SUpport to SAfety ANalysis of Hydrogen and Fuel Cell Technologies

The State-of-the-Art in Physical and Mathematical Modelling of Safety Phenomena Relevant to Fuel Cells and Hydrogen Technologies

The SUSANA project is co-funded by the European Commission within the 7th Framework Program

Authors

(randomly ordered by list of partner Institutions)

Olaf Jedicke (project coordinator)
Ke Ren
Alexei Kutchuorko
Volodymyr Shentsov
Boris Chernyavsky
Dmitriy Makarov
James Keenan
Vladimir Molkov
Daniele Baraldi
Ilias Tolias
Stella Giannissi
Alexandros Venetsanos
Simon Coldrick
Shane Slater
Frank Verbecke
Audrey Duclos

Contents

1. Physical and Mathematical Modelling of Hydrogen Releases and Dispersion (NCSRD)

1.1 Hydrogen safety engineering relevant problems and phenomena (NCSRD)

1.1.1 Laminar, transitional and turbulent flows (physical process differences description) (NCSRD)

Turbulent flows are the most often encountered flow type in every day life. Typical turbulent flows are the movement of the air around buildings in cities, the flow around cars and airplanes and the movement of the smoke out of the factories. Even though its very frequent appearance and the common sense of the word “turbulence”, it is a difficult task to make an exact definition of it (Tsinober, 2001). Many different researchers have given different definition. As a precise definition of turbulence is difficult to give, turbulence is usually defined by describing its main characteristics (Tennekes & Lumley, 1972). Therefore, a turbulent flow exhibits the following features:

- Irregularity. Turbulent flow has a seemingly random behaviour. The velocity and all other flow properties vary in a random and chaotic way. The motion is intrinsically unsteady even with constant imposed boundary conditions. The flow consists of an extremely large range of lengths and time scales. The largest eddies are of the order of the characteristic length of the geometry (e.g. height of a building, jet width, boundary layer thickness) whereas the smallest eddies have very small length scale which can be for example of the order of a micrometre (even though the smallest eddies have very small scales, these scales are larger than the molecular scale thus the continuum hypothesis is still valid). Despite the irregularity of the turbulent flows, the phenomenon is deterministic and it can be described by the Navier-Stokes equations. The sensitivity to initial conditions of the Navier-Stokes equations leads to the chaotic behaviour of the solution and thus to turbulence.
- Diffusivity. One of the main features of turbulent flows is the apparently increased diffusivity of mass momentum and heat. Particles of the fluid which are initially away from each other can be brought together by the motion of the eddies. This results in high level of mixing. Other effects of turbulent diffusivity is the reduction or the delay of the flow separation on air foils and bluff bodies, the increased resistance in internal flows such as in channels and pipes and the increase of the heat transfer rates. In brief, we can say that turbulent flows have the same effects as molecular diffusion but on much shorter time scale. This characteristic is very important in turbulence modelling.
- Three dimensionality. Turbulent flows are characterized by high levels of vorticity. Vortex stretching is an important mechanism which is absent in two dimensional flows (Tennekes & Lumley, 1972). Even though some of the turbulence characteristics can appear in two dimensional flows, turbulence is always considered as a three-dimensional phenomenon.
- Dissipation. Turbulent flow is dissipative, which means that the kinetic energy of the large eddies is dissipated to the smaller ones. The largest eddies extract energy from the mean flow and the energy of the smallest eddies is dissipated into internal energy by viscosity. This transfer of energy from the largest turbulent scales to the smallest is called “energy cascade” and results in energy losses.

In a turbulent flow velocity and pressure achieve fluctuations of high frequency. The chaotic behaviour of fluid properties makes impossible the analytic expression of turbulent flow field

variables as function of time and space. As a result a turbulent flow field is described with statistical terms.

On the other hand, laminar flows are flows in which the motion of the fluid particles is smooth in parallel layers. Fluid elements do not move macroscopically from one layer to the other. The only mixing mechanism between layers is the molecular diffusion which takes place microscopically in molecular level. There is no velocity component perpendicular to the main direction of the flow, so we have no eddies.

The first person who systematically studied turbulence was O. Reynolds. Reynolds invented an experiment in order to study the transition from laminar to turbulent flows (Reynolds, 1883). He injected a dye streak in a flow inside a pipe and he observed how it is affected by the main flow (Figure 1.1). He discovered the existence of a dimensionless number, which now known as Reynolds number, which can characterize the type of the flow:

$$\mathrm{Re} = \frac{\rho U L}{\mu} = \frac{U L}{\nu} \tag{1.1}$$

where ρ is the density, U is the typical value of fluid velocity, L is the characteristic length scale (e.g. radius of pipe), μ is the dynamic viscosity of the fluid and ν is the kinematic viscosity. Reynolds has found that approximately for $\mathrm{Re} \le 2000$ the dye is following a straight line in the flow and that it mixes with the flow only through molecular diffusion. For Reynolds number $2000 < \mathrm{Re} < 2300$ dye streak stops following a straight line and becomes wavy. Yet the mixing with the surrounding fluid is low. The flow is still laminar and the transition to turbulent occurs. For $\mathrm{Re} \ge 2300$ the flow becomes turbulent and the mixing of the dye streak with the flow is greatly enhanced.

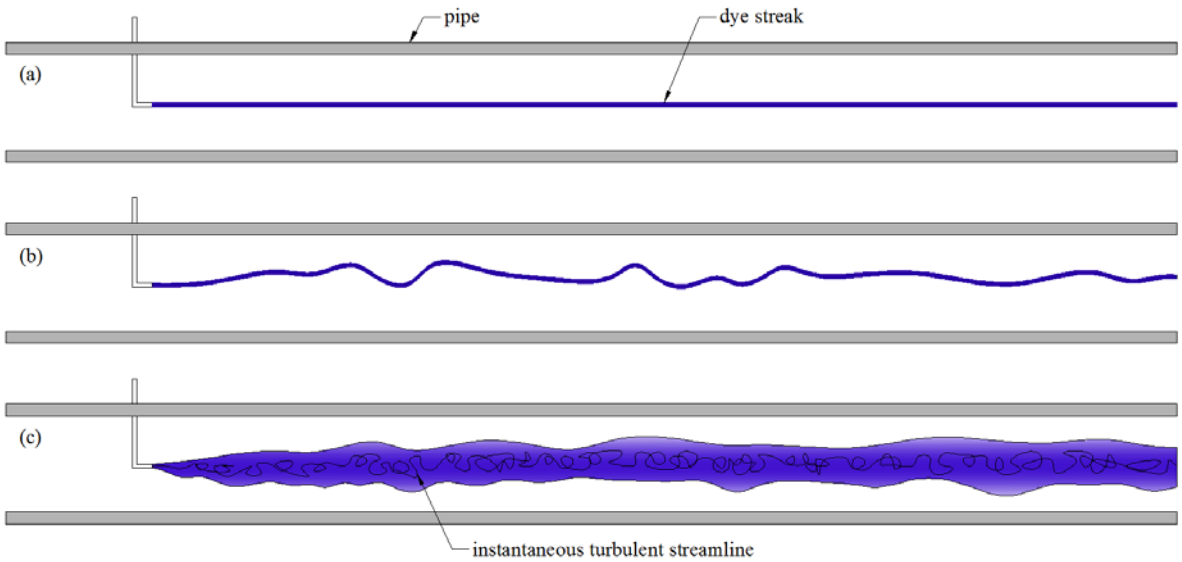

Figure 1.1: Reynolds experiment. (a) Laminar flow, (b) transition to turbulent flow, (c) turbulent flow.

By physical meaning, Reynolds number represents the ratio of the inertial to viscous forces. At low Reynolds numbers the viscous forces dominates over the inertial forces. In this case viscous forces damp the small perturbations of the flow which results in a smooth steady fluid

motion (laminar flow). On the other hand, at high Reynolds numbers the inertial forces are dominant. This has as a result the conservation and the growth of the small perturbations which leads to the formation of turbulence. The critical Reynolds numbers at which laminar flow turns into turbulent is not a universal constant number but depends upon many factors such as the type of the flow (e.g. jet flow, boundary layer flow, pipe flow), the geometry, the initial perturbations of the flow, the pressure gradient and the roughness of the solid boundaries.

The phenomenon of the transition from laminar to turbulent flow is very complex and a lot of research in this area has been done. Transition from laminar to turbulent flow happens when small perturbations of the flow start to amplify (after some length or time). Stability analysis can give an insight into the mechanism and the conditions at which the transition occurs (White, 1991). The analysis identifies as unstable the condition at which the velocity distribution contains an inflexion point (Figure 1.2). This profile is associated with jet flows, mixing layers and wakes. The importance of the hydrodynamic instability in the transition to turbulence has been studied extensively in the literature (Lin, 1955), (Chandrasekhar, 1961), (Betchov & Criminale, 1967), (Drazin & Reid, 2004), (Holmes et al. 1998).

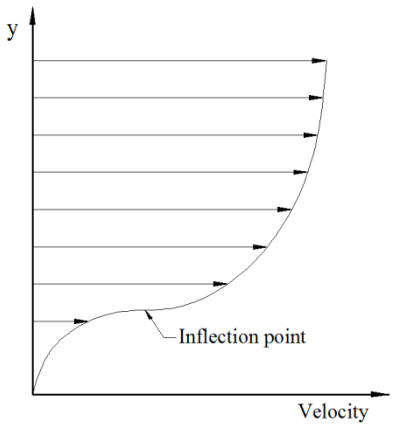

Figure 1.2: Unstable velocity profile.

Jet flows (i.e., flows coming out from a nozzle to the ambient environment - Figure 1.3) is important for hydrogen safety applications. In the case of accidental release, hydrogen can escape the infrastructure by forming a jet. Jet flows contains inflexion points, which result in turbulent flow even for small Reynolds number (Versteeg & Malalasekera, 2007). As a result jet flows are almost never laminar (Landa & McClintock, 2004). When the laminar flow exits the orifice and enters the ambient environment, rolling up vortexes are produced. The perturbations of the flow which always exist at the nozzle exit are greatly amplified and distort the vortexes. The vortexes breaks down into smaller ones and the flow turns quickly at a short distance from the source into fully turbulent regime.

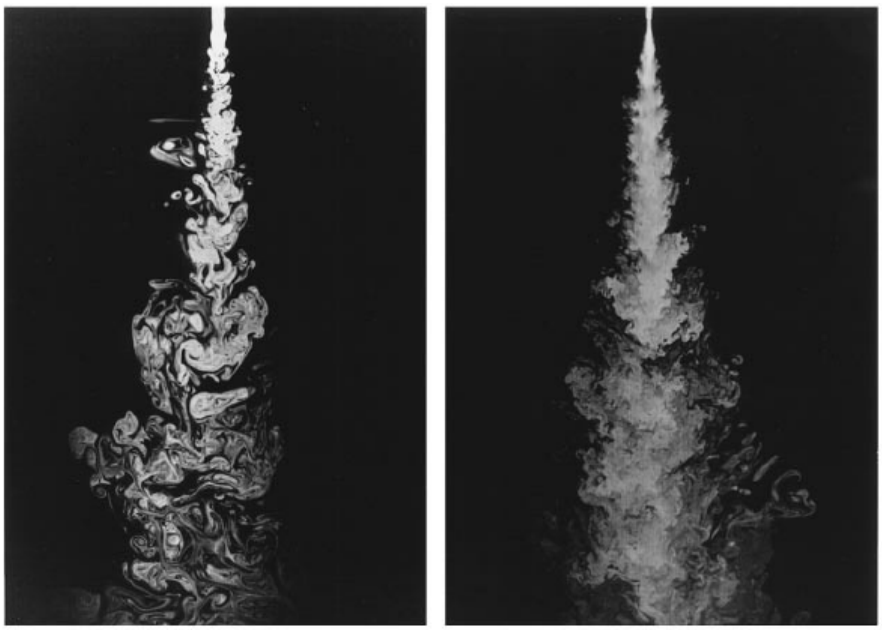

Figure 1.3: Turbulent jet flow in the plane of symmetry for Re ~ 2500 (left) and Re ~ 10000 (right), (Dimotakis, 2000).

1.1.2 Compressible and incompressible flows (NCSRD)

Incompressible flows are the flows where the density of the fluid particles remains constant (Panton, 2005). Mathematically this means that the material derivative of the density is equal to zero:

$$\frac{d\rho}{dt} = \frac{\partial \rho}{\partial t} + \vec{u} \cdot \nabla \rho = 0 \tag{1.2}$$

where $d\rho/dt$ is the material derivative of the density with respect to time, $\partial\rho/\partial t$ is the partial derivative, $\vec{u}$ is the velocity vector and $\nabla\rho$ is the density gradient. The continuity equation states that:

$$\frac{\partial \rho}{\partial t} + div(\rho \vec{u}) = \frac{\partial \rho}{\partial t} + \vec{u} \cdot \nabla \rho + \rho div(\vec{u}) = 0 \tag{1.3}$$

By combining the last two equations, we conclude that for an incompressible flow, the divergence of the velocity should be zero. An incompressible flow is not necessarily a steady state flow. We observe from the equation (1.2) that incompressible flow can occur in the case where:

$$\frac{\partial \rho}{\partial t} = -\vec{u} \cdot \nabla \rho \tag{1.4}$$

In this case, the flow is unsteady and the density field is non-uniform.

Despite of the above definition, it is common to use the term “incompressible” in the case where the density is independent of pressure, i.e. $\partial\rho/\partial p = 0$. In that case the density isn’t necessarily constant but it can be dependent on temperature or concentration. According to that definition, there are two significant concepts, which appear in compressible flows: acoustic waves (speed of sound) and chocked flow. Speed of sound is the speed at which an infinitesimally small pressure wave travels through a medium. In the case of incompressible

medium the speed of sound is infinite. In the compressible case, the process can be considered as isentropic and it can be shown (Saad, 1985) that the speed of sound c is equal to:

$$c = \sqrt{\left(\frac{\partial p}{\partial \rho}\right)_s} \tag{1.5}$$

where p is the pressure, ρ the density and s the entropy. In the case of a perfect gas this equation reduces to:

$$c = \sqrt{\gamma RT} \tag{1.6}$$

where γ is the specific heat ratio of the fluid, R is the specific gas constant and T the temperature. For example, the speed of sound for air at $T = 15^o C$ is 340.43 m/s. An important parameter in the analysis of compressible flow is the Mach number M, which is the ratio of the actual velocity V of the fluid (or of an object moving in the fluid) to the speed of sound in the same fluid:

$$M = \frac{V}{c} \tag{1.7}$$

According to Mach number the flow can be categorized into the following regimes:

- $M < 1$: subsonic flow
- $M = 1$: sonic flow
- $M > 1$: supersonic flow
- $M >> 1$: hypersonic flow

For Mach number close to 1 (i.e. from 0.8 to 1.4) the flow is also called transonic.

Choked flows can be analysed if we consider the case of a steady state one-dimensional isentropic flow through a duct. The following relation holds in every cross section of the duct due to the mass balance:

$$\dot{m} = \rho A V = constant \tag{1.8}$$

where $\dot{m}$ is the mass flow rate and A the area of the section. If we differentiate the above equation and then divide by the mass flow rate we will obtain:

$$\frac{d\rho}{\rho} + \frac{dA}{A} + \frac{dV}{V} = 0 \tag{1.9}$$

The conservation of energy for a steady state isentropic flow without work or heat interactions can be expressed as:

$$h + \frac{V^2}{2} = constant \Rightarrow dh + VdV = 0 \overset{isentropic}{\Rightarrow} \frac{dP}{\rho} + VdV = 0 \tag{1.10}$$

Combining the previous two equations we get:

$$\frac{dA}{A} = \frac{dP}{\rho}\left(\frac{1}{V^2} - \frac{d\rho}{dP}\right) \Rightarrow \frac{dA}{A} = \frac{dP}{\rho V^2}\left(1 - \mathrm{M}^2\right) = -\frac{dV}{V}\left(1 - \mathrm{M}^2\right) \tag{1.11}$$

This equation leads to some significant results. In subsonic flows dA and dP must have the same sign. As a result, the pressure of the fluid increases in diverging ducts (subsonic

diffuser) and decreases in converging ducts (subsonic nozzle). On the other hand, in supersonic flow dA and dP have opposite signs and as a result, the pressure of the fluid decreases in diverging ducts (supersonic nozzle) and increases in converging ducts (supersonic diffuser). Furthermore, the last equality of equation (1.11) gives:

$$\frac{dA}{dV} = -\frac{A}{V}\left(1-\mathrm{M}^2\right) \tag{1.12}$$

We observe that in order to accelerate the fluid in subsonic flows we need a convergence nozzle. However the highest possible velocity that we can achieve is the sonic velocity (M=1) at the exit of the nozzle. A divergence section should be added in order to achieve supersonic velocities. The result is a converging-diverging nozzle. Even if supersonic velocity is achieved in the diverging section, the fluid will always have M=1 at the nozzle throat (chocked flow). In Figure 1.4 the variations of the flow properties in subsonic and supersonic nozzles and diffusers are shown.

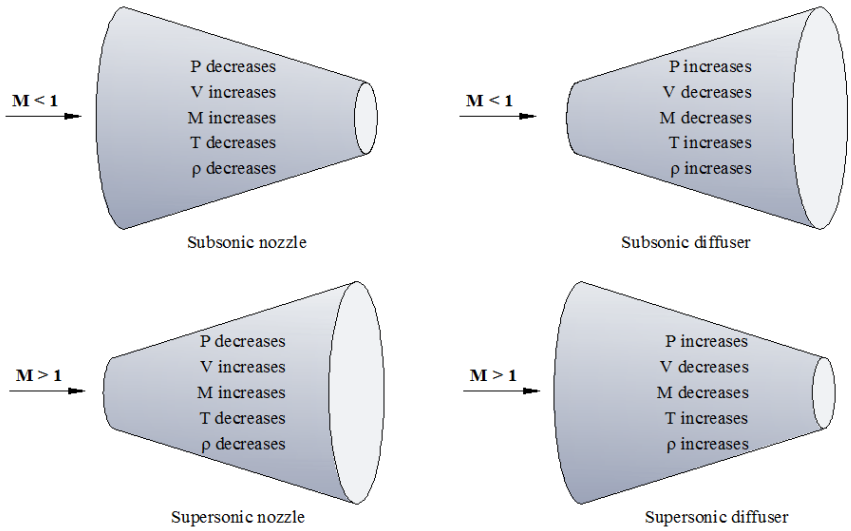

Figure 1.4: Variation of flow properties in subsonic and supersonic nozzles and diffusers.

As we will see in paragraph 1.1.7, the above types of flow is very important in hydrogen safety, as they can appear in the case of an accidental release from a high pressure storage vessel.

Stagnation pressure p_0, i.e. the pressure that a fluid attains when brought to rest isentropically, is given for an isentropic flow of an ideal gas with constant heat capacity C_p from the relation:

$$\frac{p_0}{p} = \left(1+\frac{\gamma-1}{2}M^2\right)^{\frac{\gamma}{\gamma-1}} \tag{1.13}$$

If we expand as a binomial series the right side of the above equation, we will get:

$$\frac{p_0}{p} = 1+\frac{\gamma}{2}M^2\left(1+\frac{1}{4}M^2+\frac{2-\gamma}{24}M^4+\ldots\right) \tag{1.14}$$

and if we use the relation $\frac{\gamma}{2}pM^2 = \frac{\gamma}{2}p\frac{V^2}{\gamma RT} = \frac{1}{2}\rho V^2$ then we can conclude to:

$$\frac{p_0 - p}{\frac{1}{2}\rho V^2} = 1 + \frac{1}{4}M^2 + \frac{2-\gamma}{24}M^4 + \ldots \quad (1.15)$$

The right side of the above equation is an indicator of the error for incompressible flow approximation. We observe that for low velocities (small Mach number) $p_0 - p = \frac{1}{2}\rho V^2$ and the flow can be treated as incompressible. For $M = 0.3$ the ratio of pressure difference to dynamic pressure is equal to 1.023. Usually, for $M < 0.3$ the flow can be considered incompressible without great loss of accuracy. On the other hand, for $M > 0.3$ compressibility effects should be taken into account.

1.1.3 Wind effects (HSL)

Before looking at the effects of the atmosphere on hydrogen dispersion, it is useful to compare the properties of hydrogen and dry air, as shown in Table 1.1.

Table 1.1: The properties of dry air and hydrogen.

	Air	Hydrogen
Molecular weight (kg $kmol^{-1}$)	28.96	2.016
Vapour density at 20 ^oC (kg m^{-3})	1.2	0.083
Vapour density at boiling point (kg m^{-3})	Components will boil at different temperatures	1.2
Liquid heat capacity (kJ $kg^{-1}K^{-1}$)	1.86	9.62
Vapour heat capacity (kJ $kg^{-1}K^{-1}$)	1.01	14.3

The low molecular weight of hydrogen means that a gaseous release into calm air will be buoyant whereas a liquid release may result in different behaviour due to the density effects of entrained air. While the vapour density at the boiling point is similar to that of the ambient air, when this air is entrained into the vapour cloud and cooled, it becomes significantly heavier. The lower heat capacity of air also means that it will be readily cooled to this state of higher density. The relative density of the cloud will also depend on the concentration level used to define its extent. However, relative densities are not sufficient to define the behaviour of a cloud, especially when there is relative movement of either the cloud, or the ambient air. A more appropriate criterion is the Richardson number, defined as the ratio of disturbing inertia forces to the restoring buoyancy forces:

$$Ri = \frac{g'L}{U^2} \quad (1.16)$$

where L is a characteristic length scale, U is a characteristic velocity and g' is the reduced gravity, which is given by:

$$g' = g\frac{(\rho_\infty - \rho)}{\rho_\infty} \quad (1.17)$$

where ρ is the density of the plume and ρ_∞ the ambient air density.

Liquid releases of hydrogen will also be complicated by its low boiling point of -252.78 ^{o}C and in a flashing jet, the temperature may fall lower than this value. A major consideration, however, is the fact that at these temperatures, oxygen and nitrogen will condense out of the air and as they condense, they will release latent heat. Furthermore, the density of the mixture may be increased by the presence of the hydrogen/oxygen/nitrogen/water aerosol.

The atmosphere

A fundamental feature of the atmosphere that can have a significant effect upon dispersion is its stability. In a stable atmosphere, the temperature increases with height and the air close to the ground is denser than the air above it. When turbulence within the atmosphere lifts a parcel of air from near the ground to a higher level, the parcel has a higher density than the surrounding air and buoyancy forces act to push it back down towards the ground. This means that under these conditions, buoyancy forces act to reduce the motion of eddies and turbulence is suppressed.

In an unstable atmosphere, the temperature decreases with height and the density of the air close to the ground is less than the air at higher levels. If a parcel of air is lifted up from the ground, it has a density less than the surrounding air and the buoyancy forces act to push it still higher into the atmosphere. Turbulence is therefore enhanced under these conditions.

The limiting state between the stable and unstable atmospheric conditions is termed “neutral”. Since the pressure falls with height in the atmosphere, the temperature of dry air naturally reduces with height under neutral conditions at a rate of 0.98°C per 100 m height gain (the dry adiabatic lapse rate). The criteria for stable or unstable conditions are therefore (Hanna et al., 1982):

Unstable: $(\partial T\_e)/\partial z < -0.98\ ^{o}C/100$ m

Neutral: $(\partial T\_e)/\partial z = -0.98\ ^{o}C/100$ m

Stable: $(\partial T\_e)/\partial z > -0.98\ ^{o}C/100$ m

An unstable atmosphere is typical of daytime conditions when there is ground heating resulting from insolation. A neutral atmosphere is typical of cloudy or windy conditions, and a stable atmosphere is often associated with night time, where the ground surface is cooler due to radiative heat losses.

The temperature variation with height in the atmosphere is usually expressed as a function of the potential temperature, ø, which is the temperature that a parcel of fluid would reach if it were expanded adiabatically from a reference pressure, P_0 , to its current pressure, P, and temperature, T:

$$\emptyset = T\left(\frac{P_0}{P}\right)^{R/C_p} \tag{1.18}$$

where R and C_p are the gas constant and specific heat of air respectively.

The stability of the atmosphere can be characterized in terms of the gradient Richardson number, Ri_{gr}:

$$Ri_{gr} = \frac{g}{T}\frac{\partial \emptyset/\partial z}{(\partial \bar{u}/\partial z)^2} \tag{1.19}$$

This expresses the ratio of buoyancy forces (in terms of the temperature gradient, $\partial\emptyset/\partial z$) to the inertial forces (in terms of the mean velocity gradient, $\partial u\bar{}/\partial z$). In strongly sheared flows

where the velocity gradient is large, turbulent mixing may be sufficient to overcome a stable or unstable temperature gradient and result in neutral conditions.

Observations have suggested (Blackadar, 1998) that a critical value, R_c, of the gradient Richardson number is 0.25 and for values of Ri_{gr} above this, turbulence is usually suppressed. Unfortunately, the Richardson number cannot be used to specify the atmosphere because its distribution relies on the wind distribution (Blackadar, 1998) and therefore other parameters are required.

Specifying the atmosphere

The flow behaviour in the atmosphere is characterised using similarity profiles which describe the change in velocity, temperature and turbulence conditions with height, based on other dimensionless quantities. Dyer (1974) notes that profiles are easily measured, but fluxes are not, hence the need for relationships that link the two. The following paragraphs describe profiles for the surface layer which occupies the lower part of the atmosphere, typically up to 50-100 m from the ground. Above the surface layer, these relationships become less valid with increasing height. The behaviour of the atmosphere above the surface layer is described in Section 1.2.5.

Friction velocity

The mean velocity distribution within the atmosphere is affected by convective, viscous and turbulent fluxes of momentum. If the atmosphere is approximated as a simple shear flow, where the air flows over continuous flat ground and there are no gradients in velocity in the streamwise and spanwise directions, the momentum flux in the vertical direction has two components: a viscous and a turbulent part. The viscous flux represents the transfer of momentum due to viscous shearing, and the turbulent flux represents the transfer by turbulent fluctuations. The contribution of viscous effects in atmospheric flows is usually several orders of magnitude smaller than the contribution from turbulent fluctuations and it is therefore generally ignored.

The turbulent flux is usually expressed as a Reynolds stress:

$$\tau = \bar{\rho}\overline{u'w'} \tag{1.20}$$

where u' and w' are the fluctuating velocities in the streamwise and vertical direction, respectively. The overbar is used to signify Reynolds averaging (i.e. a time or ensemble average). In a simple shear flow, this Reynolds stress can be treated as the product of a diffusion coefficient (or eddy-viscosity), K_m, and the gradient of the mean velocity:

$$\tau = -\bar{\rho}\overline{u'w'} = \bar{\rho}K_m\frac{\partial\bar{u}}{\partial z} \tag{1.21}$$

In the Prandtl mixing length model, this diffusion coefficient is treated as a product of the square of the mixing length (l_m) and the strain rate:

$$K_m = (l_m)^2\frac{\partial\bar{u}}{\partial z} \tag{1.22}$$

Within the surface layer, the mixing length increases linearly with height:

$$l_m = \kappa z \tag{1.23}$$

where the constant of proportionality is the von Karman constant, κ, which has a value close to 0.4.The scaling parameter that is used to characterise the velocity in the surface layer is the "friction velocity", u*, which is given by

$$u^* = \sqrt{\frac{\tau_{wall}}{\bar{\rho}}} \tag{1.24}$$

where τ_{wall} is the shear stress on the ground. In a simple atmospheric boundary layer with no streamwise or spanwise velocity gradients, the shear stress (τ) is constant in the vertical direction and equal to τ_{wall}. The friction velocity is therefore given by:

$$u^* = \sqrt{\overline{u'w'}} \tag{1.25}$$

Monin-Obukhov length

There are two forces within the atmosphere that generate turbulent kinetic energy (k): a shear force due to the changes in air velocity, and a buoyancy force due to density (resulting from temperature differences). The sign of the gradient Richardson number can give an indication of which of these two effects is dominant. In a stable atmosphere, the temperature increases with height and this results in positive values of Ri_{gr}. Conversely, in an unstable atmosphere, the temperature decreases with height and this results in negative values of Ri_{gr}.

Another means of characterising the stability of the atmosphere and its effect on the turbulent kinetic energy is the Monin (or Monin-Obukhov) length, L. This expresses the height at which the buoyancy production term, B, is equal to the shear production term, M, in the conservation equation for turbulent kinetic energy, i.e.:

$$L = \frac{M}{B} z \tag{1.26}$$

where

$$M = -\bar{\rho}\overline{u'w'}\frac{\partial \bar{u}}{\partial z}$$

$$B = g\overline{\rho'w'}$$

If the shear stress is assumed to remain constant across the surface layer and the mixing-length model is used to approximate the eddy viscosity, the Monin-Obukhov length becomes:

$$L = \frac{\bar{\rho}u_*^3}{\kappa g \overline{\rho'w'}} \tag{1.27}$$

Numerous different definitions for L exist, based on different assumptions and approximations for the shear stress and the density-velocity correlation, $\overline{\rho'w'}$.

In a neutral atmosphere, the buoyant production term becomes zero, Ri is zero and L becomes infinite. Stable conditions are characterised by a positive value of L and unstable conditions by a negative value.

Wind and scalar profiles

In neutral conditions, the rate at which the mean wind speed increases with height can be expressed in terms of the von Karman constant as follows:

$$\frac{\partial \bar{u}}{\partial z} = \frac{u_*}{kz} \tag{1.28}$$

This can be integrated to give an expression for the mean velocity that is commonly known as the “log-law”:

$$\bar{u} = \frac{u_*}{k} ln\left(\frac{z}{z_0}\right) \tag{1.29}$$

The constant, z_0 , that arises in this expression is the roughness length and it represents the height at which the wind speed drops to zero.

Under stable or unstable conditions, the buoyancy forces act to suppress or enhance turbulence and this has an influence on the velocity profile. The buoyancy effect on the log-law can is accounted for using the following stability parameter:

$$\zeta = \frac{z}{L} \tag{1.30}$$

The magnitude of ζ diminishes to zero as the atmosphere approaches neutral conditions, when L is infinite.

Monin-Obukhov similarity theory provides wind speed profiles according to the non-dimensional wind shear, ϕ_m, which is a function of ζ:

$$\phi_{m(\zeta)} = \frac{kz}{u_*}\frac{\partial \bar{u}}{\partial z} \tag{1.31}$$

Empirically-based formulae for ϕ_m have been derived for a range of different stability classes. For a summary, see Dyer (1974). Under stable conditions, an approximate value of ϕ_m is 1+5(z/L) which can be integrated to give:

$$u = \frac{u_*}{k} ln\left(\frac{z}{z_0} + 5\left(\frac{z}{L}\right)\right) \tag{1.32}$$

In unstable conditions, an approximate value of ϕ_m is $(1\text{-}16(z/L))^{-1/4}$ and the integration becomes more complicated.

Under neutral conditions, when L is infinite, ϕ_m is 1 and the result is Equation (1.28).

Temperature and scalar concentration gradients across the surface layer are treated in a similar manner to this. Luketa-Hanlin et al. (2007) give an overview of the implementation of these profiles in CFD modelling of liquefied natural gas (LNG) spills where the cold LNG vapours behave as a dense gas.

Whilst Monin-Obukhov similarity theory provides a quantitative method for parameterising the atmospheric boundary layer, it has the drawback that it requires values for the friction velocity and surface heat flux which are not routinely measured or readily derived from other sources. In many dispersion modelling applications, it is sufficient to have a rough estimate of the stability. With this in mind, Pasquill (1961) introduced a classification scheme for atmospheric stability that can be derived from simple observed quantities. These classes are given in many texts on dispersion modelling and are reproduced from Blackadar (1998) in Tables Table 1.2 and Table 1.3.

Table 1.2: Atmospheric stability classes.

A	Extremely unstable	D	Neutral
B	Moderately unstable	E	Slightly stable
C	Slightly unstable	F	Moderately stable

Table 1.3: Determining stability classes.

Daytime insolation				Night-time conditions	
Wind speed	Strong	Moderate	Slight	Thin overcast or cloudiness ≥4/8	Cloudiness ≥3/8
<2	A	A-B	B		

2	A-B	B	C	E	F
4	B	B-C	C	D	E
6	C	C-D	D	D	D
>6	C	D	D	D	D

Pasquill stability classes are often used to specify the weather conditions in software for modelling atmospheric dispersion. These classes are converted to the Monin-Obukhov length through a correlation such as that given by Seinfield and Pandis (1998):

$$\frac{1}{L} = a + b \log z_0 \qquad (1.33)$$

where the coefficients *a* and *b* are given in Table 1.4.

Table 1.4: Conversion from Pasquill stability class to Monin-Obukhov length (from Seinfield and Pandis (1998).

Pasquill stability class		Coefficients	
		a	b
Extremely unstable	A	-0.096	0.029
Moderately unstable	B	-0.037	0.029
Slightly unstable	C	-0.002	0.018
Neutral	D	0	0
Slightly stable	E	0.004	-0.018
Moderately stable	F	0.035	-0.036

In stable and unstable conditions, the friction velocity, u*, can also be determined from the Monin-Obukhov length using relationships given by Seinfield and Pandis (1998).

In some cases, a good approximation of the logarithmic wind profile can be made using a power law where the mean wind speed is given as an empirical function of height:

$$\frac{\bar{u}}{\overline{u_1}} = \left(\frac{z}{z_1}\right)^P \qquad (1.34)$$

where $\overline{u_1}$ is a wind speed at a known height, z_1 and p is an exponent which can be varied to give the desired wind profile. Several sources, such as Seinfield and Pandis (1998), give values of p as a function of L and surface roughness, z_0.

Ground roughness

The roughness length, z_0, must be estimated based upon the local terrain. Typical values are given in Table 1.5, taken from Blackadar (1998). The roughness length is approximately one tenth of the actual obstacle height.

Table 1.5: Typical surface roughness lengths.

Surface	Roughness length z_0 (m)
Mud flats or smooth ice	1.0×10^{-5}
Smooth snow	5.0×10^{-5}
Grass up to 1 cm	0.001
Grass up to 60 cm	0.05
Pasture land	0.2
Suburban landscapes	0.6
Forests and cities	1 to 5

Turbulence

CFD modelling requires specification of the turbulence quantities in addition to the mean wind and temperature distributions. A convenient assumption often used in ABL modelling is that, for neutral conditions, the shear production of turbulent kinetic energy and its dissipation rate are equal. Profiles of turbulent kinetic energy, k, and its dissipation rate, ε, are then given by the frequently used relations:

$$k(z) = \frac{u_*^2}{\sqrt{C_\mu}} \tag{1.35}$$

and

$$\varepsilon(z) = \frac{u_*^3}{\kappa(z + z_0)} \tag{1.36}$$

Högström (1996) suggests that there is some evidence that the assumption of equilibrium production and dissipation might not hold true as some turbulent energy is being fed into the surface layer from above. Under non-neutral conditions, the production of turbulent kinetic energy due to buoyancy also becomes significant and this needs to be accounted for in the profiles of k and ε. The dependence on buoyancy is usually introduced through an empirical function of L. Profiles for k and ε for different levels of stability were given by Han *et al.* (2000). For stable conditions in the surface layer these are:

$$k(z) = 6u_*^2 \tag{1.37}$$

and

$$\varepsilon(z) = \frac{u_*^3}{\kappa z}\left(1.24 + 4.3\frac{z}{L}\right) \tag{1.38}$$

Various other formulations for k and ε for have been proposed. For example, Pontiggia *et al.* (2009) suggested the following profiles:

$$k(z) = \frac{u_*^2}{\sqrt{C_\mu}}\sqrt{\frac{\phi_\varepsilon(z/L)}{\phi_m(z/L)}} \tag{1.39}$$

and

$$\varepsilon(z) = \frac{u_*^3}{\kappa z}\phi_\varepsilon \tag{1.40}$$

where

$$\phi_\varepsilon = \left(1 + 4\frac{z}{L}\right) \tag{1.41}$$

Yang *et al.* (2009) adopted a slightly different approach in which the equations for k and ε were modified to fit experimental data obtained from wind tunnel studies. An important consideration when modelling atmospheric boundary layers is that the boundary conditions applied at the edges of the domain are consistent with the inlet wind and turbulence profiles. This is discussed further in Section 1.2.5.

Above the surface layer

The Monin-Obukhov similarity theory which characterises the surface layer is generally valid up to heights of between 50 and 100 m. Gryning *et al.* (2007) showed that beyond this region, deviations gradually occurred. The region above the surface layer is termed the outer layer where the shear stress is no longer constant but varies with height along with a corresponding

reduction in the friction velocity. Gryning *et al*. (2007) presented a method for extending the wind profile above the surface layer based upon a scaling length *l*, which takes the place of the height, *z*, in Equation 13 to give:

$$\frac{\partial \bar{u}}{\partial z} = \frac{u_*}{kl} \tag{1.42}$$

The scaling length, *l*, was calculated from three terms by inverse summation:

$$\frac{1}{l} = \frac{1}{L_{SL}} + \frac{1}{L_{MBL}} + \frac{1}{L_{UBL}} \tag{1.43}$$

where L_{SL}, L_{MBL} and L_{UBL} are the length scales in the surface layer, middle layer and upper layer respectively. Gryning *et al*. (2007) presented expressions for the three length scales for different levels of stability, along with the friction velocity, which was given by:

$$u_*(z) = u_{*0}(1 - z/z_i)^{\alpha} \tag{1.44}$$

where u_{*0} is the friction velocity near the ground, z_i is the height of the boundary layer and α is a factor that depends on the stability of the boundary layer. A value of α = 1 gives a linear variation of friction velocity with height.

1.1.4 Impinging jets (NCSRD)

Impinging jets have been used extensively in the industry as they offer an effective way to transfer heat and mass. Impinging jets can produce heat transfer coefficients that are up to three times higher at a given maximum flow speed compared to a wall-parallel flow (Zuckerman & Lior, 2006). Typical heat transfer applications include cooling of material in material forming processes, cooling of electronic components, heating of optical surfaces for defogging and cooling of turbine components. Some examples of mass transfer applications are drying and removal of small surface particulates. Impinging jets can also appear as side effects of other applications, for example in the case of a vertical take off or landing system.

In hydrogen applications, impinging jets can be formed in various scenarios. Hydrogen vehicles are provided with pressure release vent which might be located at the bottom of the storage system. As a result in the case of a release, hydrogen will escape as high momentum jet impinging to the ground. Hydrogen impinging jets can be formed also in the case of an accidental release in closed rooms. Such a case has been studied experimentally in (Friedrich et al. 2007) and numerically in (Middha et al. 2010). Hydrogen impinging flames have been studied in (Schefer et al. 2011), (Ranga Dinesh et al. 2012) and (Mira Martinez & Jiang 2013).

Impinging jets involves very complex physics. As we can see in Figure 1.5, impinging jets has three distinct main flow regions with distinct flow physics: free jet, stagnation and wall jet. When the flow exits the nozzle, the surrounding fluid entrains into the jet reducing the jet velocity. The mixing region surrounds a core area where the fluid velocity at the centerline is almost equal to the exit velocity. The end of the core region is typically defined as the point where the velocity reaches the 95% of its value at the exit of the nozzle. The length of this region is usually equal to six to eight nozzle diameters. In the case where the flow hasn't reached the target, a decaying jet region follows caused by large shear stresses at the jet boundary. In this region, the axial velocity decreases as we move away from the centre forming a Gaussian like profile (Figure 1.5). This profile becomes wider as we move away from the nozzle. As the flow approaches the wall, it enters the stagnation or deceleration region. The axial velocity is rapidly decreased and its direction changes. The static pressure of the flow is increased, transmitting the effect of the wall upstream. High normal and shear

stresses are developed due to the non-uniform turning of the flow. Vortices are stretched and turbulence increases. Typical value for the thickness of this region is 1.2 nozzle diameters. Next, the flow enters the wall jet region where it moves parallel to the wall. The wall jet has its minimum thickness at a distance of 0.75 to 3 nozzle diameters from the jet axis and then it continually thickens. The flow has a shearing layer influenced by both the wall and the velocity gradient with respect to the surrounding stationary fluid. As the flow moves parallel to the wall, the wall jet entrains the surrounding fluid, its thickness grows and its average velocity decreases.

The complex nature of impinging jets makes their numerical simulation a tough task. The main difficulty in the accurate prediction of the phenomenon is the turbulence modelling and the modelling of the interaction with the wall. A thorough analysis of impinging jet modelling strategies can be found in (Zuckerman & Lior 2006).

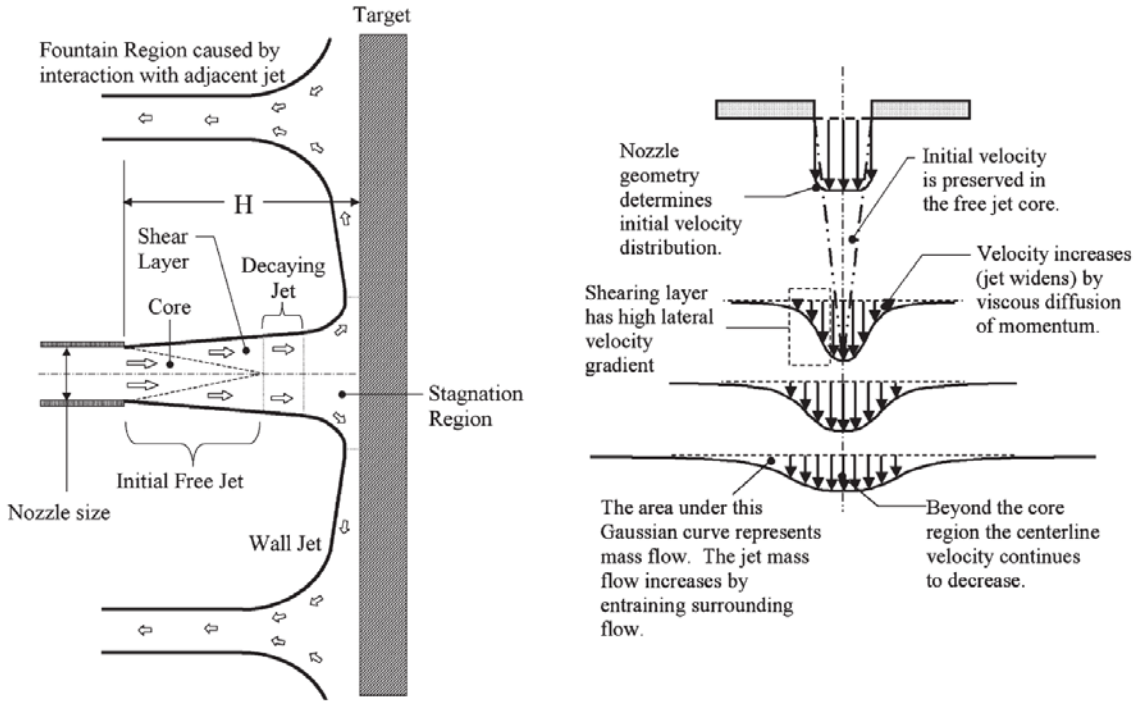

Figure 1.5: Flow regions of an impinging jet (left) and flow details of a free submerged jet (right) (Zuckerman & Lior 2006).

1.1.5 Passive and forced ventilation (HSL, UU)

Passive ventilation of the enclosure with one or more vents has been investigated by a number of researchers. Passive ventilation is driven by buoyancy effects. The pressure within and outside the compartment varies hydrostatically with height. The vertical pressure gradient inside the enclosure is lower than the vertical pressure gradient outside due to the lower density of gas mixture inside the enclosure and therefore lower weight of the fluid column of a given height. The difference between these pressure gradients leads to a buoyancy-driven flow through the vent(s). The height at which these pressure gradients intersect (internal pressure is equal to external) is designated as neutral plane. Above the neutral plane the internal pressure is higher than external, resulting in gas mixture outflow from the enclosure through the vent(s), while below neutral plane the external pressure is higher, driving fresh air into the enclosure through the vent(s) located below neutral plane (Figure 1.6).

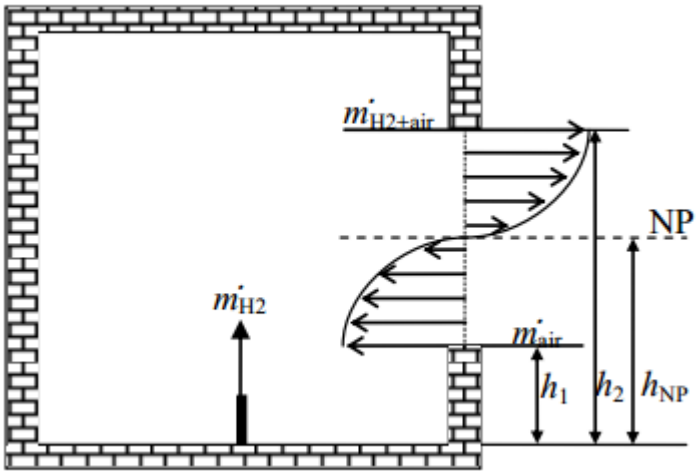

Figure 1.6: Bi-directional flow through the vent with hydrogen-air mixture escaping above the neutral plane and fresh air inflow below (Molkov et al., 2014).

In certain simple cases, for example for a well-stirred gas mixture, producing uniform mixture density across the enclosure, it is possible to find an analytical solution for the hydrogen concentration produced by a steady hydrogen release.

One such solution for a single vent and uniform gas mixture within the enclosure had been proposed by University of Ulster. The derivation was based on hydrogen and air mass balances and results in equation

$$X = f(X) \cdot \left[\frac{Q}{C_D A (g' H)^{1/2}} \right]^{2/3} \tag{1.45}$$

where C_D is the discharge coefficient, X is hydrogen molar fraction, A is the vent area (m^2), Q is the release flow rate (m^3/s), $g' = g \frac{\rho_{air} - \rho_{H_2}}{\rho_{air}}$ (m/s^2) is the reduced gravity, ρ_{air} and ρ_{H_2} (kg/m^3) are the air and hydrogen density, respectively, and H (m) is the height of the vent. Equation (1.1.5.1) differs from the one previously proposed by Linden (1999), which assumed so called 'natural' ventilation with neutral plane being located at exactly half the vent height, by additional function *f(x)* reflecting the variable height of neutral plane

$$f(X) = \left(\frac{9}{8}\right)^{1/3} \cdot \left\{ \left[1 - X \left(1 - \frac{\rho_{H_2}}{\rho_{air}} \right) \right]^{1/3} + (1 - X)^{2/3} \right\} \tag{1.46}$$

The model has been compared against experimental data on uniform and non-uniform distribution of helium concentration in the enclosure with one vent of different size and various release flow rates and have shown a good agreement with maximum hydrogen concentration levels observed in the experiments (i.e., demonstrated to be conservative).

More complex cases, including multiple vents and non-uniform mixture distribution may require CFD modelling in order to obtain hydrogen distribution within enclosure.

Forced ventilation involves suction of hydrogen-air mixture, or blowing of fresh air into the enclosure by means of external force (e.g., fan) and is applied when the passive ventilation is

not sufficient to prevent hydrogen concentration to rise above flammable level for the expected release rate.

Enclosed spaces may be ventilated by natural (passive) or forced (mechanical) ventilation. In passive ventilation, the flows through the openings and cracks in the enclosure are driven by wind or buoyancy effects arising from differing temperatures or gas densities. Buoyancy effects are particularly important with hydrogen due to its low molecular weight, but the geometry of the enclosure and the form and location of the openings also play an important role in passive ventilation. A large amount of research has been carried out on passive ventilation, which has arisen mainly from the need for energy efficient buildings. However, it is also relevant to hazard analysis such as pollutant ingress. Much of this previous work has involved the development of simple analytical or empirical models. These are often based on empirical correlations for the airtightness of standard building components and have proven to be effective in predicting infiltration rates. Modelling passive ventilation with CFD is challenging because these empirical correlations cannot always be used in the same way, and flows through openings and cracks in enclosures may instead need to be modelled explicitly. Modelling of air flow in rooms with forced ventilation is often simpler than in those that are naturally ventilated as information is usually available on the characteristics of the ventilation system, and the flow tends to be less sensitive to small differences in temperature and wind-driven pressures.

Modelling buoyant flows in an enclosure

Linden *et al*. (1990) developed a framework for modelling buoyancy-driven ventilation. Their work was aimed at thermal sources of buoyancy, but can equally be applied to releases of buoyant gases, such as hydrogen (Cariteau and Tkatschenko, 2011). Linden *et al*. (1990) separated buoyancy-driven ventilation into displacement and mixing regimes. In the mixing regime, incoming air mixes with fluid in the enclosure to produce a homogeneous environment. Conversely, in the displacement regime, a stratified environment is produced in which the incoming and outgoing fluids do not mix.

Displacement Ventilation

An idealised displacement ventilation scenario is shown in Figure 1.7 and Figure 1.8, along with the notation used by Linden *et al*. (1990), which is adopted here. In Figure 1.7, a buoyant plume rises from the floor of an enclosure, which has a height *H*. Two ventilation openings are present in the room: a high vent with area *a1* and a low vent with area *a2*. After some time, a steady-state is reached in which the buoyant plume maintains a buoyant layer, which drives a flow through the vents (Figure 1.7).

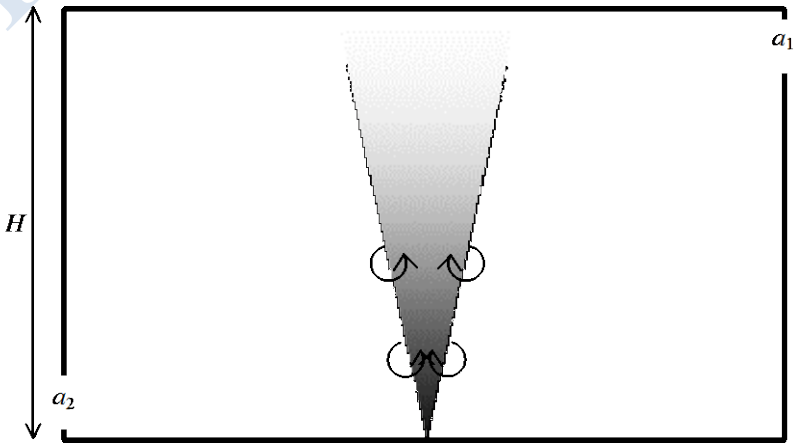

Figure 1.7: An idealised displacement ventilation scenario in which a buoyant plume rises from the floor of an enclosure with high and low vents.

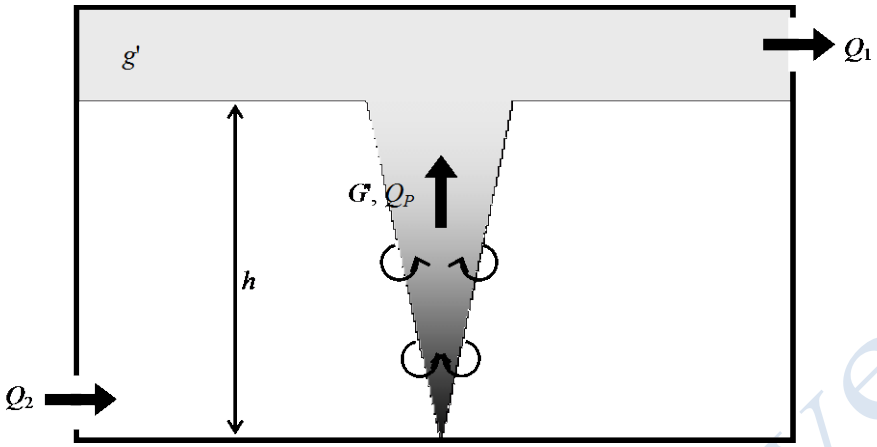

Figure 1.8: After some time a steady-state is reached in which the buoyant plume maintains a buoyant layer, which drives a flow through the vents.

Mixing Ventilation

An idealised mixing ventilation scenario is shown in Figure 1.9. A buoyant plume rises from the floor of an enclosure, which has a single high vent with area *A*. The buoyant plume fills the enclosure with a well-mixed buoyant fluid, which drives an exchange flow through the vent as shown in Figure 1.10.

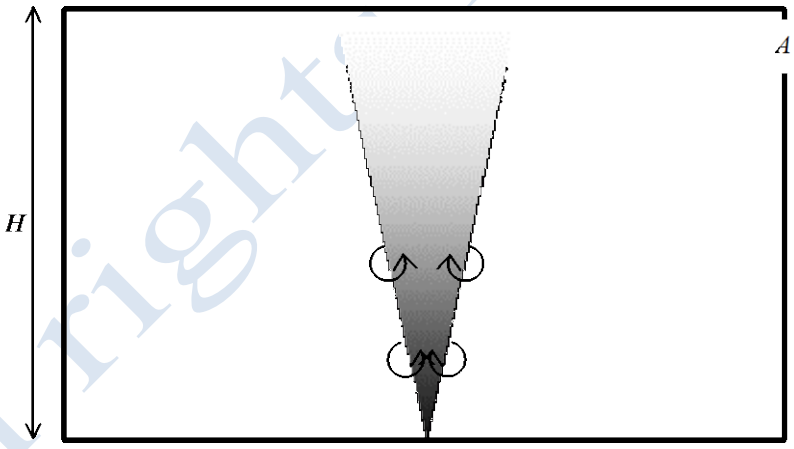

Figure 1.9: An idealised mixing ventilation scenario in which a buoyant plume rises from the floor of an enclosure with a single high vent.

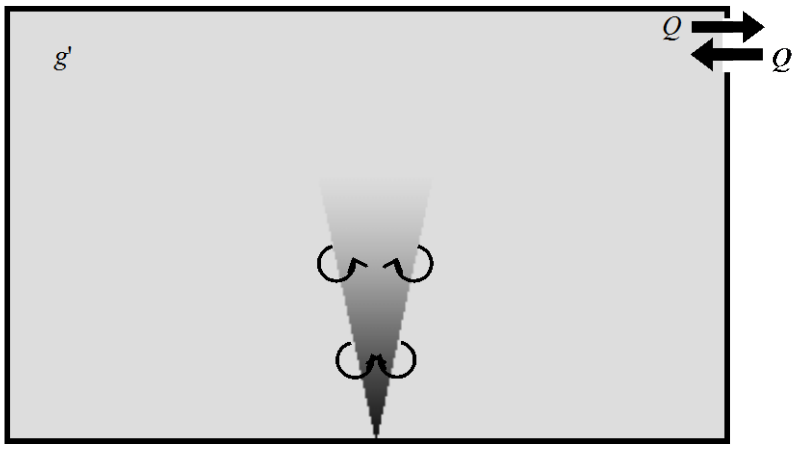

Figure 1.10: After some time a steady-state is reached in which well mixed buoyant fluid inside the enclosure drives an exchange flow through the single high vent.

Modelling the wind effects on the enclosure

Wind can enhance or oppose buoyancy-driven ventilation. The case of opposing wind and buoyancy forces is of interest because it often leads to a worst-case scenario, in terms of the gas-cloud size. The model developed by Hunt and Linden (2005) for opposing wind and buoyancy-driven ventilation is shown schematically in Figure 1.11 and Figure 1.12. A buoyant plume rises from the floor of an enclosure with high and low vents. A wind flows from right to left such that it opposes buoyancy-driven ventilation.

Hunt and Linden (2005) showed that two steady-state ventilation regimes are possible, depending on the relative strengths of the wind and buoyancy forces. For weak opposing winds, there is buoyancy-driven displacement ventilation. In this case, the wind inhibits buoyancy forces leading to a lower stratification height, as shown in Figure 1.12a. For a strong opposing wind, Hunt and Linden (2005) showed that there is wind-driven mixing ventilation, with reversed flow through the vents, as shown in Figure 1.12b.

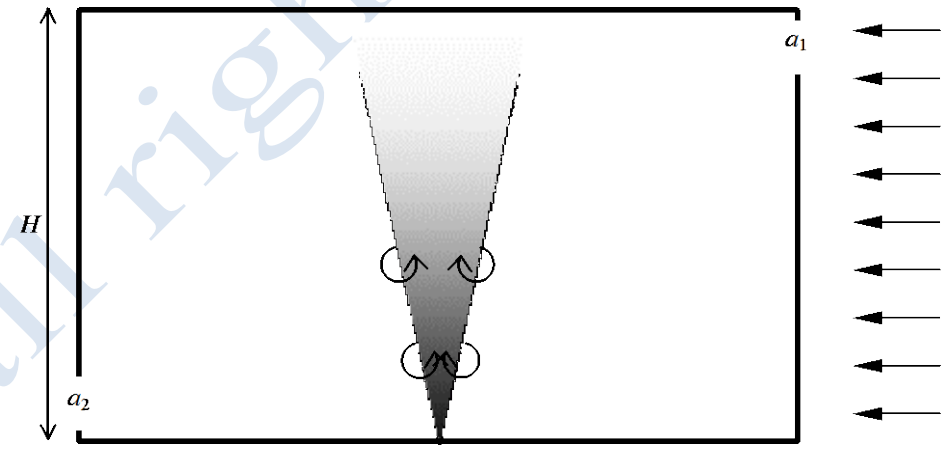

Figure 1.11: Opposing wind and buoyancy-driven ventilation, the opposing wind flows from right to left.

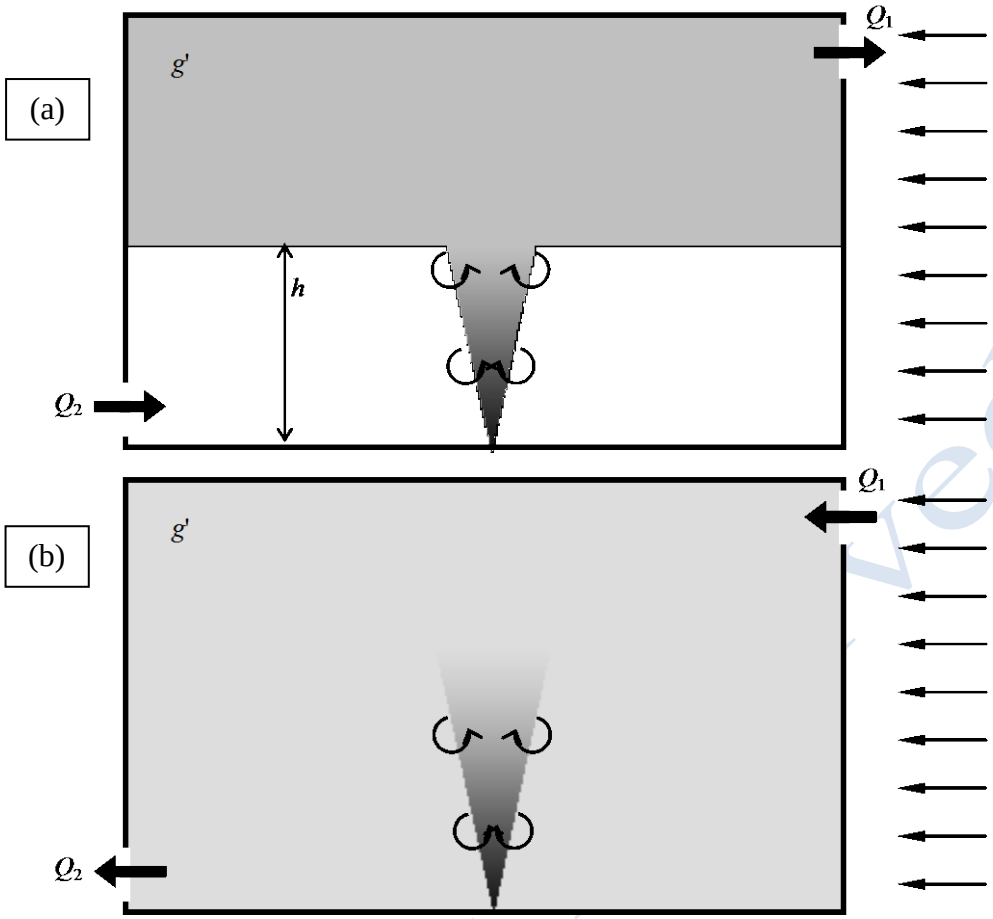

Figure 1.12: A weak opposing wind (a) inhibits buoyancy-driven ventilation, whilst a strong opposing wind (b) leads to wind-driven ventilation, with reversed flow through the vents

Modelling infiltration

The enclosures shown in Figure 1.7 to Figure 1.12 have idealised openings of known geometry. In practice, some openings may have a well-defined geometry, but in many cases there are cracks and small irregular openings in the enclosure walls. These "adventitious" openings do not have well-defined geometry and are particularly difficult to model.

In the construction industry, the air-tightness of buildings is often measured using pressurisation tests where a fan is used to pressurise a building. The total flow rate is then measured for a given pressure difference, and this is used to determine the total air change rate for an enclosure. Over the years, pressure test data have also been accumulated for a wide variety of standard building components and these are tabulated in various forms in the literature. One common method used to compare this data is to express the leakage flow rate, Q, in terms of a flow coefficient, C, and exponent, n, for a given pressure drop, ΔP:

$$Q = C(\Delta P)^n \quad (1.47)$$

Values of C and n are then provided for individual building components, such as different types of windows and doors.

Network ventilation models provide a means of using this pressure test data to predict the air change rate within buildings. The models typically involve assembling a network of all the leakage paths or openings in an enclosure as a system of equations. Each opening is defined

as a flow rate, Q, which is expressed in terms of a pressure drop, ΔP. This can either take the form of Equation 1.1.5.3 above or, alternatively, for openings of known geometry:

$$Q = C_d A \sqrt{\frac{2\Delta P}{\rho}} \tag{1.48}$$

where C_d is the discharge coefficient and A is the cross-sectional area of the opening. By iterating on the internal pressure in the enclosure and ensuring conservation of mass, it is possible to determine the flow rate through each opening. Network models can take into account external wind effects through specification of a surface pressure coefficient for each face on the enclosure. The external wind pressure then appears as a contributor to ΔP in Equations 1.1.5.3. and 1.1.5.4. For further details of network methods, see AIVC (1996).

For enclosures that have a complex shape, it may be necessary to use CFD to simulate the external air flow around the enclosure in order to determine the wind pressures on different faces of the building. CFD can also be used to model the flow through the leakage paths into the enclosure and the internal flow field. For an example of this type of CFD application, see Ramponi and Blocken (2012), who used a simple geometry with relatively large openings.

The flow through infiltration openings is sensitive to buoyancy effects arising from temperature differences between the inside and outside of the building, and also the buoyancy from the gas being released (especially hydrogen). These will interact with the wind-driven flows through the openings. There is the potential for some of the openings to change over time from being inlets to outlets, as the gas accumulates within the enclosure. CFD models that adopt a prescribed velocity and direction approach for the ventilation openings would be unable to take this into account. Instead, the flow through the openings ideally needs to be able respond over time to changes in pressure within the building.

In some cases, it may be possible to de-couple the CFD modelling into two parts:

1. External aerodynamics simulations of the building using prescribed wind speeds, in order to determine the surface pressures on different infiltration openings in the building fabric.
2. Internal ventilation simulations of the flow inside the building. These simulations may include the hydrogen source and the presence of any obstructions within the building. The main reason for de-coupling the external and internal flows in this way is for computational efficiency. This de-coupled approach assumes that infiltration has no effect upon the external wind-driven aerodynamics flow, i.e. that small leaks do not affect significantly the wind-driven pressure on the enclosure faces.

If it is necessary to couple the external wind and internal ventilation models, two alternative approaches are available. The first is to design the geometry of the CFD model to explicitly include the small gaps or holes around the doors, windows etc. where leakage paths are present. The second approach is to use empirical correlations for the leakage rates of different building elements, described above. The external pressure could be taken from simulations of the external enclosure aerodynamics and the internal pressure would be calculated by averaging the surface pressure over the particular building element surface in the CFD model, such as a window. Equation 1.1.5.3 could be used to relate the volumetric flow rate through the opening (Q) as a function of the pressure difference between the inside and outside of the building (ΔP).

The first approach has a number of disadvantages. Firstly, it is very difficult to specify correctly the shape of the infiltration openings in the CFD model geometry. These could involve long cracks a millimetre or less in width, with a convoluted internal flow path between the inside and outside of the building. Not only would it be time-consuming to determine the size of each crack, but the shape of the internal flow path would probably be unknown, and as a result the accuracy of the CFD model would be uncertain. Secondly, the computational grid would need to be very fine in the vicinity of these cracks, with cell dimensions of a millimetre or less. This would result in a very large overall grid size (probably, many millions of cells) which would lead to very long computing times.

In the second approach, the CFD model geometry would be much easier to define, since it would involve large building elements, such as windows and doors, rather than many small, intricately-shaped cracks. The computational grid needed would be coarser, which would result in a model that runs quickly. One of the limitations of the second approach is that it would lump together the leaks in various building element into a single ventilation flow through the whole area. This means that close to the element itself such as a window, the flow behaviour will be poorly represented. Instead of a high-velocity flow through a crack, the model would simulate a lower velocity flow through the whole window face.

Another limitation is that under certain conditions involving strongly buoyancy-affected flows, air may flow out of the top part of an element and in through the lower half. This would produce much higher exchange rates between the inside and outside of the building than is the case if just the net infiltration (inflow minus outflow) were modelled.

Forced ventilation

In many industrial settings, a forced ventilation system is installed. The aims of the system typically include some or all of the following:

- To control the temperature in the enclosures
- To remove exhaust gases or toxic products
- To disperse accidental releases of toxic or flammable gases
- To control admission of fresh air in the case of a fire

A ventilation system may include a number of components, for example:

- Fans which can push air into and/or pull air out of the enclosure
- Ducts through which air is transported to and from the enclosure
- Devices that condition the incoming air to control its temperature and/or humidity
- Devices that condition the incoming air to control its temperature and/or humidity
- Fire dampers or smoke ventilation openings which are activated when a fire is detected

Often, CFD models of enclosures with forced ventilation use prescribed velocities at the ventilation openings. However, this approach is unable to account for changes in the ventilation behaviour due to changes in pressure that may arise due to the build-up of a gas cloud or a fire within the enclosure. An alternative is to specify the flow rates through the ventilation openings using a ventilation network model. There are alternative approaches available to model the ventilation network, which vary in complexity.

“Simple” Ventilation Network Model

In a simple ventilation network model, the ventilation system is parameterised in terms of duct lengths, diameters and loss coefficients, fan characteristics and locations (nodes) where ducts interconnect. One-dimensional conservation equations are then solved for mass, momentum and energy through the system. An example of this type of model is given in the Fire Dynamics Simulator (FDS) CFD code. The network ventilation model in FDS model does not account for any accumulation of material in the network, hence the mass flow into a

node at a given time step must leave the node at the same time step. The model is capable of simulating the activation of any fire dampers, which is of particular interest in the types of application for which FDS is often used. The computational overhead incurred in using FDS with the implemented network model is very modest. Other options available in alternative CFD codes are to combine pre-existing network models such as COMIS or CONTAM with CFD simulations of the flows within the enclosure.

Complex Ventilation Network Model

An alternative to the simple 1D network models is to construct a three-dimensional CFD model of the ventilation network. This is a more physically realistic approach, but the increased computational overhead might not be justified even if the conditions in the network, such as temperatures, pressure and volumetric flow rates could potentially be more accurate.

1.1.6 Buoyancy-controlled and momentum-dominated subsonic jets (HSL)

Vertical buoyant plumes and free-jets are related phenomena, both having a core region of higher momentum flow surrounded by shear layers bounding regions of quiescent fluid. However, whereas for jets the driving force for the fluid motion is a pressure drop through an orifice, for plumes the driving force is buoyancy due to gradients in fluid density. Plumes can develop due to density gradients caused by temperature differences, for example in fires, or can be generated by fluids of different density mixing, such as a release of hydrogen in air. For a good introduction to turbulent jets and plumes, see Chen and Rodi (1980) or List (1982 a,b). A more general discussion of buoyant flows is given in Gebhart *et al*. (1988).

A free vertical buoyant plume can be split into a number of regions, see Figure 1.13. Close to the source, the flow is affected by details of the particular release conditions. This could include inertial effects if, for example, the flow involves a release of buoyant fluid through a nozzle under pressure. Other complexities near the source may be associated with combustion in fire plumes. At a sufficient distance further downstream, the effects of the source conditions are lost, buoyancy forces dominate the flow and it exhibits plume behaviour. Between the near-source and far-field regions, there is a transitional region.

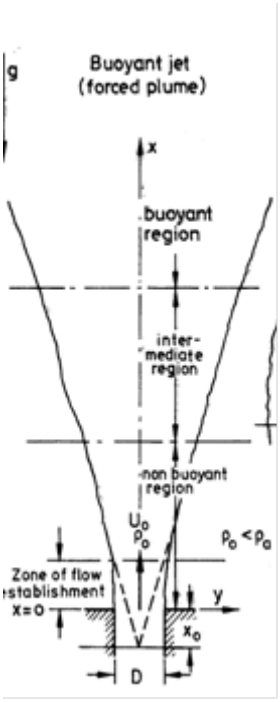

Figure 1.13: Flow development of a buoyant jet, from Chen and Rodi (1980).

Plumes arising from continuous releases of buoyant fluid with significant initial momentum are termed "thermals" or "puffs". "Starting plumes" refer to the advancing front from a continuous buoyancy source in the initial phase of the release before a steady plume becomes established.

In buoyant jets, the location where transition occurs from jet to plume behaviour is often characterised using the densimetric Froude number, *Fr*, given by:

$$Fr = \frac{U}{\sqrt{\left[gD\left(\frac{\rho_\infty - \rho}{\rho_\infty}\right)\right]}} \qquad (1.49)$$

where U is the mean velocity, g gravity, D a characteristic length-scale, and ρ density. Subscript ∞ refers to the far-field value[1]. The Froude number represents the ratio of inertial forces to buoyancy forces. It ranges in value from near zero for pure plumes, towards infinity for jets with negligible buoyancy. Chen and Rodi (1980) analysed a number of jet and plume experiments and, using dimensional analysis, produced the graph reproduced in Figure 1.13, which shows the transition from jet- to plume-like behaviour with increasing Fr^2.

Figure 1.14 shows how the difference in mean density between the axis of the plume and the far field value decays with distance from the inlet. In the jet-like region near the source, the density difference decays at a rate $(x - x_0)^{-1}$ whereas in the fully-developed plume region it decays faster of $(x - x_0)^{-5/3}$. Here, x is the axial coordinate and x_0 is the "virtual" source location (see Figure 7. Empirical correlations for the decay rate of mean velocity and scalars in buoyant jets are given in Gebhart *et al*. (1988)). Both jets and plumes spread linearly in a uniform environment, although at different rates.

[1] In some cases, the densimetric Froude number is defined with the density difference made dimensionless using the plume source density, ρ, instead of the ambient density ρ_∞, e.g. Chen and Rodi (1980) and Hossain and Rodi (1982).

[2] The local Froude number in this case is evaluated on the plume centreline. Note, the *Fr* defined by Chen and Rodi (1980) is the square of the definition of *Fr* given above.

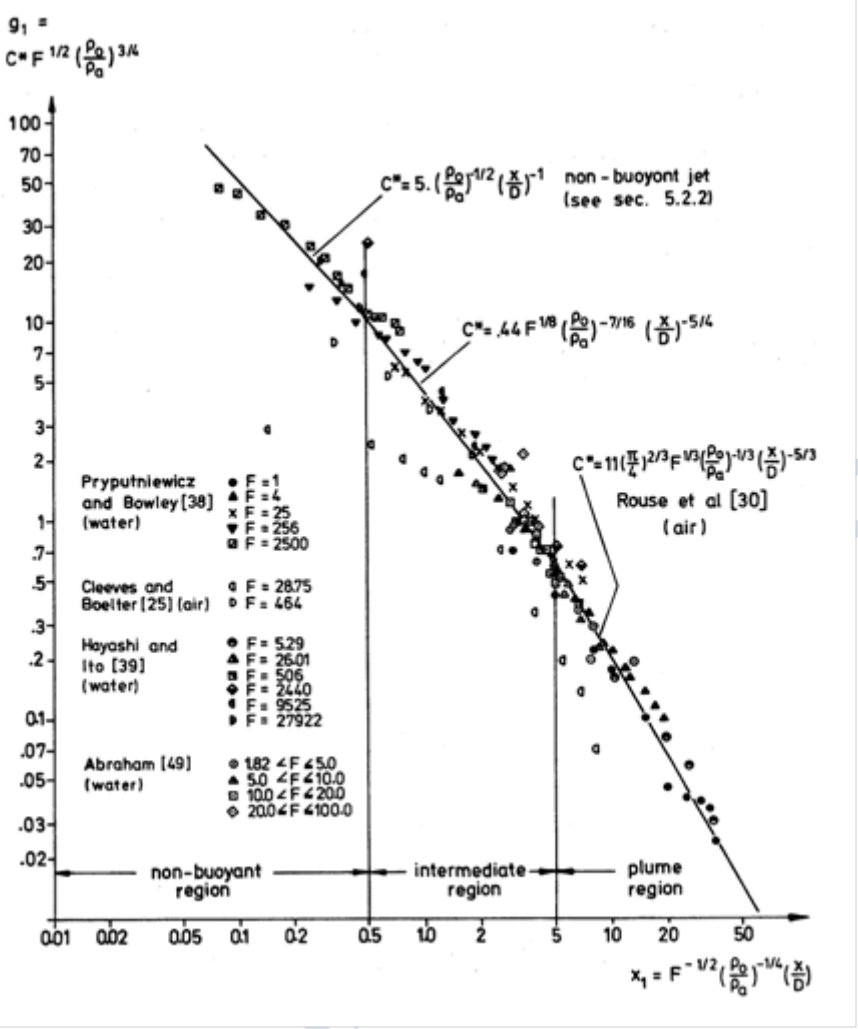

Figure 1.14: Decay of centreline density in round plumes from Chen and Rodi (1980).

Another common measure used to assess when buoyant jets reach a fully-developed state is the Morton length scale, l_M:

$$I_M = \frac{M_0^{3/4}}{F_0^{1/2}} \tag{1.50}$$

where M_0 and F_0 are the specific momentum and buoyancy added at the source of the plume:

$$M_0 = 2\pi \int_0^{r_0} U^2 r \, dr, \qquad F_0 = 2\pi \int_0^{r^0} U g \frac{\Delta\rho}{\rho_\infty} r \, dr \tag{1.51}$$

For plumes with uniform properties at the source, this is equivalent to:

$$I_M = \frac{Fr_0 D}{(\pi/4)^{1/4}} \tag{1.52}$$

where Fr_0 is the source densimetric Froude number at the source and D the inlet source diameter.

Papanicolau and List (1988) suggest that jet-like conditions occur in turbulent buoyant jets for $(x\text{-}x_0)/L_M < 1$ and fully-developed plume-like conditions for $(x\text{-}x_0)/L_M > 5$. However, there is some debate in the literature over the distance required to reach fully-developed plume conditions, see for example Dai *et al*. (1994) and Shabbir & George (1994). Mean parameters (velocity, temperature etc.) require a shorter distance to reach a fully-developed state than statistical quantities such as Reynolds stresses.

An important feature of the mean flow in the fully-developed region of turbulent buoyant plumes is “self-similarity” or “self-preserving” behaviour. In positively-buoyant plumes, as the less dense fluid rises and spreads, the mean velocity peak on the plume centreline decays and the plume becomes wider. However, the shape of the mean velocity profile remains the same. If the dimensionless radial profiles of the mean velocity are plotted at different vertical positions in the plume on the same graph axes, the curves all fall on top of one another. Self-similarity is also exhibited in the dimensionless temperature and species concentration profiles and in the dimensionless RMS turbulent fluctuations of velocity, temperature and concentration ($\sqrt{u^2/U_0}$, $\sqrt{v^2/U_0}$, $\sqrt{\theta^2/\Theta_0}$ or $\sqrt{c^2/C_0}$). Sample data from the experiments of Papanicolaou and List (1988) and Dai *et al*. (1994) shown in Figure 1.15 and Figure 1.16 demonstrate this behaviour.

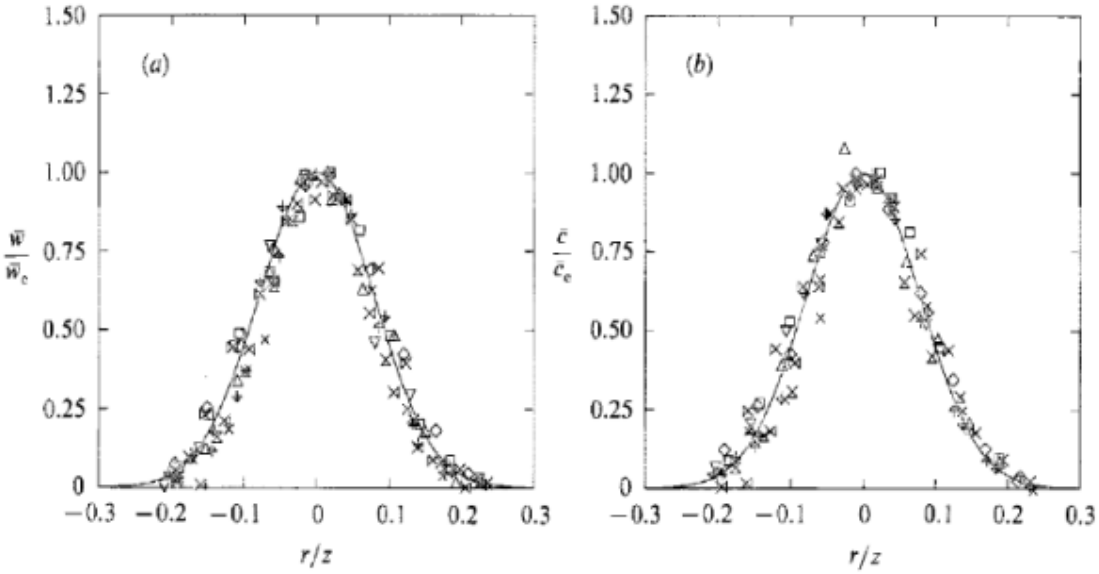

Figure 1.15: Dimensionless mean velocity and mean concentrations profiles in a turbulent axisymmetric plume, from Papanicolaou and List (1988).

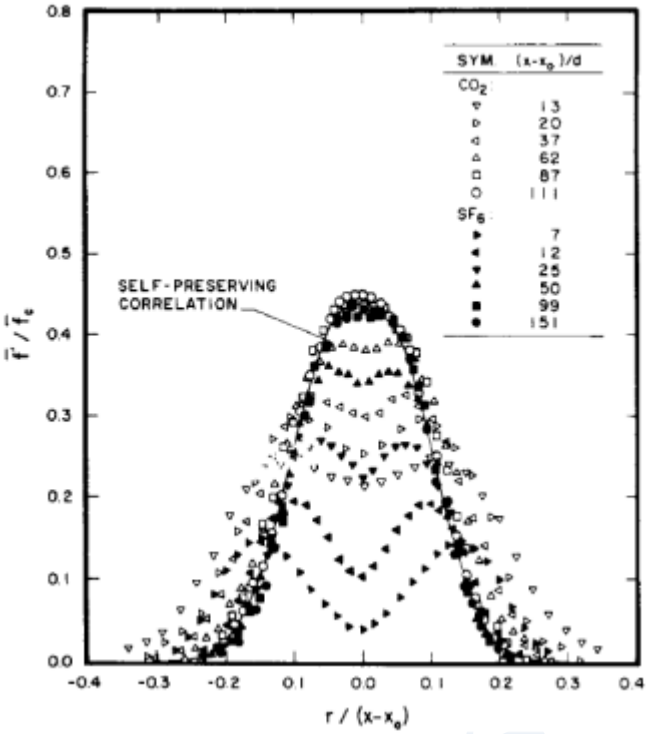

Figure 1.16: Dimensionless mixture fraction fluctuation profiles in a turbulent axisymmetric plume, from Dai *et al*. (1994).

CFD studies

CFD simulations of fully-developed, self-similar turbulent buoyant plumes have, to date, mainly used turbulence models based on the Reynolds-Averaged Navier Stokes (RANS) equations. The alternative class of Large Eddy Simulation (LES) turbulence models require significantly greater computing resources and have mainly been used to simulate just the near-field flow behaviour of buoyant plumes (see, for example, DesJardin *et al*., 2004). An exception to this is the LES study by Zhou *et al*. (2001a,b), in which the thermal plumes of George *et al*. (1977), Shabbir and George (1994) and Cetegen (1997) were examined. Whilst axisymmetric RANS simulations of these flows would involve meshes with around 4,000 cells, the large-eddy simulations of Zhou *et al*. (2001a,b) used more than 4 million cells.

One of the most comprehensive early CFD studies of buoyant plumes was undertaken by Hossain and Rodi (1982). They examined the performance of an algebraic stress and heat flux model in axisymmetric and plane plumes, buoyant jets and pure jets. Their model was based on the differential stress model of Gibson and Launder (1978). The proposed algebraic model shared some features with the standard $k - \varepsilon$ model but used modified expressions for the stresses and heat fluxes and a more sophisticated diffusion term. It also incorporated an empirical correction for the round-jet/plane-jet anomaly first proposed by Rodi (1972). To simulate the axisymmetric plume, they used a parabolic method where the numerical grid was automatically adjusted in the downstream direction to match the plume width. The results from their study should be interpreted with care, since subsequent work by El Baz *et al*. (1993) showed that the parabolic approximation led to over-predictions of the spreading rates by more than 10% in axisymmetric round jets (due mainly to the neglect of source terms arising from streamwise gradients, particularly of ε).

A number of more recent CFD simulations of axisymmetric buoyant plumes have also used variants of the standard $k - \varepsilon$ turbulence model. Nam and Bill (1993) performed simulations

of pool fires using the commercial code PHOENICS and modified the standard Launder and Spalding (1972) model by changing, arbitrarily, the values of the effective Prandtl number, σ_{eff}, and the model constant, c_{μ}, to obtain improved results in buoyant plumes. The consequences of changing these constants on the model's performance in other flows was not explored.

Hara and Kato (2004) used a standard $k - \varepsilon$ model and presented results using different meshes with various modifications to the $c_{\varepsilon 3}$ constant in the buoyancy production term of the ε-equation. They compared results to the experiments of Yokoi (1960), which involved releases of buoyant fluid through a circular orifice, but modelled this as a square orifice to enable the use of hexahedral Cartesian grids. Results were found to be grid-sensitive and recommendations regarding resolution were provided. Differences in the $c_{\varepsilon 3}$ constant were found to have no effect on results.

The study by Brescianini and Delichatsios (2003) also examined the $k - \varepsilon$ model in combination with different sub-models for the turbulence production due to buoyancy, including the Boussinesq Simple Gradient Diffusion Hypothesis (SGDH), the Generalized Gradient Diffusion Hypothesis (GGDH) of Daly & Harlow (1970) and the algebraic model of Hossain and Rodi (1982). They compared CFD predictions mainly to the experimental measurements of Dai *et al*. (1994) and examined both axisymmetric and plane plumes. None of the model variants was found to capture all the flow details of both axisymmetric and plane plumes and no firm conclusions were drawn regarding the best turbulence buoyancy production model. They concluded that given the overall satisfactory performance of the $k - \varepsilon$ model in predicting the mean-flow quantities, there was no real advantage to be gained in using a higher-order closure model to study buoyant plumes.

Yan and Holmstedt (1999) compared two $k - \varepsilon$ model variants against the George *et al*. (1977) experiments for the axisymmetric plume. The first variant was a standard $k - \varepsilon$ model with SGDH and the second involved an additional algebraic stress model for the production term in the *k*-equation combined with GGDH for the production due to buoyancy. The additional algebraic stress model was based on a second-moment-closure correction devised by Davidson (1990). The standard $k - \varepsilon$ model with SGDH was found to under-predict the spreading rate of the plume, producing overly-high temperatures and velocities in the core. Their modified model produced better results for the axisymmetric plume.

Van Maele and Merci (2006) examined both an axisymmetric and a plane buoyant wall plume using SGDH and GGDH variants of the standard $k - \varepsilon$ model and a realizable $k - \varepsilon$ model with the commercial code, Fluent. The SGDH source term was shown to have little effect in the axisymmetric plume case, and consequently the turbulent kinetic energy was underpredicted and the centreline velocity and temperature were over-predicted. The GGDH model was found to perform well with either of the two $k - \varepsilon$ model variants. For the axisymmetric plume case, results were compared to the experimental data of George *et al*. (1977).

Finally, Craft *et al*. (1996) mentioned briefly the results for the buoyant plume in discussing developments of their Two-Component Limit (TCL) second-moment-closure model. Predictions using the TCL model were compared to the experiments of Cresswell *et al*. (1989) and results from a "basic" second-moment-closure model. The spreading rate of the self-similar buoyant plume was found to be better predicted using the more sophisticated TCL model.

Further recommendations on best-practice for CFD modelling of buoyant plumes using RANS and LES models is provided in the ERCOFTAC Knowledge Base (http://www.ercoftac.org/products_and_services/wiki/, accessed 20 June 2014).

1.1.7 Expanded and under-expanded jets (UU)

1.1.7.1Expanded jets

Hydrogen release from a relatively low pressure reservoir (below ~ 1.9 standard atmospheres) results in an expanded jet, where the pressure at the nozzle exit is equal to the atmospheric pressure. It has been shown that expanded turbulent jets of practical interest can be adequately described using similarity laws (Molkov, 2012). Ricou and Spalding (1961) demonstrated by using the dimensional analysis that when the fluid density is uniform, the Reynolds number is high, and the distance x from the nozzle along the jet axis is much larger the diameter of the orifice D, then the total mass flow rate $m(x)$, including entrained surrounding gas, through a cross-section at right angle to the jet axis, is proportional to distance from the nozzle x

$$m(x) = K_1 M_0^{1/2} \rho_S^{1/2} x \tag{1.53}$$

where $M_0 = \rho_N U^2 \pi D^2 / 4$, is the momentum flux of the jet at orifice, ρ_N and ρ_S are the densities at the nozzle and in the surrounding gas, respectively, K_1 is numerical constant and U is the velocity in the nozzle (Molkov, 2012).

Ricou and Spalding (1961) had experimentally shown that numerical constant K_1 has the value 0.282 irrespective of the density ratio, the equation for mass flow rate holds for non-uniform density provided that buoyancy effects are negligible; and that the presence of combustion reduces K_1. The experimental data for isothermal injection of different gases (hydrogen, air, propane, carbon dioxide) into stagnant air therefore obey the following simple relation derived from (1.53)

$$\frac{m(x)}{m_N} = 0.32 \frac{x}{D} \sqrt{\frac{\rho_S}{\rho_N}} \tag{1.54}$$

where m_N is the mass flow rate of the gas in the nozzle.

A mass fraction of fuel averaged through the jet cross-section area can be calculated as a reciprocal to the left-hand side of equation (1.54)

$$C_{av} = 3.1 \sqrt{\frac{\rho_N}{\rho_S}} \frac{D}{x} \tag{1.55}$$

A mean mass fraction of fuel on a jet axis is higher compared to the fuel mass fraction averaged through the jet cross-section. The axial concentration can be calculated by similarity laws (Chen and Rodi, 1980) for round and plane jets respectively

$$\frac{C_{ax}}{C_N} = 5.4 \sqrt{\frac{\rho_N}{\rho_S}} \frac{D}{x} \text{(round jet)} \tag{1.56}$$

$$\frac{C_{ax}}{C_N} = 2.13 \sqrt{\frac{\rho_N}{\rho_S}} \sqrt{\frac{D}{x}} \text{ (plane jet)} \tag{1.57}$$

where C_N is the mass fraction of hydrogen in the nozzle (C_N =1 for pure hydrogen release) and C_{ax} is hydrogen mass fraction at the jet axis.

It is seen from the similarity laws (1.55) and (1.56) that for the hydrogen released to a stagnant air the distance from the nozzle to a location of a given axial concentration in percent by mass (e.g. to the lower flammability limit) depends only on the nozzle diameter. Furthermore, a plane jet decays slower than the round jet ($\sim\sqrt{D}$ *versus* $\sim D$) of the same size (for an infinite plane jet). Plane jets with limited length to width ratio were shown not to obey (1.57), at least at a far field where they are decaying similar to round jets (Molkov et al., 2010).

The mass fraction of a specie C_M can be calculated by its volumetric (mole) fraction C_V using equation

$$\frac{1}{C_M} = 1 + \left(\frac{1}{C_V} - 1\right) \cdot \frac{M_S}{M_N} \tag{1.58}$$

where M_N and M_S are molecular masses of hydrogen and surrounding gas (28.84 g/mol is accepted for air in calculations) (Molkov, 2012).

It should be noted that the correlations (1.56) and (1.57) by Chen and Rodi (1980) were only validated by concentration measurements in vertical jets up to value *x/D* = 50. Their applicability beyond this range is uncertain.

Theoretical and experimental study on hydrogen concentration decay in unignited hydrogen jets into stagnant air performed by Shevyakov et al. (1980) produced similar relations. It was shown, in particular, that for momentum-controlled jets (at high nozzle Froude number $Fr = U^2/gD > 10^5$) the dimensionless distance to 30% of hydrogen by volume $(x/D)_{30\%}$ is a constant *x/D*= 47.9. This is an excellent agreement with work by Chen and Rodi (1980) that gives value 49.3. The theoretical formula derived by Shevyakov et al. (1980) gives an estimate for the flammable envelope length $(x/D)_{4\%}$ = 410, which is close to the Chen and Rodi's value of $(x/D)_{4\%}$ = 493.

1.1.7.2 Under-expanded jets

Hydrogen release from a high pressure reservoir results in a highly under-expanded (pressure at the nozzle exit is above atmospheric pressure) turbulent jet that behaves significantly differently from the expanded jets discussed above (Molkov, 2012). At high pressures a velocity in a constant diameter nozzle (simple orifice, ruptured pipe, triggered pressure relief device (PRD), etc.) remains locally sonic, but the exit pressure rises above ambient. As the result the expansion down to ambient conditions takes place outside the nozzle.
The critical pressure ratio for establishing sonic flow of compressible gas is about 1.9 according to the chocked flow equation

$$\frac{P_R}{P_N} = \left(\frac{\gamma+1}{2}\right)^{\gamma/(\gamma-1)} \tag{1.59}$$

where P_R and P_N are pressures in the reservoir and the nozzle exit respectively, and γ is the ratio of specific heats (γ = 1.4 for diatomic gases at the normal atmospheric conditions).

For under-expanded jet the flow expansion occurs near the nozzle exit and is characterised by the complex shock structure, which is well documented and published (e.g., Abramovich, 1963). The schematic presentation of an under-expanded shock structure is given in Figure 1.17 (Dulov and Luk'yanov, 1984). Figure 1.17 shows that local sonic velocity is established at the nozzle exit with Mach number M=1. Outflowing gas undergoes rapid expansion and quickly accelerates to high Mach numbers (up to M=8 for 70 MPa storage pressure) with decrease in pressure and density. A series of expansion waves are formed at the nozzle exit edge. These expansion waves are reflected as compression waves from the free surface at the jet flow boundary, coalesce and form a barrel shock and a Mach disk. As gas with very high Mach number crosses the Mach disk, it undergoes an abrupt decrease in velocity to subsonic speeds and increases in pressure (to the atmospheric) and density. The resulting flow structure after the Mach disk comprises of subsonic core (M<1) surrounded by supersonic shell (M>1). These two regions are divided by the slip line, which is a shear layer generating turbulent eddies.

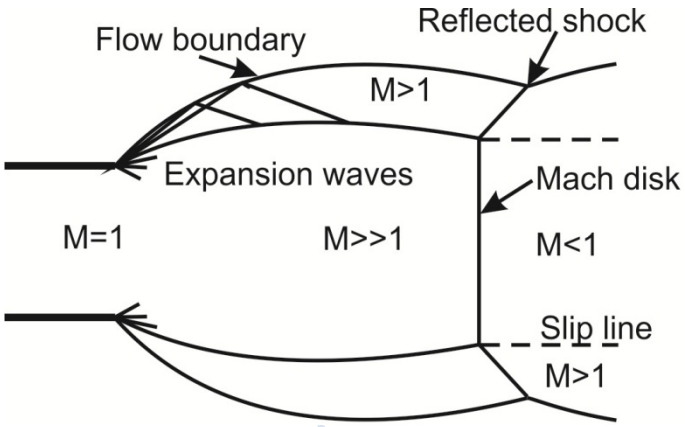

Figure 1.17: The schematic presentation of an under-expanded jet structure (Dulov and Luk'yanov, 1984).

For high ratios of nozzle exit to atmospheric pressure above 40, the barrel shock terminates with a strong Mach disk without a diamond structure, and below this critical pressure ratio of 40 – with the diamond structure. This estimate of the critical pressure ratio is based on simulations of hydrogen under-expanded jets carried out at the HySAFER Centre. The ratio of a storage pressure in a vessel to a nozzle pressure can be roughly estimated as 2 for cases without losses (short nozzles). This means that no diamond structure can be expected for under-expanded hydrogen jets to the atmosphere at storage pressures below about 8 MPa. This preliminary conclusion yet has to be confirmed by experiments.

Schlieren image of shock structure of under-expanded hydrogen jet near nozzle exit was photographed by Ruggles and Ekoto (2011). Figure 1.18 shows a mean image of the Mach disk structure (left), and a mean image of Mach disk and diamond shock structure (right). Nominal pressure ratio was 10:1 and nozzle diameter was 0.75 mm.

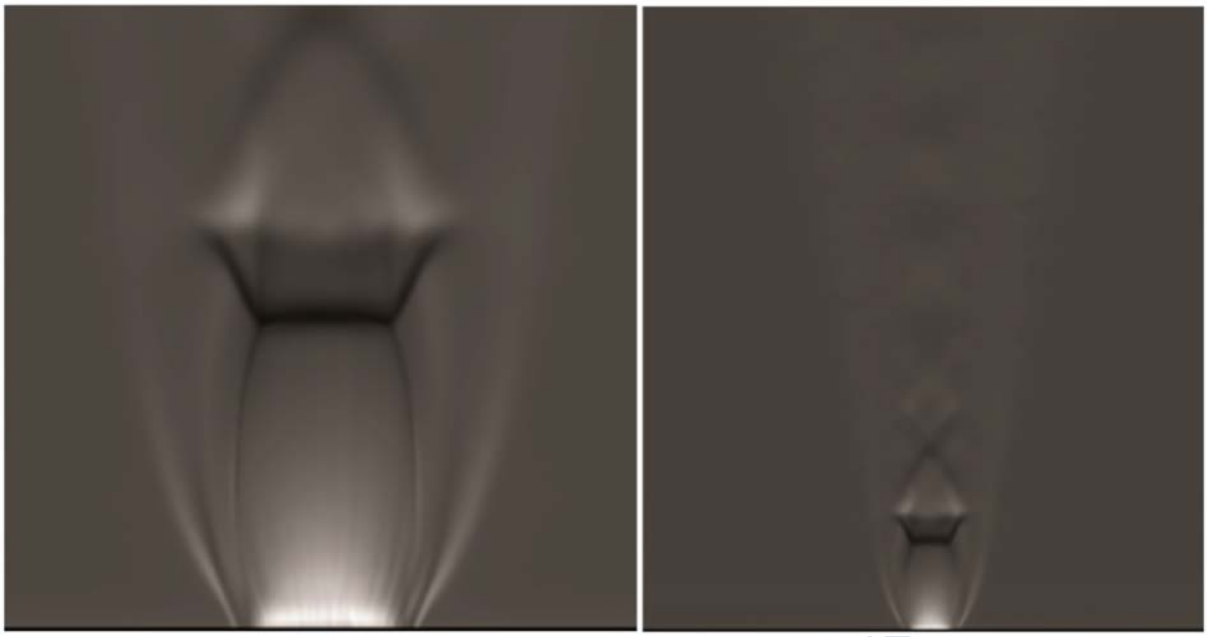

Figure 1.18: Images of the Mach disk structure (left), and Mach disk and diamond shock structure (right) (Ruggles and Ekoto, 2011).

In engineering applications it may be computationally expensive and impractical to simulate detailed shock structure of under-expanded jet, especially when interested in problems involving large geometrical scales. Instead, it is advantageous to substitute simulation of under-expanded jet issued from actual nozzle with simulation of an expanded jet from the so-called effective or notional nozzle.

A number of notional nozzle theories have proposed, introducing the concept of effective source diameter, whereby the shock structure formed in the under-expanded jet is replaced by a notional nozzle. Birch et al (1984) developed the concept of an effective source diameter, based on the area which would be occupied by the same mass flow rate at ambient pressure and temperature with a uniform sonic velocity. Birch et al. (1984) showed that the behaviour of under-expanded jets is similar to classical subsonic free jets provided that an appropriate scaling factor is employed to describe the effective size of the jet source.

While Birch et al. (1984) model remains one of the most frequently cited, this model is built on the ideal gas equation of state and thus not applicable to gas storage pressures above 10-20 MPa when effects of gas non-ideality must be accounted for. Indeed, the Abel-Noble equation of state $p = Z\rho R_{H_2} T$, where $Z=1/(1- b\rho)$ is the compressibility factor, has value Z = 1.01 at 1.57 MPa, Z = 1.1 at 15.7 MPa, and Z = 1.5 at 78.6 MPa (at temperature 293.15 K).
The first theory of under-expanded jet that accounts for non-ideal behaviour of highly compressed hydrogen has been published by Schefer et al. (2007). The notional nozzle diameter calculations by Schefer et al. (2007) are similar to Birch et al. (1984) except for the Abel-Noble equation (Chenoweth, 1983) being applied in place of the ideal gas equation of state, and the assumption by Birch et al. about the speed of sound at the notional nozzle being relaxed. As a result the theory of Schefer et al. (2007) predicts uniform super-sonic velocities at the notional nozzle exit at high storage pressures.

Molkov et al. (2009) developed the alternative to Schefer et al. (2007) under-expanded theory which is based on mass and energy conservation equations rather than mass and momentum (Schefer et al., 2007). Similar to Birch et al. (1984) the model developed by Molkov and

colleagues is based on the assumption of uniform sonic flow through the notional nozzle. The under-expanded jet scheme is shown in Figure 1.19.

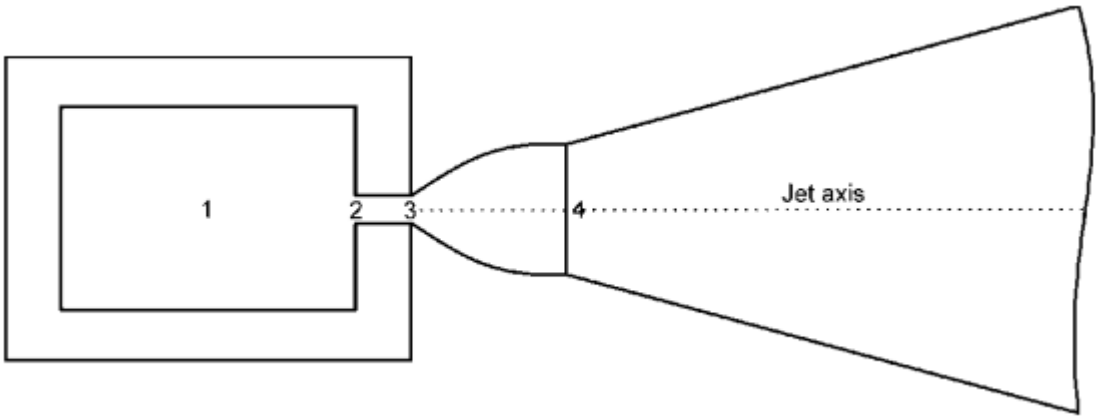

Figure 1.19: The under-expanded jet scheme: 1 – storage vessel, 2 – nozzle entrance, 3 – nozzle exit, 4 – notional nozzle exit.

It is assumed that the gas in the high pressure storage tank "1" is quiescent. The flow parameters at the entrance to the leak channel are referred to by variables with subscript "2", and those at the actual nozzle exit by variables with subscript "3". For sonic and super-sonic releases the flow becomes choked at the nozzle exit 3, and the nozzle exit velocity therefore is equal to the local speed of sound (Mach number equals unity, M=1). The notional nozzle is situated between the actual nozzle exit "3" and the notional nozzle exit "4" where flow parameters correspond to fully expanded jet with the pressure equal to ambient and uniform flow velocity equal to local speed of sound.

Notional nozzle theory by Molkov et al. (2009) assumes that gas expansion from the reservoir "1" to the nozzle exit "3" (Figure 1.19) is isentropic and governed by Abel-Noble law. The losses incurred in the flow between nozzle entrance "2" and nozzle exit "3" are neglected. It is further assumed that there is no air entrainment to an expanding jet between the actual nozzle exit "3" and the notional nozzle exit "4". Gas release can be described by a following system of nine equations with nine unknown parameters ($\rho_1, \rho_3, u_3, T_3, p_3, \rho_4, u_4, T_4, A_4$):

- three equations of state for gas parameters at the reservoir, 1, the real nozzle exit, 3, and the notional nozzle exit, 4:

$$\rho_1 = \frac{p_1}{bp_1 + R_{H_2} T_1} \quad \rho_3 = \frac{p_3}{bp_3 + R_{H_2} T_3} \quad \rho_4 = \frac{p_4}{bp_4 + R_{H_2} T_4} \tag{1.60}$$

- two equations of energy conservation, one between the reservoir "1" and the actual nozzle exit "3" and another between the actual nozzle exit "3" and the notional nozzle exit "4":

$$c_p T_1 = c_p T_3 + \frac{u_3^2}{2} \quad c_p T_3 = c_p T_4 + \frac{u_4^2}{2} \tag{1.61}$$

- two equations for the speed of sound, one for choked flow in the nozzle exit "3" and another for the assumption of the speed of sound at the notional nozzle exit "4":

$$u_3^2 = a_3^2 = \frac{\gamma p_3}{\rho_3(1-b\rho_3)} \qquad u_4 = a_4 = \sqrt{\gamma R_{H_2} T_4} \tag{1.62}$$

- and finally mass conservation equation between entrance to the notional nozzle "3" and exit from the notional nozzle "4":

$$\rho_3 u_3 A_3 = \rho_4 u_4 A_4 \tag{1.63}$$

Known parameters are p_1, T_1, A_3, p_4 and constants c_p, R_{H_2}, b, γ, where ρ is the density (kg/m^3), u is the gas velocity (m/s), A is the cross-section area (m^2), T is the temperature (K), $\gamma = c_p / c_v$ is the ratio of specific heats at constant pressure c_p and constant volume c_v respectively (both in J/mol/K), R_{H_2} is the hydrogen gas constant (4124.24 J/kg/K) and b is the co-volume constant for the Abel-Noble equation ($b = 7.69 \cdot 10^{-3}$ m^3/kg).

The isentropic expansion equation between the reservoir "1" and the actual nozzle exit "3" can be expressed as

$$p_1\left(\frac{1}{\rho_1} - b\right)^{\gamma} = p_3\left(\frac{1}{\rho_3} - b\right)^{\gamma} \tag{1.64}$$

Equation for energy conservation between the reservoir "1" and the actual nozzle exit "3" (1.62) can be rewritten as

$$\frac{T_1}{T_3} = 1 + \frac{u_3^2}{2c_p T_3} \tag{1.65}$$

Multiplying numerator and denominator in the second term of the right-hand side by square of the speed of sound (expressed for Abel-Noble gas as $a^2 = \frac{\gamma p}{\rho(1-bp)}$), eq. (1.65) is transformed into

$$\frac{T_1}{T_3} = 1 + \frac{\gamma p_3}{\rho_3(1-b\rho_3)} \frac{R_{H_2} M_3^2}{2c_p R_{H_2} T_3} \tag{1.66}$$

where M_3 is Mach number of the flow in state 3. Taking into account that $\frac{R_{H_2}}{c_p} = \frac{\gamma}{\gamma - 1}$ (1.65) transforms into

$$\frac{T_1}{T_3} = 1 + \frac{\gamma p_3}{\rho_3(1-b\rho_3)} \frac{\gamma}{\lambda - 1} \frac{M_3^2}{2R_{H_2} T_3} = 1 + \frac{(\gamma-1)M_3^2}{2(1-b\rho_3)}\left[\frac{p_3}{\rho_3 R_{H_2} T_3}\right] \tag{1.67}$$

By substitution $\frac{p_3}{\rho_3 R_{H_2} T_3} = \frac{1}{1-b\rho_3}$ and accounting for chocked flow in the actual nozzle exit 3 ($M_3 = 1$) the following equation is derived

$$\frac{T_1}{T_3} = 1 + \frac{(\gamma-1)M_3^2}{2(1-b\rho_3)^2} = 1 + \frac{(\gamma-1)}{2(1-b\rho_3)^2} \tag{1.68}$$

Equation (1.64) can be rewritten using the Abel-Noble equation of state

$$\left(\frac{\rho_1}{1-b\rho_1}\right)^{\gamma} = \left(\frac{\rho_3}{1-b\rho_3}\right)^{\gamma} \frac{\rho_1 R T_1}{1-b\rho_1} \frac{1-b\rho_3}{\rho_3 R T_3} \tag{1.69}$$

By uniting the density terms in (1.69) and substituting the temperature ratio from (1.68), (1.69) can be further rewritten as

$$\left(\frac{\rho_1}{1-b\rho_1}\right)^{\gamma-1} = \left(\frac{\rho_3}{1-b\rho_3}\right)^{\gamma-1} \left(1+\frac{\gamma-1}{2(1-b\rho_3)^2}\right) \tag{1.70}$$

The notional (or effective) nozzle diameter can be than calculated as follows (Molkov et al., 2009):

The first step is to calculate hydrogen density in the reservoir from the Abel-Nobel equation of state $p = Z\rho R_{H_2} T$. Solving a transcendental equation of isentropic expansion (1.70) provides density at the actual nozzle exit. Temperature T_3 at the actual nozzle exit can be obtained from the eq. (1.68) and the pressure p_3 from the Abel Noble equation. At the actual nozzle exit 3, the flow is chocked and hydrogen velocity can be calculated using the equation for the speed of sound $a^2 = \frac{\gamma p}{\rho(1-bp)}$. From the energy conservation equation between the actual nozzle exit and the notional nozzle exit (1.61) written per unit mass, and with the assumption that hydrogen velocity at the notional nozzle exit is equal to the local speed of sound $a_4^2 = \gamma R_{H_2} T_4$, it is possible to derive the temperature at the notional nozzle exit as

$$T_4 = \frac{2T_3}{(\gamma+1)} + \frac{(\gamma-1)}{(\gamma+1)} \frac{p_3}{\rho_3(1-b\rho_3)R_{H_2}} \tag{1.71}$$

Hydrogen density at the notional nozzle can be calculated by noting that p_4 is equal to the ambient pressure and gas velocity $u_4 = a_4$. Finally, from the continuity equation it follows that the notional nozzle exit diameter is

$$d_4 = d_3 \sqrt{\frac{\rho_3 u_3}{\rho_4 u_4}} \tag{1.72}$$

This approach can be further extended to derive the theory for calculation of the parameters of notional nozzle in the presence of losses (Molkov and Bragin, 2009). Minor losses in gas flow represent entrance to the channel, abrupt reduction or increase in channel cross-section area, presence of valves, elbows, etc. They are described in this theory through the minor losses factor *K*. Frictional losses are considered to be due to friction on walls. They are described through equation $F = fL/d$, where *f* is the friction factor, *L* is the channel/nozzle length, and *d* is channel diameter. The system of 12 equations describing this process has been derived in (Molkov and Bragin, 2009) and given in Table 1.6. The system of equations in Table 1.6 can be reduced to the following two equations with two unknown parameters u_3 and T_3

$$\frac{u_3}{b}\left(1-\frac{\sqrt{\gamma R_{H_2}T_3}}{u_3}\right)\cdot\left[\sqrt{\frac{R_{H_2}T_3}{\gamma}}+\left(\frac{K+F}{4}\right)\cdot\sqrt{\frac{2}{K}\left(c_pT_1-c_pT_3-\frac{u_3^2}{2}\left(\frac{F}{4}+1\right)\right)}+u_3\left(\frac{F}{4}+1\right)\right]-p_1=0$$

$$\frac{u_3}{b}\left(1-\frac{\sqrt{\gamma R_{H_2}T_3}}{u_3}\right)\cdot\left[\frac{R_{H_2}\left(T_1-\left(T_1-T_3-\frac{u_3^2}{2c_p}\left(\frac{F}{4}+1\right)\right)\frac{K+1}{K}\right)}{\sqrt{\frac{2}{K}\left(c_pT_1-c_pT_3-\frac{u_3^2}{2}\left(\frac{F}{4}+1\right)\right)}-u_3+\sqrt{\gamma R_{H_2}T_3}}+\right.$$

$$\left.+\left(\frac{K}{4}+1\right)\sqrt{\frac{2}{K}\left(c_pT_1-c_pT_3-\frac{u_3^2}{2}\left(\frac{F}{4}+1\right)\right)}\right]-p_1=0 \qquad (1.73)$$

After u_3 and T_3 are found by solving the system of two equations (1.73), the rest of parameters in the under-expanded jet can be easily calculated.

Table 1.6: The system of equations for the under-expanded jet notional nozzle model with losses (Molkov and Bragin, 2009).

$p_2-p_1+\rho_2u_2^2(K/4+1)=0$	$\rho_2u_2=p_3u_3$
$c_pT_1=c_pT_2+(K+1)\cdot u_2^2/2$	$u_3=\sqrt{\gamma R_{H_2}T_3}/(1-b\rho_3)$
$\rho_2=p_2/(bp_2+R_{H_2}T_2)$ or $p_2=\rho_2R_{H_2}T_2/(1-b\rho_2)$	$u_4=a_4=\sqrt{\gamma R_{H_2}T_4}$
$p_3-p_2+\rho_2u_2^2(F/4-1)+\rho_3u_3^2(F/4-1)=0$	$\rho_4=p_4/(R_{H_2}T_4)$
$c_pT_2+u_2^2/2=c_pT_3+(F/4+1)\cdot u_3^2/2$	$c_pT_3+u_3^2/2=c_pT_4+u_4^2/2$
$\rho_3=p_3/(bp_3+R_{H_2}T_3)$	$\rho_3u_3A_3=p_4u_4A_4$

1.1.8 Blowdown (UU)

Blowdown phenomena refers to the high flow rate release of the hydrogen from a high pressure storage reservoir in which the pressure in the reservoir significantly drops as the hydrogen escapes from the storage tank. While it is common in CFD modelling to assume constant inflow boundary conditions, blowdown scenario requires utilization of variable boundary conditions. Blowdown simulations usually utilize models developed for modelling of under-expanded jets, with the inflow parameters adjusted according to the drop of tank pressure. This requirement can present a problem for the simulations using notional nozzle approach, since the change in the tank parameters would affect the diameter of notional nozzle, require implementation of the movable mesh or risking loss of resolution at the nozzle and associated loss of accuracy. An alternative approach to handling blowdown modelling was proposed at University of Ulster, introducing volumetric source which adjusts for changing tank parameters by altering mathematical source terms in the volumetric source region, keeping its dimensions constant. Volumetric source approach is described in details in section 1.2.4.

Notional nozzle model described section 1.1.7.2, coupled with volumetric source approach (section 1.2.4) was used to simulate pressure dynamics in the hydrogen storage tank during

an under-expanded jet release (blowdown) in experiments by UK Health and Safety Laboratory (HSL), described in (Molkov et al., 2009). The HSL high-pressure hydrogen experimental facility was equipped with 2 vessels of 49 litres capacity each, initial pressure was P_1=208 bar, initial temperature was estimated as T_1=288 K. These conditions correspond to 3.025 kg of hydrogen mass stored in the facility. Valve with throat wide open provided a minimum orifice diameter of 9.5 mm in the pipeline. The discharge pipeline was installed at 1.2 m height and directed horizontally.

Two simulations were performed using adiabatic discharge from the high-pressure vessel (no heat transfer), and discharge under the constant temperature conditions (ideal heat transfer). Simulated pressure dynamics in the hydrogen storage vessel in comparison with the experimental pressure record is shown in Figure 1.20, showing good pressure dynamics agreement with experiment.

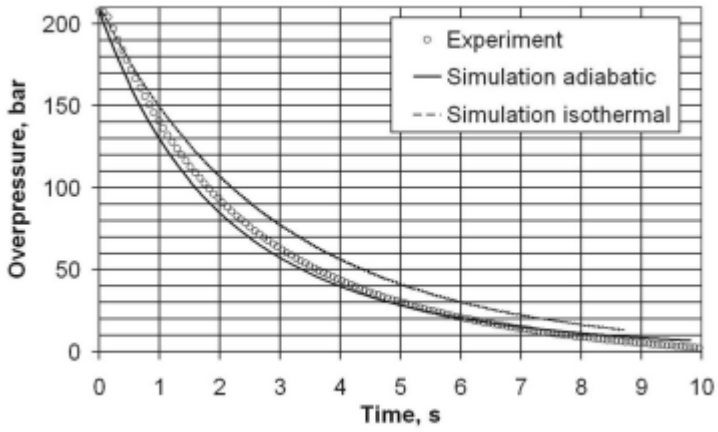

Figure 1.20: Simulated blowdown pressure dynamics (Molkov et al., 2009).

1.1.9 Releases in presence of obstacles and along surfaces (NCSRD)

The study of releases and dispersion of hazardous and flammable substances due to an accidental release or equipment failure is of great significance not only because it can help in designing mitigation/prevention equipment (e.g. detection alarms, shutdown procedures etc.) , but also it can help decide on taking actions that may prevent any escalation of the accident.

Releases can take place outdoors, or indoors, on a flat unobstructed plain, in a confined area, or in the presence of obstacles. The consequences of the release are greatly dependent on the geometry and the characteristics of the surrounding area, and it can result in deflagration/explosion, leading to catastrophic consequences. The presence of obstacles can have either negative or positive effect dependent on the case. For instance, obstacles can confine the vapour cloud and hinder its dispersion, and, consequently, restrain the hazardous area. However, if the vapour cloud is circulated by obstacles it can accumulate, and it is more possible to form a flammable cloud and could even cause explosion with catastrophic damages, as was happened in the Stockholm accident (“Gasexplosionen på Brahegatan I Stockholm den 3Mars 1983). Therefore, the presence of obstacles and its effect on the flow field should be studied thoroughly.

In addition, even in the case of releases that take place on unobstructed terrain, when the release is along surfaces (e.g. along the ground), the characteristics of the surfaces, such as the roughness length, the surface’s properties etc., influence the dispersion. In this section the

physics related to the release in the presence of obstacle and along surfaces will be discussed, in order to understand their effect on dispersion.

Turbulence is a very important factor in the mixing and the dilution of gaseous releases, and especially in atmospheric flows, it is the dominant mechanism. The presence of obstacles, such as buildings, equipment of the facility, etc. in a flow field causes recirculation areas, separation, vortex shedding and wakes dependent on the size and the shape of the obstacle and of the flow characteristics. Consequently, the turbulence is enhanced.

Moreover, the velocity is decreased downstream the obstacle. The decrease in velocity depends on the total area of the object facing the velocity direction. The velocity reduction increases with height and length of the obstacle, and it is more pronounced close to the obstacle and close to the ground. Figure 1.21 illustrates the flow streamlines around an obstacle. The recirculation region and the formed eddies (wakes) upwind and downwind the obstacle are displayed. In the area above the obstacle the velocity is increased and in the area behind the obstacle (downstream) the velocity is decreased. Away from the obstacle (a few obstacle's height downwind) the velocity profile takes again the unperturbed profile that had upwind the obstacle. Unless if another obstacle block the flow path.

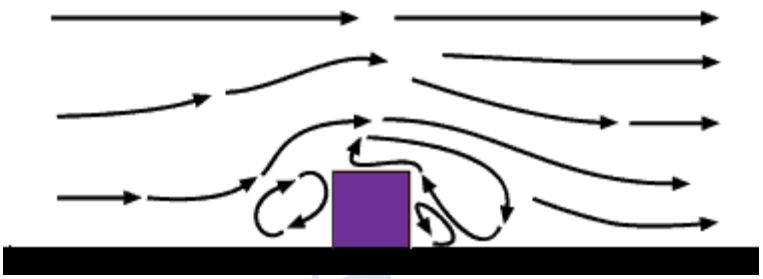

Figure 1.21: Schematic diagram of the flow streamlines around an obstacle.

Based on Reynolds number, different regimes of flow can be observed for the problem of flow around obstacle (Franke, 1991). At very low Reynolds numbers (Re << 1), viscous forces dominate the flow, and no separation occurs. With the increase of Reynolds number, flow separates at trailing edge and forms a recirculation region. Size of recirculation zone increases with an increase of Reynolds number and by reaching the critical Reynolds number, von Kármán vortex street (Theodor von Karman, 1994) with repeating pattern of swirling vortices happens (for flow around cylindrical objects). With further increase of Reynolds number beyond this critical value, separation will occur in the leading edge.

In flows with recirculation areas the released substance of interest may be trapped in these areas, leading to hazardous regions with high concentration of the substance. Especially, in the case of release and dispersion in a street canyon the hazardous gas can be trapped inside the canyon. A street canyon is a formulation of two long parallel buildings side-by-side, along with the street between them. Since a city is practically formed of street canyons, they have attracted the scientific interest in examining the flow characteristics and the pollution trapping. When the flow is perpendicular to the street canyon a complex structure occurs. As we see in Figure 1.22, a recirculation zone is formed inside the canyon. The recirculation is formed mainly if the velocity of the free flow is higher than 2 m/s although lower values can still produce recirculation in some cases (Caton, Britter, & Dalziel, 2003).

The ratio of the height of the buildings H to the width of the canyon W is important. A typical flow velocity inside the canyon for ratio H/W equal to 1 is the 2/3 of the velocity on the top of

the buildings (Nakamura & Oke, 1988). As the ratio H/W gets bigger, the coefficient 2/3 gets smaller.

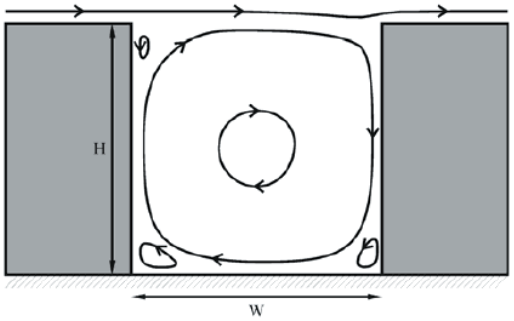

Figure 1.22: Recirculation zone in a street canyon for ratio H/W=1.

The value of the ratio H/W is critical regarding the position and the number of the recirculation zones. As the ratio becomes greater than one, the centre of the recirculation zone moves higher. As we see in Figure 1.23, for ratios greater than 2 a second primary recirculation zone can be formed and for ratios greater than 3 a third one. This recirculation zone has small velocities and it is unstable.

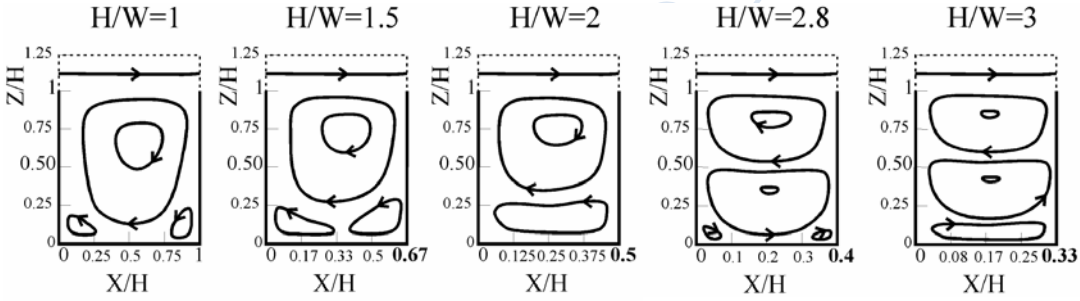

Figure 1.23: Recirculation zones for different values of H/W.

Detailed analysis about flows in street canyon can be found in (Vardoulakis, Fisher, Pericleous, & Gonzalez-Flesca, 2003), (Caton et al., 2003), (Afiq, Azwadi, & Saqr, 2012) and (Koutsourakis, 2010).

In case of release along a surface a boundary layer is formed. The definition of the boundary layer follows: *A boundary layer is the layer of fluid in the immediate vicinity of a bounding surface where the effects of viscosity are significant.*

A boundary layer can be either laminar or turbulent. In case with heat transfer a thermal boundary layer (laminar or turbulent) is also formed. The thickness of the boundary condition is defined as the distance from the solid body at which the viscous flow velocity is 99% of the free stream velocity (the surface velocity of an inviscid flow). Similar for the thermal boundary layer the thickness is defined as the distance from the solid body at which the temperature is 99% of the temperature found from an inviscid solution.

It can be said that the most characterizing parameter of the profile is the roughness length which is creating the turbulence and thus the boundary layer itself, profile and height of it. A definition of the roughness length could be “the height above the ground at which the mean wind velocity is zero” (Dyrbye & Hansen, 1997). The terrain is divided into different categories depending on its surface material and thus its roughness and goes from smooth to

rough terrain, e.g. plane ice, open sea, coastal areas, and open land. There are several tables in the bibliography which provide information about the roughness length of each terrain. The data might vary slightly from one source to another but despite that they have a good agreement. A terrain classification in terms of effective surface roughness length can be found in (Desmond, 2000).

The equations that are applied in the boundary layer are a simplification of the Navier-Stokes equations of viscous fluid. Notably, the characteristic of the partial differential equations (PDE) becomes parabolic, rather than the elliptical form of the full Navier–Stokes equations, resulting in a great simplification of the governing equations within the boundary layer. By making the boundary layer approximation for a sufficiently high Reynolds number the flow over a surface can be divided into an outer region of inviscid flow unaffected by viscosity (the majority of the flow), and a region close to the surface where viscosity is important (the boundary layer).

For an incompressible, two dimensional flow the continuity equation and the Navier-Stokes equations in the boundary layer become (Batchelor, 2000):

$$\frac{\partial u_x}{\partial x}+\frac{\partial u_y}{\partial y}=0 \tag{1.74}$$

$$u_x\frac{\partial u_x}{\partial x}+u_y\frac{\partial u_x}{\partial y}=\frac{1}{\rho}\frac{\partial p}{\partial x}+\nu\frac{\partial^2 u_x}{\partial y^2} \tag{1.75}$$

u_x is the streamwise velocity, u_y is the transverse (wall normal) velocity, P is the pressure, ρ is the density, and ν is the kinematic viscosity.

And for flows where the pressure does not change in the direction of the flow the equation (1.75) becomes:

$$u_x\frac{\partial u_x}{\partial x}+u_y\frac{\partial u_x}{\partial y}=\nu\frac{\partial^2 u_x}{\partial y^2} \tag{1.76}$$

In turbulent flows, the boundary layer is divided in a laminar (viscous) sublayer near the wall and a turbulent sublayer above it. In the laminar sublayer the turbulent viscosity is neglected, and in the turbulent sublayer the laminar viscosity is neglected. From the above simplified Navier-Stokes the relationships that calculate the mean velocity in each sublayer, called wall functions, are derived:

For the laminar sublayer

$$u^+=y^+ \tag{1.77}$$

where

$$u^+=\frac{u}{u_*} \tag{1.78}$$

$$y^+=\frac{yu_*\rho}{\mu} \tag{1.79}$$

u_* is the shear velocity, and μ the dynamic viscosity.

For the turbulent sublayer:

$$u^+ = \frac{1}{\kappa}\ln y^+ + c \tag{1.80}$$

The constant c can take values ranged from 4.9-5.5, and the von Karman constant, κ, is equal to 0.41.

A very important factor in releases along surfaces is the heat transfer from the solid object to the cloud. The heat transfer rate can be calculated using the Newton's law of cooling (Burmeister, 1993):

$$\dot{q} = h \cdot (T_s - T) \tag{1.81}$$

where $\dot{q}$ is the heat transfer rate per unit area, T is the fluid temperature, T_s is the surface temperature, and h is the heat transfer coefficient. The heat transfer coefficient depends upon physical properties of the fluid and the physical situation in which convection occurs. For laminar flows, the heat transfer coefficient is rather low compared to turbulent flows; this is due to turbulent flows having a thinner stagnant fluid film layer on the heat transfer surface. In addition, in case of liquid hydrogen release, in the area where the liquid is in contact with the solid surface the heat transfer coefficient follows the boiling curve of the liquid. According to the boiling curve the heat transfer coefficient depends on the temperature difference between the liquid and the solid surfaces, and it changes dynamically during the release as the solid surface gets colder. More detailed information about the boiling curve can be found later on in Section 1.1.13.

1.1.10 Releases and dispersion indoors (NCSRD)

1.1.10.1 Pressure peaking (UU)

Pressure peaking is the phenomenon unique for lighter than air gases occurring during high flow rate releases in the vented confined space. In order for pressure peaking to occur, the hydrogen flow rate should be such that the hydrogen concentration in the enclosure reaches 100%, completely displacing air.

Consider hydrogen fully occupying an enclosure to which it is released. Steady state conditions are reached when hydrogen mass flow rate from the enclosure through a vent $\dot{m}_{vent}$ is equal to hydrogen inflow mass flow rate (e.g., from the nozzle of the Pressure Relief Device (PRD)) $\dot{m}_{nozz}$ to the enclosure, i.e. $\dot{m}_{vent} = \dot{m}_{nozz}$. Simple models such as the orifice equation for a subsonic regime (Molkov, 1995)

$$\dot{m}_{vent} = CA\left\{\left(\frac{2\gamma}{\gamma-1}\right)P_S\rho_{encl}\left[\left(\frac{P_S}{P_{encl}}\right)^{2/\gamma} - \left(\frac{P_S}{P_{encl}}\right)^{\frac{\gamma+1}{\gamma}}\right]\right\}^{1/2} \tag{1.82}$$

and the Bernoulli's equation in the assumption of zero flow velocity in the enclosure

$$P_{encl} - P_S = \frac{1}{2\rho_{H_2}}\left(\frac{\dot{m}_{nozz}}{A}\right)^2 \tag{1.83}$$

can be used to estimate the steady state overpressure within the enclosure. In this equations C is the discharge coefficient; A is the vent area, m^2, γ is the ratio of specific heats, P_S is the

surrounding pressure, Pa; P_{encl} is the pressure in the enclosure, Pa, and ρ_{H_2} is the density of hydrogen at the surrounding conditions, kg/m^3.

The above equations are obtained in assumption of pure hydrogen within the enclosure. However, neither of two equations accounts for the injection of a lighter gas into a heavier gas and the subsequent overpressure in the garage to "push" the heavier gas air after the start of the release, and the corresponding higher inflow volumetric rate compared to outflow rate in the beginning of the process. Thus, the following system of equations is used to predict the development of the overpressure within the enclosure with time in the assumption of a perfect stirred reactor (i.e., instantaneous perfect mixing of released hydrogen with a mixture already available within the garage, Brennan et al., 2011):

$$m_{encl}^{t+\Delta t} = m_{encl}^{t} + \left(\dot{m}_{nozz}^{t} - \dot{m}_{vent}^{t}\right)\Delta t \tag{1.84}$$

$$n_{encl}^{t+\Delta t} = n_{encl}^{t} + \left(\frac{\dot{m}_{nozz}^{t}}{M_{H_2}} - \frac{\dot{m}_{vent}^{t} n_{encl}^{t}}{m_{encl}^{t}}\right)\Delta t \tag{1.85}$$

$$P_{encl}^{t+\Delta t} = \frac{n_{encl}^{t+\Delta t} RT}{V} \tag{1.86}$$

$$\dot{m}_{encl}^{t+\Delta t} = C \cdot \left(\frac{m_{encl}^{t+\Delta t} A}{V}\right) \cdot \left(\frac{2\left(P_{encl}^{t+\Delta t} - P_S\right)}{m_{encl}^{t+\Delta t}}\right)^{1/2} \tag{1.87}$$

where superscripts "t" and "$t+\Delta t$" denote previous and next time steps respectively; m is the mass of gas, kg; $\dot{m}$ is the mass flow rate, kg/s; n in the number of moles; Δt is the time step, s; V is the enclosure volume, m^3 and P is the pressure, Pa.

In order to illustrate the application of pressure peaking model (1.84)-(1.87) it was applied to simulation of the hydrogen release through a PRD in a residential garage (Brennan and Molkov, 2013). Calculations of PRD diameter required to safely blow-down storage tanks with inventories of 1, 5 and 13 kg hydrogen were calculated for a range of garage volumes and natural ventilation rates expressed in air changes per hour (ACH).

(Molkov et al., 2009) model was used to simulate blow-down of hydrogen from the storage tank. This model takes into account the under-expanded jet theory given in the same work (Molkov et al., 2009) and can be used to calculate decay of pressure and mass flow rate during a release from a storage tank of known volume through an orifice of known diameter. The heat transfer during blowdown was not accounted for; an isothermal approach which assumed a temperature of 288 K was used based on available experimental data for blow-downs at such pressures through orifices of similar size. A validation of this approach is given in (Molkov et al., 2009). For a given diameter, storage pressure, and hydrogen inventory, the output of the blow-down model (mass flow rate) was used as an input to the phenomenological model to predict overpressure in a garage with a known volume and ACH.
In order to make this work more widely applicable, steps were taken to relate garage volume and vent areas to ACH. However, whilst values of ACH characteristic of residential garages can be found in the literature (InsHyde D74, 2009), (TIAX, 2004), there was some uncertainty as to how ACH could be translated to vent area for a specific volume. ACH is defined as the volumetric air flow rate per hour, Q_{hr} (m^3/hr) per unit volume V (m^3)

$$ACH = Q_{hr} / V \tag{1.88}$$

Bernoulli's equation can be used to express volumetric flow rate per second Q_s as a function of vent area, A, density of air, ρ, and pressure differential between the volume (e.g. garage) and the atmosphere, ΔP, i.e.

$$Q_S = CA\sqrt{2\Delta P / \rho} \tag{1.89}$$

Value of ΔP in eq. (1.89), i.e. the pressure differential assumed between the interior and exterior of the enclosure will obviously have an influence on the vent area calculated for a given ACH, the larger the "standard" ΔP, the smaller the corresponding vent area for a given volume and given ACH.

Figure 1.24 illustrates the overpressure dynamics for a release of 5 kg of hydrogen at an initial storage pressure of 350 bar, in a garage of volume 30 m^3 with an ACH of 0.18. The figure shows that the maximum overpressure for a currently typical PRD diameter of 5 mm may reach as much as 1.7 bar compared with 0.20 bar for the "safe" diameter, found to be 0.55 mm in this case. From Figure 1.24 it is demonstrated that for this specific case the PRD diameter should be reduced by an order of magnitude compared with a "typical" PRD diameter.

Figure 1.25 (Brennan and Molkov, 2013) illustrates nomograms allowing calculation of blowdown time for a tank containing 5 kg of hydrogen at storage pressure of 350 bar and 700 bar, based on assumption that maximum overpressure in the pressure peaking process shall not exceed 20 kPa. The nomograms allow one to determine "safe" PRD diameter for a given enclosure volume and ACH, as well as the duration of the blowdown process from initial tank pressure to a specified overpressure value. It can be seen that this "safe" PRD diameter is significantly smaller than "typical" PRD diameters currently being used. It can also be seen that for the lower ACH values the blowdown time through a "safe" diameter can take several hours. This is currently an unrealistic requirement for fire resistance rating and thus more innovative approaches should be considered for PRD and tank design.

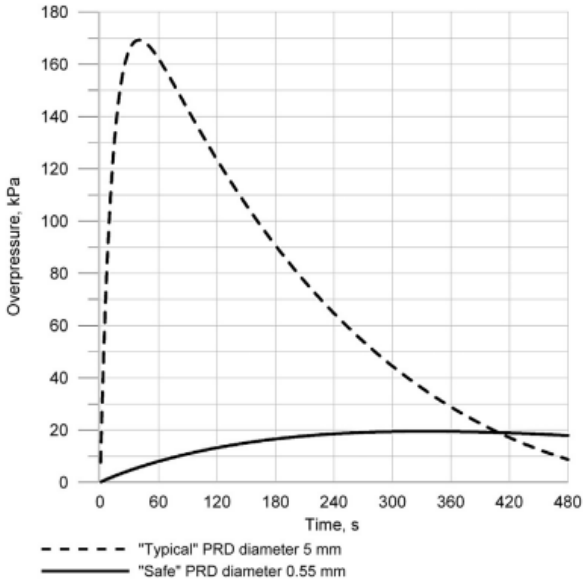

Figure 1.24: Overpressure dynamics in a 30 m^3 garage, ACH = 0.18, 5 kg of hydrogen at 350 bar, PRD diameters of 5 mm and 0.55 mm.

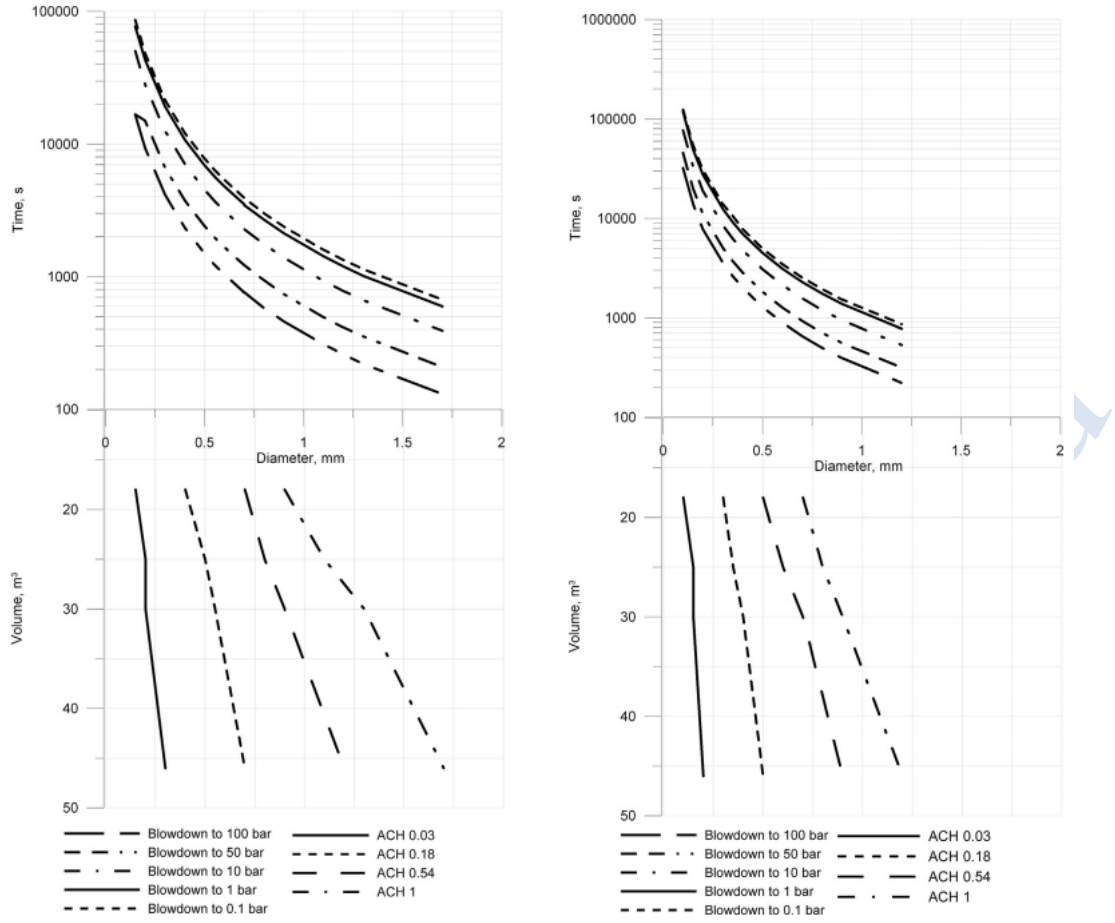

Figure 1.25: Nomogram for blowdown time assuming 5 kg hydrogen inventory stored at 350 bar (left) or 700 bar (right) pressure (Brennan and Molkov, 2013).

1.1.10.2 Stratified/layered versus uniform mixture regimes (NCSRD, UU)

Development of a stratified mixture composition in an enclosure with a single enclosed volume was experimentally studied and analysed by Cleaver et al. (1994) for a release of natural gas or propane from nozzles of diameter from 0.6 to 30 mm at pressure from 0.01 to 7 MPa (velocity from 4 m/s to sonic under-expanded jets, Cleaver et al., 1994). Experiments were conducted in three different enclosures of British Gas of size 3×3×3 m, 3×6×3 m, and 5.4×5.4×2.4 m. They were nominally unventilated with a hole of 12 mm diameter at base to prevent pressurisation. It was established that, in the range of geometrical configurations considered, to a first approximation the gas concentration in the bulk atmosphere of the enclosure was uniform across any given horizontal section. Typically, an upper well-mixed layer of constant depth was formed with a lower stratified layer growing beneath it (Cleaver et al., 1994). For any given release from a fixed position in the enclosure, an upward release produces a smaller well-mixed layer than the same release directed horizontally, and the largest well-mixed layer is formed if the release is aimed downwards as observed by Marshall (1983). Marshall also noted that whilst changes in the horizontal position of leak within the enclosure produced minor differences in mixing behaviour, the most significant changes arose when the height of the leak above the floor was varied.

Using the analysis by List (1979) and Chen and Rodi (1980) the length scale after which the momentum-dominated jet becomes buoyancy-controlled plume was given by Cleaver et al.

(1994) as

$$L = \frac{\alpha \cdot D}{2\sqrt{Ri_N}} \tag{1.90}$$

where α is the constant whose value is approximately 1.5, and the Richardson number of the inlet flow

$$Ri_N = \frac{D \cdot g_0'}{2u_N^2} \tag{1.91}$$

where u_N is the nozzle velocity, and the reduced gravity is $g_0' = g\left|\rho_{air} - \rho_{H_2}\right| / \rho_{H_2}$, in which ρ_{H_2} the hydrogen density and ρ_{air} is the density of air initially in the enclosure.

Under-expanded jet velocity and radius were calculated in (Cleaver, 1994) using the pseudo-source (notional nozzle) approach of Birch et al. (1984). For a horizontal release, the jet will turn up at a distance O(L) from the nozzle (Cleaver, 1994) . For a vertically downwards release, the jet penetrates a distance *L* before turning upwards. For a vertically upwards jet, at distance *L* the momentum flux produced by buoyancy is comparable with the initial momentum flux.

Cleaver et al. (1994) suggested a parameter which in their opinion provides some measure of the ability of the jet to promote mixing within the nominally closed space with a characteristic size $V^{1/3}$:

$$Ri_V = \frac{V^{1/3} \cdot g_0'}{u_N^2} \tag{1.92}$$

They argued that this parameter represents the ratio of the potential energy necessary to mix the gas uniformly throughout the enclosure compared with the kinetic energy of the jet. Unfortunately, the Ri_V criterion expressed by Eq. (1.92) is not applicable to estimate mixture uniformity for ventilated enclosure.

Linden (1999) described three canonical forms of stratification. Stable stratification when the horizontal interface separates denser fluid below the interface and lighter above the interface. Unstable stratification is characterised by denser fluid being above the interface. The gravity current is another form of stratification when a vertical interface separates regions of different density. Of these three, the stable stratification is the persistent feature, and the other two lead to rapid motion and redistribution of the density field towards the stable case.

Hydrogen releases and dispersion in enclosure can be divided in two main categories: release in closed enclosure and release in enclosure with openings for natural ventilation. In both categories according to the release rate different hydrogen distribution regimes can be formed. In the second category the vent size influences the characteristics of the each regime, such as the thickness of the homogeneous layer and the maximum concentration.

Closed enclosure:

When hydrogen is released vertically upwards in a closed enclosure the light hydrogen rises, reaches the ceiling, spreads to the sidewalls and then descends. Based on a work from CEA (Cariteau, 2010) depending on the volumetric Richardson number, three different distribution regimes can be identified in a closed enclosure (see Figure 1.26). The volumetric Richardson number is calculated by:

$$R_{iv} = g\frac{\rho_a - \rho_0}{\rho_0}\frac{V^{1/3}}{u_0^2} \quad (1.93)$$

where g is the gravitational acceleration, ρ_a is the air density, ρ_0 is the hydrogen density, V is the volume of the enclosure and u_0 is the average source velocity.

For very low volumetric Richardson number ($R_{iv} < 2.5 \cdot 10^{-3}$) the upper layer descends almost until the bottom of the enclosure and a homogeneous mixture inside the enclosure is formed.

For $0.0025 < R_{iv} < 3$, a homogeneous layer is formed in the upper layer of the enclosure, while a more or less stratified layer is formed in the lower part of the enclosure.

For $R_{iv} > 3$, stratification without homogenous layer is observed. This stratification regime could be linear or parabolic.

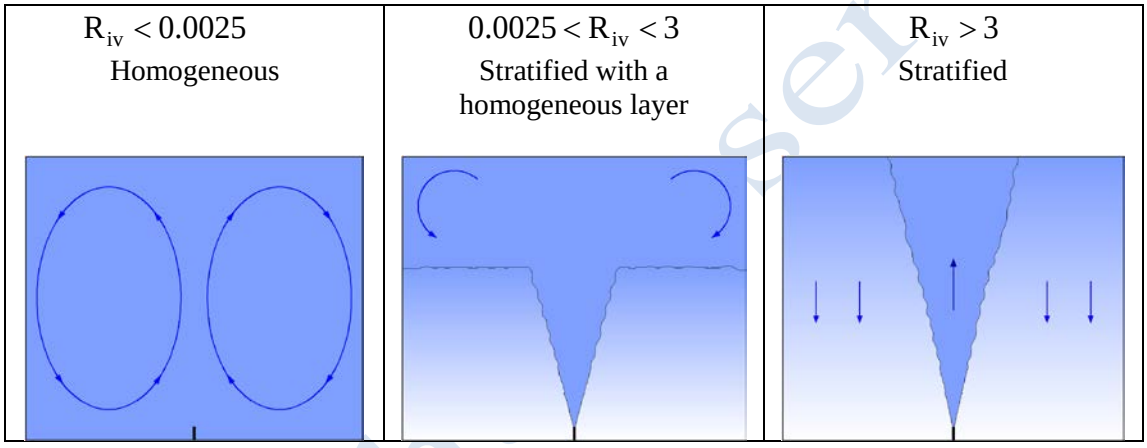

Figure 1.26: The different distribution regimes in a closed enclosure according to the volumetric Richardson number.

Enclosure with one vent:

In the case with a vent near the ceiling of the enclosure the distribution regimes are mainly defined by the volumetric Richardson number. When the R_{iv} becomes small compared to unity, an increase of the homogeneous layer in the upper part of the enclosure is observed (Cariteau, 2013). In very low R_{iv} values the dispersion is homogeneous over the height of the enclosure. The critical value of R_{iv} to reach the homogeneous mixture inside the enclosure is the approximately same as in the closed case, ie. 0.0023.

For $R_{iv} > 1$ the hydrogen distribution inside the enclosure exhibits some common characteristics regardless the vent size. There is an upper homogeneous layer followed by a steep gradient and a lower homogenous layer. Depending on the vent size, these regimes are characterized by different thickness, concentration and gradient. Large vent surface and vertical extension form a weakly apparent top homogeneous layer and small in thickness. Decreasing the vent surface, but keeping the vertical extension large, the top homogeneous layer is more apparent. In case of vent with very small vertical extension an additional zone with highly diluted layer of low thickness is formed (Cariteau, 2013).

Enclosure with two vents:

Consider the case of an enclosure with two vents: one close to the ceiling and the other one close to the floor. In that case the layer of buoyant fluid near the ceiling will drive a flow through the openings; inflow through the bottom vent and outflow through the top vent. A layer is formed near the ceiling whose thickness will increase as the layer is fed with buoyant fluid through the source, and the interface between the hydrogen-air mixture and the air will descend and approach the source (Prasad and Yang, 2011).

Also in this case the volumetric Richardson number defines the distribution regimes. For high volumetric Richardson numbers (small release rates) the dispersion regime is stratified, whilst for low volumetric Richardson number a bi-layer regime (homogeneous lower and upper layers with steep gradient in between) is formed (Houssin-Agbomson et al. 2013). The bi-layer regime appears for flow rates higher than 20NL/min.

1.1.11 Hydrogen propagation by diffusion (NCSRD)

Hydrogen is commonly stored in pressurized tanks. Compressed hydrogen can diffuse through the walls of the storage tank (permeation). If the storage tank is located in an enclosed structure, e.g. a garage, permeation can form a flammable hydrogen-air mixture, especially if the enclosure is not adequately ventilated. Therefore, the study of hydrogen propagation by diffusion (permeation rate) is of major concern. Previous studies have been focused on this subject (Saffers et al., 2011), (Adams, et al., 2011). The permeation rate is an issue for containers with non-metallic (polymer) liners, whilst is considered negligible for metallic containers or containers with metallic liners.

The permeation rate through a membrane is derived by:

$$J = P\frac{\sqrt{p_r}}{\ell} \tag{1.94}$$

where P is the material's permeability, p_r is the tank pressure and ℓ the membrane thickness.

Hydrogen molecules inside the walls of the tank are subjected to Brownian motion, i.e. the random movement of particles suspended in a fluid (a liquid or a gas) resulting from their collision with the quick atoms or molecules in the gas or liquid. According to Einstein's law (Einstein, 1905) the displacement of Brownian particle in direction of the x-axis, or precise, the root-mean-square displacement is:

$$\overline{\Delta x^2} = 2 \cdot D \cdot t \tag{1.95}$$

where D is the mass diffusivity.

The maximum displacement of molecules is $\sqrt{2 \cdot D \cdot t}$, where t is the time after the start of the permeation. The volume comprising all permeated hydrogen molecules

$$V_{mix} = A_r\sqrt{2 \cdot D \cdot t} \tag{1.96}$$

The number of moles of permeated hydrogen in this volume is

$$n = J \cdot t \cdot A_r \tag{1.97}$$

The volumetric hydrogen concentration on the tank's surface at time t, assuming the uniform distribution of hydrogen molecules in V_{mix} can be calculated as

$$xv_{h_2} = 100\frac{n \cdot V_m}{V_{mix}} \Rightarrow xv_{h_2} = 100\frac{J \cdot V_m}{\sqrt{2 \cdot D}} \times \sqrt{t} \quad (1.98)$$

where V_{H_2} is the molar volume of ideal gas in specific temperature.

The maximum hydrogen concentration in the tank's surface is obtained when quasi-steady state is reached. The quasi-steady state is established when diffusion and buoyancy balance each other. Based on the second Newton's law the displacement of mixture by buoyancy can be calculated by

$$L_x = \left(\frac{\rho_{air}}{\rho_{mix}} - 1\right) \cdot \frac{g \cdot t^2}{2} \quad (1.99)$$

And the density of the mixture is derived by the following equation

$$\rho_{mix} = \frac{xv_{H_2}}{100}\left(\rho_{H_2} - \rho_{air}\right) + \rho_{air} \quad (1.100)$$

By combining equations (1.98), (1.99) and (1.100) we can estimate the time, when quasi-steady state is reached

$$\sqrt{2 \cdot D \cdot t} = \left(\frac{\rho_{air}}{\frac{J \cdot t \cdot V_m}{\sqrt{2 \cdot D \cdot t}}\left(\rho_{H_2} - \rho_{air}\right) + \rho_{air}} - 1\right) \cdot \frac{g \cdot t^2}{2} \quad (1.101)$$

Finally, having estimated the time when quasi-steady state has been established we can also calculate the maximum hydrogen concentration on the tank's surface using equation (1.98). For instance, assuming permeation rate equal to 1 NmL/hr/L quasi-steady state is reached 37s after the start of the permeation process and the maximum hydrogen concentration is $2.4 \cdot 10^{-4}$% by volume (Saffers et al., 2011).

1.1.12 Hydrogen permeation and dispersion (UU)

Permeation is defined as diffusion through the walls or interstices of a container vessel, piping or interface material (SAE J2578, 2009). It is especially pronounced for hydrogen as it is the smallest element with a highest diffusivity. It is worth noting that hydrogen permeation is atomic through metals and molecular through polymers (Schultheiß 2007). Permeation may be categorised as a long term slow hydrogen release from a CGH2 system (Molkov, 2012). Controlling permeation has long been recognised as a key enabler in the development of hydrogen storage technologies (Mitlitsky et al., 2000). For metallic containers or containers with metallic liners the permeation rate can be considered negligible (Molkov, 2012). It can, however become an issue for containers with non-metallic (polymer) liners, i.e. so called Type IV containers (Commission Regulation, 2009).

The permeability of hydrogen for a particular material can be calculated as (Scheffer et al., 2006)

$$P = P_0 \exp(-E_0 / RT) \quad (1.102)$$

where the pre-exponential factor P_0 (mol/s/m/MPa$^{1/2}$) and the activation energy E_0 (J/mol) are material dependent and T is the temperature (K). The permeation rate through a single material's membrane is calculated using the equation (Scheffer et al., 2006)

$$J = P\frac{\sqrt{P_R}}{l} \tag{1.103}$$

where J is permeation rate (mol/s/m^2), l is reservoir thickness and P_R is the pressure in the reservoir. The permeation rate increases with an increase of storage pressure P_R and a decrease of membrane thickness l. Equations (1.102) and (1.103) are valid for metallic and non-metallic materials (Schultheiß, 2007) and applicable to a single membrane's wall but under limited range of pressure and temperature (from 10 Pa to 50 MPa and ambient temperature less than 1273 K) (San Marchi, et al., 2007).

For serial membranes of different materials like the ones used in type IV tanks the total permeability for z layers can be calculated using other correlations found in literature, e.g. (Crank, 1975)

$$\frac{l}{P} = \sum_{i=1}^{z}\frac{l}{P_i} \tag{1.104}$$

Dispersion of permeated hydrogen is a physical phenomenon essentially different from classical plumes and jets. Hydrogen "leaks" in very small amounts uniformly along the surface of high-pressure storage tank during permeation. Then hydrogen is driven out of the surface by diffusion and buoyancy. In order to evaluate the hydrogen concentration produced by the permeation from the reservoir in an enclosure through either analytical or numerical means, it is important to consider what maximum concentration of permeated hydrogen will be achieved at a tank surface.

Using Einstein's law (1905) for Brownian motion, the root-mean-square displacement of the hydrogen molecules can be estimated, and, assuming uniform distribution of hydrogen molecules in mixture volume V_{mix}, the volumetric concentration of hydrogen on the tank's surface at the time t can be calculated as

$$\left[H_2\right]_t = 100\frac{JV_{m25}}{\sqrt{2D}}\times\sqrt{t} \tag{1.105}$$

where V_{m25} is the molar volume of ideal gas at 25ºC (0.0244 m^3/mol) and $D = 7.79\times10^{-5}$ m^2/s is the hydrogen diffusion in air at 25ºC (Saffers et al., 2011), t – time (s).

The buoyancy effect increases with the increase of hydrogen concentration in air. Thus, the hydrogen concentration on the tank surface increases with time as per (1.105) until the buoyancy will overcome diffusion transport of hydrogen. A quasi-steady state will be established when diffusion and buoyancy will balance each other. It can be shown (Saffers et al., 2011) that displacement of hydrogen by buoyancy becomes of the same order as the displacement of hydrogen by diffusion and concentration at the reservoir surface reaches the quasi-steady state when

$$\sqrt{2Dt} = \left(\frac{\rho_{air}}{\frac{JtV_{m25}}{\sqrt{2Dt}}\left(\rho_{H_2}-\rho_{air}\right)+\rho_{air}}-1\right)\cdot\frac{gt^2}{2} \tag{1.106}$$

where g is the acceleration of gravity.

Permeation rate is highly dependent on the temperature of container walls (Mitlitsky et al., 2000). It was concluded (Adams et al., 2011), however, that the only time the temperature of the container would approach the maximum values currently specified by existing Regulation, Codes and Standards (RCS) would be shortly after fast refuelling and of relatively short duration.

1.1.13 LH2 releases and dispersion (NCSRD)

A practice to handle, store and distribute hydrogen is its liquefaction at elevated pressure and low temperatures. Therefore, the risks of an accidental cryogenic release should be evaluated in order to prevent the possible catastrophic consequences and to mitigate the danger. A prior condition for the development of a risk and safety assessment is the fully understanding of the phenomenon and the physical mechanisms. A failure of the cryogenic tank, any of the pipes, control valves, etc. could cause the spill of the liquid hydrogen and the formation of a flammable cloud. The risk associated vary and depend on the release and surrounding conditions (confined area, open area, obstacle or not, wind etc.).

It is necessary to define the conditions that determine the danger and to define the safety zones in each possible scenario in order to take the appropriate measures to minimize the risks. This need led also the research community to orient towards the liquefied hydrogen (LH2) release and dispersion study. Those analyses are conducted utilizing both experiments and simulations.

In this section, we present the physical theory explaining the LH2 release and dispersion in the most concise and explanatory way.

During a LH2 release, a flashing jet is formed. Both vapour and liquid phase of the hydrogen coexist in the pipe exit, and a two phase flow is created in which liquid droplets- follows the vapour phase.

The flashing releases can be divided to three regions downstream the release point (Kelsey 2002):

1. Initial non-equilibrium region: In this region the flashing happens as the released liquid adjusts from the nozzle exit conditions -approximately ambient temperature and equivalent saturation pressure- to a point where thermal equilibrium at atmospheric pressure is attained. In this region it is assumed that no mixing and energy exchange with the surrounding occurs. At the end of this region vapour and droplets coexist in thermal equilibrium at the saturation temperature of the atmospheric pressure.

2. Momentum jet: In this region air entrainment takes place. Initially, the jet consists of droplets, vapour and air. Air entrainment replaces the vapour and results in a vapour concentration fall. Thus, in order to reach equilibrium with the vapour partial pressure, the droplets evaporate and their temperature drops, since heat is consumed for their evaporation. The freezing and condensation of the air and of the ambient humidity that entrains the jet is also an additional heat source.

3. Only vapour phase: In this region, most of droplets have already evaporated, and the temperature starts to increase due to the entrainment of the relatively hot ambient air.

If the evaporation rate of the droplets is low enough, some may precipitate creating a liquid pool that will exist until its evaporation (see Figure 1.27).). In this way, a cryogenic pool is created which expands radially away from the release point depending on the volume spilled and the spill rate, and which starts to vaporize immediately. Several heat sources may heat up

the pool, namely, the ground, the ambient atmosphere, and in case of a burning pool the flame radiation. (Dienhart 1995) reported that the dominant heat source for all cryogens is the ground heat conduction. Especially, for LH2 and in non-burning pool cases the estimated error of neglecting all other sources appears to be about 2%. An additional heat source that should be considered is the condensation and solidification of air falling into the pool, due to the extremely low temperatures, below air's boiling point. The contribution of humidity condensation and solidification could be also a significant heat input.

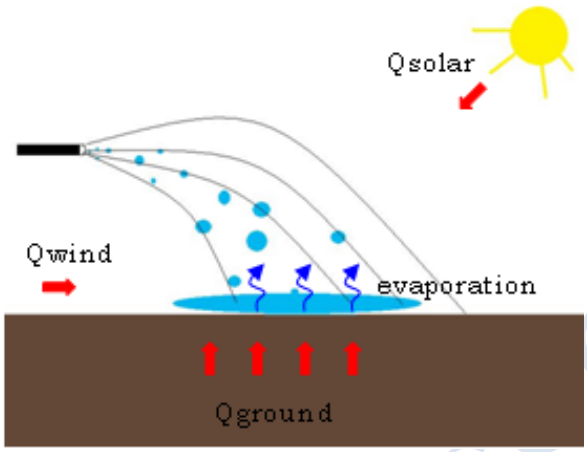

Figure 1.27: Heat sources from the surroundings to the cloud and the cryogenic pool.

The main characteristics of the cryogenic pool are its extremely low temperature (equal to the saturation temperature at atmospheric pressure), and its large temperature difference with the ground at the beginning. As time passes, the ground gets colder, and the temperature difference decreases. The heat conduction from the ground changes in different regimes that variate according to the temperature difference, as shown in Figure 1.28. In Figure 1.29 the boiling curve of liquid hydrogen is displayed as reported in (Louis 1987).

When the liquid hydrogen gets initially in contact with the ground the temperature difference is the largest, and the liquid vaporizes without delay and generates a vapour cushion between the ground (hot) and the liquid (Film Boiling regime). As the ground becomes colder the temperature difference decreases until a moment (the Leidenfrost point) at which the heat flux from the ground to the pool is the minimum. From this moment, the heat flux rises with a decreasing temperature difference (Transition regime), because the vapour film becomes unstable and gradually it collapses, resulting in a larger heat transfer through a closer contact between the pool and the ground. This regime continues until a point where a maximum heat transfer (Critical heat flux) is achieved. At this stage the heat transfer coefficient has reached a maximum and any increase in temperature difference is balanced with the reduction of heat transfer due to the bubbles that hinder the liquid to completely wet the ground and receive its corresponding heat. Below this point the regime is called Nucleate Boiling. This regime is characterized by the existence of bubbles that escape from the liquid forming columns and jets and allowing a more intense motion of the liquid near the surface, and consequently a more efficient heat flux. In his region the heat transfer growths with an increase of the temperature difference until the critical heat flux is reached. Below point A in Figure 1.28 (Onset temperature) the natural convection takes place.

In the case where the release is above liquid, e.g. above water surface, the liquid hydrogen that will fall on the water will be spread over the surface quite rapidly, considering that it is lighter than the liquid substrate. The water is exposed to a fluid with much lower temperature

and in case of a prolonged contact an ice layer might form which thickness will increase with time. The presence of an ice layer changes the heat transfer rate to the LH2 and leads to the collapse of the film boiling, altering the heat transfer mechanism. However, if the spill happens on unconfined water surface and/or in deep water, an ice layer is difficult to form, because of the high heat capacity of water. In addition, the water currents and waves prevent the ice formation. In this case it is most likely that only film boiling would occur.

The amount of liquid hydrogen that has not fallen to the ground travels along with the vapour cloud in form of droplets. The droplets are of different size and shape. However, in the modelling they are considered to be spherical, which is an acceptable assumption. The droplets evaporate absorbing heat from their surroundings and their size decreases in time until they are totally evaporated. Until all droplets are evaporated, they can influence the vapour dispersion and the vapour dispersion can influence them, as in any typical two phase particulate flow. The vapour influences the droplets via drag and turbulence, and so the droplets influence the vapour's mass, momentum and energy. The void fraction of the liquid phase determines the interaction of the two phases (vapour and liquid). For those cases characterized by low liquid void fractions ($<10^{-6}$), or with very large ratio of droplets' distances to centres to droplets' diameter (>100), the flow is characterized dilute and it has one way coupling. One way coupling means that the vapour phase affects the motion and temperature of the droplets, but the droplets do not affect the velocity or thermal flow fields. In case with intermediate liquid void fraction, or intermediate ratios of droplets' centre distance to droplets' diameter, the flow is characterized dilute too, but it has two way coupling. Two way coupling is the mutual interaction between phases. Finally, in very large liquid void fraction ($>10^{-3}$), or small ratios of droplets' centre distance to droplets' diameter (<10) the flow is characterised as dense flow and it is four-way coupled. In four-way coupling the droplets' collisions are very significant and could also result in coalescence. The way the flow is coupled is important in order to apply the best modelling approach.

Furthermore, several forces are acting on the formed droplets. Among them the most important are the drag force, lift force and virtual mass force, i.e. the inertia added to a system because an accelerating or decelerating particle must move (or deflect) some volume of the surrounding fluid as it moves through it. In the modelling the later two are usually neglected and only the first one (drag force) is considered important.

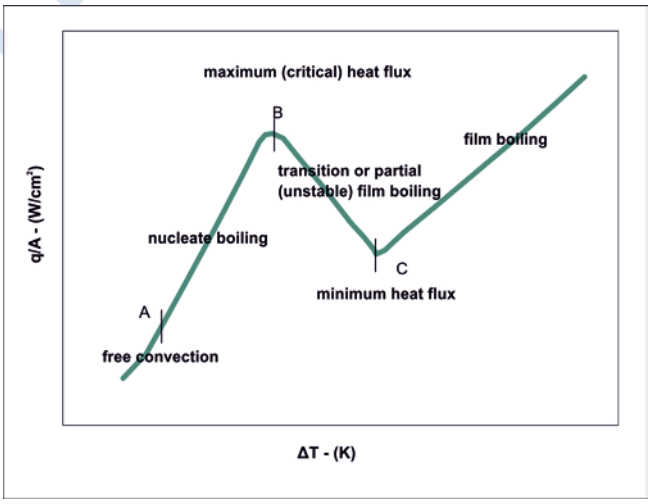

Figure 1.28: Quantitative boiling curve of liquids and the distinct regimes.

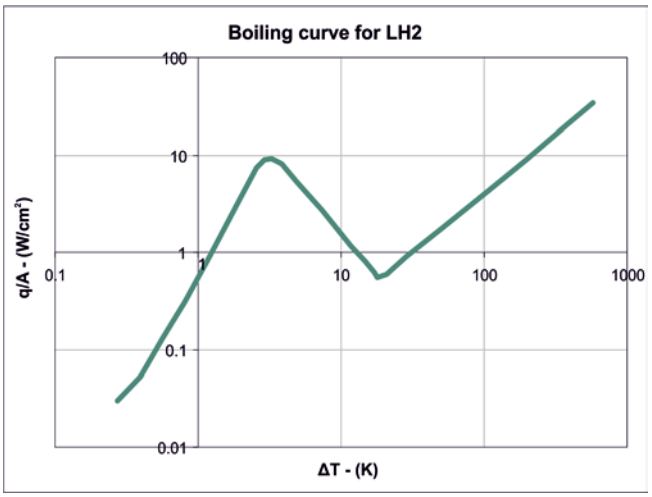

Figure 1.29: The characteristic boiling curve for LH2.

Finally, in LH2, and in general cryogenic releases and dispersion, air condensation and freezing takes place due to the very low prevailing temperatures. In particular, the air components are condensed or even frozen (oxygen and nitrogen). By means of condensation and freezing an amount of heat equal to the enthalpy of vaporization and fusion of oxygen and nitrogen is released. When the air is humid, the humidity is also condensed and solidified releasing an extra amount of thermal energy. The phase change of air components and humidity turns the two phase jet (liquid + vapour hydrogen) into three phase mixture with four components (solid water, nitrogen and oxygen plus liquid water, nitrogen, oxygen and hydrogen plus vapour water, nitrogen, oxygen and hydrogen). The formed air and water droplets and/or ice crystals can be treated similarly to the hydrogen droplets as described above. The air phase change is most likely to take place in a region near the spill point, while the humidity phase change takes place in amore extended area and its affect might be more significant.

1.2 Models (NCSRD)

The flow of a fluid can be described mathematically by a system of equations that represents the three basic conservation laws of:

- Mass
- Momentum
- Energy

The following section describes the conservation laws in terms of Cartesian coordinates for a fixed fluid element.

1.2.1 Navier-Stokes equations, continuity, energy and species transport (HSL)

Continuity equation – Conservation of mass

A mass balance across a fluid element can be written as:

(1.107)

$$\frac{\partial \rho}{\partial t} + \frac{\partial \rho U_i}{\partial x_i} = 0$$

where ρ is the fluid density, U_i is the velocity component in spatial coordinate "i", t is time and x_i is the spatial coordinate in the i-direction.

Navier-Stokes equations – Conservation of momentum

The Navier-Stokes equations describe the conservation of momentum in the three spatial directions:

$$\frac{\partial \rho U_i}{\partial t} + \frac{\partial \rho U_i U_j}{\partial x_j} = -\frac{\partial P}{\partial x_i} + \mu \frac{\partial^2 U_i}{\partial x_j^2} + \rho g_i \quad (1.108)$$

where P is the pressure, μ is the viscosity and g_i is the gravitational acceleration in the i-direction. The terms on the left represent inertia and those on the right represent body forces arising from pressure, viscosity and other body forces such as gravity.

Conservation of energy

Conservation of energy is represented by the transport of enthalpy (h):

$$\frac{\partial \rho h}{\partial t} + \frac{\partial \rho U_i h}{\partial x_i} = \frac{\partial}{\partial x_i}\left[\lambda \frac{\partial T}{\partial x_i}\right] + \frac{\partial p}{\partial t} + \Phi + S \quad (1.109)$$

where λ is the thermal conductivity, S is the source term and Φ represents the energy addition through viscous shearing. This term, called the "viscous work term" is often ignored as it is small in most flows.

Species transport equations

Transport of additional species is represented by a general transport equation:

$$\frac{\partial \rho Y_k}{\partial t} + \frac{\partial \rho U_i Y_k}{\partial x_i} = \frac{\partial}{\partial x_i}\left[\mathrm{D} \frac{\partial Y_k}{\partial x_i}\right] + S \quad (1.110)$$

where Y_k is the mass fraction of species k, D is the diffusivity of the species and S is the source term. The density, ρ, is the density of the mixture.

1.2.2 Laminar model (NCRD)

In the Laminar model, the equations which were presented in the previous paragraph are solved without modifications. In order to make reliable predictions, the modelled flow needs to be laminar. In the case of turbulent flows a turbulent model need to be used, as we will discuss in paragraph 1.2.3. However weakly turbulent flows may be simulated with satisfactory accuracy with laminar model, mainly in the case where a dense grid is used.

1.2.3 Turbulence closure models (NCSRD)

1.2.3.1 RANS (k-e, SST, etc.) (NCSRD)

The equations in the paragraph 1.2.1 refer to the instantaneous values of the variables. Unfortunately as we describe in paragraph 1.1.1 in turbulent flows the values of these variables change rapidly in both space and time. In such flows the numerical solution of the equations demands an extremely large number of grid points and a very small time step. As a result, the simulation of medium or large scale scenarios is impossible with the today computational power.

In order to be able to simulate turbulent flows in real case scenarios, we average the balance equations in order to describe only the mean flow field. Therefore, we calculate the mean values of the variables and not the instantaneous. In other words, the local fluctuations and turbulent structures are integrated in mean quantities and they are not resolved in the simulation. The first person who formulated this procedure for incompressible flows was Reynolds (Reynolds 1895) and as a result the numerical procedure is called Reynolds Averaged Navier-Stokes (RANS).

In this method, each quantity f (for example velocities, density, pressure, temperature) is decomposed into a mean $\overline{f}$ and a fluctuation f':

$$f = \overline{f} + f' \tag{1.111}$$

The mean value can be defined by the equation:

$$\overline{f} = \frac{1}{\Delta t}\int_{t_0-\Delta t/2}^{t_0+\Delta t/2} f dt \tag{1.112}$$

where Δt must be bigger than the turbulence time scale but smaller than the time scale which characterize the unsteadiness behaviour of the mean flow field. By definition we have that:

$$\overline{f'} = 0 \tag{1.113}$$

Some useful relations coming out from the above equations are:

$$\overline{f+g} = \overline{f} + \overline{g},\ \overline{\overline{f}g'} = 0,\ \overline{\overline{f}g} = \overline{f}\,\overline{g},\ \overline{\frac{\partial f}{\partial s}} = \frac{\partial \overline{f}}{\partial s} \tag{1.114}$$

The above formulation is more appropriate for incompressible flows. For flows where density variations cannot be omitted, the above averaging introduces many extra terms to the averaged equations. For example, if we average the continuity equation we conclude to the equation:

$$\frac{\partial \overline{\rho}}{\partial t} + \frac{\partial}{\partial x_i}\left(\overline{\rho}\,\overline{u_i} + \overline{\rho' u_i'}\right) = 0 \tag{1.115}$$

where the velocity-density fluctuations correlation $\overline{\rho' u_i'}$ appears. To avoid the explicit modelling of such correlations, a mass weighted (Favre) average is preferred (Favre 1992). In this method, each quantity f is decomposed into a mean $\tilde{f}$ and a fluctuating part f'':

$$f = \tilde{f} + f'' \tag{1.116}$$

where

$$\tilde{f} = \frac{\overline{\rho f}}{\bar{\rho}} \tag{1.117}$$

Some useful relations coming out from the above equations are:

$$f'' = 0 \ , \ \overline{\rho f''} = 0 \, , \ \overline{f''} \neq 0 \tag{1.118}$$

Favre averaged equations

Next the Favre averaged balance equations (Cebeci, 1974), (Poinsot & Veynante 2005) are presented using the Einstein summation convention. The average **continuity equation** is:

$$\frac{\partial \bar{\rho}}{\partial t} + \frac{\partial}{\partial x_j}\left(\bar{\rho}\tilde{u}_j\right) = 0 \tag{1.119}$$

We notice that no extra term is appeared in the average equation. The average **momentum equations** are ($i = 1, 2, 3$):

$$\frac{\partial \bar{\rho}\tilde{u}_i}{\partial t} + \frac{\partial}{\partial x_j}\left(\bar{\rho}\tilde{u}_j\tilde{u}_i\right) = -\frac{\partial \bar{p}}{\partial x_i} + \frac{\partial \bar{\tau}_{ij}}{\partial x_j} - \frac{\partial}{\partial x_j}\left(\bar{\rho}\overline{u_i''u_j''}\right) + \bar{\rho}g_i \tag{1.120}$$

where g_i is the acceleration of gravity in i direction. The average viscous stresses for a Newtonian fluid are equal to:

$$\bar{\tau}_{ij} = \mu\left[\left(\frac{\partial \tilde{u}_i}{\partial x_j} + \frac{\partial \tilde{u}_j}{\partial x_i}\right) - \frac{2}{3}\delta_{ij}\frac{\partial \tilde{u}_k}{\partial x_k}\right] + \mu\left[\left(\frac{\partial \overline{u_i''}}{\partial x_j} + \frac{\partial \overline{u_j''}}{\partial x_i}\right) - \frac{2}{3}\delta_{ij}\frac{\partial \overline{u_k''}}{\partial x_k}\right] \tag{1.121}$$

where we omit the variations of viscosity μ. The second bracket of the above equation is usually small and is neglected so the above equation is reduced to:

$$\bar{\tau}_{ij} = \mu\left[\left(\frac{\partial \tilde{u}_i}{\partial x_j} + \frac{\partial \tilde{u}_j}{\partial x_i}\right) - \frac{2}{3}\delta_{ij}\frac{\partial \tilde{u}_k}{\partial x_k}\right] \tag{1.122}$$

We observe that equation (1.120) differs from the original (non-average) momentum equations by the quantities $\bar{\rho}\overline{u_i''u_j''}$. These quantities are called Reynolds stresses. Turbulent modelling provides an approximation for these terms, as we will see next.

The average equation for the **conservation of species *k*** is ($k = 1, 2, \ldots$):

$$\frac{\partial \bar{\rho}\tilde{Y}_k}{\partial t} + \frac{\partial}{\partial x_j}\left(\bar{\rho}\tilde{u}_j\tilde{Y}_k\right) = -\frac{\partial}{\partial x_j}\left(-\bar{\rho}\bar{D}_k\frac{\partial \tilde{Y}_k}{\partial x_j}\right) - \frac{\partial}{\partial x_j}\left(\bar{\rho}\overline{u_j''Y_k''}\right) + \bar{\dot{\omega}}_\kappa \tag{1.123}$$

where $\bar{\dot{\omega}}_\kappa$ is the mean reaction rate and $\bar{D}_k$ is the species molecular diffusion for species k. In the above equation the assumption that $-\overline{\rho D_k \frac{\partial Y_k}{\partial x_j}} = -\bar{\rho}\bar{D}_k\frac{\partial \tilde{Y}_k}{\partial x_j}$ is made. The new quantity $\bar{\rho}\overline{u_j''Y_k''}$ which appears because of the averaging needs to be modelled. The common practice is to treat it like it is a turbulent analogue to the molecular diffusion (gradient assumption) (Poinsot & Veynante 2005). Thus:

$$\overline{\rho}\widetilde{u_j''Y_k''} = -\frac{\mu_t}{Sc_{kt}}\frac{\partial \tilde{Y}_k}{\partial x_j} \tag{1.124}$$

where μ_t is the turbulent viscosity which is estimated from the turbulent model and Sc_{kt} is the turbulent Schmidt number for species k which is defined as the ratio of the turbulent momentum diffusivity and the turbulent mass diffusivity. Turbulent Schmidt number usually takes values around 0.7 but in general the optimum value can be varied dependent on the case (see for example (Tominaga & Stathopoulos 2007)).

The average equation for the **conservation of energy** can take many forms, for example conservation of enthalpy, total enthalpy, energy, total energy and temperature. The averaged conservation equation of the enthalpy of the mixture H is:

$$\begin{aligned}\frac{\partial \overline{\rho}\tilde{H}}{\partial t} + \frac{\partial}{\partial x_j}\left(\overline{\rho}\tilde{u}_j\tilde{H}\right) = \overline{\frac{Dp}{Dt}} + \overline{\tau_{ij}\frac{\partial u_i}{\partial x_j}} + \frac{\partial}{\partial x_j}\left(\overline{\lambda\frac{\partial T}{\partial x_j}} - \overline{\rho}\widetilde{u_j''H''}\right) \\ -\frac{\partial}{\partial x_j}\sum_{k=1}^{N}\tilde{H}_k\left(-\overline{\rho}\overline{D}_k - \frac{\mu_t}{Sc_{kt}}\right)\frac{\partial \tilde{Y}_k}{\partial x_j} + \dot{\bar{\omega}}_T\end{aligned} \tag{1.125}$$

where $\dot{\bar{\omega}}_T$ is the source term, λ is the thermal conductivity and H_k is the enthalpy of the species k. The term $\overline{\frac{Dp}{Dt}}$ is modelled as $\overline{\frac{Dp}{Dt}} = \frac{\partial \overline{p}}{\partial t} + \overline{u_i\frac{\partial p}{\partial x_i}} \approx \frac{\partial \overline{p}}{\partial t} + \tilde{u}_i\frac{\partial \overline{p}}{\partial x_i}$ and the term $\overline{\lambda\frac{\partial T}{\partial x_j}}$ as $\overline{\lambda\frac{\partial T}{\partial x_j}} = \overline{\lambda}\frac{\partial \tilde{T}}{\partial x_j}$. The new quantity $\overline{\rho}\widetilde{u_j''H''}$ which appears because of the averaging is modelled by using again the gradient assumption like in the conservation of species case:

$$\overline{\rho}\widetilde{u_j''H''} = -\frac{\mu_t c_p}{\mathrm{Pr}_t}\frac{\partial \tilde{T}}{\partial x_j} \tag{1.126}$$

where c_p is the specific heat coefficient at constant pressure, Pr_t is the turbulent Prandlt number which is defined as the ratio of the turbulent momentum diffusivity and the turbulent thermal diffusivity. Turbulent Prandlt number usually takes values around 0.7.

Reynolds stresses

The above formulation introduce six more unknown in the equations, the Reynolds stresses $\overline{\rho}\widetilde{u_i''u_j''}$. There are two main types of models, which tries to estimates these stresses. The first one is called *first order closures* and is based in Boussinesq hypothesis (Wilcox 1994). The second type is called *second order closures*. The main representative of the second type of model is the Reynolds Stress Model (RST) (Launder et al. 1975) which solves a transport equation for each of the six stresses. As a result this model has great computational demands. Furthermore each transport equation introduces addition unknowns which need to be modelled. On the other hand it can produce good results in cases where the other models fail. Because of its complexity however it is rarely used in large scale simulations. Next we will discuss only RANS type of models which are based on Boussinesq hypothesis. Those models have been mainly used in hydrogen safety applications.

As we saw in paragraph 1.1.1, turbulence extracts energy from the main flow and turns it into thermal energy (dissipation). Furthermore, it increases the heat, mass and momentum transfer to the normal to the main flow direction (diffusivity). An analogue exists in laminar flows, where the same phenomenon are observed driven by viscosity. As a results it is a natural choice to try to model the unknown Reynolds stresses like viscous stresses (eq. (1.122)) by introducing the quantity of turbulent viscosity μ_t (Boussinesq hypothesis):

$$-\bar{\rho}\widetilde{u_i''u_j''} = \mu_t\left(\frac{\partial\tilde{u}_i}{\partial x_j}+\frac{\partial\tilde{u}_j}{\partial x_i}\right)-\frac{2}{3}\delta_{ij}\left(\mu_t\frac{\partial\tilde{u}_k}{\partial x_k}+\bar{\rho}k\right) \tag{1.127}$$

where k is the turbulent kinetic energy defined by the equation:

$$k=\frac{1}{2}\widetilde{u_k''u_k''}=\frac{1}{2}\left(\widetilde{u_1''u_1''}+\widetilde{u_2''u_2''}+\widetilde{u_3''u_3''}\right) \tag{1.128}$$

The term $\bar{\rho}k$ in equation (1.127) have been added for consistency: if we add the three normal stresses $\rho\widetilde{u_1''u_1''}$, $\rho\widetilde{u_2''u_2''}$ and $\rho\widetilde{u_3''u_3''}$ for an incompressible flow field (where the sum $\frac{\partial\tilde{u}_k}{\partial x_k}$ is zero due to the continuity equation) the equation for the turbulent kinetic energy (1.127) will be derived.

As we saw in the previous paragraph, the Favre averaged equations are very similar to the instantaneous one. The only difference between the equations is the introduction of the turbulent viscosity μ_t in the averaged one. In next, the basic turbulence models which estimate turbulent viscosity will be presented. Usually turbulence models assume that turbulent viscosity is proportional to a characteristic velocity and to a characteristic length of turbulence. Thus, the turbulence models differ from each other basically in the way they estimate these characteristic quantities. Turbulence models can be categorized based on the number of transport equations that they need to solve in order to calculate these quantities. There are three main approaches: algebraic expressions which do not require any additional balance equation (zero-equation models), one-equation models and two-equation models.

Mixing length model

In zero-equation model also called mixing length models, the turbulent viscosity is calculated by algebraic expressions which are functions of the mean variables of the flow without the need of additional transport equations. As a result these models may not be able to account properly for history effects of turbulence such as convection and diffusion of turbulent energy. On the other hand they are simple to implement and they do not require additional computing power.

Prandlt suggested (Prandtl, 1925) the following equation for the turbulent viscosity which uses the shear deformation rate as the characteristic velocity of turbulence:

$$\mu_t = C\bar{\rho}l_m^2\left|\tilde{S}\right| \tag{1.129}$$

where C is a model constant, l_m is a mixing length and $\left|\tilde{S}\right|$ is equal to:

$$\left|\tilde{S}\right| = \sqrt{2S_{ij}S_{ij}}\ ,\ \tilde{S}_{ij} = \frac{1}{2}\left(\frac{\partial \tilde{u}_i}{\partial x_j} + \frac{\partial \tilde{u}_j}{\partial x_i}\right) \tag{1.130}$$

Equations providing mixing length for some types of flow can be found in (Rodi 1993).

Other popular zero-equation model which are variants of the mixing length model, are the Baldwin-Lomax model and the Cebeci-Smith model (Wilcox 1994).

One-equation model

One typical example of one-equation turbulence model is the Prandtl-Kolmogorov model (Wilcox 1994), (Poinsot & Veynante 2005). It uses the square root of turbulent kinetic energy as characteristic turbulence velocity in order to calculate turbulent viscosity:

$$\mu_t = C_\mu \bar{\rho} l \sqrt{k} \tag{1.131}$$

where C_μ is a model constant (usually $C_\mu = 0.09$) and l a characteristic length. The transport equation for turbulent kinetic energy is:

$$\frac{\partial \bar{\rho} k}{\partial t} + \frac{\partial}{\partial x_j}\left(\bar{\rho}\tilde{u}_j k\right) = \frac{\partial}{\partial x_j}\left[\left(\mu + \frac{\mu_t}{\sigma_k}\right)\frac{\partial k}{\partial x_j}\right] + P + G - \bar{\rho}\varepsilon \tag{1.132}$$

where G represents the generation of turbulence kinetic energy due to buoyancy and P the generation due to the mean velocity gradient. G and P are given by the relations:

$$G = -\frac{\mu_t}{\rho \,\mathrm{Pr}_t}\frac{\partial \rho}{\partial x_i} g_i \tag{1.133}$$

$$P = \mu_t \left(\frac{\partial \tilde{u}_i}{\partial x_j} + \frac{\partial \tilde{u}_j}{\partial x_i}\right)\frac{\partial \tilde{u}_i}{\partial x_j} \tag{1.134}$$

σ_k is the turbulent Prandlt number for k and it is usually considered equal to 1.0. ε is the (isotropic part of) dissipation rate of turbulent energy which is defined as:

$$\varepsilon = \frac{\mu}{\rho}\overline{\frac{\partial u_i'}{\partial x_j}\frac{\partial u_i'}{\partial x_j}} \tag{1.135}$$

and which is modeled as:

$$\varepsilon = C_D \frac{k^{3/2}}{l} \tag{1.136}$$

where the constant C_D takes values between 0.07 and 0.09. The unit of ε is m^2/s^3.

k-ε model

The better known two-equations turbulence model is the k-ε model (Launder & Spalding 1974). In this model two transport equations are solved, one for the turbulent kinetic energy (eq. (1.132)) and one for the dissipation rate of turbulent energy ε. The model uses the square root of turbulent kinetic energy as characteristic turbulence velocity and the amount

$k^{3/2}/\varepsilon$ as the characteristic length. Therefore the turbulent viscosity is estimated by the relation:

$$\mu_t = \bar{\rho} C_\mu \frac{k^2}{\varepsilon} \tag{1.137}$$

where the usual value of C_μ is 0.09. The transport equation of the dissipation rate ε is:

$$\frac{\partial \bar{\rho}\varepsilon}{\partial t} + \frac{\partial}{\partial x_j}\left(\bar{\rho}\tilde{u}_j \varepsilon\right) = \frac{\partial}{\partial x_j}\left[\left(\mu + \frac{\mu_t}{\sigma_\varepsilon}\right)\frac{\partial \varepsilon}{\partial x_j}\right] + C_{1\varepsilon}\frac{\varepsilon}{k}\left(P + C_{3\varepsilon}G\right) - C_{2\varepsilon}\bar{\rho}\frac{\varepsilon^2}{k} \tag{1.138}$$

where the usual choice for the constants are $C_{1\varepsilon} = 1.44$ and $C_{2\varepsilon} = 1.92$, and for the turbulent Prandlt number σ_ε is 1.3. The constant $C_{3\varepsilon}$ defines the degree at which buoyancy affects ε (Markatos & Pericleous 1984). One choice for it is (Venetsanos et al. 2010) $C_{3\varepsilon} = 0$ if $G \le 0$ (stable stratification) and $C_{3\varepsilon} = 1$ if $G > 0$ (unstable stratification). Another choice is to use the equation $C_{3\varepsilon} = \tanh\left|\frac{w}{u}\right|$ (Henkes et al. 1991) where w is the velocity component at the direction of gravity and u is the velocity component at the perpendicular to gravity direction. The values of $C_{3\varepsilon}$ is between 0 (when flow direction is perpendicular to the direction of gravity) and 1 (when flow direction is the same as the direction of gravity).

k-ε model have been extensively used with success in various application. It has shown good predicted capabilities in hydrogen dispersion applications too (Matsuura et al. 2008), (Papanikolaou et al. 2010).

RNG k-ε model

The RNG k-ε model was developed by using a statistical technique called Renormalisation group theory in order to account for the effects of all turbulent scales (Yakhot et al. 1992). In k-ε model the turbulent viscosity is determined from a single turbulence length scale. As a result turbulent diffusion is calculated based on a specific scale, whereas in reality all turbulent scales are contribute to turbulence.

Its formulation is similar to the k-ε model. Two balance equations are solved, one for the turbulent kinetic energy k and one for the dissipation rate ε:

$$\frac{\partial \bar{\rho}k}{\partial t} + \frac{\partial}{\partial x_j}\left(\bar{\rho}\tilde{u}_j k\right) = \frac{\partial}{\partial x_j}\left(\frac{\mu_{eff}}{\sigma_k}\frac{\partial k}{\partial x_j}\right) + P + G - \bar{\rho}\varepsilon \tag{1.139}$$

$$\frac{\partial \bar{\rho}\varepsilon}{\partial t} + \frac{\partial}{\partial x_j}\left(\bar{\rho}\tilde{u}_j \varepsilon\right) = \frac{\partial}{\partial x_j}\left(\frac{\mu_{eff}}{\sigma_\varepsilon}\frac{\partial \varepsilon}{\partial x_j}\right) + C_{1\varepsilon}\frac{\varepsilon}{k}\left(P + C_{3\varepsilon}G\right) - C_{2\varepsilon}\bar{\rho}\frac{\varepsilon^2}{k} - R_\varepsilon \tag{1.140}$$

where $\mu_{eff} = \mu + \mu_t$. The main difference from the equations of k-ε model is the introduction of the new term R_ε in the equation of ε. This term improves the accuracy of the model in rapidly strained flows. R_ε is given from the relation:

$$R_\varepsilon = \frac{C_\mu \bar{\rho}\eta^3\left(1-\eta/\eta_0\right)}{1+\beta\eta^3}\frac{\varepsilon^2}{k} \tag{1.141}$$

where $\eta = \left|\tilde{S}\right| k/\varepsilon$. Turbulent viscosity is given form equation (1.137) as in k-ε model. The constants of the model are derived analytically from the theory and are equal to:

$$\eta_0 = 4.38,\ \beta = 0.012,\ C_{1\varepsilon} = 1.42,\ C_{2\varepsilon} = 1.68,\ C_\mu = 0.0845 \tag{1.142}$$

The numbers σ_k, σ_ε, Pr_t and Sc_t in RNG k-ε model are not user defined constants but are given from the relation:

$$\frac{\mu}{\mu_t} = \left|\frac{1/\sigma_t - 1.3929}{1/\sigma - 1.3929}\right|^{0.6321}\left|\frac{1/\sigma_t + 2.3929}{1/\sigma + 2.3929}\right|^{0.3679} \tag{1.143}$$

where σ_t is one of σ_k, σ_ε, Pr_t, Sc_t and σ is the corresponding number in laminar flow (equal to 1.0 in the case of σ_k and σ_ε).

k-ω model

k-ω turbulence model was the first two-equation turbulent model which was suggested by Kolmogorov in 1942 and was developed greatly over the years by various researchers (Wilcox 1994). This model solves a transport equation for the turbulent kinetic energy k and another one for ω which can be considered as the rate of dissipation per unit turbulent kinetic energy, i.e. the ratio of ε to k. It can also be interpreted as a frequency of turbulence as it has units 1/sec. There are many versions of the model. Here, we present one of the latest as described in (Wilcox 2008). A more primitive k-ω model can be found in e.g. (Wilcox 1994). The equations for k, ω and μ_t are:

$$\frac{\partial \bar{\rho}k}{\partial t} + \frac{\partial}{\partial x_j}\left(\bar{\rho}\tilde{u}_j k\right) = \frac{\partial}{\partial x_j}\left[\left(\mu + \frac{\mu_t'}{\sigma_k}\right)\frac{\partial k}{\partial x_j}\right] + \bar{\rho}\tau_{ij}\frac{\partial \tilde{u}_i}{\partial x_j} - \bar{\rho}\beta^* k\omega \tag{1.144}$$

$$\frac{\partial \bar{\rho}\omega}{\partial t} + \frac{\partial}{\partial x_j}\left(\bar{\rho}\tilde{u}_j \omega\right) = \frac{\partial}{\partial x_j}\left[\left(\mu + \frac{\mu_t'}{\sigma_\omega}\right)\frac{\partial \omega}{\partial x_j}\right] + \alpha\frac{\omega}{k}\bar{\rho}\tau_{ij}\frac{\partial \tilde{u}_i}{\partial x_j} - \bar{\rho}\beta\omega^2 + \sigma_d\frac{\rho}{\omega}\frac{\partial k}{\partial x_j}\frac{\partial \omega}{\partial x_j} \tag{1.145}$$

$$\mu_t' = \bar{\rho}\frac{k}{\omega} \tag{1.146}$$

$$\mu_t = \bar{\rho}\frac{k}{\hat{\omega}},\quad \hat{\omega} = \max\left(\omega, C_{\lim}\sqrt{\frac{2\tilde{S}_{ij}\tilde{S}_{ij}}{\beta^*}}\right),\ C_{\lim} = 0.875 \tag{1.147}$$

$$\bar{\rho}\tau_{ij} = 2\mu_t\tilde{S}_{ij} - \frac{2}{3}\bar{\rho}k\delta_{ij} \tag{1.148}$$

$$\tilde{S}_{ij}=\frac{1}{2}\left(\frac{\partial\tilde{u}_i}{\partial x_j}+\frac{\partial\tilde{u}_j}{\partial x_i}\right)-\frac{1}{3}\frac{\partial\tilde{u}_k}{\partial x_k}\delta_{ij} \tag{1.149}$$

This version of the model has two key modifications compared to the previous ones: the extra cross diffusion term in the equation of ω and the stress limiter modification of equation (1.147). Thus, the k-ω model improves the prediction capabilities in both boundary layers and free shear flows. Moreover it is less sensitive to freestream boundary conditions (Wilcox 2008). The turbulent diffusion terms in the equations of k and ω use the turbulent eddy viscosity of equation (1.146). This is done to avoid any influence from the stress limiter that equations (1.147) impose. The closure coefficients of the model are:

$$\alpha=0.52\,,\ \beta^*=0.09\,,\ \sigma_k=5/3\,,\ \sigma_\omega=2.0 \tag{1.150}$$

$$\sigma_d=\begin{cases}0 & \dfrac{\partial k}{\partial x_j}\dfrac{\partial\omega}{\partial x_j}\le 0\\ \sigma_{d0} & \dfrac{\partial k}{\partial x_j}\dfrac{\partial\omega}{\partial x_j}>0\end{cases},\quad \sigma_{d0}=0.125 \tag{1.151}$$

$$\beta=\beta_0 f_\beta,\ \beta_0=0.0708,\ \ f_\beta=\frac{1+85\chi_\omega}{1+100\chi_\omega} \tag{1.152}$$

$$\chi_\omega=\left|\frac{\tilde{\Omega}_{ij}\tilde{\Omega}_{jk}\hat{S}_{ki}}{\left(\beta^*\omega\right)^3}\right|,\ \hat{S}_{ki}=\frac{1}{2}\left(\frac{\partial\tilde{u}_k}{\partial x_i}+\frac{\partial\tilde{u}_i}{\partial x_k}\right)-\frac{1}{2}\frac{\partial\tilde{u}_m}{\partial x_m}\delta_{ki},\ \tilde{\Omega}_{ij}=\frac{1}{2}\left(\frac{\partial\tilde{u}_i}{\partial x_j}-\frac{\partial\tilde{u}_j}{\partial x_i}\right) \tag{1.153}$$

SST k-ω model

The Shear-Stress Transport (SST) k-ω model (Menter 1994) is a two equation turbulence model which combines the k-ε and the k-ω models. It uses the k-ω model in the near-wall region and the k-ε model in the free-stream area. The SST k-ω model has shown very good behavior in adverse pressure gradient and separating flows (Menter 1994). The transport equations are derived by multiplying the equations of k-ε and k-ω model with a blending function and then by adding them together. An extra damped cross-diffusion term has also been added in the transport equation of ω. The transport equations are:

$$\frac{\partial\bar{\rho}k}{\partial t}+\frac{\partial}{\partial x_j}\left(\bar{\rho}\tilde{u}_j k\right)=\frac{\partial}{\partial x_j}\left[\left(\mu+\frac{\mu_t}{\sigma_k}\right)\frac{\partial k}{\partial x_j}\right]+\bar{\rho}\tau_{ij}\frac{\partial\tilde{u}_i}{\partial x_j}-\bar{\rho}\beta^* k\omega \tag{1.154}$$

$$\begin{aligned}\frac{\partial\bar{\rho}\omega}{\partial t}+\frac{\partial}{\partial x_j}\left(\bar{\rho}\tilde{u}_j\omega\right)=&\frac{\partial}{\partial x_j}\left[\left(\mu+\frac{\mu_t}{\sigma_\omega}\right)\frac{\partial\omega}{\partial x_j}\right]+\alpha\frac{\bar{\rho}}{\mu_t}\bar{\rho}\tau_{ij}\frac{\partial\tilde{u}_i}{\partial x_j}-\bar{\rho}\beta\omega^2+\\ &2\left(1-F_1\right)\frac{\bar{\rho}}{\sigma_{\omega2}}\frac{1}{\omega}\frac{\partial k}{\partial x_j}\frac{\partial\omega}{\partial x_j}\end{aligned} \tag{1.155}$$

where $\bar{\rho}\tau_{ij}$ is given from equation (1.148). Furthermore,

$$\sigma_k = \frac{1}{F_1/\sigma_{k,1} + (1-F_1)/\sigma_{k,2}},\ \sigma_\omega = \frac{1}{F_1/\sigma_{\omega,1} + (1-F_1)/\sigma_{\omega,2}} \tag{1.156}$$

$$\beta = F_1\beta_1 + (1-F_1)\beta_2,\ a = F_1 a_1 + (1-F_1)a_2 \tag{1.157}$$

$$a_1 = \frac{\beta_1}{\beta^*} - \frac{1}{\sigma_{\omega 1}}\frac{\kappa^2}{\sqrt{\beta^*}},\ a_2 = \frac{\beta_2}{\beta^*} - \frac{1}{\sigma_{\omega 2}}\frac{\kappa^2}{\sqrt{\beta^*}} \tag{1.158}$$

where the values of the parameters are:

$$\beta^* = 0.09,\ \sigma_{\omega 1} = 2.0,\ \sigma_{\omega 2} = 125/107,\ \sigma_{k1} = 20/17,\ \sigma_{k2} = 1.0,$$
$$\beta_1 = 0.075,\ \beta_2 = 0.0828,\ \kappa = 0.41 \tag{1.159}$$

The blending function is:

$$F_1 = \tanh\left(\arg_1^4\right)$$
$$\arg_1 = \min\left[\max\left(\frac{\sqrt{k}}{0.09\omega d}, \frac{500\mu}{\bar{\rho} d^2 \omega}\right), \frac{4\bar{\rho}k}{\sigma_{\omega,2} CD_{k\omega} d^2}\right] \tag{1.160}$$

where d is the distance to the nearest wall and $CD_{k\omega}$ is the positive part of the cross-diffusion term:

$$CD_{k\omega} = \max\left[2\bar{\rho}\frac{1}{\sigma_{\omega,2}}\frac{1}{\omega}\frac{\partial k}{\partial x_j}\frac{\partial \omega}{\partial x_j}, 10^{-20}\right] \tag{1.161}$$

Finally, the turbulent viscosity is defined by:

$$\mu_t = \frac{\alpha_1 \bar{\rho} k}{\max\left[\alpha_1 \omega, \Omega F_2\right]} \tag{1.162}$$

where $\alpha_1 = 0.31$, $\Omega = \sqrt{2\tilde{\Omega}_{ij}\tilde{\Omega}_{ij}}$ is the magnitude of vorticity and

$$F_2 = \tanh\left(\arg_2^4\right)$$
$$\arg_2 = \max\left[\frac{2\sqrt{k}}{0.09\omega d}, \frac{500\mu}{\bar{\rho} d^2 \omega}\right] \tag{1.163}$$

1.2.3.2 Large Eddy Simulation and Direct Numerical Simulation (UU)

LES concept and comparison with other turbulence modelling approaches

Separation of large and small turbulence scales illustrated in Figs. 1.2.3.1 and 1.2.3.2 is accomplished by applying filtering procedure to fluid flow governing equations. The most commonly used in LES technique filtering method for variable density flows is Favre or density weighted filtering:

$$\Phi = \tilde{\Phi} + \Phi''' \tag{1.164}$$

$$\tilde{\Phi} = \frac{\overline{\rho\Phi}}{\bar{\rho}} \tag{1.165}$$

where $\tilde{\Phi}$ is the filtered and Φ'' is the fluctuating part.

Applying Favre filtering to a set of compressible Navier-Stokes, energy and species transport equations results in a following system:

$$\frac{\partial \bar{\rho}}{\partial t} + \frac{\partial}{\partial x_j}\left(\bar{\rho}\tilde{u}_j\right) = 0 \tag{1.166}$$

$$\frac{\partial \bar{\rho}\tilde{u}_i}{\partial t} + \frac{\partial}{\partial x_j}\left(\bar{\rho}\tilde{u}_j\tilde{u}_i\right) = -\frac{\partial \bar{p}}{\partial x_i} + \frac{\partial}{\partial x_j}\left(\mu+\mu_t\right)\left(\frac{\partial \tilde{u}_i}{\partial x_j} + \frac{\partial \tilde{u}_j}{\partial x_i} - \frac{2}{3}\frac{\partial \tilde{u}_k}{\partial x_k}\delta_{ij}\right) + \bar{\rho}g_i \tag{1.167}$$

$$\frac{\partial}{\partial t}\left(\bar{\rho}\tilde{E}\right) + \frac{\partial}{\partial x_j}\left(\tilde{u}_j\left(\bar{\rho}\tilde{E}+\bar{p}\right)\right) =$$

$$\frac{\partial}{\partial x_j}\left(\left(\lambda + \frac{\mu_t c_p}{Pr_t}\right)\frac{\partial \tilde{T}}{\partial x_j} - \sum_m \tilde{h}_m\left(-\left(\rho D + \frac{\mu_t}{Sc_t}\right)\frac{\partial \tilde{Y}_m}{\partial x_j}\right)\right) + \tag{1.168}$$

$$\frac{\partial}{\partial x_j}\left(\tilde{u}_i\left(\mu+\mu_t\right)\left(\frac{\partial \tilde{u}_i}{\partial x_j} + \frac{\partial \tilde{u}_j}{\partial x_i} - \frac{2}{3}\frac{\partial \tilde{u}_k}{\partial x_k}\delta_{ij}\right)\right) + S_E$$

$$\frac{\partial \bar{\rho}\tilde{Y}_{H_2}}{\partial t} + \frac{\partial}{\partial x_j}\left(\bar{\rho}\tilde{u}_j\tilde{Y}_{H_2}\right) = \frac{\partial}{\partial x_j}\left(\left(\rho D + \frac{\mu_t}{Sc_t}\right)\frac{\partial \tilde{Y}_{H_2}}{\partial x_j}\right) + S_{H_2} \tag{1.169}$$

There are four conceptual steps in LES (Pope, 2000):

(i) A filtering operation is defined to decompose the velocity *U(x,t)* into the sum of a filtered (or resolved) component $\overline{U}(x,t)$) and a residual (or subgrid-scale, SGS) component *u'(x, t).* The filtered velocity field $\overline{U}(x,t)$ - which is three-dimensional and time-dependent - represents the motion of the large eddies.

(ii) The equations for the evolution of the filtered velocity field are derived from the Navier-Stokes equations. These equations are of the standard form, with the momentum equation containing the residual- stress tensor (or SGS stress tensor) that arises from the residual motions.

(iii) Closure is obtained by modelling the residual-stress tensor, most simply by an eddy-viscosity model.

(iv) The model filtered equations are solved numerically for $\overline{U}(x,t)$, which provides an approximation to the large-scale motions in the turbulent flow.

The principal operation in large eddy simulation is low-pass filtering. This operation is applied to the Navier–Stokes and/or other transport equations to eliminate small scales of the solution. This reduces the computational cost of the simulation. The governing equations are thus transformed, and the obtained solution describes a filtered velocity, energy and species concentration(s) field. Choice of filter size (which is most commonly taken as equal to mesh size) determines what length and time scales of turbulent motion are “resolved” and what

scales are "small" enough and will be "filtered out" (effectively removed). Filter size is selected according to turbulence theory and available computational resources.

The filtering operation in large eddy simulation can be implicit or explicit. Implicit filtering recognizes that the subfilter scale model will dissipate in the same manner as many numerical schemes. In this way, the grid, or the numerical discretization scheme, can be assumed to be the LES low-pass filter. While this takes full advantage of the grid resolution, and eliminates the computational cost of calculating a subfilter scale model term, it is difficult to determine the shape of the LES filter that is associated with some numerical issues (Pope, 2000). Explicit filtering results in appearance of terms associated with turbulence scales smaller than the filter width. These scales, known as Sub Grid Scales (SGS), are not resolved in LES and have to be modelled by separate SGS models. The relatively smaller contribution of sub-grid scales together with their more universal nature in a broad range of flows, justifies the use of relatively simple SGS models. A number of different SGS models had been proposed over years.

Smagorinsky model

One of the first SGS models was the model proposed by Smagorinsky (1963).

In this model the turbulence stress tensor is closed with

$$\tau_{ij} - \frac{1}{3}\tau_{kk}\delta_{ij} = -2(C_s\Delta)^2\left|\overline{S}\right|S_{ij} \tag{1.170}$$

It was subsequently expanded by Lilly, with eddy viscosity modelled as

$$\mu_{SGS} = \rho(C_S\Delta)^2\left|\overline{S}\right| \tag{1.171}$$

where filter width

$$\Delta = (V_{CV})^{1/3} \tag{1.172}$$

and

$$\overline{S} = \sqrt{2S_{ij}S_{ij}} \tag{1.173}$$

The effective viscosity is calculated from

$$\mu_{eff} = \mu_{mol} + \mu_{SGS} \tag{1.174}$$

The Smagorinsky SGS is based on the assumption of local equilibrium (i.e. production and dissipation of SGS turbulent kinetic energy are in balance) and is strictly limited to scales in the inertial subrange. In many LES a coarser resolution is employed and this cut-off is not strictly respected.

The popularity of the Smagorinsky model is based on its simplicity and relative robustness, which is in part due to the fact that the model is strictly dissipative. On the other hand, the model requires some calibration. Thus, the original Smagorinsky model uses a value of C_s = 0.18 determined from isotropic turbulence. In practice this value is too large and introduces excessive dissipation in most engineering shear flows and consequently it is corrected to C_s = 0.15 in a free high Reynolds-number turbulent flows (Pope, 2000). The constant is attenuated near walls (compared with its value in high-Reynolds-number free turbulent flows) by a

damping function (van Driest type) due to anisotropic turbulence (Pope, 2000). Smagorinsky model with a constant value coefficient C_s is also not well suited for transitional (laminar-turbulent) flows, particularly in laminar flow it should be equal to zero. In addition, it does not account for backscatter (transfer of turbulent kinetic energy is unidirectional from large to small scales).

Dynamic SGS models

The limitations of the Smagorinsky model lead to the formulation of more general sub-grid-scale models. These included dynamic sub-grid-scale models by Germano et al., (1991) with important modifications and its extensions provided by Lilly (1992) and Meneveau et al. (1996). These models can be considered as a modification of the Smagorinsky model, as the dynamic model allows the Smagorinsky constant C_S to vary in space and time, being computed dynamically as the calculation progresses, rather than set apriori. Germano model is based on an algebraic identity between the sub-grid-scale stresses at two different filtered levels and the resolved turbulent stresses.

In Germano et al. (1991) approach the variable model coefficient C, replacing Smagorinsky constant C_S is calculated locally in each time-step based upon two filterings of the flow variables, denoted in the following equations by the overbar and a caret over the overbar. These filters are called the grid filter and the test filter, respectively, with the test filter width assumed to be larger than the grid filter width (a ratio of 2 was demonstrated to produce optimal results (Germano et al., 1991).

The SGS stress tensor τ_{ij} can be expressed as

$$\tau_{ij} = \left(\overline{u}_i\overline{u}_j - \overline{u_i u_j}\right) \tag{1.175}$$

Application of stress tensor *S* closure to (1.175) produces

$$\tau_{ij} - \frac{1}{3}\delta_{ij}\tau_{kk} = 2C\Delta^2\left|\overline{S}\right|\overline{S}_{ij} \tag{1.176}$$

where δ_{ij} is a Kronecker delta operator $\delta_{ij} = \begin{cases} 1; i = j \\ 0; i \neq j \end{cases}$, $\overline{S}_{ij} = \left(\frac{\partial \overline{u}_i}{\partial x_j} + \frac{\partial \overline{u}_j}{\partial x_i}\right)/2$, $\left|\overline{S}\right| = \sqrt{2\overline{S}_{kl}\overline{S}_{kl}}$, Δ is the grid filter width, and $C = C_S^2$ is a new Smagorinsky coefficient, equal to the square of the original quantity.

The "subtest" scale stress $T_{ij} = \left(\widehat{\overline{u}_i}\widehat{\overline{u}_j} - \widehat{\overline{u_i}\overline{u_j}}\right)$ can be similarly expressed as

$$T_{ij} - \frac{1}{3}\delta_{ij}\tau_{kk} = 2C\hat{\Delta}^2\left|\hat{\overline{S}}\right|\hat{\overline{S}}_{ij} \tag{1.177}$$

where $\hat{\Delta}$ is the test filter width.

Recognizing that consistency between (1.176) and (1.177) depends on a proper selection of C, Germano et al. (1991) were able to introduce Germano identity

$$\mathcal{L}_{ij} = T_{ij} - \hat{\tau}_{ij} = -\widehat{\overline{u}_i\overline{u}_j} + \widehat{\overline{u}}_i\widehat{\overline{u}}_j \tag{1.178}$$

where $\mathcal{L}_{ij}$ is the resolved turbulent stress. The right hand side of Eq. (1.178) can be explicitly evaluated by subtracting the test-scale average (1.176) from (1.177), producing

$$\mathcal{L}_{ij} = \frac{1}{3}\delta_{ij}L_{kk} = 2CM_{ij} \tag{1.179}$$

where

$$M_{ij} = \hat{\Delta}^2 \left|\hat{\bar{S}}\right| \hat{\bar{S}}_{ij} - \Delta^2 \widehat{|\bar{S}|\bar{S}_{ij}} \tag{1.180}$$

Multiplying both sides of (1.180) by $\bar{S}_{ij}$ the model coefficient C can be found as

$$C = \frac{1}{2}\left(\frac{\mathcal{L}_{ij}\bar{S}_{ij}}{M_{ij}\bar{S}_{ij}}\right) \tag{1.181}$$

Lilly (1992) proposed alternative closure by using least squares approach to minimize the error in the solution of equation system (1.179). Defining Q as the square of error in eq. (1.179) one can write

$$Q = \left(\mathcal{L}_{ij} - \frac{1}{3}\delta_{ij}L_{kk} - 2CM_{ij}\right)^2 \tag{1.182}$$

Appling the condition $\frac{\partial Q}{\partial C} = 0$, and observing that $\frac{\partial^2 Q}{\partial C_S^2} > 0$, C corresponding to minimum Q can be found as

$$C = \frac{1}{2}\left(\frac{\mathcal{L}_{ij}M_{ij}}{M_{ij}M_{ij}}\right) \tag{1.183}$$

Note, that this procedure can lead to numerical instability since to ensure stability C must be positive, which is not guaranteed by dynamic procedure since the numerator of (1.183) can become negative. Accordingly, to improve the robustness of the method, additional averaging in the homogeneous direction of the flow (if any) is often employed.

The sub-grid-scale stresses obtained using the dynamic model vanish in laminar flow and at a solid boundary, and have the correct asymptotic behaviour in the near-wall region of a turbulent boundary layer (Germano et al., 1991), alleviating major shortcomings of Smagorinsky model.

Further development of dynamic models included dynamic localization model of Ghosal et al. (1995) and Lagrangian averaging model of Meneveau et al (1996); however Lilly dynamic model retains its popularity due to simplicity of implementation and relatively little computational expense (10-15% compared to constant coefficient Smagorinsky model).

Renormalization Group (RNG) SGS model

Another commonly used model is RNG SGS model, which was developed from Renormalization theory by Yakhot and Orszag (1986) and is conceptually similar to the one originally applied to $k-\varepsilon$ RANS model. In this model the effective viscosity μ_{eff} is equal

$$\mu_{eff} = \mu\left[1 + H\left(\frac{\mu_s \mu_{eff}}{\mu^3} - 100\right)\right]^{1/3} \tag{1.184}$$

where

$$\mu_s = \tilde{\rho}\left[C_{RNG} V_{CV}^{1/3}\right]^2 \sqrt{2\tilde{S}_{ij}\tilde{S}_{ij}} \tag{1.185}$$

$C_{RNG} = 0.157$ is the model constant, V_{CV} is the volume of control volume, H is the Heaviside function defined as $H(x) = \begin{cases} x; x > 0 \\ 0; x \le 0 \end{cases}$, and the rate of strain tensor

$$\tilde{S}_{ij} = 1/2\left(\frac{\partial \tilde{u}_i}{\partial x_j} + \frac{\partial \tilde{u}_j}{\partial x_i}\right) \tag{1.186}$$

The RNG model is similar to the Smagorinsky's model , but does not contain adjustable or *ad hoc* parameters and is capable to describe transitional and laminar flow regimes: in the laminar flow the Heaviside function argument is negative and the effective viscosity recovers molecular viscosity, $\mu_{eff} = \mu$. The effective Prandtl number can be calculated according to the RNG theory (Yakhot and Orszag, 1986) for non-reactive flows and was equal to the effective Schmidt number:

$$\left|\frac{1/\mathrm{Pr}_{eff} - 1.3929}{1/\mathrm{Pr} - 1.3929}\right|^{0.6321} \left|\frac{1/\mathrm{Pr}_{eff} + 2.3929}{1/\mathrm{Pr} + 2.3929}\right|^{0.3679} = \frac{\mu}{\mu_{eff}} \tag{1.187}$$

MILES approach

Monotone Integrated LES (MILES) technique was introduced by Boris et al. (1990) belongs to implicit filtering technique. The idea is that turbulence is characterised by high levels of fluctuating vorticity, and therefore sharp velocity gradients, which usually requires high-order monotone schemes to properly resolve. These high-order monotone schemes, however, are highly dissipative, possessing an inherent truncation error that acts as a numerical diffusion (Oran and Boris, 1993), which can emulate the effects of physical viscosity, see Grinstein and Guirguis (1992). Using a finite-volume approach, the cell averaging discretisation of the data can be considered to be implicit filter. Therefore, these components naturally mimic LES approach. Furthermore, it was demonstrated by Ghosal (1996) that the numerical error in LES codes can be of a similar order of magnitude to the SGS model, and mask its effect. It has also been shown by Fureby et. al. (1997) and Menon et. al. (1996) that in certain flows the gross scale features appear to be insensitive to the choice of SGS model, particularly if the spatial resolution is high enough.

It should be noted that a number of LES based modelling strategies have also been proposed primarily to extend the feasibility of LES-like simulations, these include notably VLES (Very Large Eddy Simulations) and DES (Detached Eddy Simulations). VLES is aimed at unsteady flow simulations with intermediate resolution and where a significant portion of the turbulent energy spectrum needs to be modelled by the SGS. The matter of selection of adequate mesh resolution for LES, and therefore the boundary between LES proper and VLES, is a subject of considerable debates within CFD community. One of the commonly accepted criteria is that

the LES filter and mesh should be sufficiently fine to resolve 80% of the energy; if the filter and/or mesh are too coarse for that, the simulation becomes VLES (Pope, 2000).

Overall, LES provides a good compromise between good predictive capability and acceptable, if still high, computational resources requirements.

DNS approach to turbulence modelling

A direct numerical simulation (DNS) is a simulation in which the Navier-Stokes equations are explicitly solved numerically resolving all the scales of motion without any turbulence model. DNS requires the simulation to be able to resolve the entire range of spatial and temporal scales of the turbulence. Conceptually it is the simplest approach and, when it can be applied, it is unrivalled in accuracy and in the level of description provided. However, it is important to appreciate that the cost is extremely high; and the computer requirements increase so rapidly with Reynolds number that the applicability of the approach is limited to flows of low or moderate Reynolds numbers (Pope, 2000). In terms of thermocouple analogy, used in description of RANS and LES approaches, the thermocouple now have almost instantaneous measurement speed, allowing measurement of even small scale fluctuations.

All the spatial scales of the turbulence must be resolved within the computational mesh, down to the smallest (Kolmogorov) dissipative scales. The Kolmogorov scale η is given by

$$\eta = (\upsilon^3 / \varepsilon)^{1/4} \tag{1.188}$$

where v is the kinematic viscosity and ε is the rate of dissipation of kinetic energy. Resolving Kolmogorov scale typically requires utilization of ultra-fine grids with resolution inversely proportional to $Re^{¾}$ (Dimotakis, 2005), where Re is Reynolds number and computational cost increasing rapidly with the Reynolds number approximately as Re^3 (Pope, 2000).

DNS provide the most accurate results at the expense of very high computational resources requirements driven by the necessity to resolve the flowfield down to Kolmogorov scales. This requirement usually made DNS unsuitable for simulation of flows of practical interest which usually involve complex geometries and/or large scale flows.

1.2.4 Volumetric source model for release and dispersion (UU)

Specification of inflow velocity for solution of momentum equations (called in mathematics Dirichlet or first-type of boundary condition) for modelling hydrogen release and dispersion in some practical problems may be non-trivial or not convenient from modelling point of view. Examples of such practical situations may include:

- modelling high-pressure storage blowdown using notional nozzle parameters, where notional nozzle parameters are changing with time,
- underexpanded jet with sonic inflow velocity requiring compressible formulation and subject to low time step value due to Courant-Fridrichs-Levy stability criteria,
- modelling of hydrogen inflow with large disparity between scale of inflow orifice and overall problem size,
- high-velocity inflow in a congested environment, leading to large velocity gradients and poor stability and/or convergence, etc.

Numerical constraints stipulated by inflow boundary in above situations may be relaxed using volumetric source model for hydrogen inflow as described in (Molkov et al. 2009). With such

an approach a small portion of calculation domain around inflow is designated for volumetric release, where volumetric sources are applied to momentum, energy, species and other equations to mimic parameters of the modelled inflow. One may expect the volumetric source model to provide reasonably accurate solution as long as

- conservation of governing parameters is fulfilled, i.e. inflow of mass, momentum, energy, species etc. between the physical inflow and the one modelled using volumetric sources are the same,
- problem scale, where we are interested in the solution, is significantly larger than the volumetric source (in the near to the source volume field the solution is likely to be affected by the finite size of the source).

With such an approach the size of the region where volumetric source is applied may be kept all the time constant, but the source values can be adjusted in time to reflect changing with time flow parameters (e.g., parameters at the notional nozzle).

Implementation of volumetric release source may be demonstrated using example of transient hydrogen jet modelled within RANS framework using standard k-ε turbulence model. The governing equations are (see section 1.2.3.1 for the k-ε equation set):

– conservation of mass,
– conservation of momentum,
– conservation of energy,
– conservation of hydrogen mass fraction,
– conservation of turbulent kinetic energy,
– conservation of turbulent kinetic energy dissipation rate.

For the development of the described methodology one needs to know parameters at inflow: mass flow rate $\dot{m}_{in}$, inflow velocity u_{in}, temperature T_{in}, turbulent kinetic energy k_{in} and its dissipation rate ε_{in}. If turbulence intensity I and length scale l at inflow are known, turbulent kinetic energy may be calculated as $k_{in} = 3/2\left(u_{in} \cdot I\right)^2$, and dissipation rate as $\varepsilon_{in} = C_\mu^{3/4} k_{in}^{3/2} / l$, where C_μ - constant of k-ε turbulence mode, equal for the standard model 0.09.

For mass inflow rate $\dot{m}_{in}$, then inflow rates of other variables in the equation set are:

– momentum $\dot{m}_{in} \cdot u_{in}$,
– energy $\dot{m}_{H2} \cdot \left(h_{H2} - h_{H2\,f}^0\right) = \dot{m}_{H2} \cdot c_{p_{H2}} \cdot \left(T_{H2} - T_0\right)$,
– species $\dot{m}_{in}$ (assuming 100% fraction of hydrogen at inflow),
– turbulent kinetic energy $\dot{m}_{H2} \cdot k_{in}$, and
– turbulent kinetic energy dissipation rate $\dot{m}_{H2} \cdot \varepsilon_{in}$.

Knowing volume of region of calculation domain designated for source term application V_{source}, values of source terms in corresponding equations become:

conservation equation of mass

$$S_m = \dot{m}_{H2} / V_{source}, \tag{1.189}$$

conservation equation of momentum

$$S_u = \dot{m}_{H2} \cdot u_{H2} / V_{source} , \quad (1.190)$$

conservation equation of energy (specific heat of hydrogen is $c_{p_{H2}} = 14283 \mathrm{J/(kgK)}$ at normal atmospheric conditions)

$$S_E = \dot{m}_{H2} \cdot (h_{H2} - h_{H20}) / V_{source} = \dot{m}_{H2} \cdot c_{p_{H2}} \cdot (T_{H2} - T_0) / V_{source} , \quad (1.191)$$

conservation equation of inflowing species (hydrogen)

$$S_{H2} = \dot{m}_{H2} / V_{source} , \quad (1.192)$$

conservation equation of turbulent kinetic energy

$$S_k = \dot{m}_{H2} \cdot k / V_{source} , \quad (1.193)$$

conservation equation of turbulent kinetic energy dissipation rate

$$S_\varepsilon = \dot{m}_{H2} \cdot \varepsilon / V_{source} . \quad (1.194)$$

The method was validated against experimental data by Health and Safety Laboratory, UK (Roberts, 2006) on quasi steady-state under-expanded hydrogen jet issued from a storage at p=100 bar overpressure and temperature T=14^{0}C through a 3 mm diameter orifice, experimentally estimated mass flow rate was equal m = 0.045 kg/s. Source terms were applied in a region having cubic geometry. Simulations with different sizes of the region were performed, where the volume was characterised in terms of so called effective or notional nozzle diameter (i.e. flow diameter where sonic velocity is established), which was calculated according to (Molkov, 2012) and was equal to 21.8 mm. Ratio of the release region size to the effective nozzle diameter was changing from 1 to 8. Comparison of experimentally measured hydrogen volume fractions with simulation results are shown in Figure 1.30. The simulated and experimentally observed hydrogen volume fractions are in a good agreement, provided that the ratio of the release volume size to the notional nozzle diameter D_{eff} is up to 4. Table 1.7 gives flow parameters at the exit from volumetric source region for all tested cases.

It is important to note two factors leading to potential deterioration of numerical results near the volumetric release source:

- as the volumetric source region is not separated from the rest of the domain, air entrainment is allowed and hydrogen fraction near the source decreases below 1.0 in the volumetric source region,
- larger size of the volumetric source region leads to large entrainment and, as a result, to decrease of the maximum jet velocity.

On the other hand, in case of source region size equal to four effective (notional) nozzle diameters D_{eff} Mach number is equal to M=0.28, which makes flow effectively incompressible, relaxing numerical constraints and allowing faster convergence of the numerical solution procedure.

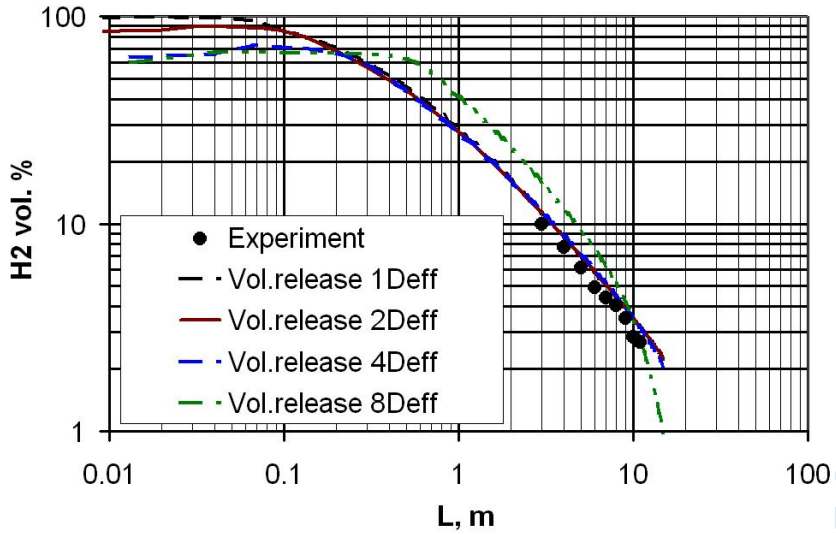

Figure 1.30: Comparison of measured and simulated hydrogen vol. fraction for various sizes of the release volume (Molkov et., 2009).

Table 1.7: Parameters at volumetric source: hydrogen volume fraction, velocity and maximum Mach number

Size of source region	H_2 vol. fraction	Jet velocity	Mach number
$1D_{eff}$	0.99	1032 m/s	0.87
$2D_{eff}$	0.90	415 m/s	0.46
$4D_{eff}$	0.72	164 m/s	0.28
$8D_{eff}$	0.67	72 m/s	0.15

1.2.5 Near surface wind distribution model (HSL)

To model atmospheric dispersion using CFD, it is necessary to specify mean wind speed profiles, as described in Section 1.1.3. This is not entirely straightforward for a number of reasons. Perhaps the most prominent of these is the use of turbulence models with wall functions. These wall functions consist of profiles of velocity, temperature and turbulence parameters (or modified transport equations) that are applied just within the computational cells adjoining the ground. The reason why these wall functions are used is that the flow behaviour close to the wall changes very rapidly. Rather than resolve these steep gradients, which would require a very fine grid near the ground and long computing times, it is advantageous to use a coarser grid and prescribe the flow behaviour within this region of the flow. Problems then arise because the scales under which atmospheric flows operate are not compatible with the scaling assumptions used in near wall cells.

These difficulties in modelling the ABL were examined by Hargreaves and Wright (2007) who showed that it is difficult to maintain the wind and turbulence profiles along the length of the computational domain. The standard near wall functions in the k-ε turbulence model tend not to preserve the applied upstream profiles of wind and turbulence, so that the quantities decay by the time the flow reaches the region of interest.

The approach commonly used to model ABLs in atmospheric dispersion simulations was developed by Richards and Hoxey (1993), who modelled a neutral boundary layer using the following inflow conditions:

$$u = \frac{u_*}{k} ln\left(\frac{z + z_0}{z_0}\right) \quad (1.195)$$

$$k(z) = \frac{u_*^2}{\sqrt{C_\mu}} \quad (1.196)$$

$$\varepsilon(z) = \frac{u_*^3}{\kappa(z + z_0)} \quad (1.197)$$

Together with a shear stress applied at the bottom boundary of:

$$\tau_g = \rho u_{*g}^2 \quad (1.198)$$

with turbulence values of:

$$k = \frac{u_{*g}^2}{\sqrt{C_\mu}} \quad (1.199)$$

and:

$$\varepsilon = \frac{\sqrt{C_\mu} k u_{*g}}{\kappa(z_g + z_0)} \quad (1.200)$$

where the subscript *g* refers to the near ground values. Richards and Hoxey (1993) were able to maintain the ABL profiles throughout the computational flow domain by modifying the expressions for *k* and *ε* in the near wall cell within the CFD code. Users of commercial CFD codes usually do not have the ability to modify the code in this way. Hargreaves and Wright (2007) acknowledged this shortcoming and noted that it may be useful to site the inlet boundary close to the region of interest within the computational domain, in order to avoid the ABL profiles changing significantly by the time that the flow reaches the area of interest.

An alternative approach to modelling the ABL was described in Blocken *et al*. (2007) where the lower boundary is modelled as a rough wall using the following standard approach:

$$u = \frac{u_*}{k} ln(y^+) + B - \Delta B(k_s) \quad (1.201)$$

where y^+ is the dimensionless wall distance, *B* is a constant and $\Delta B(k_s)$ is a function that accounts for the surface roughness, based on the equivalent sand grain roughness, k_s. Blocken *et al*. (2007) showed that it was possible to replicate an ABL profile using this standard wall function if the equivalent sand grain roughness, k_s, was set to a value of:

$$k_s = 30 z_0 \quad (1.202)$$

However, they pointed out that this method often cannot be used because the requirements for the near-wall meshing are incompatible with the values of k_s that typically arise. Many CFD codes require that the sand grain roughness length is smaller than the distance, y_p, to the centre of the near wall cell. If this rule is enforced, it can lead to overly large near wall cells which would poorly resolve the flow near the ground. Blocken *et al*. (2007) suggested a number of remedial measures that may be used when the $k_s > y_p$:

- Variable height of wall adjacent cells
- Explicit modelling of roughness elements

- Minimisation of the upstream domain length
- Generation of upstream profiles using an “empty” domain
- Specification of the wall shear stress on the bottom of the domain

The latter measure was also recommended by Richards and Hoxey (1993) and was found by Blocken *et al*. (2007) to result in a very good horizontal homogeneity. However, it is only applicable to flat, unobstructed terrain where there are no disturbing elements such as buildings and the wall shear stress can be prescribed. Since CFD models are mostly used to study complex geometries that cannot be examined using simpler integral models, this is a serious limitation of the approach.

The importance of consistency between the inflow boundary and the upper (sky) and ground boundaries was highlighted by O’Sullivan *et al*. (2011), who implemented the inlet profiles of Yang *et al*. (2009) in conjunction with different upper and lower boundary conditions. They found that the standard approach of using zero gradients to specify the turbulence quantities on the boundaries was inconsistent with the applied profiles and led to errors in the streamwise flow predictions.

Further guidance on CFD modelling of atmospheric boundary layers can be found in the reports produced by the European COST Action 732 on “Quality assurance and improvement of microscale meteorological models” (Frank *et al*., 2007; Schatzmann *et al*., 2010). In France, a government-led CFD modelling working group is currently in the process of drafting guidance on the simulation of atmospheric boundary layers using CFD models that will prescribe the approach that must be taken in industrial safety analyses. Some background information on the motivation for this new guidance can be found in the paper by Lacome and Truchot (2013).

1.2.6 LH2 releases and dispersion (NCSRD)

The release of cryogenic fluids, such as liquefied hydrogen (LH2), is a complex physical phenomenon, which results in two phase flow. There are several modelling approaches of the two phase flows and thus of the LH2 dispersion. This section analyses the modelling approaches that can and have been used in the past to simulate the LH2 dispersion. We distinguish two main categories: gas phase only release and flow models, and two-phase release and flow models. The difference between the two approaches is that the gas phase models simplify the flow from two-phase to single phase flow, while the two-phase models take into account both liquid and vapour hydrogen. The gas phase models are describing in section 1.2.6.1 and the two-phase models in section 1.2.6.2.

1.2.6.1 Gas-phase only release model (UU)

University of Ulster proposed a method of modelling the consequences of liquid hydrogen spill based on the modelling of gaseous phase only (Molkov et al., 2005). Release of liquefied hydrogen is modelled as gaseous inflow with $Y_{H_2} = 1.0$, at boiling temperature T=20 K. The hydrogen mass inflow was assumed constant, calculated based on the total evaporated hydrogen mass over evaporation period and the hydrogen inflow velocity calculated as $v_{\inf} = \dot{m}/\left(\rho_{H_2} A\right)$, where $\rho_{H_2} = 1.219$ kg/m^3 is the gaseous hydrogen density at T=20 K and A –inflow area.

In (Molkov et al., 2005) this method was applied to set an LES simulation of dispersion of hydrogen cloud resulted from LH_2 spill, mimicking conditions of experiment described by

Chirivella and Witcofski (1986). Hydrogen mass flow was set to $\dot{m} = 8.41$ kg/s, which corresponded to release of total LH_2 mass of 361.78 kg during 43 s (Chirivella and Witcofski, 1986). Two numerical simulations were performed using different hydrogen inflow boundary radius. In the first simulation, the boundary radius was assumed to grow from R=1.0 to R=2.5 m during 10 s, while in the second it was kept constant at R=2.5 m. In order to model turbulence resulting from a violent evaporation, sinusoidal oscillations were superimposed over hydrogen inflow velocity, resulting in following expression for the local inflow velocity $v = v_{\text{inf}}\,(1 + I\sin(2n\pi(x - v_{\text{inf}}\,t)) \cdot \sin(2n\pi\, z)$, where I is the "turbulence level", n = 0.5. In the first simulation (S1) "turbulence level" was set to be equal I = 0.99 for the entire duration of the whole hydrogen release, while the second simulation (S2) used I = 0.99 for the first 10 s and subsequently I = 0.10.

Comparison of resulting hydrogen contours is illustrated in Figure 1.31. Comparison of simulation results for S1 and S2 show that the initial hydrogen inflow boundary condition along with a difference in geometry (pool's boundary and diffuser) and grid resolution have strong effect on the dynamics of simulated hydrogen distribution. In S1 the hydrogen inflow velocity was initially higher than in S2, which caused hydrogen-air cloud to rise higher and predetermined more non-uniform structure of H_2-air cloud. Overall, the general behaviour of the simulated H_2-air cloud was in agreement with experimental data for both simulations with inclination angle between the cloud and ground level being close to the one observed in experiment which was reported to rise at an angle about 30^0, (Witcofski and Chirivella, 1984).

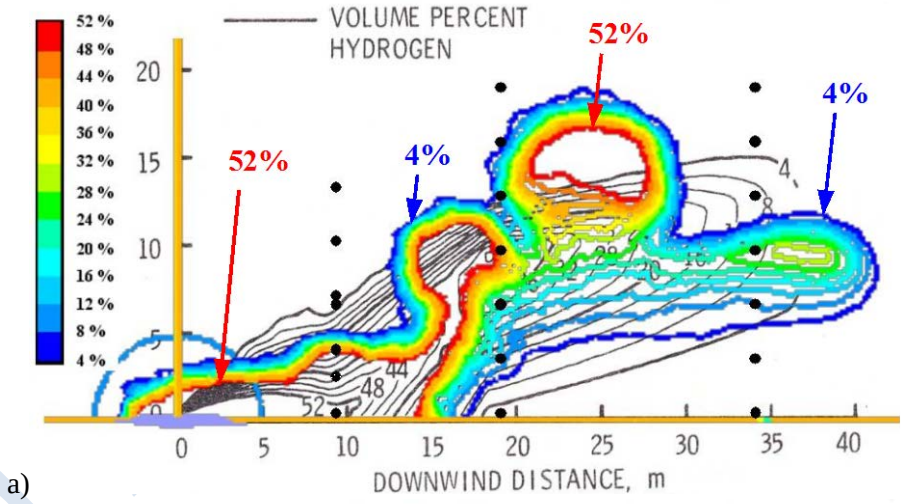

a)

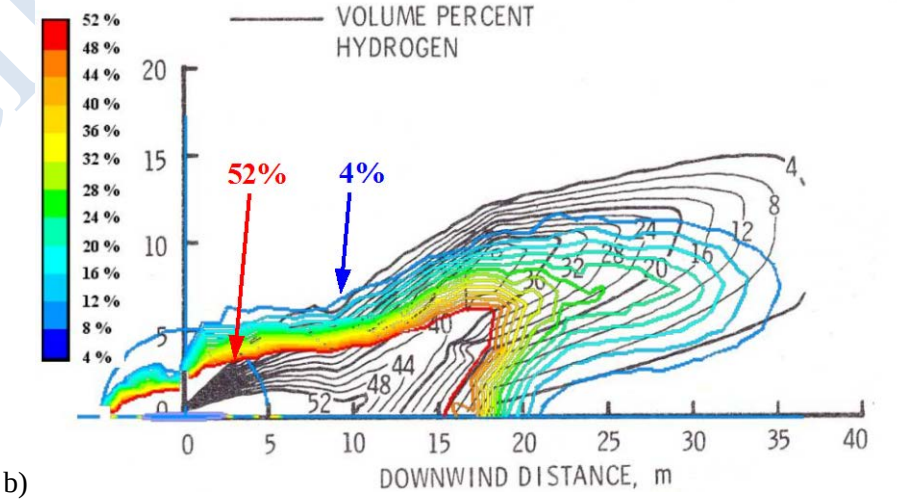

b)

Figure 1.31: Comparison of the experimental (t = 21.33 s) and simulated H_2 concentrations (vol. %): a) S1 (t = 21.36 s), b) S2 (t = 21.35 s), (Molkov et al., 2005),

1.2.6.2 Two-phase flow modelling (NCSRD)

In this section we will adduce the modelling approaches that have been used till today to simulate the liquefied hydrogen (LH2) dispersion by taken under consideration both the vapour and liquid phase of hydrogen.

In LH2 releases, the most common tool for simulating the dispersion is the CFD codes. CFD codes solve the 3D transient mass, momentum and energy conservation equations along with some turbulence model. In the past, for other cryogenic liquid dispersions, e.g. LNG, apart from CFD codes other dispersion models have been used, such as Gaussian plume model and integral models. Winters et al. (2011) is the only reference which uses a three stage buoyant turbulent entrainment model to predict the trajectory, concentration and temperature of a hydrogen jet in liquid based systems, and makes use of the Gaussian model.

Nomenclature

x_i	Cartesian j co-ordinate (m)	M	molecular weight
u_i	i component of velocity (ms^{-1})	*Greek*	
p	pressure (Pa)	μ	viscosity ($kgm^{-1}s^{-1}$)
g_i	gravity acceleration in the i-direction (ms^{-2})	ρ	density
q	mass fraction of component (dimensionless)	*Subscripts*	
t	time (s)	nv	non vapour
h	enthalpy (Jkg^{-1})	ℓ	liquid
Sc, Pr	Schmidt and Prandtl number (dimensionless)	sl	slip
τ	Shear stress tensor (kg/s^2m)	eff	effective (laminar+turbulent)
d	diffusivity (m^2/s)	sat	saturation
α	volume fraction (dimensionless)		

Modelling approaches in the CFD simulations

The CFD softwares solve the conservation equations of the flow system. There are two different specifications of the flow field in case of two-phase flows: the Eulerian and the Lagrangian. The Eulerian specification is a way of looking at fluid motion that focuses on specific locations in the space through which the fluid flows as time passes. Both phases (vapour and liquid) are treating as continuous phases. In the Lagrangian specification of the flow field the observer follows an individual fluid parcel as it moves through space and time. The liquid phase is the dispersed phase, and can be considered as large number of liquid droplets which enters the domain. Each droplet obeys the 2nd Newton law and dependent on

the forces that act on the droplet its velocity can be calculated. The vaporization rate of each droplet should be also taken into account. Coupled with the droplets' equation the Eulerian form of conservation equations of the vapour phase (hydrogen and air) are solved with extra source terms due to the interaction of the phases. Pereira et.al. (1996) has used this specification to simulate the sudden depressurization of liquefied propane into atmospheric environment In the Lagrangian specification the number and size distribution of the droplets at the source should be specified. Due to lack of such information in accidental cryogenic releases, this specification is not generally preferred. However, Witlox et al. (2005) present several correlations for the calculation of the droplet diameter in flashing liquid jets. The Lagrangian specification and its modelling process are out of the scope of this review, since it has not been used in LH2 dispersion yet.

In the Eulerian specification of the flow field, two different approaches were adopted in the CFD simulations: the mixture model and the multi-fluid model.

Mixture model

The following equations are the general differential form of the mass, momentum (Navier-stokes) and energy conservation equations for fully compressible flows using the mixture model:

$$\frac{\partial \rho}{\partial t}+\frac{\partial \rho u_j}{\partial x_j}=S_m \tag{1.203}$$

$$\frac{\partial \rho u_i}{\partial t}+\frac{\partial \rho u_j u_i}{\partial x_j}=-\frac{\partial P}{\partial x_i}+\frac{\partial}{\partial x_j}\left(\tau_{ij}\right)+\rho g_i-\frac{\partial}{\partial x_j}\left(\rho q_\ell u_{sj}\left(1-q_\ell\right)u_{si}\right)+S_{ui} \tag{1.204}$$

$$\begin{aligned}\frac{\partial \rho h_i}{\partial t}+\frac{\partial \rho h_j u_j}{\partial x_j}=&\frac{dP}{dt}+\frac{\partial}{\partial x_j}\left(\lambda\frac{\partial T}{\partial x_j}+\sum_i \rho d_i h_i\frac{\partial q_i}{\partial x_j}\right)\\&+\frac{\partial}{\partial x_j}\left[\rho q_\ell u_{sj}\left(h-h_\ell\right)\right]-q_\ell u_{sj}\left(1-\frac{\rho}{\rho_\ell}\right)\frac{\partial P}{\partial x_j}+S_e\end{aligned} \tag{1.205}$$

The viscous dissipation term is given by:

$$\tau_{ij}=\mu\left[\left(\frac{\partial u_i}{\partial x_j}+\frac{\partial u_j}{\partial x_i}\right)-\frac{2}{3}\delta_{ij}\frac{\partial u_k}{\partial x_k}\right] \tag{1.206}$$

In the source term of energy equation the heat produced by shear stress can be included, but usually is neglected. Only in cases with very large velocity gradients this term is important.

The above equations are solved for the mixture. Therefore, all variables are referred to the mixture. Both phases are assumed to have the same energy, and the hydrogen mass fraction conservation equation is also solved:

$$\frac{\partial \rho q_n}{\partial t}+\frac{\partial \rho u_j q_n}{\partial x_j}=\frac{\partial}{\partial x_j}\left(\frac{\mu_{eff}}{Sc_{eff}}\frac{\partial q_n}{\partial x_j}\right)-\frac{\partial \rho q_\ell u_{sj}\left(1-q_n\right)}{\partial x_j} \tag{1.207}$$

q is the total mass fraction of the component (vapour + liquid). The main issue of the mixture model is on how the liquid mass fraction of each component will be calculated. This matter will be discussed later.

A simplification of mixture model, called Homogeneous Equilibrium Model (HEM) is to assume that the phases are also in local kinetic equilibrium, so the slip terms in the conservation equations are neglected. This approach has two main advantages: the conservation equations are similar to those in single phase flows, and limited information about the source is required.

Slip velocity

In the set of equations (1.203)-(1.207) the slip terms are met which contain the slip velocity. Slip velocity is defined as the velocity of the liquid phase relative to the velocity of the vapour phase.

$$\vec{u}_s = \vec{u}_\ell - \vec{u}_v \tag{1.208}$$

Several models have been developed to calculate the slip velocity. The most common model is the algebraic slip model. According to the algebraic slip model the slip velocity is derived by:

$$\vec{u}_s = \frac{\tau_p}{f_{drag}} \frac{\rho_\ell - \rho_m}{\rho_\ell} \vec{\alpha} \tag{1.209}$$

where τ_p is the particle (droplet) relaxation time

$$\tau_p = \frac{\rho_\ell d_\ell^2}{18\mu_v} \tag{1.210}$$

The drag function defines the flow regime between laminar, transition and turbulent. Here, we provide the Schiller and Naumann formula (Manninen et al. 1996):

$$f_{drag} = \begin{cases} 1+0.15Re_p^{0.687}, & Re_p \le 1000 \\ 0.01833Re_p, & Re_p > 1000 \end{cases} \tag{1.211}$$

The relative Reynolds number is:

$$Re_p = \frac{\rho_v |\vec{u}_v - \vec{u}_\ell| d_\ell}{\mu_v} \tag{1.212}$$

The term $\vec{\alpha}$ is the acceleration and is calculated by:

$$\vec{\alpha} = \vec{g} - (\vec{u}_m \cdot \nabla)\vec{u}_m - \frac{\partial \vec{u}_m}{\partial t} \tag{1.213}$$

The simplest algebraic slip model is the one that takes into account only the gravity acceleration. So, in equation (1.213) the last two terms on the right side are neglected.

In the algebraic slip model the diameter of the droplet should be known. In cryogenic releases the formed droplets do not have the same size, but they follow a distribution around a mean diameter. Usually, in mechanical break-up, or, flashing break up the droplet's diameter can be described by the Rosin-Rammler distribution, or the log normal distribution (Witlox & Bowen 2001). However, information about the droplet's mean diameter from experiments of

LH2 releases is not available. Therefore, it is a complex task to estimate the droplet's characteristics.

Although most of the studies related to LH2 dispersion when solving with the mixture model neglect the slip terms, the last years an effort has been made by Giannissi et al. (2013) to take into account the slip terms. In their study the Ogura and Takahashi empirical model for water (Ogura & Takahashi 1971) is used to calculate the slip velocity. According to this model the slip velocity is calculated with the help of the liquid hydrogen mass fraction. At this point we should mention that Giannissi et al. studied the effect of the liquefaction and freezing of the ambient humidity on the dispersion, and therefore, apart from liquid hydrogen there were also liquid and solid water in the mixture. The Ogura and Takahashi empirical model for water have been used mostly for rain precipitation, but has been also used by Venetsanos et al. (2003) in propane and ammonia two phase releases. It assumes that the droplets are spherical and their diameter is distributed according to the Marshal Palmer distribution (Marshall & Palmer 1948), and the slip velocity is derived by the equation:

$$w_s = -31.21 \cdot \left(\frac{\rho q_{nv}}{\rho_{H_2O}}\right)^{0.125} \tag{1.214}$$

where index nv is for both liquid and solid phase. w_s is the velocity component along z-direction. Only in that direction was assumed that the slip terms are important due to the gravitational acceleration. That slip model does not distinguish between the non-vapour hydrogen and the non-vapour water and treats them the same. That was acceptable in that work because the area occupied by liquid hydrogen was limited to the area near the spill point and much less compared to the area occupied by the condensed and solidified water.

In Giannissi et al. (2014) a modified model of Ogura and Takahashi empirical model for the calculation of the slip velocity was developed and tested with the help of LH2 dispersion experiments. This model is expanded for all liquids. The droplet's size is distributed according to the Marshal Palmer distribution and it takes into account all the flow regimes (laminar, turbulent, transition) according to the droplet's size.

Analytically, the model calculates the mean diameter with the help of the liquid mass, solving the following equation with respect of the mean diameter:

$$\frac{\rho q_\ell}{\rho_\ell} = \int_0^\infty N \frac{\pi}{6} D^3 dD = \pi N_0 \bar{D}^4 \tag{1.215}$$

The vertical liquid flux is derived by the following relationship:

$$\rho q_\ell w_{sl} = \int_0^\infty N \rho_\ell \frac{\pi}{6} D^3 w_{sl} dD \tag{1.216}$$

The integral in the right side of the above equation is calculated numerically. The slip velocity in the integral is calculated with the help of the particle's diameter. The regime can be either laminar or turbulent dependent on diameter size. The equation is

$$w_{sl} = \frac{1}{18 \mu f_{drag}} \left(\rho_\ell - \rho\right) g D^2 \tag{1.217}$$

The drag function, f_{drag}, defines the flow regime, and its value is given by equation (1.211).

Having calculated the integral (1.216) and knowing the quantity ρq_ℓ in each cell, the slip velocity in the cell can be computed.

Liquid mass fraction calculation

As mentioned before the mixture model despite its simplicity it encounters a significant problem: the calculation of the liquid mass fraction. Since each phase is not solved separately as in the multi fluid model, a methodology to predict the mass fraction of each phase should be employed. In the bibliography of LH2 dispersion two different methodologies are met.

Venetsanos et al. (2007)-(Baraldi et al. 2009) use the Raoult's law for multi-component mixtures in order to calculate the liquid mass fraction.

More specific, if the temperature is above the mixture saturation (dew) temperature (T_S), then all mixture components are in the vapour phase. Liquid phase will appear when the temperature is equal or lower than the mixture saturation temperature:

$$T \le T_{sat} \tag{1.218}$$

The mixture saturation temperature is obtained iteratively from the following relation:

$$P = \frac{\sum \frac{q_n}{M_n}}{\sum \frac{q_n}{M_n P_{satn}(T)}} \tag{1.219}$$

where M_n and q_n are the molecular weight and total mass fraction of component-n, $P_{Sn}(T)$ is the saturation pressure of component-n and P is the total pressure.

It should be noted that according to the above equilibrium model any phase changes are assumed to occur instantaneously.

The liquid mass fraction is calculated according to Raoult's law for ideal multi-component mixtures. According to this law under two-phase equilibrium conditions the following relationship is applied which can be solved iteratively and calculate the liquid mass fractions

$$\alpha_{vi} P = \alpha_{\ell i} P_{sati} \quad i = 1, \kappa \tag{1.220}$$

Ichard et al. (2012) in their work present a different methodology. Instead of solving the total mass fraction conservation equation, two mixture fraction equations are solved, one for the vapour and one for the liquid phase.

$$\frac{\partial \rho f_*}{\partial t} + \frac{\partial \rho u_j f_*}{\partial x_j} = \frac{\partial}{\partial x_j}\left(\frac{\mu_t}{Sc_t}\frac{\partial f_*}{\partial x_j}\right) + S_{f_*} \tag{1.221}$$

index $_*$ represents either vapour or liquid phase.

The mixture fractions with the mass fraction are related with the following relationship:

$$q_n = q_{n0}^a + f_v q_{n0}^v + f_\ell q_{n0}^\ell \tag{1.222}$$

$$\sum_n q_n = 1 \tag{1.223}$$

where q_{n0}^{a} is the initial mass fraction of component n inside the surrounding atmosphere, q_{n0}^{v} is the initial mass fraction of component n inside the gas phase at the source, and q_{n0}^{ℓ} is the initial mass fraction of component n inside the liquid phase at the source. Evaporation of the liquid phase is taken into account by ensuring thermodynamic equilibrium. Thermodynamic equilibrium implies that the partial pressure of the component in the vapour phase is the saturation pressure at the mixture temperature. The partial pressure of the component is deduced from the Dalton's law:

$$P_v = a_v P_{atm} = P_{sat}(T) \tag{1.224}$$

The mixture temperature is calculated iteratively with the help of the mixture enthalpy, which is derived by (1.205) equation.

Iteration on the temperature is performed until equilibrium is attained. Equilibrium is achieved when the enthalpy is equal to the initial enthalpy in the control volume.

Multi-fluid model

The other approach of the Eulerian formulation is the multi-fluid model which solves each component and phase separately. In that case the set of equations (1.203)-(1.205) are solved weighted with the volume fraction of each component in each phase, and they turn into the following form:

$$\frac{\partial \rho^{p}\alpha^{p}}{\partial t} + \frac{\partial \rho^{p}\alpha^{p}u^{p}_{j}}{\partial x_j} = S^{p}_{m} \tag{1.225}$$

$$\frac{\partial \rho^{p}\alpha^{p}u^{p}_{i}}{\partial t} + \frac{\partial \rho^{p}\alpha^{p}u^{p}_{j}u^{p}_{i}}{\partial x_j} = -\alpha^{p}\frac{\partial P^{p}}{\partial x_i} + \frac{\partial}{\partial x_j}\left(\alpha_p \tau^{p}_{ij}\right) + \rho^{p}\alpha^{p}g_i + S^{p}_{ui} \tag{1.226}$$

$$\frac{\partial \rho^{p}\alpha^{p}h^{p}}{\partial t} + \frac{\partial \rho^{p}\alpha^{p}h^{p}u^{p}_{j}}{\partial x_j} = -\alpha^{p}\frac{\partial P^{p}}{\partial t} + \alpha^{p}\tau_{ij}\frac{\partial u^{p}_{i}}{\partial x_j} - \frac{\partial \vec{q}^{p}}{\partial x_j} + S^{p}_{e} \tag{1.227}$$

where the index p is for the each phase of each component.

The source terms in the mass equation is the mass source for each component/phase, which could be either a specific mass flow rate from an external source or mass transfer between phases ($\dot{m}^{pq}$). For instance, in non-reacting LH2 release the source terms related to the mass transfer between phases are non zero when phase change of the component takes place (evaporation and/or liquefaction). In the vapour mass equation this term represents the net change of the vapour that has been formed (vapour that has formed minus vapour that has liquefied). In the liquid mass equation the source term is equal with the one in the vapour equation but with opposite sign.

The source terms in the momentum equation include the momentum change between phases, and the forces due to particle (e.g. droplets) existence, such as drag force, lift force, virtual mass force etc.. From the forces due to particle existence usually the drag force is considered important and the other forces are neglected. According to the above the source term in momentum equation is taken the form:

$$S_u^p = \dot{m}^{pq}\vec{u}^{pq} - \dot{m}^{qp}\vec{u}^{qp} + \vec{R}^{qp} + \vec{F}_d \quad (1.228)$$

The interphase velocity $\vec{u}^{pq}$ is defined as follows: if $\dot{m}^{pq} > 0$ (i.e. phase mass p is being transferred to phase q), $\vec{u}^{pq} = \vec{u}^{p}$; if $\dot{m}^{pq} < 0$ (i.e. phase mass q is being transferred to phase p), $\vec{u}^{pq} = \vec{u}^{q}$. Likewise, if $\dot{m}^{qp} > 0$ then $\vec{u}^{qp} = \vec{u}^{q}$, and if $\dot{m}^{qp} < 0$ then $\vec{u}^{qp} = \vec{u}^{p}$.

Finally, the drag force per volume unit is equal to:

$$\vec{F}_d = \frac{f\alpha_\ell \rho_\ell}{\tau_p}\left(\vec{u}_v - \vec{u}_\ell\right) \quad (1.229)$$

f is the drag function as defined in (1.24) equation. τ_p is the "particle relaxation time", which derived by:

$$\tau_p = \frac{\rho_\ell d_\ell^2}{18\mu_v} \quad (1.230)$$

In the energy equation $\vec{q}$ is the heat flux and S_e is a source term that includes sources of enthalpy (e.g., due to chemical reaction or radiation) and heat exchange between phases. The viscous dissipation term of each phase p is derived by (1.206) equation by substituting the mixture viscosity with the viscosity of each phase, μ^p. However, it can be neglected as mentioned in the respective equation of mixture model.

In this model equation (1.207) for the mass fraction is not solved. The number of equations that are solved is dependent on the assumptions made. One can solve the mass and momentum equations of all the components and phases separately. However, in order to reduce the computational cost, it is common to make some simplifications and decrease the number of equations. For instance, in the case that liquid hydrogen is dispersed in dry air it could be considered that the vapour phases of all components (air + hydrogen) have the same velocity, while the hydrogen liquid phase has its own velocity. In this way, two momentum equations are solved instead of three. Vandroux-Koenig et al. (1997) made that assumption in modelling liquid propane release. Chitose et al. (2002) used also this approach to simulate LH2 dispersion based on the NASA experiments: three mass conservation equations, two momentum equations and two energy equations were solved. The three mass equations were for the liquid hydrogen, the vapour hydrogen and the air. The air was assumed to consist only of nitrogen. One momentum and one energy equation were solved for the vapour phase of hydrogen and nitrogen which are treated as one fluid with the same velocity and energy. Finally, one momentum and one energy equation were solved for the liquid hydrogen. By using similar approach and with the same code (CHAMPAGNE), Chitose et al. (2000) simulated also the WE-NET experiments related to LH2 dispersion with main objective to improve the evaporation model of the formed liquid pool.

Source modelling

In the case of cryogenic releases, such as the LH2 release, an important factor is the way the source itself is modelled. The release under cryogenic conditions is actually a two-phase release. In case of an accidental release of liquid hydrogen due to an equipment failure (of the cryogenic tank, of the pipe, etc.) the flow becomes two-phase, because a fraction of the hydrogen is vaporized immediately as it is spilled. In practice, the hydrogen is stored in the

tank at temperature below its boiling point and usually under pressure. When it is released an amount of hydrogen is vaporized spontaneously due to the pressure relief from system to atmospheric pressure. This process is called flash vaporization. The remaining liquid either disperses in form of spray along with the vapour phase until it is evaporated or falls to the ground forming a cryogenic pool. The formed liquid pool absorbs heat from its surroundings, the ground, the air, etc., evaporates and enriches the cloud with the vapour phase. So, there are two sources of vapour hydrogen in the domain, the one from the fracture, and the one that comes from the evaporation of the formed liquid pool. One should consider the best possible way to model the source in order to describe the physical two-phase release conditions.

In two-phase release models the source is modelled as a homogeneous two phase jet. It is located at the exact location of the release point and both liquid and vapour hydrogen are spilled at the release's direction. The main challenge of this approach is to define the vapour mass fraction at the release point. Either isenthalpic or isentropic expansion from storage conditions to atmospheric conditions can be assumed in order to calculate the flashed vapour mass fraction. Sometimes in reality, it is possible the flash to take place in the pipeline before the spill in the atmosphere, but in the modelling it is common to simplify and assume that flash is occurred only at the pipe exit.

Statharas et al. (2000) in the BAM experiments simulation used the isentropic assumption to calculate the inlet liquid hydrogen mass fraction. According to this assumption the hydrogen mass fraction at the exit is found by:

$$q_\ell = \frac{S_v\left(P_{atm}\right) - S_\ell\left(P_{st}\right)}{S_v\left(P_{atm}\right) - S_\ell\left(P_{atm}\right)} \tag{1.231}$$

The index st symbolizes the storage conditions, and the index atm is for the atmospheric conditions.

Verfondern et al. (1997), Venetsanos et al. (2007) and Giannissi et al. (2011) used the isenthalpic assumption (adiabatic flash) to calculate the flashed vapour mass fraction. The flashed vapour mass fraction is derived by the following equation which is simply a heat balance around the nozzle (spill point):

$$q_v = \frac{h_u^\ell - h_d^\ell}{h_d^v - h_d^\ell} \tag{1.232}$$

In fact small differences are detected between isentropic and isenthalpic assumption for low storage pressure.

The mixture density at the exit can now be calculated using the equation:

$$\frac{1}{\rho} = \frac{q_v}{\rho_v} + \frac{q_\ell}{\rho_\ell} \tag{1.233}$$

where

$$q_\ell = 1 - q_v \tag{1.234}$$

And with the help of the nozzle's area and the mass flow rate, the exit velocity that will be set as source boundary condition can be calculated:

$$u = \frac{Q}{\rho A} \tag{1.235}$$

Pool spreading and evaporation

Another important factor in the modelling approach of two-phase releases is the pool spreading and evaporation. Two main different approaches exist and have been use to model the pool formation and spreading in LH2 dispersions.

A simplified model is introduced by Venetsanos et al. (2007). When liquid mass fraction is calculated in a boundary cell (on the ground) it is assumed that a pool is formed with size equal to the area of the cell projected to the ground. In this way the pool formation and spreading is predicted. Heat flux from the ground and the surrounding is taken into account.

A more rigorous rain out and pool model is introduced by Ichard et al. (Ichard et al. 2012) and implemented in the FLACS code. Rain-out is due to the jet impingement either directly on the ground or on obstacles. Ichard et al. in their work (Ichard et al. 2012) coupled the rain out model with the HEM approach. According to the model if there is a jet impinging on an obstacle located at a distance L in the positive x- direction, the amount of liquid that rains out at each time step and at the cells directly adjacent to the obstacle is estimated with the help of the following equation:

$$\begin{aligned} &m_{RO}\left(\vec{x}\right)=\sum_{n,k} q^{\ell}_{n,k}\, m_k \text{ if } T\left(\vec{x}\right)\le T_{NBP} \\ &m_{RO}\left(\vec{x}\right)=0 \text{ if } T\left(\vec{x}\right)> T_{NBP} \\ &\vec{x}=\left[x(i),y(j),z(k)\right] \end{aligned} \tag{1.236}$$

where i, j, k are the cell nodes.

Rain-out occurs only if the temperature of the mixture is less than or equal to the normal boiling point of the mixture. The sum on the index k in equation (1.236) is performed over all grid cells located at a distance less or equal than ℓ_{RO} from the wall. The characteristic length scale ℓ_{RO} for the rain-out process is defined as the product of the characteristic velocity $\left(\vartheta_{RO}\right)$ and characteristic time $\left(\tau_{RO}\right)$ scales for the rain-out process. As characteristic velocity for the rainout process $\left(\vartheta_{RO}\right)$ is taken the local maximum velocity in regions of the flow where evaporation takes place and thermodynamic equilibrium has been attained. This can be justified by the fact that the main contribution to the mass of liquid that deposits on the ground or on obstacles comes from droplets with the largest diameters, since they have larger inertia than fluid particles, and hence have an extended memory of their maximum velocities. Finally, the characteristic time τ_{RO} over which the rain-out process occurs is assumed to be the time needed by the flow to achieve a new thermodynamic equilibrium. Appropriate source terms are added in the mixture fraction (1.221) and mixture enthalpy transport equations. The amount of liquid that is removed from the flow is injected inside the pool model.

For the modelling of the liquid pool on the ground the two-dimensional (2D) shallow layer equations are solved to calculate the behaviour of the pool. The assumption behind the shallow water theory is that the pool properties (temperature, velocity, etc.) are uniform across the thickness of the pool and, thus, are only a function of the horizontal coordinates. Therefore, the shallow layer equations are an approximation of the equations of fluid motion, which is accurate when the thickness of the liquid pool is small in comparison with its horizontal dimensions. The use of the 2D shallow layer equations to calculate the pool spread and vaporization has an advantage: it account for the effect of terrain features or obstacles on

the spread of the pool. The shallow layer model solves a system of non-linear differential equations that allows for description of pool height and velocity as functions of time and location based on the mass and momentum conservation (Ichard et al. 2012) and (Middha et al. 2011).

Mass conservation equation:

$$\frac{\partial h}{\partial t}+\frac{\partial\left(u_i h\right)}{\partial x_i}=\frac{\dot{m}_\ell-\dot{m}_v}{\rho_\ell} \tag{1.237}$$

Momentum conservation equation:

$$\frac{\partial u_i}{\partial t}+u_j\frac{\partial u_i}{\partial x_j}=F_{g,i}+F_{\tau,i} \tag{1.238}$$

The terms on the right side of equation (1.48) are the force terms. $F_{g,i}$ is the gravity term and is modelled as:

$$F_{g,i}=g\delta\frac{\partial\left(h+z\right)}{\partial x_i} \tag{1.239}$$

where z is to include the elevation from the ground. The parameter δ is a reduction factor that accounts for the penetration of the pool to the substrate. If the substrate is solid then $\delta=1$. For spills on water $\delta=\left(1-\rho_\ell/\rho_w\right)$. $F_{\tau,i}$ is the shear stress between the liquid pool and the substrate and is given by the general formula:

$$F_{\tau,i}=\frac{1}{8}f_f u_i\left|\vec{u}\right| \tag{1.240}$$

This model has been used also by Verfondern et al. (1997), (2007), in order to predict the pool spreading and evaporation that is formed by LH2 spills. However, the prediction was limited in the pool formation and it was not coupled with the vapour dispersion.

For the pool energy the enthalpy conservation equation can be solved taking into account all heat sources (heat due to the continuous spill, air convection, air radiation, ground conduction and heat loss due to evaporation).

$$\rho_\ell h\frac{\partial\theta}{\partial t}+\rho_\ell h u_j\frac{\partial\theta}{\partial x_j}=\dot{m}_\ell\left(\theta_\ell-\theta\right)+\dot{q}_c''+\dot{q}_{rad}'+\dot{q}_g''+\dot{q}_{evap}'' \tag{1.241}$$

where θ is the specific enthalpy.

In case of a boiling pool the total enthalpy (temperature) of the liquid pool remains constant during boiling and is assumed uniform over the entire mass of the pool. Therefore, the evaporation rate can be calculated by dividing the net heat transfer flux between the pool and the surroundings, Q'', with the latent heat of vaporization of hydrogen.

$$\dot{m}_v''=\frac{Q''}{L} \tag{1.242}$$

Due to the fact that the dominant heat input is the heat conduction from the ground the other heat inputs can be neglected and thus the evaporation rate in solid grounds can be approximated as being proportional to $t^{-1/2}$ (Verfondern et al. 2007).

For the calculation of the heat transfer from the ground the interface temperature should be estimated first. In general, two boundary conditions can be applied: 1) constant temperature: it is assumed that the temperature at the ground-pool interface is equal to the pool temperature. This boundary condition is imposed by (Ichard et al. 2012) and 2) equate the heat fluxes at the interface (heat conduction from the ground is equal to heat convection from the pool at the interface ground-pool), in order to calculate the interface temperature at each time step. Applying the first boundary condition the ground heat conduction is given by,

$$\dot{q}_g'' = \frac{\lambda_g \left(T_g^0 - T_\ell\right)}{\sqrt{\pi \alpha_g \left(t - t_\ell\right)}} \tag{1.243}$$

where λ_g and α_g are the thermal conductivity and thermal diffusivity of the substrate, T_g^0 is the initial temperature of the substrate, T_ℓ is the pool temperature and t_ℓ is the time at which the substrate comes first in contact with the pool.

Applying the second boundary condition we have,

$$-\lambda_g \frac{(T_g - T_i)}{\Delta z} = h_c \left(T_i - T_\ell\right) \tag{1.244}$$

where T_i is the temperature at the interface. Iterations on T_i are performed until the above equation is satisfied.

In boiling pools the boiling correlations can be employed to calculate the heat transfer coefficient, h_c, in equation (1.244). In case of solid substrate the use of boiling correlations is expected to affect the dispersion only at the initial stage of the spill due to fast cooling of the ground. Moreover, the temperature at the interface would become very soon equal to the pool temperature and thus the constant temperature boundary conditions (first boundary condition above) is considered a good approximation in cryogenic pools. However, in case of water substrate the boiling correlations would affect the dispersion over the entire spill duration. The heat flux would be in the film boiling regime over the entire spill, because the water temperature can be assumed constant. In that case a constant heat flux can be set at the interface equal to the heat flux that corresponds to film boiling. To take into account the effect of pool motion a total heat transfer coefficient equal to the sum of the film boiling coefficient and a forced convection coefficient can be used.

1.2.7 Volumetric source permeation model (UU)

Though phenomena of hydrogen permeation is defined as diffusion of hydrogen ions through walls or interstices, in terms of hydrogen safety it may be seen as a slow long term hydrogen release relevant to compressed hydrogen storage systems. Analytical analysis made in (Adams et al. 2011) demonstrated that hydrogen concentration on the surface of high-pressure container, driven by processes of hydrogen permeation through a wall and its diffusion in atmosphere, is significantly below 100% (of the order 0.01%). First type of boundary conditions (prescribed inflow velocity and 100% hydrogen fraction at inflow) is not well suited for simulation of hydrogen diffusion, accumulation and distribution resulting from hydrogen permeation, and alternative modelling approach is required. The volumetric source term model, described in Section 1.2.4, may be utilised for this purpose.

Example of such application is given in (Saffers et al. 2011). The problem formulation included a typical compressed hydrogen tank installed with 0.5 m clearance in a garage like

enclosure. The tank was 0.672 m long and 0.505 m in diameter with hemispherical volumes at each end with diameter of 0.505 m; surface area of the tank was equal 1.87 m^2, volume of tank was about 0.2 m^3. The garage enclosure sizes were $L \times W \times H$=5×3×2.2 m, total volume was equal 33 m^3. The ambient temperature was equal 298 K. Two scenarios were simulated with different permeation rates: 1 NmL/hr/L (normal mille-litres per hour per litre of tank volume) and 8 NmL/hr/L. To comply with incompressible problem formulation two small openings were maintained in the enclosure floor, where outflow boundary condition was specified. The purpose of the simulations performed in (Saffers et al. 2011) was to investigate if the hydrogen distribution, resulting from permeation, is capable to form a non-uniform and combustible layered mixture with air.

The applied CFD model was based on solution of incompressible three-dimensional Navier-Stokes equations, laminar flow, energy and species (hydrogen) transport equations. Hydrogen appearing on the tank surface due to permeation was modelled using volumetric source in a thin layer of control volumes of 1 mm thickness around the tank. Values of the source terms themselves were calculated as follows:

- with the permeation rate of 1 NmL/hr/L and 45 NmL/hr/L for a tank with volume 200 L a volume of permeated hydrogen is $5.6 \cdot 10^{-8}$ m^3/s and $2.5 \cdot 10^{-6}$ m^3/s respectively, which corresponds to mass flow rates $\dot{m}_{H2} = 4.5 \cdot 10^{-9}$ kg/s and $\dot{m}_{H2} = 2.0 \cdot 10^{-7}$ kg/s;
- region of calculation domain designated for source term had 1 mm thickness around the tank, with the tank having surface area $A_t = 1.87$ m^2, which makes this region volume $V_r = 1.87 \cdot 10^{-3}$ m^3;
- then, value of source terms in mass and hydrogen conservation equations were calculated as $S_{H2} = \dot{m}_{H2} / V_r$ and were equal to $2.43 \cdot 10^{-6}$ kg/s/m^3 and $1.09 \cdot 10^{-4}$ kg/s/m^3 for each permeation rate respectively.

The hydrogen permeation process was simulated for 133 min (8000 s). Time step was kept equal to 0.05 s during the whole simulation to maintain high numerical precision. The latter was controlled monitoring overall hydrogen mass balance, which relative error was below 0.1%. Simulation results obtained in (Saffers et al. 2011) demonstrated that permeation process, over long period of time, will result in formation of a nearly uniform hydrogen-air mixture in a garage. Difference of hydrogen concentrations between the garage ceiling and floor was practically constant during whole simulation period and negligible in practical sense: $2 \cdot 10^{-3}$% by vol. for the permeation rate 1 NmL/hr/L and $5 \cdot 10^{-2}$% by vol. for rate 45 NmL/hr/L, see Figure 1.32. Maximum hydrogen concentration, reached after 133 minutes, was equal to $6.24 \cdot 10^{-3}$% by vol. for the lower permeation rate and $1.82 \cdot 10^{-1}$% by vol. for the lager one.

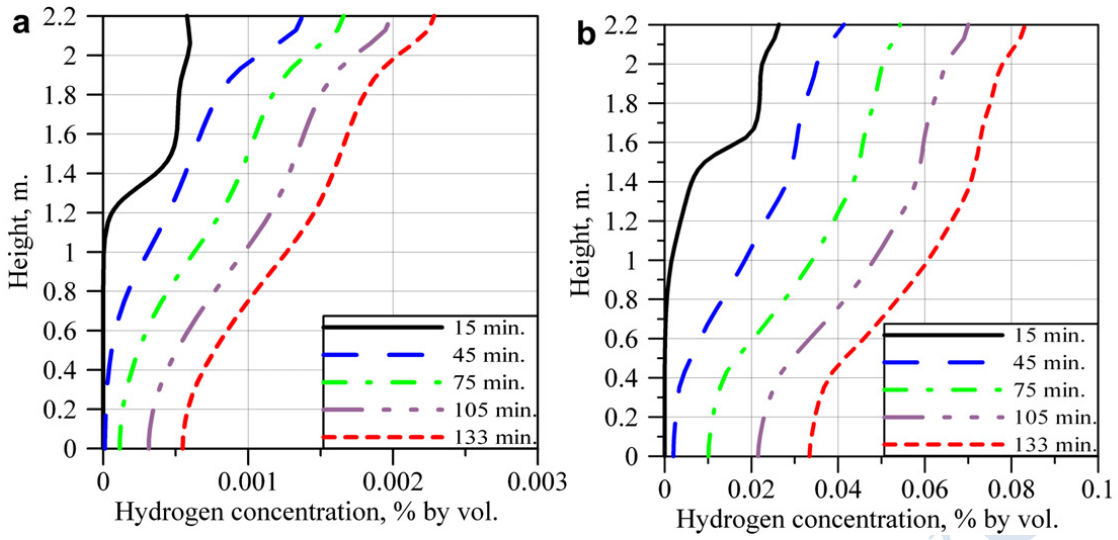

Figure 1.32: Hydrogen concentration profile across the garage height with time: (a) permeation rate 1 NmL/hr/L; (b) permeation rate 45 NmL/hr/L (Saffers et. 2011).

1.2.8 Fast filling of hydrogen storage tanks (JRC)

The deployment of hydrogen powered vehicles requires the definition of the filling protocols to be used at refuelling stations during the refilling of hydrogen tanks. As it described in Melideo et al. (2014), drivers are used to re-fill the vehicle tank in a few minutes with conventional fuels and they have similar expectations towards new technologies like hydrogen powered vehicles. The requirement of a reasonable short filling time produces a new challenge since the increase of temperature due to the quick compression inside the vessel, (e.g. from low pressure up to 700 bar) could be detrimental for the mechanical properties of the tank material. Because of safety reason, the maximum allowed temperature inside tanks is set to 85 C (358 K) by the majority of the international standards and regulations (e.g. the European regulation (2010), the SAE (2013, 2014), the global technical regulation (2013), and the international standard ISO 15869 (2009)).

Moreover, the higher the temperature is, the lower the gas density is and the smaller the amount of gas that can be filled inside the cylinder is. Higher temperatures cause the decrease of the state of charge (SoC) of the tank and therefore the decrease of the distance that a vehicle can travel with one filling. The state of charge is defined as the ratio between the density at the end of the filling process and the density at 70 MPa and 15 $^{\circ}$C or at 87.5 MPa and 85 $^{\circ}$C (40.2 kg/m3). The technological solution envisaged to tackle the fast filling issues is to pre-cool the gas before injecting it into the tank. However the addition of the heat exchanger to the refuelling installation causes a significant increase in the initial cost of the station and in the running costs in terms of energy consumption.

Several research teams performed CFD validation studies e.g. (Dicken and Merida, 2007) (Kim et al., 2010) (Zhao et al., 2010) (Heitsch et al., 2011) (Takagi et al., 2011) (Galassi et al., 2011) (Suryan et al., 2012) (Zhao et al., 2012) (Suryan et al., 2013) (Melideo et al., 2014). By comparing the simulation results with the experimental measurements they demonstrated that the current CFD models are capable of capturing the temperature histories inside the tank with a sufficient level of accuracy. In all the above CFD papers, the size of the tank is limited to 100-150 L and the ratio length to diameter of the vessels is limited to about 3.5. For those

tanks CFD can be instrumental in identifying the most suitable filling protocols for the regulations codes and standards.

For larger tanks stronger inhomogeineties and gradients are produced in the temperature field inside the tank as shown by experiments and therefore describing the fast filling of larger cylinders can be more challenging for the CFD models. Only future validation exercises with larger and longer tanks will show whether CFD can achieve the same level of accuracy that was demonstrated for the smaller vessels.

An example of the comparison between experiments and simulations is shown in Figure 1.33 (Galassi et al., 2014). In (Galassi et al., 2014), the compressible Navier-Stokes equations were solved and the turbulence closure was achieved by means of a modified k-ε model (Ouellette et al., 2000) which corrects jets spreading rate over-prediction typical of the standard k-ε model (Pope, 1978) (Magi at al., 2001). The conjugate heat transfer (CHT) capability in the model allowed the calculation of the thermal conduction through solid materials coupled with the calculation of temperature in the working fluid. The Redliche-Kwong (Redliche et al., 1949) equation of state was applied to include the real-gas behaviour at high pressure. The gravitational source term was included into the momentum equation and within the turbulent kinetic energy and dissipation equations, in order to consider buoyancy effects. The same modelling strategy was successfully applied in (Melideo et al., 2014).

In (Suryan et al., 2013) a comparative study of four turbulence models was carried out: the standard k-ε model, the Realizable k-ε model, the RNG k-ε model, and the SST k-ω model.

The simulations results were compared with the experimental data of (Dicken et Merida, 2007) and the realizable k-ε model and the Reynolds Stress Model were identified as the most accurate turbulence models for the simulation of hydrogen gas fast filling process. It was shown that the Reynolds-stress model is capable of capturing some flow details that cannot be modelled by the eddy viscosity models. Nevertheless the authors state that the marginal improvements on the mean variables with the Reynolds-stress model compared to the realizable k-ε model does not justify the preference of the Reynolds-stress model over the realizable k-ε model because of the longer computing time that is required with the Reynolds-stress model, especially for fully 3D simulations.

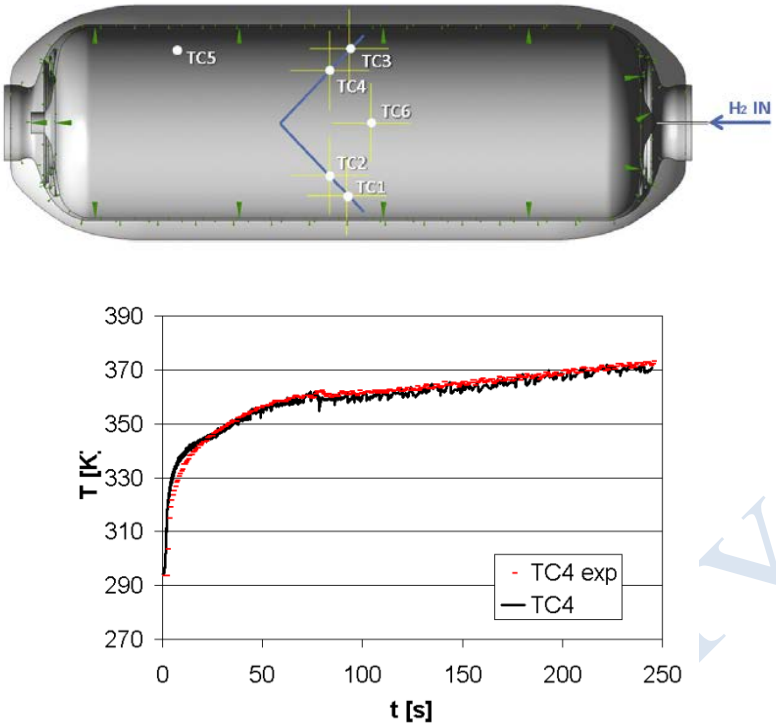

Figure 1.33: Top: tank geometry and position of the sensors. Bottom: comparison between simulation results (black) and experimental data (red) for the temperature history during the filling of a tank (Galassi et al., 2014).

1.3 References

Abramovich, G.N. (1963) *The theory of turbulent jets*. Cambridge, Mass.:M.I.T. Press.

Adams, P., Bengaouer, A., Cariteau, B., Molkov, V. and Venetsanos, A.G. (2011) Allowable hydrogen permeation rate from road vehicles, *Intl. J. of Hydrogen Energy*, 36:2742-2749.

Afiq, W. M. Y., Azwadi, C. S. N., and Saqr, K. M. (2012) Effects of buildings aspect ratio, wind speed and wind direction on flow structure and pollutant dispersion in symmetric street canyons: a review. *Intl. J. of Mech. and Materials Engg.* 7(2).

AIVC (1996) *A guide to energy efficient ventilation*. Air Infiltration and Ventilation Centre (AIVC), International Energy Agency, University of Warwick Science Park, Coventry, UK, ISBN 0 946075 85 9.

Baraldi, D. , Venetsanos, A.G., Papanikolaou, E., Heitsch, M. and Dallas, V. (2009) Numerical analysis of release, dispersion and combustion of liquid hydrogen in a mock-up hydrogen refuelling station. *J. of Loss Prevention in the Process Ind.*, 22(3):303–315.

Batchelor, G. (2000). An introduction to fluid dynamics. Gambridge University Press.

Betchov, R. and Criminale, W.O. (1967) *Stability of parallel flow*. Academic Press.

Birch, A. D., Brown, D. R., Dodson, M. G. and Swaffield, F. (1984) The structure and concentration decay of high pressure jets of natural gas. *Comb. Sc. and Tech.* 36: 249-261.

Blackadar, A. K. (1998) *Turbulence and diffusion in the atmosphere*, Springer-Verlag.

Blocken, B., Stathopoulos, T., Carmeliet, J. (2007) CFD simulation of the atmospheric boundary layer: wall function problems. *Atmos. Environ*, 41:238–252.

Boris J.P. (1990), On Large Eddy Simulation Using Subgrid Turbulence Models, in Whither Turbulence? Turbulence At The Crossroads, J.L. Lumley Ed., Springer, New York, p. 344.

Brennan, S., Makarov, D. and Molkov, V. (2011) Dynamics of flammable hydrogeneair mixture formation in an enclosure with a single vent. In: *Proceedings of the 6th International seminar on fire and explosion hazards*. England: Research Publishing; July 2011. ISBN 978-981-08-7724-8.

Brennan, S. and Molkov, V.V. (2013) Safety assessment of unignited hydrogen discharge from onboard storage in garages with low levels of natural ventilation. *Intl. J. of Hydrogen Energy*, 38: 8159-8166.

Brescianini, C. P., Delichatsios, M. A. (2003) New evaluation of the k-epsilon turbulence model for free buoyant plumes. *Numerical Heat Transfer, Part A.* 43:731-751.

Burmeister, L. C. (1993) *Convective Heat Transfer* (p. 107). 2nd ed. Publisher Wiley-Interscience.
Cariteau, B., Tkatschenko, I. (2011) Experimental study of the effects of vent geometry on the dispersion of a buoyant gas in a small enclosure. *Intl. Conference on Hydrogen Safety*, San Francisco.
Cariteau, B. (2010) *Résultats expérimentaux sur les régimes de dispersion d'un jet d'hélium dans une enceinte*. SFME/RT/2010-013.
Cariteau, B. (2013) Experimetnal study of the effect of vent geometry on the dispersion of a buoyant gas in a small enclousre, *Intl. J. of Hydrogne Energy*, 38:8030-8038.
Caton, F., Britter, R. E., and Dalziel, S. (2003). Dispersion mechanisms in a street canyon. *Atmos. Environ.*, 37(5):693–702.
Cebeci, T., Smith, O. (1974) Analysis of turbulent boundary layers, Academic press inc., London.
Cetegen B. M. (1997) Behavior of naturally unstable and periodically forced axisymmetric buoyant plumes of helium and helium-air mixtures, *Phys. Fluids*, 9:3742-3752.
Chandrasekhar, S. (1961). *Hydrodynamic and Hydromagnetic Stability*. Dover Publications.
Chen, C. J. and Rodi, W. (1980) *Vertical buoyant jets: a review of experimental data*. New York: Pergamon.
Chen, C.J. and Rodi, W. (1980) *HMT – the science and applications of heat and mass transfer, vol. 4*. Oxford: Pergamon Press.
Chenoweth, D.R. (1983) *Gas-transfer analysis*. Section H - Real gas results via the van der Waals equation of state and virial-expansion extensions of its limiting Abel-Noble form. Livermore, CA, Sandia National Laboratories.
Chirivella, J.E. and Witcofski, R.D. (1986) Experimental Results from Fast 1500 Gallon LH2 spills. *Am. Inst. Chem. Eng. Symp*. 82(251):120-140.
Chitose, K., Takeno, K., Hayashi, K., Hishida, M. and Maruyama, F. (2000) Activities on hydrogen safety for the WE-NET project - experiment and simulation of the hydrogen dispersion. *Proceedings of the 13th World Hydrogen Energy Conference, Bejiing*, pp.1–11.
Chitose, K., Takeno, K., Hayashi, K., Hishida, M. and Okamoto, M. (2002) Analysis of a Large Scale Liquid Hydrogen Dispersion Using the Multi-Phase Hydrodynamics Analysis Code (CHAMPAGNE). *Energy Resour. Technol.* 124(4):283–289.
Cleaver, R.P., Marshall, M.R. and Linden, P.F. (1994) The build-up of concentration within a single enclosed volume following a release of natural gas. *J. Haz. Materials.* 36:209-226.
Commission Regulation (2009) (EC) No 79/2009 Of The European Parliament & Of The Council of 14 Jan. 2009 on type-approval of hydrogen-powered motor vehicles, & amending Dir.2007/46/EC, *Off. J. of the Eur. Union*, 4.2.2009.
Commission Regulation (EU) No 406/2010 of 26 April 2010 implementing regulation (EC) No 79/2009 on type-approval of hydrogen-powered motor vehicles. *Off J. Eur Union.* 18.05.2010. L 122/1-107.
Cox G. and Kumar S. (2000) *Modelling enclosure fires using CFD*. SFPE Handbook, 3rd Edition.
Craft, T. J., Ince, N. Z., Launder, B. E. (1996) Recent developments in second-moment closure for buoyancy-affected flows. *Dynamics of Atm. and Oceans*. 23:.99-114.
Crank, J. (1975*) The mathematics of diffusion*. 2nd ed. USA: Oxford University Press.
Cresswell R., Haroutunian V., Ince N. Z., Launder B. E., Szczepura R. T. (1989) Measurement and modelling of buoyancy-modified elliptic turbulent flows, in Proc. 7th Symp. on Turbulent Shear Flows, (Eds).
Dai, Z., Tseng, L.-K. and Faeth G. M. (1994) Structure of round, fully-developed, buoyant turbulent plumes. *J. Heat Transfer*. 116:409-417.
Daly, B. J. and Harlow F. H. (1970) Transport equations in turbulence. *Phys. Fluids.* 13:2634-2649.
Davidson, L. (1990) Second-order correction of the k-epsilon model to account for non-isotropic effects due to buoyancy. *Intl. J. Heat Mass Transfer*. 33:2599-2608.
DesJardin P. E., O'Hern, T. J. and Tieszen, R. (2004) Large eddy simulation and experimental measurements of the near-field of a large turbulent helium plume. *Phys. Fluids.* 16:1866-1883
Desmond, B. T. (2000) *Meteorological Monitoring Guidance for Regulatory Modeling Applications Meteorological Monitoring Guidance*, EPA-454/R-99-005.
Dicken, C.J.B. and Merida, W. (2007) Modeling the transient temperature distribution within a hydrogen cylinder during refueling. *Numerical Heat Transfer, Part A: Applications.* 53:685–708.
Dienhart, B. (1995) *Ausbreitung und Verdampfung von flüssigen Wasserstoff auf wasser und festem Untergrund*. Report Jül-3155. Research Center Jülich, Germany.
Dimotakis, P. (2005). Turbulent mixing. *Annu. Rev. Fluid Mech*. 37:329–356.
Dimotakis, P.E. (2000) The mixing transition in turbulent flows. *J. of Fluid Mech*. 409:69–98.
Drazin, P.G. and Reid, W.H. (2004) *Hydrodynamic Stability* (Cambridge Mathematical Library). Cambridge University Press.
Dulov, V.G. and Luk'yanov G.A. (1984) *Gasdynamics of the outflow processes*. Novosibirsk: Nauka.
Dyer A. J. (1974) A review of flux-profile relationships. *Boundary-Layer Meteorology*. 7: 363-372.
Dyrbye, C., and Hansen, S. O. (1997). *Wind loads on structures*. Wiley.

ECE/TRANS/WP.29/2013/41 (2013) *Proposal for a global technical regulation on hydrogen and fuel cell vehicles*.

Einstein, A. (1905) On the motion of small particles suspended in liquids at rest required by molecular kinetic theory of heat. *Annalen der Physik.* 17:549-560.

El Baz, A., Craft, T.J., Ince, N.Z. and Launder, B.E. (1993) On the adequacy of the thin-shear-flow equations for computing turbulent jets in stagnant surroundings, *Int. J. Heat Fluid Flow*. 134:164-169.

Favre, A. (1992) Formulation of the statistical equations of turbulent flows with variable density. In: *Studies in Turbulence*, pp. 324–341. New York: Springer.

Franke, J., Hellsten, A., Schlünzen, H. and Carissimo, B. (Eds) (2007) *Best practice guideline for the CFD simulation of flows in the urban environment*. COST Action 732 on "Quality Assurance and Improvement of Microscale Meteorological Models", COST Office, Brussels, Belgium, ISBN: 3-00-018312-4.

Franke, R. (1991) *Numerische Berechnung der instationnaren Wirbelablosung hinter zylindrischen Korpern*. University of Karlsruhe, Ph.D.

Friedrich, A., Grune, J., Kotchourko, A., Kotchourko, N., Sempert, K., Stern, G. and Kuznetsov, M. (2007) Experimental study of jet-formed hydrogen-air mixtures and pressure loads from their deflagrations in low confined surroundings. In: *Proceedings of 2nd International Conference on Hydrogen Safety*. San Sebastian, Spain.

Fureby, C., Tabor, G., Weller, H.G. and Gosman, A.D. (1997) Differential subgrid stress models in large eddy simulations. *Physics of Fluids.* 9:3578–3580.

Galassi, M.C., Papanikolaou, E., Heitsch, M., Baraldi, D., Acosta Iborra B. and Moretto, P. (2014) Assessment of CFD models for hydrogen fast filling simulations. *Intl J of Hydrogen Energy.* 39:6252-6260.

Gasexplosionen på Brahegatan I Stockholm den 3 Mars 1983, Kommittén (Kn 1981:02) för undersökning avallvarliga olyckshäandelser, Utredningsrapport Nr.2, 1983, Stockholm (summarized translation in English). (n.d.).

Gebhart, B., Jaluria, Y., Mahajan, R. L. and Sammakia, B. (1988) *Buoyancy-induced flows and transport*. New York: Hemisphere Pub. Corp..

George Jr., W. K., Alpert, R. L. and Tamanini, F. (1977) Turbulence measurements in an axisymmetric buoyant plume. *Int. J. Heat Mass Transfer.* 20:1145-1154.

Germano, M., Piomelli, U., Moin, P. and Cabot, W. (1991) A dynamic subgrid-scale eddy viscosity model. *Physics of Fluids A.* 3 (7):1760–1765.

Ghosal, S. (1996) An Analysis of Numerical Errors in Large-Eddy Simulations of Turbulence. *J. of Comp. Physics.* 125:187–206.

Ghosal, S., Lund, T., Moin, P. and Akselvoll, K. (1995) A dynamic localization model for large eddy simulation of turbulent flows. *J. of Fluid Mech.* 286:229–255.

Giannissi, S.G., Venetsanos, A.G, Bartzis, J., Markatos, N., Willoughby, D.B. and Royle, M. (2011) CFD modeling of LH2 dispersion using the ADREA-HF code. *Proceedings of 4th International Conference on Hydrogen Safety*, pp.1–12.

Giannissi, S.G., Venetsanos, A.G., Markatos, N. and Bartzis, J.G. (2014) CFD modeling of hydrogen dispersion under cryogenic release conditions, *Intl. J. of Hydrogen Energy*, in press.

Giannissi, S.G., Venetsanos, A.G., Markatos, N., Willoughby, D.B. and Royle, M. (2013) Simulation of hydrogen disperison under cryogenic release conditions. In: *Proceedings of 5th International Conference on Hydrogen Safety*, pp.1–12.

Gibson, M. M. and Launder, B. E. (1978) Ground effects on pressure fluctuations in the atmospheric boundary layer. *J. Fluid Mech*. 86(3):491-511.

Grinstein, F.F. and Guirguis, R.H. (1992) Effective viscosity in the simulation of spatially evolving shear flows with monotonic FCT models. *J of Comp Physics*, 101:165–175.

Gryning, S. E., Batchvarova, E., Brümmer, B., Ejsing, J., Hans, L. and Søren, E. (2007) On the extension of the wind profile over homogeneous terrain beyond the surface boundary layer. *Boundary-Layer Meteorology.* 124:251-268.

Han, J., Pal Arya, S., Shen, S. and Lin, Y-L. (2000) *An Estimation of Turbulent Kinetic Energy and Energy Dissipation Rate Based on Atmospheric Boundary Layer Similarity Theory*. NASA/CR-2000-210298.

Hanna, S. R., Briggs, G A., Hosker Jr., R. P. (1982) *Handbook on atmospheric diffusion*. Technical Information Center, US Department of Energy, DOE/TIC-11223 (DE82002045).

Hara, T., Kato, S. (2004) Numerical simulation of thermal plumes in free space using the standard k-epsilon model. *Fire Safety Journal.* 39:105-129.

Hargreaves , D. M. and Wright N. G. (2007) On the use of the k–ε model in commercial CFD software to model the neutral atmospheric boundary layer. *J. Wind Eng. Ind. Aerod*. 95:355–369.

Heitsch, M., Baraldi, D., Moretto, P., (2011) Numerical investigations on the fast filling of hydrogen tanks. *Intl J of Hydrogen Energy* 36, p. 2606–2612.

Henkes, R.A.W.M., Van Der Vlugt, F.F. & Hoogendoorn, C.J., 1991. Natural-convection flow in a square cavity calculated with low-Reynolds-number turbulence models. *International Journal of Heat and Mass Transfer*, 34(2), pp.377–388.

Högström, U. (1996) Review of Some Characteristics of the Atmospheric Surface Layer. *Boundary-Layer Meteorology*. 78:215-246.

Holmes, P., Lumley, J.L. and Berkooz, G. (1998) *Turbulence, Coherent Structures, Dynamical Systems and Symmetry*. Cambridge University Press.

Hossain, M. S. and Rodi, W. (1982) A turbulence model for buoyant flows and its application to vertical buoyant jets. In: *Turbulent Buoyant Jets and Plumes*, W. Rodi (Eds). Pergamon Press.

Houssin-Agbomson, D. , Gilles, B.-M., Cariteau, B. and Jallais, S. (2013) Influence Of The Location Of A Buoyant Gas Release In Several Configurations Varying The Height Of The Release. *Int. Conference on Hydrogen Safety*, Brussels, Paper 161.

Hunt, G.R. and Linden, P.F. (2005) Displacement and mixing ventilation driven by opposing wind and buoyancy. *J. Fluid Mech*. 527:27-55.

Ichard, M., Hansesn, O.R., Middha, P. and Willoughby, D. (2012) CFD computations of liquid hydrogen releases. *Intl. J. of Hydrogen Energy*. 37(22):17380–17389.

InsHyde D74 (2009*) Allowable hydrogen permeation rate for automotive applications*. Deliverable D74, InsHyde project, accessible at: http://www.hysafe.org/download/1855/HySafe/D74/Permeation/Rev7/Final/Corr/1.pdf; June 2009.

International Standard Organization (2009) *Gaseous hydrogen and hydrogen blends land vehicle fuel tanks*. ISO/TS 15869.

Kelsey, A. (2002) *CFD modelling of flashing jets: Simulation of flashing propane jets*. CM/00/02.

Kim, S.C., Lee, S.H. and Yoon, K.B. (2010) Thermal characteristics during hydrogen fueling process of type IV cylinder. *Intl J of Hydrogen Energy*. 35:6830–6835.

Koutsourakis, N. (2010) Flow and Pollutant Dispersion in Street Canyons: A Review. *Technika Chronika Scientific Journal of the TCG*. 1(1): 175–189.

Lacome, J.-M. and Truchot, B. (2013) Harmonization of practices for atmospheric dispersion modelling with the framework of risk assessment. *15th Conference on "Harmonisation within Atmospheric Dispersion Modelling for Regulatory Purposes"* (Harmo'15), Madrid, Spain, 6-9 May 2013.

Landa, P.S. and McClintock, P.V.E. (2004) Development of turbulence in subsonic submerged jets. *Physics Reports*. 397(1):1–62.

Launder, B. E. and Spalding, D. B. (1972) *Mathematical models of turbulence*. London: Academic Press.

Launder, B.E. and Spalding, D.B. (1974) The numerical computation of turbulent flows. *Comp. Methods in Applied Mech. and Engg.* 3(2):269–289.

Launder, B.E., Reece, G.J. & Rodi, W. (1975). Progress in the development of a Reynolds-stress turbulence closure. *Journal of Fluid Mechanics*, 68(03), p.537.

Lilly, D. K. (1992), A proposed modification of the Germano subgrid scale closure model, *Phys. of Fluids*, 4: 633–635.

Lin, C.C. (1955) *The Theory of Hydrodynamic Stability*. Cambridge University Press.

Linden, P. F., Lane-Serff, G. F. and Smeed, D. A. (1990) Emptying filling boxes: the fluid mechanics of natural ventilation, *J. Fluid Mech*. 212:309-335.

Linden, P.F. (1999) The fluid mechanics of natural ventilation. *Annu. Rev. Fluid Mech.* 31: 201–238.

List, E. J. (1982a) Turbulent jets and plumes. *Ann. Rev. Fluid Mech*. 14:189-212.

List, E. J. (1982b) Mechanics of turbulent buoyant jets and plumes, in Turbulent Buoyant Jets and Plumes, Rodi, W. (Eds), Pergamon Press.

List, E.J. (1979) Turbulent jets and plumes. In: Fischer HB, Koh RCY, Imberger J, Brooks NH, eds. *Mixing in inland and coastal waters*, 9. New York, Ch: Academic Press; 1979: 315-389.

Louis, I.B. (1987) *Cryogenic Liquid Heat Transfer Analysis*. Aerospace Structures Information and Analysis, Report No. 187.1A.

Luketa-Hanlin, A., Koopman, R. P. and Ermak, D. L. (2007) On the application of computational fluid dynamics codes for liquefied natural gas dispersion, *J. of Haz. Materials.* 140(3):504-517.

Magi, V., Iyer, V. and Abraham, J. (2001) The k-e model and computed spreading in round and plane jets. *Num Heat Transfer J*. 40:317-334.

Manninen, M., Taivassalo, V. and Kallio, S. (1996) *On the mixture model for multiphase flow*. VTT Publication 288.

Markatos, N. & Pericleous, K., 1984. Laminar and turbulent natural convection in an enclosed cavity. *International Journal of Heat and Mass*, 27(5), pp.755–772.

Marshall M.R. (1983) The effect of ventilation on the accumulation and dispersal of hazardous gases. In: *Proceedings of the 4th international symposium on loss prevention and safety promotion in the process*

industries. Harrogate, 12-16 September 1983, IChemE Symp. Ser. No.81. Oxford: Pergamon Press; 1984.

Marshall, J. and Palmer, W. (1948) The distribution of raindrops with size. *J. of Meteorology*. 5:165–166.

Matsuura, K., Kanayama H., Tsukikawa, H. and Inoue, M. (2008) Numerical simulation of leaking hydrogen dispersion behavior in a partially open space. *Intl. J. of Hydrogen Energy*. 33(1):240–247.

Melideo, D., Baraldi, D., Galassi, M.C., Ortiz Cebolla, R., Acosta Iborra, B. and Moretto, P. (2014) CFD model performance benchmark of fast filling simulations of hydrogen tanks with pre-cooling. *Intl. J. Hydrogen Energy*. 39:4389–95.

Meneveau, C., Lund, T.S. and Cabot, W. (1996) A Lagrangian dynamic subgrid-scale model of turbulence. *J. of Fluid Mech*. 319:353-385.

Menon, S., Yeung, P.-K. and Kim, W.-W. (1996) Effect of subgrid models on the computed interscale energy transfer in isotropic turbulence. *Computers and Fluid*. 25: 165–180.

Menter, F.R. (1994) Two-equation eddy-viscosity turbulence models for engineering applications. *AIAA J.* 32(8):1598–1605.

Middha, P., Hansen, O.R., Grune, J. and Kotchourko, A. (2010) CFD calculations of gas leak dispersion and subsequent gas explosions: validation against ignited impinging hydrogen jet experiments. *J. of Haz. Materials*, 179(1-3):84–94.

Middha, P., Ichard, M. and Arntzen, B.J. (2011) Validation of CFD modelling of LH2 spread and evaporation against large-scale spill experiments. *Intl. J. of Hydrogen Energy*. 36(3):2620–2627.

Mira Martinez, D. and Jiang, X. 2013. Numerical investigations of a hydrogen impinging flame with different finite-rate chemical kinetic mechanisms. *Fuel*, 109:285–296.

Mitlitsky, F., Weisberg, A.H. and Blake, M. (2000) Vehicular hydrogen storage using lightweight tanks. *Proceedings of the 2000 U.S. DOE Hydrogen program review*. Lawrence Livermore National Laboratory, NREL/CP-570-28890, USA.

Molkov, V., Shentsov, V. and Quintiere, J. (2014) Passive ventilation of a sustained gaseous release in an enclosure with one vent. *Int. J. of Hydrogen Energy*. 39(15):8158–8168.

Molkov, V.V, Makarov, D.V. and Prost, E. (2005) On numerical simulation of liquefied and gaseous hydrogen releases at large scales. *Proceedings of the First International Conference on Hydrogen Safety*. Pisa Italy, 8-10 September 2005.

Molkov, V.V. (1995) Theoretical generalization of international experimental data on vented explosion dynamics. In: *Proceedings of the first international seminar*, pp. 166-181. Moscow: VNIIPO.

Molkov, V.V. (2012) *Fundamentals of hydrogen safety engineering*. In 2 volumes. www.bookboon.com.

Molkov, V.V., Makarov, D.V. and Bragin, M. (2009) Physics and modelling of under-expanded jets and hydrogen dispersion in atmosphere. In: *Proceedings of the 24th International conference on interaction of intense energy fluxes with matter*, pp. 143-145. Elbrus, Chernogolovka.

Molkov, V., Bragin M., Brennan S., Makarov, D. and Saffers, J.-B. (2010) Hydrogen Safety Engineering: Overview of Recent Progress and Unresolved Issues. *Proceedings of the International Congress on Combustion and Fire Dynamics*. 20-23 October 2010, Santander, Spain.

Molkov, V.V. and Bragin, M. (2009) High-pressure hydrogen leak through a narrow channel. In: *Nonequilibrium Phenomena: Plasma, Combustion, Atmosphere*, pp. 332-338. Moscow: Torus Press.

Nakamura, Y. and Oke, T. R. (1988) Wind, temperature and stability conditions in an east-west oriented urban canyon. *Atmospheric Environment.* 22(12):2691–2700.

Nam, S. and Bill, R. G. Jr. (1993) Numerical simulation of thermal plumes. *Fire Safety Journal.* 21:213-256.

O'Sullivan, J. P., Archer, R.A. and Flay, R. G. J. (2011) Consistent boundary conditions for flows within the atmospheric boundary layer, *J. of Wind Engg. and Ind. Aerodynamics*. 99(1):65-77.

Ogura, Y. and Takahashi, T. (1971) Numerical simulation of the life cycle of a thunderstorm cell. *Monthly Weather Review*. 99:895-911.

Oran, S. and Boris, J.P. (1993) Computing Turbulent Shear Flows - A Convenient conspiracy. *Computers in Physics.* 7:523.

Ouellette, P. and Hill, P.G. (2000) Turbulent transient gas injections. *J Fluids Eng*, 122:743-753.

Panton, R.L. (2005) *Incompressible Flow*. Wiley.

Papanicolaou, P. N. and List, E. J. (1988) Investigations of round vertical turbulent jets. *J. Fluid Mech*. 195:341-391.

Papanikolaou, E.A., Venetsanos, A.G., Heitsch, M., Baraldi, D., Huser, A., Pujol, J., Garcia, J. and Markatos, N. (2010) HySafe SBEP-V20: Numerical studies of release experiments inside a naturally ventilated residential garage. *Intl. J. of Hydrogen Energy*. 35(10):4747–4757.

Pasquill, F. (1961) The estimation of the dispersion of windborne material. *The Meteorological Magazine*. 90(1063):33-49.

Pereira, J. and Chen, X. (1996) Numerical calculations of unsteady heavy gas dispersion. *J. of Haz. Materials.* 46(2-3):253-272.

Poinsot, T. and Veynante, D. (2005) *Theoretical and Numerical Combustion.* 2nd Ed.. R.T. Edwards, Inc.
Pontiggia, M., Derudi, M., Busini, V. and Rota, R. (2009) Hazardous gas dispersion: A CFD model accounting for atmospheric stability classes, *J. of Haz. Materials.* 171(1–3):739-747
Pope, S.B. (1978) An explanation of the turbulent round-jet/plane-jet abnormality. Tech Note, *AIAA J* , 16:279-291.
Pope, S. B. (2000) *Turbulent Flows.* Cambridge University Press.
Prandtl, L. (1925) Investigations on turbulent flow. *Zeitschrift fur angewandte Mathematik und Mechanik*, 5, 136.
Prasad, K. and Yang, J. (2011) Vertical release of hydrogen in a partially enclosed compartment: Role of wind and buoyancy. *Intl. J. of Hydrogen Energy.* 36:1094-1106.
Ramponi R. and Blocken B. (2012) CFD simulation of cross-ventilation for a generic isolated building: impact of computational parameters. *Building and Environment.* 53:34-48.
Ranga Dinesh, K.K.J., Jiang, X. and van Oijen, J.A. (2012) Numerical simulation of hydrogen impinging jet flame using flamelet generated manifold reduction. *Intl. J. of Hydrogen Energy*. 37(5):4502–4515.
Redlich, O. and Kwong J.N.S. (1949) On the thermodynamics of solutions: V. An equation of state: fugacity of gaseous solutions. *Chem Rev*, 44:233-244.
Reynolds, O. (1883) An Experimental Investigation of the Circumstances Which Determine Whether the Motion of Water Shall Be Direct or Sinuous, and of the Law of Resistance in Parallel Channels. *Philosophical Transactions of the Royal Society of London.* 174: 935–982.
Reynolds, O. (1895) On the Dynamical Theory of Incompressible Viscous Fluids and the Determination of the Criterion. *Philosophical Transactions of the Royal Society A: Mathematical, Physical and Engineering Sciences.* 186:123–164.
Richards P. J. and Hoxey R. P. (1993) Appropriate boundary conditions for computational wind engineering models using the k–ε turbulence model. *J. Wind Eng. Ind. Aero.* 46 and 47:145–153.
Ricou, F.P. and Spalding, D.B. (1961) Measurements of entrainment by axisymmetrical turbulent jets. *J. Fluid Mech*.. 8:21-32.
Roberts, P.T., Shirvill, L.C., Roberts, T.A., Butler C.A. and Royle, M. (2006) Dispersion of hydrogen from high pressure sources. *Proc. Of Hazards XIX Conference*. 28-30 March 2006, Manchester, UK.
Rodi, W. (1972) *The prediction of free turbulent boundary layers by use of a two-equation model of turbulence.* PhD Thesis, University of London, UK.
Rodi, W. (1993) *Turbulence Models and Their Application in Hydraulics - A State of the Art Review.* CRC Press.
Ruggles, A.J. and Ekoto, I.W. (2011*) Ignitability and mixing of underexpanded hydrogen jets*. Proceedings of the Fourth International Conference on Hydrogen Safety, paper ID 125, 12-14 September 2011, San Francisco, USA.
Saad, M.A. (1985) *Compressible Fluid Flow*. Englewood Cliffs, NJ: Prentice-Hall, Inc.
SAE J2578 (2009). *Recommended practice for general fuel cell vehicle safety, a surface vehicle recommended practice*. Detroit, Michigan, USA: SAE International; January, 2009.
SAE J2579. (2013) *Technical information report for fuel system in fuel cells and other hydrogen vehicles*. Revised. SAE International; March 2013.
SAE J2601 (2014) *Fueling protocols for light duty gaseous hydrogen surface vehicles*. SAE International.
Saffers, J-B., Makarov D.V. and Molkov, V.V. (2011) Modelling and numerical simulation of permeated hydrogen dispersion in a garage with adiabatic walls and still air. *Intl. J. of Hydrogen Energy.* 36:2582-2588.
San Marchi, C., Somerday, B.P. and Robinson, S.L. (2007) Permeability, solubility and diffusivity of hydrogen isotopes in stainless steels at high gas pressures, *Intl. J. Hydrogen Energy.* 32:100-116.
Schatzmann, M., Olesen, H. and Franke, J. (Eds) (2010) *COST 732 Model evaluation case studies: approach and results.* COST Action 732 on "Quality Assurance and Improvement of Microscale Meteorological Models". COST Office, Brussels, Belgium, ISBN: 3-00-018312-4.
Schefer, R.W., Houf, W.G., San Marchi, C., Chernicoff, W.P. and Englom, L. (2006), Characterisation of leaks from compressed hydrogen dispensing systems and related components. *Int J Hydrogen Energy.* 31:1247-1260.
Schefer, R. W., Houf, W. G., Williams, T. C., Bourne, B. and Colton, J., (2007) Characterization of high-pressure, under-expanded hydrogen-jet flames, *Intl J. of Hydrogen Energy*. 32(12):2081–2093.
Schefer, R.W., Merilo, E.G., Groethe, M.A. and Houf, W.G. (2011) Experimental investigation of hydrogen jet fire mitigation by barrier walls. *Intl. J. of Hydrogen Energy*. 36(3):2530–2537.
Schultheiß D. (2007) *Permeation barrier for lightweight liquid hydrogen tanks*. Der Online-Publikationsserver der Universitat Augsburg; 2007.
Seinfeld, J. H. and Pandis, S. N. (1998) *Atmospheric chemistry and physics: From air pollution to climate change*. John Wiley and Sons, Inc.

Shabbir, A. and George W. K. (1994) Experiments on a round turbulent buoyant plume. *J. Fluid Mech.* 275:1-32.

Shabbir, A. and Taulbee T. B. (1990) Evaluation of turbulence models for predicting buoyant flows. *J. Heat Transfer*. 112:945-951.

Shevyakov, G.G., Tomilin, V.P. and Kondrashkov, Yu. A. (1980) *Engineering Physical Journal*, deposit with VINITI, N3671-80 (in Russian).

Smagorinsky, J. (1963) General circulation experiments with the primitive equations I. The Basic Experiment. *Month. Wea. Rev*. 91(3):99–164.

Statharas, J.C., Venetsanos, A.G., Bartzis J.G., Wurtz, J. and Schmidtchen, U. (2000) Analysis of data from spilling experiments performed with liquid hydrogen. *J. of Haz. Materials.* 77(1-3):57–75.

Suryan, A., Kim, H.D. and Setoguchi, T. (2012) Three dimensional numerical computations on the fast filling of a hydrogen tank under different conditions. *Intl J of Hydrogen Energy.* 37:7600-7611.

Suryan, A., Kim, H. D. and Setoguchi, T. (2013) Comparative study of turbulence models performance for refueling of compressed hydrogen tanks. *Intl J of Hydrogen Energy.* 38:9562-9569.

Takagi, Y., Sugie N., Takeda K., Okano Y., Eguchi T., Hirota K., (2011) Numerical investigation of the thermal behaviour in a hydrogen tank during fast filling process. *Asme/Jsme* 2011, Honolulu, Hawaii, USA.

Tennekes, H. and Lumley, J.L. (1972) *A First Course in Turbulence*. Cambridge, Mass.: The MIT Press.

TIAX (2004) Safety evaluation of the fuelmaker home refuelling concept. Presented to Sacramento, USA: Natural Gas Vehicle Technology Forum, http://www.nrel.gov/vehiclesandfuels/ngvtf/pdfs/fuelmaker_ngvtf_sac.pdf; April 15, 2004.

Tominaga, Y. and Stathopoulos, T. (2007) Turbulent Schmidt numbers for CFD analysis with various types of flowfield. *Atmospheric Environment.* 41(37):8091–8099.

Tsinober, A. (2001) *An Informal Introduction to Turbulence.* Springer.

Van Maele, K. and Merci, B. (2006) Application of two buoyancy modified k-epsilon turbulence models to different types of buoyant plumes. *Fire Safety Journal*. 41:122-138.

Vandroux-Koenig, S. and Berthoud, G. (1997) Modelling of a two phase momentum jet close to the breach, in the containment vessel of a liquefied gas. *J. of Loss Prevention in the Process Industries*, 10(1):17–29.

Vardoulakis, S., Fisher, B. E. ., Pericleous, K., and Gonzalez-Flesca, N. (2003) Modelling air quality in street canyons: a review. *Atmospheric Environment*, 37(2):155–182.

Venetsanos, A.G., Bartzis J.G., Wurtz J., and Papailio D.D. (2003) DISPLAY-2: a two-dimensional shallow layer model for dense gas dispersion including complex features. *J. of Haz Materials*, 99(2):111–144.

Venetsanos, A. and Bartzis, J. (2007) CFD modeling of large-scale LH2 spills in open environment. *Intl. J. of Hydrogen Energy.* 32(13):2171–2177.

Venetsanos, A.G., Papanikolaou, E.A. & Bartzis, J.G. (2010). The ADREA-HF CFD code for consequence assessment of hydrogen applications. *International Journal of Hydrogen Energy*, 35(8), pp.3908–3918.

Verfondern, K. and Dienhart, B. (1997) Experimental and theoretical investigation of liquid hydrogen pool spreading and vaporization. *Intl. J. of Hydrogen Energy.* 22(7):649–660.

Verfondern, K. and Dienhart, B. (2007) Pool spreading and vaporization of liquid hydrogen. *Intl. J. of Hydrogen Energy.* 32(2):256–267.

Versteeg, H. and Malalasekera, W. (2007) *An Introduction to Computational Fluid Dynamics: The Finite Volume Method*. 2nd Ed. Prentice Hall.

von Karman, T. (1994.). *Aerodynamics*. Dover.

White, F.M. (1991) *Viscous Fluid Flow*. 2nd ed. McGraw-Hill.

Wilcox, D., (2008) Formulation of the k-ω Turbulence Model Revisited. *AIAA Journal*. 46(11):2823–2838.

Wilcox, D.C. (1994) *Turbulence Modeling for CFD*. DCW Industries, Inc., La Canada, California.

Winters, W.S. and Houf, W.G. (2011) Simulation of small-scale releases from liquid hydrogen storage systems. *Intl. J. of Hydrogen Energy.* 36(6):3913–3921.

Witcofski, R.D. and Chirivella, J.E. (1984) Experimental and Analytical Analyses of the Mechanisms overning the Dispersion of Flammable Clouds Formed by Liquid Hydrogen Spills. *Int. J. Hydrogen Energy.* 9(5): 425-435.

Witlox, H. and Bowen, P. (2001) *Flashing liquid jets and two-phase dispersion: A review.* HSE Contract Report 4403/2002. HSE Books.

Witlox, H., Harper, M., Bowen, P.J. and Cleary, W.M. (2005) Flashing liquid jets and two-phase droplet dispersion. Proc. of 'Mary Kay O'Connor' Symp. Houston, October 2005.

Yakhot, V. and Orszag, S. (1986) Renormalization group analysis of turbulence: I. Basic theory. *J. Sci. Comput*. 1(1):13–51.

Yakhot, V., Orszag, S.A., Thangam, S., Gatski, T.B. and Speziale, C.G. (1992) Development of turbulence models for shear flows by a double expansion technique. *Physics of Fluids A: Fluid Dynamics.* 4(7):1510.

Yan, Z. and Holmstedt, G. (1999) A two-equation model and its application to a buoyant diffusion flame. *Int. J. Heat Mass Transfer.* 42:1305-1315.

Yang, Y., Gu, M., Chen, S. Q. and Jin, X. Y. (2009) New inflow boundary conditions for modeling the neutral equilibrium atmospheric boundary layer in Computational Wind Engineering. *J. of Wind Engineering and Industrial Aerodynamics.* 97:88-95.

Yokoi, S. (1960) Study on the prevention of fire-spread caused by hot upward current. *Building Research Institute Report No. 34*.

Zhao, L., Liu, Y., Yang, J., Zhao, Y., Zheng, J., Bie, H. and Liu, X. (2010) Numerical simulation of temperature rise within hydrogen vehicle cylinder during refueling. *Intl J of Hydrogen Energy* 35:8092–8100.

Zhao, Y., Liu, G., Liu, Y., Zheng, J., Chen, Y., Zhao, L., Guo, J. and He, Y. (2012) Numerical study on fast filling of 70 MPa type III cylinder for hydrogen vehicle. *Intl J of Hydrogen Energy*, 37:17517-17522.

Zhou, X., Luo, K. H. and Williams, J. J. R. (2001a) Large-eddy simulation of a turbulent forced plume. *Eur. J. Mech. B – Fluids.* 20:233-254.

Zhou, X., Luo, K. H. and Williams, J. J. R. (2001b) Study of density effects in turbulent buoyancy jets using large-eddy simulation. *Theoret. Comput. Fluid Dynamics.* 15:95-120.

Zuckerman, N. and Lior, N. (2006) Jet Impingement Heat Transfer: Physics, Correlations, and Numerical Modeling. *Advances in Heat Transfer*. 39(6):565–631.

2. Physical and Mathematical Models of Ignition (UU)

2.1 Hydrogen safety engineering relevant problems and ignition mechanisms (HSL)

2.1.1 Ignition Mechanisms (HSL)

There are a number of different potential ignition sources. (BS EN 1127-1:2011) gives a list of potential ignition sources to consider:

Hot surfaces, flames and hot gases (including hot particles), mechanically generated sparks, electrical apparatus, stray electric currents, cathodic corrosion protection, static electricity, lightning, radio frequency (RF) electromagnetic waves from 10^4 Hz to $3 \cdot 10^{11}$ Hz, electromagnetic waves from $3 \cdot 10^{11}$ Hz to $3 \cdot 10^{15}$ Hz, ionizing radiation, ultrasonic, adiabatic compression and shock waves, exothermic reactions, including self-ignition of dusts.

A review was carried out by (Astbury & Hawksworth, 2005) into the so-called "spontaneous ignition" of hydrogen releases into air, ruling out a number of mechanisms for spontaneous ignition at ambient temperatures while identifying others for further research, particularly the potential for what is often termed diffusion ignition, and also corona discharges. A significant amount of work has been done since that review paper and much of it is summarized in this report.

Potential ignition mechanisms for hydrogen are discussed below.

2.1.2 Hot surfaces (HSL)

2.1.2.1 Auto-ignition and pressure dependence in enclosed volumes

Vapour can auto-ignite if the temperature exceeds the so-called Auto Ignition Temperature (AIT). This temperature is not a well-defined quantity. The temperature varies depending on the method used to measure it. One possible scenario is when the gas is in contact with a hot surface whose temperature is above the auto-ignition temperature of the gas. However, the duration of the time the gas is in contact with the surface is also of importance.

Generally auto-ignition results from the exothermic chain branching character of the oxidation reactions that at certain conditions self-accelerate to reach high conversion and heat release rates. Auto-ignition limits can be established by testing experimentally, or theoretically, a homogeneous mixture of volume V filling a vessel whose walls have a temperature T_w. Once the heat release rate in the volume due to reactions exceeds the heat lost to the walls or if the reaction rates in the vessel exceed the reaction quenching (termination) rates by the walls or in the gas a thermal or branched chain (isothermal) auto-ignition occurs. As all combustion reactions are exothermic, chain auto-ignitions cause also self-heating and are accelerated by both factors. Obviously auto-ignition limits are not only a feature of the mixture composition and parameters (pressure, temperature) but also of the vessel size, wall properties and internal flow conditions.

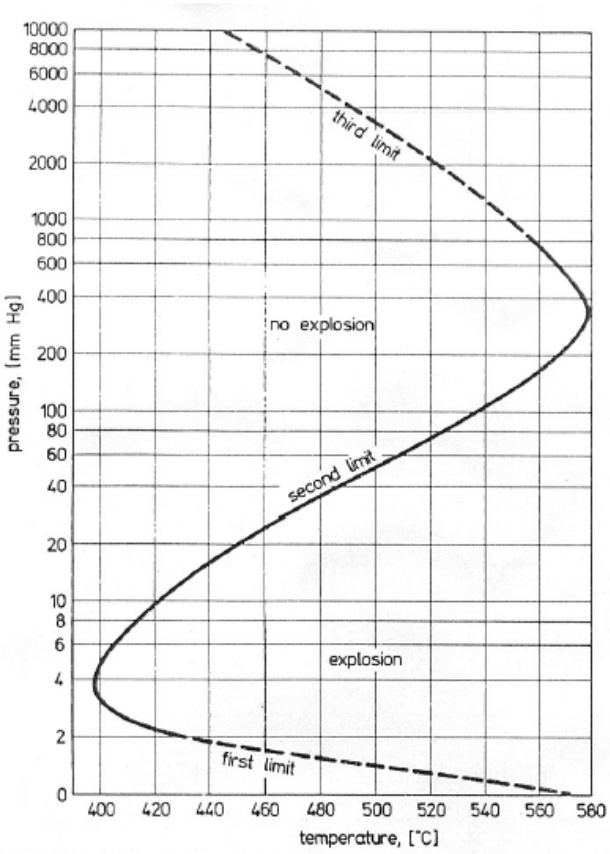

Figure 2.1 Explosion limits of a stoichiometric H2-O2 mixture in a spherical HCl coated vessel of 7.4 cm diameter.

This is illustrated in Figure 2.1 which shows the auto-ignition limits often called also explosion limits for a stoichiometric mixture of hydrogen and oxygen (Lewis and von Elbe, 1987) providing the important parameters of the test vessel. Note that the logarithmic scale of pressure and linear scale of temperature show that pressure effects on reaction rates are weaker than temperature effects as one would expect by the consideration of Arrhenius chemistry.

The first and second limits, although interesting from the fundamental point of view, correspond to very low pressure (up to about 0.3 bar, 30 kPa) and are thus of little practical interest. The third limit follows the trend that one would expect from simple density considerations. As the pressure increases, the initial densities of the reactants increase and a lower temperature is necessary for the reactions to reach a critical reaction rate for explosion. For safety considerations explosions in large volumes where wall effects can be neglected at atmospheric conditions and the most violently reacting, i.e. stoichiometric mixtures, are considered. Thus, in typical safety manuals a temperature of 585 °C is given as the auto-ignition temperature for hydrogen air systems.

The initial reaction rate in auto-ignition is very small thus a certain time must pass before the reaction has reached a defined rate. This time interval is called ignition delay. Ignition delays are particularly important for operation of engines as they provide the engine speed limits where operation is possible due to auto-ignition (compression ignition engines) or where auto-ignition can be avoided when detrimental (knock in spark ignition engines).

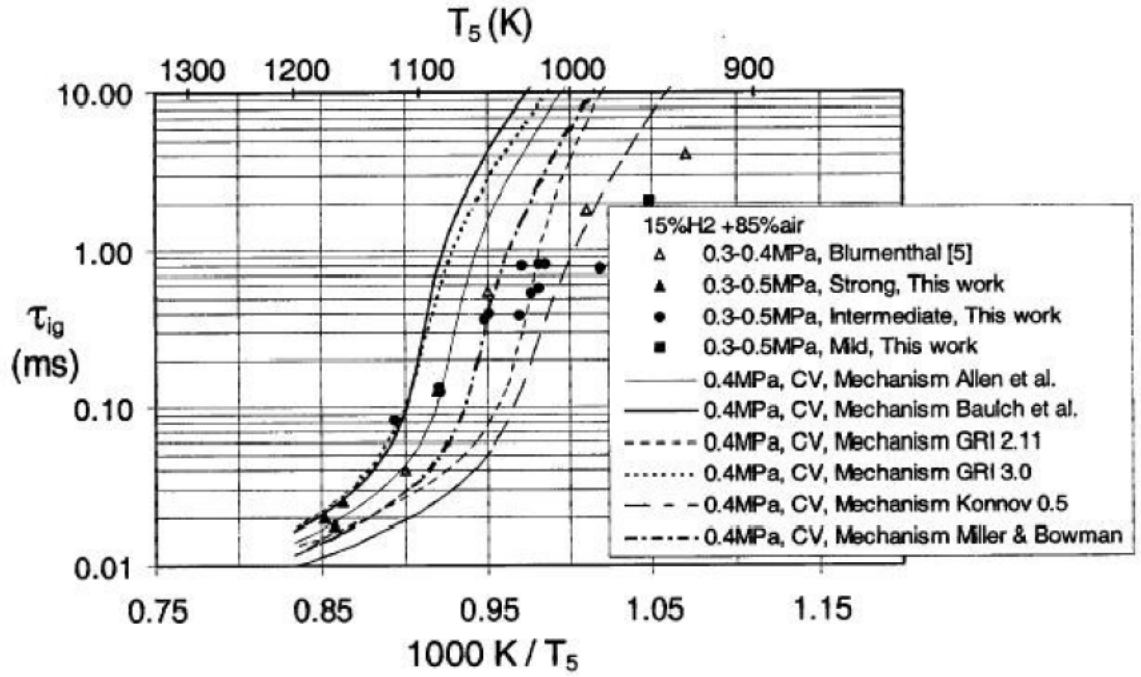

Figure 2.2 Measured and calculated ignition delay times in a H2-air mixture.

Most accurate ignition delay measurements can be performed in shock tubes in wall reflected shocks where the heating of the mixture is practically instantaneous. A research issue is then prediction of the ignition delays using available kinetic data. The state of the art in this field is far from satisfactory as illustrated in Figure 2.2, after Wang et al., (2003), where a comparison of measured and calculated ignition delay times using different chemical reaction mechanisms is provided.

In the low temperature range the measured ignition delay times are much shorter (even by orders of magnitude) than the theoretically predicted ones. Partially this is because in shock wave ignition mild and strong ignition regimes are possible. For the case of mild ignition multiple and random ignition kernels appear in the mixture. In the case of strong ignition typically reproducible direct transitions to detonation occur. Mild ignition is extremely sensitive to homogeneity of the mixture, impurities, and wall properties of the shock tube and particularly to presence of even minute obstacles causing shock reflections, shock focusing and thus generating local hot spots. Thus, this form of ignition is very difficult to control particularly in natural conditions. If the volume of the mixture is large enough deflagration to detonation transition will eventually occur even after mild ignition causing convergence of effects of both types of ignition in accidental explosions.

2.1.2.2 Ignition by hot surfaces that do not enclose the hydrogen / air mixtures

Ignition by a hot surface which does not fully enclose the hydrogen / air mixture occurs as a result of local heating of the fuel-oxidant mixture to the point where a sufficiently large volume reaches the auto-ignition temperature and the combustion reaction is initiated. For this to occur the surface generally needs to be at a temperature well above the auto-ignition temperature (Powell, 1984). However, the actual temperature depends on a number of factors in addition to the usual considerations of mixture concentration, ambient temperature, etc. These additional factors determine the hot surface ignition behaviour of flammable gases which include the size and shape of the hot surface, the degree of confinement around

the surface, the strength of the convection currents across the surface (Laurendeau, 1982) and the material of the surface (Lewis & Elbe, 1987, page 380).

For a particular hot surface, ignition is characterized by an ignition delay which, under ideal circumstances, multiplied by the power for ignition gives a linear relationship between the product (energy) and ignition delay (Lewis & Elbe, 1987 page 365) (Carleton et al., 2000).

The temperatures required to cause ignition of mixtures of hydrogen with air and oxygen (see review in (Buckel & Chandra, 1996); (Carleton et al., 2000); (Hawksworth et al., 2005) range from 640 °C to 930 °C, the spread of temperatures being explained by the size and geometry effects. While the temperatures quoted are above the auto ignition temperature, the increase is much less for hydrocarbon-fuel air mixtures, as illustrated by the IIA curve in Figure 2.3. In terms of simple modelling of hot surface ignition, Laurendeau (1982) presents a simple model in terms of a one-step reaction chemical kinetics model.

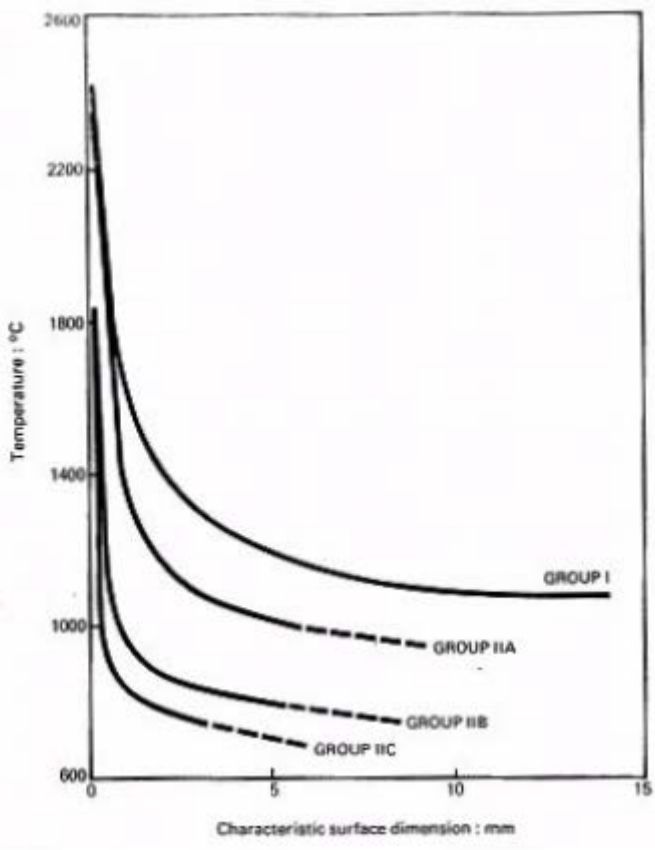

Figure 2.3 Dependence of hot surface ignition temperature as a function of characteristic surface dimension (hydrogen is represented by the curve for Group IIC gases).

Interestingly, the most easily ignited mixture of hydrogen with air lies lean of stoichiometric (Calcote et al., 1952) while work using very small hot surfaces (Carleton et al., 2000; Hawksworth et al., 2004) suggests that mixtures containing as low as 10 to 15% hydrogen are the most easily ignited. For hydrogen-oxygen mixtures, the work of Buckle and Chandra (1996) indicates a fairly flat H_2 concentration dependence (slight positive slope with increasing hydrogen concentration) between roughly 20 and 90% hydrogen in oxygen.

Catalytic surfaces (that is to say platinum) have a dramatic effect on the ignition temperature required (Cho & Law, 1986), ignitions reported at temperatures as low 70 °C.

It is entirely possible that either a hot particle or burning droplet could ignite a flammable gas cloud, although the presence of the hot particle alone is not sufficient to cause ignition; there are a number of conditions that will have to be met. The particles / droplets must pass through a region where a fuel-air mixture is present, the fuel concentration in that region must also be in the flammable range, and finally the residence time of the particle in the flammable gas cloud must be long enough so that ignition can occur. The temperature of a hot particle may be reduced as the particle falls through the air due to convective and radiative heat losses, unless it is itself combusting (e.g. smouldering). The criteria for igniting a flammable gas cloud are the same for burning droplets as for hot particles, although burning droplets may consume all their fuel during the time it takes for the droplet to fall, and hence ignition would not be possible.

Open flames, often associated with hot working such as welding, will in any circumstance ignite a flammable fuel-air mixture.

2.1.3 Mechanical sparks / frictional ignition (HSL)

There are a number of key properties of burning metal particles or sparks that are relevant to their ability to cause ignition of a flammable atmospheres. These include: size, material, velocity, temperature, number, combustion rate and time. There is a metal-to-metal contact pressure and relative velocity threshold for spark production during impact, rubbing or grinding. Above the threshold metal particles are lost from the weaker of the two materials. Generally, particles are only produced when the relative velocity between the two surfaces exceeds 1 m s^{-1} (Bernend & Ritter, 2000).

Brearley & Tolson (1995) measured power levels and contact loads required to ignite flammable gas mixtures by a 25 mm cube of stainless steel frictionally heated through rubbing against a stainless steel wheel at circumferential velocities of 5 and 20 m s^{-1}. In these tests a contact load of 750 N was required to ignite hydrogen. This equates to a dissipated power of approximately 2 kW and a power density of approximately 0.5 W mm^{-2}. No temperature recordings were made in the tests. It was noted that in most cases the ignition was caused by the hot spot close to the point of contact.

In Powell's review (Powell, 1986) he summarises data from various experiments breaking them into two categories with rubbing speeds above and below 10 m s^{-1}. Table 2.1 includes results for Group IIC gases (for example hydrogen).

The frictional ignition of gases was investigated as part of the EU Mech-Ex project and approaches to assessing the problem were discussed (Hawksworth et al., 2004). It was found that the temperature of the hot surface required for the ignition of simple hydrocarbons was higher than the measured AIT of the gas, whereas this was not the case for hydrogen. At low rubbing speeds, hydrogen was ignited at a temperature close to the auto-ignition temperature. The conditions were: power 0.7 kW and rubbing speed 0.7 m s^{-1} which caused ignition at 530 °C. Ignition occurred from the hot surface with few sparks produced from the low speed conditions.

Table 2.1 Summary of rubbing tests (Powell, 1986).

Group	***I or N***	***Rubbing < 10 m s^{-1}***	***Rubbing > 10 m s^{-1}***
Group I Methane, etc.	I	• Sandstone on sandstone (500-750 W) • Rusty steel and light metals and alloys	• Steel on buffing disk (460 W) • Mild steel on mild steel • Thermosetting plastics on materials with melting point > 723 K (22 m

		• Tungsten carbide tipped machine picks on sandstone • Mild steel on mild steel (> 3700 W) – 1 % P cast irons on mild steel	s^{-1}) • Sandstone, Al bronze 197, mild steel on Al bronze disk • AB197, AB2 on mild steel disk • CMA2, mild steel on CMA2 disk • Brass on light alloy Si (90 m s^{-1}) – 1 % P cast irons on mild steel
	N	• 0.5 % Cr cast iron on mild steel • 3 % P cast iron on mild steel • Brass on sandstone	• Mild steel on buffing disk (460 W) • Drill steel on grindstone (1000 W) • CMA2, mild steel on mild steel disk disk (46 m s^{-1}) • 70/30 brass on mild steel disk (90 m s^{-1})
Group IIA Propane, etc.	I		• Grinding steels – from hot surfaces, not sparks • Ti, Mg steels on runway materials • Ti alloy, stainless steel on anodised Al disk
	N	• 0.5 % Chromium cast iron on mild steel	• Al alloy on runway materials (18 m s^{-1})
Group IIB Ethylene, etc.	I	• Steel on steel (400 W)	• Steels on grindstone • Rusty steel on copper disk (75 m s^{-1}) • AB197, AB2, CMA2 on mild steel (46 m s^{-1}) • 70/30 brass, Copper on mild steel disk (90 m s^{-1}) • 0.5 % Chromium cast iron on mild steel
	N		• 60/40 brasses on mild steel disk (90 m s^{-1}) • Light alloy on light alloy (140 m s^{-1}) • Non-metallic composite brake material on mild steel
Group IIC Hydrogen, etc.	I		• Stainless steel on Al alloy and GRP disks • Al on GRP disk • CuBe, Ni alloy, phosphorous bronze on steel wheel • Cooper on rusty steel wheel (90 m s^{-1}) • Steel on copper wheel • Bronzes, CuBe, copper alloys on grindstone if long enough
	N		• Sparks from high alloy and chromium steels on grindstone

			• CuBe and cu alloy sparks from grindstone • Carborundum on Al alloy and GRP disks • Al on Al disk (90 m s^{-1}) • AlZn and their alloys on grindstone

2.1.4 Impact (HSL)

In his paper, Powell (1984) states how little energy is needed to ignite flammable gases and vapours with impact of light metals and their alloys, producing burning particles with temperatures in excess of 2000 °C from light impacts (<1 J) with material such as Cerium, Titanium, Zirconium, Hafnium and their alloys. Impacts on smears of aluminium or magnesium on rusty steel are also equally incentive. There is therefore a high probability of igniting hydrogen under these conditions.

Powell reports on ignitions caused by impacts between very hard steels with a Vickers Pyramid Number (VPN) greater than 550 (Powell, 1986). Energies of 250 to 1000 J are required to ignite methane-air, with slightly lower energies igniting IIA vapours. For steel with VPN of approximately 550, an energy of 180 J was sufficient to cause ignition. Ignition of hydrogen-air mixtures from impacts involving very hard steels are therefore very likely.

Thermite sparks can be highly energetic. The energy is released in a highly exothermic reaction. A typical case could be a tool made of aluminium being dropped onto a rusty steel plate, such as a walkway on an offshore installation (BOMEL, 2002). Studies have shown that the energy in a thermite spark arising from impacts involving tools such as a hammer may be sufficient to ignite flammable dust clouds and so would be more than capable of igniting hydrogen / air mixtures (Gibson et al., 1968). More recent work by (Averill et al., 2014) reports that the incendivity of a thermite spark depends more on the sliding velocity of the surfaces and the normal force of impact rather than the overall kinetic energy of the impact.

2.1.5 Electrical ignition sources (HSL)

Electrical ignition sources result from either electrical discharges or hot surfaces (see section 2.1.2). Electrical equipment typically operates at relatively low voltages (few hundred volts) compared to the high voltages associated with electrostatic phenomena (see section 2.1.6).

Electrical discharges and the mechanism for ignition are discussed in general terms below.

2.1.5.1 Electrical discharges

Electrical sparks are defined as discontinuous electrical discharges across a gap, in an otherwise complete electric circuit, between at least two electrodes occurring when the voltage exceeds the breakdown voltage. The characteristics of the discharge depend very much on the discharge circuit involving capacitors, resistors and inductors. In many technical applications, especially in spark ignition engines, optimized, standard ignition systems are used. Typically the systems are based on a capacitor to store the energy supplied by a high voltage generator, complemented by a circuit of low induction and resistance containing an electronic device triggering the spark for control and synchronization purposes. In Figure 2.4 a schematic diagram of the voltage and current of ignition spark as a function of time is presented after (Maly & Vogel, 1979).

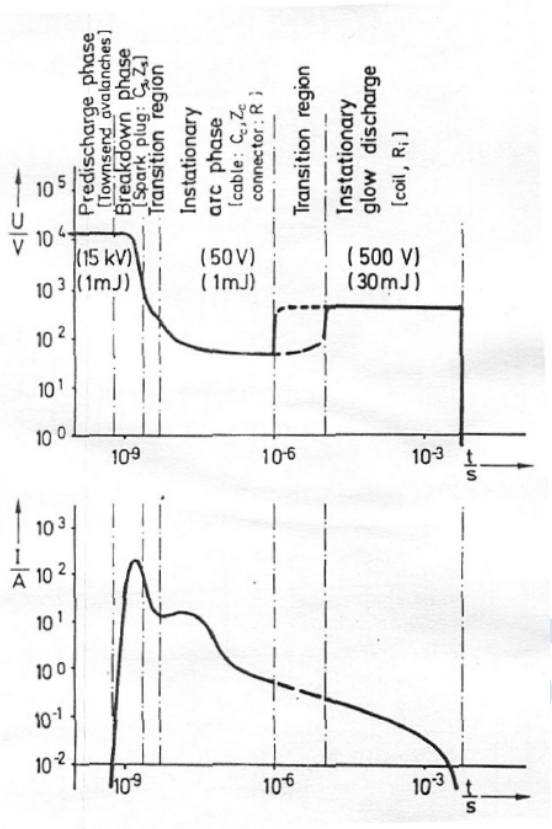

Figure 2.4 Schematic diagrams of voltage and current of technical ignition systems as functions of discharge time. Typical values are given in parentheses, circuit parameters responsible for a discharge mode are indicated in brackets.

As it can be seen a typical electrical spark of a commercial ignition system can be divided in three phases. First a breakdown phase is initiated which creates in the gas a small diameter (≈10μm) conducting plasma channel between the two electrodes. The phase is very short (1-10 ns) and characterized by high voltages (≈10 kV) and currents (≈200 A). Temperatures in the plasma channel reach up to 60 000 K, the molecules are fully dissociated and ionized causing the pressure to jump to 200 bar creating an intense shock wave and expansion of the discharge zone. The high conductivity of the plasma reduces the voltage provided by the circuit and the arc phase is initiated. The arc voltage is low (<100 V) although the current may be as high as the electrical circuit permits (up to several kA). The maximum temperature in the discharge zone drops to about 6000 K and ionization falls to a 1% level. The arc expands mainly due to conduction and diffusion producing bell shaped temperature and ionization profiles. Heat losses create appreciable cathode and anode voltage falls and the glow phase begins during which currents drop to a 200 mA level, the gas temperature is less than 3000 K and ionization less than 0.01 %. The conversion efficiency of electrical to thermal energy of the gas decreases from the breakdown to the glow phase mostly due to the heat losses to the electrodes. To initiate a flame shortly after breakdown the chemical reaction must produce enough energy to overcome heat losses and the ignition kernel has to grow beyond a critical size for the flame to develop, typically two times larger than the laminar flame thickness. Obviously the electrodes, their separation, shapes and material play an important role in this process.

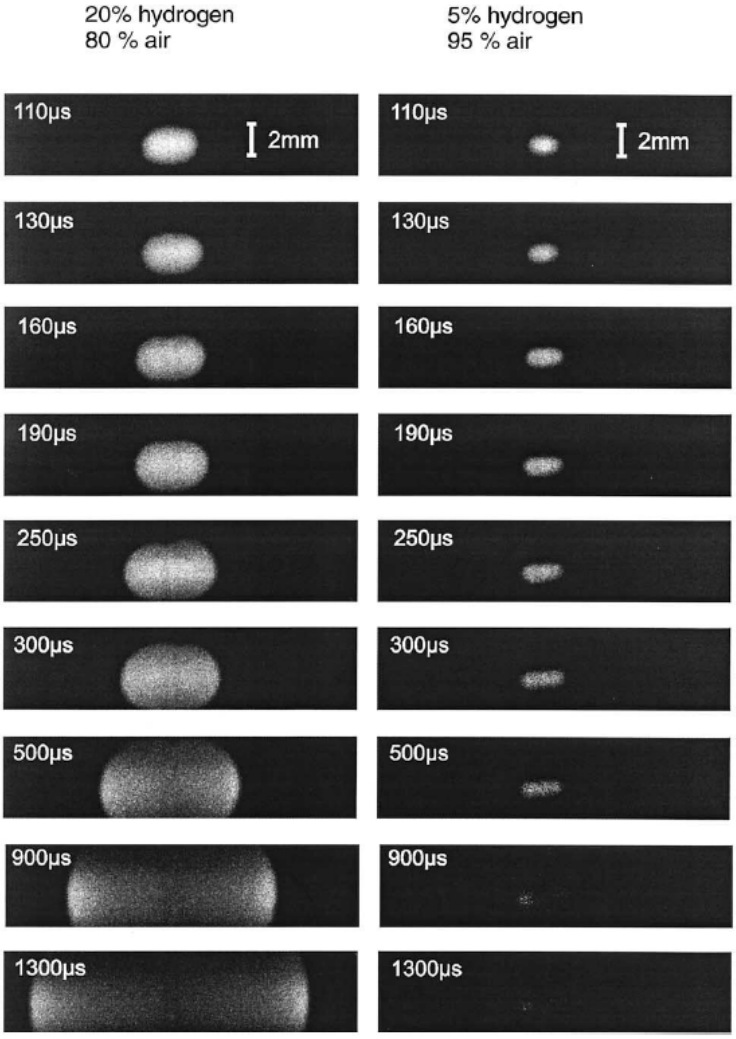

Figure 2.5 Temporal evolution of a flame kernel visible as a relative OH concentration profiles recorded by PLIF for an ignitable and below the ignition limit mixture of hydrogen and air. Spark duration was 100 µs.

Spark ignition constitutes a very complex interplay between plasma kinetics, chemical kinetics, molecular transport processes and fluid dynamics. Experimental investigations of spark kernels and their transition to flame kernels are rendered difficult because of very short process times, extremely high core temperatures and large gradients in the refractive index. In general, only flame propagation subsequent to spark ignition can be studied by laser diagnostic methods. Therefore, internal structures of the plasma core remain mostly unknown. A complete mathematical simulation of a spark ignition is also a difficult task because of the enormous numerical problems; due to the stiffness and high dimensionality of the problem (each chemical species introduces an additional conservation equation). Recently Thiele et al. (2002) have conducted detailed two dimensional numerical modelling of spark ignition of hydrogen-air mixtures. Their model considered heat conduction from the gas phase to the electrodes, detailed chemistry and molecular transport as well as the coupling of the gas dynamics to the properties of the electrical discharge through heating by the electrical current. They also performed spark ignition experiments using a highly reproducible ignition system. Shapes of early flame kernels were monitored by 2-D laser-induced fluorescence PLIF imaging of OH radicals produced during the ignition and the combustion process, see Figure 2.5. In addition, for a central position within the flame kernel, temperatures were measured

using coherent anti-Stokes Raman spectroscopy (CARS). Results from experiments and simulations suggest the birth of a self-sustaining flame propagation for process times between 50-70 ms after arc breakdown.

2.1.5.2Electrical equipment

Electrical discharges in electrical equipment may arise as a result of brushes within a motor, the operation of switches or thermostats, or faults. There are three main types of electrical discharge that are of concern in relation to ignition hazards; spark, arc and glow discharges. The characteristics of these are described in section 2.1.5.1. In electrical equipment the discharge is often initiated by the breaking of contacts, causing high temperatures at the point of the break which results in plasma formation and the initiation of the discharge. This may take the form of a short duration spark, or may develop into an arc discharge.

An electric circuit may contain capacitors, resistors and inductance all of which influence the ignition potential of a discharge from the circuit.

In order to avoid arcing in a purely resistive circuit, the current or voltage need to be restricted, depending upon the flammable gas type as shown in Figure 2.6.

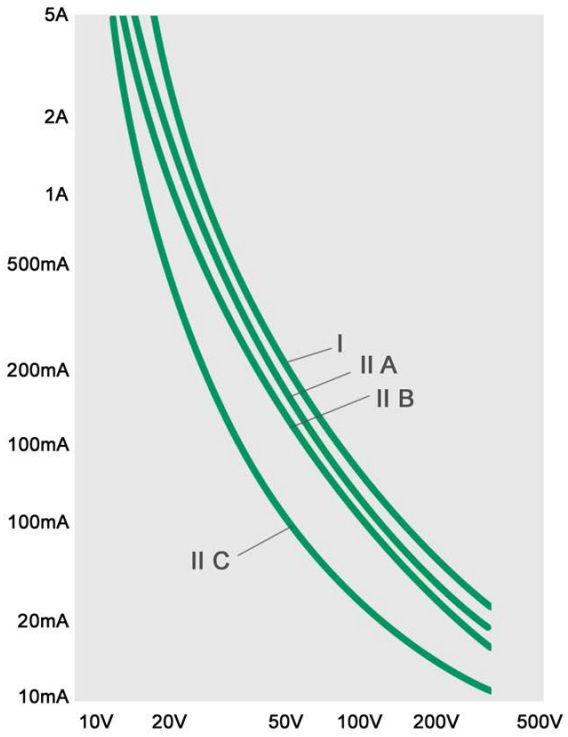

Figure 2.6 Current / voltage limits for resistive circuits (for indication, based on data in BS EN 60079-11:2012).

For circuits containing inductance, the maximum current in the circuit need to be restricted, depending on the gas type, as shown in Figure 2.7.

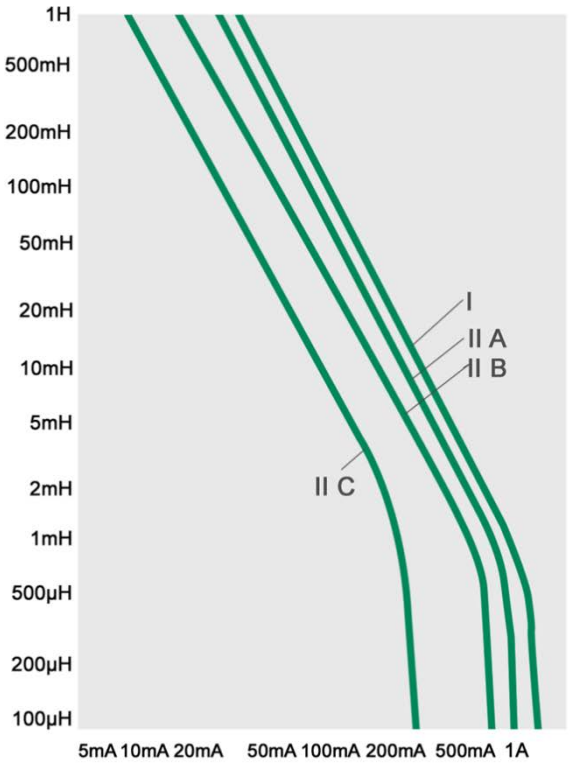

Figure 2.7 Current limits for inductive circuits (for indication, based on data in BS EN 60079-11:2012).

2.1.6 Electrostatic discharges (HSL)

Electrostatic discharges are generally associated with relatively high voltages, typically > 1 kV, compared to those associated with typical electrical equipment. They can occur from charged surfaces (both electrically conducting and insulating), including liquids, or indeed from charged clouds of particles or droplets (e.g. lightning). Lightning is of course a very powerful ignition source and will not be discussed further here.

The ignition hazards posed by static electricity require specific precautions to be taken. The IEC international guidance document on electrostatic hazards, PD (IEC/TS 60079-32-1:2013) does not specifically refer to hydrogen but does refer to the flammable gas Group IIC, to which hydrogen belongs, and the ignition hazards associated with static electricity.

The three main types of electrostatic discharges that are of concern in the ignition of hydrogen are capacitive sparks from conducting items, brush discharges from insulating surfaces and corona discharges.

2.1.6.1Capacitive spark

The energy in a purely capacitive discharge is approximately equal to that stored on the capacitor, i.e.

$$E = \frac{1}{2}CV^2 \qquad (2.1)$$

where E is the energy stored on the capacitor (J), C is the capacitance of object (F) and V is the voltage of object (V).

The minimum spark ignition energy for hydrogen in air has been reported as 0.016 mJ at 28% v/v (Britton 1992). This would equate to a voltage of less than 2 kV for a human with a typical capacitance of 100 pF. Such voltages could readily be obtained by a person and the discharge itself would be barely noticeable.

The spark energy required for the ignition of hydrogen / air mixtures that are richer or leaner than 28 % v/v are higher as shown in Figure 2.8 (Drell and Bell, 1957), which also shows the effect of pressure on the ignition energy.

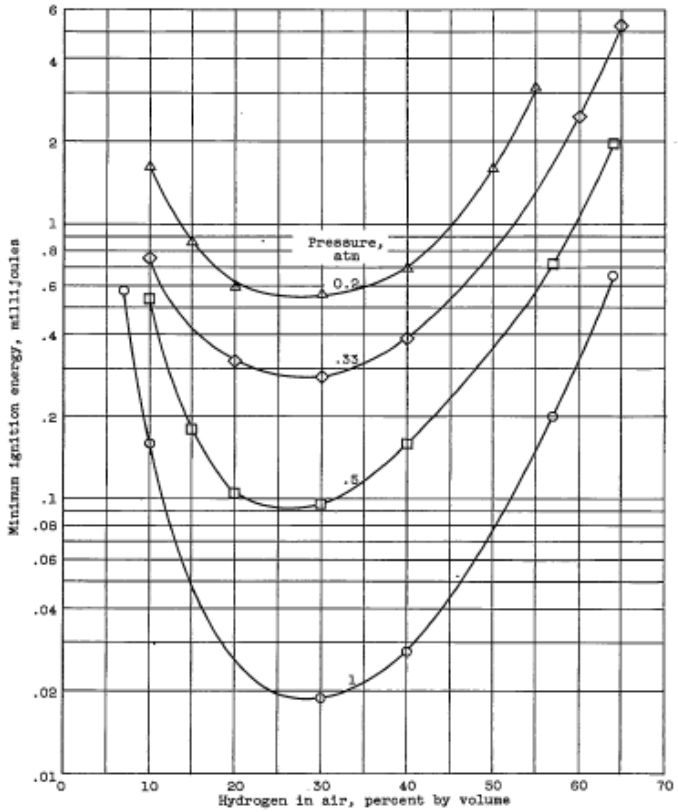

Figure 2.8 Spark ignition energy of hydrogen / air mixtures.

2.1.6.2Brush discharge from insulating materials

These are typified by a discharge between a charged insulator and a conducting earthed point. They are characterised by many separate plasma channels, combining at the conductor, and are typical of those from insulating plastics. As the charged surface is a non-conductor, a capacitance and hence energy cannot be determined. However, the ignition properties can be compared to those of a spark discharge between two conductors. The comparison has been discussed by Gibson & Harper (1988), who proposed the term incendivity to compare the quantity of charge transferred with its capability to ignite a flammable mixture with a given minimum ignition energy. Typical equivalent energies were found to be about 4 mJ for brush discharges from flat polyethylene sheets (Glor, 1996) and (Ackroyd & Newton, 2003).

Further work (von Pidoll et al., 2004) gives specific guidance on the maximum tolerable charge transfer to ensure freedom from ignition. However, he has correlated the charge transferred with minimum ignition energy and the gas groups defined by the International Electrotechnical Commission in their standard, but does not take account of the temporal and spatial characteristics of the discharge.

PD (IEC/TS 60079-32-1:2013) presents the maximum tolerable charge transfer values in the presence of the IEC gas groups (IIC gases include hydrogen). The maximum tolerable charge transfer for IIC gas / air mixtures is given as “no measureable discharge” for areas where an almost permanent flammable atmosphere is present (Zone 0) and 10 nC where a flammable atmosphere is less likely to form (Zones 1 and 2). This reflects the fact that a very small quantity of charge is required to ignite the IIC gases, and hence hydrogen is extremely prone to ignition from electrostatic discharges from insulating or non-conductive materials.

Restricting the maximum area of an insulating surface limits the maximum charge that can be transferred in the form of a brush discharge. PD (IEC/TS 60079-32-1:2013) also presents the maximum areas of insulating materials that are acceptable in the presence of the IEC gas groups. The restriction on the size of chargeable surfaces depends on the ignitability of the gases and vapours and the classification of the hazardous area:

- For sheet materials the area is defined by the exposed (chargeable) area;
- For curved objects the area is the projection of the object giving the maximum area;
- For long narrow materials, such as cable sheaths or pipes, the maximum size is defined by the transverse dimension.

Table 2.2 shows the chargeable surface area restrictions and the restrictions on width for narrow materials for IIC gases:

Table 2.2 Restriction on chargeable surface area and width depending on zones for IIC gases.

Zone	Maximum area, [mm^2]	Maximum width, [mm]
0	400	1
1	2000	20
2	No limit	No limit

There have been several instances in the past where accidental hydrogen releases have ignited spontaneously. Whilst these have been investigated, no satisfactory explanation has been produced, but there have been suggestions that some form of electrostatic charging has been present, resulting in an ignition. In view of the very low ignition energy of hydrogen, such ignitions are a distinct possibility.

Whilst electrostatics can be due to an obvious charging mechanism, such as the discharge from a sheet of insulating plastic as described above, ignition of hydrogen from electrostatics generated from or by the hydrogen itself is a far more difficult mechanism to define. Generally, there is no particular propensity for pure gases to become electrostatically charged, as described by (CENELEC, 2003). As reported by Astbury & Hawksworth (2005), work at the U.K. Health and Safety Laboratory on releasing high pressure (15 MN m^{-2}) hydrogen through various nozzles from 0.5 to 12 mm in diameter did not result in any spontaneous ignition at all. This would suggest that straightforward pure hydrogen does not in itself ignite. However, there have been reports, particularly one by the periodical Engineering (Anon, 1922) reporting work undertaken by Nusselt in Germany, after a spontaneous ignition of hydrogen. While electrostatic ignition was considered, much of this work centred on the possibility of a catalytic effect from fine rust that was present.

2.1.6.3Corona discharges

Corona discharges are not discrete spark discharges, like capacitive or brush discharges, but are a quasi-constant current emitted from a pointed object that is at a different potential to its surroundings. The corona current is initiated when the potential is high enough to cause the local electric field to exceed a threshold value which depends upon curvature of the point. The potential required for the onset of a corona discharge is given by (Cross, 1987)

$$Vc = 18\sqrt{r}, \quad (2.2)$$

where V_c is the threshold potential (kV) and R is the radius of curvature of the point (cm).

The magnitude of the current thereafter has been found experimentally (Cross 1987, Hooker et al 2011) to be related to the applied potential in an equation of the form

$$I = KV(V - V_c), \quad (2.3)$$

where V_c is the threshold potential (V) V is the applied potential (V) and K is a constant (specific for the system, including the geometry and gas).

Unlike most hydrocarbon fuels, there is evidence that hydrogen may be ignited by corona discharges. There has been anecdotal evidence of corona discharges igniting hydrogen, such as in Engineering 1922 (Anon, 1922) which reports that when hydrogen was released in the dark through a nozzle fitted with a funnel and a wire probe, corona discharges were seen, and on tapping the nozzle to disturb the rust, an ignition took place. However, there is not much published quantitative data on the subject. The maximum equivalent energy of corona discharges, in terms of incendivity, has been reported as being approximately 0.1 mJ (Britton, 1999). It has been reported (Hooker et al., 2011) that hydrogen between 28% v/v and 32% v/v was to ignited by positive corona discharges at a current of +150 μA and a potential of +20 kV using a 0.38 mm wire point and plate electrode system with a 30 mm separation. No ignition was observed with negative currents of up to–290 μA and potential of –28 kV. Experiments were carried out in which hydrogen at up to 200 bar was released into a pile of up to 160 g of iron oxide dust or plastic powder; no ignitions occurred, although electric fields were generated by the charged dust clouds. It was concluded that ignition of hydrogen releases by corona discharges appears to be unlikely for low level, well-earthed systems, although the electric potential at the top of vent stacks may be sufficient to generate high corona currents, especially in conditions of high atmospheric elctric fields. Coal gas, which contains hydrogen, has also been reported as having ignited as a result of corona discharges between pointed metal electrodes which passed a current with a magnitude of approximately 300 μA (Sloane, 1935).

In a corona discharge the current will flow, and hence energy deposited, in a path that depends upon the geometry of the electrode system. Further work would be required to understand the influence of electrode geometry on the propensity to ignition.

2.1.7 Radiofrequency electromagnetic waves up to 10^{11} Hz (HSL)

Radiofrequency (RF) waves will induce electric currents and voltages in any conducting structure on which they impinge. The magnitude of the currents and voltages will depend upon the size and shape of the structure, and the wavelength and strength of the RF signal. Although a high RF potential may exist between two parts of a structure, RF discharges most easily occur if two parts of a structure initially in contact are drawn apart (i.e. a break-spark occurs), and discharges across a fixed gap are not considered to be a significant problem.

Guidance on avoiding the accidental ignition of flammable gases, including Group IIC gases (of which hydrogen is one) is given in PD CLC/TR 50427:2004, Assessment of inadvertent ignition of flammable atmospheres by radio-frequency radiation - Guide.

2.1.8 Electromagnetic waves from 3 x 10^{11} Hz to 3 x 10^{15} Hz (HSL)

Radiation in this spectral range can be a source of ignition, especially when focussed, through absorption by explosive atmospheres or solid particles. Lasers are able to transmit a high power density over large distances. Hydrogen ignitions from lasers (optical sources) can be split into, explosion initiation by pulsed or continuous light sources and explosion initiation by optical irradiation of combustible materials within a flammable hydrogen atmosphere. The propensity for ignition of a flammable hydrogen atmosphere from laser ignition is further dependant on; laser wavelength, the material the light falls on (target material), hydrogen concentration, atmospheric pressure, the size of the irradiated area and the length of time the area is irradiated for (Carleton et al., 2000).

Carleton et al. (2000) found that the minimum ignition power and temperature increased linearly with pressure and that hydrogen concentration had little effect on minimum ignition power. This work also found that hydrogen has a relatively high ignition power in spite of its low MIE. Previous testing of ignitions due to optics (McGeehin, 1994), found that fibre diameters below 62.5③m did not cause a decrease in minimum ignition powers. Table 2.3 shows selected scenarios from the work of Carleton et al. (2000), that produced the lowest minimum ignition energies.

Table 2.3 Minimum ignition energies for various optical ignition scenarios

Optical Ignition Scenario	Ignition Criterion	Irradiation Area	Exposure Time	Hydrogen Concentration, (%)	Laser Wavelength, (nm)	Fibre Diameter, (m)	Minimum Ignition Crieterion
Continuous wave irradiation	Minimum power	Small	Tends to infinity	10	805	62.5	140 mW
Pulsed irradiation	Minimum energy	Small	Tends to zero	13	1064	400	3.3 mJ
Pulsed irradiation	Minimum energy	92 m^2	70 s	21	1064	NA	88 J

2.1.9 Ionizing radiation (HSL)

Ionizing radiations may act as an ignition source as a result of energy absorption, especially in dust particles. Alternatively, the radioactive source itself may heat up by internal absorption of radiation energy. The hot surfaces may cause ignition if at a sufficiently high temperature above the AIT of the surrounding atmosphere. BS EN 1127-1:2011 gives advice on avoiding ignition by ionizing radiation.

2.1.10 Ultrasonics (HSL)

A large portion of the energy in ultrasonic sound waves is absorbed by solids or liquids, causing them to heat up. The hot surfaces may cause ignition if at a sufficiently high temperature above the AIT of the surrounding atmosphere. BS EN 1127-1:2011 give advice on avoiding ignition as a result of ultrasonic sound waves, such as avoiding waves with a frequency of more than 10 MHz, and limiting the power density to no more than 1 mW/mm2.

2.1.11 Spontaneous / diffusion ignition (HSL)

There has been, for some time, anecdotal evidence of “spontaneous ignition” of hydrogen leaking from pressurised containers into the air. The first “scientific” investigations into the mechanism for shock wave induced ignition were published by Wolanski & Wojcicki (1973) who described the mechanism as “diffusion ignition”.

A number of papers have been published describing this interesting case of shock wave induced ignition in which hydrogen ignites when gas kept at high pressure is rapidly released from a volume into air at atmospheric pressure, such as when a bursting disc ruptures. As the compressed hydrogen is released, a shock wave is generated ahead of the hydrogen jet. The air behind the shock wave is heated to temperatures greater than the autoignition temperature of hydrogen. Mass transfer occurs across the contact region resulting in a flammable mixture which will ignite if the required conditions are achieved. This mechanism of ignition is referred to by researchers both as diffusion ignition and spontaneous ignition.

Experimental work in which spontaneous ignition was carried out in straight tubes has been reported, such as Golub et al. (2006) and Grune et al. (2011). The work by Golub et al. (2006) reported that the propensity for ignition was increased if either pressure or initial temperature were increased. Other experimental work has been reported in which pressurised hydrogen ignited as a result of being released into the air through pipework containing common “real-world” pipeline fittings, such as Dryer et al. (2007) and Hooker et al. (2011). Dryer et al. (2007) reported that, for a downstream geometry consisting of a 2” long, 1/2” NPT union, a 1/2” to 3/8” NPT reducer and a 3/8” NPT to 1/4” Swagelok reducer, there was a zero probability of ignition with burst pressures less than 20.4 atm, but certain ignition at 22.1 atm. When the length of the 1/2” connection was reduced to 1 1/2” in length a higher pressure was required for ignition, as was also the case when the diameter of the reduced fittings was increased. In the experiments reported by Hooker (2011), using nominally the same downstream geometry as Dryer, ignition occurred at as low as 36 bar with no ignition at 25 bar. It was also reported that soft bursting discs (in this case aluminum) were less likely to result in ignitions. No ignitions occurred when hydrogen was released directly from the storage (by opening a valve with no bursting disc or restrictive or reflective downstream geometries) at pressures up to 831 bar.

The mechanism and modelling of diffusion ignition has been reported by a number of authors. A review of the physics of spontaneous ignition was published by Bragin & Molkov (2009). This paper highlighted the difficulties of drawing conclusions from experimental data alone, since apparently minor changes in the experimental arrangements (for example, surface roughness, bursting disc rupture behavior, etc.) may play a large role in determining the critical conditions required for ignition. While the “real-world” experiments are useful for guidance in hydrogen safety engineering the complexity of the geometries and the number of poorly controlled variables make such data difficult to use for validating predictive models. In the same paper by Bragin and Molkov, large-eddy simulation (LES) of the spontaneous ignition dynamics within a straight tube were found to be in good agreement with experimental results in terms of distance from the rupture disc to ignition , and also showed that ignition is initiated in the wall boundary layer.

Numerical simulations reported by Wen et al. (2009) indicated that the rate of rupture of the pressure boundary is important in determining whether spontaneous ignitions occur in a straight pipe, with more rapid rupture being more likely to result in ignition. This was also indicated in experimental work reported by Hooker et al. (2011) where a higher rate of

pressure rise in the piping downstream of the bursting disc was more likely to result in ignition.

In further papers, Xu & Wen (2011, 2012, 2014), numerically investigated the effects of changing internal geometries downstream of the pressure boundary. Four types of geometry were considered; local contraction, local enlargement, abrupt contraction and abrupt enlargement. The work showed that the presence of internal geometry changes can significantly increase the propensity to spontaneous ignition, with reflected shock and shock interactions further increasing the temperature of the hydrogen – air mixture. The geometry changes also enhance turbulent mixing of the shock heated air and the hydrogen resulting in a larger volume of flammable mixture. It was also reported that the presence of forward facing vertical planes (i.e. constrictions) appears to result in a greater propensity to ignition than backward facing planes (i.e. expansions) since the reflected shock from the side walls are relatively weak for backward facing planes. Such information would be useful in equipment design, such as pressure relief systems.

Spontaneous ignition within a tube or other fitting may not always transition into a jet-fire at the tube exit. Experiments carried out by Grune et al. (2014) using a tube containing some transparent sections demonstrated that in some cases ignition was initiated within the tube but failed to develop into a jet fire at the nozzle exit. Bragin & Molkov (2009) assumed that the transition from initial ignition to a sustained jet flame is largely dependent on the initial jet formation stage where the developing vortex pushes the burning mixture into the recirculation zone. If the flame is stabilised near to the tube exit, it acts a pilot flame to ignite the emerging jet and establish the jet fire.

2.1.12 Explosives (HSL)

An explosive is a powerful ignition source and will readily ignite a flammable fuel/air mixture and even under the right conditions directly initiate a detonation in an unconfined mixture. No data has been found in the literature on the minimum amount of explosive required to ignite a fuel/air mixture, but there have been a number of experimental and theoretical studies to determine the minimum amount of explosive required to initiate an unconfined detonation by (Bull et al., 1978; Bull, 1979).

As might be predicted from the general behaviour with other ignition sources the mass of explosive required to initiate an unconfined detonation in a hydrogen/air mixture is very much less than that required for less reactive fuel/air mixtures such as propane or methane. Table 2.1.1 compares the minimum amount of tetryl required to initiate an unconfined detonation in the most detonable hydrogen/air mixture and other common fuel/air mixtures. For hydrogen and the other fuels listed in Table 2.4, apart from acetylene, the most detonable mixture lies within a stoichiometry range of between 1.1 and 1.3. For acetylene the value for the most detonable mixture is 2.05. For all fuels the minimum amount of explosive required increases rapidly as the mixture approaches the detonation limits. In the case of hydrogen it is predicted there is about a hundred-fold increase in the mass of tetryl required to initiate a detonation in near limit mixtures compared to the most detonable mixture (stoichiometry of about 1.1).

Table 2.4 Minimum mass of tetryl required to initiate unconfined detonation

Fuel	Mass of Tetryl, [g]
Hydrogen	0.8
Methane	16,000
Propane	37

Ethylene	5.2
Acetylene	0.4

2.1.13 Ignition of liquid hydrogen and solid oxygen mixtures (HSL)

Liquid hydrogen has properties which set it apart from the other cryogenic fuel of liquefied natural gas, in that its atmospheric boiling point is much lower than that of air. Pipe-work and vessels at liquid hydrogen temperatures of about 20 K will condense air from the atmosphere. It will also be cold enough to condense and freeze water and carbon dioxide from the air, see Table 2.5.

Work undertaken by Perlee et al. (1964) indicated that liquid hydrogen can condense and freeze oxygen. The resultant solid oxygen in an excess of liquid hydrogen can be detonated by impact. Using a rifle and with a muzzle velocity of 600 m s^{-1}, detonation always occurred when the bullet impacted the mixture. Detonation was indicated by the use of thin metal strip gauges which deflected permanently when a detonation occurred. The results indicated that the explosive yield of liquid hydrogen-solid oxygen mixtures was greater than those for equal weights of trinitrotoluene (TNT). Various experiments were carried out in which there was a large excess of liquid hydrogen. The specific gravity of liquid hydrogen is typically about 0.07, and that for the solid oxygen in the αstate is about 1.426. The sonic velocities in the hydrogen and solid oxygen phases are similar due to the two gases having nearly identical ratios of specific heat capacities.

Table 2.5 Melting and boiling points of selected gases (Yarwood & Castle, 1961).

Gas	Melting point, [K]	Boiling point, [K]
Methane	14	20
Helium	1	4
Oxygen	54	90
Nitrogen	63	77
Carbon dioxide	Sublimes	195

Hall et al. (2014) investigated the dispersion of liquid hydrogen released from a simulated rupture of a 1” diameter transfer hose. For ground level releases solid / liquid, air / hydrogen deposits were often formed on the ground near to the release point as shown in Figure 2.9. In some of the tests the resulting hydrogen cloud was deliberately ignited resulting in the burn back of the cloud to the release point followed by a continuous steady fire. However, in one of reported tests, an explosion occurred after several seconds of steady burning. It is thought that the explosion was caused by the rapid combustion, potentially detonation, of the hydrogen / air deposit, possibly due to oxygen enrichment of the solidified air. It was estimated that the explosion involved of the order of hundreds of grams of hydrogen.

Figure 2.9 Formation of solid/liquid deposit of air and hydrogen.

2.1.14 Ignition probabilities (HSL)

There are a large number of releases of flammable material every year. However, not all releases will be ignited even if the quantity of released flammable gas is relatively large. The probability of a release igniting can be obtained from

- Observations of ignition in experiments (which allows for some measure of control)
- Analysis of incident data

A number of experimental campaigns have addressed the ignition probability issue (Birch et al., 1981; Ahmed & Mastorakos, 2005; Swain et al., 2007; Gant et al., 2011; Schefer et al., 2011). Ignition probability plays a crucial role in the Quantified Risk Assessment of a plant. Since risk is calculated as

$$risk = probability\ x\ consequence \quad (2.4)$$

it is clear that an as accurate an estimate of the ignition probability as possible is required to arrive at a measure of a representative risk. We are here leaving aside the question of inaccuracies in the consequence modelling.

In two studies, (Birch et al., 1979, 1981) investigated the ignition probability of natural gas releases using laser Raman spectroscopy. Some interesting findings were (Birch et al., 1979):

- The fluctuation in the natural gas volume fraction was found to be around 30 %;
- The ignition probability is considerably lower for lower temperatures, below about 25 % of that at T = 1000 K;
- The probability density function of the mean concentration was Gaussian along the centreline of the jet flame; and
- The probability density function of the mean concentration was highly non-Gaussian in the intermittent region off-axis.

In the follow up paper, (Birch et al., 1981) showed that the ignition probability was high, around 30%, even though the mean concentration of fuel was below the LFL near the edge of the jet. One graph, graph 2, showed that the flammable boundary (complete light-up of the jet) could extend out to a region where the mean concentration was approximately 10 % LFL.

The results of experiments on sub-sonic releases of hydrocarbon / carbon dioxide mixtures (Gant et al., 2011) revealed that ignition was possible in regions where the flammable gas concentration was below the LFL and above the UFL.

(Swain et al., 2007) reported that high pressure jets of hydrogen required a concentration of 8% v/v for ignition to occur along the axis of the jet, which is considerably greater than the LFL of 4% v/v determined using a standard method.

The work of (Schefer et al., 2011) somewhat confirmed the results of Swain in that a hydrogen concentration of 8 – 10% v/v was required for ignition along the axis of the jet. However, light-up of the jet was possible at as low as 0.5% v/v hydrogen radially out from the jet axis (i.e. almost 10% of the LFL of hydrogen).

The results confirm that that in a turbulent flow it is not meaningful to consider just the mean concentration in order to define the flammability or probability of ignition (e.g. Birch et al., 1981).

This is relevance to the mathematical modeller since calculations using a Reynolds Averaged Navier-Stokes approach will yield only the mean concentration field, which is not sufficient to define the boundary of flammability or ignition probability. Birch et al. (1981) showed that intermittency or fluctuations were of utmost importance. From a modelling point of view, it would necessitate the use of a Large Eddy Simulation approach, possibly in conjunction with a RANS model in the near-wall region, which could provide more realistic fluctuation estimates and thus give some hope of capturing the behaviour described by (Birch et al., 1979, 1981).

The above considers the ignition probability where the ignition source is large enough to ignite a flammable atmosphere and, therefore, the ignition probability is a function only of the gas concentration. Where an ignition source is close to the minimum required for ignition (for example, spark ignition energy) the probability of ignition will be less than unity even in a quiescent, uniform mixture. An example of this for spark ignition energy of methane / hydrogen mixtures is reported by Hankinson et al. (2009). The statistical nature of electrostatic brush discharges as an ignition source has also been demonstrated by Gibson & Harper (1988).

2.1.15 Ignition modelling (HSL)

Westbrook et al. (1996) used the following definition: "*ignition consists of a rapid growth in the radical pool of a chemically reactive mixture which may be entirely gaseous or may include fuel droplets or particles*". Ignition of a flammable mixture is brought about if a sufficient amount of heat is imparted locally on the mixture. The amount of energy required must exceed the energy loss mechanisms.

It is feasible to model the ignition process, but some of the simple combustion models are not capturing the physics and hence cannot be used. However, the ignition processes have been represented by a single-step, irreversible Arrhenius-type reaction, for example for modelling deflagration-to-detonation transition and it works satisfactorily in some cases (Buckmaster et al, 2005). Rate ratio asymptotics has been used to model the ignition processes. This has identified different ignition regimes (Buckmaster et al., 2005). This approach was used to

determine the cross over temperature, the rate-determining elementary and global reactions and overall activation energies. The research has been extended to multi-step rate-ratio asymptotics.

It is important to model the production and destruction of the highly reactive radicals, for example the hydrogen radical (H), the oxygen radical (O) and the hydroxyl radical (OH), as these and other radicals the mechanism by which the combustion can progress. A detailed kinetics scheme will contain all the important chemical species, radicals and reaction pathways. It has been shown that a reduced chemical kinetics scheme, which includes a sub-mechanism for the combustion of hydrogen, will suffice for hydrocarbon fuels, at pressures below approximately 100 atm and temperatures above 1000 K (Buckmaster et al., 2005; Petrova & Williams, 2006). The kinetic scheme has also been tested for the autoignition of hydrogen (Del Alamo et al., 2004). Further testing of the reduced kinetics scheme for hydrogen has been carried out by Saxena & Williams (2006) who investigated its effectiveness for laminar burning velocity and diffusion flame extinction.

2.1.16 Conclusions (HSL)

Although there is a generally a reasonable understanding of the mechanisms by which hydrogen may be ignited, there are a number of areas where further development of knowledge is required.

In the case of diffusion ignition, simple geometries have investigated successfully using CFD, and the methods have been used to predict behaviour in some slightly more complex geometries. More comparison of CFD simulations versus experiments with complex geometries would be desirable, as would the development of simplified predictive tools.

In terms of the ignition of hydrogen by corona discharges, a more complete understanding of the ignition potential for different electrode systems is desirable, as is the understanding of the role of hydrogen concentration.

Although some success has been achieved in modelling ignition and light-up probabilities, more work is required to improve predictions for differing release conditions, including attached jets where releases are close to or impinging on surfaces.

2.2 Spontaneous diffusion ignition model (UU)

2.2.1 Spontaneous diffusion ignition phenomenon (UU)

Spontaneous diffusion ignition presents a particular interest among the ignition phenomena listed in section 2.1. Part of the importance of the spontaneous ignition phenomena lies in its importance for the safety analysis of hydrogen infrastructure. The conditions which were observed to lead to the spontaneous diffusion ignition are commonly encountered during the release of hydrogen under high pressure, e.g., after failure of the pipe or storage tank. Furthermore the exact conditions which determine ignition event are still not completely understood. Since high pressure hydrogen storage facilities are an inherent part of hydrogen infrastructure, it is of paramount importance for hydrogen safety engineering to be able to predict if the release results in immediate ignition. Accordingly, research into spontaneous ignition has been a subject of vigorous experimental and numerical research in recent years.

It is well-known that a sudden hydrogen release from a high pressure equipment into air can be spontaneously ignited at pressures far below of storage pressures up to 100 MPa used in

today's hydrogen and fuel cell applications (Golub et al., 2010). The phenomenon was first observed in the experiments by (Wolanski & Wojcicki, 1973) and was named as "diffusion" mechanism of spontaneous ignition. In spite of recent experimental and numerical studies there is still limited understanding and validated models able to reproduce the pressure limit of spontaneous ignition of hydrogen, especially in complex geometries like pressure relief devices (PRD) requiring 3D simulations.

Numerical studies by (Liu et al., 2005), (Bazhenova et al., 2006), (Xu, Wen, et al., 2009; Xu, Hima, et al., 2009) were focused on unconfined release from high-pressure storage directly into the atmosphere. While spontaneous ignition for direct release into the atmosphere was predicted by numerical simulations, no experimental proof exists up to date. However, spontaneous ignition was observed in experiments that included pipes located downstream of a rupture disk (Dryer et al., 2007; Pinto et al., 2007; Golub et al., 2008; Mogi et al., 2008), etc.

Dryer et al. (2007) speculate on the importance of the initial stage of a membrane rupture on the mixing and subsequent spontaneous ignition process. They concluded that at low pressures, the chemical ignition time becomes the limiting factor, while at high pressures the mixing time to achieve significant flammable mixture volume limits the process, with typical characteristic time scale in the release tube estimated to be less than 100 μs (Dryer et al., 2007). When pressurized hydrogen is released into an ambient environment via a length of tube through fast rupturing of a pressure boundary, strong shock waves are generated inside the tube. The leading shock wave is driven into the ambient air and the temperature of the air behind the shock is elevated. The shock-heated air mixes with the released hydrogen at the contact region. Ignition might occur inside the tube first under specific conditions and then the initiated flame might also survive the high under-expansion while spouting from the tube and transit to a turbulent jet fire.

Although the mechanism of the actual turbulent mixing process is still not well understood, it has been found that the rupturing process, which generates strong multi-dimensional shock waves, plays an important role in the mixing (Hooker, 1961; Levine, 1970; Vasil'eva et al., 1985). As shock waves reflected from the tube wall sweep through the contact region, the misalignment of the pressure and density gradients cause a deposition of vorticity through the baroclinic production mechanism and produce significant turbulent mixing via Rayleigh–Taylor instability.

Accordingly, more recent numerical studies investigated more complex conditions focusing on the features known from the experiments to promote onset of self-ignition. These included modelling of non-instantaneous membrane opening time studies (Xu, Wen, et al., 2009; Xu, Hima, et al., 2009; Wen et al., 2009), burst disk shape (Lee & Jeung, 2009) and the release tube internal geometry (Xu & Wen, 2012), (Xu & Wen, 2014) and presence of obstacles (Xu et al., 2011), confirmed their significance for initiation of the spontaneous ignition process.

The 2D analysis of pressure-boundary rupture rate on hydrogen spontaneous ignition during release through a 3 mm hole in a wall of 0.1 mm thickness directly to atmosphere was carried out in (Xu et al., 2009). Characteristic cell sizes used were 15-30 μm across the contact surface. It was found that spontaneous ignition will not occur if the rupture rate is below a certain threshold value. As the rupture rate increases, the temperature of the shock heated region grows more quickly owing to earlier flow expansion and once the rupture rate is sufficiently high, spontaneous ignition can occur.

Lee & Jeung, (2009) investigated the effect of a burst disk shape on the ignition process at pressure of a burst disk rupture of 8.6 MPa and release into a tube. The burst disk had a semi-

spherical shape and was assumed to be opened instantaneously. Cartesian grid with a cell size of 19 μm was used. The spontaneous ignition first occurred in a boundary layer and consequently spread throughout a cross-section of the tube, i.e. through the contact surface between air and hydrogen where mixing takes place, which was similar to the results of 3-D study (Bragin & Molkov, 2009) investigating an instant opening of a flat membrane.

Hydrogen releases through a tube of 3-6 mm internal diameter and length of 30-60 mm long for storage pressures in a range 5-15 MPa were simulated in (Wen et al., 2009). It was demonstrated that spontaneous ignition is governed by focusing of reflected shocks from the tube wall. The influence of internal tube geometry had been investigated in (Xu & Wen, 2012, 2014). Hydrogen had been released through a tube of 3 mm diameter and 6 cm long with featuring local contraction and enlargement. Study demonstrated that internal geometries with a forward-facing vertical plane can significantly increase the propensity to spontaneous ignition by producing an elevated flammable mixture and turbulent enhanced mixing. The backward facing vertical plane was found to be less likely to cause spontaneous ignition as the reflected shock from the side wall is relatively weak.

Numerical modelling of the shock-related turbulent mixing problem is mathematically challenging due to the presence of the thin diffusion layer and strong shock waves. One of the primary challenges is the substantial scale difference between diffusion and advection and the reactive flow with strong shock waves. Utilization of the direct numerical simulation (DNS) approach would be desirable, but often proves to be prohibitive for more complex problems due to its requirement on computing power for such shock-containing flows, prompting researchers to consider less computationally intensive methods such as large eddy simulation (LES). Furthermore, many researchers considered reduction of the problem to 2-D and in some cases to 1-D, often taking advantage of axisymmetric geometry, in order to reduce mesh size requirements. While effectively reducing computation requirements, 1-D and 2-D models, however, suffer from the inability to correctly model the physics of turbulent mixing which had been shown to be one of the main drivers of self-ignition. Both DNS and LES approaches had been applied to modelling of spontaneous ignition, producing a range of 1-D, 2-D and 3-D models described in the following sections.

2.2.2 1-D models (UU)

Maxwell & Radulescu, (2011) developed a model addressing the ignition problem of a one-dimensional unsteady diffusion layer of fuel and oxidizer, undergoing volumetric expansion. This model was applied to shock induced diffusion-ignition of pressurized fuel jets that are released into an oxidizing atmosphere. Upon the sudden release of a pressurized gaseous fuel into the ambient atmosphere through a hole, a strong shock wave forms, driven by rapid expansion of the forming jet. The model follows the thin diffusion layer at the head of the jet in Lagrangian coordinates, with its rate of expansion dictated by the local pressure evolution of the surrounding gas flow.

Sudden transient release of gas from a pressurized tank into the ambient atmosphere produces a strong shock wave, driven by the piston action of the jet head (Radulescu & Law, 2007). The shock wave heats the material that it has compressed, and the diffusive interface between the two gases may lead to local ignition without any other external sources. This type of shock induced ignition can occur when the air is sufficiently hot due to a sufficiently strong shock driven by a large initial pressure difference between the fuel and air (Dryer et al., 2007). The process is illustrated in Figure 2.10. Following the initial compression at the start of the process, the interface between the two gases, experiences very strong expansion owing to the growth of the jet head (see Figure 2.10). The model applies only to the evolution of the

jet head, in Lagrangian coordinates in the frame of reference of the jet head itself, in order to determine a conservative ignition criterion. Since the jet head is the location where the flow is the hottest point in the flow at any given time during the release (Radulescu & Law, 2007), a failure for ignition to occur at the jet head means that spontaneous ignition will not occur at any other location either.

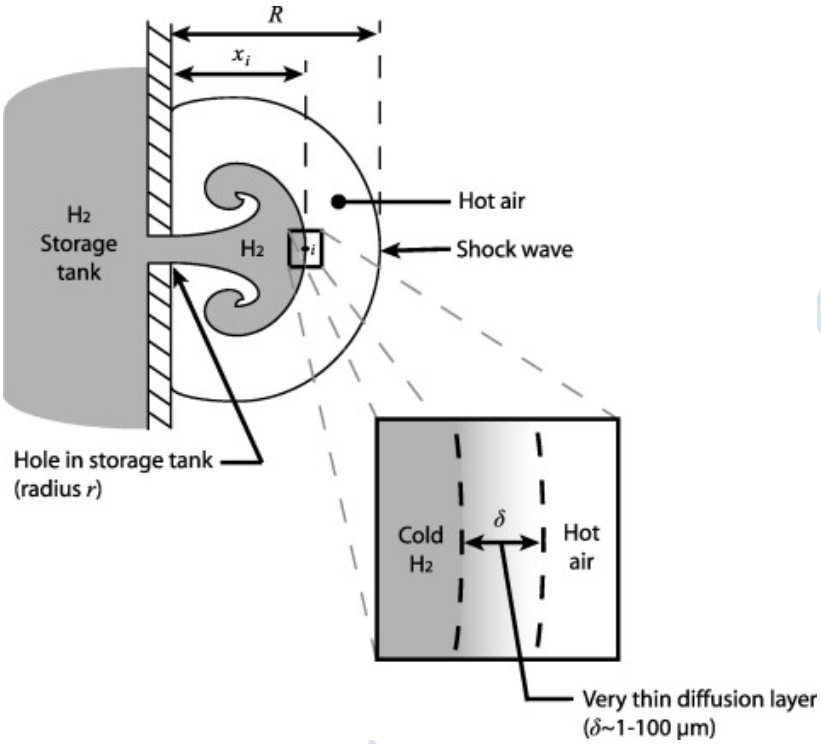

Figure 2.10 Structure of the thin diffusion layer at the head of the jet resulting from an accidental release of hydrogen from a high pressure storage tank. The diffusion layer is where the hydrogen mixes with shocked air, ultimately leading to diffusion-ignition (Maxwell & Radulescu, 2011).

The evolution of the entire reactive jet expansion problem illustrated in Figure 2.10 is governed by the Navier–Stokes equations for a chemically reactive fluid augmented by the evolution of each chemical reactive species. Neglecting viscous effects and spatial pressure gradients within the diffusion layer due to its dimension being very small compared to that of the jet, decouples the momentum equation from the evolution of the diffusion layers. Furthermore, owing to the thinness of the diffusion layer, its curvature can be neglected, restricting the analysis to a single space dimension perpendicular to the diffusion layer. Further neglecting body forces, viscous dissipation and radiation transfer, the equation system reduces to:

$$\frac{D\rho}{Dt} = -\rho\frac{\partial u}{\partial x}, \tag{2.5}$$

$$\rho\frac{DY_i}{Dt} = \omega_i - \frac{\partial(\rho Y_i u_{d,i})}{\partial x} \tag{2.6}$$

$$\rho c_p \frac{DT}{Dt} = \frac{Dp}{Dt} h_i \omega_i + \frac{\partial}{\partial x}\left(k \frac{\partial T}{\partial x} \right) - \sum_{i=1}^{N} \rho Y_i c_{p,i} u_{d,i} \frac{\partial T}{\partial x} \tag{2.7}$$

This system is further simplified by using a mass-weighted Lagrangian coordinate to follow the diffusion layer. This permits the elimination of the requirement of solving the continuity equation and the velocity field, since each mass element travels with its material velocity. The transformation follows the same approach as Rogg & Wang (1984) where the Eulerian spatial coordinates are transformed into the mass-weighted Lagrangian coordinates, i.e.,

$$(x,t) \rightarrow (m,t)\,. \tag{2.8}$$

In this approach the spatial coordinate, x, is transformed into a mass-based coordinate, m, by integrating the density from some reference coordinate, xo, to x:

$$m(x,t) = \int_{x_0}^{x} \rho(x,t)dx\,, \tag{2.9}$$

and system (2.2.1) – (2.2.3) further reduces to

$$\rho \frac{\partial Y_i}{\partial t} = \omega_i - \rho \frac{\partial (\rho Y_i u_{d,i})}{\partial m}, \tag{2.10}$$

$$\rho c_p \frac{\partial T}{\partial t} = \frac{\partial p}{\partial t} - \sum_{i=1}^{N} h_i \omega_i + \rho \frac{\partial}{\partial m}\left(k\rho \frac{\partial T}{\partial m} \right) - \sum_{i=1}^{N} \rho^2 Y_i c_{p,i} u_{d,i} \frac{\partial T}{\partial m}, \tag{2.11}$$

where partial derivatives with respect to time denote Lagrangian derivatives, i.e. keeping the mass coordinate constant.

For calculating transport properties of the gasses (i.e. diffusion velocity of each specie and thermal conductivity), the model uses mixture-averaged expressions described in (Coffee & Heimerl, 1983) and also developed in (Kee et al., 2000). These expressions provide a good estimate for the transport properties and are much less expensive to employ than multi-component expressions described in (Dixon-Lewis, 1968) and (Williams, 1985). Finally, in order to compute the thermodynamic properties ($c_{p,i}$, h_i, etc.) and production rates of each chemical species, ω_i, a reaction mechanism is required which provides the details of reactions involved including the required thermo-chemical data. The reaction mechanism used for this model had been developed by Li et al. (2004) for high pressure hydrogen combustion, 0.3–87 atm.

It have previously determined in (Radulescu & Law, 2007) that the scaling parameters for under-expanded, non-reactive jets both analytically and numerically for non-reactive releases. In their analysis, the pressure–time history at the interface between the gasses for different jet conditions was found to obey a similarity solution. The dependence on hole size is through the non-dimensional time τ, which depends on the discharge flow rate, and hence the size of

the hole through which the gas escapes as well as the choked velocity at the hole. The dependence $p(\tau)$ in this model was found by curve-fitting the numerical results of (Radulescu & Law, 2007). As shown in Figure 2.11, a power-law

$$\frac{p}{p_{air_0}} = 12.2\tau^{-0.68} \tag{2.12}$$

provides good approximation for a wide range of discharge conditions. The scaling parameter τ is given by

$$\tau = \left(\left(\frac{\rho_{air_0}}{\rho_{H_{2_0}}} \right) \left(\frac{2}{\gamma_{H_2}+1} \right)^{-1/(\gamma_{H_2}-1)} \right)^{1/2} \frac{t a_{H_{2_0}}}{1.2r} \left(\frac{2}{\gamma_{H_2}+1} \right)^{1/2}, \tag{2.13}$$

where the subscript ‘o’ denotes the initial undisturbed state. The rate of change of pressure at the jet head is then simply the time derivative of p, yielding

$$\frac{\partial p}{\partial t} = \frac{\partial p}{\partial \tau}\frac{\partial \tau}{\partial t} = -8.3 p_{air_0} \tau^{-1.68} \frac{\partial \tau}{\partial t} \tag{2.14}$$

where $\frac{\partial \tau}{\partial t}$ is simply the time derivative of Eq. (2.13). Thus

$$\frac{\partial \tau}{\partial t} = \left(\left(\frac{\rho_{air_0}}{\rho_{H_{2_0}}} \right) \left(\frac{2}{\gamma_{H_2}+1} \right)^{-1/(\gamma_{H_2}-1)} \right)^{1/2} \frac{a_{H_{2_0}}}{1.2r} \left(\frac{2}{\gamma_{H_2}+1} \right)^{1/2}. \tag{2.15}$$

The pressure at the interface does not change instantaneously upon the beginning of the release, but remains constant for the time required for the lateral expansion from the edge of the hole to reach the axis of the jet. To account for this delay, the value of τ is calculated from Eq. (2.12) for the moment when $\frac{p}{p_{air_0}}$ is equal to the initial pressure of the jet head, obtained from the shock tube solution. The simulations are then started at time zero of the release process, incorporating this period of constant pressure.

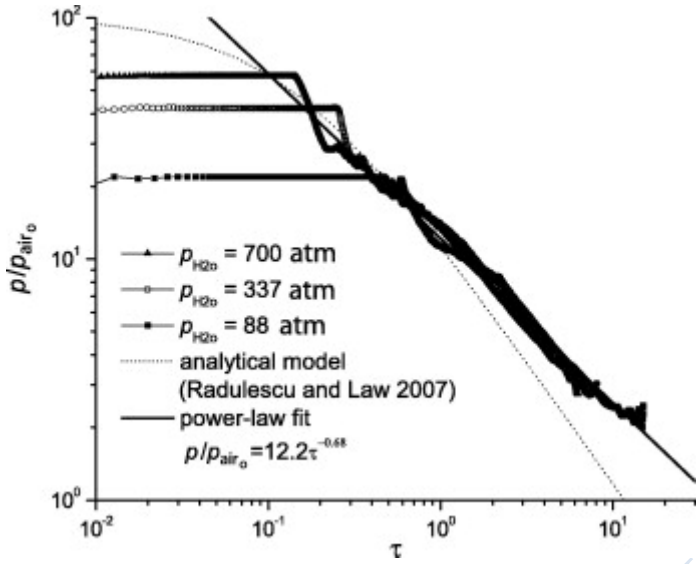

Figure 2.11 Evolution of the contact surface pressure along the jet axis of round jets for various storage pressure to ambient pressure ratios (Radulescu & Law, 2007).

Simplified governing equations (2.10) – (2.11) are integrated numerically using an *operator splitting* technique (LeVeque, 2007) which solves the diffusion, reaction, and source terms separately, over one time step. Each operation is solved independently based on information known from the previous operation. Once each of the three steps, explained below, are executed throughout a single time step, the process is repeated over the next time step. The operator-splitting process is similar to the process outlined in (Karasalo & Kurylo, 1981). For the first operation (diffusion step), the governing equations are discretized using central difference approximations (Anderson, 1995)(Anderson, 1995) on the diffusive terms and explicit time stepping (Anderson, 1995) for the unsteady terms. For the second operation (reaction step), the reaction terms are solved over the same time step using the solution obtained from the first step. Due to the Arrhenius dependence on temperature in the reaction terms, the equations that are solved in this operation are very stiff and highly coupled. To handle the stiffness of the equations, the Sundials (Hindmarsh et al., 2005) CVODE (Cohen et al., 1996) integrator is used. This particular solver is specifically designed for solving stiff, nonlinear systems of equations implicitly for each time step using Newton iteration (Cohen et al., 1996). For the final operation, the expansion term, $\partial p/\partial t$ in the energy Eq. (2.11) is treated as a source term and is prescribed by Eq. (2.14) and the pressure of the system is updated accordingly. Finally, in all steps, the thermodynamic and transport properties are evaluated at each operation using the Cantera libraries (Goodwin, 2009). The same kinetic mechanism as in. (Li et al., 2004) was used for calculating the reaction rates and thermodynamic data for each chemically reacting specie.

2.2.3 2-D models (UU)

A number of researchers carried out 2-D (including axisymmetric) numerical simulations of the diffusion spontaneous ignition phenomenon.

Pinto et al. (2007) employed Direct Numerical Simulation (DNS) approach utilizing compressible two-dimensional axisymmetric Navier-Stokes equations, the conservation of mass, total energy, chemical species, and the equation of state, and the detailed chemical reactions mechanism to simulate the behaviour of the hydrogen jet discharged of 10 mm diameter tube with 50 mm length and 3.8 MPa initial hydrogen pressure. Model used the

reduced kinetic mechanism (Petersen & Hanson, 1999) with 9 species (H_2, O_2, O, H, OH, HO_2, H_2O_2, H_2O, and N_2) and 18 elementary reactions, which provided good performance for ignition delay time and heat release within a wide pressure range from 1 to 600 atm. The diffusion flux was evaluated using Fick's law with binary diffusion coefficients. The transport coefficients of each chemical species: viscosity, heat conductivity, and binary diffusion coefficient, are evaluated using the Lennard-Jones intermolecular potential model (Chapman & Cowling, 1970), and those of the gas mixture are calculated by Wilke's empirical rule (Wilke, 1950)(Wilke, 1950). The enthalpy of each chemical species is derived from NIST database (NIST). The buoyancy, bulk viscosity, Soret and Dufour effects are neglected.

The governing equations were discretized in a finite difference formulation. The convective terms were evaluated using the second-order explicit Harten-Yee non-MUSCL modified-flux type TVD scheme, considering the properties of the hyperbolic equations. The viscous terms were evaluated with the standard second-order central difference formulae. The time integration method was the second-order Strang-type fractional step method. Chemical reactions were treated by a point implicit way to avoid stiffness. Uniform rectangular grid with a cell size of 20 x 20 μm was used to carry out simulations with maximum mesh size reaching 27 million cells.

The model was subsequently used by Yamada et al., (2009) to simulate hydrogen release from a tube of 4.8 mm diameter and 71 mm long with the inlet pressure of 3.6, 5.3 and 21.1 MPa, resulting from initial pressure in the large hydrogen tank of 6.8, 10 and 40 MPa. Grid cell size measured 20-45 μm, which was estimated to be close to the Kolmogorov scale (Cheng et al., 1992; Mizobuchi et al., 2002). The total grid size was 4 million cells. Simulations showed spontaneous ignition of the hydrogen for the releases with 5.3 and 21.1 MPa inlet pressure. Additional simulations performed for the hydrogen released from a hole in the tank without a tube. No continuous ignition has been observed for the 5.3 MPa release from the tube, which confirmed the importance of the vortexes generated around the exit from the tube for achieving autoignition. Similar model had been used by (Liu et al., 2005) for modelling of autoignition of hydrogen escaping from the tank with initial pressure of 10, 40 and 70 MPa.

Different numerical model had been used in (Lee & Jeung, 2009). They used numerical scheme based on the cell-centered finite volume method to solve unsteady, compressible two dimensional axi-symmetric Navier–Stokes equations for a chemically reactive multi-species mixture of ideal gases. The convective numerical fluxes were evaluated by the AUSM-DV scheme (Wada & Liou, 1997), which is accurate and robust for resolving shock and contact (stationary and moving) discontinuities. Second-order spatial accuracy is attained by using MUSCL extrapolation on primitive variables with limited slopes by the Superbee limiter for the Total Variation Diminishing (TVD) constraint. The viscous terms were evaluated by second-order central differencing discretization. For time integration, the second-order Strang-type method is employed, splitting convection–diffusion terms and chemical source terms. A memory-efficient type of four-step Runge–Kutta scheme (Blazek, 2001) is used for the integration of convection and diffusion terms, while a stiff ODE solver named RADAU5 (Hairer & Wanner, 1996), an implicit Runge–Kutta method of order five with step size control, is used in order to overcome the stiffness caused by the chemical source terms. A comprehensive kinetic model of hydrogen combustion, recently updated in (Li et al., 2004) and based on the mechanism of presented in (Mueller et al., 1999), is used for describing the reaction kinetics with nine species (H_2,O_2,H,O, OH, H_2O, HO_2, H_2O_2, N_2) and nineteen reactions. The evaluation of thermodynamic properties, transport properties, and chemical source terms is assisted by the Cantera library (Goodwin, 2009) with its interface for Fortran. Thermodynamic properties of the species are based on NASA polynomials (McBride et al.,

1993). The viscosity, thermal conductivity, and binary diffusion coefficients for each species are determined using Lennard–Jones potentials (Chapman & Cowling, 1970) and kinetic theory. In (Wilke, 1950) and (Mathur et al., 1967) formulae were used for calculation of mixture-averaged values.

Simulations of hydrogen spontaneous ignition in air using the model accounting for viscous gas transport, multi-component diffusion, heat transfer, and incorporating a kinetic scheme of hydrogen oxidation with 9 equations were performed by (Golub et al., 2010). The authors studied experimentally and numerically in 2D axisymmetric formulation the self-ignition in cylindrical and rectangular tubes and concluded that governing mechanism for hydrogen spontaneous ignition is diffusion ignition on the contact surface assisted by the boundary layer effects. Combustion starts as kinetic one and then acquires diffusion character. Heat release and flame turbulence intensify mixing of reagents and such burning cloud may propagate along the tube far enough. Simulation with and without the boundary layer were also carried out and a conclusion is drawn that when boundary layer is not taken into account, ignition occurs at the tube axis, whereas it occurs near the wall if boundary layer is taken into account.

While DNS remains the most accurate approach, it carries very high cost in terms of required computational resources, particularly where resolution of shock waves is desirable. Ultra-fine grids are required to resolve the Kolmogorov scale which is inversely proportional to $Re^{3/4}$(Dimotakis, 2005). It is also well known that high-order numerical schemes designed for DNS (e.g. spectral or high-order finite-difference) are incapable of capturing shock containing flows due to Gibbs oscillations (Wen et al., 2009). Furthermore, it is impossible to fully resolve shocks with typical length scale of less than one micron in a macroscopic simulation. These considerations make a DNS approach impractical for the simulation involving modelling of shock interactions and complex geometries.

Accordingly, a number of researchers (Mosedale & Drikakis, 2007; Berglund & Fureby, 2007; Xu et al., 2007; Wen et al., 2009; Berglund et al., 2010) has turned to alternative approaches, such as Large Eddy Simulation (LES). In LES, the large scale motions of turbulent flow are solved directly, while the effect of the unresolved (subgrid) scales (SGS) is modelled. These works utilized Implicit LES (ILES) approach, which, as suggested by (Drikakis, 2003), can be more suitable than explicit LES for simulation of supersonic flows featuring shock waves. ILES is based on the hypothesis that the action of sub-grid scale (SGS) on the resolved scale is equivalent to a strictly dissipative action of a numerical scheme. Therefore, no explicit SGS model is required in the ILES approach. The Navier–Stokes equations are implicitly filtered by the discretization and the implicit dissipative truncation error from the numerical scheme for the convection terms is regarded as an adaptive numerical dissipation to model the unresolved small scales in the same manner as an explicit sub-grid scale model in LES. ILES is often utilized in cases where the flow dynamic mechanisms stretch the capability of numerical modelling because they are either unknown or too complicated to be modelled exactly and explicitly, such as shock/turbulence interaction (Lele, 1994).

In study by Xu et al., (2007) they developed spontaneous ignition model utilizing ILES approach to investigate spontaneous ignition of hydrogen. The simulations were performed by solving the unsteady Navier–Stokes equations of a chemically reactive multicomponent mixture of ideal gases using the KIVA-3V code (O'Rourke & Amsden, 1986). The equation system used in this model consists of a set of Navier-Stokes equations supplemented by equations of state. The closure terms necessary to complete equation system were formulated as follows:

$$\mu = \sum_{k=1}^{k} \frac{X_k \mu_k}{\sum_{j=1}^{k} X_j \Phi_{kj}}, \tag{2.16}$$

where μ_k is pure specie viscosity and X_j is molar fraction of specie *j* and

$$\Phi_{kj} = \frac{1}{\sqrt{8}} \left(1 + \frac{M_k}{M_j}\right)^{-1/2} \left(1 + \left(\frac{\mu_k}{\mu_j}\right)^{1/2} \left(\frac{M_j}{M_k}\right)^{1/4}\right)^2, \tag{2.17}$$

where M_k is the molecular weight of specie *k*.

Mixture thermal conductivity λ was expressed as

$$\lambda = \frac{1}{2}\left(\sum_{k=1}^{K} X_k \lambda_k + \frac{1}{\sum_{k=1}^{K} X_k / \lambda_k}\right), \tag{2.18}$$

where λ_k is pure species thermal conductivity, and mixture average diffusion coefficient D_{ma} as

$$D_{ma} = \frac{\sum_{j \neq k}^{K} (X_j + \varepsilon) M_j}{\overline{W} \sum_{j \neq k}^{K} (X_j + \varepsilon) D_{ij}}, \tag{2.19}$$

where $\varepsilon = 10^{-12}$ is a small number to prevent denominator to be zero for pure species, and D_{ij} is binary diffusion coefficient.

Thermal diffusion coefficient for specie *m* was determined by equation

$$D_m^T = \rho D_{ma} \Theta_m M_m / \overline{M}, \tag{2.20}$$

where Θ_m is a thermal diffusion ratio (Chapman & Cowling, 1970) and $\overline{M}$ is the average molecular weight of the mixture.

Pure species viscosity μ_k and binary diffusion coefficient D_{ij} are calculated according to the standard kinetic theory (Hirschfelder et al., 1964), and pure species thermal conductivity λ_k is computed according to Warnatz (1982).

Chemical source terms were defined as follows

$$\dot{\rho}_m^c = M_m \sum_r (b_{mr} - a_{mr}) \dot{\omega}_r, \tag{2.21}$$

$$\dot{Q}^c = \sum_r Q_r \dot{\omega}_r, \tag{2.22}$$

where a_{mr} and b_{mr} are integral stoichiometric coefficients for reaction *r*, Q_r is the negative of the heat of reaction at absolute zero

$$Q_r = \sum_m (a_{mr} - b_{mr})(\Delta h_f^0)_m \tag{2.23}$$

and $(\Delta h_f^0)_m$ is the heat of formation of specie *m* at absolute zero.

Chemical reaction rate $\dot{\omega}_r$ was defined as

$$\dot{\omega}_r = k_{fr} \prod_m (\rho_m / M_m)^{a_{mr}} - k_{br} \prod_m (\rho_m / M_m)^{b_{mr}} , \tag{2.24}$$

where the coefficient k_{fr} was assumed to be of an Arrhenius form

$$k_{fr} = A_{fr} T^{\varsigma_{fr}} e^{-E_{fr}/RT} \tag{2.25}$$

$$k_{br} = k_{fr} / K_{cr} . \tag{2.26}$$

K_{cr} is the equilibrium constant which can be calculated by thermodynamic data (Kee et al., 2000).

The numerical implementation was based on an arbitrary Lagrangian and Eulerian (ALE) method (Hirt et al., 1974) in which convective terms are solved separately from the other terms. Each time cycle is divided into two phases: a Lagrangian phase and a rezone phase. Considering the substantial scale difference between diffusion and advection, different numerical schemes were adopted in the two phases. In the Lagrangian phase, a second-order Crank-Nicolson scheme is used for the diffusion terms and the terms associated with pressure wave propagation, a two-stage, second-order MacCormack method (MacCormack, 2003) is used in the rezone phase to solve the convective terms. The coupled semi-implicit equations in the Lagrangian phase are solved by a SIMPLE type algorithm with individual equations solved by a conjugate residual method (O'Rourke & Amsden, 1986). For spatial differencing, a second-order total variation diminishing (TVD) scheme (Amsden et al., 1989) was used for the convection terms and the second-order central differencing scheme was used for all the other terms.

A mixture-averaged multi-component approach (Kee et al., 2000) had been used for the calculation of molecular transport with consideration of thermal diffusion which is important for non-premixed hydrogen combustion. Instead of using one of the existing subgrid combustion models, which could be inappropriate for self-ignition modelling due to the strong shock/combustion interactions, the model employs fine grid resolution to directly resolve the thin flame. This approach requires adoption of 15 – 30 μm grid resolution across the contact region. Although the diffusion flame is directly resolved, such ''direct" approach can still be classified as LES as the flow field is not fully resolved (Norris & Edwards, 1997).

For autoignition, detailed chemistry scheme by (Saxena & Williams, 2006) involving eight reactive species and 21 elementary steps had been used. To deal with the stiffness problem of the chemistry, the chemical kinetic equations were solved by a variable-coefficient ODE solver (Brown et al., 1989).

This model was subsequently improved by replacing a second-order TVD scheme for spatial differencing with high order WENO scheme (Xu et al., 2008; Xu, Wen, et al., 2009). It was

found that the second-order TVD schemes are overly dissipative to capture the mixing process and higher order weighted essentially non-oscillatory (WENO) shock-capturing schemes can better resolve the underlying physical process with the same grid resolution (Mosedale & Drikakis, 2007). Since the ILES approach used numerical dissipation to model the unresolved small scales, the accuracy order of the numerical schemes applied to the convection terms is essential. Several high order WENO schemes had been investigated (Xu et al., 2008). It had been shown that 9^{th}-order scheme results in numerical oscillations leading to unphysical results on the contact surface. Accordingly, subsequent works (Xu, Wen, et al., 2009; Wen et al., 2009) used 5^{th}-order upwind WENO scheme (Balsara & Shu, 2000) for the convection terms. Furthermore, second order MacCormack method used in the rezone phase to solve the convection terms was replaced with a 3^{rd}-order TVD Runge–Kutta method (Balsara & Shu, 2000). This updated model had been used in a number of follow up works aimed at investigation of the effects of the obstacles and non-instantaneous membrane opening (Xu & Wen, 2011, 2014; Xu et al., 2011).

2.2.4 University of Ulster 3-D LES model (UU)

In spite of a measure of success achieved by 2-D models, capture of correct physics of the turbulent mixing requires implementation of the fully 3-D model. Furthermore, utilization of 3-D models is required in order to be able to perform simulations and reproduction of experimental results obtained in a complex realistic geometries, where 2-D simulations cannot be applied. Such a 3-D model, using large eddy simulation (LES) approach had been developed at University of Ulster in order to model the dynamics of spontaneous ignition in the complex realistic geometries. The unavoidable consequence of extending the model into 3^{rd} dimension is a coarser grid. This increase in mesh size is “compensated” by an advanced sub-grid scale (SGS) modelling of the combustion by the eddy dissipation concept with a detailed chemistry and the turbulence by the renormalization group (RNG) theory. The University of Ulster model had originally been applied to simulate dynamics of spontaneous ignition of hydrogen emerging into air within simple geometries (Bragin & Molkov, 2009). It had been subsequently modified to investigate transitional phenomena on the lower pressure limit of spontaneous ignition and assess the model’s predictive capability against experimental data obtained in a 3-D geometry of the T-shaped channel (see Figure 2.12) at different pressures, which is a mock-up of a pressure relief device (PRD) (Bragin et al., 2013).

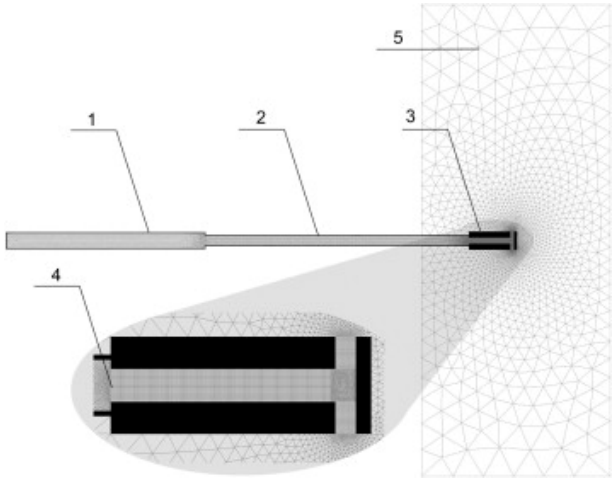

Figure 2.12 The geometry of T-shaped pressure relief device (PRD) simulated in (Bragin et al., 2013) and associated computational domain: 1 and 2 – high-pressure tubes, 3 – PRD, 4 – burst disk, and 5 – external domain.

Conservation equations

The governing equations, employed for LES, are filtered over the control volume three-dimensional instantaneous conservation equations for mass, momentum (Navier-Stokes), energy, and species for compressible Newtonian fluid

$$\frac{\partial \overline{\rho}}{\partial t}+\frac{\partial}{\partial x_j}\left(\overline{\rho}\tilde{u}_j\right)=0, \tag{2.27}$$

$$\frac{\partial \overline{\rho}\tilde{u}_i}{\partial t}+\frac{\partial}{\partial x_j}\left(\overline{\rho}\tilde{u}_i\tilde{u}_j\right)=-\frac{\partial \overline{p}}{\partial x_i}+\frac{\partial}{\partial x_j}\left(\mu_{eff}\left(\frac{\partial \tilde{u}_i}{\partial x_j}+\frac{\partial \tilde{u}_j}{\partial x_i}-\frac{2}{3}\frac{\partial \tilde{u}_k}{\partial x_k}\delta_{ij}\right)\right)+\overline{\rho}g_i, \tag{2.28}$$

$$\frac{\partial}{\partial t}\left(\overline{\rho}\tilde{E}\right)+\frac{\partial}{\partial x_j}\left(\tilde{u}_j\left(\overline{\rho}\tilde{E}+\overline{p}\right)\right)=$$
$$=\frac{\partial}{\partial x_j}\left(\frac{\mu_{eff}c_p}{Pr_{eff}}\frac{\partial \tilde{T}}{\partial x_j}-\sum_m \tilde{h}_m\left(-\frac{\mu_{eff}}{Sc_{eff}}\frac{\partial \tilde{Y}_m}{\partial x_j}\right)+\tilde{u}_i\,\mu_{eff}\left(\frac{\partial \tilde{u}_i}{\partial x_j}+\frac{\partial \tilde{u}_j}{\partial x_i}-\frac{2}{3}\frac{\partial \tilde{u}_k}{\partial x_k}\delta_{ij}\right)\right)+\sum_m R_m H_C, \tag{2.29}$$

$$\frac{\partial}{\partial t}\left(\overline{\rho}\tilde{Y}_m\right)+\frac{\partial}{\partial x_j}\left(\overline{\rho}\tilde{u}_j\tilde{Y}_m\right)=\frac{\partial}{\partial x_j}\left(\frac{\mu_{eff}}{Sc_{eff}}\frac{\partial \tilde{Y}_m}{\partial x_j}\right)+R_m. \tag{2.30}$$

The effective viscosity μ_{eff} is calculated using the renormalization group (RNG) theory (Yakhot & Orszag, 1986). The RNG model is capable to reproduce not only turbulent, but also transitional and laminar flows. At low Reynolds numbers the effective viscosity becomes equal to molecular viscosity. This allows the model to perform better in the vicinity of walls (Shah et al., 2001). The effective viscosity is calculated in RNG model as

$$\mu_{eff}=\mu\left[1+H\left(\mu_s^2\,\mu_{eff}/\mu^3-100\right)\right]^{1/3}, \tag{2.31}$$

where $\mu_s = \overline{\rho}\left(C_{RNG} V_{CV}^{1/3}\right)^2 \sqrt{2\widetilde{S}_{ij}\widetilde{S}_{ij}}$, V_{CV} is the volume of control volume, C_{RNG} is constant and $H(x)$ is Heaviside function.

In highly turbulent regions of the flow $\mu_{eff} \approx \mu_s$ and the RNG model reduces to the Smagorinsky model. In laminar flow regions the argument of Heaviside function becomes negative and the model recovers molecular viscosity, $\mu_{eff} = \mu$. The effective Prandtl and Schmidt numbers are calculated following the RNG theory by purely theoretical equations (Yakhot & Orszag, 1986):

$$\left|\frac{1/N_{eff} - 1.3929}{1/N - 1.3929}\right|^{0.6321} \left|\frac{1/N_{eff} + 2.3929}{1/N + 2.3929}\right|^{0.3679} = \frac{\mu}{\mu_{eff}}, \tag{2.32}$$

where N stands for laminar Prandtl or Schmidt numbers. Laminar Prandtl and Schmidt numbers are calculated according to kinetic theory.

Combustion model

The Eddy Dissipation Concept (EDC) model (Magnussen, 1981) with updates that incorporates detailed Arrhenius chemical kinetics in turbulent flames was applied as the combustion sub-model. EDC gives an expression for a combustion rate based on an assumption that chemical reactions occur in so-called fine structures of Kolmogorov's scale where the dissipation of turbulence energy takes place. In a flow of moderate to intense turbulence these fine structures are concentrated in isolated areas occupying only a small fraction of the flow. The characteristic size of the fine structures is much smaller than a LES filter width (cell size in the described case), and it needs to be computed as a function of flow parameters and a cell size.

In the EDC model adopted in FLUENT a source term in the species transport Eq. (2.30) is modelled as

$$R_m = \frac{\rho\left(\xi^*\right)^2}{\tau^*\left[1-\left(\xi^*\right)^3\right]}\left(Y_m^* - Y_m\right), \tag{2.33}$$

where R_m is a net rate of production of specie m by chemical reactions, ξ^* is the length fraction of the fine scale turbulent structures where the reaction occurs, Y_m^* is the fine scale species mass fraction (specie m) after reacting over the time τ^*, Y_m is a species mass fraction for specie m in the surrounding fine scales state. The multiplier in Eq. (2.33) with a square of the length fraction of fine scales represents the mass exchange between the surrounding and fine structure regions. The length fraction of fine structures is evaluated in this LES model similar to EDC RANS model as

$$\xi^* = C_\xi u_\eta / u_{SGS}, \tag{2.34}$$

where the volume fraction constant is taken as C_ξ = 2.1377 similar to RANS. The upper limit ξ^* = 1 is applied when the fine scales velocity is larger than residual SGS velocity.

The scale of a LES residual velocity at the sub-grid scale (SGS) level is

$$u_{SGS} = \mu_t / (\rho \cdot L_{SGS}), \tag{2.35}$$

where μ_t is turbulent viscosity, and the SGS length scale is determined as

$$L_{SGS} = C_{RNG} V^{1/3} \ . \tag{2.36}$$

The Kolmogorov's velocity u_η is

$$u_\eta = \left(\frac{\mu \cdot u_{SGS}^3}{\rho \cdot L_{SGS}} \right)^{1/4}, \tag{2.37}$$

where μ is laminar viscosity.

Characteristic sub-grid eddy and Kolmogorov's timescales are respectively

$$\tau_{SGS} = L_{SGS} / u_{SGS} \text{, and} \tag{2.38}$$

$$\tau_\eta = \left(\frac{\mu \cdot L_{SGS}}{\rho \cdot u_{SGS}^3} \right)^{1/2} \ . \tag{2.39}$$

The volume fraction of the fine scales is calculated as ξ^{*3} and species are assumed to react in the fine structures over a time scale

$$\tau^* = C_\tau \tau_\eta \text{,} \tag{2.40}$$

where a time scale constant is taken equal to C_τ = 0.4082 similar to applied in the EDC RANS model.

Magnussen (1989) assumes that all the fine scales in the cell are perfectly stirred reactors with a residence time τ^*. Combustion at the fine scales is assumed in this model to take place as a constant-pressure reactor. The reactor type is determined by the choice of a mixing rate $1/\tau^*$ and a time-step Δt. In FLUENT initial conditions at the constant pressure reactor are taken as the current species and temperature in the cell. Arrhenius reactions governed by Eq. (2.41) proceed over the time scale τ^*. The *in situ* adaptive tabulation ISAT algorithm (Pope, 1997), offering substantial reductions in run-times by up to three orders of magnitude, is applied.

All of the reactions considered in the chemical mechanism involved are elementary (reversible). For reversible reaction the molar rate of creation or destruction of species *i* in reaction *r* is given by Eq. (2.41)

$$\hat{R}_{m,R} = \Gamma \left(\nu''_{m,r} - \nu'_{m,r} \right) \left(k_{f,r} \prod_{n=1}^{N} \left[C_{n,r} \right]^{\nu'_{m,r}} - k_{b,r} \prod_{n=1}^{N} \left[C_{n,r} \right]^{\nu''_{m,r}} \right), \tag{2.41}$$

where N is number of chemical species in the system; $\nu'_{m,r}$ is stoichiometric coefficient for reactant m in reaction r; $\nu''_{m,r}$ is stoichiometric coefficient for product m in reaction r; $k_{f,r}$ is forward rate constant for reaction r; $k_{b,r}$ is backward rate constant for reaction r. Γ represents the net effect of third bodies on the reaction rate and is given by

$$\Gamma = \sum_{n=1}^{N} \gamma_{n,r} C_n \text{,} \tag{2.42}$$

where $\gamma_{m,r}$ is the third-body efficiency of *m*-th species in the *r*-th reaction.

The forward rate constant for reaction *r* without pressure dependency is computed in conventional form of Arrhenius equation

$$k_{f,r} = AT^{\beta_r} \exp\left(-E_r / RT\right). \tag{2.43}$$

All reactions are reversible, the backward rate constant for reaction *r* is calculated from the forward rate Eq. (2.43) and the equilibrium constant K_r using the equation

$$k_{b,r} = k_{f,r} / K_r \,. \tag{2.44}$$

The equilibrium constant K_r computed as

$$K_r = \exp\left(\frac{\Delta S_r^0}{R} - \frac{\Delta H_r^0}{RT}\right) \cdot \left(\frac{P_{atm}}{RT}\right)^{\sum_{i=1}^{N}\left(\nu''_{m,r} - \nu'_{m,r}\right)}, \tag{2.45}$$

where P_{atm} denotes atmospheric pressure (101,325 kPa). The term within the exponential function represents the change in Gibbs free energy and its components are computed as

$$\frac{\Delta S_r^0}{R} = \sum_{i=1}^{N}\left(\nu''_{m,r} - \nu'_{m,r}\right)\frac{S_m^0}{R}, \tag{2.46}$$

$$\frac{\Delta H_r^0}{RT} = \sum_{i=1}^{N}\left(\nu''_{m,r} - \nu'_{m,r}\right)\frac{h_m^0}{RT}, \tag{2.47}$$

where S_m^0 and h_m^0 are entropy and enthalpy respectively of the *m*-th species respectively evaluated at temperature *T* and atmospheric pressure.

Specific heats of mixtures were approximated as piecewise-polynomial functions of temperature with polynomial coefficients calculated according to mass-weighted mixing law.

Chemical reaction mechanism

In this study the detailed 21-step chemical reaction mechanism of hydrogen combustion in air employing 37 elementary reactions is applied (Gutheil et al., 1993). The effect of nitrogen chemistry is taken into account by considering detailed mechanism of NO formation. The specific reaction rate constants are given in Table 2.6. The forward reaction rate constants are presented in the table, and backward rates for reversible reactions are calculated through the equilibrium constants Eq. (2.44).

Table 2.6 Specific reaction rate constants (Gutheil et al., 1993).

No.	Reactions	*A*, KJ/mol	β_r,	E_r, mol/m^3
1	H+O2=OH+O	2.00E+14	0.00	70.30
2	H2+O=OH+H	1.80E+10	1.00	36.93
3	H2O+O=OH+OH	5.90E+09	1.30	71.25
4	H2+OH=H2O+H	1.17E+09	1.30	15.17
5	H+O2+M=HO2+M	2.30E+18	-0.8	0.00
	Third-body chaperon efficiencies H2/1./ H2O/6.5/ O2/0.4/ N2/0.4/			
6	H+HO2=OH+OH	1.50E+14	0.00	4.20

7	H+HO2=H2+O2	2.50E+13	0.00	2.93
8	OH+HO2=H2O+O2	2.00E+13	0.00	4.18
9	H+H+M=H2+M	1.80E+18	-1.00	0.00
	Third-body chaperon efficiencies H2/1./ H2O/6.5/ O2/0.4/ N2/0.4/			
10	H+OH+M=H2O+M	2.20E+22	-2.00	0.00
	Third-body chaperon efficiencies H2/1./ H2O/6.5/ O2/0.4/ N2/0.4/			
11	HO2+HO2=H2O2+O2	2.00E+12	0.00	0.00
12	H2O2+M=OH+OH+M	1.30E+17	0.00	190.38
13	H2O2+OH=H2O+HO2	1.E+13	0.00	7.53
14	O+HO2=OH+O2	2.E+13	0.00	0.00
15	H+HO2=O+H2O	5.E+12	0.00	5.90
16	H+O+M=OH+M	6.2E+16	-0.60	0.00
	Third-body chaperon efficiencies H2O:5, others 1			
17	O+O+M=O2+M	6.17E+15	-0.50	0.00
18	H2O2+H=H2O+OH	1.E+13	0.00	15.02
19	H2O2+H=HO2+H2	4.79E+13	0.00	33.26
20	O+OH+M=HO2+M	1.E+16	0.00	0.00
21	H2+O2=OH+OH	1.7E+13	0.00	200.0
	Nitrogen Chemistry			
22	O+N2=N+NO	1.82E+14	0.00	319.02
23	O+NO=N+O2	3.8E+09	1.00	173.11
24	H+NO=N+OH	2.63E+14	0.00	210.94
25	NO+M=N+O+M	3.98E+20	-1.50	627.65
26	N2+M=N+N+M	3.72E+21	-1.60	941.19
27	N2O+O=NO+NO	6.92E+13	0.00	111.41
28	N2O+O=N2+O2	1.E+14	0.00	117.23
29	N2O+N=N2+NO	1.E+13	0.00	83.14
30	N+HO2=NO+OH	1.E+13	0.00	8.31
31	N2O+H=N2+OH	7.6E+13	0.00	63.19
32	HNO+O=NO+OH	5.01E+11	0.50	8.31
33	HNO+OH=NO+H2O	1.26E+12	0.50	8.31
34	NO+HO2=HNO+O2	2.E+11	0.00	8.31
35	HNO+HO2=NO+H2O2	3.16E+11	0.50	8.31
36	HNO+H=NO+H2	1.26E+13	0.00	16.63
37	HNO+M=H+NO+M	1.78E+16	0.00	203.7

The FLUENT software is used as the computational engine. The solver used explicit linearization of the governing equations with explicit method for solution of linear equation set. A second-order upwind scheme with AUSM flux splitting was applied for flow discretization. The four step Runge–Kutta algorithm was employed for advancement of simulations in time. The time-step was determined from Courant–Friedrichs–Lewy condition, where the CFL number was equal to 0.2 to ensure stability.

2.3 References

Ackroyd, G.. & Newton, S.. (2003) An Investigation of the Electrostatic Ignition Risks Associated with a Plastic Coated Metal, *Journal of Electrostatics* 59 (2): 143–151

Ahmed, S. & Mastorakos, E. (2005) Measurements of the Probability of Ignition and Subsequent Flame Propagation Speed in Turbulent Non-Premixed Jets, *In*: *Proc. 20th ICDERS*,

Amsden, A.A., O'Rourke, P.J. & Butler, T.D. (1989) *KIVA-2: A Computer Program for Chemically Reactive Flows with Sprays*, Los Alamos National Laboratory

Anderson, J.D. (1995) *Computational Fluid Dynamics: The Basics with Applications*, New York: McGraw-Hill

Anon (1922) Spontaneous Ignition of Hydrogen, *Engineering* (113): 502

Astbury, G.R. & Hawksworth, S.J. (2005) Spontaneous Ignition of Hydrogen Leaks: A Review of Postulated Mechanisms,

Averill, A.F., Ingram, J.M., Battersby, P., Holborn, P.G. & Nolan, P.F. (2014) Ignition of Hydrogen/air Mixtures by Glancing Mechanical Impact, *International Journal of Hydrogen Energy* 39 (35): 20404–20410

Baker, J., Calvert, M.E. & Murphy, D.W. (2002) Structure and Dynamics of Laminar Jet Micro-Slot Diffusion Flames, *Journal of Heat Transfer* 124 (4): 783

Balsara, D.S. & Shu, C.-W. (2000) Monotonicity Preserving Weighted Essentially Non-Oscillatory Schemes with Increasingly High Order of Accuracy, *Journal of Computational Physics* 160 (2): 405–452

Ban, H., Venkatesh, S. & Saito, K. (1994) Convection-Diffusion Controlled Laminar Micro Flames, *Journal of Heat Transfer* 116 (4): 954

Bazhenova, T.V., Bragin, M.V., Golub, V.V. & Ivanov, M.F. (2006) Self-Ignition of a Fuel Gas upon Pulsed Efflux into an Oxidative Medium, *Technical Physics Letters* 32 (3): 3

Berglund, M., Fedina, E., Fureby, C., Tegnér, J. & Sabel'nikov, V. (2010) Finite Rate Chemistry Large-Eddy Simulation of Self-Ignition in Supersonic Combustion Ramjet, *AIAA Journal* 48 (3): 540–550

Berglund, M. & Fureby, C. (2007) LES of Supersonic Combustion in a Scramjet Engine Model, *Proceedings of the Combustion Institute* 31 (2): 2497–2504

Bernend, E. & Ritter, K. (Eds.) (2000) Mechanically Produced Sparks, *In*: *Section 2.4 of the Handbook of Explosion Protection, Steen, H. (Ed.) [HSE translation No 2000/20]*, Weinheim, Germany: Wiley-VCH,

Birch, A.D., Brown, D.R. & Dodson, M.G. (1981) Ignition Probabilities in Turbulent Mixing Flows, *Symposium (International) on Combustion* 18 (1): 1775–1780

Birch, A.D., Brown, D.R., Dodson, M.G. & Thomas, J.R. (1979) Studies of Flammability in Turbulent Flows Using Laser Raman Spectroscopy, *Symposium (International) on Combustion* 17 (1): 307–314

Blazek, J. (2001) *Computational Fluid Dynamics: Principles and Applications*, Amsterdam ; New York: Elsevier

BOMEL, L. (2002) *Materials Other than Steel and Concrete*, Sudbury: OFFSHORE TECHNOLOGY REPORT 2001/017 Available from: <http://www.hse.gov.uk/research/otopdf/2001/oto01017.pdf> [Accessed:

Bragin, M. & Molkov, V. (2009) Physics of Spontaneous Ignition of High-Pressure Hydrogen Release and Transition to Jet Fire, *In*: *Proceedings of Third International Conference on Hydrogen Safety*, Ajaccio, France,

Bragin, M.V., Makarov, D.V. & Molkov, V.V. (2013) Pressure Limit of Hydrogen Spontaneous Ignition in a T-Shaped Channel, *International Journal of Hydrogen Energy* 38: 8039–8052

Brearley, D. & Tolson, P. (1995) *The Frictional Ignition Properties of (18/8) Stainless Steel, HSL Internal Report, IR/L/IC/95/02.*,

Britton, L.G. (1999) *Avoiding Static Ignition Hazards in Chemical Operations*, New York: Center for Chemical Process Safety of the American Institute of Chemical Engineers

Brown, P.N., Byrne, G.D. & Hindmarsh, A.C. (1989) VODE: A Variable-Coefficient ODE Solver, *SIAM Journal on Scientific and Statistical Computing* 10 (5): 1038–1051

BS EN 1127-1:2011 Explosive Atmospheres. Explosion Prevention and Protection. Basic Concepts and Methodology, Available from: <http://shop.bsigroup.com/ProductDetail/?pid=000000000030198044> [Accessed: 2 September 2015]

BS EN 60079-11:2012 Explosive Atmospheres. Equipment Protection by Intrinsic Safety 'I', Available from: <http://shop.bsigroup.com/ProductDetail/?pid=000000000030314832> [Accessed:

Buckel, J. & Chandra, S. (1996) Hot Wire Ignition of Hydrogen-Oxygen Mixtures, *International Journal of Hydrogen Energy* 21 (1): 39–44

Buckmaster, J., Clavin, P., Liñán, A., Matalon, M., Peters, N., Sivashinsky, G., *et al.* (2005) Combustion Theory and Modeling, *Proceedings of the Combustion Institute* 30 (1): 1–19

Bull, D.C. (1979) Concentration Limits to the Initiation of Unconfined Detonation in Fuel/air Mixtures, *In*: *Transactions of the IChem, 57*, pp.219–227

Bull, D.C., Elsworth, J.E. & Hooper, G. (1978) Initiation of Spherical Detonation in Hydrocarbon/air Mixtures, *Acta Astronautica* 5 (11-12): 997–1008

Butler, M.S., Moran, C.W., Sunderland, P.B. & Axelbaum, R.L. (2009) Limits of Hydrogen Leaks That Can Support Stable Flames, *International Journal of Hydrogen Energy* 34: 5174–5182

Calcote, H.F., Gregory, C.A., Barnett, C.M. & Gilmer, R.B. (1952) Spark Ignition. Effect of Molecular Structure., *Industrial & Engineering Chemistry* 44 (11): 2656–2662

Carleton, F.B., Bothe, H., Proust, C. & Hawksworth, S. (Eds.) (2000) *Prenormative Research on the Use of Optics in Potentially Explosive Atmospheres, PROPEX: Final Report*, Luxembourg: Off. for Off. Publ. of the Europ. Communities

CENELEC (2003) *Electrostatics. Code of Practice for the Avoidance of Hazards due to Static Electricity, CEN-CENELEC Report No. CLC/TR 50404:2003*, Brussels, Belgium

Chapman, S. & Cowling, T.G. (1970) *The Mathematical Theory of Non-Uniform Gases: An Account of the Kinetic Theory of Viscosity, Thermal Conduction, and Diffusion in Gases*, Cambridge ; New York: Cambridge University Press

Cheng, T.S., Chao, Y.-C., Wu, C.-Y., Li, Y.-H., Nakamura, Y., Lee, K.-Y., *et al.* (2005) Experimental and Numerical Investigation of Microscale Hydrogen Diffusion Flames, *Proceedings of the Combustion Institute* 30 (2): 2489–2497

Cheng, T.S., Chen, C.-P., Chen, C.-S., Li, Y.-H., Wu, C.-Y. & Chao, Y.-C. (2006) Characteristics of Microjet Methane Diffusion Flames, *Combustion Theory and Modelling* 10 (5): 861–881

Cheng, T.S., Wehrmeyer, J.A. & Pitz, R.W. (1992) Simultaneous Temperature and Multispecies Measurement in a Lifted Hydrogen Diffusion Flame, *Combustion and Flame* 91 (3-4): 323–345

Cho, P. & Law, C.K. (1986) Catalytic Ignition of Fuel/oxygen/nitrogen Mixtures over Platinum, *Combustion and Flame* 66 (2): 159–170

Coffee, T.P. & Heimerl, J.M. (1983) Sensitivity Analysis for Premixed, Laminar, Steady State Flames, *Combustion and Flame* 50: 323–340

Cohen, S.D., Hindmarsh, A.C. & Dubois, P.F. (1996) CVODE, A Stiff/Nonstiff ODE Solver in C, *Computers in Physics* 10 (2): 138–143

Cross, J. (1987) *Electrostatics: Principles, Problems and Applications*, Bristol: Hilger

Del Alamo, G., Williams, F.A. & Sanchez, A.L. (2004) Hydrogen-Oxygen Induction Times above Crossover Temperatures, *Combustion Science and Technology* 176 (10): 28

Dimotakis, P.E. (2005) TURBULENT MIXING, *Annual Review of Fluid Mechanics* 37 (1): 329–356

Dixon-Lewis, G. (1968) Flame Structure and Flame Reaction Kinetics. II. Transport Phenomena in Multicomponent Systems, *Proceedings of the Royal Society A: Mathematical, Physical and Engineering Sciences* 307 (1488): 111–135

Drikakis, D. (2003) Advances in Turbulent Flow Computations Using High-Resolution Methods, *Progress in Aerospace Sciences* 39 (6-7): 405–424

Dryer, F.L., Chaos, M., Zhao, Z., Stein, J.N., Alpert, J.Y. & Homer, C.J. (2007) Spontaneous Ignition of Pressurized Releases of Hydrogen and Natural Gas into Air, *Combustion Science and Technology* 179: 663–694

Gant, S.E., Pursell, M.R., Lea, C.J., Thyer, A.M. & Connolly, S. (2011) Flammability of hydrocarbon/CO2 Mixtures: Part 2. Predictive Models for Gas Jet Ignition, *In*: *Proc. IChemE Hazards XXII Conference, Liverpool, UK*, pp.11–14 Available from: <http://s177835660.websitehome.co.uk/research/gant_etal_2011_hazards_flammability_part2.pdf> [Accessed: 3 September 2015]

Ge, X. & Sutton, W.H. (2006) Analysis and Test of Compressed Hydrogen Interface Leakage by Commercial Stainless Steel (NPT) Fittings Available from: <http://papers.sae.org/2006-01-0130/> [Accessed: 11 September 2015]

Gibson, N. & Harper, D.J. (1988) Parameters for Assessing Electrostatic Risk from Non-Conductors - a Discussion, *Journal of Electrostatics* 21 (1): 27–36

Gibson, N., Lloyd, F.C. & Perry, G.R. (1968) Fire Hazards in Chemical Plant from Friction Sparks Involving the Thermite Reaction, *In*: *Chem. E. Symposium Series*, Available from: <http://www.oneportlandplace.co.uk/icheme_home/communities/subject_groups/safety%20and%20loss%20prevention/resources/hazards%20archive/~/media/Documents/Subject%20Groups/Safety_Loss_Prevention/Hazards%20Archive/III/III-Paper-04.pdf> [Accessed: 2 September 2015]

Glor, M. (Ed.) (1996) *Quoted by Lees, F.P Loss Prevention in the Process Industries*, Oxford: Elsevier Butterworth-Heinemann

Golub, V.V., Baklanov, D.I., Golovastov, S.V., Ivanov, M.F., Laskin, I.N., Saveliev, A.S., *et al.* (2008) Mechanisms of High-Pressure Hydrogen Gas Self-Ignition in Tubes, *Journal of Loss Prevention in the Process Industries* 21 (2): 185–198

Golub, V.V., Bazhenova, T.V., Bragin, M.V., Ivanov, M.F. & Volodin, V.V. (2006) Hydrogen Auto-Ignition During Accidental or Technical Opening of High Pressure Tank, *In*: *Proceedings of the 6th International Symposium on Hazards, Prevention and Mitigation of Industrial Explosions*, [Accessed: 3 September 2015]

Golub, V.V., Volodin, V.V., Baklanov, D.I., Golovastov, S.V. & Lenkevich, D.A. (2010) Experimental Investigation of Hydrogen Ignition at the Discharge into Channel Filled with Air, *In*: *Physics of Extreme States of Matter*, Chernogolovka, pp.110–113

Goodwin, D.G. (2009) Cantera - An Object-Oriented Software Toolkit for Chemical Kinetics, Thermodynamics, and Transport Processes. - Google Project Hosting, Available from: <https://code.google.com/p/cantera/> [Accessed: 4 September 2015]

Grune, J., Sempert, K., Kuznetsov, M. & Jordan, T. (2011) Experimental Study of Ignited Unsteady Hydrogen Jets into Air, *In*: *International Conference on Hydrogen Safety*, San Francisco, Available from: <http://linkinghub.elsevier.com/retrieve/pii/S0360319910008542> [Accessed: 25 March 2014]

Grune, J., Sempert, K., Kuznetsov, M. & Jordan, T. (2014) Experimental Study of Ignited Unsteady Hydrogen Releases from a High Pressure Reservoir, *International Journal of Hydrogen Energy* 39 (11): 6176–6183

Gutheil, E., Balakrishnan, G. & Williams, F.A. (1993) Structure and Extinction of Hydrogen-Air Diffusion Flames, *In*: Peters, N. & Rogg, B. eds. *Reduced kinetic mechanisms for applications in combustion systems*, *Lecture notes in physics*, New York: Springer-Verlag, pp.177–195

Hairer, E. & Wanner, G. (1996) *Solving Ordinary Differential Equations II*, Berlin, Heidelberg: Springer Berlin Heidelberg Available from: <http://link.springer.com/10.1007/978-3-642-05221-7> [Accessed: 4 September 2015]

Hall, J.E., Hooker, P. & Willoughby, D. (2014) Ignited Releases of Liquid Hydrogen: Safety Considerations of Thermal and Overpressure Effects, *International Journal of Hydrogen Energy* 39 (35): 20547–20553

Hankinson, G., Mathurkar, H. & Lowesmith, B. (2009) IGNITION ENERGY AND IGNITION PROBABILITY OF METHANE-HYDROGEN –AIR MIXTURES, *In*: *3rd International conference on hydrogen safety*, Palais de Congress, Ajaccio, France,

Hawksworth, S., Rogers, R., Beyer, M., Proust, C., Lakic, D., Gummer, J., *et al.* (2005) MECHEX - Criteria for Assessing the Likelihood of Ignition by Mechanical Sources,

Hawksworth, S., Rogers, R., Proust, C., Beyer, M. & Schenk, S. (2004) Mechanical Ignition Hazards in Potentially Explosive Atmospheres - EC Project MECHEX,

Hindmarsh, A.C., Brown, P.N., Grant, K.E., Lee, S.L., Serban, R., Shumaker, D.E., *et al.* (2005) SUNDIALS: Suite of Nonlinear and Differential/algebraic Equation Solvers, *ACM Transactions on Mathematical Software* 31 (3): 363–396

Hirschfelder, J.O., Curtiss, C.F. & Bird, R.B. (1964) *Molecular Theory of Gases and Liquids*, New York,NY: Wiley

Hirt, C.., Amsden, A.. & Cook, J.. (1974) An Arbitrary Lagrangian-Eulerian Computing Method for All Flow Speeds, *Journal of Computational Physics* 14 (3): 227–253

Hooker, P., Royle, M., Gummer, J., Willoughby, D. & Udensi, J. (2011) Self Ignition of Hydrogen by Various Mechanisms*Symposium Series No.156*, Liverpool,

Hooker, W.J. (1961) Testing Time and Contact-Zone Phenomena in Shock-Tube Flows, *Physics of Fluids* 4 (12): 1451

IEC/TS 60079-32-1:2013 Explosive Atmospheres – Part 32 - 1: Electrostatic Hazards, Guidance,

Kalghatgi, G.T. (1981) Blow-out Stability of Gaseous Jet Diffusion Flames. Part I: In Still Air, *Combustion Science and Technology* 26 (5): 233–239

Karasalo, I. & Kurylo, J. (1981) On Solving the Stiff ODE's of the Kinetics of Chemically Reacting Gas Flow, *Journal of Computational Physics* 40 (1): 167–182

Kee, R., Rupley, F., Miller, J., Coltrin, M., Grcar, J., Meeks, E., *et al.* (2000) CHEMKIN Collection, Release 3.6, Reaction Design, *Inc., San Diego, CA*

Laurendeau, N.M. (1982) Thermal Ignition of Methane □air Mixtures by *Combustion and Flame* 46: 29–49

Lecoustre, V.R., Sunderland, P.B., Chao, B.H. & Axelbaum, R.L. (2010) Extremely Weak Hydrogen Flames, *Combustion and Flame* 157 (11): 2209–2210

Lecoustre, V.R., Sunderland, P.B., Chao, B.H. & Axelbaum, R.L. (2013) Modeled Quenching Limits of Spherical Hydrogen Diffusion Flames, *Proceedings of the Combustion Institute* 34 (1): 887–894

Lee, B.J. & Jeung, I.-S. (2009) Numerical Study of Spontaneous Ignition of Pressurized Hydrogen Release by the Failure of a Rupture Disk into a Tube, *International Journal of Hydrogen Energy* 34: 8763–8769

Lele, S.K. (1994) Compressibility Effects on Turbulence, *Annual Review of Fluid Mechanics* 26 (1): 211–254

LeVeque, R.J. (2007) *Finite Volume Methods for Hyperbolic Problems*, Cambridge: Cambridge Univ. Press

Levine, M.A. (1970) Turbulent Mixing at the Contact Surface in a Driven Shock Wave, *Physics of Fluids* 13 (5): 1166

Lewis, B. & Elbe, G. von (1987) *Combustion, Flames and Explosions of Gases*, New York: Academic Press Inc.

Li, J., Zhao, Z., Kazakov, A. & Dryer, F.L. (2004) An Updated Comprehensive Kinetic Model of Hydrogen Combustion, *International Journal of Chemical Kinetics* 36 (10): 566–575

Liu, Y.-F., Tsuboi, N., Sato, H., Higashino, F., Hayashi, A.K. & Gakuin, A. (2005) Direct Numerical Simulation of Hydrogen Fuel Jetting from High Pressure Tank, *In*: *20th International Colloquium on the Dynamics of Explosions and Reacting Systems*,

MacCormack, R. (2003) The Effect of Viscosity in Hypervelocity Impact Cratering, *Journal of Spacecraft and Rockets* 40 (5): 757–763

Magnussen, B. (1981) On the Structure of Turbulence and a Generalized Eddy Dissipation Concept for Chemical Reaction in Turbulent Flow, *In*: *American Institute of Aeronautics and Astronautics*, Available from: <http://arc.aiaa.org/doi/abs/10.2514/6.1981-42> [Accessed: 11 February 2014]

Magnussen, B.F. (1989) Modelling of Pollutant Formation in Gas Turbine Combustors Based on the Eddy Dissipation Concept, *In*: *Proceedings of the CIMAC Conference*, Tianjin, China,

Maly, R. & Vogel, M. (1979) Initiation and Propagation of the Flame Fronts in Lean CH-Air Mixtures by Three Modes of the Ignition Spark, *In*: *Proceedings of the Combustion Institute*, *1*, Pittsburgh, Pennsylvania, USA: The Combustion Institute, pp.821–831

Mathur, S., Tondon, P.K. & Saxena, S.C. (1967) Thermal Conductivity of Binary, Ternary and Quaternary Mixtures of Rare Gases, *Molecular Physics* 12 (6): 569–579

Matta, L.M., Neumeier, Y., Lemon, B. & Zinn, B.T. (2002) Characteristics of Microscale Diffusion Flames, *Proceedings of the Combustion Institute* 29 (1): 933–939

Maxwell, B.M. & Radulescu, M.I. (2011) Ignition Limits of Rapidly Expanding Diffusion Layers: Application to Unsteady Hydrogen Jets, *Combustion and Flame* 158 (10): 1946–1959

McBride, B.J., Gordon, S., Reno, M.A., McBride, B.J., Gordon, S. & Reno, M.A. (1993) *Coefficients for Calculating Thermodynamic and Transport Properties of Individual Species*,

McGeehin, P. (1994) *OPTICAL TECHNIQUES IN INDUSTRIAL MEASUREMENT: SAFETY IN HAZARDOUS ENVIRONMENTS*, Available from: <http://bookshop.europa.eu/et/optical-techniques-in-industrial-measurement-pbCDNA16011/downloads/CD-NA-16-011-EN-C/CDNA16011ENC_001.pdf;pgid=y8dIS7GUWMdSR0EAlMEUUsWb0000zgSdQLHf;sid=di_YlxRfKhjYmkc6MFhGMHZ6O0zG5Vk8aF0=?FileName=CDNA16011ENC_001.pdf&SKU=CDNA16011ENC_PDF&CatalogueNumber=CD-NA-16-011-EN-C> [Accessed:

Mizobuchi, Y., Tachibana, S., Shinio, J., Ogawa, S. & Takeno, T. (2002) A Numerical Analysis of the Structure of a Turbulent Hydrogen Jet Lifted Flame, *Proceedings of the Combustion Institute* 29 (2): 2009–2015

Mogi, T., Kim, D., Shiina, H. & Horiguchi, S. (2008) Self-Ignition and Explosion during Discharge of High-Pressure Hydrogen, *Journal of Loss Prevention in the Process Industries* 21: 199–204

Molkov, V. (1995) Theoretical Generalization of International Experimental Data on Vented Explosion Dynamics, *In*: *First international seminar*, Moscow: VNIIPO, pp.166–181

Molkov, V. (2012) *Fundamentals of Hydrogen Safety Engineering*, bookboon.com, free download online book

Mosedale, A. & Drikakis, D. (2007) Assessment of Very High Order of Accuracy in Implicit LES Models, *Journal of Fluids Engineering* 129 (12): 1497

Mueller, M.A., Kim, T.J., Yetter, R.A. & Dryer, F.L. (1999) Flow Reactor Studies and Kinetic Modeling of the H2/O2 Reaction, *International Journal of Chemical Kinetics* 31 (2): 113–125

Nakamura, Y., Yamashita, H. & Saito, K. (2006) A Numerical Study on Extinction Behaviour of Laminar Micro-Diffusion Flames, *Combustion Theory and Modelling* 10 (6): 927–938

Norris, J. & Edwards, J. (1997) Large-Eddy Simulation of High-Speed, Turbulent Diffusion Flames with Detailed ChemistryAmerican Institute of Aeronautics and Astronautics, Available from: <http://arc.aiaa.org/doi/abs/10.2514/6.1997-370> [Accessed: 7 September 2015]

O'Rourke, P.J. & Amsden, A.A. (1986) *Implementation of a Conjugate Residual Iteration in the KIVA Computer Program*, Los Alamos National Laboratory

PD CLC/TR 50427:2004 Assessment of Inadvertent Ignition of Flammable Atmospheres by Radio-Frequency Radiation. Guide,

Perlee, H., Litchfield, E. & Zebatakis, M. (1964) *Review of Fire and Explosion Hazards of Flight Vehicle Combustibles*, AF Aero Propulsion Laboratory, Wright-Patterson Air Force Base, Ohio, Technical Report No. ASD TR 61-278

Petersen, E.L. & Hanson, R.K. (1999) Reduced Kinetics Mechanisms for Ram Accelerator Combustion, *Journal of Propulsion and Power* 15 (4): 10

Petrova, M. & Williams, F. (2006) A Small Detailed Chemical-Kinetic Mechanism for Hydrocarbon Combustion, *Combustion and Flame* 144 (3): 526–544

von Pidoll, U., Brzostek, E. & Froechtenigt, H.-R. (2004) Determining the Incendivity of Electrostatic Discharges Without Explosive Gas Mixtures, *IEEE Transactions on Industry Applications* 40 (6): 1467–1475

Pinto, D., Aizawa, K., Liu, Y.F., Sato, H., Hayashi, A.K. & Tsuboi, N. (2007) Auto-Ignition of High Pressure Hydrogen Release, *In*: *Proceedings of the 21 st International Colloquium on the Dynamics of Explosions and Reactive Systems*, Poitiers,

Pope, S.B. (1997) Computationally Efficient Implementation of Combustion Chemistry Using in Situ Adaptive Tabulation, *Combustion Theory and Modelling* 1: 41–63

Powell, F. (1984) Ignition of Gases and Vapours by Hot Surfaces and Particles - A Review, *In*: *9th Intl. Symp. on the Prevention of Occupational Accidents and Diseases in the Chemical Industry*, Luzer, pp.267–292

Powell, F. (1986) Can Non-Sparking Tools and Materials Prevent Gas Explosions?, *Gas-Wasser-Abwasser* 66 (6)

Radulescu, M.I. & Law, C.K. (2007) The Transient Start of Supersonic Jets, *Journal of Fluid Mechanics* 578: 331–369

Rogg, B. & Wang, W. (1984) RUN-1DL : The Laminar Flame and Flamelet Code; User Manual, *In*: *Lehrstuhl fur Stromungsmechanik Institut fur Thermo-und Fluiddynamik, Ruhr-Universitat Bochum, D-44780 Bochum, Germany*,

SAE J2579 (2009) Technical Information Report for Fuel Systems in Fuel Cell and Other Hydrogen Vehicles, *In*: *SAE International*, Detroit MI, U.S.,

Saxena, P. & Williams, F.A. (2006) Testing a Small Detailed Chemical-Kinetic Mechanism for the Combustion of Hydrogen and Carbon Monoxide, *Combustion and Flame* 145: 316–323

Schefer, R.W., Evans, G.H., Zhang, J., Ruggles, A.J. & Greif, R. (2011) Ignitability Limits for Combustion of Unintended Hydrogen Releases: Experimental and Theoretical Results, *International Journal of Hydrogen Energy* 36 (3): 2426–2435

Shah, R.K., Heikal, M.R., Thonon, B. & Tochnon, P. (2001) Progress in the Numerical Analysis of Compact Heat Exchanger Surfaces, *In*: Hartnett, J.P. ed. *Advances in Heat Transfer Vol. 34*, San Diego, USA: Academic Press,

Sloane, R.W. (1935) The Ignition of Gaseous Mixtures by the Corona Discharge, *The London, Edinburgh, and Dublin Philosophical Magazine and Journal of Science* 19 (129): 998–1011

Sunderland, P. (2010) Hydrogen Microflame Hazards, *In*: *Proceedings of the 8th International Short Course and Advanced Research Workshop in the series 'Progress in Hydrogen Safety', Hydrogen and Fuel Cell Early Market Applications*, University of Ulster, Belfast,

Swain, M.R., Filoso, P.A. & Swain, M.N. (2007) An Experimental Investigation into the Ignition of Leaking Hydrogen, *International Journal of Hydrogen Energy* 32 (2): 287–295

Takahashi, M., Tamura, Y., Suzuki, J. & Watanabe, S. (2008) Investigation of the Allowable Flow Rate of Hydrogen Leakage on Receptacle, *SAE International Journal of Passenger Cars - Mechanical Systems* 1 (1): 590–597

Thiele, M., Warnatz, J., Dreizler, A., Lindenmaier, S., Schießl, R., Maas, U., *et al.* (2002) Spark Ignited Hydrogen/air Mixtures: Two Dimensional Detailed Modeling and Laser Based Diagnostics, *Combustion and Flame* 128 (1-2): 74–87

Vasil'eva, R.V., Zuev, A.D., Moshkov, V.L., Tkhorik, L.G. & Shingarkina, V.A. (1985) Turbulent Mixing of Driver and Driven Gases in a Shock Tube Channel, *Journal of Applied Mechanics and Technical Physics* 26 (2): 271–277

Wada, Y. & Liou, M.-S. (1997) An Accurate and Robust Flux Splitting Scheme for Shock and Contact Discontinuities, *SIAM Journal on Scientific Computing* 18 (3): 633–657

Wang, B.L., Olivier, H. & Grönig, H. (2003) Ignition of Shock-Heated H2-Air-Steam Mixtures, *Combustion and Flame* 133 (1–2): 93–106

Warnatz, J. (1982) *Numerical Methods in Laminar Flame Propagation*, Braunschweig ; Wiesbaden: Vieweg

Wen, J.X., Xu, B.P. & Tam, V.H.Y. (2009) Numerical Study on Spontaneous Ignition of Pressurized Hydrogen Release through a Length of Tube, *Combustion and Flame* 156 (11): 2173–2189

Westbrook, C.K., Pitz, W.J., Curran, H.J., Gaffuri, P. & Marinov, N.M. (1996) Chemical Kinetic Modelling of Hydrocarbon Ignition, *In*: Wolfrum, J., Volpp, H.-R., Rannacher, R., & Warnatz, J. eds. *Gas Phase Chemical Reaction Systems*, Berlin, Heidelberg: Springer Berlin Heidelberg, pp.279–290 Available from: <http://www.springerlink.com/index/10.1007/978-3-642-80299-7_22> [Accessed: 3 September 2015]

Wilke, C.R. (1950) A Viscosity Equation for Gas Mixtures, *The Journal of Chemical Physics* 18 (4): 517

Williams, F.A. (1985) *Combustion Theory: The Fundamental Theory of Chemically Reacting Flow Systems*, Cambridge, Mass: Perseus Books

Wolanski, P. & Wojcicki, S. (1973) Investigation into the Mechanism of the Diffusion Ignition of a Combustible Gas Flowing into an Oxidizing Atmosphere,

Xu, B.P., Hima, L.E., Wen, J.X., Dembele, S. & Tam, V.H.Y. (2007) Numerical Study of Spontaneous Ignition of Pressurized Hydrogen Release into Air, *In*: *2nd International Conference on Hydrogen Safety*, Available from: <www.hysafe.org/conference> [Accessed:

Xu, B.P., Hima, L.E., Wen, J.X., Dembele, S., Tam, V.H.Y. & Donchev, T. (2008) Numerical Study on the Spontaneous Ignition of Pressurized Hydrogen Release through a Tube into Air, *International Journal of Hydrogen Energy* 21: 205–213

Xu, B.P., Hima, L.E., Wen, J.X. & Tam, V.H.Y. (2009) Numerical Study of Spontaneous Ignition of Pressurized Hydrogen Release into Air, *International Journal of Hydrogen Energy* 34 (14): 5954–5960

Xu, B.P. & Wen, J.X. (2011) Numerical Study of Spontaneous Ignition of Pressurized Hydrogen Release through a Length of Tube with Local Contraction,

Xu, B.P. & Wen, J.X. (2012) Numerical Study of Spontaneous Ignition in Pressurized Hydrogen Release through a Length of Tube with Local Contraction, *International Journal of Hydrogen Energy* 37 (22): 17571–17579

Xu, B.P. & Wen, J.X. (2014) The Effect of Tube Internal Geometry on the Propensity to Spontaneous Ignition in Pressurized Hydrogen Release, *International Journal of Hydrogen Energy* 39 (35): 20503–20508

Xu, B.P., Wen, J.X., Dembele, S., Tam, V.H.Y. & Hawksworth, S.J. (2009) The Effect of Pressure Boundary Rupture Rate on Spontaneous Ignition of Pressurized Hydrogen Release, *Journal of Loss Prevention in the Process Industries* 22 (3): 279–287

Xu, B.P., Wen, J.X. & Tam, V.H.Y. (2011) The Effect of an Obstacle Plate on the Spontaneous Ignition in Pressurized Hydrogen Release: A Numerical Study, *International Journal of Hydrogen Energy* 36 (3): 2637–2644

Yakhot, V. & Orszag, S. (1986) Renormalization Group Analysis of Turbulence. I. Basic Theory, *Journal of Scientific Computing* 1: 3–51

Yamada, E., Watanabe, S., Hayashi, A.K. & Tsuboi, N. (2009) Numerical Analysis on Autoignition of a High-Pressure Hydrogen Jet Spouting from a Tube, *Proceedings of the Combustion Institute* In print. Available online

Yarwood, T.M.C. & Castle, F. (1961) *Physical and Mathematical Tables*, Macmillan Available from: <https://books.google.co.uk/books?id=iG5RnQEACAAJ> [Accessed:

3. Physical and Mathematical Models of Fires (UU)

3.1 Physical and Mathematical Modelling of Fires (UU)

3.1.1 Microflames (UU) – DONE

A small leak in a hydrogen system could ignite, burn undetected for a long time, and potentially degrade surrounding materials or ignite any hydrogen release that may occur nearby (Butler et al., 2009). Hydrogen leaks can support combustion at flow rates much lower than leaks of other gaseous fuels. The technical information report SAE J2579, (2009) states that a localised hydrogen leak from a typical compression fitting cannot sustain a flame (that can subsequently weaken material and cause a loss of containment), when the mass flow rate is below 28 μg/s. For a miniature burner, the lowest leak flow rate capable of sustaining a flame is 5 μg/s.

Leak flames resemble micro diffusion flames and, while only a few studies have specifically evaluated leak flames (e.g., Takahashi et al., 2008), there have been a number of studies of micro diffusion flames (Ban et al., 1994; Baker et al., 2002; Matta et al., 2002; Cheng et al., 2005, 2006; Nakamura et al., 2006). Micro diffusion flames are typically associated with an application, e.g., a microcombustor for power generation. Nonetheless, it is possible that they could arise unexpectedly. For example, if a fuel leak from a crack or hole in a fitting, tube or storage vessel of a plumbing system were ignited, this could be characterized as a micro diffusion flame.

Some of the weakest self-sustaining steady flames ever observed have been reported by Lecoustre et al., (2010). Lecoustre et al. (2010) carried out experiments in which flames were produced by a downward oriented burner made from a stainless steel hypodermic tube with an internal diameter of 0.15 mm and an outside diameter of 0.30 mm. Near their quenching limits these flames had hydrogen flow rate of 3.9 μg/s and 2.1 μg/s in air and oxygen, respectively (Lecoustre et al., 2010), with uncertainties in the quenching limit flow rates measurements estimated to be approximately ±10%. Assuming complete combustion, the associated heat release rates were 0.46 W and 0.25 W (based on hydrogen's lower heating value of 119.9 kJ/g). Buoyancy has been found to play an insignificant role in hydrogen microflames (Cheng et al., 2005).

Microflames are associated with small flow rates of subsonic laminar releases from cracks. The equation for volumetric flow rate from a leak can be written as (Molkov, 2012)

$$\dot{V}_{vent} = CA\left\{\left(\frac{2\gamma}{\gamma-1}\right)\frac{P_S}{\rho_{orif}}\left[\left(\frac{P_S}{P_{orif}}\right)^{\frac{2}{\gamma}} - \left(\frac{P_S}{P_{orif}}\right)^{\frac{\gamma+1}{\gamma}}\right]\right\}^{\frac{1}{2}}, \qquad (3.1)$$

where $\dot{V}_{vent}$ is the volumetric flow rate (m^3/s), γ is the ratio of specific heats, P is the pressure (Pa), ρ is the density (kg/m^3), with subscripts "S" and "orif" corresponding to surrounding (ambient) conditions and conditions at the orifice respectively, A is the orifice area (m^2) and C is the discharge coefficient (Molkov, 1995). It can be seen from Eq.(3.1), that for the same pressure at the orifice the highest volumetric flow rate through leaks will be produced by a gas with the lowest density, i.e. hydrogen.

From a safety perspective, it is important to determine if a small scale hydrogen leak would be able to support a flame. Although hydrogen flames can be sustained over a relatively large range of flow rates, very low and very high flow rates will lead to flame extinction (Sunderland, 2010). The very low flow rate limit is known as the quenching limit. It is

associated with kinetic extinction, which occurs at high scalar dissipation rates (low Damköhler numbers) and may occur with or without external losses (i.e., losses other than chemical enthalpy loss) (Lecoustre et al., 2013). The upper flow rate limit corresponds to so-called flame blow-off and will be discussed in details in section 3.1.4.

Quenching and blow-off limits of different gases were measured by (Kalghatgi, 1981; Baker et al., 2002; Matta et al., 2002; Cheng et al., 2006) for a variety of fuels including propane, methane and hydrogen. At the quenching limits the flame length is comparable to the quenching distance for a premixed hydrogen flame. Matta et al. (2002) and Nakamura et al. (2006) observed that a flame is not able to exist when its predicted length became less than the measured stand-off distance. Significantly smaller quenching limits for hydrogen were also observed for leaking compression fittings (Butler et al., 2009). These studies showed that hydrogen mass flow rate blow-off limits are higher than those for methane and propane. Butler et al., (2009) examined weak hydrogen flames that might be associated with the fire hazards of small hydrogen leaks. They observed quenching limits of diffusion flames on small round burners and for the leaky compression fittings and found the quenching mass flow rates for hydrogen to be about an order of magnitude lower than those for methane and propane. For a given leak size, there is a range of mass flow rates where hydrogen is able to support a stable flame but methane and propane flames would be extinguished.

For isentropic choked flows the mass flow rate is linear with pressure upstream of the orifice P_0 (Pa) and area of the leak A (m^2):

$$\dot{m} = CAP_0\left(\frac{\gamma M}{RT_0}\right)^{1/2}\left(\frac{2}{\gamma+1}\right)^{\frac{\gamma+1}{2(\gamma-1)}}, \qquad (3.2)$$

where T_0 is the temperature upstream of the release orifice (K), γ - is the specific heat ratio, M – is the gas molar mass (kg/mol) and R is the universal gas constant (J/mol/K). Equation (3.2) can be used to correlate orifice diameter and upstream pressure at the quenching limit(Butler et al., 2009). The results of these calculations are shown in Figure 3.1 for hydrogen, methane, and propane. For each of the three gases the dependence line starts at the minimum upstream pressure for choked flow and ends at the maximum pressure anticipated in alternative fuel vehicles. It is seen from Figure 3.1 that for a given storage pressure, hydrogen is susceptible to leak flames for smaller hole diameters than those for methane or propane.

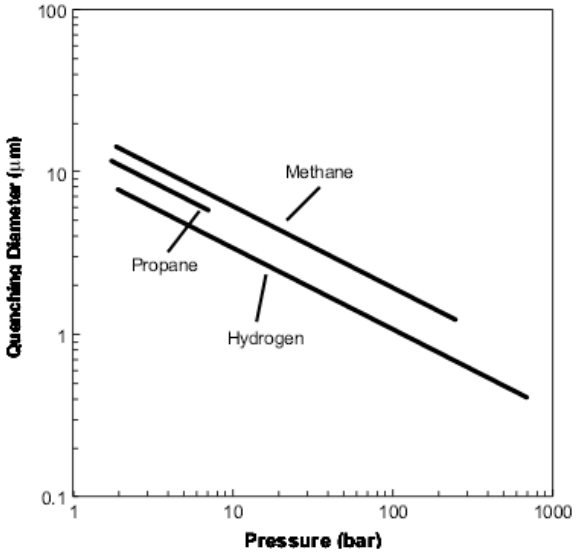

Figure 3.1 Quenching diameter as a function of upstream absolute pressure assuming isentropic choked flow(Butler et al., 2009).

Ge & Sutton (2006) conducted research on hydrogen interface leakage in national pipe thread (NPT) fittings. The tests were run at a pressure drop of 7 MPa. They found that the best performing fittings leaked hydrogen at rates of 1 μg/s, while the leak rates for the worst performing fittings were far higher. They found that the tightening torque was less important in sealing the threads than the choice and proper application of thread sealant material. An alternative type of fitting, often used with gases at high pressure, is a compression fitting (Sunderland, 2010). An advantage of using compression fittings over pipe thread fittings is the absence of Teflon tape, which greatly simplifies disassembly and reattachment of the fittings. Compression fittings, however, can be subject to over-tightening, which damages the ferrule and increases the likelihood of leaks occurring (Sunderland, 2010).

Figure 3.2 (left) shows measured ignition flow rates for hydrogen, methane, and propane releases through a leaky fitting in a vertical orientation (Butler et al., 2009). The minimum flow rate necessary for sustained ignition is plotted versus pressure. The upper limit on pressure for propane is lower than that of the other gases because the vapour pressure of propane at 21^{o} C is 0.76 MPa (110 psig). The measured ignition mass flow rates shown in Figure 3.2 (left) can be converted into volumetric flow rates using the measured temperature and pressure (Butler et al., 2009). The resulting volumetric flow rates are plotted in Figure 3.2 (right) versus upstream pressure. Within experimental uncertainties, the minimum fuel mass and volumetric flow rates are independent of pressure. Figure 3.2 (right) illustrates that although hydrogen has the lowest mass flow rate necessary to sustain fittings microflame, propane has the lowest volumetric flow rate to sustain a microflame. The volumetric flow rates for hydrogen, methane and propane are 0.337, 0.581, and 0.187 mL/s, respectively. It should be noted, that for leaky fittings, the quenching flow rates for hydrogen, methane, and propane are about an order of magnitude higher than the corresponding flows for tube burners (Butler et al., 2009), which need to be taken into account when applying the results of experiments using micro-burners to leak problems. This is attributed to additional heat losses in the leaky fittings, where the flames burn near thick concave metal surfaces.

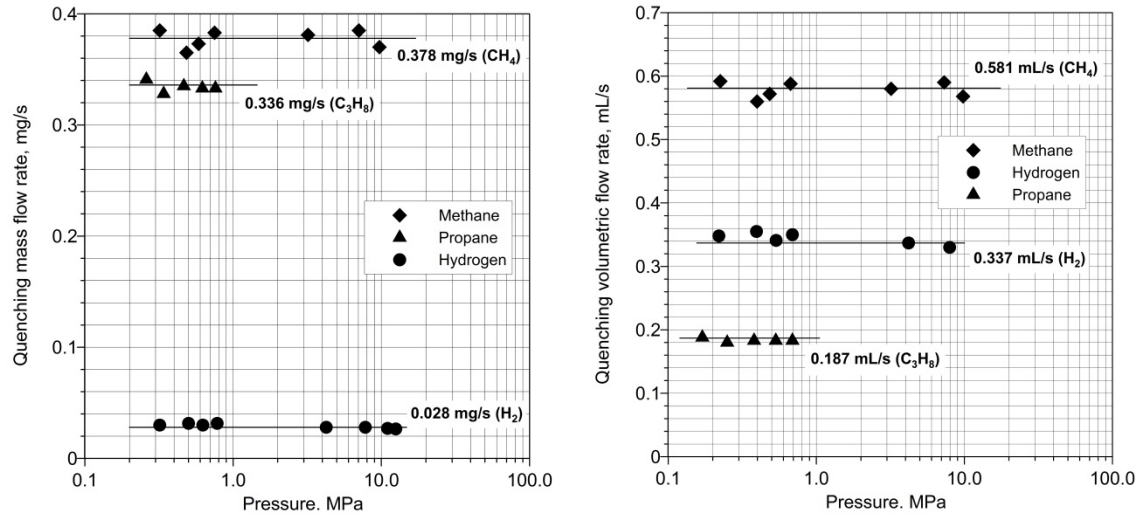

Figure 3.2 Quenching limits for hydrogen, methane, and propane releases through vertically orientated fittings: mass flow rate limit (left; Butler et al., 2009) and volumetric flow rate limit (right; Sunderland, 2010).

Butler et al., (2009) also investigated the effect of release orifice or leaky fitting orientation (vertical, horizontal, inverted) on the quenching limit. The effects of fitting orientation are shown in Figure 3.3 (left), and reveal that orientation has little or no effect on the quenching limits of the hydrogen flames, which supports the observation that flames near extinction are driven by mechanisms other than buoyancy. This is anticipated as these flames are small at their limits and the results are consistent with those of similar experiments using round orifice burners. As can be seen in Figure 3.3 (left), however, fitting orientation did affected the quenching limits of propane and methane flames, with the inverted orientation yielding limits about 20% lower than the vertical orientation.

The effects of fitting diameter on quenching limits are examined in Figure 3.3 (right). Diameter had a significant impact on the quenching limits in all cases; on average as tube diameter doubles, the fuel mass flow rate at which quenching occurs increases by 30%. This is attributed to increased heat losses associated with larger fittings (Butler et al., 2009).

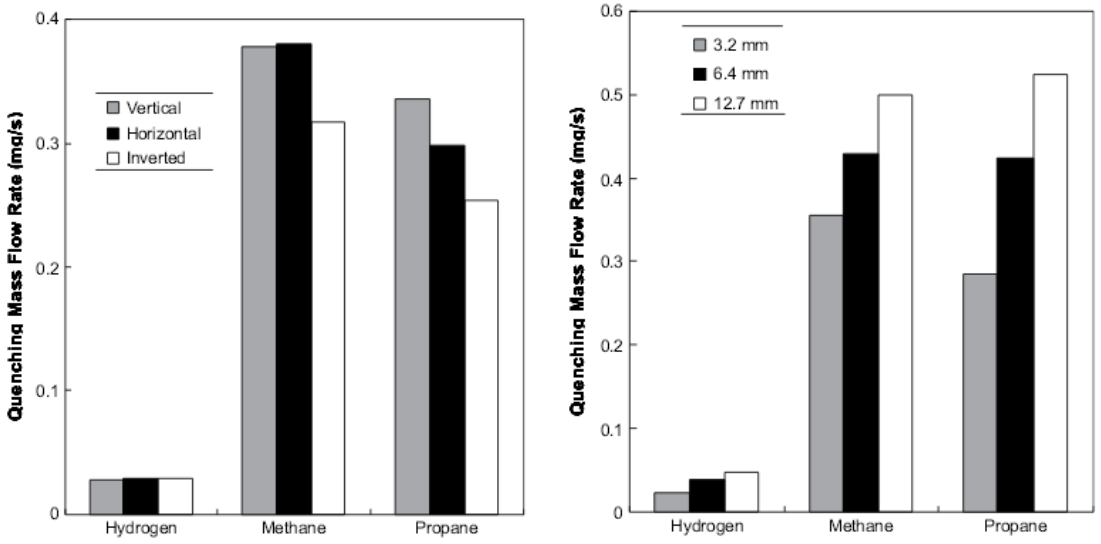

Figure 3.3 Hydrogen, methane, and propane quenching limits for leaky compression fittings: tube diameter 6.3 mm and vertical, horizontal and inverted release orientations (left);

vertically oriented releases and tube diameters 3.1, 6.3 and 12.6 mm (right). The upstream absolute pressure was 4 bar (Butler et al., 2009).

3.1.2 Jet fires (UU)

Jet fire types and length

A jet fire is a typical scenario for hydrogen accidents. Statistics show that in most situations accidental hydrogen releases will be ignited (Astbury & Hawksworth, 2007). One of the key parameters necessary for hydrogen safety engineering and assessment of the safety of a specific engineering installation is the jet flame length. The jet flame length is a key parameter because it is required to calculate separation distances.

The prediction of laminar and turbulent non-premixed hydrogen jet flame lengths has been the subject of studies starting from the seminal work of Hawthorne et al. (1949). Traditionally, the research concentrated on the development of correlations for the dimensionless flame length in terms of the burner nozzle diameter and Froude number (Fr). These early studies neglected to quantify the flame length in terms of the Reynold (Re) number or Mach (M) number.

To distinguish between purely diffusion flames, when a flow from a burner is laminar, and turbulent flames from the same burner the last are referred as turbulent non-premixed flames. Figure 3.4 shows progressive change of the flame height with the nozzle velocity during transition from laminar diffusion to fully developed turbulent non-premixed flame as observed by Hawthorne et al. (1949). In the beginning the increase of nozzle velocity leads to the increase of flame length for laminar flames. As the jet velocity at the nozzle increases, the laminar flame height reaches its maximum and starts to decline as the flame becomes turbulent stating from its tip. This transition from vertical laminar diffusion flame to turbulent flame occurs at a Reynolds number of around 2000. After transition to turbulent flame is complete, further increase of fuel gas flow rate has no effect on the flame length as long as it is sufficient to produce a fully developed turbulent flame according to experiments with expanded jets conducted by Hawthorne et al. (1949).

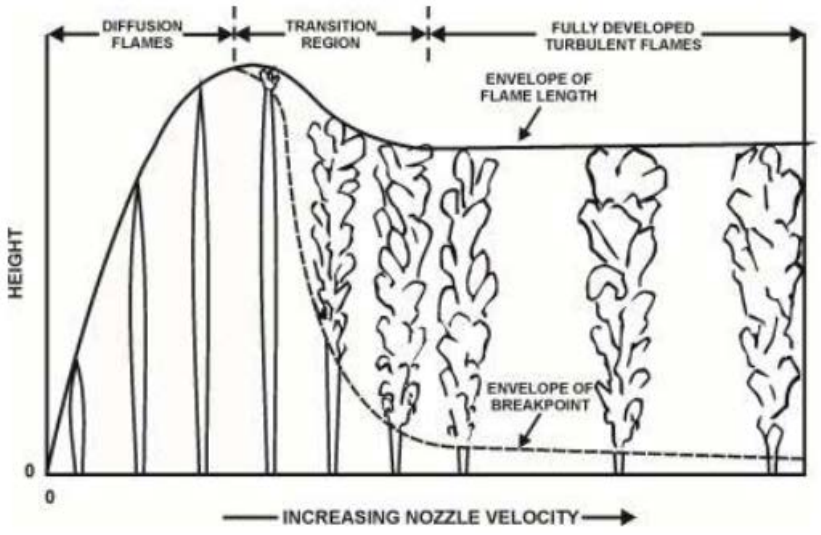

Figure 3.4 Progressive change from laminar diffusion flame to fully developed turbulent non-premixed flame (Hottel & Hawthorne, 1949).

Based on the experiments with expanded jets, Hawthorne et al. (1949) concluded, that for the fully developed turbulent flames the flame length L_F is proportional only to the nozzle diameter D and does not depends on the release rate. The dimensionless length of a free turbulent flame jets can be expressed as

$$\frac{L_F - s}{D} = \frac{5.3}{C_{st}} \sqrt{\frac{T_{ad}}{\alpha_T T_N} \left[C_{st} + (1 - C_{st}) \frac{M_S}{M_N} \right]}, \tag{3.3}$$

where s is the distance from the breakpoint (see Figure 3.4) to the nozzle, α_T is the ratio of reactant moles to product moles for a stoichiometric mixture, T_{ad} is the adiabatic flame temperature, T_N is the temperature of fluid in the nozzle, C_{st} is the mole fraction of the gas released from the nozzle in a stoichiometric mixture with air and M_S/M_N is the ratio of molecular masses of the ambient and released from gases. Using Eq. (3.3), Hawthorne et al. (1949) calculated the dimensionless expanded jet flame length to be equal to L_F/D = 152.

Hawthorne et al. (1949) also demonstrated that the actual variation of hydrogen concentration (normalised by axial concentration) over a cross-section of turbulent jet fire (normalised by a jet width where concentration is half of the maximum concentration) is independent of the distance from the nozzle. This is an important observation which can be used for validation of computational fluid dynamics (CFD) simulations of subsonic jet fires.

Hawthorne's pioneering work was followed by a large body of experimental and theoretical research, producing measurements of jet flame length under a variety of release conditions. These experimental data and theoretical considerations have been used in the development of correlations aimed at predicting the jet flame length as a function of the release parameters.

Golovichev & Yasakov (1972) theoretically predicted the maximum flame length to nozzle diameter ratio L_F/D = 220. The maximum measured value for a subsonic release, i.e. expanded jet, was L_F/D = 205 at a velocity of 365 m/s. (Baev et al., 1974; Baev & Yasakov, 1974) undertook a systematic attempt to investigate flame length over the entire range of release rates from plumes to jets (Becker & Liang, 1978), conducting more than 70 experiments with release Mach number ranging from 0.25 to 3.08 and nozzle diameter from 1 mm to 16.65 mm. The basic flame length equation derived in these studies is similar to Eq. (3.3) obtained by Hottel & Hawthorne (1949), but additionally accounts for the effects of compressibility (Becker & Liang, 1978). The resulting flame length correlation was presented in terms of the Froude number. In spite of the understanding of the role of the Re and M numbers, the experimental flame length data were presented as a function of the Froude number $Fr = \frac{U_N^2}{gD}$. Baev et al. (1974) had theoretically shown that for momentum-dominated jets the flame length is proportional to the Reynolds number $L_F \sim Re$, which means that the dimensionless flame length L_F/D is constant for sonic (choked) expanded jets assuming that both the density and the viscosity remain constant.

For the lower Reynolds numbers, (Baev & Yasakov, 1974) showed theoretically that depending on the nozzle diameter (and therefore Froude number) there will be a characteristic peak in $L_F(Re)$ function, previously mentioned by Hottel & Hawthorne (1949) (Figure 3.5).

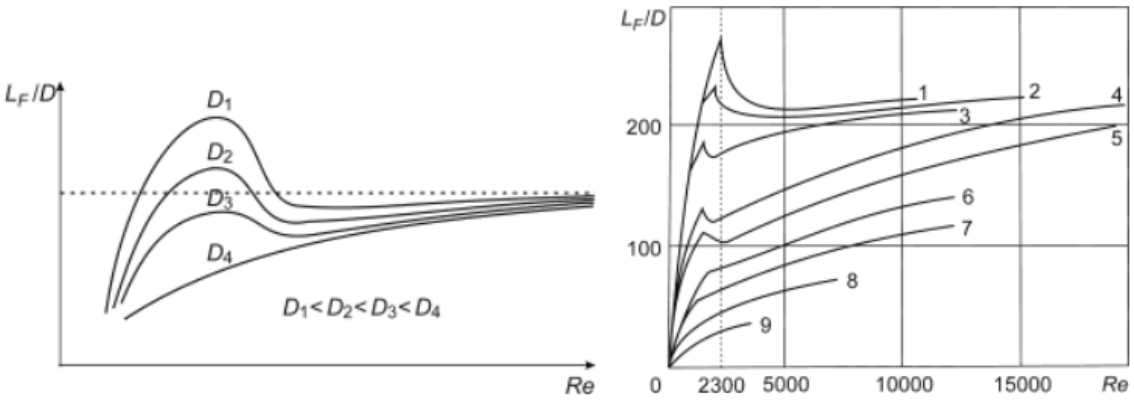

Figure 3.5 The theoretical (left, Baev & Yasakov, 1974) and experimental (right, Shevyakov & Komov, 1977) dependence of the flame length to diameter ratio L_F/D as a function of Reynolds number (Re) for different nozzle diameters D. Dotted horizontal line indicates a turbulent flame length limit (Baev & Yasakov, 1974). Numbers on the right figure correspond to different nozzle diameters D, mm: 1 – 1.45; 2 – 1.9; 3 – 2.9; 4 – 4.0; 5 – 6.0; 6 – 10.75; 7 – 15.5; 8 – 21; 9 – 51.7 (Shevyakov & Komov, 1977).

Baev & Yasakov (1974) analysis suggested that the ratio of maximum laminar to maximum turbulent flame length is L_l/L_t = 1.74 and is independent of fuel type. This ratio decreases with the increase of nozzle diameter D (see Figure 3.5, left). Their experimental data gave a maximum L_F/D = 230 for laminar jet flames and a L_F/D = 190 for turbulent jet fires. These theoretical conclusions were confirmed by experiments carried out by Shevyakov & Komov (1977) that are shown in Figure 3.5 (right). In these experiments dimensionless flame length L_F/D measurements were similar to those predicted by Baev & Yasakov (1974) for small nozzle diameters, and approached a limit of L_F/D = 220-230 at high Reynolds numbers. This experimental data is above a turbulent jet flame limit L_F/D = 190 measured by Baev & Yasakov (1974) and similar to the limit L_F/D = 230 measured by (Baev et al., 1974) for laminar jet flames.

A wide range of experiments for subsonic vertical hydrogen jet fires, covering the range of conditions from buoyancy-controlled to subsonic momentum-dominated, had been conducted by Shevyakov and colleagues (Shevyakov & Komov, 1977; Shevyakov & Savelyeva, 2004). Application of regression analysis to these results plotted against Froude number lead to the piecewise-linear correlation

$$\begin{cases} L_F / D = 15.8 \cdot Fr^{1/5} & (Fr < 10^5) \\ L_F / D = 37.5 \cdot Fr^{1/8} & (10^5 < Fr < 2 \cdot 10^6), \\ L_F / D = 230 & (Fr > 2 \cdot 10^6) \end{cases} \quad (3.4)$$

which can be used to reconcile the differences in measured L_F/D experimental data by different researchers at different Froude numbers.

Kalghatgi (1984) published experimental data from more than 70 tests with nozzle diameters in the range 1.08-10.1 mm, both with subsonic and sonic hydrogen jet flames (Figure 3.6, left). The maximum measured flame lengths agree well with the modified Shevyakov's correlation (Eq. (3.4)). Examination of Figure 3.6 (left) leads to two important conclusions valid for both subsonic and sonic flows: 1) flame length grows with mass flow rate when the nozzle diameter is fixed (D = const), and 2) flame length grows with nozzle diameter when the mass flow rate is fixed ($\dot{m} = const$). It is seen that the hydrogen flow rate does appear to

be a factor in determining jet flame length. The dependence of flame height on mass flow rate implies that non-ideal behaviour of hydrogen at high pressures should be accounted for in the development of jet flame length correlations. Flame length dependence on both flow rate and nozzle diameter observed by Kalghatgi (1984) was later confirmed by (Schefer, 2006).

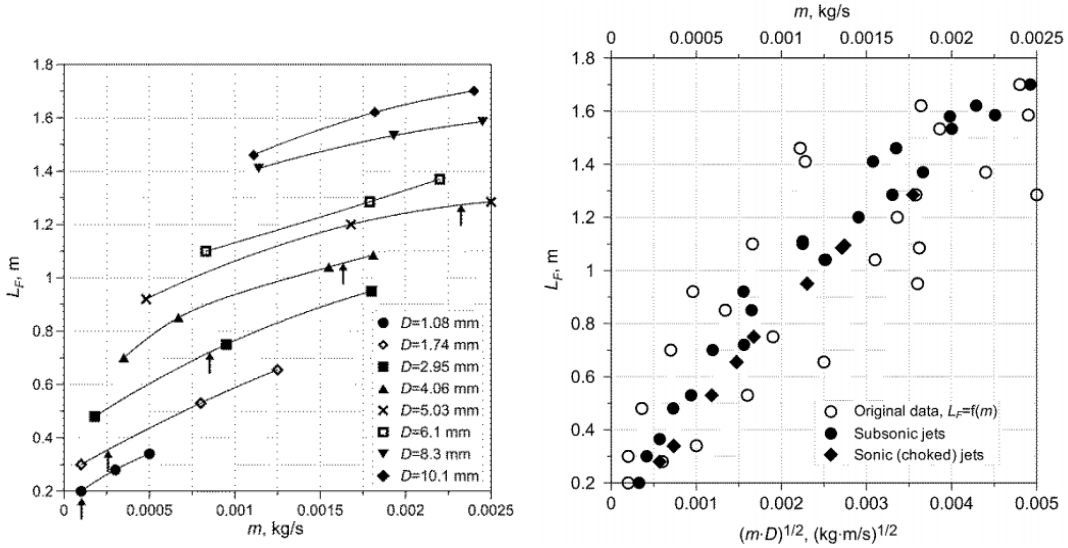

Figure 3.6 Experimental data by Kalghatgi (1984) on hydrogen jet flame length for subsonic and sonic jet fires for different nozzle diameters and different mass flow rates plotted in the original $L_f - \dot{m}$ (left), and new $L_f - (\dot{m} \cdot D)^{1/2}$ (right, Molkov & Saffers 2013) coordinates. Arrows in the left figure indicate the transition from subsonic (to the left of the arrow) to sonic flow. Hollow circles in the right figure correspond to original coordinates, filled circles to subsonic and filled diamonds – sonic jet fires.

Accordingly, Molkov, (2009) proposed a correlation based on the similitude analysis, which includes the dependence of flame length on both nozzle diameter and mass flow rate. Utilization of the new similarity group $(\dot{m} \cdot D)^{1/2}$ has significantly improved the convergence of the flame length data by Kalghatgi (1984) for both subsonic and sonic jets (see Figure 3.6 right).

Studies of jet flame length in the wide range from buoyancy- to momentum-controlled turbulent non-premixed expanded jet flames was performed by (Delichatsios, 1993), suggesting the relation in the form $L_F / D = 23(\nu + 1)(\rho_N / \rho_S)^{1/2}$, where ν is the air to fuel mass stoichiometric ratio, which gives maximum L_F/D = 210 ratio for the release of expanded hydrogen into the still air.

Blake & McDonald (1993) showed that for upward turbulent diffusion flames the dimensionless flame length L_F/D is a function of a density weighted Froude number (inverse Richardson number) and a flame density to ambient density ratio.

Mogi et al. (2005) studied horizontal hydrogen jet flames from convergent nozzles of 0.1-4.0 mm exit diameter in the range of overpressures 0.01-40 MPa. The experimentally measured dimensionless flame length increases with the spouting pressure (static pressure measured close to nozzle exit) as $L_F / D = 523.5 \cdot P^{0.436}$, where pressure P is measured in MPa. This correlation gives maximum L_F/D = 254 for subsonic flows (at the spouting pressure 0.19 MPa), which is somewhat above the maximum value L_F/D = 230 obtained for expanded jets. These results prompted Mogi et al. (2005) to propose that a flame length can be expressed as

a function of flow rate regardless of nozzle diameter; this however lead to significant scattering of experimental data obtained for different nozzle diameters, similar to the one observed by Kalghatgi (1984).

Further experiments were conducted by (Schefer, 2006), who investigated hydrogen vertical hydrogen jet flames for both subsonic and sonic (choked) flows at pressures up to 17.2 MPa. This study confirmed Kalghatgi (1984) conclusion that flame length increases with both mass flow rate and jet nozzle diameter. Imamura et al. (2008) carried out a series of experiments investigating the dependence of flame shape on the nozzle diameter (in a range of 1 – 4 mm) and spouting pressure (in a range of 0.5 – 3.0 MPa). Proust et al. (2011) published experimental results on horizontal hydrogen jet flame in the widest range of pressures 1-90 MPa and leak diameters 1, 2, 3 and 10 mm. Studer et al. (2009) published results of experimental study on hydrogen jet fires. Hydrogen was released horizontally from a storage tank at 10 MPa through a flexible pipe with internal diameter of 15 mm.

The majority of the correlations for jet flame length proposed by these and other researchers were based on the Froude number in one or another form. One of the exceptions was previously mentioned work by Mogi et al. (2005), whose proposed correlation was based on the flow rate. Correlation proposed by (Schefer, 2006; Schefer et al., 2007) incorporates data on under-expanded jet fires. To include under-expanded jet fires into the dimensionless correlation (Schefer et al., 2006) substituted actual nozzle diameter by effective (notional) nozzle diameter in the form $D_{eff} / D = (\rho_N U_N / \rho_S U_S)^{1/2}$. Molkov & Saffers (2013) consolidated experimental data reported by different authors in the Fig. 3.1.2.4, using coordinate system proposed by (Schefer et al., 2007).

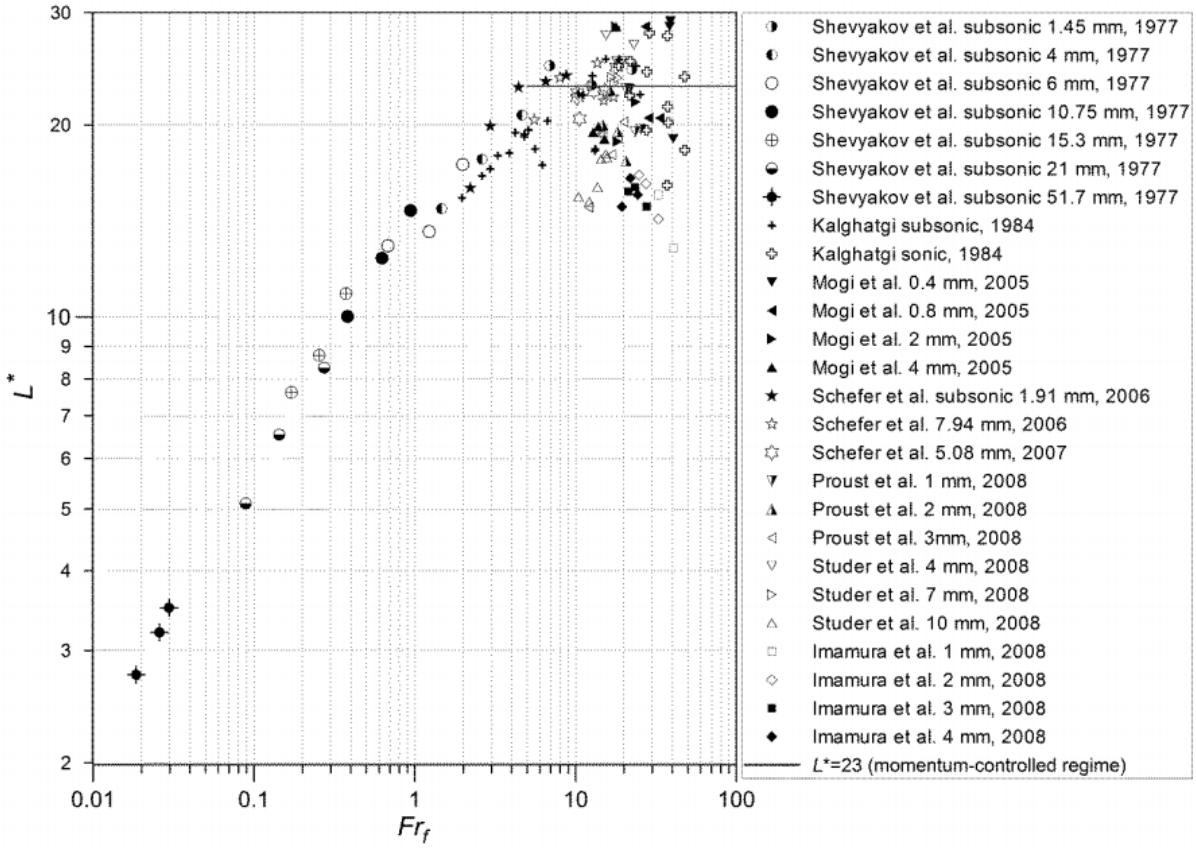

Figure 3.7 The Froude number-based flame length correlation in coordinates used by Schefer et al. (2007) with the extended range of experimental data on under-expanded jet fires (Molkov & Saffers, 2013).

Parameters at the notional nozzle exit, used to build the correlation in Figure 3.7 for the flame length, were calculated using the under-expanded jet theory by Schefer et al. (2007). The dimensionless flame length and Froude number coordinates in the Figure 3.7 can be expressed as

$$L^* = \frac{L_F f_S}{D_{eff}(\rho_{eff}/\rho_S)^{1/2}}, \tag{3.5}$$

$$Fr_f = \frac{U_{eff} f_S^{3/2}}{\left[(\Delta T_f / T_S) g D_{eff}\right]^{1/2} (\rho_{eff}/\rho_S)^{1/4}}, \tag{3.6}$$

Schefer et al. (2007), where f_S is mas fraction of fuel at stoichiometric conditions, ΔT_f is the peak flame temperature rise due to combustion heat release, and T_S is the ambient air temperature.

Figure 3.7 demonstrates that flame length data become unacceptably scattered in the momentum-dominated area of the correlation with large Froude numbers, which are characteristic for leaks from high pressure hydrogen equipment. It confirms the conclusion drawn from the analysis of Kalghatgi (1984) was later confirmed by (Schefer et al., 2006) results, that the flame length correlations based on the functional dependence on Froude number alone does not work well for under-expanded jet fires.

Molkov (2009) used the same $L_f - (\dot{m} \cdot D)^{1/2}$ similitude analysis inspired coordinates, which was successfully used to collapse Kalghatgi's (1984) experiments results (Figure 3.6, right), to a wider range of experiments. Resulting correlation is shown in Figure 3.8.

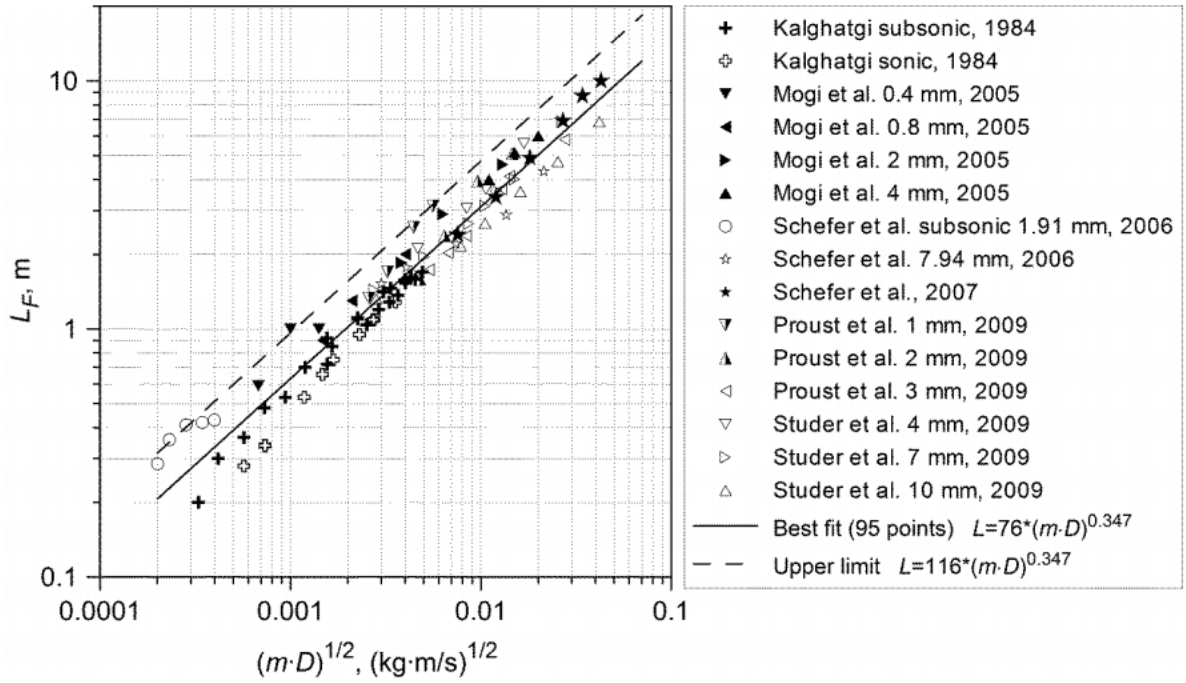

Figure 3.8 The dimensional correlation for hydrogen jet flame length (Molkov, 2009a).

In Figure 3.8 the experimental data obtained by different research groups are collapsed onto the same curve. The best fit line can be expressed as

$$L_f = 76 \cdot (\dot{m} \cdot D)^{0.347}, \quad (3.7)$$

where L_F is the dimensional flame length (measured in meters), D is the actual nozzle diameter, m, and $\dot{m}$ is the mass flow rate, kg/s. Additional advantage of this correlation over the one depicted in Figure 3.7 is that it requires knowledge of only the actual leak diameter and the mass flow rate, rather than the parameters at the notional nozzle. The mass flow rate can be calculated using any validated under-expanded jet theory.

The upper limit curve for the experimental flame lengths in Figure 3.8 (i.e., conservative estimate), can be written as

$$L_f = 116 \cdot (\dot{m} \cdot D)^{0.347}, \quad (3.8)$$

which produces flame length 50% longer than the best fit line described by Eq. (3.7). It can be seen from Figure 3.8 that the dimensional correlation Eq. (3.7) provides good agreement with experimental data for high flow rate jet fires. It is somewhat worse for the smaller flow rate flames. The characteristic peak in the dependence L_F/D = f(Re) for small diameters (see Figure 3.5) is one of possible reasons for the larger scattering in the experimental data in the low flow rate limit. Caution, therefore, must be exercised when applying the correlation to small diameter leaks.

Most of the previously discussed correlations distinguished two regimes of jet fires. The first regime is buoyancy-controlled jet fire. This regime is characterised by lower Froude number, and the dimensionless flame length L_F/D grows with Fr number. The second regime is momentum-dominated jet flame. This regime is characterised by higher Froude numbers compared to the buoyancy-controlled regime. For this regime it has been demonstrated that the dimensionless flame length is independent of Froude number.

This statement, however, was only derived for expanded jets. Hydrogen jets from storage tanks and equipment at pressures up to 100 MPa, commonly used in hydrogen-related infrastructure, will be mainly in a form of under-expanded jet. The under-expanded jet is defined as a jet with pressure at the nozzle exit is above the atmospheric pressure (see section 1.1.7). Jet fires originating from under-expanded jets present a particular important problem for hydrogen safety studies, since under-expanded hydrogen flames can reach tens of meters from current pressure relief devices for on-board storage of hydrogen-fuelled vehicles, and up to hundreds of meters for large diameter high pressure industrial hydrogen pipes. Recent study (Molkov & Saffers, 2013) expands the current classification of jet fires to include under-expanded jet fires through the development of a novel correlation for jet fires that comprises dependence on Fr, Re and M numbers.

As have been shown in the preceding discussion, theoretical and experimental results indicate that the flame length has to be a function of not only the Froude number (Fr) but also the Reynolds (Re) number and the Mach (M) number. The analysis of previous research leads to a conclusion that it is impossible to build a universal correlation applicable to both expanded and under-expanded jet fires based on only one of these three similarity groups. Molkov & Saffers (2013) proposed a new approach to correlation of the experimental data by introducing dimensional correlation.

The dimensional correlation of the type $L_F = 76 \cdot (\dot{m} \cdot D)^{0.347}$ (Molkov, 2012) can be approximated as $L_F \sim (\dot{m} \cdot D)^{1/3}$. The mass flow rate, by definition, is $\dot{m} \sim D^2$. After substituting $\dot{m} \sim D^2$ into relationship for L_F it appears that the dimensionless flame length

L_F / D does not depend explicitly on the diameter *D*. This basic hypothesis has been used by Molkov & Saffers (2013) to develop a novel dimensionless correlation for the jet flame length, which is supported by the experimental data analysis. After eliminating *D*, the only remaining dependence of the dimensionless flame length, L_F / D is on the "residual" parameters in the mass flow rate, i.e. density ρ_N and velocity U_N at the nozzle exit, which for simplicity are assumed to be uniform. The density and velocity are normalized as ρ_N / ρ_S and U_N / U_S respectively, where U_N is the speed of sound at conditions of gas in the nozzle and ρ_S is the density of the surrounding air. Assuming that the kinetic energy flux in the nozzle exit is a conserved scalar of the process, density and the velocity in the dimensional group can be related as $(\rho_N / \rho_S) \cdot (U_N / C_N)^3$.

Figure 3.1.2.6 presents a novel dimensionless hydrogen flame length correlation (Molkov & Saffers, 2013). In this correlation the experimental data on flame length are normalized by the actual (not notional) nozzle diameter, and are correlated with the product of the dimensionless density ratio ρ_N / ρ_S and the Mach number (ratio of the flow velocity to the speed of sound at the actual nozzle exit) to the power of three $M^3 = (U_N / C_N)^3$.

One of the advantages of this correlation is that it utilizes parameters at the exit of the actual rather than notional nozzle. These parameters are nozzle diameter, hydrogen density and flow velocity, the speed of sound at the pressure and temperature at the nozzle exit. The use of the correlation requires application of an under-expanded jet theory described in the section 1.1.7. Calculation of flow parameters in the actual nozzle exit can be carried out with less uncertainty compared to uncertainties at the notional nozzle. Indeed, it is well known that there exists a strong non-uniformity of velocity immediately downstream of the Mach disk that deviates from the common for all under-expanded jet theories assumption of uniform velocity at the notional nozzle exit. By utilizing the parameters at the actual nozzle it is possible to ovoid these complications.

The hydrogen flow parameters at the nozzle exit for experiments presented in Figure 3.9 are taken either directly from the experiments or calculated by the under-expanded jet theory (Molkov et al., 2009). The details of experiments used to underpin the dimensionless correlation are given in (Molkov & Saffers, 2013). New correlation covers the whole spectrum of hydrogen reacting leaks, including laminar and turbulent flames, buoyancy- and momentum-controlled fires, expanded (subsonic and sonic) and under-expanded (sonic and supersonic) jet fires.

The dimensionless group derived for correlating the dimensionless flame length can be rewritten in terms of Re and Fr numbers as follows

$$(\rho_N / \rho_S) \cdot (U_N / C_N)^3 = \frac{g \mu_N}{\rho_S C_N^3} \cdot \mathrm{Re} \cdot Fr \,, \qquad (3.9)$$

where the viscosity was calculated as $\mu_N = \mu_{293} \left((293 + K_{suth})(T_N + K_{suth}) \right) \cdot \left(T_N / 293 \right)^{3/2}$ (Sutherland constant for hydrogen was taken as K_{Suth} = 72 K and the dynamic viscosity as $\mu_{293} = 8.76 \times 10^{-6}$ Pa s), and Re and Fr numbers are determined by parameters of hydrogen flow in the actual nozzle exit as $\mathrm{Re} = (\rho_N \cdot U_{N.} \cdot D) / \mu_N$ and . $Fr = U_N^2 / (g \cdot D)$

The form of the dimensionless group in the left hand side of Eq. (3.9) suggests that for subsonic flows, when M < 1, the dimensionless flame length depends only on the nozzle Mach number, since the density ratio ρ_N / ρ_S is, assuming constant temperature in the nozzle, effectively a constant for expanded jets (Molkov & Saffers, 2013). For choked flows (M = 1), the dimensionless flame length depends only on the hydrogen density in the nozzle exit ρ_N. The density increases with the increase of storage pressure and the decrease of temperature. The form of the right hand side of Eq. (3.9) indicates that at a constant temperature of hydrogen in the nozzle exit (that provides the constancy of the speed of sound C_N) the dimensionless flame length depends on both Re and Fr numbers, contradicting previous correlations built on Froude number only.

New correlation allows to identify three distinct parts (see Figure 3.9, from the left to the right): traditional buoyancy-controlled, traditional momentum-dominated "plateau" (expanded jets), and new momentum-dominated under-expanded jet fire "slope" part. These three parts can be approximated by the following equations (conservative curves) respectively

$$L_F / D = 1403 \cdot X^{0.196} \text{ for } X = \frac{\rho_N}{\rho_S}\left(\frac{U_N}{C_N}\right)^3 < 0.0001;$$

$$L_F / D = 230 \text{ for } 0.0001 < X = \frac{\rho_N}{\rho_S}\left(\frac{U_N}{C_N}\right)^3 < 0.07; \quad (3.10)$$

$$L_F / D = 805 \cdot X^{0.47} \text{ for } X = \frac{\rho_N}{\rho_S}\left(\frac{U_N}{C_N}\right)^3 > 0.07.$$

There is a saturation of L_F / D for expanded jet fires as the flow velocity in the actual nozzle exit is approaching the speed of sound. The value of this saturation limit L_F / D = 230 reproduces results of a number of previous studies with expanded jets, though in the new coordinates. However, there is no saturation of the dimensionless flame length for choked under-expanded jet flames. Reported in recent under-expanded jet fire experiments (Proust et al., 2011) values are significantly higher compared to the limit L_F / D = 230 – up to and above L_F / D = 3000, indicating that the previous assumption of momentum dominated flame length is constant is incorrect.

In the new correlation, three distinct regimes of jet fires are identified, changing from traditional buoyancy-controlled at low values of dimensionless group $(\rho_N / \rho_S) \cdot (U_N / C_N)^3$, to traditional momentum-dominated "plateau" at moderated values, and finally to momentum-controlled under-expanded jet fire regime at higher values of $(\rho_N / \rho_S) \cdot (U_N / C_N)^3$.

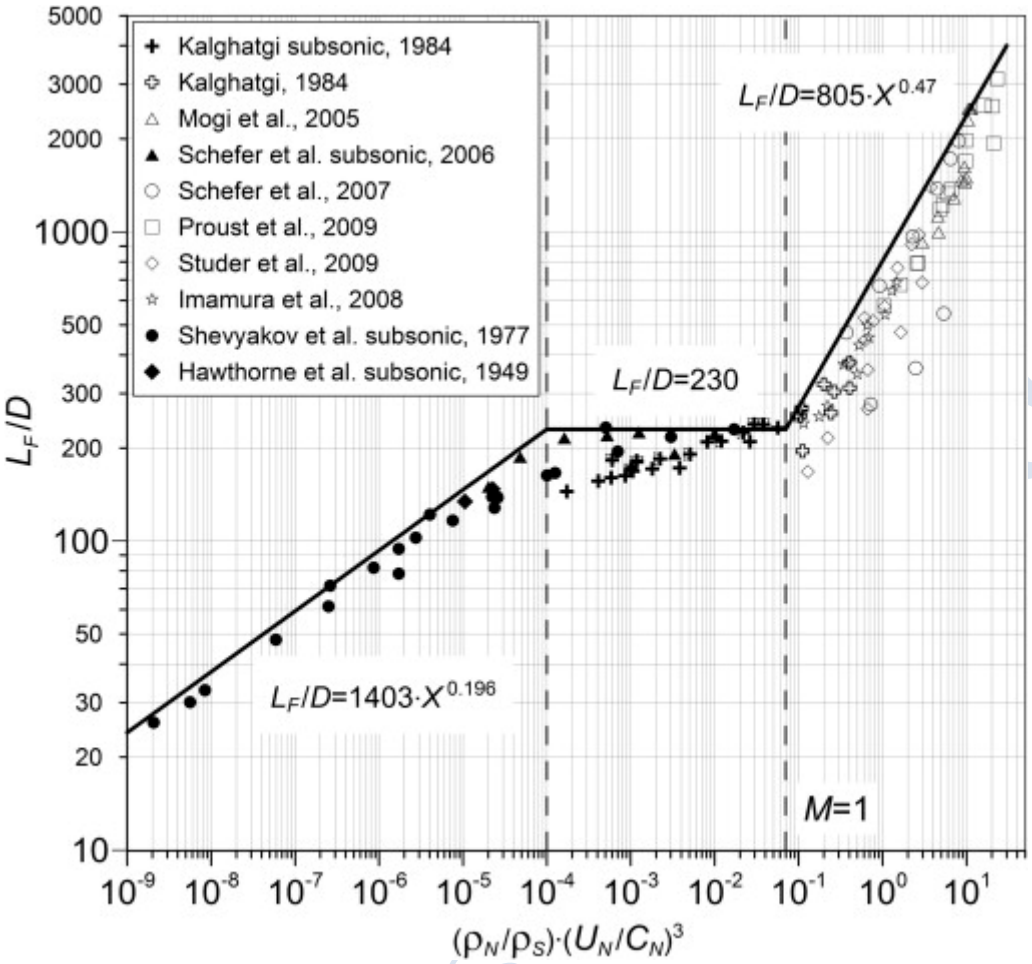

Figure 3.9. The dimensionless correlation for hydrogen jet flames (in formulas "*X*" denotes the similarity group $((\rho_N/\rho_S)\cdot(U_N/C_N)^3$ (Molkov & Saffers, 2013).

The shape of data in Figure 3.9 has a physical meaning based on the knowledge of jet flame behaviour. For example, the dimensionless flame length, L_F/D, increases for laminar and transitional flames (usually identified as "buoyancy-controlled" regime, low Re), then it is practically constant for transitional and fully developed turbulent expanded flames ("momentum-dominated" regime, moderate Re), and it increases again for under-expanded jets (higher Re). The last is due to the fact that the dimensionless flame length is defined through the actual nozzle exit diameter, which is a constant, while in reality the under-expanded jet expands to atmospheric pressure at the notional nozzle exit which increases with increase of density in the nozzle.

Figure 3.10 demonstrates changes of dimensionless numbers Re, Fr, M (for the experiments used for the development of the dimensionless correlation) as a function of the similarity group $(\rho_N/\rho_S)\cdot(U_N/C_N)^3$. The analysis of Re, Fr, M functional dependence on the similarity group shows that for under-expanded jets the dimensionless flame length growth depends practically on Re only. Indeed, the nozzle flow for under-expanded jets is choked, i.e. local M = 1, and the nozzle Fr number is practically constant also (the scattering of Fr is due to difference in nozzle diameters of about one order of magnitude).

There are five dashed thick lines in Figure 3.10. Line Re = 2000 indicates the start of transition from laminar to turbulent nozzle flow. Close to (or immediately above) this line there are experimental points with laminar jet flames and jet flames in the transitional regime.

Horizontal line M = 1 indicates a choked flow limit. Subsonic expanded jets have M < 1 and sonic and supersonic (relevant to flow in the notional nozzle) under-expanded jets have M = 1 in the nozzle exit. There is some scattering of data around M = 1 due to experimental data and data processing errors. Horizontal line Fr = 10^6 is an approximate division between buoyancy-controlled (Fr < 10^6) and momentum-dominated (Fr > 10^6) jets established previously for expanded jets.

Vertical line at a value of the similarity group $(\rho_N / \rho_S) \cdot (U_N / C_N)^3 = 0.0001$ conditionally separates buoyant jet fires (to the left from the line) and momentum jet fires (to the right from the line). Finally, vertical line denoted M = 1 divides subsonic (to the left) and sonic or chocked (to the right) jets in the nozzle exit.

In log–log coordinates used in Figure 3.10, Froude number increases linearly with the similarity group $(\rho_N / \rho_S) \cdot (U_N / C_N)^3$ for expanded jet fires. There is practically no change of Fr for under-expanded jets in this system of coordinates (scattering is mainly due to difference in nozzle sizes). There is a slight growth of Re with the similarity group for buoyant jets, moderate increase in traditional momentum-dominated area, and comparatively steep growth of Reynolds number in the area of under-expanded jet fires that are all momentum-dominated.

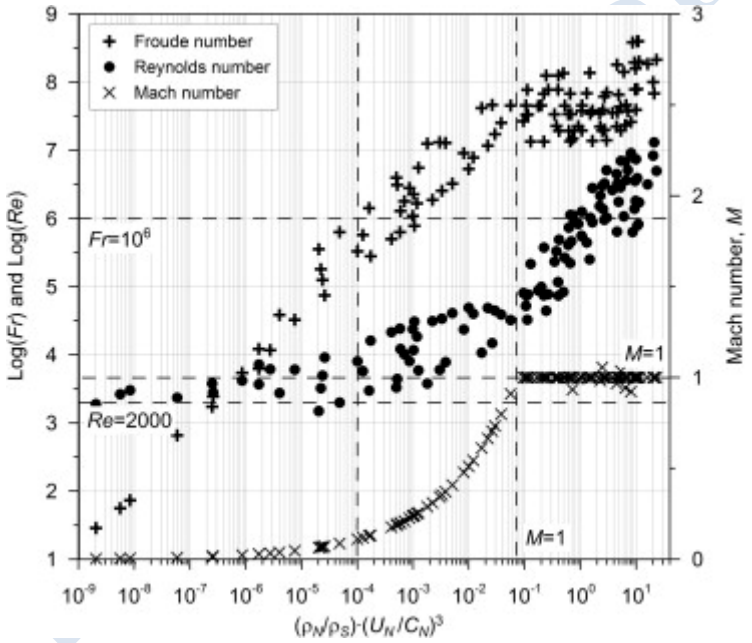

Figure 3.10. Dimensionless numbers *Re*, *Fr*, *M* as a function of the new similarity group for experiments used to build the dimensionless correlation.

Effect of nozzle shape on flame length

The effect of the nozzle shape on hydrogen flame length and width was experimentally investigated by Mogi & Horiguchi (2009). Experiments were carried out at the release pressure of 40 MPa, ensuring that the reacting flow was in the momentum-dominated regime.

The measured flame lengths and widths are presented in Figure 3.11 (Mogi & Horiguchi, 2009). For plane nozzles the flame length is approximately twice shorter than for the round nozzle of the same cross-section area, whereas the maximum flame width is approximately twice wider than that for the round nozzle.

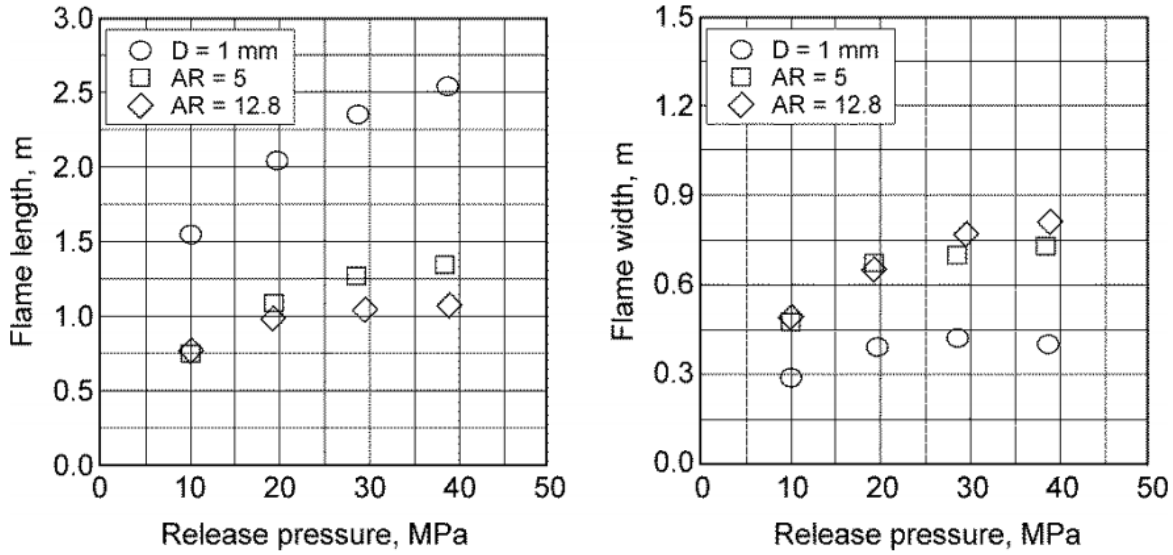

Figure 3.11. Flame length (left) and flame width (right) for three different nozzles of the same cross -section area: round nozzle of 1 mm diameter, plane nozzle with aspect ratio AR=5, plane nozzle with AR=12.8 (Mogi & Horiguchi, 2009).

Effect of jet attachment on flame length

It is known from fire safety science that the flame length of fire increases when the fire source is attached to wall. The effect is even stronger if the same fire is placed in a corner. The phenomenon is explained by the change in the air entrainment rate.

Royle & Willoughby (2009) measured the increase of the flame length due to attachment to ground. In these experiments hydrogen was released horizontally from storage at 20.5 MPa through nozzles of various diameters listed in Table 3.1.2.1 and ignited producing jet fire. For the free jet series of experiments the nozzle was located 1.2 m above the ground, while for the attached jet series the nozzle located only 0.11 m above the ground.

The increase of the flame length due to the jet attachment is apparent from the Table 3.1. It can be noted that the effect of jet flame attachment on its length growth decreases with the increase of the nozzle diameter. This can be explained by the change of air entrainment conditions, as well as the effect of momentum losses of the high velocity jet on the surface due to nonslip conditions.

Table 3.1. Free and attached jet flame length comparison (Royle & Willoughby, 2009).

D (mm)	Free jet flame length (m)	Attached jet flame length (m)
1.5	3	5.5
3.2	6	9
6.4	9	11
9.5	11	13

3.1.3 Impinging jets (HSL) – DONE

3.1.3.1 Introduction

In the context of hydrogen installations, and in particular hydrogen refuelling stations, an impinging fire could result from an ignited jet impacting upon an object, such as a process vessel. This may result in a number of consequences:

- Displacement of the object hit by a high momentum jet release
- Ablation of any passive fire protection material (if present)
- Vessel failure due to high temperatures and/or thermal expansion
- Boiling Liquid Evaporating Vapour Explosion (BLEVE) due to evaporation of flammable liquid within the vessel leading to vessel failure and ignition

To protect against impinging jet fires, barriers in the form of metal sheets, brick or breeze block walls are sometimes used. The effectiveness of these barriers against ignited high pressure releases were investigated experimentally in the HyPer project (Hyper project). Similar experiments have also been performed by Sandia National Laboratories in the USA (Diop et al., 2008). One of the findings of these experiments was that the barrier could in fact increase the radiative heat transfer received by an object depending on the angle of the wall/barrier, distance and height of the release point in relation to the barrier.

The behaviour of high-pressure, impinging jets is complex and challenging to model using CFD. The following processes are involved:

- Fluid flow
- Combustion
- Convective heat transfer from the flame to the surface of the object
- Conductive heat transfer (both through the fluid and the solid object)
- Radiative heat transfer within the flame and between the flame and its surroundings.

The following sections review flow behaviour and turbulence modelling approaches:

In a high-pressure gas release, close to the jet exit the under-expanded jet may feature complex shock structures, such as oblique and normal shockwaves. To model this behaviour accurately using CFD requires a fine mesh resolution and short time steps. The turbulence model may also need to be modified to account for compressibility effects (Sarkar & Lakshmanan, 1991). When the jet impacts upon the solid surface there is a stagnation point and strong streamline curvature. Within this region, turbulence is generated from high normal strain rates (rather than shear strain rates). Standard turbulence models that assume turbulence to be in local equilibrium therefore generally do not perform well.

Often the flow behaviour close to jet exit within the under-expanded region is not of great interest. Instead, the main focus of the study may be to understand the effect of the jet impinging on the obstacle. In such cases, rather than to resolve the complex near-field flow behaviour, a pseudo-source approach can be used. The region between the jet exit and the point where the pressure has fallen to reach atmospheric pressure is then not simulated. Instead, a new jet inlet is applied in the CFD model a short distance downstream from the actual jet exit. The flow conditions at this new inlet are calculated from empirical correlations (see, for example: (Birch et al., 1984, 1987; Ewan & Moodie, 1986; Houf & Schefer, 2007)). There are a number of advantages of the pseudo-source approach. A coarser mesh resolution

can be used with larger time steps thus leading to shorter computer run times. It may also be unnecessary to apply corrections for compressibility effects to the turbulence model.

There are various options available to account for the effect of turbulence in the flow downstream from the under-expanded region. The two main types of approach involve Reynolds-Averaged Navier-Stokes (RANS) or Large Eddy Simulation (LES) models.

RANS models range in complexity from simple algebraic expressions to complex Reynolds stress transport models (RSTMs) that involve the solution of seven or more transport equations. For industrial flow applications, the most popular RANS models are the two-equation k-ε , k-ω and SST models.

The standard k-ε model (Launder & Spalding, 1972; Jones & Launder, 1972) is known to produce poor predictions in impinging jets. The problems are particularly acute when the low Reynolds number variant of the model is used (Launder & Sharma, 1974), where a fine near-wall grid is needed to resolve the flow behaviour close to the wall surface. This weakness stems from the fact that the model assumes the production of turbulence energy to be proportional to the strain rate squared ($Pk \propto S^2$), whereas in reality it is proportional to the strain rate at the stagnation point ($Pk \propto S$). As a consequence, the k-ε model over-predicts the turbulence energy, which leads to excessively high predictions of heat transfer at the stagnation point.

Various corrections have been proposed to overcome this problem. The “Yap” correction (Yap, 1987) and differential length-scale correction of Iacovides & Raisee (1997) both help to decrease the turbulent kinetic energy, but the predicted heat transfer rate may still be over-predicted by a factor-of-two at the stagnation point. An alternative solution was proposed by Durbin (1996), who proposed a realizability limit on the turbulence time-scale ($T = k/\varepsilon$). Abdon & Sundén (2001) showed that this correction improves heat transfer predictions when used in conjunction with a k-ε model in impinging jet flows. Behnia et al. (1997, 2005) also demonstrated that it performs well with the four-equation v^2-f turbulence model

The Shear Stress Transport (SST) model (Menter, 1992, 1994) is a hybrid turbulence model that uses the k-ω model (Wilcox, 1988, 2006) in near-wall regions and the k-ε model elsewhere in the flow domain. It was shown to accurately predict the heat transfer in impinging jets well by (Vieser et al., 2004).

A slightly dated but informative comparison of the relative performances of different turbulence models was produced by Zuckerman & Lior (2006) (see

Table 3.2). They suggested that the SST model or the v2-f model, while not perfect, offered the best compromise between accuracy and computational effort.

Table 3.2. Comparison of turbulence models used for modelling impinging jet heat transfer (Zuckerman & Lior, 2006).

Turbulence model	Computational cost	Impingement jet transfer coefficient	Ability to predict second peak
k-ε	****[3] Low	* Poor; Nu error 15-60%	* Poor
k-ω	**** Low-moderate	** Poor-fair; expect errors to be at least 10-30%	** Fair; may predict incorrect location or magnitude
Realizable k-ε and other variants	**** Low	** Poor-fair; expect errors to be 15-30%	** Poor-fair; may predict incorrect location or magnitude
Algebraic stress transport model	**** Low	** Poor-fair; expect Nu error to be at least 10-30%	* Poor
Reynolds stress transport models	** Moderate-high	* Poor; anticipate Nu error to be 25-100%	** Fair
Shear stress transport (SST)	*** Low-moderate	*** Anticipate Nu error to be 20-40 %	** Fair
v^2-f	*** moderate	**** Excellent; Nu error between 2–30 %	**** Excellent
DNS/LES	* Very High	**** Good-excellent	**** Good-excellent

The use of LES models to simulate impinging jets involves significantly greater computing resources than for RANS models. An early example of LES being used to simulate heat transfer from a hot jet to a wall is the work by Hällqvist (2006), who used an implicit LES approach without a sub-grid scale (SGS) model and without explicit filtering. Hällqvist (2006) found that the shape of the mean inlet velocity profile had a significant influence on the model predictions, whereas the characteristics of the turbulent fluctuations imposed on the

[3] The number of stars indicates the level of suitability of a model's characteristics for modelling impinging jet heat transfer; more stars indicate greater suitability. The size of the error in the calculated Nusselt number comes from Zuckerman and Lior (2006).

inlet profiles had only secondary effects. The best approach to create the jet inlet profiles involved using a precursor pipe flow simulation.

More recently, (Bovo, 2011) modelled heated jets impinging on a flat plate using three different approaches: i) steady RANS (standard k-ε and v2-f models), ii) Detached Eddy Simulation (i.e. a blend of LES with a near-wall RANS model), and iii) LES. The best agreement between the calculated and measured heat transfer was achieved with the v2-f model.

In addition to the choice of turbulence model, the choice of wall treatment can have a significant impact on the accuracy of CFD model predictions in impinging flows. Standard wall functions typically assume zero pressure-gradient, wall-parallel flow, which can lead to poor predictions in impinging flows where the boundary layer is not in equilibrium. This issue was investigated by Craft et al. (2004), who compared a standard log-law wall function to an alternative embedded-grid wall function and a boundary-layer resolving approach in an impinging jet flow. The heat transfer rate was predicted poorly using the standard wall function. Good results were obtained by both the embedded-grid wall function and the boundary-layer resolving approach with a non-linear version of the *k-ε* model.

3.1.3.2Combustion

There are a number of CFD combustion models of different degrees of complexity. The popular Eddy Dissipation Concept (EDC) model (Magnussen & Hjertager, 1977) is based on the Eddy BreakUp (EBU) model originally proposed by Spalding (Spalding, 1971, 1977). Various refinements have been made to the original EDC model by (Magnussen, 1981; Byggstøyl & Magnussen, 1985; Ertesvåg & Magnussen, 2000), and it has been shown to provide a good compromise between accuracy and affordability for a number of different non-premixed flames.

Johnson et al. (1999) modelled some of the propane and natural gas jet fire tests that were performed in Phase 2 of the Blast and Fire Topside Structures (BFETS). The simulations resolved the barrel region hence a fine mesh and short time steps were required. In the case of the propane jet fires, the impinged object was located just beyond the lift-off height of the flame. It was found that a modified version of the premixed laminar flamelet combustion model proposed by Gu, (1993) gave the best agreement with the experiments for the lift-off region of the flame. However, Johnson et al. (1999) also reported that the non-premixed combustion model, laminar flamelet with a ß–Probability Density Function, also provided accurate predictions for the bulk of the flame. It is important to note the some of the model constants were adjusted for the different combustion models. A Monte Carlo radiation model was used and the absorptivity and emissivity was calculated using a wide-band model. Comparison of calculated and measured received radiative heat flux on an impinged vertical flat surface in a propane jet fire showed that the calculated fluxes were considerably lower for many of the radiometer locations.

Modelling of under-expanded hydrogen jet flames impinging on walls and barriers were carried out in the HyPer project, in which the calculated temperatures and heat fluxes were compared against experiments carried out by Sandia National Laboratories and University of Alabama. Information on these tests can be found on the HyPer project website[4] and in the paper by Diop et al. (2008).

[4] http://www.hyperproject.eu/, accessed 24 July 2014.

Further information on best practice CFD modelling of under-expanded jets, impinging jets and combustion can be found on the online ERCOFTAC Knowledge Base[5].

3.1.4 Flame lift-off and blow-off phenomena (UU)

A turbulent jet diffusion flame with a sufficiently low release rate will stabalise on the orifice. If the fuel flow rate is increased, eventually a critical exit velocity will be exceeded and the jet flame will detach from the orifice and re-stabilize at some axial distance downstream. This phenomenon is known as flame lift-off and the critical exit velocity at which it occurs is called the lift-off velocity.

A number of studies, such as Muñiz & Mungal (1997) and (Watson et al., 2000, 2003; Watson, Lyons, Carter, et al., 2002; Watson, Lyons, Donbar, et al., 2002), have investigated stable lifted flame reaction zone structures that settle at moderate downstream positions. If the flow rate continue to increase, the reaction zone moves further downstream and eventually it enters a region that can no longer support combustion due to the low fuel concentration. This condition is known as flame blow-out or blow-off and it leads to flame extinction. The blow-off condition has been investigated by (Kalghatgi, 1981; Pitts, 1989a; Coats, 1996; Chao et al., 2000, 2004).

Flame stability, therefore, is usually characterized by lift-off velocity, lift-off height, and blow-out velocity. The lift-off velocity is defined as the mean jet velocity at which the flame becomes detached from the jet exit rim. If the jet velocity is further increased, the flame moves downstream to a position where it stabilizes. Lift-off height is the distance between the lifted flame base and the jet exit. When the jet velocity reaches the blow-out velocity, the reaction cannot be sustained and the flame is extinguished. For positions between the jet exit and the flame base, a turbulent mixing region exists which is very similar to that for the unignited jet. The stability limits of turbulent jet diffusion flames are important for operation of combustion systems and have safety implication for handling combustible fuels. The lift-off and blow-out behaviours of the turbulent jet diffusion flames have been the subject of numerous research efforts.

The flame lift-off phenomenon has been investigated by many investigators, including (Scholefield & Garside, 1948; Wohl et al., 1948; Hottel & Hawthorne, 1949; Peters & Williams, 1983; Broadwell et al., 1985; Takahashi et al., 1985; Birch & Hargrave, 1989; Dahm & Dibble, 1989; Pitts, 1989a; Yoon et al., 1994). A review of these works is provided in Peters (2000). The most successful theories to explain the lift-off and blow-off phenomena and predict the lift-off height are the premixed flame propagation models, treating diffusion flames as being premixed at the base of the lifted flame, based on the studies of the structure of the lifted diffusion flame by Vanquickenborne & van Tiggelen, (1966). Jet fire lift-off and stabilization research utilizing this approach include works carried out by (Brzustowski, 1980; Giinther et al., 1981; Kalghatgi, 1984; Broadwell et al., 1985; Pitts, 1989a,b, 1991), and in the context of flame stability, by Annushkin & Sverdlov (1979) and Hall et al. (1980). A characteristic of premixed flames is the existence of a flame velocity at which the flame propagates with respect to the unburnt mixture. In the diffusion flame mixing is considered to occur prior to onset of combustion, and the base of the diffusion flame is assumed to be stabilized by propagation of a turbulent premixed flame against the mean flow.

This approach is convenient for predicting lift-off heights and blow-off velocities. Under turbulent conditions, turbulent mixing can be calculated without combustion to obtain local

[5] http://www.ercoftac.org/products_and_services/wiki, accessed 24 July 2014.

average values for the mixture ratio, the flow velocity and the turbulence intensity and scale, which in turn provides a turbulent burning velocity (from measurements of premixed flames). Near the orifice, the average flow velocity exceeds the turbulent burning velocity. Further downstream a position is reached where these two velocities become equal, defining lift-off height. Increasing jet exit velocity increases the local average flow velocity and thereby causes the lift-off height to increase. At sufficiently high lift-off velocities the stabilization plane is so far downstream from the nozzle that the average concentration becomes fuel lean across the entire jet and the turbulent burning velocity sharply decreases. Blow-off then occurs as a consequence of either inability to satisfy the equality between flame and flow velocities or due to reaching a lower flammability limit (Peters & Williams, 1983).

The importance of the isothermal mixing process of the jet for jet fire lift-off phenomenon was emphasised by Pitts (1989a,b, 1991). The turbulent burning velocity has been one of the focus points of the premixed flame stabilization approach. Kalghatgi (1984) assumed that the ratio of burning velocity to laminar burning velocity was proportional to the square root of the local turbulence Reynolds number based on the integral length scale. He successfully correlated the experimental data for CH_4, C_2H_4, C_3H_8 and H_2 into a single formula. Studies by Broadwell et al. (1985) and Burgess & Lawn (1999) focused on the role of intermittence and large scale eddies associated with premixed combustion.

A number of researchers had questioned the assumption of quasi-premixed nature of flame in lift-off phenomenon (e.g., (Janicka & Peters, 1982), (Peters & Williams, 1983)). In the conditions of lifted diffusion flames to those of premixed flames it is implicitly assumed that mixing occurs at the molecular level since premixed turbulent flame-speed data assume uniform mixtures. Estimation of whether sufficient time is available for a fluid element of lifted diffusion flames to approach uniformity prior reaching the flame shows that it appears unlikely that sufficient amount of premixing on the molecular level can occur to justify the use of the premixed flame concept. Accordingly, Peters (1983) proposed an alternative approach in which it has been suggested that the lift-off as well as blow-out characteristics of turbulent jet diffusion flames can be explained in terms of the extinction of laminar flamelets. Byggstøyl & Magnussen (1985) considered extinction as the mechanism of stabilization as well, but focused on the smallest eddies in the flow, rather than strain caused by large scale structures. Like the model of Peters & Williams (1983), this theory assumes little premixing occurs before the fuel and air reach the flame zone a certain distance downstream of the jet exit. This assumption had been called into question by Pitts (1989a) based on the experimental results which indicate that the actual case may be more complicated, involving a significant degree of premixing at the leading edge ahead of the reaction zone. Subsequent work by Watson (1999) and Stårner et al. (1996) support this conclusion. Furthermore, Stårner et al. found that the base of lifted flames lies within the flammability limits and the maximum temperature gradients occur along the stoichiometric contour.

A number of theories have been developed to determine the mechanism controlling blowout. For turbulent flames, Broadwell et al. (1985) proposed that at the blowout velocity, the combustion ceases because there is not enough time for the ignition of incoming fuel/air mixtures by entrained hot products. This work and research by Miake-Lye & Hammer (1989) pointed to the primary role of large-scale structures in facilitating hot-product transport. Similarly, Dahm & Dibble (1989) applied a blowout parameter from Broadwell et al. (1985) for turbulent jets in coflow and showed that an increased coflow velocity decreased the jet blowout velocity. The blowout parameter, based on characteristic ignition time and mixing time ratios, was shown to correctly predict blowout trends. Han & Mungal (2000) focused

their explanations of blowout phenomenon on the inability of the reaction zone to counter-propagate against incoming reactants at blowout. Research performed by (Dahm & Mayman, 1990; Montgomery et al., 1998; Brown et al., 1999; Burgess & Lawn, 1999) addressed the related elements of flame blowout; further overview of research in blowout is contained in Chao et al. (2004). More recently, Wu et al. (2006) reported on lifted flames near blowout, with detailed comments on triple flames in the pulsating region, and describe a proposed mechanism of flame pulsation and blowout. Nevertheless, the mechanisms that cause jet-flame blowout, are still not completely understood and remain the area of active research.

The relation between flame blow-off and release pressure and orifice diameter has been investigated experimentally by Mogi & Horiguchi, (2009) and Okabayashi et al. (2007). The combustion states of the flame were investigated under various nozzle diameters and the release pressures of hydrogen. Figure 3.12 illustrates the boundaries of a region of flame blow-off in the "release pressure – nozzle diameter" space (Mogi & Horiguchi, 2009). It is seen that for the release pressure below critical, which is 1.9 times of the atmospheric pressure, the flame was found to be lifted, irrespective of the nozzle diameter.

The lower limit of the pressure for the blow-off is weekly dependent of the nozzle diameter. However, the upper limit for blow-off is strongly affected by both the release pressure and the nozzle diameter. The release pressure at the upper blow-off limit decreases with an increase of the nozzle diameter. For diameters 0.1-0.2 mm the blow–off occurred even in the cases where release pressure was increased up to 40 MPa and no self-sustained flames were observed. The flame blow-off became impossible for release nozzle diameters exceeding 1.5 mm at any pressures.

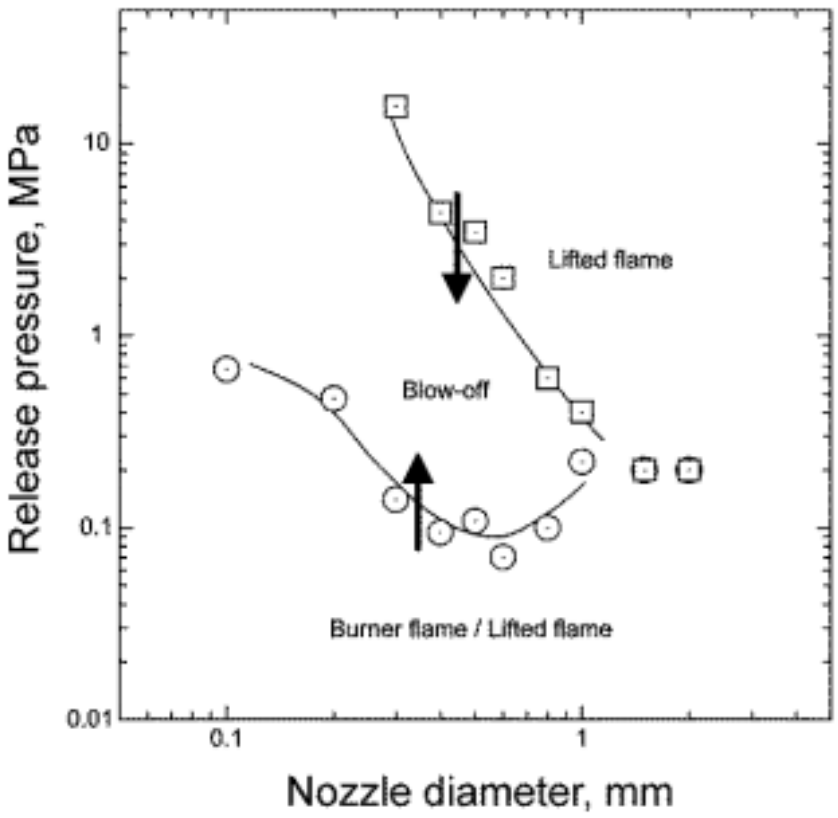

Figure 3.12. Hydrogen jet flame blow-off region as a function of different leak diameters and release pressures (Mogi & Horiguchi, 2009).

Figure 3.13 shows similar results by Okabayashi et al. (2007), illustrating the blow-off limits obtained with more experiments carried out at high pressures and small diameters. They confirmed that sustained jet flame become unachievable for the nozzles with diameters less than 0.1 mm even at very high release pressures.

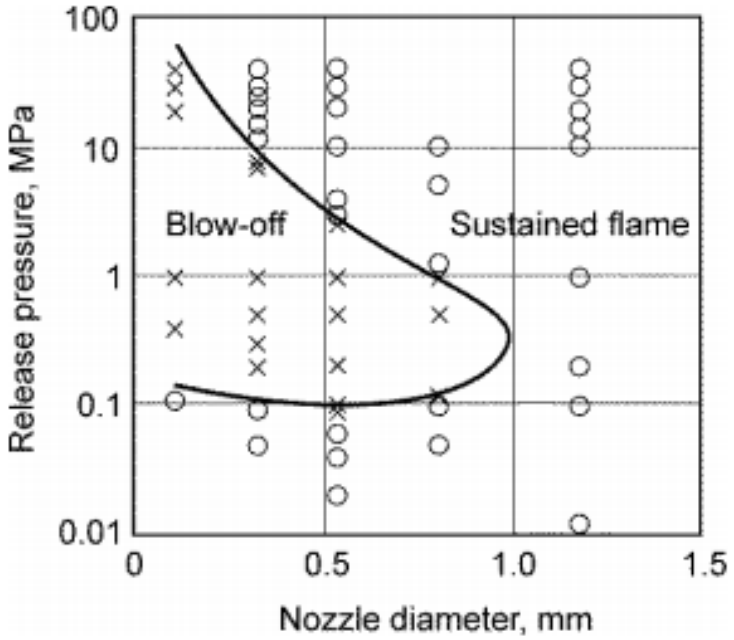

Figure 3.13. Regions of flame blow-off and sustained hydrogen jet flames(Okabayashi et al., 2007).

3.1.5 Fire in enclosure

The behaviour of a hydrogen fire in a vented enclosure depends on the hydrogen release rate and the size of the vent or vents. Three different regimes are possible: well-ventilated internal fire, under-ventilated internal fire (sometimes with exterior flames) and external fire. Numerical experiments (Molkov et al., 2014) show that for a fixed vent size increasing the hydrogen flow rate results in a transition from a well-ventilated internal fire, to an under-ventilated internal fire and then to an external fire.

Relatively low release rates in an enclosure with a relatively large vent result in a well-ventilated fire regime. Figure 3.14, (Molkov et al., 2014) illustrates the dynamics of a well-ventilated hydrogen jet fire (central cross-section area of the enclosure is shown). The vertical vent is located at the left wall. At the end of the numerical experiment the fire is in quasi-steady state conditions. Bottom left image in Figure 3.14 shows that there is a very slow depletion of the initial oxygen layer at the bottom of the enclosure, explained by the substantial intake of fresh oxygen from outside the enclosure through the lower part of the vent, sufficient to sustain the flame. Temperature contours (Figure 3.14, bottom right) confirm the presence of the layer at the bottom where the ambient temperature is maintained.

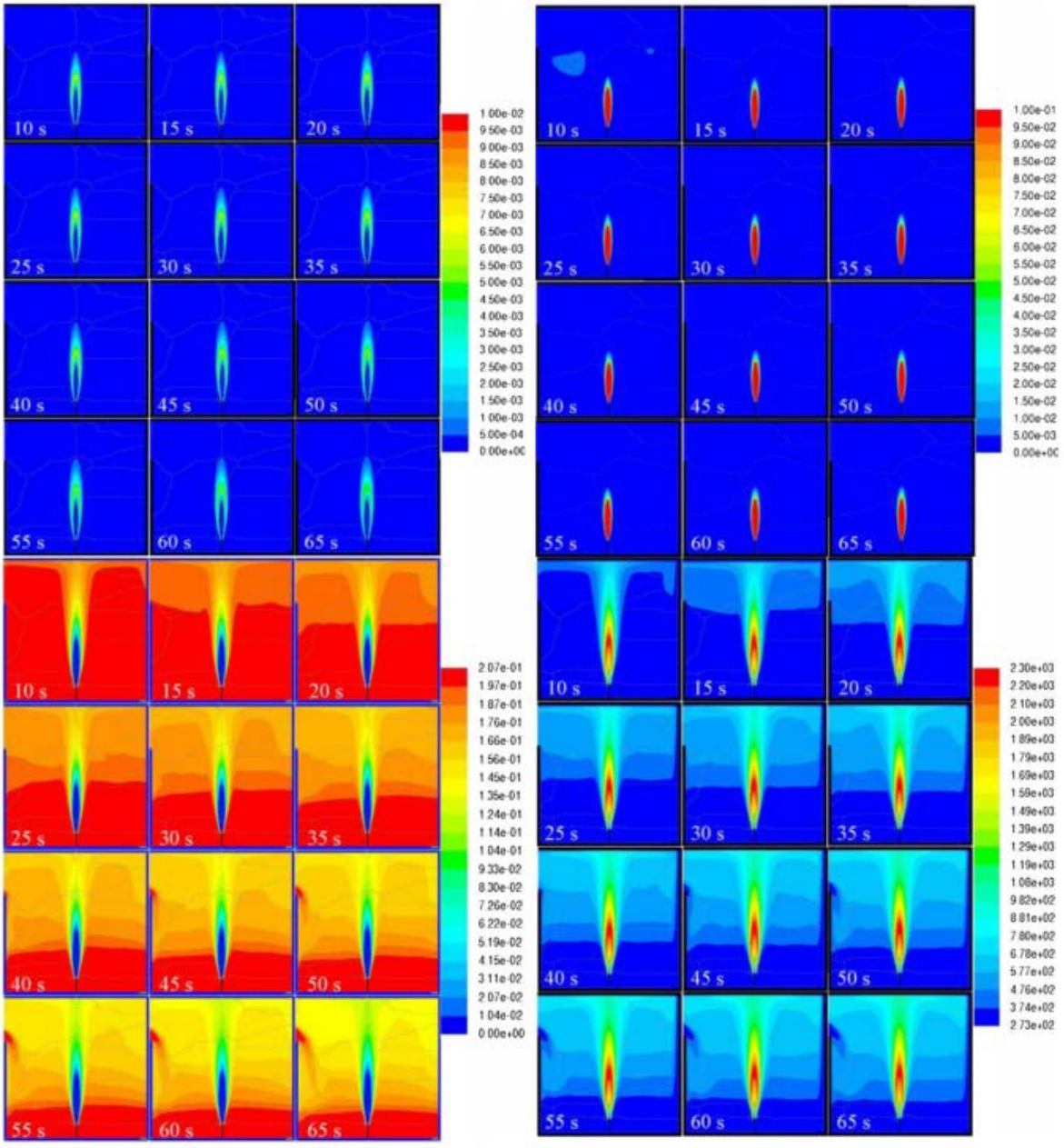

Figure 3.14 Mole fractions of OH (top left), H_2 (top right), O_2 (bottom left), and temperature (bottom right) on a 2D slice through the enclosure centre-line from a simulation of a well-ventilated fire (Molkov et al., 2014).

Figure 3.15 shows the transition from a well-ventilated internal jet fire to an under-ventilated internal jet fire with external flames from a simulation in which the hydrogen flow rate is gradually increased. At early times the fire is similar to the well-ventilated fire with hydroxyl mole fraction in the flame at 10 s equal to 0.01 which is characteristic for combustion at normal atmospheric conditions (not shown in Figure 3.15). The maximum OH mole fraction, however, quickly reduces along with shrinking of the zone where highest mole fraction of OH is present. This can be explained by the dilution of the jet flame by entrained combustion products. As the combustion rate inside the enclosure decreases after 20 s, the reaction zone starts to move out of the enclosure through the vent, setting an external flame which can be seen above the enclosure after 50 s. The two top pictures in Figure 3.15 clearly show that the

reaction ceases first on the jet flame side that is opposite to the vent which is located at the top of the left wall.

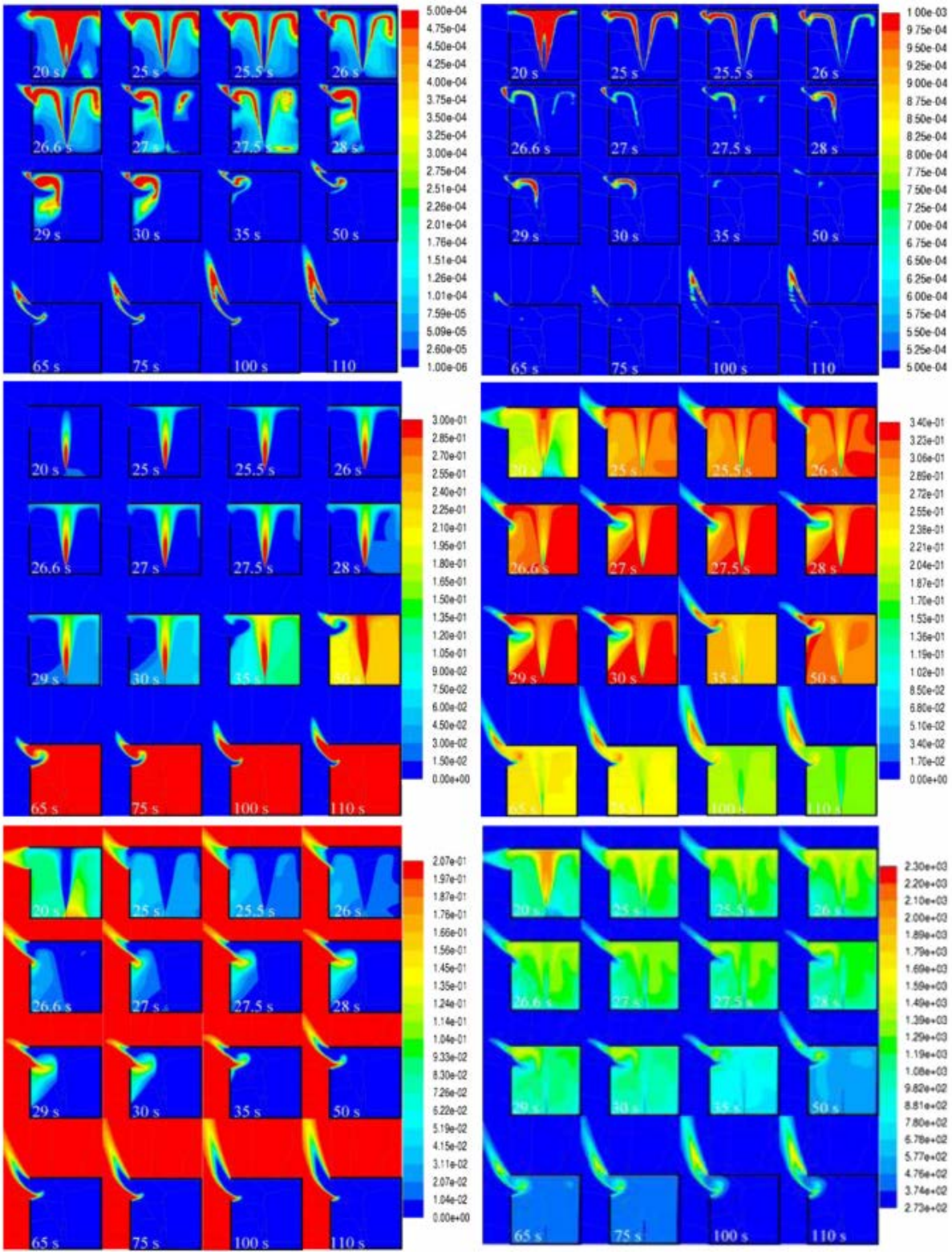

Figure 3.15. Mole fractions of OH in the range 1×10^{-6} ~ 5×10^{-4} (top left) and OH in the range 5×10^{-4} ~ 1×10^{-3} (top right), H_2 (middle left), H_2O (middle right), O_2 (bottom left) and temperature (bottom right) on a 2D slice through the enclosure centre-line from a simulation of an under-ventilated jet fire resulting in an external flame (Molkov et al., 2014).

Figure 3.15 (top left) demonstrates that there is a continuous reaction zone on both sides of the vent. This zone separates fresh air that is entering the enclosure from a mixture of hydrogen and combustion products that is flowing out of the enclosure. These two opposite direction flows through the vent create a reacting eddy that sits within the enclosure close to the vent and stabilises the lower flame edge. The upper edge of the external flame is attached to the top edge of the vent.

Further increase in hydrogen flow rate or reduction of the vent area results in the extinction of the flame inside the enclosure. The extinction of a hydrogen flame indoors was first studied by Molkov et al., (2013), who considered less effective horizontal vent. It was found that there is a period of time from 27.5 s to 70 s when the entire vent area is occupied by the flow of air into the enclosure. This is not the case for the transition to the external flame regime where the flow out of the enclosure, is always present.

3.2 Models (UU)

3.2.1 Governing equations for reacting flows (UU)

The governing equations for turbulent combustion flows may be expressed in different forms; however, they are normally represented as transport equations for conservation of mass, momentum and additional scalars that can be used to spatially and temporally resolve the thermodynamic state of the mixture (Echekki & Mastorakos, 2011). These equations are augmented by initial and boundary conditions, as well as constitutive relations for atomistic processes (e.g. reaction, molecular diffusion, equations of state). Therefore, in addition to density, transport equations for the evolving composition (e.g. mass or mole fractions, species densities or concentrations) and a scalar measure of energy (e.g. internal energy, temperature, or enthalpy) have to be solved as well. The following equations represent the compressible form of the instantaneous governing equations in non-conservative form for the mass density, momentum, species mass fractions and internal energy. A more detailed discussion on the various forms and their equivalence, especially for the energy equation can be found in the textbooks by Williams (1994) or Poinsot & Veynante (2011).

• Continuity

$$\frac{\partial \rho}{\partial t} + \nabla \cdot \rho \vec{u} = 0\,, \tag{3.11}$$

• Momentum

$$\rho \frac{D\vec{u}}{Dt} = \rho \frac{\partial \vec{u}}{\partial t} + \rho \vec{u} \cdot \nabla \vec{u} = -\nabla p + \nabla \cdot \tau + \rho \sum_{k=1}^{N} Y_k \vec{f}_k\,, \tag{3.12}$$

• Species continuity (k=1,⋯,N)

$$\rho \frac{DY_k}{Dt} = \rho \frac{\partial Y_k}{\partial t} + \rho \vec{u} \cdot \nabla Y_k = \nabla \cdot (-\rho \vec{V}_k Y_k) + \omega_k\,, \tag{3.13}$$

• Energy

$$\rho \frac{De}{Dt} = \rho \frac{\partial e}{\partial t} + \rho \vec{u} \cdot \nabla e = -\nabla \cdot \vec{q} - p \nabla \cdot \vec{u} + \tau \times \nabla \vec{u} + \rho \sum_{k=1}^{N} Y_k \vec{f}_k \cdot \vec{V}_k\,. \tag{3.14}$$

In the above equations, ρ is the mass density; $\vec{u}$ is the velocity vector; p is the pressure; $\vec{f}_k$ is the body force associated with the *k*-th species per unit mass; τ is the viscous stress tensor; $\vec{V}_k$ is the diffusive velocity of the *k*-th species, where the velocity of the k-th species may be expressed as the sum of the mass-weighted velocity and the diffusive velocity, $\vec{u}+\vec{V}_k$; ω_k is the *k*-th species production rate; *e* is the mixture internal energy, which may be expressed as $e=\sum_{k=1}^{N} h_k Y_k - p/\rho$; $\vec{q}$ is the heat flux, which represents heat conduction, radiation, and transport through species gradients and the Soret effect.

As can be seen, a number of terms in the governing equations are not explicitly expressed in terms of the solution vector and must rely on constitutive relations, equations of state or any additional auxiliary relations. These terms include expressions for the viscous stress, the species diffusive velocities, the body forces, the species reaction rate and the heat flux. The bulk of these terms have their origin in the molecular scales, and therefore, the role of constitutive relations is to represent them in continuum models. In fact, the use of constitutive equations is the first level of multi scale treatment for the modelling of turbulent combustion flows.

It should be noted that the appropriate choice of compressible or incompressible governing equations depends on the considered phenomena. Typically, open atmosphere fires or fires in a well-ventilated enclosure may be considered as incompressible (though with varying density) – flow velocities are low and pressure variations across the domain are too small to have an appreciable effect on the density, so the density may be considered as a function of temperature and species concentration only, and pressure may be taken as a constant (i.e. atmospheric pressure). However, for fires with significant pressure variations, compressibility effects may become significant and need to be taken into account. Examples include open atmosphere jet fires resulting from releases from a high-pressure hydrogen storage involving sonic and supersonic velocities and large pressure gradients near a nozzle, or fires in sealed compartments with a significant pressure rise.

3.2.2 Arrhenius (Finite rate chemistry) model (UU)

In laminar flows, it is possible to apply a finite-rate chemistry model which computes the chemical source terms using the approach of Arrhenius (1889). The laminar model is often acceptable for combustion with relatively slow chemistry and small turbulence-chemistry interaction, such as supersonic flames.

In the finite rate chemistry approach the source term for the chemical specie *i* produced or consumed in the reaction is computed as the sum of the Arrhenius reaction sources over the *N* reactions in which this species participates:

$$R_i = M_i \sum_{r=1}^{N_R} \hat{R}_{m,i,r}\,, \tag{3.15}$$

where M_i is the molecular weight of species *i*, N_R – is the number of reactions and $\hat{R}_{m,i,r}$ is the Arrhenius molar rate of creation/destruction of species *i* in reaction *r*.

Reversible reaction *r* can be written in general form as:

$$\sum_{i=1}^{N} \nu_i' S_i \underset{k_b}{\overset{k_f}{\Leftrightarrow}} \sum_{i=1}^{N} \nu_i'' S_i \,, \tag{3.16}$$

where S_i is symbol denoting species i, N - is the number of species participating in the reaction, ν_i' and ν_i'' are the stoichiometric coefficients for reactant and products of the reaction, respectively, and k_f and k_b are the forward and backward reaction constants. For non-reversible reactions $k_b = 0$.

The molar rate of species creation/destruction can be expressed as

$$\hat{R}_{i,r} = \Gamma(\nu''_{i,r} - \nu'_{i,r}) \left(k_{f,r} \prod_{j=1}^{N} [C_{j,r}]^{\eta'_{j,r}} - k_{b,r} \prod_{j=1}^{N} [C_{j,r}]^{\eta''_{j,r}} \right), \tag{3.17}$$

where, $\hat{R}_{i,r}$ is the molar rate of creation/destruction of species m in reaction r, N is the number of chemical species in the system; $\nu'_{i,r}$ is the stoichiometric coefficient for reactant i in reaction r; $\nu''_{i,r}$ is the stoichiometric coefficient for product i in reaction r; $k_{f,r}$ and $k_{b,r}$ are forward and backward rate constants for reaction r respectively; $C_{j,r}$ is the molar concentration of species j in reaction r; $\eta'_{j,r}$ and $\eta''_{j,r}$ are rate exponent for reactant species j and product species j in reaction r respectively. Γ represents the net effect of third bodies on the reaction rate and is equal $\Gamma = \sum_{j=1}^{N} \gamma_{j,r} C_j$, where $\gamma_{j,r}$ is the third body efficiency of j-th species in the r-th reaction. The rate constants for reaction r, $k_{f,r}$ and $k_{b,r}$ can be computed using the Arrhenius (1889) equation:

$$k_{f,r} = A_r e^{-E_r / RT} \,. \tag{3.18}$$

where A_r is the pre-exponential constant, E_r is the activation energy, R is the universal gas constant and T is the temperature.

This model is exact for laminar flames, but is generally inaccurate when applied to turbulent flames modelled using time averaged (RANS models) or space-filtered (LES models) approaches. Spalding (1971) reported that utilization of mean temperature values in this model often produces incorrect reaction rate results. This is due to highly non-linear Arrhenius chemical kinetics dependence on temperature, fluctuations that are not resolved with RANS or LES approaches.

Due to exponential dependence on temperature this model is mathematically stiff and typically requires very small time steps resulting in high computational costs. It is therefore usually restricted to relatively low Reynolds number small scale simulations, e.g. spontaneous ignition DNS simulations described in section 2.

3.2.3 Eddy Break-Up model (UU)

As mentioned above, the expression for the Arrhenius reaction rate cannot be used when turbulent flow is not resolved explicitly and any turbulence modelling approach (RANS or LES) is used. As a result, a turbulence combustion model should be used to simulate chemical reaction in turbulent flows.

The Eddy Break-Up (EBU) model is an example of a so-called “mixed is burned” turbulent combustion model, in which it is assumed that the chemical kinetics rates are much faster than the flow rates, and that the combustion rate therefore is limited by the turbulent mixing rate controlling delivery of fresh reactants to the reaction zone. In the EBU model, originally proposed by Spalding (1971), it is argued that since turbulent mixing can be viewed as a cascade process from integral length scales down to molecular length scales, as long as the mixing rather than the chemistry is controlling the reaction rates, the chemical reactions are also controlled by the turbulence cascade process (Peters, 2000). Turbulent combustion is therefore controlled by the supply of reactants carried by turbulent eddies. The chemical time scales can then be replaced by the turbulent time scale, and the reaction rate can be found based on the species concentration fluctuations and the rate of break-up of eddies, which can be expressed through the ratio of turbulence dissipation rate ε to the turbulence kinetic energy k (Mason & Spalding, 1973)

$$\bar{\dot{\omega}} = \rho C_{EBU} \frac{\varepsilon}{k} \left(\overline{Y''^2} \right)^{1/2}, \tag{3.19}$$

where C_{EBU} is the Eddy Break-Up constant and $\overline{Y''^2}$ is the variance of the product mass fraction.

This model was later generalized by Magnussen & Hjertager (1977), who proposed using mean concentrations of intermittent quantities instead of concentration fluctuations used in the original Spalding model. The model takes the minimum of three rates, calculated for the fuel, the oxidizer and the products. This version of the model became known as the Eddy Dissipation Model (EDM)

$$\bar{\dot{\omega}}_F = A_{EB} \frac{\varepsilon}{k} \min \left[\bar{C}_F, \frac{\bar{C}_O}{\nu}, B_{EB} \frac{\bar{C}_P}{(1+\nu)} \right], \tag{3.20}$$

where $\bar{C}_F$, $\bar{C}_o$ and $\bar{C}_p$ are the concentrations of fuel, oxygen and products, respectively, ν is the stoichiometric ratio and A_{EB} and B_{EB} are empirical constants with typical values of 0.5 and 4.0 respectively. The advantage of this formulation is that unlike Eq. (3.19) it does not require solving equations for the variance of the product mass fraction, $\overline{Y''^2}$. The dependence on the products concentration is introduced based on the assumption that without products the temperature would be too low for reactions to occur.

The advantage of the EBU and EDM models lies in the simplicity of their implementation and relatively low computational cost. Furthermore, due to their “mixed is burned” assumption, EBU type models usually do not require artificial ignition in order to initiate combustion, as the reaction starts as soon as the reactants mix (realisation of the model in some CFD codes may require none-zero concentration of combustion products as “ignition source”). It is therefore popular with engineering CFD models, particularly where large scale/long duration reacting flows need to be modelled, as the computational cost is often critical for these applications. This popularity leads to inclusion of EBU models, particularly the Magnussen & Hjertager (1977) formulation, in many commercial engineering software packages. The model

applicability is limited to the flows where the reactions are fast and the system can be considered to be purely mixing limited. The original EBU and EDM models are independent of chemical kinetics and this leads to their main limitation, namely their inability to model a full range of physical phenomena associated with fires where finite rate chemistry is also important, e.g., flame lift-off. The constants C_{EBU} (or A_{EB} and B_{EB}) are also found to require "tuning" within a wide range in order to obtain reasonable results for a particular problem (Peters, 2000).

In many studies the EBU model is used in an extended form, which allows for the use of finite rate chemistry

$$\overline{\dot{\omega}}_{F,r_j} = \min\left[A_{EB}\frac{\varepsilon}{k}\overline{C}_F, A_{EB}\frac{\varepsilon}{k}\frac{\overline{C}_O}{\nu_{r_j}}, \overline{\dot{\omega}}_{k,r_j} \right], \tag{3.21}$$

where $\overline{\dot{\omega}}_{k,r_j}$ is the kinetic reaction rate and r_j denotes the j^{th} reaction. This approach is suitable for modelling multistep reactions. Despite the limitations associated with using mean quantities in the calculation of the reaction rates, this form of the EBU model has produced encouraging results (Magel et al., 1995).

Many variations of the EBU model have subsequently been developed addressing specific types of problems, including, for example an extension developed by Naji et al. (1989)

$$\tilde{\omega} = C_{EBU}\frac{\varepsilon}{k}\left(1+\frac{4.4}{1+3.2\dfrac{k^{1/2}}{U_L}}\right)\tilde{Y}\left(1-\frac{\tilde{Y}}{\tilde{Y}^0}\right), \tag{3.22}$$

which takes into account difference between the movement of flamelets and the turbulence itself. Naji et al. (1989) have shown that the mean reaction rate strongly depends on the ratio of turbulent kinetic energy k to laminar flame velocity U_L (when $k^{1/2}$ is of the order of U_L, i.e., when the reaction rate is defined not only by the turbulence, but also influenced by flamelets properties, which are related to U_L. In the limit when $k^{1/2} >> U_L$ the extended model is reduced to the classic Eddy-Break-Up model, i.e., this model can be regarded as an extension of the EBU model for flames with lower turbulence intensities. This model had been successfully used by Kotchourko et al. (1999) for hydrogen flame modelling.

An example of the EBU model being applied to hydrogen fire modelling can be found in Makarov & Molkov, (2013) who used it in conjunction with a RANS turbulence model to simulate large-scale round and planar hydrogen jets fires. The EBU combustion model of Magnussen & Hjertager, (1977) was used to model combustion. The hydrogen source term (mass burning rate per unit volume) was modelled as

$$S_{H_2} = -C\overline{\rho}\frac{\overline{\varepsilon}}{k}\min\left\{\tilde{Y}_{H_2}, \frac{\tilde{Y}_{O_2}}{\nu}\right\}, \tag{3.23}$$

where C = 4.0 is an empirical coefficient, Y_{H_2} is the mass fraction of hydrogen, Y_{O_2} is the mass fraction of oxygen and ν = 8.0 is the stoichiometric coefficient for hydrogen–oxygen reaction. The primary focus of Makarov & Molkov (2013) was the prediction of the axisymmetric and plane turbulent non-premixed flame lengths. Due to its mixed is burned assumption, the EBU combustion model is unable to predict lift-off of turbulent flames and it was therefore necessary to neglect the effect of lift-off on the jet flame length. Experimental works, however, indicated that the impact of lift-off on the jet flame length for the conditions considered in Makarov & Molkov, (2013) is insignificant. Indeed, the lift-off distance of hydrogen flames was found to be less than 0.08 m (Mogi et al., 2005), while the length of experimental jet fires in (Mogi & Horiguchi, 2009) was in the range 1.0 m to 2.6 m.

3.2.4 Linear Eddy Model (UU)

The Linear Eddy Model (LEM) was first developed by Kerstein (1988). LEM is a method of simulating flame structure through the molecular mixing in a one-dimensional domain embedded in a turbulent flow. In the Linear Eddy approach various physical processes, such as advection, mixing, diffusion and chemical reactions are resolved on their relevant length and time scales.

In every computational cell a molecular, diffusion and chemical model is defined as

$$\frac{\partial}{\partial t}(\rho Y_k) = \frac{\partial}{\partial \eta}\left(\rho D_k \frac{\partial Y_k}{\partial \eta}\right) + \dot{\omega}_k , \tag{3.24}$$

where η is a spatial coordinate. The scalar distribution obtained can be seen as a one-dimensional reference field between Kolmogorov scale and grid scales.

In a second stage a series of re-arranging stochastic events take place.

The model is based on the following assumptions: 1) small scale turbulence is locally homogeneous and isotropic; 2) the effect of heat release and the associated thermal expansion of the flow is the same in all directions.

The resolution within a 1-D domain is chosen to resolve all scales down to the Kolmogorov and reaction-diffusion mechanism scales.

These events represent the effects of a certain turbulent structure of size *l*, smaller than the grid size at a location η_0 within the one-dimensional domain. This vortex distort the η field obtain by the one-dimensional equation, creating new maxima and minima in the interval $(\eta_0, \eta + \eta_0)$. The vortex size *l* is chosen randomly based on the inertial scale range while η_0 is obtained from a uniform distribution in η. The number of events is chosen to match the turbulent diffusivity of the flow.

LES-LEM approach

In the LEM model (Kerstein, 1988, 1989, 1991a,b) the various physical processes, such as large scale advection, small scale mixing, molecular diffusion and chemical reaction are resolved at their relevant length and time scales. The basic premise of using LEM in LES is that the scalar field evolution can be split into two parts (Sankaran et al., 2004): large scale advection and turbulent stirring at the small scale, where the terms “large scale” and “small scale” are defined with respect to the LES filter size. Physical processes such as molecular diffusion, chemical reactions and the volumetric heat release are small-scale processes

occurring locally within each LES cell. A reduced one-dimensional reaction-diffusion equation is solved inside each LES cell with a resolution time fine enough to resolve all turbulent scales between the filter (grid) size and the Kolmogorov scale η. Sub-grid reaction-diffusion process is, therefore considered locally exact and the finite-rate kinetics can be included in exact form without requiring any closure. Furthermore, molecular diffusion is also included in an exact manner, which is important for predicting turbulent combustion, particularly for reaction involving hydrogen (Genin et al., 2003).

Unfiltered reactive scalar Φ evolution can be written in the Eulerian form as

$$\rho\frac{\partial\Phi}{\partial t}+\rho u_i\frac{\partial\Phi}{\partial x_i}+\rho\frac{\partial}{\partial x_i}\left[-D_\Phi\frac{\partial\Phi}{\partial x_i}\right]=\dot{\omega}_\Phi\,. \tag{3.25}$$

In this equation the second term on the left hand side represents total (both large and small scale) convection, the third term on the left hand side represents the molecular diffusion and the term on the right hand side represents the source term describing chemical reactions.

u_i can now be split into the contributions of resolved (large) and sub-grid (small) scales (Genin et al., 2003)

$$u_i=(\bar{u}_i+u_i')\,. \tag{3.26}$$

(3.2.4.3)

Dividing convection into large and small-scales and grouping molecular diffusion and chemical reaction with small scale processes, Eq. (3.25) can now be split into two equations:

$$\rho\frac{\Phi^*-\Phi}{\Delta t_{LES}}+\rho\bar{u}_i\frac{\partial\Phi}{\partial x_i}=0\,, \tag{3.27}$$

and

$$\rho\frac{\partial\Phi^*}{\partial t}+\rho u_i'\frac{\partial\Phi^*}{\partial x_i}+\rho\frac{\partial}{\partial x_i}\left[-D_\Phi\frac{\partial\Phi^*}{\partial x_i}\right]=\dot{\omega}_\Phi\,, \tag{3.28}$$

representing three-dimensional large-scale processes and small-scale processes respectively. Δt_{LES} here is the fluid dynamics/acoustic LES time-step and Φ^* is the intermediate solution of the large-scale convection processes. Together, Eqs. (3.27) and (3.28) account for complete evolution of the scalar fields.

Small-scale Eq. (3.28) is solved within each LES cell on a 1-D line segment, referred to as LEM domain. For the species and the temperature, the reaction-diffusion Eq. (3.28) written in non-conservative form become

$$\rho\frac{\partial Y_k}{\partial t}+u\frac{\partial Y_k}{\partial s}+\rho\frac{\partial}{\partial s}\left(-D_k\frac{\partial Y_k}{\partial s}\right)=\dot{\omega}_k M_k\,, \tag{3.29}$$

and

$$\rho c_p\frac{\partial T}{\partial t}+u\frac{\partial T}{\partial s}-\sum_{k=1}^{N}\rho c_{p,k}D_k\left(\frac{\partial Y_k}{\partial s}\right)\left(\frac{\partial T}{\partial s}\right)-\frac{\partial}{\partial s}\left(k\frac{\partial T}{\partial s}\right)=-\sum_{k=1}^{N}h_k\dot{\omega}_k M_k\,, \tag{3.30}$$

respectively. Here Y_k, M_k, $c_{p,k}$, h_k, D_k and $\dot{\omega}_k$ are the mass fraction, the molecular weight, the specific heat at constant pressure, the enthalpy, the mixture averaged diffusivity, and the mass reaction rate of the *k*-th specie, respectively. T and ρ in the Eq. (3.30) are sub-grid temperature and mass density, respectively, *k* is the mixture thermal conductivity, c_p is the mixture averaged specific heat at constant pressure and *s* is the coordinate direction of 1-D domain. The orientation of the 1-D domain is typically chosen to align with the direction of maximum scalar gradient (Kerstein, 1989). The length of the 1-D domain is taken to be equal to that of the local LES filter width.

The effect of the sub-grid velocity field (second terms in Eqs. (3.29) and (3.30)) on the sub-grid scalar fields are modelled using stochastic re-arrangement events called triplet maps (Kerstein, 1989). Each triplet map represents the action of an isotropic turbulent eddy on the sub-grid scalar field. Figure 3.16 illustrates the rationale behind the triplet map approach. Consider a mixing layer configuration shown in Figure 3.16 (top) with a plane material surface separating specie A from specie B. The bold straight line running from the top to the bottom shown in the box (dashed line) represents the initially uniform concentration gradient. Straight vertical lines represent the concentration isopleths at the initial time. Figure 3.16 (bottom) shows the distortion caused by stretching and compression of the concentration isopleths due to action of an eddy or vortex roll-up. The initial linear concentration profile evolves into a form resembling the profile obtained by applying triplet map to the linear profile.

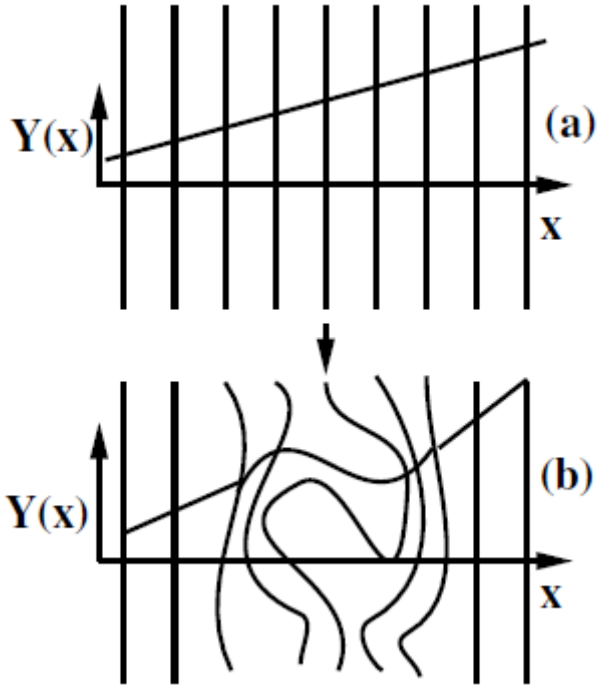

Figure 3.16. Triplet mapping approach (Kerstein, 1989).

In order to implement turbulent stirring it is necessary to obtain eddy size *l*, eddy location within 1-D domain, and the stirring frequency λ. The eddy size in the range from filter width Δ to Kolmogorov's scale η is determined by eddy size distribution *f(l)*, obtained using inertial range scaling in 3-D turbulence (Kerstein, 1989)

$$f(l) = \frac{5}{3}\frac{l^{-8/3}}{\left(\eta^{-5/3} - \Delta^{-5/3}\right)}, \tag{3.31}$$

where η is determined from inertial range scaling law

$$\eta = N_\eta \frac{\Delta}{\mathrm{Re}_\Delta^{3/4}}, \tag{3.32}$$

where N_η is an empirical constant (Smith & Menon, 1997), and Re_Δ is the sub-grid scale Reynolds number based on filter width. The location of the event is chosen randomly from a uniform distribution, and the event mapping mean frequency per unit of length is (Krstein, 1989)

$$\lambda = \frac{54}{5}\frac{\nu\,\mathrm{Re}_\Delta}{C_\lambda \Delta^3}\left[\frac{(\Delta/\eta)^{5/3} - 1}{1 - (\eta/\Delta)^{4/3}}\right]. \tag{3.33}$$

Time interval between the events is

$$\Delta t_{st} = \frac{1}{\lambda \Delta}, \tag{3.34}$$

where Δ is the length of 1-D domain equal to local filter width. These mappings are implemented as a Poisson process in time.

The final sub-grid process in LEM requiring definition is volumetric heat expansion. Since the sub-grid convection is modelled explicitly using triplet maps, volumetric expansion can also be expressed explicitly as

$$\Delta V^*_{LEM} = \frac{\rho_i^n}{\rho_i^*}, \tag{3.35}$$

where ΔV^*_{LEM} is the change in volume of LEM cell *i*. ρ_i^n and ρ_i^* are, respectively, densities of the *i*-th cell at the previous and current time integration level in the sub-grid simulation.

Since LES-LEM does not require explicit filtering of the reaction rate, the exact rates can be calculated using direct integration (Kerstein, 1992; Menon et al., 2003).

3.2.5 Flamelet PDF model (UU)

Some of the effects of reaction chemistry on combustion may be accounted for by using a flamelet PDF model.

The flamelet model is one of the topology-based turbulent combustion models. In this model, the integrity of the laminar flame structure is conserved. The impact of the turbulence on an element of flame is evaluated in terms of equivalent control parameters in a laminar flame experiment, such as the imposed strain. The turbulent combustion in itself is not different from the laminar case and the key point of the turbulent combustion modelling is the route to translate turbulent flow dynamics near the reaction zone into control parameters of a separated laminar flame configuration.

The flamelet model takes advantage of the hierarchy problem appearing in turbulent combustion, namely, the fact that the turbulence structures cover a spectrum of scales while the typical thickness of a flame is on the low end of that spectrum. This hierarchy decouples the mixing of the species that is operated by the turbulent cascade from the chemistry that happens exclusively in the flame.

Rather than solving conservation equation for each species, the flamelet-PDF method uses a mixture fraction approach (Bilger, 1976). The approach is based on the assumption that the diffusivity of all species is equal. It allows simplification of calculations by decoupling simulation of the flow from the relatively complex reaction chemistry. The mixture fraction is introduced as:

$$Z = \frac{sY_F - Y_o + Y_o^0}{sY_F^0 + Y_o^0}, \tag{3.36}$$

where Y_F^0 and Y_o^0 are the mass fractions of fuel in the pure fuel stream and oxidizer in the pure oxidizer stream respectively, Y_F and Y_o are the fuel and oxidizer mass fraction values at the position where the mixture fraction Z is calculated, s is the mass stoichiometric ratio, $s = (Y_o / Y_F)_{st}$ at stoichiometric conditions. It can be shown (Poinsot & Veynante, 2011) how the species equations can be replaced by a single conserved scalar conservation equation for the mixture fraction Z with no source term. The unfiltered equation for the mixture fraction is:

$$\frac{\partial \rho Z}{\partial t} + \frac{\partial}{\partial x_j}(\rho u_j Z) = \frac{\partial}{\partial x_j}\left(\rho D \frac{\partial Z}{\partial x_j}\right), \tag{3.37}$$

where ρD denotes the molecular diffusion. The filtered transport equation for the mixture fraction is:

$$\frac{\partial \overline{\rho}\overline{Z}}{\partial t} + \frac{\partial}{\partial x_j}(\overline{\rho u}_j \overline{Z}) = \frac{\partial}{\partial x_j}\left(\overline{\rho D}\left(\frac{\partial \overline{Z}}{\partial x_j}\right)\right). \tag{3.38}$$

In the case of chemical equilibrium (assumption of infinitely fast chemistry and infinitely thin flame thickness) all combustion products, thermo-chemical scalars i.e. the species fractions, density, and temperature depend solely on the instantaneous fresh mixture composition, which is represented by the mixture fraction Z. If the chemistry is not infinitely fast, and instead occurs in a narrow but finite thickness reaction zone, then assumptions must be made about the turbulent flame structure so that temperature and species concentration may be calculated accounting turbulence-combustion interaction.

The laminar flamelet approach for application to non-premixed flame was developed by (Peters, 1988). The approach assumes that the turbulent flame brush can be approximated as a system of instantaneous laminar flamelets, where species concentrations and temperature are described as a function of mixture fraction (Poinsot & Veynante, 2011). The flamelet equations solved are as follows (FLUENT, 2006; Poinsot & Veynante, 2011):

$$\rho \frac{\partial Y_k}{\partial t} = \dot{\omega}_k + \frac{1}{2}\rho\chi \frac{\partial^2 Y_k}{\partial Z^2}, \tag{3.39}$$

$$\rho\frac{\partial T}{\partial t}=\frac{1}{2}\rho\chi\frac{\partial^2 T_k}{\partial Z^2}-\frac{1}{c_p}\sum_k H_k\dot{\omega}_k+\frac{1}{2c_p}\rho\chi\left[\frac{\partial c_p}{\partial Z}+\sum_k c_{p,k}\frac{\partial Y_k}{\partial Z}\right]\frac{\partial T}{\partial Z}, \tag{3.40}$$

where $\chi=2D\left(\frac{\partial Z}{\partial x_j}\right)^2$ is scalar dissipation representing the flame stretch. The scalar dissipation varies along the axis of the flamelet and the inverse of χ can be interpreted as the characteristic diffusion time across the flame. In adiabatic systems the laminar flamelets are completely parameterised by χ_{st} (value of flame stretch at flame location) and Z, and can hence be used to determine instantaneous values of species mass fraction and mixture temperature. The density-weighted mean species mass fractions and temperature can then be determined from the probability density function (PDF) of χ_{st} and Z; this is described in the next section, therefore for adiabatic cases the energy equation is not solved explicitly at each time step.

The effect of turbulence on the chemistry should be accounted for. PDF is used here as a closure model for these effects. The averaged values of species mass fraction, temperature and density are a function of both their instantaneous values and the joint PDF of Z and χ_{st}:

$$\bar{\phi}_i=\iint p(Z,\chi_{st})\phi(Z,,\chi_{st})dZd\chi_{st}, \tag{3.41}$$

where $\bar{\phi}_i$ represents the averaged value of ϕ which can be the species mass fraction or temperature. The shape of the PDF needs to be specified in order to determine the local mean fluid state at all points in the flow field. The PDF describes SGS temporal fluctuations in the properties which are obtained from the flow field, i.e. the mixture fraction and the scalar dissipation. Z and χ_{st} are assumed to be statistically independent and so there are separate PDF functions for each. In practice this PDF is unknown and is modelled as a mathematical function that approximates the actual PDF shapes that have been observed experimentally. Eq. (3.41) can therefore be rewritten as:

$$\bar{\phi}_i=\iint p(Z)\,p(\chi_{st})\phi(Z,\chi_{st})dZd\chi_{st}, \tag{3.42}$$

In practice *p(Z)* is unknown and must be modelled – or assumed – based on experimentally observed PDF shapes. The sub filter PDF of a conserved scalar can be approximated by a beta function (Richardson et al., 1953). The b-function PDF is a function of Z and its SGS variance Z_0

$$p(Z)=\frac{Z^{\alpha-1}(1-Z)^{\beta-1}}{\int Z^{\alpha-1}(1-Z)^{\beta-1}dZ}, \tag{3.43}$$

where $\alpha=\bar{Z}\left[\left(\bar{Z}(1-Z)/Z'^2\right)-1\right]$, $\beta=\left(1-\bar{Z}\right)\left[\left(\bar{Z}(1-Z)/Z'^2\right)-1\right]$, and $\overline{Z'^2}$, the mixture fraction variance, is modelled using $\overline{Z'^2}=C_{\text{var}}L_s^2\left|\nabla\bar{Z}\right|^2$, where C_{var} is computed dynamically in the same way as C_s, and $L_s=\min(kd,C_sV^{1/3})$

As specified in (FLUENT, 2006) fluctuations in χ_{st} are ignored so that the PDF of χ is a delta function $p(\chi) = \delta(\chi - \overline{\chi})$. The mean scalar dissipation $\overline{\chi_{st}}$ is modelled using formula $\overline{\chi_{st}} = C_{\chi}(\mu_t + \mu/\rho\sigma_t)|\nabla Z|^2$ where $C_{\chi} = 2$.

Solving the flamelet equations at each time step would be computationally intensive. Thus, flamelet ''libraries'' are generated in advance of the simulation. The flamelet equations are solved for a range of values of Z and χ_{st}. Similarly, the assumed shape PDF functions for Z and χ_{st} are calculated in advance for a range of values of mixture fraction, scalar dissipation and mixture fraction variance. The flamelets are then convoluted with the assumed shape PDFs and look up tables are constructed. The look up table contains information on species mass fraction and temperature for given values of mixture fraction, mixture fraction variance and scalar dissipation rate. The density of the flow is then calculated based on the mixture composition.

3.2.6 Eddy Dissipation Concept (EDC) model (UU)

The eddy dissipation concept (EDC) model is an extension of the eddy dissipation model to include chemical reaction mechanism in a turbulent flow (Magnussen, 1981). It assumes that reactions occur in small turbulent structures, called fine-scales.

Chemical reactions take place when reactants are mixed at the molecular scale at sufficiently high temperature. In turbulent flow the reactant consumption is strongly dependent on the molecular mixing. It is known that the misroscale processes which are decisive for the molecular mixing as well as dissipation of turbulent kinetic energy into heat are severely intermittent, i.e., concentrated in isolated regions whose entire volume is a small fraction of the volume of the fluid.

These regions are occupied by fine structures whose dimensions are small in one or two directions, but not in the third. These are believed to be vortex tubes, sheets or slabs whose characteristic dimensions are of the magnitude of Kolmogorov scales.

The fine structures are responsible for the dissipation of turbulence into heat. Within these structures one can therefore assume that reactants will be mixed at the molecular scale. These structures are thus creating the reaction space for non-uniformly distributed reactants.

One can assume that the reactants are homogeneously mixed within fine structures. In order to treat reaction within this space it is necessary to know the reaction volume and mass transfer rate between the structures and surrounding fluid.

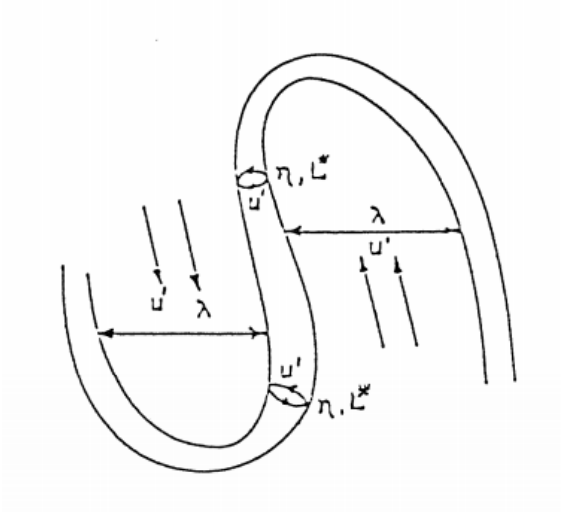

Figure 3.17. Schematic illustration of fine structure vortex (Tennekes, 1968).

Batchelor & Townsend (1949) were the first to point out the tendency towards strong dissipation intermittency, i.e. its concentration in isolated regions whose entire volume is a small fraction of the volume of the fluid, in high Reynolds number turbulence. Small scale structures which are responsible for most of the dissipation, can, therefore, be assumed to be produced in a very localized fashion (Magnussen, 1981). It can be assumed that these structures consist of large thin vortex sheets, ribbons of vorticity or vortex tubes of random extension folded or tangled throughout the flow (Figure 3.17). These fine structures are localized in certain regions, primarily highly strained areas between eddies, separating reacting and non-reacting volumes, whose linear dimensions are much larger than the fine structures (Kuo & Corrsin, 1971).

On the basis of consideration of energy transfer to these structures, it can be assumed that the mass fraction Y occupied by the fine structures can be expressed as

$$\xi = \left(\frac{u^*}{u'} \right)^3 , \tag{3.44}$$

(Magnussen, 1981), where u^* is the mass average fine structure velocity and u' is the turbulent fluctuating velocity.

If it is assumed that the fine structures are localized in nearly constant energy regions, then the mass fraction occupied by the fine structure regions can be expressed as

$$\xi = \xi^* \cdot \left(\frac{u^*}{u'} \right)^2 , \tag{3.45}$$

resulting in

$$\xi^* = \frac{u^*}{u'} . \tag{3.46}$$

Assuming nearly isotropic turbulence and introducing the turbulence kinetic energy k and its rate of dissipation ε, the mass fraction occupied by fine structure regions can be expressed as (Magnussen, 1981)

$$\xi^* = 2.13 \cdot \left(\frac{\nu \varepsilon}{k^2} \right)^{1/4}, \tag{3.47}$$

where ν is the kinematic viscosity.

On the basis of simple geometrical considerations the transfer of mass per unit of fluid and unit of time between the fine structures and the surrounding fluid can be expressed as

$$\dot{m} = 11.08 \cdot \xi^* \cdot \frac{\varepsilon}{k} = 23.6 \cdot \left(\frac{\nu \cdot \varepsilon}{k^2} \right)^{1/4} \cdot \frac{\varepsilon}{k}. \tag{3.48}$$

The mass flow rate per unit of mass of fine structures may then be expressed in terms of ν and ε as

$$\dot{m}^* = 2.43 \cdot \left(\frac{\varepsilon}{\nu} \right)^{1/2}, \tag{3.49}$$

which gives fine structure residence time

$$\tau^* = \frac{1}{\dot{m}^*} = 0.41 \cdot \left(\frac{\nu}{\varepsilon} \right)^{1/2}. \tag{3.50}$$

Reaction rate can be written as

$$\dot{Y}_F = 23.6 \cdot \left(\frac{\nu \cdot \varepsilon}{k^2} \right)^{1/4} \cdot \frac{\varepsilon}{k} \cdot \overline{Y}_{\min}, \tag{3.51}$$

(Hamworthy, 2013), where $\overline{Y}_{\min}$ is the smallest concentration of Y_F and Y_{O2}. Since it cannot be assumed that all fine structures have the same temperature level, it is necessary to take into account concentration of the hot products. Accounting for hot products introduces a correction factor

$$\chi = 2 \frac{\overline{Y}_{pr} / (1 + r_{O_2})}{\overline{Y}_{pr} / (1 + r_{O_2}) + Y_F}. \tag{3.52}$$

where r_{O_2} is the stoichiometric oxygen requirement, and Eq. (3.52) takes the form

$$\dot{Y}_F = 23.6 \cdot \left(\frac{\nu \cdot \varepsilon}{k^2} \right)^{1/4} \cdot \frac{\varepsilon}{k} \cdot \chi \cdot \overline{Y}_{\min}. \tag{3.53}$$

The EDC model offers several advantages for hydrogen fire modelling. It allows a wider variety of phenomena to be modelled compared to the EBU model and its variations, including flame lift-off and blow-out. Recent simulations using the EDC model for hydrogen and methane fire modelling include (Christo & Dally, 2005; Galletti et al., 2006; Houf et al., 2009). An example of the application of the EDC model to hydrogen fire modelling can be found in the recent work by Molkov et al. (2014), where it was used in conjunction with RANS RNG *k-ε* turbulence model for simulating hydrogen flames in an enclosure.

In the EDC model the source term in the conservation equation for the mean species was modelled as (Magnussen, 1989; ANSYS, 2012):

$$R_m = \frac{\rho(\xi^*)^2}{\tau^*\left[1-(\xi^*)^3\right]}(Y_m^* - Y_m), \tag{3.54}$$

where R_m is a net rate of production/destruction of species m by chemical reactions, ξ^* is the length fraction of the fine-scale turbulent structures where the reaction occurs, Y_m^* is the fine-scale species m mass fraction after reacting over the time τ^* and Y_m is a species mass fraction for species m in the surrounding fine-scales state (Magnussen, 1989). The multiplier in above equation with a square of the length fraction of fine-scales represents the mass exchange between the surrounding and fine-structure regions.

The length fraction of the fine-scales can be modelled as (Gran & Magnussen, 1996):

$$\xi^* = C_\xi\left(\frac{\nu\varepsilon}{k^2}\right)^{1/4}, \tag{3.55}$$

where superscript "*" denotes fine-scale quantities, C_ξ=2.1377 is the volume fraction constant and ν is the kinematic viscosity.

Time scale of species reaction in the fine structures was expressed as

$$\tau^* = C_\tau\left(\frac{\nu}{\varepsilon}\right)^{1/2}, \tag{3.56}$$

where C_τ=0.4082 is a time-scale constant.

Combustion at the fine-scales is assumed to occur as a constant pressure reactor, with initial conditions taken as the current species and temperature in the cell. Reactions proceed over the time scale τ^*, governed by the Arrhenius rates (Eq. (3.57)), and are integrated numerically using the in-situ adaptive tabulation (ISAT) algorithm by (Pope, 1997) that can accelerate the chemistry calculations by two to three orders of magnitude, offering substantial reductions in run-times:

$$\hat{R}_{m,r} = \Gamma(\nu''_{m,r} - \nu'_{m,r})\left(k_{f,r}\prod_{j=1}^{N}[C_{j,r}]^{\eta'_{j,r}} - k_{b,r}\prod_{j=1}^{N}[C_{j,r}]^{\eta''_{j,r}}\right), \tag{3.57}$$

where, $\hat{R}_{m,r}$ is the molar rate of creation/destruction of species m in reaction r, N is the number of chemical species in the system; $\nu'_{m,r}$ is the stoichiometric coefficient for reactant m in reaction r; $\nu''_{m,r}$ is the stoichiometric coefficient for product i in reaction r; $k_{f,r}$ and $k_{b,r}$ are forward and backward rate constants for reaction r respectively; $C_{j,r}$ is the molar concentration of species j in reaction r; $\eta'_{j,r}$ and $\eta''_{j,r}$ are rate exponent for reactant species j and product species j in reaction r respectively. Γ represents the net effect of third bodies on the reaction rate and is equal to $\Gamma = \sum_j^N \gamma_{j,r}C_j$, where $\gamma_{j,r}$ is the third body efficiency of j-th species in the r-th reaction. The forward rate constant for reaction r, $k_{f,r}$, is computed using the Arrhenius equation:

$$k_{f,r} = A_r T^{\beta_r} e^{-E_r/RT}. \tag{3.58}$$

Backward rate constant $k_{b,r}$ for reversible reaction r is computed from the forward rate constant using the relation $k_{b,r} = k_{f,r}/K_r$, where K_r is the equilibrium constant for the r-th reaction, is computed from:

$$K_r = \left(\frac{p_{atm}}{RT} \right)^{\sum_{i=1}^{N} (\nu''_{m,r} - \nu'_{m,r})} \exp\left(\frac{\Delta S_r}{R} - \frac{\Delta H_r}{RT} \right), \tag{3.59}$$

where p_{atm} is the atmospheric pressure equal to 101325 Pa. The term within the exponential function represents the change in Gibbs free energy, and its components are computed as follows:

$$\frac{\Delta S_r}{R} = \sum_{m=1}^{N} (\nu''_{m,r} - \nu'_{m,r}) \frac{S_m}{R} \quad \text{and} \quad \frac{\Delta H_r}{RT} = \sum_{m=1}^{N} (\nu''_{m,r} - \nu'_{m,r}) \frac{h_m}{R}. \tag{3.60}$$

The 18-step reduced chemical reaction mechanism of hydrogen combustion in air is applied that is a subset of the Peters & Rogg's (1993) mechanism that excludes H_2O_2 formation and consumption. Indeed, for the reactants at room temperature and not very large pressures up to 4 MPa, the H_2O_2 concentration is very low and does not play an important role in the structure of the flame. The reduced mechanism counts eight reactive species (H_2, O_2, H, O, OH, HO_2, H_2O, N_2). The effect of nitrogen chemistry is not taken into account and nitrogen plays a role of the third body only.

3.3 References

Abdon, A. & Sundén, B. (2001) Numerical Simulation of Turbulent Impingement CoolingASME, p.V003T01A033 Available from: <http://proceedings.asmedigitalcollection.asme.org/proceeding.aspx?doi=10.1115/2001-GT-0150> [Accessed: 22 September 2015]

Annushkin, M.Y. & Sverdlov, E.D. (1979) Stability of Submerged Diffusion Flames in Subsonic and Underexpanded Supersonic Gas-Fuel Streams, *Combustion, Explosion and Shock Waves* 14 (5): 597–605

ANSYS (2012) ANSYS CFX-Solver Theory Guide,

Arrhenius, S. (1889) *Über Die Dissociationswärme Und Den Einfluss Der Temperatur Auf Den Dissociationsgrad Der Elektrolyte*, Wilhelm Engelmann Available from: <https://books.google.co.uk/books?id=HA11PgAACAAJ> [Accessed:

Astbury, G. & Hawksworth, S. (2007) Spontaneous Ignition of Hydrogen Leaks: A Review of Postulated Mechanisms, *International Journal of Hydrogen Energy* 32 (13): 2178–2185

Baev, V.K., Kuznetsov, P.P., Mogil'nyi, I.A., Tret'yakov, P.K. & Yasakov, V.A. (1974) Length of Diffusion Flames, *Combustion, Explosion and Shock Waves* 10 (4): 420–426

Baev, V.K. & Yasakov, V.A. (1974) Influence of Buoyant Forces on the Length of Diffuse Flames, *Combustion, Explosion, and Shock Waves* 10 (6): 752–756

Baker, J., Calvert, M.E. & Murphy, D.W. (2002) Structure and Dynamics of Laminar Jet Micro-Slot Diffusion Flames, *Journal of Heat Transfer* 124 (4): 783

Ban, H., Venkatesh, S. & Saito, K. (1994) Convection-Diffusion Controlled Laminar Micro Flames, *Journal of Heat Transfer* 116 (4): 954

Batchelor, G.K. & Townsend, A.A. (1949) The Nature of Turbulent Motion at Large Wave-Numbers, *Proceedings of the Royal Society A: Mathematical, Physical and Engineering Sciences* 199 (1057): 238–255

Becker, H.A. & Liang, D. (1978) Visible Length of Vertical Free Turbulent Diffusion Flames, *Combustion and Flame* 32: 115–137

Behnia, M., Ooi, A. & Gregory, P. (2005) Prediction of Turbulent Heat Transfer in Impinging Jet Geometries, *Modelling and Simulation of Turbulent Heat Transfer* 16: 147–175

Behnia, M., Parneix, S. & Durbin, P. (1997) Accurate Modeling of Impinging Jet Heat Transfer, *Center for Turbulence Research, Annual Research Briefs*: 149–164

Bilger, R.W. (1976) Turbulent Jet Diffusion Flames, *Progress in Energy and Combustion Science* 1 (2-3): 87–109

Birch, A.D., Brown, D.R., Dodson, M.G. & Swaffield, F. (1984) The Structure and Concentration Decay of High Pressure Jets of Natural Gas, *Combustion Science and Technology* 36 (5-6): 249–261

Birch, A.D. & Hargrave, G.K. (1989) Lift-off Heights in Underexpanded Natural Gas Jet Flames, *Symposium (International) on Combustion* 22 (1): 825–831

Birch, A.D., Hughes, D.J. & Swaffield, F. (1987) Velocity Decay of High Pressure Jets, *Combustion Science and Technology* 52 (1-3): 161–171

Blake, T.R. & McDonald, M. (1993) An Examination of Flame Length Data from Vertical Turbulent Diffusion Flames, *Combustion and Flame* 94 (4): 426–432

Bovo, M. (2011) *On the Numerical Modelling of Impinging Jets Heat Transfer*, , Göteborg, Sweden: Chalmers University of Technology.

Broadwell, J.E., Dahm, W.J.A. & Mungal, M.G. (1985) Blowout of Turbulent Diffusion Flames, *Symposium (International) on Combustion* 20 (1): 303–310

Brown, C.D., Watson, K.A. & Lyons, K.M. (1999) Studies on Lifted Jet Flames in Coflow: The Stabilization Mechanism in the near-and Far-Fields, *Flow, turbulence and combustion* 62 (3): 249–273

Brzustowski, T.. (1980) Mixing and Chemical Reactions in Industrial Flares and Their Models, *In*: *2nd International Physico Chemichal Hydrodynamics Conference*, Washington, DC, pp.27–40

Burgess, C. & Lawn, C. (1999) The Premixture Model of Turbulent Burning to Describe Lifted Jet Flames, *Combustion and Flame* 119 (1-2): 95–108

Butler, M.S., Moran, C.W., Sunderland, P.B. & Axelbaum, R.L. (2009) Limits of Hydrogen Leaks That Can Support Stable Flames, *International Journal of Hydrogen Energy* 34: 5174–5182

Byggstøyl, S. & Magnussen, B. (Eds.) (1985) A Model for Flame Extinction in Turbulent Flow, *In*: *Bradbury, L.J.S., Durst, F., Launder, B.E., Schmidt, F.W. and Whitelaw, J.H. (eds), Turbulent Shear Flows 4*, Berlin, Heidelberg: Springer Berlin Heidelberg, p.381 Available from: <http://link.springer.com/10.1007/978-3-642-69996-2> [Accessed: 22 September 2015]

Chao, Y.-C., Chang, Y.-L., Wu, C.-Y. & Cheng, T.-S. (2000) An Experimental Investigation of the Blowout Process of a Jet Flame, *Proceedings of the Combustion Institute* 28 (1): 335–342

Chao, Y.-C., Wu, C.-Y., Lee, K.-Y., Li, Y.-H., Chen, R.-H. & Cheng, T.-S. (2004) Effect of Dillution on Blowout Limits of Turbulent Jet Flames, *Combustion Science and Technology* 176 (10): 1735–1753

Cheng, T.S., Chao, Y.-C., Wu, C.-Y., Li, Y.-H., Nakamura, Y., Lee, K.-Y., *et al.* (2005) Experimental and Numerical Investigation of Microscale Hydrogen Diffusion Flames, *Proceedings of the Combustion Institute* 30 (2): 2489–2497

Cheng, T.S., Chen, C.-P., Chen, C.-S., Li, Y.-H., Wu, C.-Y. & Chao, Y.-C. (2006) Characteristics of Microjet Methane Diffusion Flames, *Combustion Theory and Modelling* 10 (5): 861–881

Christo, F.C. & Dally, B.B. (2005) Modeling Turbulent Reacting Jets Issuing into a Hot and Diluted Coflow, *Combustion and Flame* 142 (1-2): 117–129

Coats, C.M. (1996) Coherent Structures in Combustion, *Progress in Energy and Combustion Science* 22 (5): 427–509

Craft, T.J., Gant, S.E., Iacovides, H. & Launder, B.E. (2004) A NEW WALL FUNCTION STRATEGY FOR COMPLEX TURBULENT FLOWS, *Numerical Heat Transfer, Part B: Fundamentals* 45 (4): 301–318

Dahm, W.J.A. & Dibble, R.W. (1989) Coflowing Turbulent Jet Diffusion Flame Blowout, *Symposium (International) on Combustion* 22 (1): 801–808

Dahm, W.J.A. & Mayman, A.G. (1990) Blowout Limits of Turbulent Jet Diffusion Flames for Arbitrary Source Conditions, *AIAA Journal* 28 (7): 1157–1162

Delichatsios, M.A. (1993) Transition from Momentum to Buoyancy-Controlled Turbulent Jet Diffusion Flames and Fame Height Relationships, *Combustion and Flame* 92 (4): 349–364

Diop, S., Agrawal, A. & Schefer, R. (2008) Barrier Optimization by Optical Analysis of Compressed Gas Leak, Combustion Fundamentals and Applications,

Durbin, P.A. (1996) On the K-3 Stagnation Point Anomaly, *International Journal of Heat and Fluid Flow* 17 (1): 89–90

Echekki, T. & Mastorakos, E. (Eds.) (2011) *Turbulent Combustion Modeling*, Dordrecht: Springer Netherlands Available from: <http://link.springer.com/10.1007/978-94-007-0412-1> [Accessed: 23 September 2015]

Ertesvåg, I.S. & Magnussen, B.F. (2000) The Eddy Dissipation Turbulence Energy Cascade Model, *Combustion Science and Technology* 159 (1): 213–235

Ewan, B.C.. & Moodie, K. (1986) Structure and Velocity Measurements in Underexpanded Jets, *Combustion Science and Technology* 45: 275–288

FLUENT (2006) FLUENT 6.3 User's Guide, Available from: <https://www.sharcnet.ca/Software/Fluent6/html/ug/main_pre.htm> [Accessed: 24 September 2015]

Galletti, C., Lenzi, M., Parente, A. & Tognotti, L. (2006) Numerical Modeling of Hydrogen Diffusion Jet Flame: The Role of the Combustion Model, *Combust. Flame*

Genin, F., Chernyavsky, B. & Menon, S. (2003) Large Eddy Simulation of Scramjet Combustion Using a Subgrid Mixing/combustion Model, *In*: *12th AIAA International Space Planes and Hypersonic Systems and Technologies*, *International Space Planes and Hypersonic Systems and Technologies Conferences*, American Institute of Aeronautics and Astronautics, Available from: <http://dx.doi.org/10.2514/6.2003-7035> [Accessed: 24 September 2015]

Ge, X. & Sutton, W.H. (2006) Analysis and Test of Compressed Hydrogen Interface Leakage by Commercial Stainless Steel (NPT) Fittings Available from: <http://papers.sae.org/2006-01-0130/> [Accessed: 11 September 2015]

Giinther, R., Horch, K. & Lenze, B. (1981) The Stabilization Mechanism of Free Jet Diffusion Flames, *In*: *First Specialists Meeting (International) of the Combustion Institute*, Bordeaux, pp.117–122

Golovichev, V.I. & Yasakov, V.A. (1972) Analysis of a Reacting Submerged Hydrogen Jet, *In*: *Combustion, Explosion and Shock Waves*, pp.41–56

Gran, I.R. & Magnussen, B.F. (1996) A Numerical Study of a Bluff-Body Stabilized Diffusion Flame. Part 2. Influence of Combustion Modeling and Finite-Rate Chemistry, *Combustion Science and Technology* 119: 191–217

Gu, X.J. (1993) *A Theoretical and Computational Study of Turbulent Flames*, , Leeds, England: University of Leeds. Available from: <uk.bl.ethos.502339> [Accessed:

Hall, D., Horch, K. & Giinther, R. (1980) Die Stabilitat von Freistahl-Diffusions Flammen, *In*: *Warme-Krajt*, Brennst, p.2631

Hällqvist, T. (2006) *Large Eddy Simulation of Impinging Jets with Heat Transfer*, , Stockholm, Sweden: Royal Institute of Technology.

Hamworthy, J.. (2013) *The John Zink Hamworthy Combustion Handbook* (C.E. Baukal, Ed.), Boca Raton, Fla.: CRC Press

Han, D. & Mungal, M.G. (2000) Observations on the Transition from Flame Liftoff to Flame Blowout, *Proceedings of the Combustion Institute* 28 (1): 537–543

Hawthorne, W.R., Weddell, D.S. & Hottel, H.C. (1949) Mixing and Combustion in Turbulent Gas Jets, *Proceedings of the Combustion Institute* 3: 266–288

Hottel, H.C. & Hawthorne, W.R. (1949) Diffusion in Laminar Flame Jets, *Proceedings of the Combustion Institute* 3: 254–266

Houf, W.G., Evans, G.H. & Schefer, R.W. (2009) Analysis of Jet Flames and Unignited Jets from Unintended Releases of Hydrogen, *International Journal of Hydrogen Energy* 34 (14): 5961–5969

Houf, W. & Schefer, R. (2007) Predicting Radiative Heat Fluxes and Flammability Envelopes from Unintended Releases of Hydrogen, *International Journal of Hydrogen Energy* 32 (1): 136–151

Iacovides, H. & Raisee, M. (1997) Computation of Flow and Heat Transfer in 2-D Rib Roughened Passages, *In*: *2nd Int. Symposium on Turbulence, Heat & Mass Transfer*, Delft, pp.21–29

Imamura, T., Hamada, S., Mogi, T., Wada, Y., Horiguchi, S., Miyake, A., *et al.* (2008) Experimental Investigation on the Thermal Properties of Hydrogen Jet Flame and Hot Currents in the Downstream Region, *International Journal of Hydrogen Energy* 33: 3426–3435

Janicka, J. & Peters, N. (1982) Prediction of Turbulent Jet Diffusion Flame Lift-off Using a Pdf Transport Equation, *Symposium (International) on Combustion* 19 (1): 367–374

Johnson, A., Shirvill, L. & Ungut, A. (1999) *CFD Calculation of Impinging Gas Jet Flames*, HSE Offshore Technology Report No. OTO-1999-011

Jones, W.. & Launder, B.. (1972) The Prediction of Laminarization with a Two-Equation Model of Turbulence, *International Journal of Heat and Mass Transfer* 15 (2): 301–314

Kalghatgi, G.. (1984) Lift-off Heights and Visible Lengths of Vertical Turbulent Jet Diffusion Flames in Still Air, *Combustion Science and Technology* 41 (1): 14–29

Kalghatgi, G.T. (1981) Blow-out Stability of Gaseous Jet Diffusion Flames. Part I: In Still Air, *Combustion Science and Technology* 26 (5): 233–239

Kerstein, A.R. (1988) Simple Derivation of Yakhot's Turbulent Premixed Flame Speed Formula, *Combustion Science and Technology* 60: 163–165

Kerstein, A.R. (1989) Linear-Eddy Modeling of Turbulent Transport. II: Application to Shear Layer Mixing, *Combustion and Flame* 75 (3-4): 397–413

Kerstein, A.R. (1991a) Linear-Eddy Modeling of Turbulent Transport. Part V: Geometry of Scalar Interfaces, *Physics of Fluids A: Fluid Dynamics* 3 (5): 1110

Kerstein, A.R. (1991b) Linear-Eddy Modelling of Turbulent Transport. Part 6. Microstructure of Diffusive Scalar Mixing Fields, *Journal of Fluid Mechanics* 231 (-1): 361

Kerstein, A.R. (1992) Linear-Eddy Modelling of Turbulent Transport. Part 7. Finite-Rate Chemistry and Multi-Stream Mixing, *Journal of Fluid Mechanics* 240 (-1): 289

Kotchourko, A., Dorofeev, S. & Breitung, W. (1999) Test of Extended Eddy Break Up Model in Simulations of Turbulent H2-Air Combustion, *In*: *17-th Int. Colloq. on the Dynamics of Explosions and Reactive Systems (ICDERS)*,

Kuo, A.Y.-S. & Corrsin, S. (1971) Experiments on Internal Intermittency and Fine-Structure Distribution Functions in Fully Turbulent Fluid, *Journal of Fluid Mechanics* 50 (02): 285

Launder, B.E. & Sharma, B.I. (1974) Application of the Energy-Dissipation Model of Turbulence to the Calculation of Flow near a Spinning Disc, *Letters in Heat and Mass Transfer* 1 (2): 131–137

Launder, B.E. & Spalding, D.B. (1972) *Lectures in Mathematical Models of Turbulence*, London, England: Academic Press

Lecoustre, V.R., Sunderland, P.B., Chao, B.H. & Axelbaum, R.L. (2010) Extremely Weak Hydrogen Flames, *Combustion and Flame* 157 (11): 2209–2210

Lecoustre, V.R., Sunderland, P.B., Chao, B.H. & Axelbaum, R.L. (2013) Modeled Quenching Limits of Spherical Hydrogen Diffusion Flames, *Proceedings of the Combustion Institute* 34 (1): 887–894

Magel, H.., Schneider, R., Risiso, B. & Hein K.R.G (1995) Numerical Simulation of Utility Boilers with Advanced Combustion Technologies, *In*: *Eigth Interational Symposium On Transport Phenomena in Combustion*, San Francisco,

Magnussen, B. (1981) On the Structure of Turbulence and a Generalized Eddy Dissipation Concept for Chemical Reaction in Turbulent Flow, *In*: *American Institute of Aeronautics and Astronautics*, Available from: <http://arc.aiaa.org/doi/abs/10.2514/6.1981-42> [Accessed: 11 February 2014]

Magnussen, B.F. (1989) Modelling of Pollutant Formation in Gas Turbine Combustors Based on the Eddy Dissipation Concept, *In*: *Proceedings of the CIMAC Conference*, Tianjin, China,

Magnussen, B.F. & Hjertager, B.H. (1977) On Mathematical Modeling of Turbulent Combustion with Special Emphasis on Soot Formation and Combustion, *Symposium (International) on Combustion* 16 (1): 719–729

Makarov, D. & Molkov, V. (2013) Plane Hydrogen Jets, *International Journal of Hydrogen Energy* 38 (19): 8068–8083

Mason, L.. & Spalding, D.. (1973) Prediction of Reaction Rates in Turbulent Premixed Boundary Layer Flows, *In*: *Combustion Institute European Symposium*, New York: Academic Press, pp.601–6012

Matta, L.M., Neumeier, Y., Lemon, B. & Zinn, B.T. (2002) Characteristics of Microscale Diffusion Flames, *Proceedings of the Combustion Institute* 29 (1): 933–939

Menon, S., Sankaran, V. & Stone, C. (2003) *Subgrid Combustion Modeling for the next Generation National Combustion Code*, NASA/CR—2003-212202, CCL–02–003: National Aeronautics and Space Administration, Glenn Research Center

Menter, F.R. (1992) Improved Two-Equation K-Omega Turbulence Models for Aerodynamic Flows, *NASA STI/Recon Technical Report N* 93: 22809

Menter, F.R. (1994) Two-Equation Eddy-Viscosity Turbulence Models for Engineering Applications, *AIAA Journal* 32 (8): 1598–1605

Miake-Lye, R.C. & Hammer, J.A. (1989) Lifted Turbulent Jet Flames: A Stability Criterion Based on the Jet Large-Scale Structure, *Symposium (International) on Combustion* 22 (1): 817–824

Mogi, T. & Horiguchi, S. (2009) Experimental Study on the Hazards of High-Pressure Hydrogen Jet Diffusion Flames, *Journal of Loss Prevention in the Processes Industries* 22: 45–51

Mogi, T., Nishida, H., Shiina, H. & Horiguchi, S. (2005) A Study of Combustion Properties of High-Pressure Hydrogen Gas Jet, *In*: *43rd Symposium (Japaneese) on Combustion*, pp.164–165

Molkov, V. (1995) Theoretical Generalization of International Experimental Data on Vented Explosion Dynamics, *In*: *First international seminar*, Moscow: VNIIPO, pp.166–181

Molkov, V. (2009) Hydrogen Non-Reacting and Reacting Jets in Stagnant Air: Overview and State-of-the-Art,

Molkov, V. (2012) *Fundamentals of Hydrogen Safety Engineering*, bookboon.com, free download online book

Molkov, V., Makarov, D. & Bragin, M. (2009) Physics and Modelling of under-Expanded Jets and Hydrogen Dispersion in Atmosphere, *In*: *Proceedings of the 24th International Conference on Interaction of Intense Energy Fluxes with Matter*, Elbrus, Chernogolovka, pp.143–145

Molkov, V. & Saffers, J.B. (2013) Hydrogen Jet Flames, *International Journal of Hydrogen Energy* 38: 8141–8158

Molkov, V., Shentsov, V., Brennan, S. & Makarov, D. (2013) Dynamics of Hydrogen Flame Self-Extinction in a Vented Enclosure, *In*: *Proceedings of the 7th International Seminar on Fire and Explosion Hazards*, Providence, RI, USA,

Molkov, V., Shentsov, V., Brennan, S. & Makarov, D. (2014) Hydrogen Non-Premixed Combustion in Enclosure with One Vent and Sustained Release: Numerical Experiments, *International Journal of Hydrogen Energy* 39 (20): 10788–10801

Montgomery, C.J., Kaplan, C.R. & Oran, E.S. (1998) The Effect of Coflow Velocity on a Lifted Methane-Air Jet Diffusion Flame, *Symposium (International) on Combustion* 27 (1): 1175–1182

Muñiz, L. & Mungal, M.G. (1997) Instantaneous Flame-Stabilization Velocities in Lifted-Jet Diffusion Flames, *Combustion and Flame* 111 (1-2): 16–31

Naji, H., Said, R. & Borghi, R.P. (1989) Towards a General Turbulent Combustion Model for Spark Ignition Engines Available from: <http://papers.sae.org/890672/> [Accessed: 24 September 2015]

Nakamura, Y., Yamashita, H. & Saito, K. (2006) A Numerical Study on Extinction Behaviour of Laminar Micro-Diffusion Flames, *Combustion Theory and Modelling* 10 (6): 927–938

Okabayashi, K., Hirashima, H., Nonaka, T., Takeno, K., Chitose, K. & Hashiguchi, K. (2007) Introduction of Technology for Assessment on Hydrogen Safety, *Mitsubishi Heavy Industries Ltd. Technical Review* 44 (1): 1–3

Peters, N. (1983) Local Quenching Due to Flame Stretch and Non-Premixed Turbulent Combustion, *Combustion Science and Technology* 30 (1-6): 1–17

Peters, N. (1988) Laminar Flamelet Concepts in Turbulent Combustion, *Symposium (International) on Combustion* 21 (1): 1231–1250

Peters, N. (2000) *Turbulent Combustion* (G.K. Batchelor, Ed.), Cambridge: Cambridge University Press

Peters, N. & Rogg, B. (Eds.) (1993) *Reduced Kinetic Mechanisms for Applications in Combustion Systems*, Berlin ; New York: Springer-Verlag

Peters, N. & Williams, F.A. (1983) Liftoff Characteristics of Turbulent Jet Diffusion Flames, *AIAA Journal* 21 (3): 423–429

Pitts, W.M. (1989a) Assessment of Theories for the Behavior and Blowout of Lifted Turbulent Jet Diffusion Flames, *Symposium (International) on Combustion* 22 (1): 809–816

Pitts, W.M. (1989b) Importance of Isothermal Mixing Processes to the Understanding of Lift-off and Blowout of Turbulent Jet Diffusion Flames, *Combustion and Flame* 76 (2): 197–212

Pitts, W.M. (1991) Large-Scale Turbulent Structures and the Stabilization of Lifted Turbulent Jet Diffusion Flames, *Symposium (International) on Combustion* 23 (1): 661–668

Poinsot, T. & Veynante, D. (2011) *Theoretical and Numerical Combustion*, Paris: CNRS

Pope, S.B. (1997) Computationally Efficient Implementation of Combustion Chemistry Using in Situ Adaptive Tabulation, *Combustion Theory and Modelling* 1: 41–63

Proust, C., Jamois, D. & Studer, E. (2011) High Pressure Hydrogen Fires, *International Journal of Hydrogen Energy* 36 (3): 2367–2373

Richardson, J.M., Howard, H.C. & Smith, R.W. (1953) The Relation between Sampling-Tube Measurements and Concentration Fluctuations in a Turbulent Gas Jet, *Symposium (International) on Combustion* 4 (1): 814–817

Royle, M. & Willoughby, D.B. (2009) Consequences of Catastrophic Releases of Ignited and Unignited Hydrogen Jet Releases,

SAE J2579 (2009) Technical Information Report for Fuel Systems in Fuel Cell and Other Hydrogen Vehicles, *In*: *SAE International*, Detroit MI, U.S.,

Sankaran, V., Genin, F. & Menon, S. (2004) Subgrid Mixing Modeling for Large Eddy Simulation of Supersonic Combustion, *In*: *42nd AIAA Aerospace Sciences Meeting and Exhibit*, *Aerospace Sciences Meetings*, American Institute of Aeronautics and Astronautics, Available from: <http://dx.doi.org/10.2514/6.2004-801> [Accessed: 24 September 2015]

Sarkar, S. & Lakshmanan, B. (1991) Application of a Reynolds Stress Turbulence Model to the Compressible Shear Layer, *AIAA Journal* 29 (5): 743–749

Schefer, R., Houf, W., Bourne, B. & Colton, J. (2006) Spatial and Radiative Properties of an Open-Flame Hydrogen Plume, *International Journal of Hydrogen Energy* 31 (10): 1332–1340

Schefer, R.W. Houf, W.G., Bourne, B., and Colton, J. (2006) Spatial and Radiative Properties of an Open Flame Hydrogen Plume, *International Journal of Hydrogen Energy* 31 (10): 9

Schefer, R.W., Houf, W.G., Williams, T.C., Bourne, B. & Colton, J. (2007) Characterization of High-Pressure, Underexpanded Hydrogen-Jet Flames, *International Journal of Hydrogen Energy* 32 (12): 2081–2093

Scholefield, D.A. & Garside, J.E. (1948) The Structure and Stability of Diffusion Flames, *Symposium on Combustion and Flame, and Explosion Phenomena* 3 (1): 102–110

Shevyakov, G.G. & Komov, V.F. (1977) Effect of Noncombustible Admixtures on Length of an Axisymmetric on-Port Turbulent Diffusion Flame, *Combustion, Explosion and Shock Waves* 13 (5): 563–566

Shevyakov, G.G. & Savelyeva, N.I. (2004) Dispersion and Combustion of Hydrogen Jet in the Open Atmosphere, *International Scientific Journal for Alternative Energy and Ecology* 1: 23–27

Smith, T.M. & Menon, S. (1997) One-Dimensional Simulations of Freely Propagating Turbulent Premixed Flames, *Combustion Science and Technology* 128 (1-6): 99–130

Spalding, D.B. (1971) Mixing and Chemical Reaction in Steady Confined Turbulent Flames, *Symposium (International) on Combustion* 13 (1): 649–657

Spalding, D.B. (1977) Development of the Eddy-Break-up Model of Turbulent Combustion, *Symposium (International) on Combustion* 16 (1): 1657–1663

Stårner, S.H., Bilger, R.W., Frank, J.H., Marran, D.F. & Long, M.B. (1996) Mixture Fraction Imaging in a Lifted Methane Jet Flame, *Combustion and Flame* 107 (3): 307–313

Studer, E., Jamois, D., Jallais, S., Leroy, G., Hebrard, J. & Blanchetière, V. (2009) Properties of Large-Scale Methane/hydrogen Jet Fires, *International Journal of Hydrogen Energy* 34 (23): 9611–9619

Sunderland, P. (2010) Hydrogen Microflame Hazards, In: Proceedings of the 8th International Short Course and Advanced Research Workshop in the series 'Progress in Hydrogen Safety', Hydrogen and Fuel Cell Early Market Applications, University of Ulster, Belfast,

Takahashi, F., Mizomoto, M., Ikai, S. & Futaki, N. (1985) Lifting Mechanism of Free Jet Diffusion Flames, *Symposium (International) on Combustion* 20 (1): 295–302

Takahashi, M., Tamura, Y., Suzuki, J. & Watanabe, S. (2008) Investigation of the Allowable Flow Rate of Hydrogen Leakage on Receptacle, *SAE International Journal of Passenger Cars - Mechanical Systems* 1 (1): 590–597

Tennekes, H. (1968) Simple Model for the Small-Scale Structure of Turbulence, *Physics of Fluids* 11 (3): 669

Vanquickenborne, L. & van Tiggelen, A. (1966) The Stabilization Mechanism of Lifted Diffusion Flames, *Combustion and Flame* 10 (1): 59–69

Vieser, W., Esch, T. & Menter, F. (2004) Heat Transfer Predictions Using Advanced Two-Equation Turbulence Models, *CFX Validation Report, Report No. CFX-VAL* 10: 0902

Watson, K. (1999) Observations on the Leading Edge in Lifted Flame Stabilization, *Combustion and Flame* 119 (1-2): 199–202

Watson, K.A., Lyons, K.M., Carter, C.D. & Donbar, J.M. (2002) Simultaneous Two-Shot CH Planar Laser-Induced Fluorescence and Particle Image Velocimetry Measurements in Lifted CH4/air Diffusion Flames, *Proceedings of the Combustion Institute* 29 (2): 1905–1912

Watson, K.A., Lyons, K.M., Donbar, J.M. & Carter, C.D. (2002) Simultaneous Two-Shot CH-PLIF and Particle Image Velocimetry Measurements in Lifted CH4-Air Diffusion Flames, *In*: *Proceedings of the 29th International Symposium on Combustion*, pp.1905–1912 Available from: <http://linkinghub.elsevier.com/retrieve/pii/S1540748902802310> [Accessed: 22 September 2015]

Watson, K.A., Lyons, K.M., Donbar, J.M. & Carter, C.D. (2003) On Scalar Dissipation and Partially Premixed Flame Propagation, *Combustion Science and Technology* 175 (4): 649–664

Watson, K.., Lyons, K.., Donbar, J.. & Carter, C.. (2000) Simultaneous Rayleigh Imaging and CH-PLIF Measurements in a Lifted Jet Diffusion Flame, *Combustion and Flame* 123 (1-2): 252–265

Wilcox, D.C. (1988) Reassessment of the Scale-Determining Equation for Advanced Turbulence Models, *AIAA Journal* 26 (11): 1299–1310

Wilcox, D.C. (2006) *Turbulence Modeling for CFD*, La Cãnada, Calif: DCW Industries

Williams, F.A. (1994) *Combustion Theory*, Cambridge, Mass: Perseus Books

Wohl, K., Gazley, C. & Kapp, N. (1948) Diffusion Flames, *Symposium on Combustion and Flame, and Explosion Phenomena* 3 (1): 288–300

Wu, C.-Y., Chao, Y.-C., Cheng, T.-S., Li, Y.-H., Lee, K.-Y. & Yuan, T. (2006) The Blowout Mechanism of Turbulent Jet Diffusion Flames, *Combustion and Flame* 145 (3): 481–494

Yap, C.R. (1987) Turbulent Heat and Momentum Transfer in Recirculating and Impinging Flows, , Manchester Univ. (England).

Yoon, Y., Donbar, J.M. & Driscoll*, J.F. (1994) Blowout Stability Limits Of a Hydrogen Jet Flame In a Supersonic, Heated, Coflowinq Air Stream, *Combustion Science and Technology* 97 (1-3): 137–156

Zuckerman, N. & Lior, N. (2006) Jet Impingement Heat Transfer: Physics, Correlations, and Numerical Modeling, *In*: *Advances in Heat Transfer*, Elsevier, pp.565–631 Available from: <http://linkinghub.elsevier.com/retrieve/pii/S0065271706390065> [Accessed: 22 September 2015]

Hyper Project, Available from: <http://www.hyperproject.eu/> [Accessed: 22 September 2015]

4. Physical and Mathematical models of deflagration (UU)

4.1 Hydrogen safety engineering relevant problems and phenomena (UU)

4.1.1 Introduction (UU)

4.1.1.1 Deflagrations – Characteristic parameters

By definition, an explosion is a sudden and rapid release of energy leading to a rapid increase in pressure, called a blast wave. The origin of energy can be either physical or chemical: examples of "physical explosions" include the explosion of a vessel due to overpressure following overfill or an increase in pressure resulting from a runaway reaction; for "chemical explosions" examples include explosions created by the combustion of gas and dust. It's possible to separate "combustion explosions" into either a deflagration or a detonation. It should be noted that the word "explosion" in this context can generate misunderstanding and as such its use will be avoided where possible in the remainder of this document, instead the terms "deflagration" or "detonation" will be used.

The main different feature between a deflagration and a detonation is the velocity of the wave front. A deflagration is a combustion reaction where the combustion wave front propagates at subsonic speed (below the speed of sound) in the unburned mixture, whereas for a detonation the combustion wave front is supersonic in the unburned mixture. As result, the pressure history of a deflagration or a detonation will be different.

Detonation phenomena will be developed in the Chapter 5 of this document.

Laminar flames

The laminar flame structure is show in Figure 4.1. As shown in this figure four zones can be readily identified:

- **Reactants zone:** contains the fresh unburnt fuel-air mixture,
- **Preheat zone:** in this zone, the heat generated by combustion is conducted toward fresh gases,
- **Reaction zone:** in this zone the combustion reaction takes place, the fuel is consumed and transformed into combustion products, heat is released and transmitted to the burnt gases which expand,
- **Products zone:** contains the burnt gases

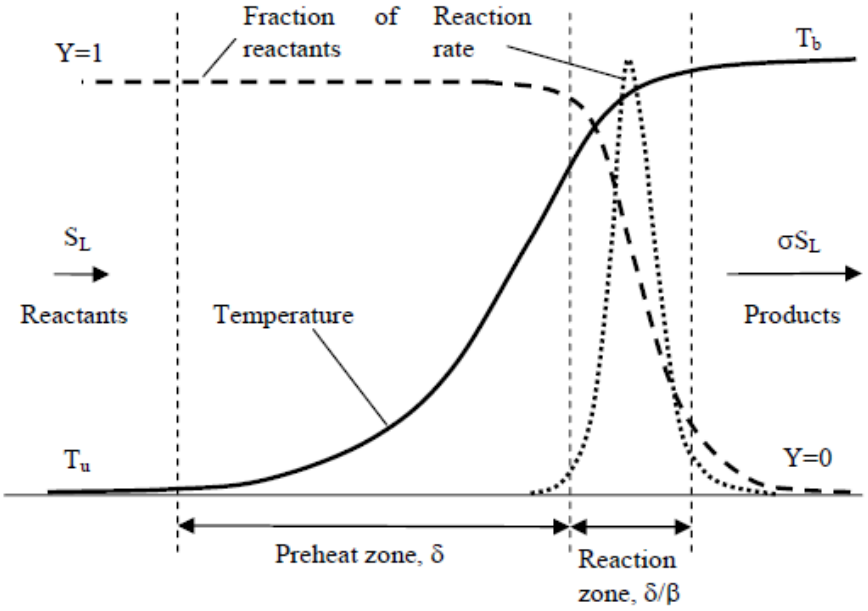

Figure 4.1 Schematic of laminar flame structure (Dorofeev, 2008).

Expansion ratio

The expansion ratio E of the combustion products is a thermo-dynamical parameter. It's defined as the ratio of the unburnt gas density to the burnt gas density.

$$E = \frac{\rho_u}{\rho_b} \approx \frac{T_b}{T_u} = \frac{\Delta H_{comb}}{C_p T_u} + 1, \qquad \text{Equation 4.1}$$

where ρ_u and ρ_b are respectively the densities of unburnt gas and burnt gas, T_u and T_b are respectively the temperatures of the unburnt gas and burnt gas in the hypothesis of an adiabatic reaction, ΔH_{comb} is the mass enthalpy of the combustion reaction at the temperature T_u and C_p is the specific heat capacity.

Expansion ratio is an "intrinsic" parameter which only depends on the mixture concentration and not on the way that the flame propagates.

Laminar flame burning velocity

If combustion occurs in an initially premixed and quiescent hydrogen-air mixture, the flame produced can be considered to be initially laminar. The laminar burning velocity is the velocity of the flame propagating through a quiescent fresh mixture from the point of view of a fixed observer moving with fresh mixture. The laminar flame burning velocity can be obtained using the relation published by Zel'dovitch et al. (Zel'dovich et al., 1980):

$$S_u = \left[\frac{2 \cdot \lambda \cdot L_e \cdot Z' \cdot R \cdot T_u^2 \cdot \exp\left(\frac{-E_a}{R_m T_u}\right)}{\rho_u \cdot E_a \cdot C_p \cdot (T_b - T_u)} \right]^{\frac{1}{2}}, \qquad \text{Equation 4.2}$$

where λ is the thermal conductivity, L_e is Lewis number, Z' is the pre-exponential factor, R is the perfect gas constant and Ea is the activation energy.

The laminar flame is also defined by a small thickness and plane flame front. This laminar flame thickness, also known as the Zeldovich thickness, is commonly expressed using the following equation:

$$\delta_L = \frac{\lambda}{C_p \cdot \rho_u \cdot S_u} = \frac{a_{th}}{S_u},$$ Equation 4.3

where the thermal diffusivity, a_{th} is defined as: $a_{th} = \lambda / C_p \cdot \rho_u$.

This relation shows that the laminar burning velocity is, similar to the expansion ratio, an "intrinsic" parameter of the flame. This relation implies that the laminar burning velocity is dependent on the burnt gas temperature as well as the mixture concentration.

The laminar flame burning velocity is well described in the literature and a wide range of values is available for each hydrogen concentration. Dahoe (Dahoe, 2005) gives a detailed comparison of the laminar burning velocities of hydrogen mixtures, as summarised below in .

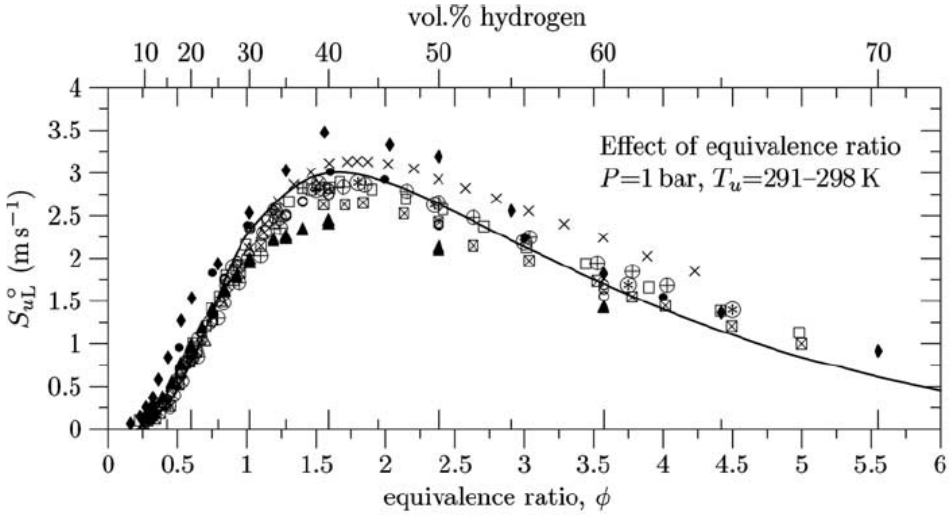

Figure 4.2 Effect of hydrogen concentration on the laminar burning velocity (Dahoe, 2005).

The laminar burning velocity is, in addition to hydrogen concentration, dependent on the initial temperature and the initial pressure. Its general expression is defined by:

$$\frac{S_{ui}}{S_{u0}} = \left(\frac{T_i}{T_0}\right)^m \cdot \left(\frac{p_i}{p_0}\right)^n$$ Equation 4.4

According to the adiabatic compression laws, this expression becomes:

$$\frac{S_{ui}}{S_{u0}} = \left(\frac{T_i}{T_0}\right)^{m_0}$$ Equation 4.5

Where m_0 is the temperature index (Verbecke, 2009) and S_{u0} is the laminar burning velocity at the temperature T_0 = 298 K.

4.1.1.2Flame instabilities

Landau-Darrieus Instability (or hydrodynamic instability)

Hydrodynamic instability, also known as the Landau-Darrieus (LD) instability due to the works of Darrieus (Darrieus, n.d.) (Darrieus, 1946) and Landau (Landau, 1944), is a consequence of gas thermal expansion, and the variation of density between the unburnt gas and the burnt one (Law, 2006) (Matalon, 2007).

The theory presented by Darrieus (Darrieus, n.d.) (Darrieus, 1946) and Landau (Landau, 1944) assumes that the flame is infinitesimally thin and forms the interface between the unburnt and burnt gases. Additionally it is assumed that the flame propagates at a constant speed, S_u, relative to the fresh unburnt mixture and that this is, by its nature, unstable. Therefore within this framework, the linear stability of a planar flame yields an expression describing the hydrodynamic instability growth rate:

$$\omega_{LD} = \frac{-E + \sqrt{E^3 + E^2 - E}}{E + 1}$$ Equation 4.6

where ω_{LD} is the growth rate of the hydrodynamic instability and E is the expansion ratio.

As illustrated in Figure 4.3 if a flame is initially lightly curved, the streamlines in the burnt gas converge behind the convex part of the front and diverge behind the concave part. This creates an additional push for the convex part of the front, which increases the initial curvature (Ciccarelli et al., 1994) thereby causing the flame to become wrinkled.

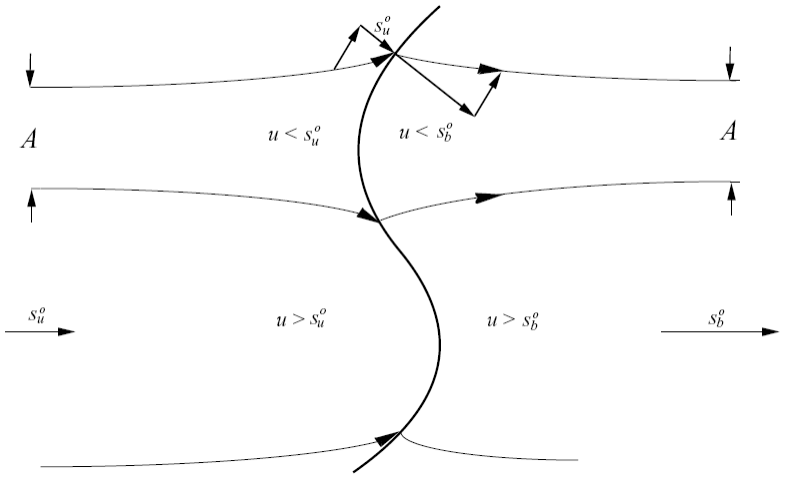

Figure 4.3 Schematic of LD instability mechanism (Law, 2006).

Thermo-diffusive instabilities

This instability is based on a competition between the thermal diffusivity (heat conductivity) and the diffusivity of the deficient reactant. To characterize this instability, the Lewis number is commonly used:

$$L_e = \frac{a_{th}}{D_m}$$ Equation 4.7

Where D_m is the molecular diffusivity of the deficient reactant and a_{th} is the molecular heat conductivity of the mixture.

It's possible to distinguish two situations:

- $Le > 1$ (and/or $\alpha_{th} > D_m$): The thermo-diffusive instability contributes to the stabilization of the flame against the hydrodynamic instability, consequently the flame stays in this planar form and keeps a burning velocity close to the laminar burning velocity. As result, in this case, there is a stabilizing effect.
- $Le < 1$ (and/or $\alpha_{th} < D_m$): In this situation, the thermo-diffusive and LD instabilities are intensified by each other, perturbations of the flame front are more important therefore the flame front area increases leading to an increase in the burning velocity increase. This effect is a destabilizing one.

If Lewis numbers greater than one are considered, at the curved in segment of the flame burning is intensified and at the curved out segment of the flame burning is weakened, this means that flame wrinkles are smoothed out and the flame tends to stabilise. However the opposite result occurs when considering Lewis numbers less than one. In this situation there is a decrease in hear losses and an increase in mass diffusion which causes an increase in the local temperature of combustion behind the turned in segment of the flame front. At such location, this leads to an increase in the burning velocity. In segments of the flame front that are turned out, the local temperature of combustion decreases leading to a reduction in the burning velocity. Overall, this causes further increases in flame wrinkling. This phenomenon was predicted by Dold (Dold, 2007) where in the case of Lewis numbers less than one the analysis carried out predicted that the flame would lose its stability due to the emergence of cellular instabilities.

Regarding hydrogen-air mixtures, the thermo-diffusive instability is common for lean mixtures. Lean hydrogen mixtures can be defined as mixtures in which hydrogen is a deficient species. Such mixtures have large mass diffusivities and low Lewis numbers, meaning that the flame becomes wrinkled and develops a cellular structure, as illustrated in Figure 4.4 (top) where $\Phi = 0.6$. In comparison rich mixtures can be defined as mixtures in which oxygen is the deficient component. Such mixtures have relatively low diffusivities and Lewis numbers greater than one, consequently the flame is smooth as illustrated in Figure 4.4 (bottom) where $\Phi = 4.0$.

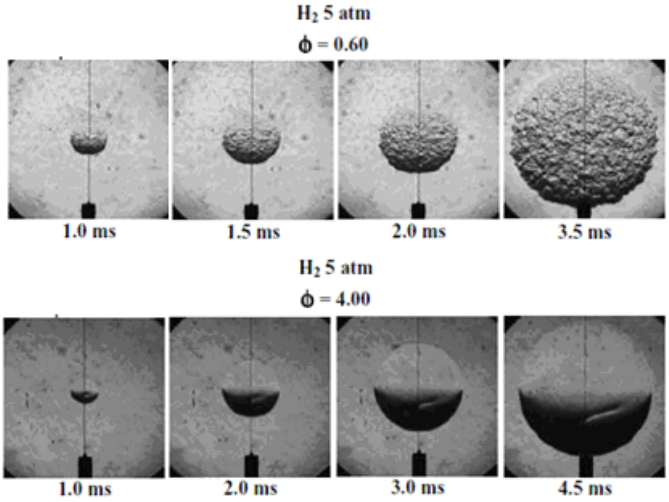

Figure 4.4 Showing spherically expanding flames of lean (Φ = 0.6) and rich (Φ = 4.0) hydrogen-air mixtures. The horizontal physical dimension of each frame is 5.4 cm (Law, 2006).

Turbulence generated by the flame front itself

Flame instabilities cause a rise in flame-generated turbulences (Sivashinsky, 1979). Flame-generated turbulence not only accelerates the transport process of heat and species but also increases the flame surface area and therefore the mass burning rate. When the flame starts to wrinkle, the subsequent enhancement of the burning rate causes a stronger flow expansion, resulting in an increase of the flow velocity. Due to this higher flow velocity the turbulence intensity levels become greater. Then, under higher flow turbulence, the instantaneous laminar flame loses its original appearance, and propagates in a chaotic manner. The flame surface increases, causing higher burning rates, and then producing stronger flow expansion and higher turbulence intensities. In summary, the flame-generated turbulence triggers a positive feedback loop, causing faster flame propagation and subsequent pressure build up.In the early 1950s, Karlovitz and his co-workers first proposed the concept of flame generated turbulence. The theory behind the mathematical formulations outlined in (Karlovitz et al., 1951) is summarised below:

- As a reactive mixture passes through a flame front, it travels with a velocity equal to the normal burning velocity, S_u.
- Its specific volume increases from V_1 (initial volume) to V_2. This change in volume is due to the gas being heated.
- The gas leaves the flame front with a velocity equal to $(V_2/V_1)\cdot S_u$
- The flame front forms a flow source which introduces a velocity into the flow of gas, which is always normal to the instantaneous flame front.
- This introduced velocity has a magnitude equal to $[(V_2 - V_1)/V_1]\cdot S_u$
- When a turbulent flame is considered the instantaneous flame front is curved and therefore small sections of it are subjected to fluctuating motions, subsequently this causes fluctuations in this flame introduced velocity.

- This introduced velocity has an average forward velocity, Ū with a direction normal to the average turbulent flame front.
- The magnitude of Ū is large for slightly turbulent flames, decreasing as the flame becomes more turbulent. When this velocity is subtracted the remaining flame-introduced velocity components are randomly distributed and constitute turbulence generated by the turbulent flame.

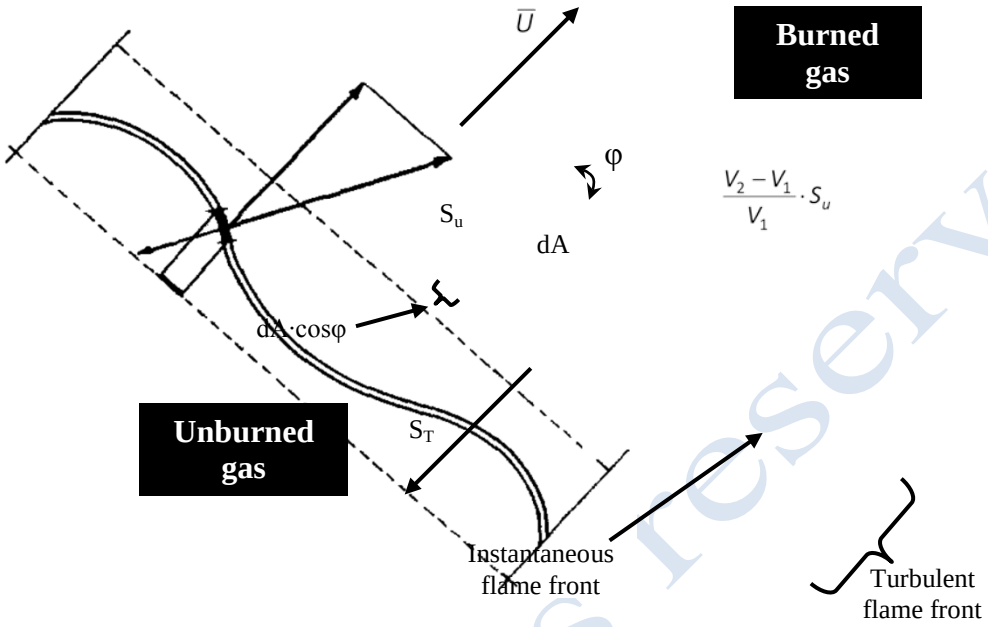

Figure 4.5 Schematic of the turbulent flame front, showing velocity vectors.

Using Figure 4.5 this theory can be formally written mathematically as per (Karlovitz et al., 1951). At the location of interest, A is considered to be the area of the flame front. Therefore the forward velocity component of the flame introduced velocity for a given element dA can be written as:

$$\frac{(V_2 - V_1)}{V_1} \cdot S_u \cdot \cos\phi \qquad \text{Equation 4.8}$$

The average value of this forward velocity is:

$$\overline{U} = \left[\frac{(V_2 - V_1)}{V_1} \cdot S_u \cdot \cos\phi\right] \qquad \overline{U} = \frac{(V_2 - V_1)}{V_1} \cdot S_u \cdot [\cos\phi] \qquad \text{Equation 4.9}$$

It should be noted that square brackets represent average values.

Since $\int_0^A \cos\phi \cdot dA = 1$ Therefore $[\cos\phi] = \frac{1}{A}$

Therefore Equation 4.9 can be rewritten as:

$$\overline{U} = \frac{(V_2 - V_1)}{V_1} \cdot S_u \cdot \frac{1}{A}$$ Equation 4.10

The area ratio A can be written as:

$$A = \frac{S_t}{S_u}$$ Equation 4.11

The area ratio is the ratio between the turbulent and normal burning velocities and can be written in this form as large-scale turbulence does not affect the structure of the instantaneous flame front.

Therefore Equation 4.10 can be written as:

$$\overline{U} = \frac{(V_2 - V_1)}{V_1} \cdot S_u \cdot \frac{S_u}{S_t}$$ Equation 4.12

The source of the additional turbulent energy is the amount of mechanical work that has been developed by the gas as it moves across the pressure drop at the flame front. To calculate this additional energy the unburned gas can be considered to be at rest. The flame can be regarded as moving with a velocity S_u into the stationary unburned zone. The burned gas can then be considered to be accelerated, due to the pressure drop across the flame front, to the velocity $[(V_2 - V_1)/V_1] \cdot S_u$, as shown in Figure 4.5.

The expansion work of the gas can be calculated as the kinetic energy of the burned gas:

$$Energy = \frac{1}{2} \cdot g \cdot \left[\frac{(V_2 - V_1)}{V_1} \cdot S_u \right]^2$$ Equation 4.13

A proportion of the expansion work which corresponds to the introduced mean forward velocity $\bar{U}$ is added to the energy of the mean flow. The remaining section of the expansion work provides the energy for the flame generated turbulence. The total intensity of this flame generated turbulence can be calculated from the energy equation, using Equation 4.14.

$$\overline{u}^2 + \overline{v}^2 + \overline{w}^2 = \left(\frac{(V_2 - V_1)}{V_1} \cdot S_u \right)^2 - \left(\frac{(V_2 - V_1)}{V_1} \cdot S_u \cdot \frac{S_u}{S_t} \right)^2$$ Equation 4.14

Where:

$\overline{u}^2, \overline{v}^2, \overline{w}^2$ Mean square values of the flame generated turbulent velocity components, m/s

As the flame becomes more turbulent, i.e. where the ratio of turbulent burning velocity to laminar burning velocity increases, the turbulence generated by the flame reaches its upper limit:

$$\overline{u}^2 + \overline{v}^2 + \overline{w}^2 = \left(\frac{(V_2 - V_1)}{V_1} \cdot S_u \right)^2$$ Equation 4.15

If it is considered that the energy distribution between these three velocity components is uniform:

$$u' = v' = w' = \frac{1}{\sqrt{3}}\left(\frac{(V_2 - V_1)}{V_1}\right)\cdot S_u \qquad \text{Equation 4.16}$$

Finally, if the flow is considered to be highly turbulent, it can be assumed that u' = S_t.

Therefore Equation 4.16 can be rewritten as:

$$S_t = \frac{1}{\sqrt{3}}\left(\frac{(V_2 - V_1)}{V_1}\right)\cdot S_u \qquad \frac{S_t}{S_u} = \frac{1}{\sqrt{3}}\left(\frac{V_2}{V_1} - 1\right) \qquad \frac{S_t}{S_u} = \frac{E_i - 1}{\sqrt{3}} \qquad \text{Equation 4.17}$$

Where:

E_i Expansion coefficient or density ratio of the combustion products, -

Therefore using the theory described above the upper limit for the flame wrinkling factor due to turbulence generated by the flame front itself has been derived for flows with high Reynolds numbers, this theory being brought together into Equation 4.17. As stated in (Karlovitz et al., 1951) this formula describing turbulent burning velocity shows that "large-scale turbulence may increase the burning velocity several fold, but its effectiveness diminishes with increasing intensity". Experimental data provided in (Karlovitz et al., 1951) confirms this.

4.1.1.3 Turbulent flames

Cellular flames

As describe in the previous paragraph, cellular flames can be observed for the mixture with a low Lewis number. When the flame becomes wrinkled due to hydrodynamic or/and thermo-diffusive instabilities, there is the formation of cells and then cellular flame structure is generated as shown in Figure 4.6 (Ciccarelli and Dorofeev, 2008).

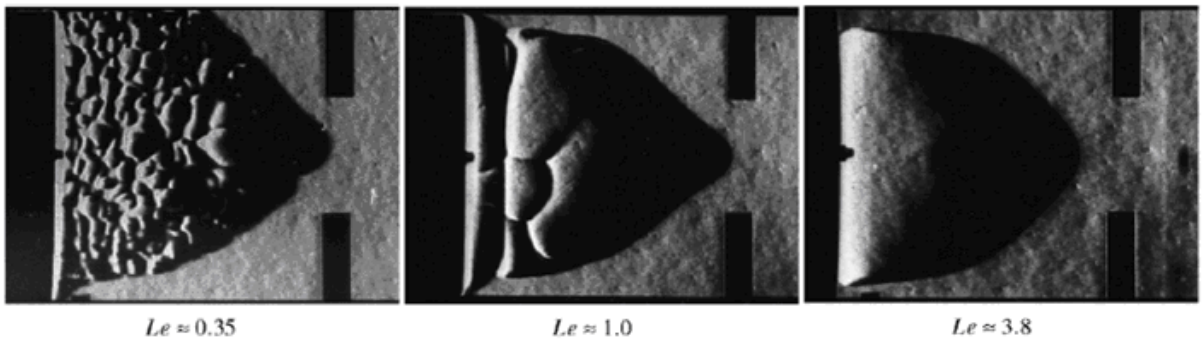

Figure 4.6 Schlieren photos of initial stage of flame propagation; From left to right: 10% H_2-air; 10% H_2 + 5% O_2+85% Ar; 70% H_2-air (Ciccarelli and Dorofeev, 2008).

Self-turbulising flames

The mathematics of fractal has been developed primarily by Mandelbrot (Mandelbrot, 1982). To describe the subject of fractals, Gouldin (Gouldin, 1987) considers the question: how long is the coastline of Great Britain? He argues that the answer depends on the measurement scale

and tends to be infinite when the measurement scale approaches zero. Assimilating Great Britain to a polygon of N sides of equal length ε (the measurement scale); the coastline length would be $N \cdot \varepsilon$, with this length increasing as ε is increased.

According to fractal theory, a straight line results when the measured lengths are plotted versus ε on a log-log scale, as shown in Figure 4.7 . Fractal nature is therefore characterized by a measured length of a curve (or the area of a surface) which depends on the measurement scale according to power dependence ε^{1-D} for curves (ε^{2-D} for surfaces). *D* is called the fractal dimension and is a non-integer for a fractal curve or surface, if the surface is smooth the fractal dimension *D* approaches 2, however if it is rough then *D* will approach 3.

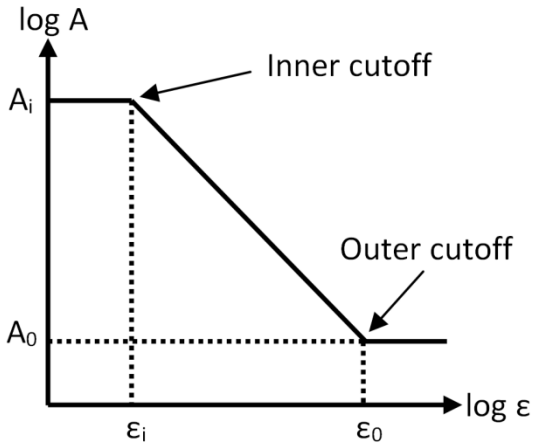

Figure 4.7 Self-similar representation of a fractal surface (Law, 2006).

As a flame continues to propagate the flame can become unstable. The formation of this instability is controlled by the Peclet number, *Pe* which is defined as the ratio of the flame radius to the flame thickness. When the flame radius becomes large enough, so that the Peclet number is larger than a specific critical value, transition from a stable to an unstable flame can occur. Then as the flame continues to expand the area of individual cells increases, until at a secondary critical Peclet number, Pe_{cl} smaller cells are then created (Gostintsev et al., 1988) (Bradley, 1999). Above this critical Peclet number the wrinkling of the flame is referred to as displaying "fractal-like flame wrinkling" (Molkov, 2010). Gostintsev (Gostintsev et al., 1988) surveyed the results of experimental measurements of flame propagation in large-scale explosions and suggested a critical Peclet number, of between 120,000 and 220,000, for the transition to a turbulent flame. Bradley (Bradley, 1998) reported that in every case the burning velocity is about three times the laminar burning velocity just after the suggested transition.

In this regime the laws of variation of *R* with time and of the visible velocity of propagation *R(t)* become virtually identical for all flames studied:

$$R = R_0 + A \cdot t^{3/2} \qquad \text{Equation 4.18}$$

$$\dot{R} = \frac{3}{2} \cdot A \cdot t^{1/2} = \frac{3}{2} \cdot A^{3/2} \cdot R^{1/3} \qquad \text{Equation 4.19}$$

where A^2 has the dimensions of the rate of energy release per unit mass [J/(kg.s)], and R_0 is the critical radius at which the self-similar regime takes place. R_0 may depend on the conditions of ignition and the existence of perturbation factors on the starting process. The constant *A* is fundamental for the self-similar regime of turbulent combustion and its value remains approximately constant from one experiment to another for each individual mixture (Gostintsev et al., 1988). As an application of an appropriate mechanism representing fractals is being considered, for fully developed turbulent flames, the critical radius (describing the

transition of the flame from laminar to the fully turbulent regime) must be considered. This regime changed can be clearly identified on the series of experimental data provided in Figure 4.8.

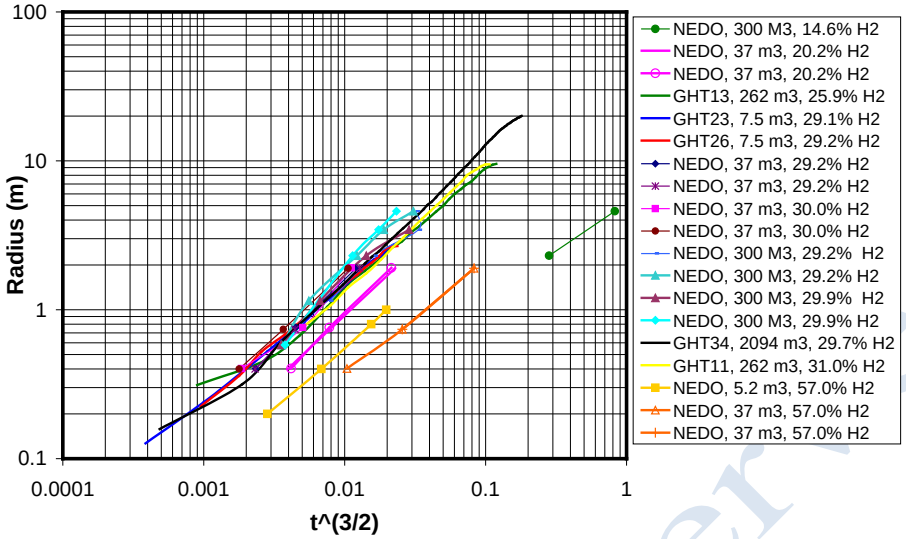

Figure 4.8 Unconfined flame propagations as a function of $t^{(3/2)}$.

According to fractal theory (Gouldin, 1987), the measured area of a surface in volume of size *R* depends on the area measurement scale ε^2 as by:

$$A_t \approx \varepsilon^{2-D} R^D \qquad \text{Equation 4.20}$$

where *D* is fractal dimension and ε is inner cut-off. The inner cut-off and the fractal dimension are difficult to model and will require additional experimental or DNS information (Fureby, 2004).

A wide range of experimental values were suggested for the fractal dimension of flames. Murayama and Takeno (Murayama and Takeno, 1989), obtained fractal dimension data varying between 2.2 and 2.35, with an average value around 2.26 for open atmosphere turbulent flames. Similar values were reported Gostintsev et al. for freely propagating premixed flames *D = 2.2 - 2.33* (Gostintsev et al., 1988). Bradley suggested a theoretical value of *D = 2.33* (Bradley, 1999). Gouldin argued that for low intensity turbulence the fractal dimension is lower than 7/3, and found *D = 2.11* for very low turbulent flow intensities (Gouldin et al., 1989). In 1990 Gülder (Gulder, 1991) reported fractal dimensions within a range *D*=2.14-2.24. North and Santavicca (North and Santivicca, 1990) defined the fractal dimension by an empirical parameterization as a function of (u'/S_u):

$$D = \frac{2.05}{u'/S_u + 1} + \frac{2.35}{S_u/u' + 1} \qquad \text{Equation 4.21}$$

where *D = 2.05* in a limit of low flow intensities and *D = 2.35* for highly turbulent flow (North and Santivicca, 1990). Peters (Peters, 1988) and Kerstein (Kerstein, 1988) suggested the Gibson scale as the inner cut-off scale of the turbulent premixed flame surfaces, $\lambda_G = \Delta \cdot (S_u/u')^3$, which is the length scale below which flame-surface fluctuations are suppressed.

Another choice for ε_i is the Kolmogorov length scale: $\lambda_K = (\nu^3/\varepsilon)^{1/4}$ which is the smallest turbulent eddy scale. Both Gouldin et al. (Gouldin et al., 1989) and Murayama and Takeno

(Murayama and Takeno, 1989) found that the inner cut-off ε_i is significantly larger than the Kolmogorov length scale η. Experimentally measured flame structures do not support either of these scalings (Gülder, 1991), but rather that $\varepsilon_i \propto \delta_L$. Murayama and Takeno (Murayama and Takeno, 1989) and Takeno et al. (Takeno et al., 1989) determined experimentally that the inner cut-off is the thickness of the laminar flame, which is the smallest dimension that can be distorted by the turbulence. Taking chemistry effects into account suggests that ε_i also should depend on the Karlovitz number, *Ka*. Based on DNS and experimental data Gülder and Smallwood (Gülder, 1991), proposed $\varepsilon_i = \delta_L\left(\alpha + Ka^{\beta}\right)$ $0.5 < u'/S_u < 6.2$, where α and β are constants.

Effect of r.m.s turbulent velocity on burning velocity

A well-known effect of turbulence on premixed combustion consists of an increase in burning velocity by r.m.s turbulence velocity. A velocity variation *u(t)* is commonly characterized by two quantities: the mean velocity $\bar{u}$ and the root mean square (r.m.s) turbulent velocity, as illustrated in Figure 4.9.

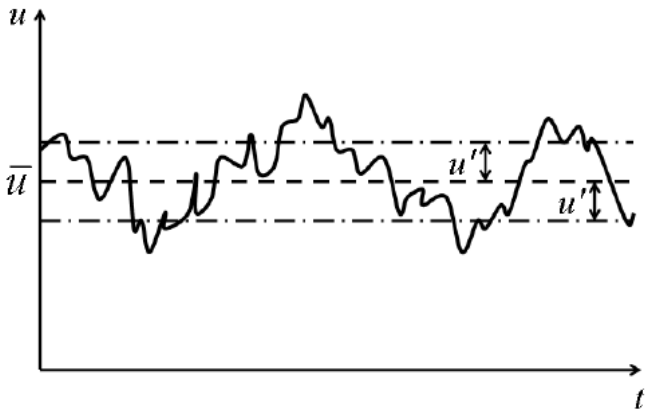

Figure 4.9 A sketch of velocity variation at a point (Lipatnikov and Chomiak, 2005).

Figure 4.9 shows the experimental data measured by Karpov and Severin (Karpov and Severin, 1978) (Karpov and Severin, 1980) to illustrate the effect of r.m.s turbulent velocity on burning velocity for different mixtures concentrations.

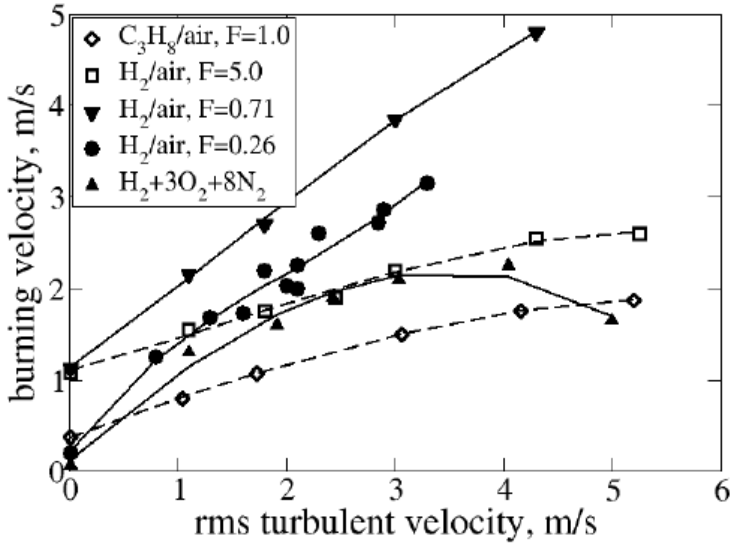

Figure 4.10 Burning velocity vs. rms turbulent velocity in several mixtures specified in legends, symbols show the data measured by Karpov and Severin (Karpov and Severin, 1980), the curves represent an approximation of the data (Lipatnikov, 2007).

The experimental data presented in Figure 4.10 shows that differences in molecular transport coefficient affect the local burning rate in premixed turbulent flames. In Particular, by comparing two hydrogen-air mixtures of different concentrations such as H_2-air of $\Phi = 0.71$ (denoted by $F = 0.71$ in Figure 4.10Figure 4.10) and H_2-air of $\Phi = 5.0$ (denoted by $F = 5.0$ in Figure 4.10), it can be clearly seen that, despite a lower initial laminar burning velocity of the former ($S_{u0} = 0.2$ *m/s* for H_2-air of $\Phi = 0.71$ against $S_{u0} = 1.1$ *m/s* for H_2-air of $\Phi = 5.0$), the turbulent burning velocity of the leaner hydrogen-air mixture ($\Phi = 0.71$) is much greater than the richer one ($\Phi = 5$) under the same r.m.s turbulent velocity, this effect being even more pronounced when considering the slopes of the corresponding curves.

Several approaches to model the influence of the difference in molecular transport coefficients on turbulent burning velocity can be considered i.e. the concept of the Markstein number, the concept of the critical stretch rate and the concept of the leading point.

The concept of the Markstein number

Markstein (Markstein et al., 1964) has suggested a linear relationship between flame speed and flame stretch. As stated by Bechtold and Matalon (Bechtold and Matalon, 1987) this dependence is characterised by a coefficient of the order of flame thickness. This has become known as the Markstein length, which is described by Clavin (Clavin, 1985) as a measure of the response of the flame to stretch. The factors that can influence Markstein length are known to include, for example, the properties of the reactant mixture, the effects of flame stretch itself and whether the flame is steady or unsteady. The Markstein number is reported by a number of authors carrying out experiments with spherically expanding flames. It has been assumed by Kwon et al. (Kwon et al., 1992) that the Markstein number is proportional to the characteristic flame thickness. Therefore the Markstein number can be defined as the ratio of the Markstein length to the thermal thickness of the flame. A flame will react differently to stretch and strain depending on the Markstein number (Markstein et al., 1964). When the Markstein number is positive flame stretch will result in a reduction in the local burning velocity (Pelce and Clavin, 1982) (Clavin and Joulin, 1983) however if the Markstein number is negative the burning velocity will increase (Dorofeev et al., 2001).

Higher (lower) mean values of the consumption velocity have been documented in many experimental and DNS studies of premixed turbulent flames characterized by high (low) diffusivity of the deficient reactant as reviewed in (Lipatnikov and Chomiak, 2005). Figure 4.11 below shows that the mean consumption velocity computed in DNS (Trouve and Poinsot, 1994) is significantly increased when the Lewis number decreases, in line with the concept of the Markstein number.

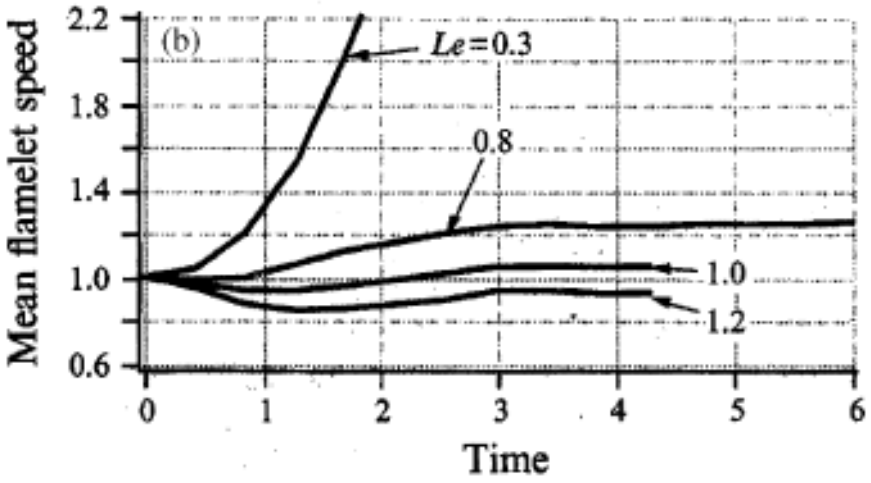

Figure 4.11 Development of the mean consumption velocity computed in DNS by Trouve and Poinsot at different Lewis numbers (Lipatnikov, 2007) from (Trouve and Poinsot, 1994).

DNS and experimental data shows that differences in molecular transport coefficient affect the local burning rate in premixed turbulent flames. It was shown in (Lipatnikov and Chomiak, 2005) that there is a qualitative agreement between the theory of weakly perturbed laminar flames – the concept of Markstein number – with dependence of S_t on D_d, where D_d is the molecular diffusivity of the deficient reactant. The concept of the Markstein number yields to a qualitatively correct dependence of S_t on Le. However the concept does not seem to be able to quantitatively predict the strong effect of Le on S_t, which is well documented in lean hydrogen-air mixtures. This limitation results from a number of assumptions (e.g. weak and steady perturbations), which the concept is based on but which do not hold in real turbulent flames. No model of premixed turbulent combustion, based in the concept of the Markstein number, has been shown to predict the strong dependence of S_t on D_d.

The concept of leading points

The crucial role played by leading points in turbulent flame propagation was highlighted by Zel'dovich (Zel'dovich and Frank-Kamenetskii, 1947) and the idea was developed by several groups in Russia.

According to Kuznetsov and Sabel'nikov (Kuznetsov and Sabel'nikov, 1990), the turbulent flame speed is controlled by the burning velocity of these leading point flamelets, where the mixture composition is locally altered due to different diffusivity of fuel and oxidiser, i.e. preferential diffusion.

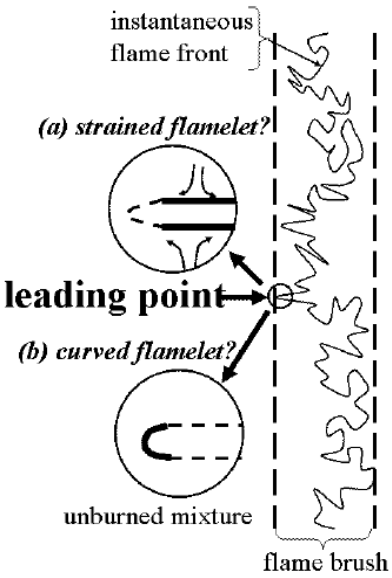

Figure 4.12 A schematic of a leading point and its possible structure (Lipatnikov, 2007).

Kuznetsov and Sabel'nikov (Kuznetsov and Sabel'nikov, 1990) have discussed the physical basis of the concept of leading points in detail and have argued that turbulent flame speed is controlled by the flamelets that advance the furthest into the unburned mixture (leading points, see Figure 4.12). The structure of the leading kernels is universal (independent of turbulence characteristics) as suggested by Baev and Tretyakov (Baev and Tretyakov, 1969).

There are two approaches to model the structure of the leading points. One, developed by Kuznetsov and Sabel'nikov (Kuznetsov and Sabel'nikov, 1990), places the focus of consideration on two almost parallel flamelets just behind the leading point (see Figure 4.12a) and considers these flamelets to be critically strained by turbulent eddies i.e. a further increase in the strain rate quenches the flamelets.

Based on the assumption of a critically strained structure for the leading point and different diffusivities of fuel and oxidiser, Kuznetsov and Sabel'nikov (Kuznetsov and Sabel'nikov, 1990) derived the model for a local change in the mixture composition within the leading point combustion zone as follows:

If $\alpha_{lp} \geq 1$, then $\alpha_{lp} = \frac{\alpha_0 (1 + C_{st}) \cdot d + d - 1}{d + C_{st}}$; if $\alpha_{lp} < 1$, then $\alpha_{lp} = \frac{\alpha_0 (C_{st} + d)}{1 + \alpha_0 \cdot C_{st} + C_{st} \cdot (1 - \alpha_0 \cdot d)}$,

where $\alpha_{lp} = 1/\phi_{lp}$ is the reciprocal of the equivalence ratio ϕ_{lp} at the leading point, α_0 is the reciprocal of the equivalent ratio ϕ in the original mixture, $d = \sqrt{D_{ox}/D_f}$, D_{ox} and D_f are the molecular diffusion coefficients of the oxidant and the fuel respectively, and C_{st} is the mass stoichiometric coefficient. Experimental data (Talantov and Gorenie, 1978), (Karpov and Severin, 1978) has shown to be consistent with this concept.

Another approach, developed later by Lipatnikov (Lipatnikov and Chomiak, 2005), (Betev et al., 1995), (Karpov et al., 1996), (Karpov et al., 1997), (Lipatnikov and Chomiak, 1998), (Karpov and Lipatnikov, 1995) highlights the tip of the conical flamelet surface (see Figure 4.12) and considers the flamelet structure at the tip to be critically curved flamelet.

Based on numerical simulation results, Lipatnikov and Chomiak (Lipatnikov and Chomiak, 1998) demonstrated that the highest burning rate is reached in the highly curved spherical

flame. For this and other reasons discussed in (Lipatnikov and Chomiak, 2005), (Karpov et al., 1997) and (Karpov and Lipatnikov, 1995), the highly curved spherical laminar flame kernel has been proposed to be used as a model of the structure of the leading kernels in turbulent flames. A method, drawing an analogy between the leading points and the so-called flame ball, studied first by Zel'dovich, was developed in (Karpov et al., 1997) to characterize the burning rate in the leading points.

Further on, Karpov and Lipatnikov (Karpov and Lipatnikov, 1995) proposed to introduce the chemical time scales of τ_{lp} and τ_{fb} to characterize the burning rate in the leading points for premixed turbulent combustion. These time chemical scales, i.e. τ_{lp} and τ_{fb}, were incorporated into the extended Zimont model by replacing the standard chemical time scale τ_c. The combined models were used to simulate the experiments of Karpov and Severin. They found that the leading point concept, associated with critically curved flamelets and supplemented with the chemical time scales of τ_{lp} allowed them to not only explain the strong effect of D_d on S_t at moderate turbulence, but also allowed them to quantitatively predict it.

Instabilities promoted by confinement and obstructions

When a flame is propagating in a closed space (an enclosure), acoustic waves are generated, which can be reflected from walls and/or obstacles and then interact with the flame front, resulting in a development of flame perturbations (Dorofeev, 2008). Consequently different instabilities can be observed: Rayleigh-Taylor (RT), Richtmyer-Meshkov (RM) and Kelvin-Helmholtz (KH).

In a confined or an obstructed space, Kelvin-Helmholtz instability corresponds to the shear instability whereas Rayleigh-Taylor instability occurs at the interface between two fluids with different densities and is developed when a lighter fluid is accelerated towards a heavier fluid. In the case of compressible fluids, Rayleigh-Taylor instability is known as Richtmyer-Meshkov instability.

Those instabilities may have a significant influence on the flame propagation (Ciccarelli and Dorofeev, 2008). They generally induce flame acceleration and in extreme cases, cause transition to detonation if the flame front is initially sufficiently fast (Kuhl, c1993.), (Thomas et al., 1997). For instance, both KH and RT instabilities are triggered when the flame is suddenly accelerated over an obstacle or through a vent.

As a summary of the instabilities previously introduced, it's possible to say that in the case of channels with obstacles, LD and thermo-diffusive instabilities are relatively weak in comparison with KH and RT instabilities, which are principally responsible of flame area increase and turbulence generation. However LD and thermo-diffusive instabilities may be involved at the initial phase of flame propagation and/or in cases of unconfined deflagrations/flames. Acoustic instabilities may be present for relatively slow flames in enclosures without obstacles. Turbulent flames can be generated by these instabilities or by a turbulent flow. The turbulent flame front is characterized by random local variations of the front position, resulting from the perturbations of the flow. Those variations result in an increase of the flame front and then an increase of the burning rate. For a turbulent flow, the following two parameters are key parameters to recognise: L_T, the characteristic length scale of turbulence, associated with the largest dimensions of turbulent motions, and u', the root mean square (r.m.s) turbulent velocity, defined by the fact that a velocity variation $u(t)$ is equal to the mean velocity $\bar{u}$ and u', recalling that $u(t) = \bar{u} + u'$) (see Figure 4.9).

Parametrization of turbulent flame burning velocity

Some authors (Bray, 1990) (Gülder, 1991) proposed an expression to calculate the turbulent flame burning velocity using the two characteristic parameters of a turbulent flow:

$$\frac{S_t}{S_{u0}} = k.\left(\frac{u'}{S_{u0}}\right)^a.\left(\frac{L_T}{\delta_L}\right)^b \qquad \text{Equation 4.22}$$

where *k*, *a* and *b* are coefficients relatively independent of the mixture. For instance, Gülder (Gülder, 1991) proposed the following coefficients: *k=0.62*, *a=0.75* and *b=0.25* and Bray (Bray, 1990) proposed: *k=1.8*, *a=0.412* and *b=0.196*.

The different combustion regimes can be described by the following dimensionless ratios u'/S_{u0} and L_T/δ_L, as in the Borghi diagram (Figure 4.13) (Borghi, 1985) (Ciccarelli and Dorofeev, 2008).

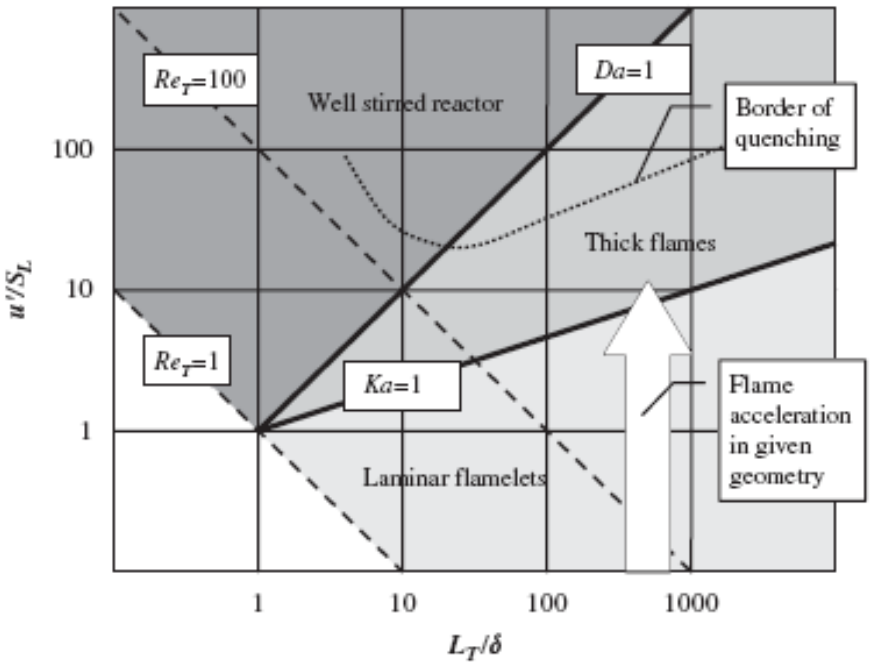

Figure 4.13 Borghi diagram of characteristic regimes of turbulent combustion (Ciccarelli and Dorofeev, 2008).

Slopes inside the Borghi diagram are expressed in function of non-dimensional numbers; the Reynolds, Damköhler and Karlovitz numbers as a function of u'/S_{u0} and L_T/δ_L ratios:

$$Re_t = \left(\frac{u'}{S_{u0}}\right).\left(\frac{L_T}{\delta_L}\right) \; ; \; Da = \left(\frac{u'}{S_{u0}}\right)^{-1}.\left(\frac{L_T}{\delta_L}\right) \; ; \; Ka = \left(\frac{u'}{S_{u0}}\right)^{3/2}.\left(\frac{L_T}{\delta_L}\right)^{-1/2} \qquad \text{Equation 4.23}$$

Those three non-dimensional numbers are linked by the following relation: $Re_t = Da^2.Ka^2$

On this diagram, it's possible to identify several combustion regimes. Each of these combustion regimes has a specific burning velocity and flame thickness dependence on turbulence.

- Laminar flame regime ($Re_t < 1$): In the wrinkled flame regime the RMS turbulent velocity is approximately equal to the laminar burning velocity. The thickness of the flame is smaller than the Kolmogorov scale. Where the flame is more strongly wrinkled, folded flames occur where the RMS turbulent velocity is greater than the

mainar burning velocity. These folded flames create pockets of unburned mixture within the burnt zone.

- Wrinkled flamelet regime ($Re_t > 1$, $Ka < 1$, $Da > 1$, $u'/S_{u0} < 1$). The thickness of the flame is still small. Burning takes place in laminar flamelets which wrinkle the surface when they pass through large eddies.
- Corrugated flamelet regime ($Re_t > 1$, $Ka < 1$, $Da > 1$, $u'/S_{u0} > 1$). Flame structure is still laminar but it's highly disturbed due to eddies passing through the flame front. 'Small tongues' of floded flames are formed which may eventually split off from the flame front. The folding process of the flamelet leads to the creation of pockets of unburned mixture pockets in combustion products.
- Thick flame regime ($Ka > 1$, $Da > 1$). Small eddies penetrated in the flame structure; several pockets of unburned mixture and combustion products are present in the flame zone. As a result, the combustion reaction occurs in thick flames.
- Well-stirred reactor regime ($Ka > 1$, $Da < 1$). Pockets of unburnt mixtures and combustion products are smeared out in space, then the reaction zone thickness becomes bigger and the reaction is slower. This process increases diffusion and rate of heat transfer to the cold mixture that leads to the observed drop in flame temperature.

4.1.2 Closed vessel deflagrations (HELION)

A closed vessel deflagration is an explosion that occurs in a vessel/enclosure which is capable of withstanding the pressure generated. In enclosures, the flame propagation velocity is sufficiently small (< 30 m/s) so that the internal pressure can be considered uniform (in the space). Even if flame propagation isn't fast, high pressures can be obtained as the vessel will prevent expansion of the burnt gas leading to pressure build up.

This condition is generally met when the ratio between the largest and the smallest dimension of the enclosure is less than 5 ($L/D < 5$; L = length; D = diameter/height/width (Proust, 2004). In the case of isochoric combustion, the maximum overpressure P_{max} depends only on the total quantity of burnt gas produced during the explosion. This overpressure cannot be greater than 12 or 13 bars (the hypothesis being reliant on the initial pressure being equal to atmospheric pressure) and almost exclusively depends on the nature of the reactant and its calorific value.

The theoretical value of the maximum overpressure is obtained for adiabatic isochoric complete combustion (AICC). Differences between the AICC pressure and the real peak pressure are related to the amount of energy lost during combustion.

The internal pressure increase between two successive instants is proportional to the volume of gas produced by combustion. The volume of gas produced is a function of the flame area, burning velocity and expansion ratio of combustion products. The curve defining pressure increase as a function of time forms an "S" shape (see Figure 4.14), which can be described using the following expression (Lewis and Von Elbe, 1987):

$$\frac{1}{P}.\frac{dP}{dt} \approx \gamma \frac{S_u A_f(t)(E-1)}{V} \qquad \text{Equation 4.24}$$

where $Af(t)$ is the flame surface, γ is the specific heat ratio ($\gamma = 1.4$ for hydrogen) and V is the volume of the enclosure.

Andrews and Bradley (Andrews and Bradley, 1972) established a relation, for a spherical propagation in a closed vessel, between the pressure increase dP_b/dt and the position of the flame (radius, r_b in the case of a sphere):

$$\frac{dP_b}{dt} = \frac{3\gamma P_b}{r_b}\left(E.S_u - V_f\right) \qquad \text{Equation 4.25}$$

where V_f is the visible/apparent flame velocity (from a fixed marker).

This kind of modelling allows, in theory, a connection to be made between the rate of pressure increase in a closed vessel, the enclosure geometry, and the rate of production of burnt gases. Considering the flame to be infinitely thin and radial propagation from the point of ignition (considering a spherical vessel of diameter D), the rate of pressure increase can therefore be calculated with good precision. Ellis and Wheeler (Ellis and Wheeler, 1927) as described in (Lewis and Von Elbe, 1987) showed that this approach is true for relatively compact equipment, considering central ignition.

$$\left(\frac{dP}{dt}\right)_{max} = \frac{6}{D}.S_c.\left(\frac{P_{max}}{P_0}\right)^{1/\gamma}.(P_{max} - P_0) \qquad \text{Equation 4.26}$$

where D is the diameter of the spherical vessel; S_c is the burning velocity (laminar or turbulent); P_{max} is the theoretical overpressure of combustion (maximum pressure at constant volume) and P_0 is the initial pressure.

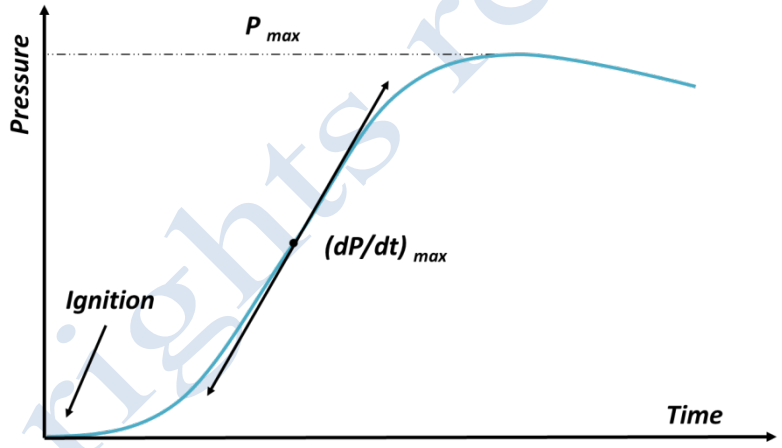

Figure 4.14 Example of explosion overpressure as a function of time in a closed vessel

The shape of the enclosure can have an impact on the pressure increase and on flame propagation. Two cases can be readily distinguished:

- An enclosure with L = D; flame propagation will be spherical (around the ignition point)
- An enclosure with L >> D (like pipes, channels or tunnels); flame propagation will be planar

When the overpressure and the flame speed are compared for these flame propagation modes, it can be shown that a higher flame velocity is required for the spherical mode than for the planar mode in order to obtain the same explosion overpressure. This can be explained by the fact that gas can expand more freely in the spherical mode than in the planar mode (Moen and Saber, 1986).

Deflagration index - Pressure increase coefficient

A characteristic parameter to evaluate closed vessel combustion is the coefficient K_G known as the deflagration index. This coefficient is used to define the "explosion violence" of a mixture and then to classify and compare different gases. It per *dP/dt*, the K_G coefficient is also strongly dependent on test conditions such as volume and geometry of the vessel, type and amount of ignition energy, temperature and pressure conditions.

This coefficient is calculated by multiplying the maximum rate of pressure increase with a characteristic length (here the cube root of the vessel volume) and defined by Equation 4.27:

$$K_G \equiv V^{\frac{1}{3}}.\left(\frac{dP}{dt}\right)_{max} \qquad \text{Equation 4.27}$$

where V is the enclosure volume.

K_G values for different gases and for a range of volumes have been tabulated in the NFPA-68 (NFPA 68, 2007). For example, for a spherical enclosure of 5 L and ignition by an electrical spark of roughly 10 J, in normal conditions, P_{max} is equal to 6.8 bars and K_G is equal to 550 bar m/s for hydrogen.

4.1.3 Open atmosphere deflagration (HELION)

Open atmosphere deflagrations are also called Unconfined Vapour Cloud Explosions (UVCE) and correspond to the ignition of an unconfined cloud formed after a leak. Due to the expansion ratio, the burnt gases produced during combustion act as "piston" on the surrounding atmosphere and generate a "pressure wave".

Leyer (Leyer, 1983) shows that the speed of this "piston effect" u_p (or the Mach number M_p) is directly linked to the speed of flame propagation V_f towards the unburnt gases (or Mach number M_f) and to the expansion ratio E. These relationships can be defined through the following expression:

$$M_p = M_f.\left(1 - \frac{1}{E}\right)^{1/3} \qquad \text{Equation 4.28}$$

The solution of the physical problem of pressure wave production by an unconfined explosion has been developed and validated several times (Guilbert-Duplantier, 1993) (Lee, 1988). Mathematically, the solution is the application of an "acoustic" model to flames (Van Den Berg, 1985) (Leyer et al., 1993) (Leyer, 1982).

Leyer (Leyer, 1982) and Deshaies (Deshaies and Leyer, 1981) provided the most significant developments. An analytical model has been developed that permits the prediction of wave propagation in the environment. Using this modelling allows for the Navier-Stokes equations to be solved by dividing the computation space into different areas namely: the flame front, the burnt gases and the unburnt gases. Near the front, the unburnt gases are considered as incompressible fluids.

At a distance from the flame front, the "acoustic" solution is:

$$\Delta P = \frac{\rho_0\left(1 - \frac{1}{E}\right)}{4\pi r}.\frac{d^2V_{flame}}{dt^2} \qquad \text{Equation 4.29}$$

with

$$\frac{\partial^2 V_{flame}}{\partial t^2} = \frac{\partial}{\partial t}\left(A_f . S_f\right)$$ Equation 4.30

where ΔP is the overpressure at the distance r from the location of ignition; ρ_0 is the density of the surrounding gas; V_{flame} is the volume of the "acoustic source" (here the ignited volume of gas); A_f is the surface of the "acoustic source" and S_f is the spatial speed of the flame.

This type of modelling forms the basis of estimation methods of pressure effects, in the case of spherical flame propagation in explosive clouds, this model being the tool base of the Multi-Energy Method (Van Den Berg, 1985).

Flow generated by an open atmosphere deflagration

The flow induced by a deflagration of an r_0-radius-spherical combustible charge in an open and infinite space can be divided into four distinct areas (see Figure 4.15):

- The first area is the area contained the burnt gas, delimited by the spherical flame front of a radius r_f. This area concerns every radius r as $0 < r < r_f$. The area containing the burnt gas is hot and is assumed to be quiescent, so that the pressure inside the "fire ball" is approximated as being constant.
- The second area corresponds to the flame front itself ($r = r_f$). The flame can be considered as an interface with a thin thickness, in comparison to the volume containing the burnt gases, where the transformation of reactants into combustion products takes place. The shape of the reactive area can be complicated particularly when turbulent eddies interact with the combustion process. Considering the expansion ratio, the maximum radius of the flame is defined, for a fuel-air mixture near stoichiometry, as:

$$r_{f_{max}} = E^{1/3} . r_0 \approx 2 . r_0$$ Equation 4.31

- The third area is the unburnt gas, which is in direct contact with the flame and the burnt gases so that the local pressure is close to the flame front pressure. In this case, the flow is correctly described by the incompressible fluid dynamic equations. The extension of this area can be written as: $r_f < r < 2r_f$.
- The fourth area is comprised between $2r_f$ and the maximum distance covered by the initial pressure wave (called the "first wave"). In this area, the pressure field obeys the acoustics laws. Beyond this area, the surrounding air isn't modified.

When the flame speed is smaller than about 120 m/s, the amplitude of the first wave is equal to zero and the pressure field doesn't create a discontinuity upstream from the flame. Above 120 m/s, the first wave is a shock wave (Leyer, 1982).

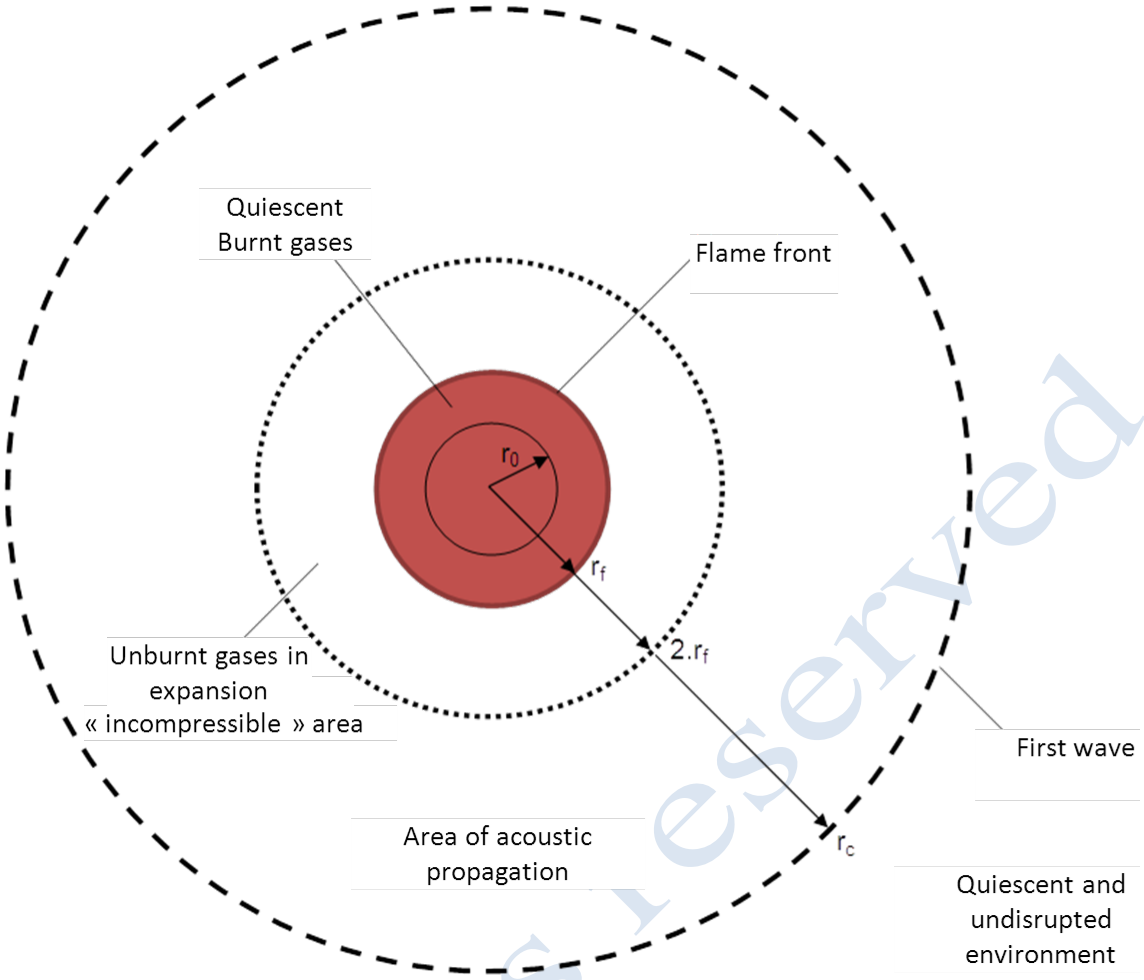

Figure 4.15 Flow generated by a spherical deflagration.

Cambray (Cambray et al., 1979) proposed general analytic solutions, also available for high Mach numbers.

Leyer (Leyer, 1982), (Leyer, 1983) and Deshaies and Layer (Deshaies and Leyer, 1981) gave a general description of the pressure signal. It appears, for example, for constant speed propagation, that the overpressure ΔP at a distance r (which is greater than the flame radius r_f) has the same shape as indicated in Figure 4.16. After the first pressure wave, the pressure increases linearly up to the quenching of the flame, that occurs when the flame has reached its maximum radius, r_{fmax} at:

$$t^+ = \frac{r_0 . E^{1/3}}{V_f}, \qquad \text{Equation 4.32}$$

The deceleration and cessation of the flame at the end of propagation leads to a rapid fall in pressure. At a fixed moment, the profile of the pressure field in the space is as shown in Figure 4.16 (picture B). In the burnt gases, the pressure is uniform and slightly lower than the maximum overpressure for the flame front. In the acoustic area, the overpressure decreases as *1/r*, moving away from the flame front. The acoustic area is linked to the surrounding air by the first wave.

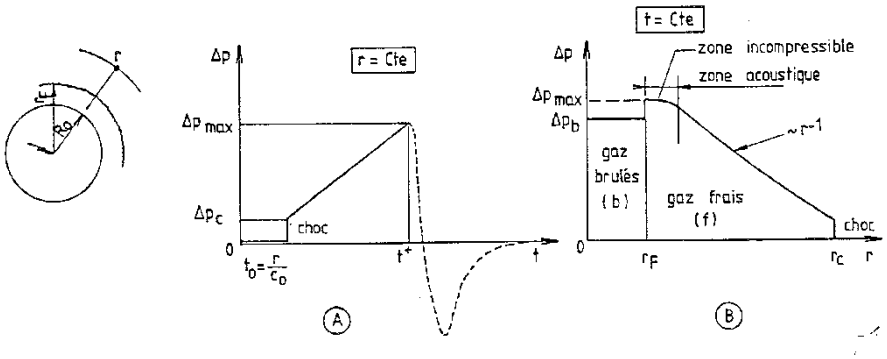

Figure 4.16 Overpressure, as a function of time (A) and distance (B), generated by a spherical deflagration (Leyer et al., 1993).

If the flame speed is moderate (i.e. clearly lower than the speed of the unburnt gases, M_f < *0.35*), an accurate analytical solution for the pressure field can be obtained:

- In the acoustic area (fourth region), the explosion effect is experienced as the effect of a monopole acoustic source that gives out an acoustic wave in the environment (similar to the sounds emitted by a speaker).

  The pressure effect is represented by the relation:

$$\Delta P(r,t) = \frac{\rho_0\left(1-\frac{1}{E}\right)}{4.\pi.r}.\frac{d^2V_{flame}(\tau)}{dt^2} \qquad \text{Equation 4.33}$$

  where $\tau = t\text{-}r/c_0$, c_0 is the speed of sound in the surrounding gas (air).

  In the case of spherical propagation, a more explicit formulation can be obtained:

$$V = \frac{4}{3}.\pi.r_f^3 \qquad \text{Equation 4.34}$$

  Finally:

$$\Delta P(r,t) = \rho_0.\left(1-\frac{1}{E}\right) * \left[2.\frac{r_f(\tau)}{r}.\left(\frac{dr_f(\tau)}{dt}\right) + \frac{r_f^2(\tau)}{r}.\left(\frac{d^2r_f(\tau)}{dt^2}\right)\right] \qquad \text{Equation 4.35}$$

- In the incompressible area (third region), the analytic solution is:

$$\Delta P(r,t) = \rho_0.\left(1-\frac{1}{E}\right) * \left[2.\frac{r_f}{r}.\left(\frac{dr_f}{dt}\right)^2 + \frac{r_f^2}{r}.\frac{d^2r_f}{dt^2} - \frac{1}{2}.\left(1-\frac{1}{E}\right).\frac{r_f^4}{r^4}.\left(\frac{dr_f}{dt}\right)^2\right] \qquad \text{Equation 4.36}$$

  When the flame is rapid (i.e. *M > 0.35; Vf < 120 m/s*), the first wave takes the profile of a shock wave and can be ignored. If *M > 0.7*, the pressure profile between the shock wave and the piston is close to the incompressible solution. Some analytic solutions had been proposed (Lannoy, 1984) but they are difficult to use.

In the case of a flame propagating at constant velocity lower than 120 m/s, the expressions describing the pressure field become:

- In the acoustic area ($r >> r_f$):

$$\Delta P(r,t) = 2.\rho_0.\left(1-\frac{1}{E}\right).\frac{r_f}{r}.V_f^2.\left(1-\frac{V_f}{c_0}\right) \quad \text{Equation 4.37}$$

- Near the flame front ($r \approx r_f$):

$$\Delta P(r,t) = 2.\rho_0.\left(1-\frac{1}{E}\right).\frac{r_f}{r}.V_f^2.\left[1-\frac{\left(1-\frac{1}{E}\right)}{4}.\left(\frac{r_f}{r}\right)^3\right] \quad \text{Equation 4.38}$$

- In the burnt gases, the pressure is uniform:

$$\Delta P_b = \rho_0.\left(1-\frac{1}{E}\right).V_f^2.\frac{1}{2}.\left(3-\frac{1}{E}\right) \quad \text{Equation 4.39}$$

This set of analytical expression allows for the calculation, in all space and at a fixed moment, of the maximum overpressure generated by the explosion. This overpressure is expressed using the square of the flame velocity, V_f and decreases according to the inverse of radius r.

Multi-Energy Method

In order to obtain graphs for the pressure effects associated with open atmosphere deflagrations, and to obtain results applicable to all ranges of Mach number, solutions such as the TNO in the Multi-Energy Method can be implemented (Van Wingerden, 1984) (Van den Berg, 1980) (Van Den Berg, 1985).

The Multi-Energy Method is based on the following hypothesis:

- The flame is propagating at a constant speed, taken as the maximum possible for the plant considered
- The maximum flame propagation velocity is calculated in an empirical way, as a function of the cloud reactivity, its geometry etc.

The energy-scaled distance is calculated from the combustion energy:

$$\bar{R} = \frac{R}{(E_{comb}/P_0)^{1/3}} \quad \text{Equation 4.40}$$

where E_{comb} is the combustion energy and P_0 is the atmospheric pressure.

The dimensionless maximum static overpressure is defined by:

$$\Delta\bar{P} = \frac{\Delta P}{P_0} \quad \text{Equation 4.41}$$

The combustion energy of the explosion is the internal energy of the charge (volume of the fuel) and can be defined as the energy of Brode:

$$E_b = \frac{\Delta P_{max}.V}{\gamma - 1} \quad \text{Equation 4.42}$$

where ΔP_{max} is the maximum overpressure of an explosion at constant volume and V the volume of the initial charge.

Noticing that $V = 4/3 \cdot \pi R_0^3$ for a spherical charge and the expansion ratio $E \approx \Delta P_{max}/P_0$ (explosion at constant volume), a one-to-one relationship can be deduced between $(E_{comb}/P_0)^{1/3}$ and the radius of the initial charge R_0:

$$\left(\frac{E_{comb}}{P_0}\right)^{1/3} = \left(\frac{4}{3}.\pi.\frac{1}{\gamma-1}.\frac{\Delta P_{max}}{P_0}\right)^{1/3}.R_0 = \left(\frac{4}{3}.\pi.\frac{E}{\gamma-1}\right)^{1/3}.R_0 \qquad \text{Equation 4.43}$$

A similar relation can be obtained for a hemispherical charge with $V = 2/3 \cdot \pi R_0^3$.

Van der Berg (Van Den Berg, 1985) proposed the following graphs where the "intensity" of each explosion is characterized by an index with a range between 1 and 10, corresponding to the maximum level of overpressure (see Figure 4.17). These graphs allow for the determination of the dimensionless overpressure and the positive phase duration as a function of the energy-scaled distance.

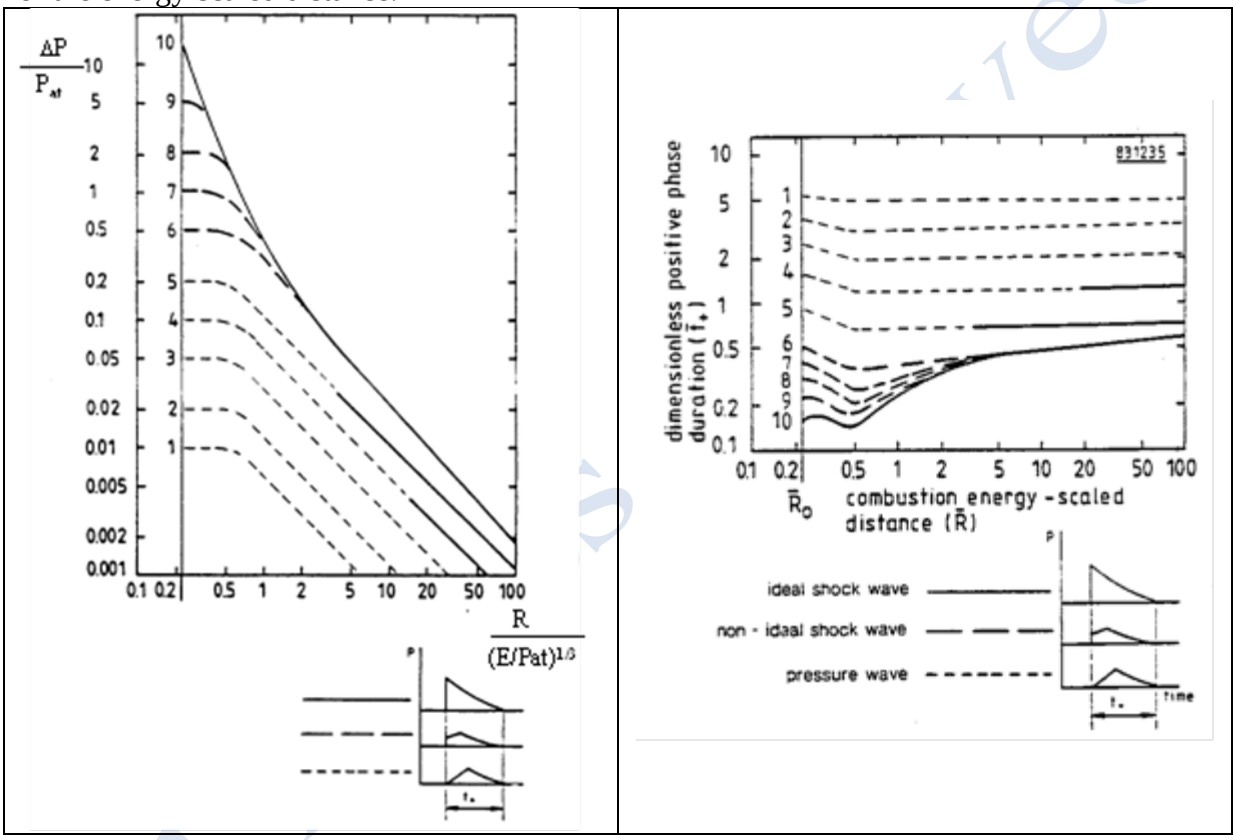

Figure 4.17 Graphs of maximal overpressure and positive phase duration in function of energy-scaled distance generated by a hemispherical deflagration at constant velocity.

The value of the impulse can be defined as:

$$I = \frac{(\Delta P.t^+)}{2} \qquad \text{Equation 4.44}$$

The determination of explosion effects (overpressure, impulse) from the graphs requires the estimation of the flame propagation velocity and the explosion energy, i.e. the size of flammable cloud.

These laws were the subject of experimental verifications. In the work of Koch and Drenckhahn (Koch and Drenckhahn, 1984), some explosion experiments using stoichiometric hydrogen-air mixtures were undertaken on a large range of volumes. The results showed the effect that a decrease in overpressure had on acoustic behaviour, decreasing as *1/r*. While in

the burnt gases, the pressure stayed constant, in agreement with the hypothesis of the deflagration model at constant speed. For a fixed flame speed (or fixed overpressure level inside the burnt gases), the experimental points lined up with an only decreasing curve of overpressure as a function of r_0/r, whatever the volume of the initial charge.

4.1.4 Vented deflagrations, including coherent deflagration phenomenon (UU)

If hydrogen is allowed to disperse in an enclosed space with the resulting mixture concentration exceeding the flammability threshold, subsequent ignition results in the deflagration phenomenon – a rapid combustion of the mixture driven by heat transfer. The heat released by the deflagration causes the combustion gases and excess air to expand. It is accompanied with a rapid rise in pressure, which can result in the collapse of the enclosure. If the enclosure is sufficiently strong to withstand the pressure, the evolution of the pressure can become quite complex with several distinct pressure peaks.

The phenomenon of double peak pressure structure for vented gaseous deflagrations has been well established since the beginning of research into this topic in the 1950s (Kommitten for Explosions Forsok, 1957), but it has not been explained on a theoretical basis for a long time (Butlin, 1975). The existence of a two-peak pressure structure during the venting of deflagrations was demonstrated theoretically by models of Yao (Yao, 1974), Pasman et al. (Pasman et al., 1974), Bradley and Mitcheson (Bradley and Mitcheson, 1978) and Molkov and Nekrasov (Molkov and Nekrasov, 1981). An example of a typical two peak structure, experimental pressure transient is presented in Figure 4.18 (Dragosavic, 1973). The first peak occurs due to vent opening and the second peak due to the high combustion rate (large surface area) at the end of the deflagration.

Later studies by Cooper et al. (Cooper et al., 1986) revealed a more complex four-peak pressure structure for rectangular enclosures and very low vent release pressures (see Figure 4.19, top graph). Analysis of film records showed that pressure peak P_1 is associated with vent opening and venting of the unburned gas from the enclosure (Figure 4.19, top, middle, bottom). Due to the higher velocity of hot gas compared to the cold gas at the same pressure drop, burned gas venting begins almost immediately after pressure peak P_1, when vent opening pressure is above 7.5 kPa (Figure 4.19, middle, bottom), and thus contributes significantly to the fall in pressure at this stage of the vented deflagration. The second peak P_2 is due to the “external explosion” or the highly turbulent combustion of the unburned mixture pushed out of the vessel, resulting in a “coherent deflagration” of unburned mixtures inside and outside of the enclosure.

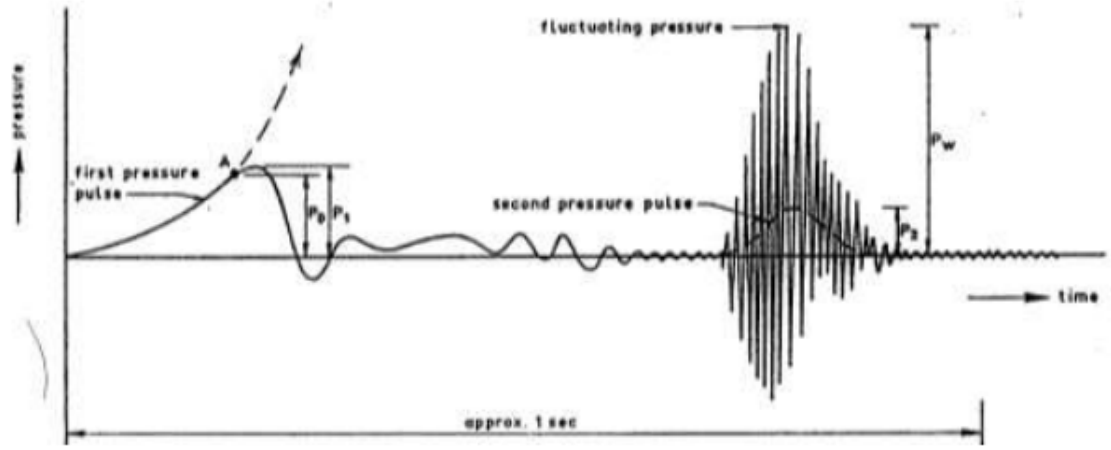

Figure 4.18 Typical experimental pressure-time curve with two characteristic peaks P_1 and P_2 (Dragosavic, 1973) Pressure P_0 corresponds to the vent opening pressure.

The coherent deflagration phenomenon refers to the multi-peak pressure evolution behaviour observed during vented deflagrations. The first pressure peak is produced by the deflagration of the hydrogen-air mixture in the enclosure. The pressure wave generated by this deflagration pushes the unburned fuel-air mixture from the enclosure through the vent, resulting in an increased concentration of combustible mixture outside of the enclosure. This mixture is subsequently ignited when the flame front reaches the vent, producing the external combustion, which exhibits high combustion velocities due to the mixture turbulisation occurring as it escapes from the enclosure. The pressure generated by this external deflagration effectively “closes” the vent, preventing the escape of combustion products from within the enclosure and producing the second recorded pressure peak. The synchronized rise of pressure outside and inside the enclosure lends the descriptor “coherent” to the phenomenon. Solberg et al. (Solberg et al., 1980) carried out one of the earliest studies highlighting the importance of external explosions.

Subsequent studies by Harrison and Eyre (Harrison and Eyre, 1987) came to the conclusion that for “large vents, where the internally generated pressures are low, the external explosion can be the dominating influence on the internal pressure” and that this influence “could be very important for large volume low strength structures such as buildings or off-shore modules”. Harrison and Eyre (Harrison and Eyre, 1987) simultaneously with Swift and Epstein (Swift and Epstein, 1987) suggested that the influence of the external explosion on the internal pressure dynamics is to decrease the mass flow rate through the vent. Theoretical analysis by Molkov (Molkov et al., 2007) based on processing the experimental data by Harrison and Eyre (Harrison and Eyre, 1987) confirmed that the turbulence factor inside the enclosure was practically not affected by the external explosion. Instead, the substantial decrease of the generalised discharge coefficient in the lumped parameter model, and thus the mass outflow, was found for tests with a distinct external combustion. It was concluded that the decrease in a pressure drop on the vent due to combustion outside the enclosure is the main reason for the reduction in the venting of the gas to outside the enclosure.

The external combustion is less important at higher vent opening pressures since only a small amount of unburned gas is ejected from the enclosure prior to its ignition. Thereby for such scenarios the second peak is no longer visible on pressure transient traces. The decrease of flame front area after the flame touches the enclosure walls is responsible for the third peak P_3. Cooper et al. (Cooper et al., 1986) stated that the fourth peak P_4 is generated when pressure waves resulting from the combustion process couples with the acoustic modes of the

vessel, setting up sustained pressure oscillations thus satisfying the Rayleigh criterion (Lord Rayleigh, 1883). The third and fourth peaks, P_3 and P_4 still occur at failure pressure 7.5 kPa (see Figure 4.19, middle). At the highest vent opening pressure of 21.7 kPa (Figure 4.19, bottom) only two peaks are observed. The second major peak is clearly due to acoustically enhanced combustion (Cooper et al., 1986). Peak P_3 is no longer observed since the onset of the rapid combustion process responsible for P_4 occurs prior to any significant reduction in flame area due to the interaction of the flame front with the enclosure walls.

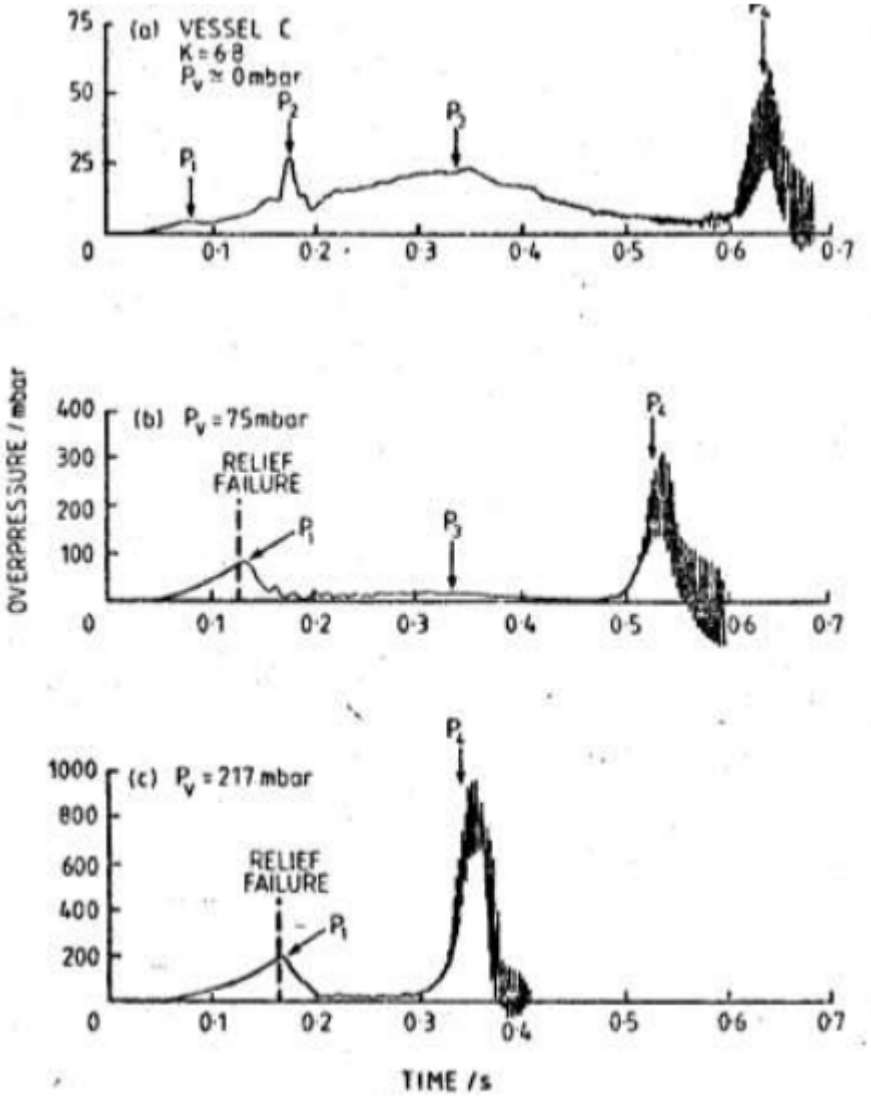

Figure 4.19 Pressure transients (Cooper et al., 1986): with four peaks at low vent opening pressure (top), three peaks at medium vent opening pressure (middle), two peaks at high vent opening pressure (bottom).

It can be noted that by increasing the failure pressure of the relief panel to above 7.5 kPa the two pressure peak structure becomes the dominant feature on the observed pressure-time profiles (Figure 4.19, middle and bottom graphs). This value has to be confirmed for hydrogen-air deflagrations as experiments by Cooper et al. (Cooper et al., 1986) were carried out using another flammable gas. Requirements in many industrial situations preclude the use of low failure pressure reliefs. In circumstances where a high failure pressure relief panel is employed the four pressure peaks identified by Cooper et al. (Cooper et al., 1986) will not all

be discernible on any pressure trace, as can be seen in Figure 4.19. Moreover, the relative ease, with which the fourth acoustically driven peak can be significantly reduced in magnitude or eliminated altogether, suggests that in most practical situations acoustically enhanced pressures will be of little or no importance (Cooper et al., 1986) (Van Wingerden and Zeeuwen, 1983).

The nature of the coherent deflagration phenomenon in a vented enclosure-atmosphere system has been investigated by Molkov and Makarov (Molkov and Makarov, 2003) using large eddy simulations (LES). Simulation results were compared against experimental observations within the SOLVEX (Shell Offshore Large Vented Explosions) research programme (Bradley et al., 2001) performed in the empty 547 m^3 vented enclosure, containing an initially quiescent methane-air mixture. A comparison between simulated and experimental pressure transients and dynamics of flame front propagation inside and outside the enclosure gave an insight into the nature of the complex simultaneous interactions between flow, turbulence and combustion inside and outside the enclosure (coherent deflagrations). Comparison of LES simulations with experimental data have shown that the substantial intensification of premixed combustion occurs only outside the empty SOLVEX enclosure and this leads to a steep coherent pressure rise in both internal and external deflagrations. The external highly turbulent premixed combustion does not affect burning rate inside the enclosure.

LES numerical model, described in detail by Makarov and Molkov (Makarov and Molkov, 2004) provided an excellent match between theory and experiment for coherent deflagrations in the empty SOLVEX facility. The rapid increase of the burning rate outside the enclosure commences not at the moment when the flame front emerges from the vent but after the flame front reaches the edges of the vent. The coherent steep pressure rise is observed both inside and outside the enclosure after this instance. The pressure rise in the atmosphere is a direct consequence of the highly turbulent deflagration outside the enclosure.

It is important to notice that the model contained only one ad hoc parameter, which is used to account for the unresolved sub-grid scale (SGS) increase of the flame surface density outside the enclosure (Molkov, 2012) due to the generation of small-scale swirling structures in the flow downstream of the vent edges. This flow phenomenon is unresolved in the simulations as a relatively coarse mesh is implemented. The LES model correctly reproduces the experimental pressures at different locations inside and outside the enclosure, as well as the development of the deflagration in the atmosphere when the ad hoc parameter is gradually increased outside the enclosure, from its default value of 1 to 2 in a time equal to the completion of the external combustion.

At the same time no increase of the burning rate inside the enclosure has been observed. The pressure rise inside the enclosure is caused by the decrease of mass flow rate from the enclosure to the atmosphere, due to the decrease of pressure drop at the vent as a result of the intensive combustion of the flammable mixture as it emerges into the atmosphere in front of the vent. The application of an ad hoc parameter inside the enclosure, or both inside and outside the enclosure, leads to inadequate dynamics of the coherent deflagrations (Molkov and Makarov, 2006).

Vented deflagrations, characterized by a rise ina number of instabilities, occurrs as the unburned mixture and combustion products escape through the vent. One of the potentially important types of instabilities occurring during vented deflagrations is Rayleigh-Taylor (RT) instability. Rayleigh-Taylor instability was first described by Lord Rayleigh (1883) and by Sir G. Taylor (1950). It occurs at the interface between two fluids of different densities, subjected to acceleration in the direction from the lighter to the heavier. Accelerations in the flow, as

described by Zeldovich et al. (Zeldovich et al., 1985), may vary periodically in magnitude and sign and as such can have a stabilizing and destabilizing effect on the flame front.

The growth of this instability has been found to occur most prominently as the flame accelerates through the vent (Tsuruda and Hirano, 1987) and also close to the vent following the expulsion of the hot combustion gases (Solberg et al., 1981). Additionally, according to previous research undertaken at Ulster University (Makarov et al., 2010b), the flow conditions required for the growth of RT instability were identified following the application of the former version of the Ulster deflagration model to analyse the experiments described in (Shirvill et al., 2007). This result provided the basis for the inclusion of RT instability during the simulation of the present vented deflagration scenarios.

Rayleigh-Taylor instability was identified as playing a major role in pressure build-up during the external deflagration encountered within large scale scenarios. A model representing this instability has been developed (Keenan et al., 2014) and added to the multi-phenomena turbulent burning velocity deflagration model. The model has been implemented in the form of a separate transport equation for the Ξ_{RT} wrinkling factor, containing source and sink terms developed based on phenomenological considerations of RT instability. A detailed description of the RT model implementation is provided in (Keenan et al., 2014).

Another potentially important instability is produced by the interaction of acoustic waves generated by a deflagration within an enclosed structure. This type of instability is difficult to account for in CFD modelling, giving rise to significant discrepancies between computed and experimentally observed results, in cases where acoustic instabilities become important.

4.1.5 Vented deflagrations with inertial vent covers (UU)

The first studies on the influence of vent cover inertia on explosion overpressure were performed in the UK in the 1950s (Wilson, 1954), (Cubbage and Simmonds, 1955). They demonstrated that in order to prevent pressure from growing above the strength of the weakest structure part, in addition to sufficient vent area, it is necessary for vent cover inertia to be sufficiently low. A recent review of the state-of-the-art in explosion venting with inertial vent covers is provided in (Molkov et al., 2004).

Pressure dynamics of vented deflagrations with inertial vent covers

As previously discussed, vented deflagration pressure dynamics typically exhibit two or more pressure peaks (Butlin, 1975). The theoretical explanation for its appearance was provided by Yao (Yao, 1974), Pasman et al. (Pasman et al., 1974), and Bradley and Mitcheson (Bradley and Mitcheson, 1978). The first peak is associated with the opening of a vent cover, while the second is typically associated with combustion of the gas mixture outside of the enclosure, which effectively prevents the combustion products within the enclosure from escaping through the vent. It was experimentally (Cubbage and Simmonds, 1955) and theoretically (Korotkikh and Baratov, 1978) shown that inertia of the vent panels affects only the first pressure peak. Experiments with identical vent areas but with vent inertia up to 200 kg/m^2 have shown a linear trend between this first pressure peak and vent cover inertia (Cooper et al., 1986).

The observation that inertia of the vent panel, at least over the range of conditions from the tests, affects only the first pressure peak and has no effect on the second pressure peak was first made by Cubbage and Simmonds (Cubbage and Simmonds, 1955). Zalosh (Zalosh, 1979) demonstrated that, for tests in a 0.19-m^3 vessel, with the same vent area and inertia free covers, but different vent release pressures (for inertia-free vent covers the first pressure peak

is equal to release pressure), the second pressure peaks were almost identical, even though the first peaks differed by a factor of 2.5. Both results are similar in the sense of independence of two pressure peaks. Korotkikh and Baratov (Korotkikh and Baratov, 1978) have theoretically shown that the inertia of the vent cover does influence the value of the first peak, but does not affect the second one (Korotkikh and Baratov, 1978), (Korotkikh, 1980). This result would be expected to be correct only in cases where the vent cover is removed fully before the completion of combustion inside the enclosure. The same result was obtained during an analysis of real explosions (Molkov, 1999a). In 1983, Pilugin (Pilugin, 1983) confirmed this finding and showed that the instantaneous breakage of glass through all venting areas at different pressures (i.e. a different first pressure peak) does not influence the second peak. A more realistic model of glass breakage, with probability of glass failure over a range of pressures, compared to simultaneous breakage of all glass, was then used. This probabilistic model substantially changed the dynamics of deflagrations: the first pressure peak disappeared, the explosion impulse (the integral of internal pressure in time) on the structure increased, and, most importantly, the second peak increased in comparison with the instantaneous opening of glass vent covers. At the same time, the opening of glass panes in succession, predicted by the use of a probability failure model, led to "oscillations" in the pressure time transient in comparison with a "smooth" breakage.

In a series of tests by Cooper et al. (Cooper et al., 1986), identically sized vents of different surface densities in the range up to about 200 kg/m^2 were allowed to rest over the vent area in a horizontal plane, restrained only by their own weight. The results suggested a linear relationship between the first pressure peak and vent cover inertia. The mass per unit area of the relief panel was found to have no significant effect on the second pressure peak. The first pressure peak depended crucially on the failure strength of the explosion venting device installed, and as the relief failure pressure P_v increased with inertia, (i.e. weight of the panel) so did the first pressure peak P_1.

Effect of venting generated turbulence

The majority of experimental data on vented gaseous explosions have been obtained under conditions of low turbulence using small-scale equipment. Most empirical formulae do not, therefore, include a parameter accounting for the increase in burning velocity (flame front area in our model) due to turbulence (Marshall, 1980), (Dobashi et al., 1994), (Dobashi, 1997a), (Dobashi, 1997b). Turbulence generated by venting can be characterised by the turbulence factor χ (equivalent of turbulent-to-laminar burning velocity), introduced by Yao (Yao, 1982). Burgoyne and Wilson (Burgoyne and Wilson, 1960) observed that the smooth opening of hinged venting plates produced a lower overpressure compare to bursting membranes, which, as they suggested, was due to the lower level of venting generated turbulence for the gradual opening of the vent. Lower than expected overpressure was observed in experimental studies employing heavy hinged swing doors (Zalosh, 1979), and in the study where vent release panels opened at different pressures in the same test (Howard and Karabinis, 1980). Swift and Epstein (Swift and Epstein, 1987) suggested that slowly growing vent area generated less turbulence, and therefore required smaller vent area for the same effect. Tamanini (Tamanini, 1996) argued that the independence of the second pressure peak, from vent panel inertia, is due to the domination of combustion instabilities and acceleration close to the final stages of venting, meaning that the method of panel deployment plays a relatively minor role on the progress of the explosion.

Until recently the turbulence factor was not predictable from first principles (Yao, 1982). For a laminar spherical flame the turbulence factor is equal to unity. Solberg (Solberg, 1982) used a time-variable turbulence factor reaching as high as 20 to 80 to calculate the maximum

pressure rise. Molkov (Molkov, 1995) has calculated values up to 100 from the processing of experimental data on vented deflagrations in an enclosure of volume 4000 m^3 with obstacles (about 25 without obstacles). These numbers, with differences of two orders of magnitude, introduce the notion of possible failures in vent sizing.

The substantial effects of vent size and turbulence are clear: combustion with high turbulence and small vent areas gives pressures much higher than that for which buildings are normally designed (Rasbash et al., 1976).

Sometimes, opposite points of view can be found in the literature with regard to venting of deflagrations by use of inertial vent covers. For example, (Howard, 1972) stated that the higher the inertia of the venting panel the higher the pressure needed to accelerate the panel to the open position. Hence, for the total venting pressure to be low, vent panels, if any, must be of the lowest feasible inertia. A contrary statement was given by Burgoyne and Wilson (Burgoyne and Wilson, 1960), who showed experimentally that a smooth opening of the vent, for example, by hinged plates, led to a decrease of the maximum explosion pressure in comparison with bursting membranes. They suggested that the reason for this phenomenon was a lower level of generated turbulence due to the gradual opening of the vent. It can be suggested that the reason for this contradiction is the consideration of different pressure peaks by different authors. This underlines the importance of a unified approach and the need to estimate and compare all pressure peaks during vent design for enclosures with inertial vent covers.

An uncovered vent opening allows for vent flow from the very beginning of the explosion. One should expect a higher maximum pressure to occur for a covered vent, which prevents venting in the initial phase of the explosion. This seems, at least for relatively slow deflagrations, not always to be the case, as is evident from pressure–time traces of propane–air deflagration in 35 m^3 (Solberg, 1982). The possible reason could be differences in the development of venting-generated turbulence.

In Zalosh's (Zalosh, 1979) tests the vents were, with one exception, heavy hinged swing doors meaning that the full vent was not immediately open. A possible explanation for the lower than expected overpressures (by theory) is that the slowly varying vent area did not create as much turbulence as might be expected if the full vent area were immediately available (Swift and Epstein, 1987).

Howard and Karabinis (Howard and Karabinis, 1980) noted, in some of their tests, lower than expected overpressures, attributing them to poor reproducibility inherent in large-scale testing. Examination of their results showed that the vent release panels opened at different pressures during the same test. This would give a varying vent area, which could result in less turbulence. These results and theoretical analysis suggest that a staged venting process, in which the vent area grows gradually as the flame ball expands, could generate less turbulence and require a smaller vent area (Swift and Epstein, 1987).

Tamanini (Tamanini, 1996) gave the following interpretation to the independence of the second pressure peak on vent inertia in some experiments. Gas explosions are strongly influenced by the final stages of the venting process, since the flame tends to accelerate as it approaches the vessel walls. Due to the importance of this phenomenon, which is attributable to the development of flame instabilities, it is reasonable to accept the conclusion that the details of panel deployment may play a relatively small role in the subsequent progress of the gas explosion.

Anthony (Anthony, 1978) concluded that, of all the approaches so far examined, the one by Yao (Yao, 1974) seemed the most promising, since it had theoretical justification and was the

most versatile. Anthony (Anthony, 1978) noted that its major weakness was the need to introduce an arbitrary turbulence factor as a multiplier to the burning velocity. After these conclusions, an advanced approach was developed to model and study vented gaseous deflagrations by Molkov (Molkov, 1995) and colleagues (Molkov et al., 1991). This new approach has been verified on numerous experimental data (Molkov, 1999a), (Molkov and Nekrasov, 1981), (Molkov et al., 1991), (Molkov, 1999b), (Molkov et al., 2000). Moreover, the correlation for turbulence factor has been obtained and is under continuous development by inclusion of new experimental data (Molkov, 1999a), (Molkov, 1999b) (Molkov et al., 2000).

Empirical correlations for overpressure

According to Tamanini (Tamanini, 1996), an early attempt to predict the dependence of the explosion pressure on panel inertia was offered by the analysis of Rust (Rust, 1979). Harmanny (Harmanny, 1993) used his own modelling results to analyse experimental data and to develop some general conclusions. These included the observation that the volume of the enclosure was important, in addition to the mass per unit area of the panel. Harmanny's (Harmanny, 1993) analysis, however, failed to identify the effect of other important variables, such as the mixture reactivity. The model developed by Tamanini (Tamanini, 1996) assumed that the flame propagated throughout the entire event at a constant effective burning velocity. Tamanini (Tamanini, 1996) admits that this is probably a fair approximation in dust explosions, where turbulence generally dominates the combustion process. However, it is not true for most situations involving gaseous mixtures, where the venting process itself is known to cause the flame to accelerate.

Cubbage and Simmonds (Cubbage and Simmonds, 1955) proposed an empirical correlation for the first peak overpressure for the relief in the top of an oven as a function of oven volume, inertia of vent cover and vent area coefficient:

$$P_1 V^{1/3} = S \cdot (0.43 \cdot K \cdot w + 2.78), \qquad \text{Equation 4.45}$$

where P_1 – first pressure peak (kPa); w – inertia of vent cover (kg/m^2); V – oven volume (m^3); S – burning velocity (m/s); K – vent area coefficient (ratio of area of oven cross section to area of relief). The correlation was obtained for oven volumes up to 14 m^3, relief inertia between 1.5 and 34.2 kg/m^2, and vent area coefficient range: 1 - 4. The formula is strictly applicable to situations in which the pressure of vent release p_v does not exceed about 2 kPa.
Later on Cubbage and Marshall (Cubbage and Marshall, 1973) suggested a correlation for maximum explosion overpressure (in kPa):

$$P_m = P_v + 2.3 \cdot S^2 \cdot K \cdot w / V^{1/3}, \qquad \text{Equation 4.46}$$

which is based on experiments in chambers of volumes up to 30 m^3, using a variety of fuel gases to maximize the range of burning velocity. The correlation was devised from experiments which used positively fixed relief panels and had to be physically broken by the explosion in order to create an open vent (p_v is larger than about 2 kPa). The fact that overpressure is proportional to the square of burning velocity, and not to S, leads to some overestimation of explosion pressure for mixtures with S > 0.5 m/s. On the basis of experiments with such mixtures, British Gas (British Gas, 1990) recommended that the coefficient should be reduced to 0.7.
Molkov et al. (Molkov et al., 2004) rewrote Equation 4.46 based on the observation of the role of venting generated turbulence in the increase of the burning rate, and on the argument that the burning velocity S may be expressed as a product of the laminar burning velocity and the deflagration-outflow interaction (DOI) number χ/μ as:

$$P_1 = P_v + 0.007 \cdot \left(S_u \cdot \frac{\chi}{\mu} \right)^2 \cdot \frac{A_{cs}}{F} \cdot \frac{w}{V^{1/3}}, \qquad \text{Equation 4.47}$$

where DOI number is ratio of turbulence factor χ to generalised discharge coefficient μ. For enclosures without essential obstructions inside, the DOI number may be correlated as:

$$\chi / \mu = \alpha \cdot \left[\frac{(1 + 10 \cdot V_{\#}^{1/3}) \cdot (1 + 0.5 \cdot Br^{\beta})}{1 + \pi_v} \right]^{0.4} \qquad \text{Equation 4.48}$$

Here the empirical coefficients α and β assume values of α = 1.75 and β = 0.5 for hydrocarbon-air mixtures, and α = 1.00 and β = 0.8 for hydrogen-air mixtures.

$V_{\#} = V / V_{1m^3}$ is the dimensionless volume (numerically equal to the enclosure volume in cubic meters); $\pi_v = P_v / P_i = (P_{stat} / P_i + 1)$ is the dimensionless vent closure release pressure; $P_{stat} = P_v - P_i$ is the vent closure release pressure used in NFPA 68 (NFPA 68, 2007), bar gauge. The Bradley number *Br* is:

$$Br = \frac{F}{V^{2/3}} \cdot \frac{c_{ui}}{S_{ui}(E_i - 1)}, \qquad \text{Equation 4.49}$$

where c_{ui} is the speed of sound at initial conditions of deflagration (m/s); S_{ui} is the burning velocity at initial conditions (m/s) and E_i is the combustion products expansion coefficient at initial conditions.

As already mentioned, the second pressure peak doesn't depend on inertia of a vent cover (if the vent area is fully opened before the completion of the deflagration). The value of the second peak could be calculated in the case of reduced pressure not exceeding 1 bar using conservative vent sizing formula (Molkov, 2001):

$$P_2 = 1 + 5.65 \cdot P_v^{2.5} \cdot Br_t^{-2.5} \quad (Br_t \geq 2), \qquad \text{Equation 4.50}$$

where the turbulent Bradley number Br_t is related to the Bradley number *Br* as:

$$Br_t = \frac{\sqrt{E_i / \gamma_u}}{\sqrt[3]{36\pi_0}} \cdot Br \cdot \frac{\mu}{\chi} \qquad \text{Equation 4.51}$$

in which π_0 is the "pi" number; γ_u is the specific heats ratio for unburned mixture. It should be emphasized that the turbulent Bradley number includes the DOI number, χ/μ, in the denominator. In order for the overpressure at the second peak to be less than 1 bar the turbulent Bradley number has to be equal to 2 or greater.

For a cost-efficiently designed explosion protection system, when the vent area is equal to its lower limit and the inertia may be equal to its upper limit, the first pressure peak value has to be equal to or less than the second peak value: $P_1 \leq P_2$. The formula for calculation of the upper limit of the inertia of a vent cover based on this assumption was derived and presented in (Molkov et al., 2004) as follows:

$$w \leq \frac{V^{1/3} \cdot (F / A_{cs})}{0.007 \cdot S_u^2 \cdot (\chi / \mu)^2} \cdot \left[1 + P_v \left(\frac{5.65 \cdot (36 \cdot \pi_o)^{5/6}}{Br^{2.5} \cdot (E_i / \gamma_u)^{5/4}} \cdot (\chi / \mu)^{2.5} \cdot P_v^{1.5} - 1 \right) \right] \qquad \text{Equation 4.52}$$

Effect of turbulence on scaling vent cover inertia

Similarity analysis of the governing equations of vented deflagration dynamics has identified an approximation of the constant turbulence factor during venting. The scaling relationship between the surface density of the cover (w), the turbulence factor (χ), initial pressure (P_i), and perimeter (per) of the vent(s) can be written as (Molkov et al., 2004):

$$\frac{w \cdot (S_u \cdot \chi)^3}{per \cdot P_i} = const \qquad \text{Equation 4.53}$$

Equation 4.52 indicates a significant interrelationship between vent cover inertia and venting generated turbulence. A 20% decrease of turbulence factor allows for the use of a twofold heavier vent cover. Increase of initial pressure could be associated with proportional increase of vent cover inertia. Inertia of multiple vents with the same total venting area as one vent could be higher as the perimeter of vents will be larger.

4.1.6 Deflagration in obstructed environments (KIT)

Starting from the pioneering works of the 50's, e.g. Shchelkin (Shchelkin, 1940) , in many topical studies, e.g. Lee (Lee et al., 1985) it was found that, obstructions on the path of the propagating flame can result in strong flame acceleration (FA) and deflagration to detonation transition (DDT). In (Lee et al., 1985), (Shepherd and Lee, 1992) it was pointed out that such phenomena (FA and DDT) are of primary importance for practical applications, e.g., for industry relevant appliance. In general, qualitatively, the sequence of events leading to FA is well known: hot combustion products push the gas before the flame; this moving flow generates growing turbulence, as it flows over and around the obstacles; and the turbulence accelerates combustion process, thus providing positive a feedback mechanism.

In numerous works it was shown that the details of the obstacle configuration can decisively influence the regime of the combustion. One of the main parameter which is commonly used for the obstruction characterization is blockage ratio. However other geometrical characteristics can and actually affect the combustion process as well. In (Ardey and Mayinger, 1996), (Durst et al., 1996) different geometrical forms were studied: it was shown that turbulent hydrogen-air flames can be strongly accelerated, if in a combustion chamber obstacles with a high blockage ratio (BR > 50%, plate with rectangular opening) or even with a low blockage ratio (BR << 50%, tube bundles, gridiron) are used. The influence of different obstacle configurations (including variation of the blockage ratio, distance between obstacles, imitation of rough walls, etc.) were studied in the works of Teodorczyk (Teodorczyk et al., 1988), (Teodorczyk, 1995). Interesting tests were also performed in a vertical facility with a partially obstructed channel (Cheikhravat et al., 2007). A parametric study on the evaluation of limits for effective flame acceleration in obstructed closed geometries was carried out in (Dorofeev et al., 2001), (Dorofeev et al., 2000).

Numerical simulation can provide additional insight into the process of flame acceleration and DDT. Deeper understanding was obtained after the remarkably detailed CFD simulations presented in (Gamezo et al., 2007). However further efforts are continuously being undertaken to improve the knowledge and understanding of the role of obstacles in the combustion process, through advances in both experiments and numerical simulations. Among recent studies, for example, in (Gaathaug et al., 2012) an onset of detonation behind a single obstacle was studied; and in (Heidari and Wen, 2014) a possibility to simulate an onset of detonation using different techniques was considered. In the frame of the EC project HyPer

(Brennan et al., 2011) a study of small foreseeable releases and a possibly catastrophic hydrogen leakage followed by combustion of the resulting mixtures inside a fuel cell cabinet for a range of leak rates, blockage ratios and vents was investigated.

On the basis of the experimental work of (Friedrich et al., 2007), (Kuznetsov et al., 2010a), (Kuznetsov et al., 2011), (Grune et al., 2013b), (Grune et al., 2013a) on the flame acceleration in flat layers, an attempt to generalize utilization of the congestion characteristics using numerical simulations was made in (Yanez et al., 2011). The correlations proposed in (Kuznetsov et al., 2011) considers dependence on blockage ratio, distance between obstacles and layer thickness, while in the numerical experiments of (Yanez et al., 2011) geometrical parameters which were considered to be the most significant parameters of the layout were taken into account. Additionally to the above mentioned, the vertical interval between obstacles, the height of the obstacles, and, as an auxiliary parameter, the distance from the first obstacle to the top were also considered. The obtained correlation introduces a new set of dimensionless parameters and provides a noticeably higher level of generality due to additionally accounting for the detailed characterization of the obstruction. It should be noted however that the obtained correlation should not be used in practical applications, without solid experimental validation.

Note also, that most of the studies are made for artificially created obstacle sets, such as repetitive periodic grids, circular orifices in the tubes at the constant mutual distance, etc., while real industrial configurations will definitely include obstacles which are irregularly placed in the volume, with very different characteristic sizes. It is well known that rough tubes without material obstacles inside them and even smooth tubes are able to promote FA and DDT (Urtiew and Oppenheim, 1966). It was found that consideration of the boundary layer can give practical results for unobstructed tubes (Kuznetsov et al., 2005). Further analyses into this area of research could yield a considerable practical outcome.

Thus, the current status is that despite broad scientific discussion and relatively wide experimental data base, it is still a challenge to make predictive forecasts of the realization of the definitive combustion regimes in the conditions close to the real industrial environments.

4.1.7 Deflagrations in non-uniform and lean mixtures (UU)

Most numerical studies are devoted to uniform gaseous deflagrations. Hydrogen safety engineering requires the prediction of pressure loads for realistic scenarios which practically always include the formation and consequently the combustion of a non-uniform flammable mixture. To be considered as a reliable predictive tool CFD models have to be validated against large-scale experiments which reproduce real life conditions. For non-reacting flows, the quantities of interest in LES are determined by the resolved large scales. In turbulent combustion, the essential rate-controlling processes of molecular mixing and chemical reaction occur at scales which are much smaller than those that are resolved (Pope, 2004). Hence, these SGS processes have to be modelled. It is generally agreed that if more than 20% of turbulent scales are not resolved and have to be modelled then the method is called very large eddy simulations (VLES) rather than LES.

The VLES model previously applied for the prediction of large scale unconfined stoichiometric hydrogen-air deflagrations, and 20-30% (by volume) hydrogen-air deflagrations in a 78.5 m long tunnel, has been developed further to reproduce dynamics of lean uniform and non-uniform (gradient) hydrogen-air premixed combustion in a 5.7 m height and 1.5 m diameter cylindrical vessel (Verbecke et al., 2009), (Makarov et al., 2010a).

Similar to the previous studies by the same authors, the turbulent burning velocity model includes three interacting mechanisms: flow turbulence that is computed by Yakhot's (Yakhot, 1988) equation for premixed turbulent combustion; evolution of the turbulence generated by flame front itself with the maximum value calculated from the Karlovitz et al. (Karlovitz et al., 1951) theory; and change of a total flame front area with the integral flame scale (outer cut-off) and the flame front thickness (inner cut-off) following the fractal theory. The fractal sub-model was modified: instead of a constant fractal dimension a fractal dimension as a function of burning velocity and r.m.s. velocity is introduced to make the fractal sub-model more universal following (North and Santivicca, 1990).

An additional mechanism based on the leading point concept as formulated by Kuznetsov and Sabel'nikov and implemented by Zimont and Lipatnikov is introduced into the described LES model. The results of numerical simulations reproduced experimental data on flame propagation in the uniform 12.8%, 14%, 16% and 20% by volume hydrogen-air mixtures in a large-scale vessel. The model is further applied to simulate a non-uniform hydrogen-air deflagration: a mixture with concentration gradient (27% by volume of hydrogen at the top of the vessel and 2.5% at the bottom, average concentration 12.6%).

Good agreement is achieved between simulations and experimental data for dynamics of both pressure and flame propagation only when the fourth mechanism, i.e. the leading point concept based on the selective diffusion phenomenon, is introduced to the LES model (Verbecke et al., 2009), (Makarov et al., 2010a).

The selective diffusion phenomenon destabilises the flat laminar flame front of lean hydrogen-air mixtures and its mechanism may be described as follows: Combustion instabilities, including preferential-diffusive-thermal and hydrodynamic, cause perturbations of the laminar flame triggering the formation of a cellular flame structure and then flame wrinkling, e.g. (Bradley, 1999), (Bradley et al., 2001), (Lipatnikov and Chomiak, 2005), (Lipatnikov, 2007), (Dorofeev, 2008) and (Ciccarelli and Dorofeev, 2008).

Wrinkles protruding (convex) into the unburned mixture propagate with a higher velocity compared to concave wrinkles, due to redistribution of hydrogen close to these wrinkles. Indeed, due to higher diffusivity of hydrogen its concentration at convex wrinkles will grow and at concave wrinkles it will decrease.

Consequently, the burning velocity will increase or decrease respectively. This will lead to an increase in the amplitude of the wrinkles. The selective diffusion effect depends on wrinkle curvature, i.e. reciprocal to radius.

There is a curvature of wrinkles at which the effect of selective diffusion on mass burning rate is maximum. Because a real flame has a spectrum of wrinkles of different curvature, the flame will be led by those wrinkles that have the optimum curvature, from a point of view of maximum burning rate curvature. These wrinkles will be responsible for propagation of the leading edge of the flame front and are called "leading points". The concept of leading points was first suggested by Zeldovich and then developed further. Thus, an increase in the flame speed results from the development of the cellular structure, in combination with the formation of leading flamelet structures, i.e. leading points (Kuznetsov and Sabel'nikov, 1990), (Bradley, 1999), (Bradley et al., 2001).

Kuznetsov and Sabelnikov (Kuznetsov and Sabel'nikov, 1990) stated that the turbulent flame speed is controlled by the burning velocity of these leading point flamelets, where the mixture composition is locally altered due to the different diffusivity of the fuel and oxidiser, i.e. preferential diffusion. Based on the assumption of a critically strained structure for the leading

point and different diffusivities of fuel and oxidiser, they derived the model for a local change in the mixture composition within the leading point combustion zone as follows:

$$\alpha_{lp} = \begin{cases} \dfrac{\alpha_0(1+C_{st})\cdot d + d - 1}{d + C_{st}}, & \alpha_{lp} \geq 1; \\ \dfrac{\alpha_0(1+C_{st})}{1+\alpha_0 \cdot C_{st} + C_{st}\cdot(1-\alpha_0 \cdot d)}, & \alpha_{lp} < 1, \end{cases} \quad \text{Equation 4.54}$$

where $\alpha_{lp} = 1/\phi_{lp}$ is the reciprocal of the equivalence ratio ϕ_{lp} at the leading point; α_0 is the reciprocal of the equivalent ratio ϕ in the original mixture; $d = \sqrt{D_{0x}/D_f}$ where D_{0x} and D_f are the molecular diffusion coefficients of oxidant and fuel respectively; and C_{st} is the mass stoichiometric coefficient. To account for preferential diffusion effects for curved hydrogen flames the leading point concept was proposed by Kuznetsov and Sabel'nikov (Kuznetsov and Sabel'nikov, 1990) and implemented by Zimont and Lipatnikov (Zimont and Lipatnikov, 1995), who determined the hydrogen concentration at the leading points and found their corresponding burning velocities by linear interpolation of the experimental data provided by Karpov and Severin. Figure 4.20 shows the augmentation of burning velocity by the leading point phenomenon. Lean mixtures are all affected by this mechanism. For example, for 10% hydrogen-air mixture the laminar burning velocity has to be multiplied by a factor as large as 2.4.

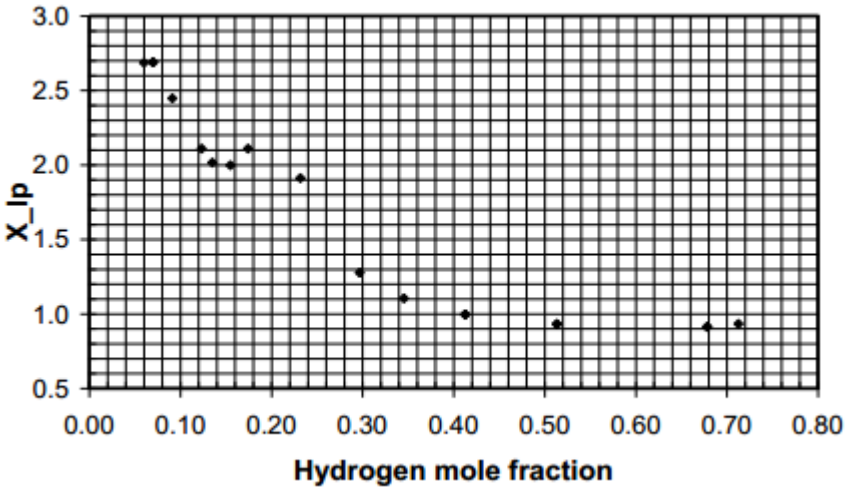

Figure 4.20 Leading point flame wrinkling factor as a function of hydrogen mole fraction (Verbecke, 2009).

The preferential diffusion effect coupled with flame curvature is pronounced for lean hydrogen-air mixtures and has to be accounted for in the premixed combustion model, for example, in the Ulster University LES combustion model it is accounted through an additional "leading point" turbulence factor (Verbecke, 2009). This mechanism of turbulent burning velocity enhancement, caused by flamelet perturbations in the proximity of these leading flamelets, cannot be resolved on meshes applied for large-scale problems and thus has to be modelled at SGS level. The leading point flame wrinkling factor Ξ_{LP} is introduced in the combustion model to correct the SGS burning velocity. It is assumed that the leading point turbulence coefficient develops linearly with radius to reach the maximum (see Figure 4.20) at half of the critical radius R_0. It remains constant after that, i.e. $\Xi_{LP} = \Xi_{LP}^{\max}$.

Four different combustion models were used in the inter-comparison exercise (Makarov et al., 2010a) to simulate lean uniform and non-uniform hydrogen-air deflagration in a closed vessel, using experiments performed by Whitehouse et al. (Whitehouse et al., 1996). The Ulster University LES combustion model accounts for the preferential diffusion mechanism of flame acceleration, which is important for combustion in non-uniform mixtures, based on the leading point concept by Kuznetsov and Sabel'nikov (Kuznetsov and Sabel'nikov, 1990) and implemented according to the Zimont and Lipatnikov (Zimont and Lipatnikov, 1995) model. Details of the leading point concept implementation in the Ulster University LES combustion model and its validation are available in (Verbecke, 2009).

The model also accounts for initially laminar flame propagation regime and major mechanisms for flame acceleration: 1) flow turbulence using the turbulent combustion model by Yakhot (Yakhot, 1988), 2) turbulence generated by the flame front itself according to the theory by Karlovitz et al. (Karlovitz et al., 1951), 3) fractal-like flame wrinkling mechanism in a fully developed turbulent combustion regime according to the experimental data by Gostintsev et al. (Gostintsev et al., 1988). The burning velocity is a function of the hydrogen concentration according to experimental data (Lamoureux et al., 2002) and dependence on pressure is accounted for as: $S_u = S_{u0}(Y_{H_2})(p/p_{0)})^{\varepsilon}$, where $S_{u0}(Y_{H_2})$ is the laminar burning velocity at initial pressure, and ε is the overall thermo-kinetic index as a function of the hydrogen concentration by volume. Three other combustion models - by Forschumcentrum Karlsruhe (presently Karlsruhe Institute of Technology, Germany), the Joint Research Centre (The Netherlands), and the Kurchatov Institute (Russia) - used burning velocity dependence on hydrogen concentration.

Bauwens et al. (Bauwens and Dorofeev, 2014) investigated the effect of initial turbulence on the overpressure produced by the deflagration of lean mixtures. The experiments were conducted at artificially elevated initial turbulence levels. Experiments were performed for lean hydrogen-air mixtures, with hydrogen concentrations ranging from 12 to 15% by volume. It was found that an increase in initial turbulence results in an increase of the overall flame propagation speed and this increased flame propagation speed translated into higher peak overpressures during the external explosion (Figure 4.21). The peak pressures generated by flame-acoustic interactions were not significantly affected by initial turbulence levels. It has been demonstrated that the burning velocity increased with flame radius as a power function of radius, with a relatively constant exponent over the range of weak initial turbulence studied and did not vary systematically with initial turbulence. The elevated levels of initial turbulence produced increase of the initial flame propagation velocities of the various mixtures. The initial turbulence thus appears to affect deflagration pressures primarily through generation of the higher initial flame wrinkling while producing minimal effect on the growth rate of the wrinkles.

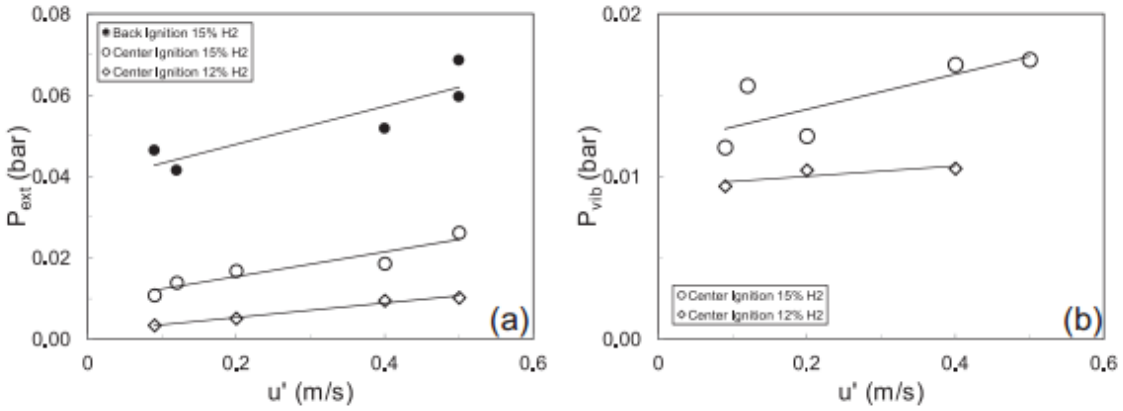

Figure 4.21 Variation in external (left) and internal (right) pressures with initial turbulence for hydrogen-air mixtures (Bauwens and Dorofeev, 2014).

4.1.8 Vent sizing correlation (UU)

Accurate modelling of the multi-peak pressure time evolution during vented deflagrations is, a complex CFD problem. For the purpose of safety engineering, however, it is sufficient to determine the maximum overpressure generated within the enclosure for the given vent area. Accordingly, a number of different empirical and semi-empirical engineering correlations aimed at predicting maximum overpressure for a specified vent size, or, conversely, allowing for the calculation of vent area required to keep overpressure below specified limit, have been developed. The same correlations may be used to cross-check the results of CFD simulations (though caution must be exercised in their application). A recent overview of equations for vent sizing and their inter-comparison and comparison against experiments with various hydrocarbon-air and hydrogen-air mixtures can be found in (Sustek and Janovsky, 2012).

One of such vent sizing technique had been under development at Ulster University since 1995 (Molkov, 1995) with its most recent version published in 2015 (Molkov and Bragin, 2015). This correlation, developed for low-strength equipment and buildings, i.e. cases when the deflagration overpressure or reduced pressure is below 0.1 MPa (initial pressure in such cases is usually atmospheric), is based on the observation that dimensionless reduced deflagration pressure depends only on the turbulent Bradley number Br_t, which in turn is uniquely dependent on the deflagration-outflow interaction (DOI) number, χ/μ. Accordingly, a general form of the correlation takes the following form (Molkov et al., 1999):

$$\pi_{red} = \lambda \cdot Br_t^{-\sigma} \qquad \text{Equation 4.55}$$

where λ and σ are empirical coefficients (theoretical value of σ is 2 (Molkov, 1996)), $\pi_{red} = P_{red}/P_i$ is dimensionless reduced deflagration pressure, P_{red} and P_i are reduced (gauge) deflagration pressure and initial absolute pressure respectively, and Br_t is the turbulent Bradley number:

$$Br_t = \frac{\sqrt{E_i/\gamma_u}}{\sqrt[3]{36\pi_0}} \cdot \frac{Br}{\chi/\mu} \qquad \text{Equation 4.56}$$

where Br is Bradley number, π_0 is "pi" number (3.1416…) and Bradley number is:

$$Br = \frac{F}{V^{2/3}} \cdot \frac{c_{ui}}{S_{ui}(E_i - 1)}$$ Equation 4.57

E_i in these equations is the combustion products expansion coefficient, γ_u is the specific heat ratio of unburned mixture, χ/μ is the Deflagration-Outflow Interaction (DOI) number, F is the vent area, V is the enclosure volume, S_{ui} is the initial laminar burning velocity, and c_{ui} is the speed of sound in the initial unburned mixture.

Examination of Equation 4.56 reveals that, in addition to geometric and thermodynamic parameters, which can be directly derived from the known experiment conditions, the major unknown parameter in Equation 4.55 is DOI number χ/μ, characterizing the effect of turbulence factor χ on the flame front coupled with the effect of generalized discharge coefficient μ. Present work follows an approach to model the χ/μ number, which had been developed in Ulster University during the past two decades and described in detail in (Molkov and Bragin, 2015), with a simplified calculation of wrinkling factors as described below.

The approach used in (Molkov and Bragin, 2015) presents DOI number as a product of different flame wrinkling factors:

$$\frac{\chi}{\mu} = \Xi_K \cdot \Xi_{LP} \cdot \Xi_{FR} \cdot \Xi_{u'} \cdot \Xi_{AR} \cdot \Xi_o$$ Equation 4.58

Individual wrinkling factors can be computed as follows: Ξ_K is the flame wrinkling due to Karlowitz turbulence generated by the flame itself (Karlovitz et al., 1951). Based on the theory by Karlovitz et al. (Karlovitz et al., 1951) and observations by Gostintsev et al. (Gostintsev et al., 1988) the following equation can be suggested for the turbulence generated by flame front itself (Molkov, 2012):

$$\Xi_K = 1 + (\psi \cdot \Xi_K^{\max} - 1) \cdot [1 - \exp(-R/R_0)]$$ Equation 4.59

where $\Xi_K^{\max}$ is the theoretical maximum of the Karlowitz wrinkling factor:

$$\Xi_K^{\max} = (E_i - 1)/\sqrt{3}$$ Equation 4.60

E_i is the combustion products expansion coefficient shown in Figure 4.22(a), ψ is the empirical coefficient characterizing how close Karlowitz number Ξ_K can approach its maximum theoretical value $\Xi_K^{\max}$ for a given hydrogen fraction in the mixture, R is the flame radius and R_0 is the characteristic flame radius for transition from laminar to fully turbulent flame.

The empirical coefficient ψ depends on the hydrogen fraction in the mixture. The precise nature of this dependence is presently unknown. It has been estimated that ψ can vary between approximately 0.5 for stoichiometric and rich mixtures (Molkov, 2012) and unity for very lean mixtures. Indeed, lean mixtures are subject to thermo-diffusive instability and may turbulise more easily. This increases the chance of achieving isotropic turbulent combustion and thus for Karlovitz turbulence to reach its theoretical maximum. Accordingly, Molkov and Bragin (Molkov and Bragin, 2015) approximated ψ with a function, as illustrated in Figure 4.22(b).

Flame radius R for the deflagration in the enclosure can be considered limited by enclosure dimensions (Molkov and Bragin, 2015) and calculated as the radius of a spherical flame with equivalent volume:

$$R = \sqrt[3]{3V / 4\pi_0} \qquad \text{Equation 4.61}$$

Studies by Gostintsev et al. (Gostintsev et al., 1988) indicated that for near stoichiometric and rich hydrogen-air mixtures with hydrogen concentration more than 20% by volume and up to the upper flammability limit of 75% by volume the transition to fully developed turbulent flame takes place at R_0 = 1 - 1.2 m. Molkov and Bragin (Molkov and Bragin, 2015) assumed that for lean hydrogen-air mixtures prone to thermo-diffusive instability the characteristic radius decreases with concentration. Accordingly, the dependence of characteristic radius from the hydrogen concentration by volume was estimate as:

$$R_0 = \begin{cases} -0.12 + 6.7X; 0.04 < X < 0.20 \\ 1.2; 0.20 < X < 0.75 \end{cases} \qquad \text{Equation 4.62}$$

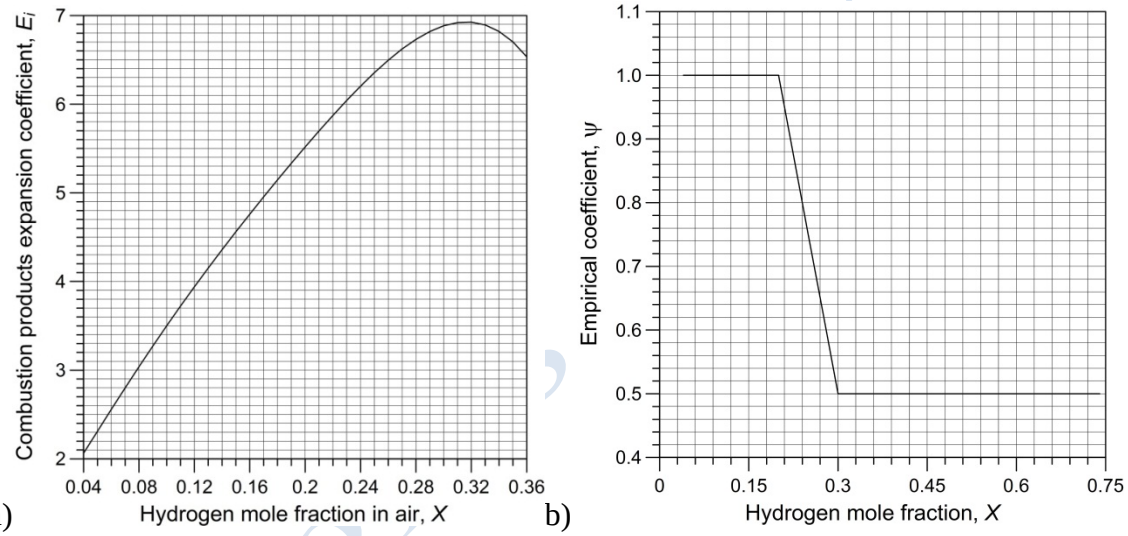

a) b)

Figure 4.22 a) Combustion product expansion coefficient E_i versus hydrogen mole fraction X ; b) Empirical coefficient ψ versus hydrogen mole fraction X (Molkov and Bragin, 2015).

The leading point wrinkling factor Ξ_{LP} accounts for the effect of preferential diffusion of hydrogen in stretched turbulent flames. It was suggested, based on results of CFD studies at Ulster University, that the leading point flame wrinkling factor Ξ_{LP} develops linearly with radius and reaches its maximum at half of the characteristic radius R_0 for Karlovitz turbulence and remains constant after this (Molkov, 2012). The leading point wrinkling factor changes linearly with radius from 1 to its maximum at $R_0/2$ as:

$$\Xi_{LP} = \begin{cases} 1 + \dfrac{(\Xi_{LP} - 1) \cdot 2R}{R_0}; \dfrac{R_0}{2} > R \\ \Xi_{LP}^{\max}; R > \dfrac{R_0}{2} \end{cases}, \qquad \text{Equation 4.63}$$

where Ξ_{LP}^{max} is the maximum leading wrinkling number, which is a function of hydrogen mole fraction in the mixture and can be approximated by the function shown in Figure 4.23(a) using piecewise polynomial approximation (Verbecke, 2009).

The wrinkling factor due to the fractal increase of flame front area is applied when the flame radius exceeds R_0 as:

$$\Xi_{FR} = \left(\frac{R}{R_0}\right)^{D-2}, \quad \text{Equation 4.64}$$

where fractal dimension $D = 2.33$ (Bradley, 1999).

The aspect ratio wrinkling factor:

$$\Xi_{AR} = A_{EW} / A_S \quad \text{Equation 4.65}$$

is responsible for the increase of the flame front surface area due to enclosure elongation, with A_{EW} equal to the internal enclosure surface area and A_S equal to the surface area of the sphere with the radius R.

The presence of the initial turbulence before the start of the deflagration process can produce additional wrinkling, which can be accounted for by introducing the wrinkling factor $\Xi_{u'}$. It is calculated through utilization of Yakhot's equation (Yakhot, 1988) for turbulent burning velocity S_t, modified as per (Molkov, 2012) by substitution of laminar burning velocity S_u by the unresolved subgrid sale (SGS) wrinkled flame velocity:

$$S_t = S_w^{SGS} \cdot \exp\left(\frac{u'}{S_t}\right)^2, \quad \text{Equation 4.66}$$

where S_w^{SGS} is the subgrid scale wrinkled flame burning velocity and u' is the RMS velocity in the unburned mixture at the start of the deflagration. Since the maximum overpressure during a deflagration is determined by the largest burning rate which is achieved by the end of combustion when the flame approaches enclosure walls and is affected by all the aforementioned wrinkling factors, S_u in Yakhot's original equation is replaced by the SGS wrinkled flame velocity.

$$S_w^{SGS} = S_u \cdot \Xi_K \cdot \Xi_{LP} \cdot \Xi_{FR} \cdot \Xi_{AR} \cdot \Xi_O \quad \text{Equation 4.67}$$

The value of the factor $\Xi_{u'}$ can subsequently be calculated as:

$$\Xi_{u'} = S_t / S_w^{SGS} \quad \text{Equation 4.68}$$

The initial laminar burning velocity can be obtained by interpolation of experimental data. Figure 4.23 shows experimental data by stretched and un-stretched laminar burning velocity obtained by (Lamoureux et al., 2003) for hydrogen concentrations above 10% by volume, extended with (Ross, 1997) data in the lean limit. Since laminar burning velocity depends on the initial temperature, this data is adjusted for the pre-deflagration mixture temperature T_i as:

$$S_{ui} = S_{u0} \cdot \left(\frac{T_i}{298}\right)^{m_0} \quad \text{Equation 4.69}$$

where m_0 is temperature index (Verbecke, 2009).

Due to the absence of obstacles in the newly added experiments under consideration, the wrinkling factor due to the presence of obstacles, Ξ_O, is assumed to be equal to unity.

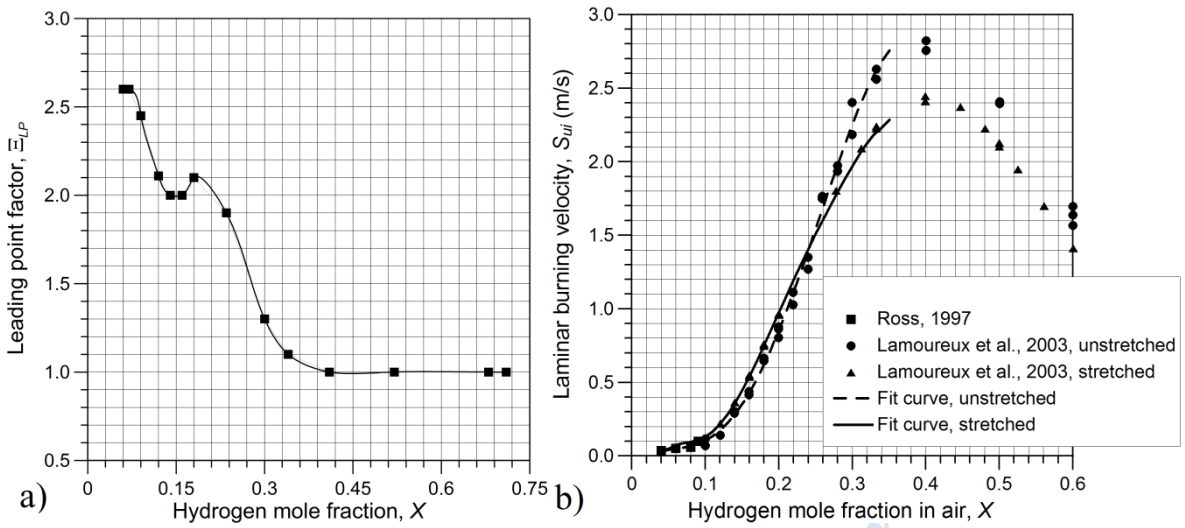

Figure 4.23 a) Maximum leading point wrinkling factor $\Xi_{LP}^{\max}$ versus hydrogen mole fraction X (Verbecke, 2009); b) Laminar burning velocity S_u versus hydrogen mole fraction X.

Empirical coefficients λ and σ in Equation 4.55 were obtained by plotting the experimental results from (Kumar, 2006), (Kumar, 2009), (Daubech et al., 2011), (Pasman et al., 1974), (Bauwens et al., 2012), (Bauwens et al., 2011) in π_{red} versus Br_t coordinates (Figure 4.24).

Fitting the entire data set using Equation 4.55 results in a best fit equation, Equation 4.70 and a conservative equation, Equation 4.71, as provided:

$$\pi_{red} = 0.33 \cdot Br_t^{-1.3}, \qquad \text{Equation 4.70}$$

$$\pi_{red} = 0.86 \cdot Br_t^{-1.3}, \qquad \text{Equation 4.71}$$

where the curve produced using the "conservative" correlation is elevated above the best fit curve, to ensure that all experimental data points lie below it.

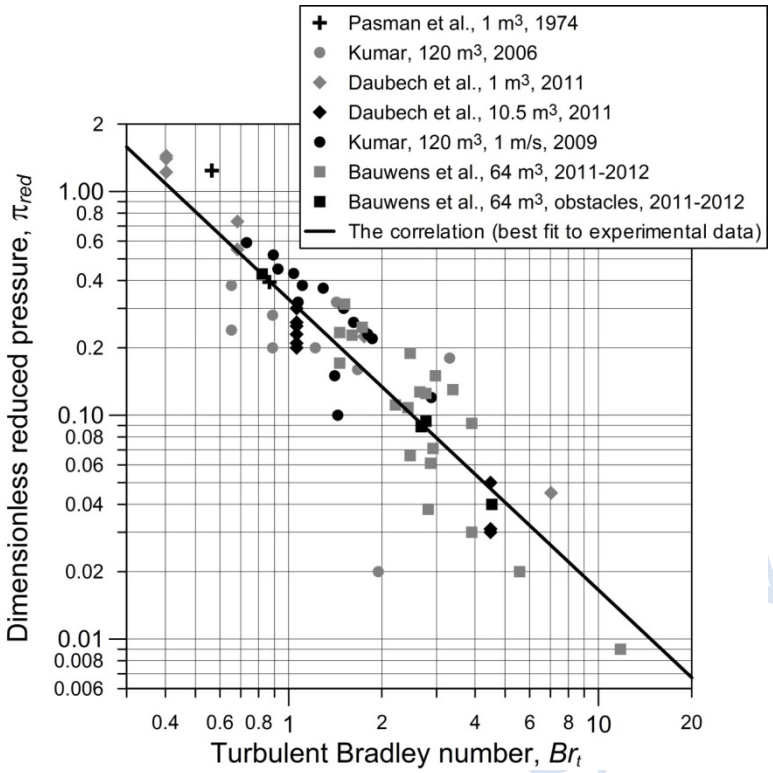

Figure 4.24 Comparison of the results of vent sizing correlation against experimental data (Molkov and Bragin, 2015).

The conservative estimate of the reduced pressure is 2.6 times higher compared to the best fit estimate (Molkov and Bragin, 2015).

The correlation presented in Figure 4.24 can be used to calculate the vent area required to keep the overpressure within the enclosure within a specified value. The procedure for calculating the vent area, as reported previously in (Molkov and Bragin, 2015) is as follows:

- Calculate the value of the dimensionless reduced explosion overpressure:
  - $\pi_{red} = (P_{max} - P_i)/P_i$;
- Based on the value of π_{red}, calculate the value of Br_t by using the relevant equation (best fit or conservative);
- Determine the appropriate values of E_i, Ξ_{LP} and S_{ui} for the mixture in the enclosure (see Figure 4.22 and Figure 4.23);
- Calculate the flame wrinkling factors and multiply them to get DOI number $\frac{\chi}{\mu}$;
- Determine the vent area using the following equation:

$$F = Br_t \cdot \frac{\chi}{\mu} \cdot \sqrt[3]{36\pi_0} \cdot V^{2/3} \cdot \frac{S_{ui} \cdot (E_i - 1)}{c_{ui} \cdot \sqrt{E_i / \gamma_u}} \qquad \text{Equation 4.72}$$

4.1.9 Layered mixture deflagrations (UU)

A majority of gas mixtures of practical interest are not uniformly mixed and exhibit at least some degree of layering or gradients of hydrogen concentration. It had been demonstrated that the presence of concentration gradients can result in faster deflagration dynamics (Whitehouse

et al., 1996). This phenomenon underscores the practical importance of the study of non-uniform mixture combustion behaviour.

The correlation discussed in Section 4.1.7 assumes that the entire volume is occupied by the explosive mixture, resulting in an overestimation of the necessary venting area and consequent costs (Tamanini, 2000), (Molkov et al., 1999). Furthermore, full-volume explosions in stratified mixtures can be more dangerous than the deflagration of a homogeneous mixture with the same amount of fuel (Whitehouse et al., 1996). The combustion of non-uniform mixtures can also occur in backdraughts (Chitty, 1996).

Overview of experimental studies

Flame propagation in stratified mixtures has being investigated experimentally since the early sixties. Phillips (Philips, 1965) demonstrated that in spite of its apparent simplicity, the combustion process in stratified mixture layers is quite complicated and, schematically, consists of three main stages:

1) Premixed flame propagation along the line of stoichiometric fuel-air composition; consuming fuel-air mixture within the flammable concentration range;
2) Diffusion combustion; involving combustion products of the primary premixed flame, which contain fuel-rich and the fuel-lean mixtures beyond the flammability limits;
3) Convection stage of combustion; when the fuel, at a concentration above the upper flammability limit, mixes with air under the action of buoyancy.

After Phillips (Philips, 1965) work, the leading premixed flame is considered to be essentially different from a conventional premixed flame. It could be coupled with a diffusion flame forming a so-called triple flame, when the time required for the mixing between the fuel-rich and air-rich layers is small. For relatively small concentration gradients, the diffusion flame may not be present at all.

Ishikawa (Ishikawa, 1983) published results of experiments, in a 10 cm confined combustor, on flame propagation through an interface between layered methane and air, in which linearly distributed concentration fields are frozen in space and time. There was no diffusion flame observed in these experiments with a constant and relatively small gradient of fuel concentration. The conclusion of this study was that the flame might propagate at a constant speed without any effects of the succeeding diffusion and convection flames.

Explosions in stratified fuel-air mixtures above ethanol spills in an 80 mm diameter vessel were studied by Sato et al. (Sato et al., 1994). The dynamics of flame propagation and pressure histories were examined as a function of the fraction of liquid surface area to horizontal cross-sectional area of the vessel, the time from the beginning of evaporation to ignition and also by initial temperature. A two-stage pressure build-up was observed in tests with a relatively short time to ignition, when the flammable layer thickness is much smaller than the vessel height. This pressure shape is due to the primary premixed flame and succeeding diffusion flame on the liquid surface. It is shown that sufficient overpressure can be generated even for a weak primary premixed flame if the succeeding diffusion combustion occurs.

Hirano et al. (Hirano et al., 1976) studied the effect of known concentration gradients over methanol or ethanol fuel on the characteristics of flame propagation from a linear central ignition source in a cylindrical combustion chamber of 20-cm diameter. The leading flame front usually propagated through a layer where the mixture composition before ignition was close to that for the maximum flame velocity in a homogeneous mixture. In accordance with a

previous finding by Feng et al. (Feng et al., 1975) it was shown that flame velocity V_f in a layered mixture is less than that in a homogeneous mixture, in the same experimental chamber. It was revealed that the dependence of flame velocity V_f on the concentration gradient, when the equivalence ratio Φ_0 at the fuel surface is constant, can be quite different. For values $\Phi_0 < 1$ for methanol, V_f decreases with increasing concentration gradient. Otherwise, for the range of studied values $1.5 < \Phi_0 < 2$ the value of V_f first increases and then decreases. However, V_f was almost constant during flame propagation throughout the combustion chamber.

Tamanini (Tamanini, 2000) has studied pressure development during flame propagation in near-floor stratified propane-air mixtures in a large-scale 63.7 m^3 room-like enclosure under both vented and unvented conditions. It was found that the diffusion combustion at the convection stage of fuel burning contributed significantly to pressure rise in confined deflagrations (up to 67% of the total overpressure). Much lower vent areas (10 times or more) were needed to protect the room compared to the recommendations in the NFPA 68 (NFPA 68, 2002) standard. Tamanini (Tamanini, 2000) suggested that, in the case of heavy vapour layers along a floor, the resulting flame should have a more turbulent appearance and greater vertical extension, due to buoyant forces, than in the case of ceiling layers.

Whitehouse et al. (Whitehouse et al., 1996) studied the vertical flame front propagation from a top and bottom located ignition source, in both uniform and stratified (gradient) hydrogen-air mixtures, in a vertical 10.7 m^3 cylinder. The flame propagated in the direction of the concentration gradient similar to Karim et al. studies (Karim and Lam, 1986), (Karim and Panlilio, 1993) which were undertaken in the eighties and nineties with methane-air mixtures, when higher flame speeds were observed in stratified gases, than those encountered under homogeneous conditions for the first time. Stratified mixtures with top ignition (13% vol. H_2 at top, 3% vol. H_2 at bottom) provided downward flame propagation even for an average concentration of 6.1% vol. H_2, which is well below the downward flame propagation limit (about 8% vol. H_2). An important result of the study undertaken by Whitehouse et al. (Whitehouse et al., 1996) is that the pressure in a stratified deflagration rises much more rapidly than that of the uniform mixture case. For bottom ignition, there is a long delay before a significant pressure rise (with higher rate of pressure rise than for the uniform case) than was seen in the stratified mixture test. The analysis of results on pressure dynamics in systems with flame propagation in the direction of concentration gradient (Whitehouse et al., 1996) clearly pointed out that the requirements to deflagration venting systems could be more severe for stratified mixtures (filling the entire enclosure volume) than for uniform ones.

Sochet et al. (Sochet et al., 2002) investigated blast waves from non-uniform gaseous cloud deflagrations ignited at different locations with various delay times. The non-uniform gaseous cloud is formed by the dispersion of a stoichiometric hydrogen-oxygen mixture initially confined in a hemispherical volume.

Girard et al. (Girard et al., 1979) performed experiments on hemi-spherically stratified hydrogen-air mixtures. The results obtained from gradient tests were dependent on the radius of the soap bubble containing air and hydrogen and the fraction of the gas present in the inner bubble. The shortest time to peak pressure and highest pressures relative to the homogeneous mixture with the same amount of fuel were observed in gradients having a high fraction of their fuel in the near stoichiometric inner bubble. Further experiments were conducted with flames propagating in the direction of the gradient by Badr and Karim (Badr and Karim, 1984), Karim and Lam (Karim and Lam, 1986) and Karim and Panlilio (Karim and Panlilio, 1993). It had been shown that the flame propagation velocities into richer mixtures were not

affected by stratification, while flame burning into less reactive mixtures had speeds up to 70% higher than corresponding flame speeds under homogeneous conditions.

Overview of basic studies on partially premixed combustion.

Premixed and diffusion combustion are two idealised regimes that are not antagonistic but lead to flames with properties that are fundamentally different. The premixed front is thin and propagates combustion naturally while the diffusion flame is more mixing controlled and does not propagate by itself. It is thus unlikely that numerical models for a diffusion flame, which are suitable for "standard" fire simulations, can properly describe both regimes (Domingo et al., 2002).

It has been revealed by both modern experimental diagnostics and numerical simulations that the fuel, air and residual products in many combustion devices are not, in fact, as spatially homogeneous as previously thought. For lean-rich systems the reaction zone can be described as a staged combustion system with a first stage corresponding to premixed combustion and producing partially burned products, followed by a second stage corresponding to non-premixed/diffusion combustion and leading to fully burned products (Helie and Trouve, 1998). It was also found that partial premixing had a negligible contribution to flame stretch and flame-surface production (Helie and Trouve, 1998).

The theoretical framework that would allow for simultaneous premixed and diffusion modes of combustion at variable mixture compositions can be briefly described as follows. Assuming global single-step chemistry, unit Lewis numbers and neglecting radiative heat transfer, this framework must use at least two scalar variables to capture partially premixed flames: one variable to describe the mixture composition (mixture fraction, Z) and a second one to describe the progress of the premixed reaction (progress variable, c), see (Birkby et al., 2000), (Domingo et al., 2002), (Helie and Trouve, 1998).

The corresponding LES filtered equations could be written as:

$$\frac{\partial}{\partial t}\left(\overline{\rho}\,\widetilde{c}\right)+\frac{\partial}{\partial x_j}\left(\overline{\rho}\,\widetilde{u}_j\widetilde{c}\right)=\frac{\partial}{\partial x_j}\left(\left[\frac{\mu}{Sc}+\frac{\mu_t}{Sc_t}\right]\frac{\partial\widetilde{c}}{\partial x_j}\right)+\overline{S}_c \qquad \text{Equation 4.73}$$

$$\frac{\partial}{\partial t}\left(\overline{\rho}\,\widetilde{Z}\right)+\frac{\partial}{\partial x_j}\left(\overline{\rho}\,\widetilde{u}_j\widetilde{Z}\right)=\frac{\partial}{\partial x_j}\left(\left[\frac{\mu}{Sc}+\frac{\mu_t}{Sc_t}\right]\frac{\partial\widetilde{Z}}{\partial x_j}\right) \qquad \text{Equation 4.74}$$

where t – time; x_j – spatial coordinates; ρ – density; u – velocity; μ and μ_t – laminar and turbulent viscosities; Sc and Sc_t – laminar and turbulent Schmidt numbers; S_c – source term in the progress variable equation (premixed combustion reaction rate); overbar and tilde denote filtered and mass-weighted Favre filtered quantities correspondingly.

Partially premixed flames propagate preferentially along surfaces of stoichiometric composition. The leading edge has been called the triple flame. The triple flame consists of three branches: the rich and lean premixed branches; and the diffusion flame behind these branches. The triple flame characteristics depend on several parameters, including mixture fraction gradient in the region of the triple point, Lewis number, self-induced strain, and heat release. The propagation velocity of the overall hybrid structure is the triple flame speed. The heat release profile shows three clearly separated peaks corresponding to reaction zones in three branches, while the temperature profile has one peak only with its maximum close to the stoichiometric line. Ruetsch et al. (Ruetsch et al., 1995) demonstrated that under standard conditions, fuel consumption in diffusion flames is more than an order of magnitude smaller

than in premixed flames. This is not always the case for convection diffusion flames during accidental combustion, when large amounts of fuel could be burned to contribute significantly in pressure build up, as proved by the experiments mentioned above.

In the laminar flamelet regime of premixed combustion, chemical kinetics enters the combustion model only through its influence on the burning velocity, S_u, the flame-turbulence interaction is purely kinematic and modelling of detailed chemistry can be omitted (Bray, 1996). Various models for the combustion reaction rate based on RANS models or subgrid closures for LES, feature strong similarities (Vervisch and Veynante, 2000).

The local mass burning rate can be described as: $\dot{m} = \rho_u \cdot S_u(Z,T,p) \cdot |\nabla c| \cdot \Xi_{SGS}$, similar to the combustion method, where ρ_u – density of unburned mixture; Ξ_{SGS} – flame wrinkling factor, which accounts for subgrid scale increase of flame surface due to flame-turbulence interaction.

In the thin flamelet combustion regime, the varying premixed front could be modelled as a collection of interacting premixed flamelets, each defined for a given mixture fraction of the non-uniform mixture (Domingo et al., 2002). For diffusion combustion modelling, approaches based on the assumption of mixing-controlled burning can be adopted. The useful concept of a flame indicator based on the scalar product of fuel and oxidiser normal vectors was first proposed by Yamashita et al. (Yamashita et al., 1996). Domingo et al. (Domingo et al., 2002), Vervisch and Veynante (Vervisch and Veynante, 2000) and Bray (Bray, 1996) have employed a similar procedure, based on resolved fields with use of the LES flame index, to associate premixed and diffusion flame descriptions in this hybrid combustion regime. The flame index is equal to 1 in premixed combustion due to fast consumption of fuel and oxidiser (fuel and oxidiser concentration gradients have the same direction). For diffusion flames the flame index is equal to zero.

Significant flow turbulence, high flame strain rates and relatively small scales of non-homogeneous regions are characteristic for most combustion devices. These features could be very different from those at large-scale stratified accidental explosions. The initial propagation of accidental deflagration usually takes place in a quiescent or moderately agitated mixture in a quasi-laminar mode. A large fraction of the fuel layer in an accidental combustion scenario could be above the upper flammability limit, giving rise to additional pressure build up during burning, in the convective diffusion mode after premixed combustion, i.e. deflagration.

4.1.10 Delayed ignition of hydrogen-air jets (UU)

If the hydrogen jet is not ignited immediately after release, hydrogen concentration in the near field of the jet can rapidly exceed the flammability threshold. Delayed ignition and consequent combustion of the unsteady highly turbulent hydrogen-air cloud formed at this stage can lead to significant overpressure in the near field of the jet. This process is basically a deflagration and takes place before the quasi-steady jet fire is established.
A number of experiments were carried out by different research teams in order to investigate the impact of ignition delay, ignition location and release nozzle diameter on the overpressure produced as a result of delayed ignition (Tanaka et al., 2007), (Takeno et al., 2007), (Royle and Willoughby, 2009), etc.
The effects of ignition delay and location of ignition source on deflagration pressure had been studied by Takeno et al. (Takeno et al., 2007). In these experiments hydrogen stored at pressures between 40 MPa and 65 MPa was released through a 10 mm diameter nozzle (pressure in the nozzle was 40 MPa). It was observed that the increase of ignition delay from

0.85 s to 5.2 s, with ignition source located at the same distance of 4 m from the nozzle, resulted in a decrease in the maximum deflagration overpressure in the near field from 90 kPa to 15 kPa. It was concluded that the shorter the ignition delay, the greater the overpressure. Takeno et al. (Takeno et al., 2007) also concluded that turbulence has a greater effect on the "explosiveness" than the total amount of leakage or the premixed volume.

Tanaka et al. (Tanaka et al., 2007) investigated the impact of ignition time on the overpressure for the jets in the open air. Experiments were conducted using a horizontal jet issued from an 8 mm diameter nozzle and ignited at a distance of 4 m. It was found that the logarithm of the peak overpressure decreased linearly with increased logarithm of time to ignition. The largest overpressure was found for a 1.2 s ignition delay.

The UK Health and Safety Laboratory (HSL) of the Health and Safety Executive performed a series of over 40 experiments with high pressure releases of hydrogen as a part of the project HYPER (HYPER, 2008), the results of which were published later by Royle and Willoughby (Royle and Willoughby, 2009). The effects on overpressure of varying the jet exit diameter, the ignition delay and position were investigated. Predominantly momentum-controlled (i.e. the flow was relatively non-buoyant up to the lower flammability limit, (Royle and Willoughby, 2009)) jets were produced by releasing hydrogen stored at 20.5 MPa through the nozzle. The exit diameter of the nozzle was controlled by flow restrictors. Ignition distance was varied in a range of 2 – 10 m from the nozzle exit.

The effect of the ignition delay was studied for the 6.4 mm nozzle diameter with ignition location 2 m from the nozzle. A maximum overpressure of 19.4 kPa was observed for the ignition delay of 600 ms, which closely corresponded to a time when the area of maximum turbulence within the front portion of the jet reached the ignition point. Longer delays resulted in lower overpressure values, while shorter delays resulted in ignition in the area with hydrogen concentration close to the flammability limits, producing a relatively slow burn and hence a small overpressure.

The same nozzle with diameter 6.4 mm was used for an investigation of the ignition location impact. Ignition delay was kept constant at 800 ms, while the ignition position varied from 2 m to 10 m from the nozzle. It was observed that the deflagration overpressure dramatically decreased with an increase of the ignition position distance from the jet source. A maximum overpressure of 15.2 kPa had been recorded for an ignition point located at the distance of 2 m from the nozzle.

Two ignition delays (400 ms, when the jet just reached the ignition point located 2 m downstream from the nozzle, and 800 ms corresponding to the formation of a larger turbulent flammable hydrogen-air cloud) were used to investigate the influence of nozzle diameter on the unsteady hydrogen jet deflagration overpressure. Nozzle diameter varied from 3.2 mm to 9.5 mm (additional tests with 1.5 mm diameter nozzle produced no recordable overpressure). The maximum recorded pressure was 16.5 kPa, 15.2 kPa and 3.5 kPa for 800 ms ignition delay for 3.2, 6.4 and 9.5 mm diameter nozzles, respectively. Experiments with 400 ms ignition delay showed a similar trend, although with significantly lower overpressure values for all nozzles (e.g. maximum overpressures of 3.3 - 5.4 kPa were recorded the for 8.5 mm nozzle).

From these experiments, it can be concluded that the leak diameter plays critical role in the determination of the overpressure after delayed ignition, and should therefore be kept as low as reasonably possible for a particular hydrogen and fuel cell technology.

Royle and Willoughby (Royle and Willoughby, 2009) concluded that the jet turbulence and size had a greater effect on a deflagration pressure than the total amount of hydrogen leaked. Particularly in the open air environment, the total released amount of hydrogen can be of lesser importance, since buoyancy continues to remove hydrogen from the release vicinity

and drives dilution of hydrogen by entrained air until it reaches the LFL of 4% by volume and beyond.
It can be further assumed that the spontaneous diffusion ignition of a sudden hydrogen release could produce a lower overpressure compared to the delayed ignition.
Utilization of barriers is often considered as a mitigation measure to reduce the hydrogen flame length. Experiments have shown, however, that barriers employment can result in an increase of overpressure produced by delayed ignition. HYPER (HYPER, 2008) experiments have shown that the deflagration overpressure peak after a delayed ignition (0.8 s) of the turbulent jet from a 9.5 mm nozzle at a storage pressure of 20.5 MPa increases from 16.5 kPa for a free jet to 42 kPa in the presence of a vertical barrier. In this case the barrier creates a quasi-confined space in which the non-uniform mixture deflagrates, which inhibits hydrogen dispersal and increases deflagration overpressure.

4.1.11 Deflagration to detonation transition (DDT) (KIT)

DDT phenomenon describes the sudden transition from deflagration-type combustion, characterized by subsonic flame-propagation velocity, to detonation, characterized by super-sonic combustion.

Early experimental works addressing the problem of detonation origin were conducted in the 1950s (Oppenheim, 1952), (Oppenheim and Stern, 1958), (Egerton et al., 1953), (Troshin, 1958), (Popov, 1958), (Salamandra et al., 1958) and (Bazhenova and Soloukhin, 1958).

An important step in understanding the DDT process was achieved in the experiments undertaken by Urtiew and Oppenheim (Urtiew and Oppenheim, 1966). They were able to capture the onset of detonation in the vicinity of the boundary layer, although the exact mechanism of DDT remained elusive.

Progress in computer state of the art and CFD opened up the possibility to study the DDT process numerically. An early numerical simulations of a two-dimensional approximation of DDT was performed by Taki and Fujiwara (Taki and Fujiwara, 1978), this work was followed and improved upon a few years later by Oran et al. (Oran et al., 1982).

Recent numerical research on DDT has included the work by Kagan and Sivashinsky (Kagan and Sivashinsky, 2003), Kuznetsov et al. (Kuznetsov et al., 2010b), and Gaathaug et al. (Gaathaug et al., 2012). Recent research has concentrated on the shock wave-boundary layer interaction (SWBLI) problem. In most cases the problem of SWBLI has been studied with non-reactive mixtures. One of the early published works on the interaction of a reflected shock with the boundary layer was by Mark (Mark, 1956). He investigated a reflected shock formed at the closed end of a shock tube. His work was subsequently confirmed and continued by Clarke et al. (Clarke et al., 1984). Dyner (Dyner, 1966) investigated density variation in reflected shock / laminar boundary layer interaction, using a strip-film Schlieren interferometer (Dzieminska and Hayashi, 2013).

The study of reactive flows in association with SWBLI, started to get attention together with a new combustor, a ram accelerator. The first concept was presented by Hertzberg et al. (Hertzberg et al., 1988) and later developed by Yungster (Yungster, 1992). Recent research also includes Dzieminska and Hayashi (Dzieminska and Hayashi, 2013) who investigated autoignition and SWBLI in the smooth tube.

The sequence of events leading to detonation in a tube containing explosive gases can be summarized as follows:

- Generation of compression waves ahead of an accelerating laminar flame (see Figure 4.25). The laminar flame front is wrinkled at this stage.
- Formation of a shock front due to coalescence of compression waves (see Figure 4.25).
- Movement of gases induced by shock, causing the flame to break into a turbulent brush (see Figure 4.25).
- Onset of "an explosion in an explosion" at a point within the turbulent reaction zone, producing two strong shock waves in opposite directions and transverse oscillations in between. These oscillations are called transverse waves (see Figure 4.26). The forward shock is referred to as superdetonation and moves into the unburned gases. In the opposite direction, a shock moves into the burned gases and is known as retonation.
- Development of a spherical shock wave at the onset of the "explosion in an explosion," with a centre located in the vicinity of the boundary layer (see Figure 4.27).
- Interaction of transverse waves with shock front, retonation wave, and reaction zone.
- Establishment of a final "steady wave" as a result of a long sequence of wave interaction processes that leads finally to the shock-deflagration ensemble: the self-sustained C-J detonation wave.

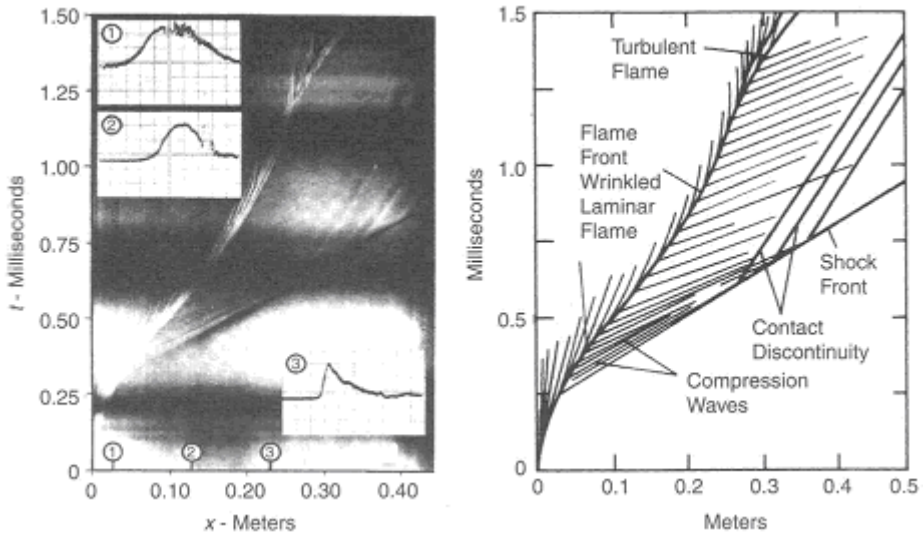

Figure 4.25 Development of detonation in stoichiometric H_2-O_2 mixture initially at normal temperature and pressure, showing the generation of pressure waves ahead of the accelerating flame.

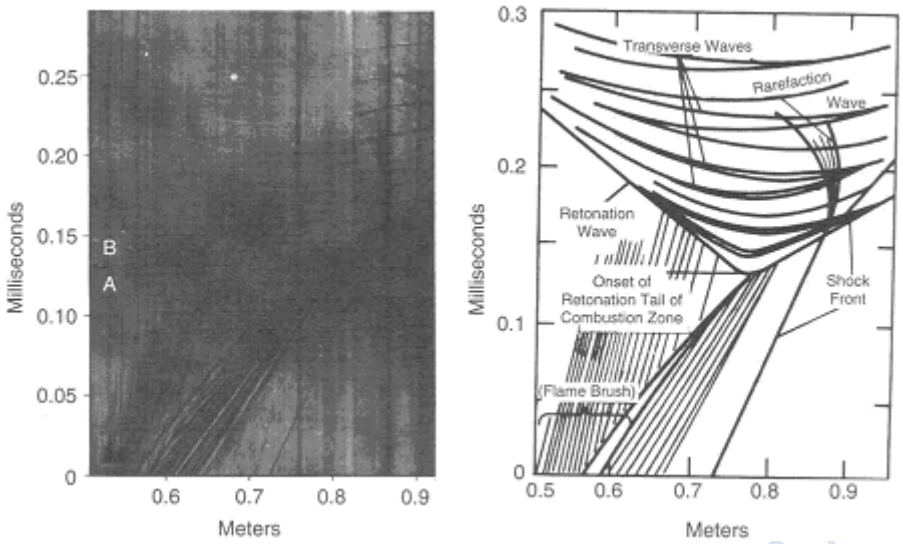

Figure 4.26 Onset of retonation, for both photographs spark ignition by discharging 1.0 mJ, electrodes located at closed end of 25 x 37 mm cross-section tube (Oppenheim et al., 1963), streak Schlieren photographs.

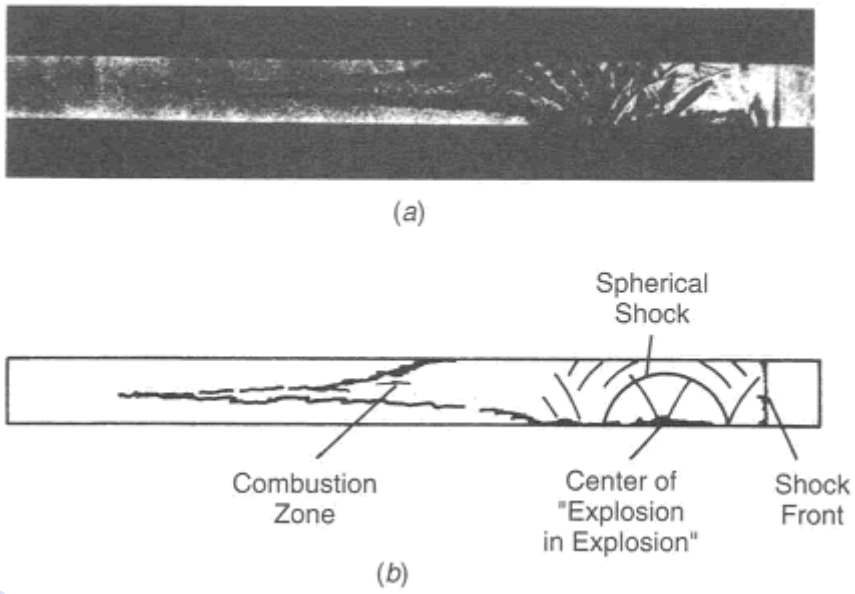

Figure 4.27 Flash Schlieren photograph of the onset of retonation in a stoichiometric H_2-O_2 mixture initially at normal temperature and pressure at an instant marked by A on streak Schlieren photo (Fig.4.1.10.1) (Oppenheim et al., 1963).

The forward-moving wave was studied using wall imprints of the detonation process, an example of which is shown in Figure 4.28. The characteristic fish-scale pattern, which corresponds to inception of the forward shock, is a distinguished feature of a self-sustained detonation front.

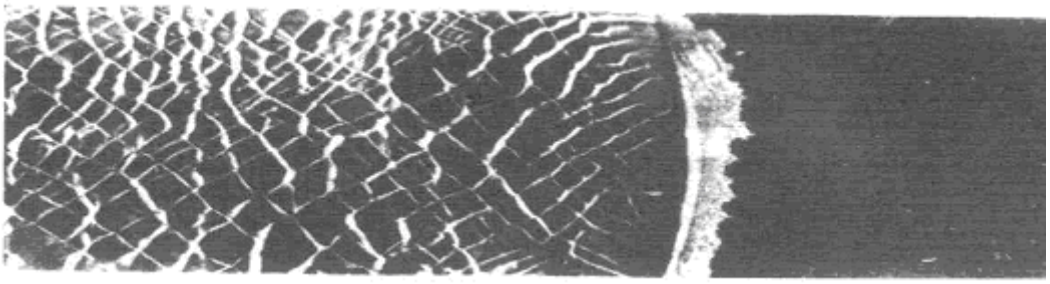

Figure 4.28 Wall imprints of the transition process.

There are generally four different modes of the transition process which have been observed and classified, based on the location of the onset of an “explosion in an explosion”:

1. Between flame and shock front (see Figure 4.25),
2. At the flame front (see Figure 4.26),
3. At shock front (see Figure 4.31), and
4. At the contact discontinuity (see Figure 4.32).

The onset of detonation depends on the particular pattern of shock fronts created by the accelerating flame. The process of DDT is unreproducible in its detailed sequence of events.

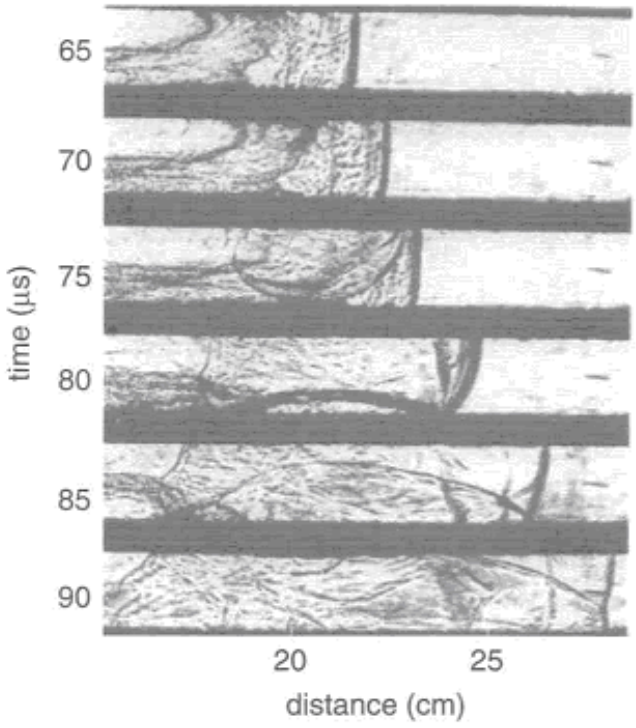

Figure 4.29 DDT observed in $2H_2+O_2$ mixture. Onset occurs between flame and shock.

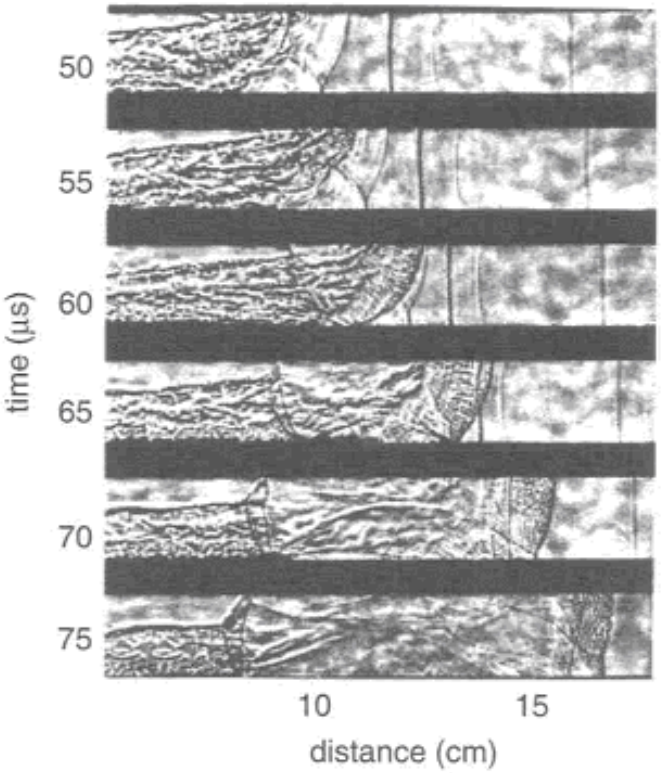

Figure 4.30 DDT observed in $2H_2+O_2$ mixture. Onset occurs at flame front.

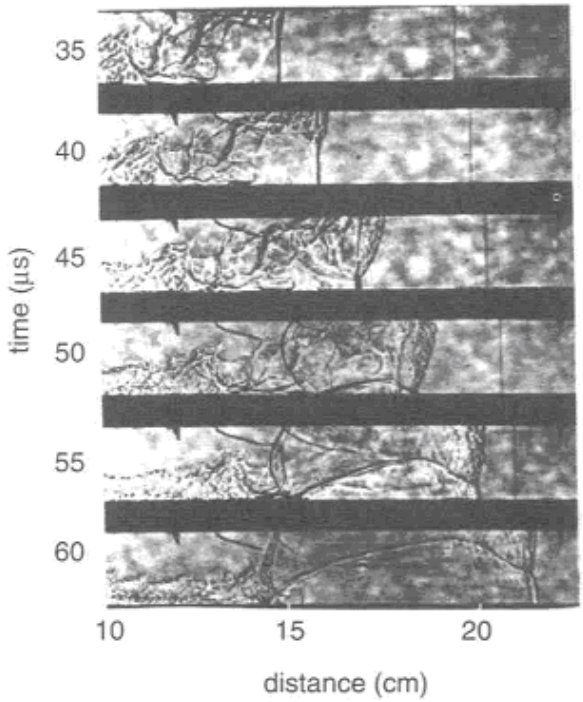

Figure 4.31 DDT observed in $2H_2+O_2$ mixture. Onset occurs at shock front.

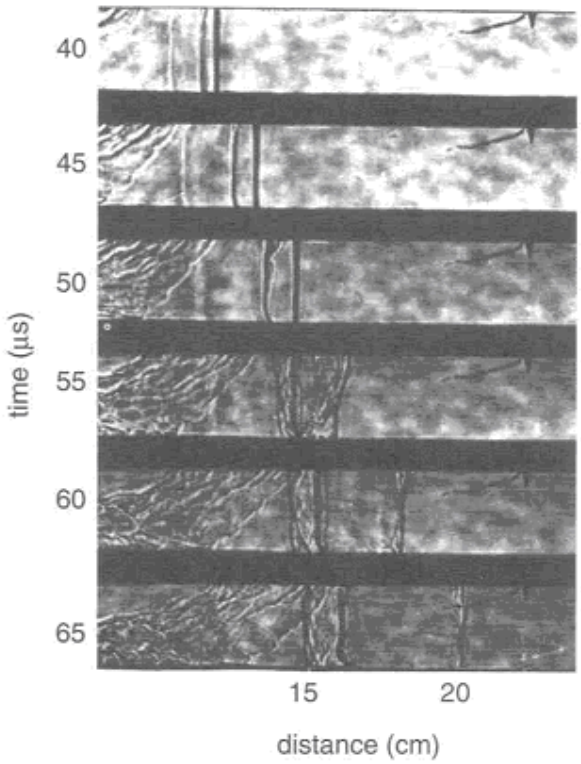

Figure 4.32 DDT observed in $2H_2+O_2$ mixture. Onset occurs at contact discontinuity.

DDT refers to the phenomena where the critical conditions for the onset of detonation are established by the combustion process itself without an external energy source. There are several ways by which the conditions necessary for transition can be achieved. These include:

- Flame acceleration to some critical speed,
- Ignition of a turbulent pocket, and
- Jet ignition.

4.2 Models (UU)

4.2.1 Governing equations for deflagration phenomena modelling (HSL)

4.2.1.1 Introduction

Deflagration is a term used to describe subsonic combustion propagating through heat transfer, where hot burning material heats the next layer of cold material and ignites it. Deflagration is different from detonation, which propagates supersonically through shock waves.

There are three main classes of models, in order of increasing complexity:

- Empirical correlations
- Zone models
- CFD models
    - Simplified approach
    - Detailed approach

There are a number of key features associated with deflagrations, these include:

- There must be a release of flammable material (in this context it is assumed that the flammable material is hydrogen gas)
- There could be a high degree of confinement, i.e. release could occur within or into an enclosure
- There could be a high degree of congestion, e.g. obstacles of various sizes and orientations
- There must be a source of ignition
- The concentration of the flammable gas cloud, consisting of fuel and air, must be in the flammable range at the ignition location

The concentration in the flammable cloud is highly unlikely to be uniform, unless it is a controlled experiment. This is an important point to remember when we come to discuss modelling vapour cloud explosions.
There are a number of potential ignition sources (see Chapter 2, Ignition). We will assume that one of these is present and that it is imparting a sufficient amount of energy and duration for the flammable mixture to ignite. There are a number of factors contributing to the severity of the deflagration:

- The greater the congestion the higher the overpressure tends to be
- Confinement of the flammable cloud tends to lead to higher overpressures
- The further the flame travels in a congested and confined region the higher the overpressure is likely to be

The pressure some distance away from the ignition location will build up slowly as the expanding flame pushes the unburnt gases ahead of the flame front. A peak overpressure is reached. This is referred to the positive phase. The pressure may then drop down below ambient pressure once the flame front has passed. This is referred to as the negative phase. The magnitude of the negative peak pressure is usually considerably lower the positive pressure peak, but the duration of the negative phase can be much longer, which has an impact on the impulse (which is a product of the pressure and the duration).
Initial turbulence in the flammable cloud may not in itself lead to higher overpressures, but it means that the rate of pressure rise is much greater than for a deflagration in a quiescent environment.

4.2.1.2 Governing equations

The equation set which must be solved is already presented in Chapter 1, Section 1.2.1. The equations included here will be limited to those associated with the analysis of deflagration scenarios.

Species transport equations — N equations

The number of species transport equations is dependent on the complexity of the combustion model. In the case of detailed chemical kinetics, the number of species could be in excess of a few hundred depending on the fuel molecule. In the case of hydrogen, and ignoring nitrogen chemistry, one would consider eight species and 27 reactions. The general form of the species transport equation is provided below:

$$\frac{\partial \rho Y_l}{\partial t} + \frac{\partial \rho U_i Y_l}{\partial x_i} = \frac{\partial}{\partial x_i}\left[\Gamma_{eff}\frac{\partial Y_l}{\partial x_i}\right] + \sum_{s=1}^{m}\omega_s, \qquad \text{Equation 4.75}$$

where Y_l is the mass fraction of species "l", ω_s is the reaction rate of reaction "s" and m is the number of reactions.

Conservation of energy — 1 equation

Conservation of energy is represented by the transport of enthalpy for the mixture (h) and the enthalpy of the individual species (h_k). The enthalpy of the species includes its heat of formation which accounts for the conversion of chemical energy into heat. A laminar flamelet model does not necessarily require an equation for the transport of energy because the temperature is instead derived from the flamelet library. The energy equation is as follows:

$$\frac{\partial \rho h}{\partial t} + \frac{\partial \rho U_i h}{\partial x_i} = \frac{\partial}{\partial x_i}\left[\frac{\mu}{\sigma_h}\frac{\partial h}{\partial x_i} + \mu\left(\frac{1}{Sc_k} - \frac{1}{\sigma_h}\right)\sum_{k=1}^{N} h_k \frac{\partial Y_k}{\partial x_i}\right] + \frac{\partial p}{\partial t} + S \qquad \text{Equation 4.76}$$

where σ_h is the mixture Prandtl number and Sc_k is the Schmidt number for the individual species. The summation term in the energy equation represents transport of energy due to diffusion along gradients of species concentration. In some cases, a simplified form can be used in which this term is neglected. The source term, S, accounts for energy loss or addition due to radiation. The ratio of the Schmidt number to the Prandtl number is known as the Lewis number (Le) and most, if not all, combustion models make the assumption that all species have the same Lewis number. In addition, it might also be assumed that the Lewis number is constant, though it has been shown that the Lewis number can be both temperature and pressure dependent. This assumption is acceptable for most major species, but is not justifiable for hydrogen.

This has implications for laminar flame calculations, where the predicted flame behaviour could be different from that observed in a real flame. A further issue is that the molecular diffusion of a species in a multi-component mixture might be significantly different to a binary system. This is a particular issue in laminar flame calculations, but it tends to be neglected in turbulent flame calculations, where usually there is no attempt at resolving the flame front.

Reaction progress variable and variance of the reaction progress variable transport equation

In premixed combustion, two variables, the reaction progress variable (c), a conserved scalar, and its variance (c''^2) are introduced:

$$c = \frac{\eta - \eta_u}{\eta_b - \eta_u} \qquad \text{Equation 4.77}$$

The variable η can either be temperature, or the concentration of one of the main species (Benim and Syed, 1998).

Mixture fraction and its variance

The two quantities used in non-premixed combustion are the mixture fraction (f), a conserved scalar, and its variance (f''^2). The transport equation for the mixture fraction is written as:

$$\frac{\partial \rho f}{\partial t} + \frac{\partial \rho U_j f}{\partial x_j} = \frac{\partial}{\partial x_j}\left[\Gamma\frac{\partial f}{\partial x_j}\right] \qquad \text{Equation 4.78}$$

where f is the mixture fraction.

The transport equation for the variance of the mixture fraction, f''^2 can be written as:

$$\frac{\partial \rho f''^2}{\partial t} + \frac{\partial \rho U_j f''^2}{\partial x_j} = \frac{\partial}{\partial x_j}\left[\Gamma \frac{\partial f''^2}{\partial x_j}\right] + C_1 \mu_t \left(\frac{\partial f}{\partial x}\right)^2 + C_2 \rho \frac{\varepsilon}{k} f''^2, \qquad \text{Equation 4.79}$$

where C_1 and C_2 are constants.

4.2.1.3 Empirical correlations and commonly used models

Empirical correlations are derived from experiments. The correlations often require a minimal amount of input and provide an instantaneous answer. Their range of applicability is limited by the conditions under which the experiments upon which the correlations are based were performed. Extreme caution should be exercised when extrapolating the empirical correlations beyond their range of applicability.

TNT Equivalency

The TriNitroToluene (TNT) Equivalency methodology is based on the assumption that pressures from gas explosions exhibit a similar behaviour to the pressure generated from high explosives. However, there are substantial differences between gas explosions and TNT. In the former the local pressure is much less than for the latter. Furthermore, the pressure decay from a TNT detonation is much more rapid than the acoustic wave from a vapour cloud explosion. Nevertheless the model has been used extensively to predict peak pressures from gas explosions due to its ease of use.

Multi-Energy Method

The Multi-Energy Method (Van Den Berg, 1985), is often referred to as MEM. MEM can be used to estimate the blast from gas explosions with variable strength. The method assumes that only the part of the gas cloud that is confined or obstructed will contribute to the blast and that unconfined vapour clouds give rise to only small over-pressures if ignited. The over-pressure increases with increasing confinement. In essence, the method is based on numerical simulations of a blast wave from a centrally ignited spherical cloud with constant velocity flames.

There are two input parameters to MEM, a combustion-energy parameter scaled distance and the charge strength. The former parameter relates the combustion energy and the cloud volume to a distance from the ignition location, while the latter parameter takes into account the layout of the deflagration source. The charge strength is given a number between one and ten, where a charge strength of ten represents a detonation. The curve associated with a charge strength of seven is commonly used for congested and confined scenarios. It can be very difficult to choose the appropriate charge strength curve.

The MEM has been developed further to address this “weakness” (Van Den Berg et al., 1991). In addition, guidance has also been published which can be used to choose the appropriate curve based on the level of congestion and confinement of the site (Kinsella, 1993).

MEM tends to give conservative answers, i.e. it over-predicts the overpressure.

Baker-Strehlow-Tang Model

The Baker-Strehlow-Tang (BST) Model takes into account the reactivity of the fuel, the level of congestion and the level of confinement where the flammable cloud exists (Baker et al., 1996). A flame Mach number can then be derived based on this assessment. The BST model was not able to give reasonable overpressure predictions for some of the experiments

performed in the MERGE and EMERGE, projects sponsored by the European Commission. It was therefore necessary to modify the expressions for the flame Mach number to take into account additional factors (Melton and Marx, 2009).

Eddy Break-Up Model

This modelling approach has already been described through its applicability to fire modelling (see Section 3.2.3). For completeness of this section the Eddy Break-Up Model is also listed here. A detailed description of how this approach can be applied to deflagration analysis can be found in Section **Error! Reference source not found.**.

Eddy Dissipation Model

The popular Eddy Dissipation Model (EDM) (Magnussen and Hjertager, 1976) is based on the Eddy Break-Up (EBU) model originally proposed by Spalding (Spalding, 1971), (Spalding, 1976).
In its original formulation, the EBU model assumed that combustion can be represented as a fast, irreversible single-step reaction. In certain implementations of the EBU model the requirement of a single-step reaction has been relaxed. However, the reaction still has to be fast in comparison to the turbulence time scale.
The EDM model proposed by Magnussen and Hjertager (Magnussen and Hjertager, 1976) introduces two model constants, *A* and *B*, The model was then re-named Eddy Dissipation Model. However, it has been found that these constants, or parameters, are not universal, as their values have been shown to be dependent on the fuel and burner configuration. However, the EBU model is frequently used with different values and the results are in reasonably good agreement with available measurements. However, a typical value for constant A is 3, but the range of values used in the literature is between 0.4 and 7 (Brizuela and Bilger, 1996). This suggests that 'tuning' of the model constant value has been carried out in order to obtain good agreement with experiments. Furthermore it shows that value selection is case dependent.
The EBU model for non-premixed combustion has a basis in theory, though the general approach of the model is questionable (Brizuela and Bilger, 1996). Brizuela and Bilger (Brizuela and Bilger, 1996) investigated values for the two model constants for diffusion flames, but it is not clear whether the findings from their investigation are also applicable to premixed combustion, or if they can be used to infer "better" values for the constants. Brizuela and Bilger (Brizuela and Bilger, 1996) derived a formulation for parameter A and used two different presumed-shape Probability Density Functions, clipped Gaussian and a β–PDF, to find the appropriate value. The authors presented a graph which showed the variation in parameter A as a function of the normalised fluctuation in mixture fraction of the limiting reactant. The values for A ranged from 0.01 to > 300. There were some differences in the calculated values when using different PDFs, but they were of the same order of magnitude. It was also noted that a value between 2 and 3 was entirely consistent with their analysis (Brizuela and Bilger, 1996). Brizuela and Bilger (Brizuela and Bilger, 1996) concluded that the value of A could be calculated in the CFD code without incurring a great computational overhead. However, to date we are not aware of any codes where this has been implemented. In addition, we are not aware of any systematic study of the effect of varying the value of parameter A on the calculations of, say the temperature and species compositions in a flame.

Eddy Dissipation Concept Model

There are a number of CFD combustion models of different degrees of complexity. The popular Eddy Dissipation Concept (EDC) model (Magnussen and Hjertager, 1976) is based

on the Eddy Break-Up (EBU) model originally proposed by Spalding (Spalding, 1971), (Spalding, 1976). Various refinements have been made to the original EDC model by Magnussen (Magnussen, 1981), Byggstoyl and Magnussen (Byggstoyl and Magnussen, 1985) and Ertesvag and Magnussen (Ertesvag and Magnussen, 2000), and it has been shown to provide a good compromise between accuracy and affordability for a number of different non-premixed flames.

4.2.2 Multi-phenomena deflagration model (UU)

VLES Model

The VLES model consists of 3D filtered conservation equations of mass, momentum, energy and species as detailed in previous publications (Molkov et al., 2006). The progress variable equation is used to model the premixed flame propagation:

$$\frac{\partial}{\partial t}\left(\overline{\rho}\,\widetilde{c}\right)+\frac{\partial}{\partial x_j}\left(\overline{\rho}\,\widetilde{u}_j\widetilde{c}\right)=\frac{\partial}{\partial x_j}\left(\frac{\mu_{eff}}{Sc_{eff}}\frac{\partial \widetilde{c}}{\partial x_j}\right)+\overline{S}_c \qquad \text{Equation 4.80}$$

where the gradient method (Prudnikov, 1967) is used to express the source term in the form $\overline{S_c}=\rho_u S_t\left|grad\,\widetilde{c}\right|$ to calculate the mass burning rate. The density of the unburnt mixture is calculated as a function of pressure p, assuming of adiabatic compression/expansion: $\rho_u=\rho_{u0}\left(Y_{H_2}\right)\left[p/p_0\right]^{1/\gamma}$, where $\rho_{u0}\left(Y_{H_2}\right)$ is mixture density at initial pressure p_0, and γ is the adiabatic index. The laminar burning velocity S_u is calculated using the formula: $S_u=S_{u0}\left(Y_{H_2}\right)\left(p/p_0\right)^{\varepsilon}$, where $S_{u0}\left(Y_{H_2}\right)$ is the laminar burning velocity at initial pressure (Lamoureux et al., 2002), ε is overall thermokinetic index as a function of the hydrogen concentration (Babkin, 2003).

In the previous studies (Molkov et al., 2006), (Molkov et al., 2007), (Molkov et al., 2008) the turbulent burning velocity S_t was modelled by three mechanisms affecting the flame surface area. The first mechanism takes into account the effect of the flow turbulence and is modelled using Yakhot's transcendental equation for the turbulent burning velocity of premixed turbulent combustion, derived from the renormalization group theory (Yakhot, 1988): $S_t=S_u\exp(u'/S_t)^2$, where S_u is laminar burning velocity, and u' is r.m.s velocity.

The second mechanism originates from the theory of Karlovitz et al. (Karlovitz et al., 1951) according to which the flame front itself generates turbulence that additionally increases the flame front area too. It was shown that the maximum theoretical value of a flame wrinkling factor associated with turbulence generated by flame front itself (high Reynolds numbers) is equal to: $\chi_{Karl_{MAX}}=(E_i-1)/\sqrt{3}$ where E_i is combustion products expansion coefficient (Molkov et al., 1991). Gostintsev et al. reported that for stoichiometric hydrogen-air mixtures the transition from laminar to self-similar (fractal) turbulent flame propagation regime takes place at a characteristic radius of about R_0=1.0-1.2 m (Gostintsev et al., 1988). To account for both mentioned results the following sub-grid scale (SGS) flame wrinkling factor has been implemented into the VLES model (ψ is an empirical coefficient):

$$\chi_{Karl}=1+\left(\psi\cdot\chi_{Karl_{MAX}}-1\right)\cdot\left[1-\exp\left(-R/R_0\right)\right] \qquad \text{Equation 4.81}$$

The third mechanism accounts for the fractal increase of flame front area with an increase of the integral flame scale (outer cut-off). It was demonstrated that this mechanism is very

important to reproduce acceleration in large-scale explosions in the open atmosphere (Molkov et al., 2006). This mechanism has been implemented into the model according to $S_t / S_{tR_0} = \left(R \cdot \varepsilon_{R_0} / R_0 \cdot \varepsilon\right)^{D-2}$. It takes effect starting from the critical radius R_0 = 1.2 m according to observation by Gostintsev et al. (Gostintsev et al., 1988).

In this study it is assumed that the inner cut-off scale, ε, is proportional to the laminar flame thickness $\varepsilon \approx \delta_L$ (Fureby, 2005). Assuming that $\delta_L = \nu / S_u = \mu / \left(\rho \cdot S_u\right)$, one can calculate $\varepsilon_{R_0} / \varepsilon = \left(\rho \cdot S_u \cdot \mu_{R_0}\right) / \left(\rho_{R_0} \cdot S_{u\,R_0} \cdot \mu\right)$.

Combining with the assumption of adiabatic compression, i.e.:

$$S_u / S_{R_0} = \left(p / p_{R_0}\right)^{\varepsilon},$$

$$\rho / \rho_{R_0} = \left(p / p_{R_0}\right)^{\frac{1}{\gamma}},$$

$$T / T_{R_0} = \left(p / p_{R_0}\right)^{\frac{\gamma-1}{\gamma}},$$

and Sutherland's viscosity equation $\mu / \mu_{R_0} = \left(T / T_{R_0}\right)^{\frac{3}{2}} \cdot \left(T_{R_0} + S\right) / \left(T + S\right)$, results in:

$$\frac{\varepsilon_{R_0}}{\varepsilon} = \left(\left(p / p_{R_0}\right)^{\frac{5}{2\gamma}+\varepsilon-\frac{3}{2}} \cdot \left(T_{R_0} \cdot \left(p / p_{R_0}\right)^{\left(\frac{\gamma-1}{\gamma}\right)} + S \right) \Big/ \left(T_{R_0} + S\right) \right) \qquad \text{Equation 4.82}$$

where $S = 110.56\,K$ is the Sutherland's constant for air in the temperature range 293 to 473 *K*.

Preferential diffusion effects are pronounced for lean hydrogen-air mixtures and have to be accounted for in the combustion model through an additional mechanism. This fourth mechanism causes flamelet perturbations in the proximity of these leading flamelets that in turn enhance the burning velocity and mass burning rate (Kuznetsov and Sabel'nikov, 1990), (Lipatnikov and Chomiak, 2005), (Lipatnikov, 2007).

Using the formulation of leading points (Kuznetsov and Sabel'nikov, 1990), Zimont and Lipatnikov (Zimont and Lipatnikov, 1995) determined the hydrogen concentration at the leading points and found their corresponding burning velocities by linear interpolation of the experimental data provided by Karpov and Severin (Karpov and Severin, 1978), (Karpov and Severin, 1980). The leading point flame wrinkling factor χ_{lp} is introduced in the combustion model to correct the SGS burning velocity. It is assumed that preferential-diffusive instability develops linearly with radius to reach its maximum at half of the critical radius R_0. It remains constant after that, i.e. $\chi_{lp} = \chi_{lp_{MAX}}$.

The turbulent burning velocity S_t model can be summarized as follows:

For the transition from laminar to fully turbulent combustion, stage ($0 < R < R_0$), the model includes effects of the flow turbulence (Yakhot's equation), the turbulence generated by flame front itself (Karlovitz turbulence), and preferential diffusion:

$$S_t = \left[S_u\left(Y_{H_2}, T, p\right) \cdot \chi_{lp} \cdot \left\{ 1 + \left(\psi \cdot \chi_{Karl_{MAX}} - 1\right) \cdot \left[1 - \exp\left(-\frac{R}{R_0} \right) \right] \right\} \right] \cdot \exp\left(\frac{u'}{S_t} \right)^2 \qquad \text{Equation 4.83}$$

For the self-similar fully developed turbulent combustion regime ($R > R_0$):

$$S_t = \left[S_u\left(Y_{H_2}, T, p\right)\cdot \chi_{lp} \cdot \left\{1+\left(\psi \cdot \chi_{Karl_{MAX}} - 1\right)\cdot\left[1-\exp\left(-\frac{R}{R_0}\right)\right]\right\}\cdot\left(\frac{\varepsilon_{R_0}}{\varepsilon}\cdot\frac{R}{R_0}\right)^{D-2}\right]\cdot\exp\left(\frac{u'}{S_t}\right)^2 \qquad \text{Equation 4.84}$$

The empirical parameterization for the fractal dimension (North and Santivicca, 1990), (Fureby, 2004) is applied (see Equation 4.21). There is only one empirical constant, i.e. ψ, available for the calibration of the VLES model.

The multi-phenomena turbulent burning velocity model for LES of large-scale deflagrations is being continuously developed at Ulster University. Recently the model has been successfully applied to simulated the distorted tulip flame in a small-scale closed duct (Xiao et al., 2012).

The compressible LES governing equations are obtained by filtering the three-dimensional conservation equations of mass, momentum, energy and the progress variable equation. The sub-grid scale (SGS) turbulence model derived from the renormalization group (RNG) theory by Yakhot and Orszag (Yakhot and Orszag, 1986) is adopted. The RNG model is purely theoretical and does not contain any empirical parameters. It is able to reproduce laminar, transitional and turbulent flows.

The progress variable equation is used to model the flame front propagation. The mass burning rate is described by the gradient method (Prudnikov, 1967). The gradient method ensures that the prescribed mass burning rate $\rho_u S_t$ takes place in the simulations independent of grid resolution. The numerical requirement to the gradient method is that a simulated flame thickness spreads over 4-5 control volumes.

The model is based on the assumption of a flamelet regime of premixed turbulent combustion that is thought to be valid for accidental combustion with comparatively large scales and moderate turbulence. In the model, the mass burning rate is determined in general as a product of the local burning velocity in a flamelet and the surface area of flamelets both being affected by different instabilities, etc.

The phenomena included in the model can be summarised as follows:

- The ***effect of pressure, temperature and concentration*** on the burning velocity are included in the model. The dependence of laminar burning velocity on temperature and pressure during deflagration simulations uses the assumption of adiabatic compression or expansion similar to previous studies (Molkov and Nekrasov, 1981):

$$S_u = S_{ui}\cdot\left(\frac{T}{T_{ui}}\right)^m\left(\frac{p}{p_{u_i}}\right)^m = S_{ui}\cdot\left(\frac{p}{p_{u_i}}\right)^{\varepsilon} \qquad \text{Equation 4.85}$$

  where S_{ui} is the burning velocity at initial temperature T_{ui} and pressure p, $\varepsilon = m + n - m/\gamma_u$ is the overall thermokinetic index, and γ_u is the adiabatic index of unburned mixture. The effect of hydrogen concentration on the burning velocity is included into a value of the initial laminar burning velocity S_{ui}, and indices m and n when it is needed.

- ***Effect of flow turbulence*** on the burning rate. When turbulence occurs in the flow during combustion wave propagation at the flame front would be distorted and the burning rate will be consequently enhanced. The flame thickness is normally a fraction of a millimetre (Aung et al., 1997) and therefore it is impractical to resolve in simulations the three-dimensional real flame thickness and the flow turbulence at all scales, i.e. it is impossible to perform DNS at the comparatively large scales characteristic of most hydrogen safety problems. The effect of flow turbulence on flame front wrinkling is partially resolved by LES at scales comparable to the applied

mesh. The effect of unresolved SGS flow turbulence is modelled following the Yakhot's (Yakhot, 1988) transcendental equation for the turbulent burning velocity of premixed turbulent combustion $S_t = S_u \cdot \exp(u'/S_t)^2$, where u' is the SGS residual velocity. This equation is derived from first principles and does not include any empirical coefficients. For laminar flow with $u' = 0$, the equation yields $S_t = S_u$.

- However, Yakhot's equation cannot be used in its original form in the LES of large-scale deflagrations as the mesh size is large compared to the flame front thickness and thus phenomena affecting the turbulent burning rate at scales of flame thickness cannot be resolved. In order to account for various mechanisms enhancing turbulent burning velocity and unresolved on a comparatively large mesh, i.e. selective diffusion and flamelet curvature, as well as turbulence generated by flame front itself and fractals structure of the flame front, the laminar burning velocity in Yakhot's original equation is substituted by a SGS wrinkling velocity in the model:

$$S_t = S_w^{SGS} \cdot \exp(u'/S_t)^2 \qquad \text{Equation 4.86}$$

This is the principle difference in the application of the Yakhot's equation compared to other studies. As the SGS physical mechanisms cannot be resolved directly, the methods used to account for these mechanisms are overviewed below.

- ***Effect of turbulence generated by the flame front itself***. The wrinkled or turbulent flame front generates additional turbulence in the near-field region (Karlovitz et al., 1951). The increase of surface area of the flame front due to the turbulence generated by the flame front itself cannot be resolved with current computing power even for moderate scale practical problems. The upper limit for a flame wrinkling factor due to the self-induced turbulence can be derived for high Reynolds number flows as (Molkov et al., 1984):

$$\chi_K^{\max} = (E-1)/\sqrt{3} \qquad \text{Equation 4.87}$$

where E is the expansion coefficient of combustion products, i.e. the ratio of densities of the unburned mixture and the burned gases. For a flame propagating in an initially quiescent mixture, this wrinkling factor gradually increases from 1 at the ignition point to the maximum value of $\chi_K^{\max}$ for fully developed turbulence. Gostintsev et al. (Gostintsev et al., 1988) reported that the critical radius for the onset of self-similar flame propagation (fully developed turbulence) for near-stoichiometric hydrogen–air mixtures is about $R_0 = 1.0 - 1.2$ m. In order to take into account these transitional effects, the following equation is applied for SGS modelling of the unresolved self-induced by flame turbulence:

$$\Xi_K = 1 + (\psi \cdot \chi_K^{\max} - 1) \cdot \left[1 - \exp(-R/R_0)\right] \qquad \text{Equation 4.88}$$

where R is the distance from the ignition point to the flame front, and $\psi \le 1$ is a model constant. This constant to following current knowledge is about ψ = 0.5 - 0.6 for near stoichiometric and moderately reach hydrogen-air mixture, and it grows to a maximum value ψ = 1 for lean hydrogen-air mixtures (Molkov and Bragin, 2015). Therefore, with the consideration of physical phenomenon of the turbulence generated by the flame front itself the following expansion for the SGS wrinkling burning velocity is obtained: $S_w^{SGS} = S_u \cdot \chi_K$.

- Flame wrinkling and combustion acceleration mechanism associated with ***preferential diffusion*** coupled with flamelet curvature (leading point) is described in detail in Section 4.1.7. The hydrogen flame with a Lewis number less than unity is affected by the preferential diffusion effect. For a given mixture composition, there exists a flame curvature radius which corresponds to the maximum mass burning rate. According to Zeldovich's the flamelets of such curvature will lead the propagation of the premixed flame. Zimont and Lipatnikov (Zimont and Lipatnikov, 1995), based on the work of Kuznetsov and Sabelnikov (Kuznetsov and Sabel'nikov, 1990), calculated a leading point coefficient $\chi_p^{\max}$ associated with this mechanism as a correction to the laminar burning velocity, dependent on mixture composition.
  In the present model, it is assumed that the diffusive-thermal instability χ_p develops linearly to the maximum value χ_{lp}^{MAX} at half of the critical radius R_0:

$$\chi_p^{\max} = \left\{1 + \frac{(\chi_p^{\max} - 1)\cdot 2R}{R_0}\right\} \qquad \text{Equation 4.89}$$

  For distances from the ignition source above the critical radius: $R > R_0$, $\chi_p = \chi_p^{\max}$.
  Taking into account the leading point mechanism, the equation for the SGS wrinkling burning velocity can be updated to $S_w^{SGS} = S_u \cdot \chi_K \cdot \chi_{lp}$.

- ***Effect of fractal surface of turbulent flame front.*** A turbulent flame has a contorted surface. Thus, the conclusions of the fractal theory are applied to model the change of the fractal surface area of a turbulent flame as a function of the outer cut-off, that is usually the flame size, and the inner cut-off, that is currently chosen as the flame front thickness. The enhancement of turbulent burning velocity by this physical phenomenon is calculated in the model as:

$$\chi_f = (R \cdot \varepsilon_{R_0} / R_0 \cdot \varepsilon)^{D-2} \qquad \text{Equation 4.90}$$

  where R_0 is the critical radius for the establishment of a fully developed turbulent flame, from which the fractal sub-model is applied; R is distance from the ignition source (outer cut-off); ε_{R_0} and ε are inner cut-off scales at R_0 and R respectively; and D is the fractal dimension. The choice of the fractal dimension from the wide range of mentioned values is ambiguous. To make the LES model more universal the fractal sub-model has to exclude, as much as possible, any parameters which can be adjusted by the user.

  The empirical parameterization of the fractal dimension, D, as a function of the ratio of the fluctuating velocity, u', to the laminar burning velocity, Su, is applied (North and Santivicca, 1990):

$$D = \frac{2.05}{u'/S_u + 1} + \frac{2.35}{S_u/u' + 1} \qquad \text{Equation 4.91}$$

  The equation for the SGS wrinkling burning velocity can now be further updated to $S_w^{SGS} = S_u \cdot \chi_k \cdot \chi_p \cdot \chi_f$.

- Finally, the multi-phenomena combustion model now includes the five different physical mechanisms affecting the turbulent burning velocity, i.e. the effects of transient hydrogen concentration, temperature and pressure on laminar burning velocity, the flow turbulence in the incoming unburned mixture, the turbulence generated by flame front itself, the leading point mechanisms, and the fractal increase of turbulent flame front area.

  The turbulent burning velocity can be modelled as:

$$S_t = S_u \cdot \chi_k \cdot \chi_p \cdot \chi_f \cdot \exp\left(\frac{u'}{S_t}\right)^2 \qquad \text{Equation 4.92}$$

The advantage of the turbulent burning velocity model for LES is its flexibility to include new mechanisms affecting the burning rate. Currently research is underway to Ulster University on the inclusion of the Rayleigh-Taylor instability into the model. The first preliminary results of this research have been published (Keenan et al., 2014).

4.2.3 Eddy break-up model (JRC)

The Eddy Break-Up (or EBU) model can be found in many commercial and research codes. Its wide spread use is due to the fact that the reaction rate is written as a simple function of known mean quantities without additional transport equations, and with a low numerical cost compared to other approaches (Poinsot and Veynante, 2012). The EBU Model was developed initially by Spalding (Spalding, 1971), (Spalding, 1976) with the assumption that at high Reynolds and Damkoler numbers (Re >> 1, Da >> 1) the reaction rate is controlled by relatively slow turbulent motions, while chemical time scale is much faster and does not play any role as it does not limit combustion rate.

Assuming infinitely thin flames, the mean reaction rate can be written as:

$$\omega = C_{EBU}\bar{\rho}\,\frac{\epsilon}{k}\,\tilde{\theta}\,\left(1-\tilde{\theta}\right) \qquad \text{Equation 4.93}$$

$$\tilde{\theta} = \frac{T - T_1}{T_2 - T_1} \qquad \text{Equation 4.94}$$

where C_{EBU} is a model constant, ρ is the density, ε/κ is the inverse of the integral time scale of the turbulent flow field, θ is a reduced temperature correlation that assumes a value equal one in the fully burned mixture and a value equal to zero in the fresh unburned mixture, T_1 is the temperature of the fresh mixture, and T_2 is the temperature of the fully burned mixture. The use of the time scale related to the integral length scale is based on the assumption that the largest vortices (close to integral length scale) have a dominant effect in the interactions between the flame and the flow field. The EBU model closure is usually achieved with the *κ-ε* turbulent model.

In (Magnussen and Hjertager, 1976) the EBU model was developed into the Eddy Dissipation Concept EDC model where the EBU assumption of flame propagation dominated by a turbulent mixing time (based on integral length scale) is extended to non-premixed combustion.

Although the EBU model has the weakness of not including any dependence on chemistry, generally the EBU model provides better results than the simple Arrhenius model in

simulations of turbulent combustion (Poinsot and Veynante, 2012). Nevertheless it is known that the EBU model tends to over-estimate the reaction rate, especially in highly strained regions (with strong shears) like walls and flame holders where the ratio ε/κ is large.

A weakness of the original EBU model is that there is not a universal value of the model constant that seems suitable for all configurations and flame regimes. The flame propagation is driven by the turbulent motions only and all other flame acceleration mechanisms are not included in the original model. In the initial stages of flame propagation, immediately after the ignition, the assumption of high Reynolds and Damkoler numbers does not hold and in some cases the stages at lower Reynolds and Damkoler numbers can contribute significantly to the flame speed and to the over-pressure history. Moreover the model is not suitable for detonation simulations where chemistry plays a major role. As described hereafter, several modifications of the model were suggested along the years in order to include more mechanisms for flame acceleration into the model, making it suitable for the modelling of a broader range of applications.

An extinction mechanism was introduced by Hjertager in the EDC model (Hjertager, 1982). According to that mechanism, when the chemical time scale (calculated with Arrhenius chemistry) is significantly larger (> 1000) than the turbulent mixing time scale, the reaction rate goes to zero. A quasi-laminar combustion modification was introduced by (Bakke and Hjertager, 1986) to take into account the quasi-laminar stages of flame propagation when the local turbulent Reynolds number is smaller than a critical value. A modification of the C_{EBU} to include some chemical features in the expression of the reaction rate was proposed by (Said and Borghi, 1988). A combustion enhancement factor E_T was added by (Hjertager and Solberg, 1999) to the expression of the turbulent combustion rate to take into account the break-up and acceleration of the flame when multiple obstacles are inside the control volume.

Another modification of the EBU model was suggested by (Meneveau and Poinsot, 1991) including the total turbulent strain rate in the original EBU model (ITNFS or Intermittent Turbulent Net Flame Stretch).

The expression of the mean reaction rate becomes:

$$\omega = C_{EBU}\bar{\rho}\,\Gamma_k\left(\frac{u'}{s_L^0},\frac{l_t}{\delta_L^0}\right)\frac{\epsilon}{k}\,\tilde{\theta}\,(1-\tilde{\theta}) \qquad \text{Equation 4.95}$$

where u' is the turbulent RMS velocity in the fresh mixture, s^0_L is the unstrained laminar flame speed, l_t is the integral length scale, δ^0_L is the thermal flame thickness, and Γ_k is the efficiency function that is fitted from DNS data.

This new expression takes into account all possible turbulent scales (and not only the integral length scale like in the original EBU model); it tends to decrease the mean reaction rate in highly strained regions, and it introduces sensitivity to chemistry. As reported in (Poinsot and Veynante, 2012), the above expression was successfully used by (Bailly et al., 1996) and (Lahjaily et al., 1998).

One potential issue with EBU/EDC models is that pre-ignition due to numerical diffusion can occur in regions with a large ε/κ ratio in front of the flame. That is non-physical behaviour of the model and it can be addressed by including a limiting condition on the relevant parameter (e.g. temperature or progress variable) into the model.

A LES-EBU model was considered by (Fureby and Lofstrom, 1994), (Fureby and Lofstrom, 1994), (Candel et al., 1999)

In the HySafe project (2004-2009) an extensive programme of CFD validation benchmark exercises were performed for hydrogen safety issues. It was shown that a EDC model (Hjertager, 1982), (Hjertager, 1993a), (Hjertager, 1993b) was capable of reproducing in RANS simulations the following experiments with different level of agreement between experimental measurements and simulation results: hydrogen deflagrations in a closed 1.5 m in diameter and 5.7 m high cylindrical vessel (Makarov et al., 2010a), hydrogen explosions in an environment simulating a vehicle refuelling station (Makarov et al., 2009), the explosion of a stoichiometric hydrogen-air mixture in a 10 m radius balloon in an unconfined configuration (Garcia et al., 2010), explosions of stoichiometric hydrogen–air mixtures in a 78.5 m long tunnel (Baraldi et al., 2009), and stoichiometric hydrogen deflagrations in a 0.95 m^3 vessel with vents of different sizes (Baraldi et al., 2010).

4.2.4 Flame surface density model (KIT)

4.2.4.1 General

The model of flame surface density created by FM global has been developing for the last years through successive developments (Bauwens et al., 2008a), (Bauwens et al., 2008b), (Bauwens et al., 2011). Between the factors contributing to pressure built-up in deflagrations, flame instabilities play a significant role especially in those problems in which the interaction with obstacles and enclosures are not significant. Surprisingly, the modelling of the flame instabilities have been introduced only in the last years (Bauwens et al., 2008a), (Bauwens et al., 2008b) for large scale calculations. Such modelling approaches are necessary as most of the spectrum of the wrinkles lies in the non-resolvable area due to resolution restrictions. In such a methodology the effective burning velocity was modelled as a product of the laminar burning velocity and a flame surface wrinkling factor Ξ.

The surface wrinkling factor is analysed taking into account (Bauwens et al., 2011) as a transport equation:

$$\frac{d\Xi}{dt} = G\,(\Xi - 1) - R\,(\Xi - 1)^{\frac{3}{2}} \qquad \text{Equation 4.96}$$

in which G and R are sub-grid wrinkling generation and removal rates. Although such a formulation allows for modelling of the included instabilities it has serious restrictions. Firstly, it disregards any interaction between disturbances with different wave numbers. Moreover, it only considers the growth of disturbances using a single wavenumber. Wavenumber is utilized also to calculate the growth rate *G*. Additionally, it was not derived from the first principles, and in some cases the solution of the transport equation was obtained using empirical parameters for *G* and *R*. Furthermore, each instability is modelled separately, and one equation, and one wrinkling factor, is required for each instability. The interaction and combination between the different factors (e.g. $\Xi = \Xi_1 \cdot \Xi_2$ in (Bauwens et al., 2011)) or $\Xi = \Xi_1 + \Xi_2$ in (Bauwens et al., 2008a), (Bauwens et al., 2008b) pose serious restrictions.

4.2.4.2 Derivation of the model for the flame wrinkling evolution

The detailed derivation of a model for the flame wrinkling and its evolution allows Rayleigh-Taylor instability to be accounted for. The model consists finally of a partial differential equation, which provides for the evolution of the wrinkling of the flame front. This wrinkling represents the flame surface enhancement due to instabilities. The source term of such a differential equation will be provided by the theory of flame instabilities.

A planar flame front is in general not stable. As a first approach, the flame can be considered as a surface of discontinuity which moves with a velocity normal to itself in every position. Based on these two assumptions a curved combustion front can be analysed utilizing the Huygen's principle (Zeldovich et al., 1985), see Figure 4.33. If the initial position and shape of the flame is known, the successive displacement of the surface can be obtained tracing the family of spheres of radius $S_L\,dt$. The enveloping surface of all these spheres represents the flame position in time $t+dt$.

Observing the surface of the flame, it is possible to distinguish convex and concave regions. In concave regions, the flame trajectories are convergent and ultimately focus on a single location to create a break in the surface of the flame.

This suggests to model the evolution of the front during the process in which the flame wrinkles as dominated by two competitive effects. These are the flame destabilization created by the instability itself and a suppression effect due to the cusp evolution.

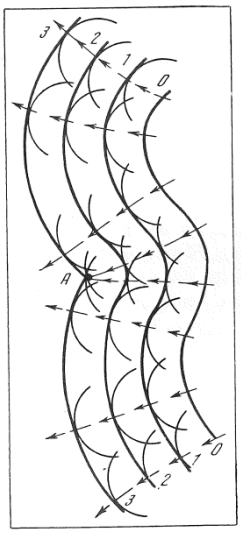

Figure 4.33 Successive locations of the flame front constructed applying the Huygen's principle (Zeldovich et al., 1985).

4.2.4.3 Source term

If the flame front is represented by the function $F(x,t)=0$ in a reference moving with the flame front, this surface divides the calculation domain into two regions $F < 0$ for the reactants and $F > 0$ for the products. Small perturbations could be considered in the surface of the flame utilizing the formulation:

$$(x,t) = A(t)exp(i\kappa x) \qquad \text{Equation 4.97}$$

The time dependent amplitude of the fluctuations can be expressed in terms of the exponential function:

$$A(t) = A_0 exp(\sigma\, t) \qquad \text{Equation 4.98}$$

Deriving, the source term representing the time dependent growth of the amplitude of the instability due to the initial perturbation, this could be expressed as a first approximation as:

$$\frac{dA}{dt} = \sigma A = \sigma k u_n A \qquad \text{Equation 4.99}$$

where sigma denotes the growth rate of the instability. This magnitude has been the subject of intensive studies and concrete formulation of this term, for any of the instabilities of interest, can be found in the literature, e.g. (Bychkov and Liberman, 2000).

The expression contained in this last equation neglects the existence of cusps in the flame surface. In the rationale that follows, it was attempted to estimate the effect of these cusps. Thus, in the following disquisitions *A* will be considered the amplitude of the front between cusp and top of the cyclic surface.

4.2.4.4 Flame surface annihilation due to cusps

We may now turn our attention to the pattern of the flame in the cusp, see Figure 4.34 and Figure 4.35.

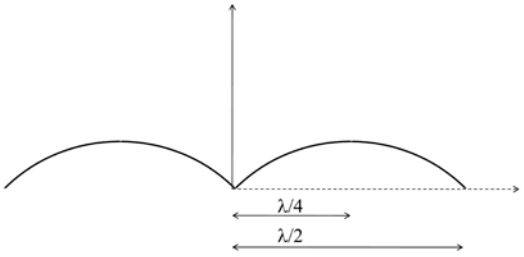

Figure 4.34 Surface of a flame with a cusp.

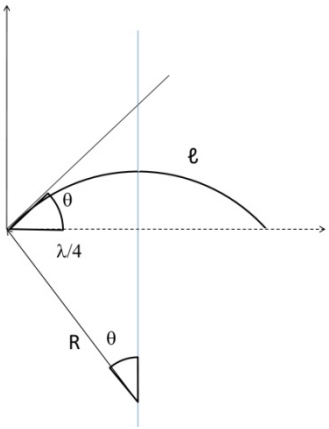

Figure 4.35 Surface of a flame with a cusp and variables utilized for its description.

If θ_c is the angle of the flame in the cusp and due to the interaction of the two convex areas the speed in the cusp is given by $S_L/cos\ \theta_c$. The suppression of amplitude due to the greater velocity of the cusps relative to the speed in convex areas is:

$$\frac{dA_c}{dt} = -S_L\left(\frac{1}{cos\theta_c} - 1\right). \qquad \text{Equation 4.100}$$

Out of the cusps the surface of the flame can be approximated with a parabola:

$$y = ax^2 + bx + c \qquad \text{Equation 4.101}$$

which intersects the points (0,0), (λ_c/2, 0) and (λ/4, A_c). This allows for the values of *a*, *b*, *c* to be obtained:

$$a = -\frac{16A_c}{\lambda_c^2}$$ Equation 4.102

$$b = \frac{8A_c}{\lambda_c}$$ Equation 4.103

$$c = 0$$ Equation 4.104

The equation of the parabola is:

$$y = -\frac{16A_c}{\lambda_c^2}x^2 + \frac{8A_c}{\lambda_c}\ x$$ Equation 4.105

and its derivative:

$$y' = -\frac{32A_c}{\lambda_c^2}\ x + \frac{8A_c}{\lambda_c}$$ Equation 4.106

Therefore, in the cusp, the slope is:

$$tg\ (\theta_c) = \frac{dy}{dx}|\_x = 0\ = 8A\_c/\lambda\_c$$ Equation 4.107

On the other side, the secant can be expressed to be:

$$\frac{1}{cos(\theta_c)} = \sqrt{tg^2(\theta_c) + 1}$$ Equation 4.108

In turn, the square root can be approximated with:

$$\sqrt{(tg^2(\theta_c) + 1)}\ \approx\ 1 + \frac{1}{2}\left(\frac{(8A_c)}{(\lambda_c)}\right)^2$$ Equation 4.109

Which allow, simplifying the previous equation, a case in which:

$$\frac{dA_c}{dt} = -\frac{S_L 8A_c^2\kappa^2}{\pi^2}$$ Equation 4.110

is obtained.

4.2.4.5 Wrinkling factor equation

The wrinkling factor represents the relation between the surface of the wrinkled and the planar flame. In the direction perpendicular to the paper the flame was considered as infinite, simplifying the problem to two dimensions, see Figure 4.35. The wrinkling factor represents the relation between the length of the arc and the chord shown in Figure 4.34. The length of the chord is directly $\lambda_c/2$. The length of the arc can be easily approximated, with first order accuracy, considering that the parabola utilized in the previous section is a circle. The first order approximation is a perfectly coherent premise taking into account that the theory for flame instabilities is based in this assumption and therefore using these assumptions the growth rate can be obtained:

$$\frac{1}{sen\theta_c} = \sqrt{1 + \left(\frac{1}{tg\theta_c}\right)^2} = \sqrt{1 + \left(\frac{\lambda_c}{8A_c}\right)^2}$$ Equation 4.111

$$R = \frac{\lambda_c}{4}\frac{1}{sen\theta_c}$$ Equation 4.112

$$\ell = 2\,\theta_c R$$ Equation 4.113

$$\theta_c \approx\ tg\,\theta_c\ = \frac{8A_c}{\lambda_c}$$ Equation 4.114

$$\ell\ = 2\frac{8A_c}{\lambda_c}\frac{\lambda_c}{4}\ \sqrt{1+\left(\frac{\lambda_c}{8A_c}\right)^2} = 4A_c\sqrt{1+\left(\frac{\lambda_c}{8A_c}\right)^2}$$ Equation 4.115

The wrinkling factor is then:

$$\Xi = \frac{\ell}{\frac{\lambda_c}{2}} = \sqrt{1+\left(\frac{8A_c}{\lambda_c}\right)^2}$$ Equation 4.116

which again in first order approximation reduces to:

$$\Xi\ \approx\ 1+\frac{1}{2}\left(\frac{8A_c}{\lambda_c}\right)^2$$ Equation 4.117

This can be reformulated into an expression involving different variables, the wrinkling factor and the wavenumber $\kappa = 2\pi/\lambda\_c$.

Under this formulation the equation can be rewritten as:

$$\Xi - 1 \approx \frac{1}{2}\left(\frac{8A_c}{\lambda_c}\right)^2 = \frac{8A_c^2\kappa^2}{\pi^2}$$ Equation 4.118

and deriving:

$$\frac{\Xi}{dt} = \frac{8\kappa^2}{\pi^2}\ 2\frac{A_c dA_c}{dt}$$ Equation 4.119

On the other side from equation:

$$A_C = \sqrt{\frac{\pi^2}{8}\kappa^2(\Xi-1)}$$ Equation 4.120

Thus:

$$\frac{d\Xi}{dt} = \frac{8\kappa^2}{\pi^2}\ 2\frac{\pi}{\sqrt{8}}\ \kappa\sqrt{\Xi-1}\frac{dA_c}{dt} = \frac{2\sqrt{2}\kappa}{\pi}2\sqrt{\Xi-1}\frac{dA_c}{dt}$$ Equation 4.121

Therefore, substituting:

$$\frac{1}{\frac{4\sqrt{2}\kappa}{\pi}}\sqrt{\backslash Xi-1}\frac{d\Xi}{dt}\ = -S_L(\Xi-1)$$ Equation 4.122

which simplifies to:

$$\frac{d\Xi}{dt} = -\frac{4\sqrt{2}\kappa}{\pi}\ S_L\ (\Xi-1)^{\frac{3}{2}}$$ Equation 4.123

4.2.4.6 Source term (instability) wrinkling factor

The previous equations can be also reformulated utilizing the wrinkling factor.

Substituting:

$$\frac{d\Xi}{dt} = \frac{4\sqrt{2}\kappa}{\pi}\sqrt{\Xi - 1}\,\sigma\,\kappa\,S_L\sqrt{\frac{\pi^2}{8\kappa^2}(\Xi - 1)} \qquad \text{Equation 4.124}$$

and thus:

$$\frac{d\Xi}{dt} = 2\sigma\kappa\,S_L\,(\Xi - 1) \qquad \text{Equation 4.125}$$

4.2.4.7 Final equation

The annihilation and source equations can be combined together to generate the model researched:

$$\frac{d\Xi}{dt} = 2\sigma\,\kappa\,S_L\,(\Xi - 1) - 4\sqrt{2}\frac{\kappa}{\pi}\,S_L\,(\Xi - 1)^{\frac{3}{2}} \qquad \text{Equation 4.126}$$

The factor σ, dimensionless growth factor can be, for the Darrieus-Landau, Rayleigh-Taylor, thermo-diffusive or acoustic-parametric instabilities, found in the literature, e.g. (Bychkov and Liberman, 2000) and provides a possibility for the modelling of the mentioned instabilities.

The equation contain a free parameter, the wavenumber that also affects the growth rate, as $\sigma = \sigma(\kappa)$. Therefore, it is necessary to define the wavenumber that should be considered inside the range of the instability. Bauwens et al. (Bauwens et al., 2011) have selected the wavenumber that produces the highest growth rate exclusively arguing that this would be the most significant wavenumber.

4.2.4.8 Limitations

The validity of a model based and resulting on the assumptions accepted in this chapter is doubtful.

Nevertheless, it offers the framework to introduce flame instabilities into the modelling in a very simple way. Between the evident shortcomings of such an approach we should mention several points. Conceptually the approach is based tracing an analogy between combustion and optics, the validity of which controversial. Additionally, it considers a single wavenumber as representative of the whole instability spectrum. Furthermore, it ignores and neglects the interaction between different wavenumbers.

4.2.4.9 Growth rate of Rayleigh-Taylor instability

The stability of a flame with an arbitrary Lewis number and with transports coefficients varying with temperature was studied i.e. in reference (Searby, 1986). Bychkov and Liberman (Bychkov and Liberman, 2000) recovers this formulation (which appears in (Searby and Rochwerger, 1991)) to analyse the stability of flames.

The stability problem could be studied by analysing the negative solutions of:

$$A\sigma^2 + U_L kB\sigma + k\,g\,C_1 + U_L^2 k^2 C_2 = 0 \qquad \text{Equation 4.127}$$

where

$$A = 1 + \frac{\theta - 1}{\theta + 1}\,kL\left(Ma - \frac{\theta}{\theta - 1}J\right) \qquad \text{Equation 4.128}$$

$$B = \frac{2\,\theta}{\theta + 1}\left(1 + \theta\,kL(Ma - J)\right) \qquad \text{Equation 4.129}$$

$$C_1 = \frac{(\theta-1)}{(\theta+1)}\left(1 \; - \; k\,L\left(Ma \; - \frac{J\,\theta}{\theta-1}\right)\right) \qquad \text{Equation 4.130}$$

$$C_2 = \left(\frac{\theta(\theta-1)}{\theta+1}\left(-1 + \frac{kL}{\theta-1}\left((3\theta-1)Ma \; - \; 2J\theta \; + 2\,\mathrm{Pr} \quad h_b(\theta-1) - J_3(2Pr-1)\right)\right)\right) \qquad \text{Equation 4.131}$$

where $\gamma = (\rho_u - \rho_b)/\rho_u = 1 - 1/\sigma$, $\vartheta = (T - T_u)/(T_b - T_u)$, $Le = \chi/D$ the Lewis number, Pr the Prandtl number, $Fr^{-1} = gd/U_L^2$ the Froude number, g the acceleration of the gravity, U_L the laminar flame speed and d the thickness of the flame.

The additional definitions provided complete the description of the previous equations:

$$H = \int_0^1 \left(h_b - h(\vartheta)\right) d\vartheta \qquad \text{Equation 4.132}$$

$$J = \frac{\gamma}{1-\gamma}\int_0^1 (h(\vartheta))/(1 + \frac{\vartheta\gamma}{1-\gamma}) \; d\vartheta \qquad \text{Equation 4.133}$$

$$Ma = \frac{J}{\gamma} - \frac{1}{2}\,Ze\,(\,Le - 1)\int_0^1 \frac{h(\vartheta)ln(\vartheta)}{1 + \frac{\vartheta\gamma}{1-\gamma}}\,d\vartheta \qquad \text{Equation 4.134}$$

where

$$h(\vartheta) = \frac{\left(\lambda(\vartheta)C_{P_u}\right)}{\lambda_u C_P(\vartheta)} = \frac{\rho(\vartheta)\chi(\vartheta)}{\rho_u\chi_u} \qquad \text{Equation 4.135}$$

4.2.4.10 Rayleigh-Taylor instability results

For the Rayleigh-Taylor instability, the calculations were performed with 7 different accelerations. In the case where g = 0 the growth rate coincides with the Darrieus-Landau instability.

Additionally three positive and three negative accelerations were included in the graphics.

The approximate value of 10000 m/s^2 was obtained from a rough estimation of typical acceleration to be achieved in obstructed combustion tubes with flames moving at 100 m/s.

Even bigger values could be achieved in the reality.

Of course those values are problem dependent and will depend on the fuel content of the reactive mixture.

The results obtained for all concentrations were included in the Figure 4.36 and Figure 4.37.

The dependence of the growth rate on the concentration can be very clearly appreciated.

Therefore, the effect of acceleration on the RT instability is much stronger for lean mixtures than for rich ones.

Additionally the interval of wavenumbers to be considered as unstable also grows strongly for lean mixtures.

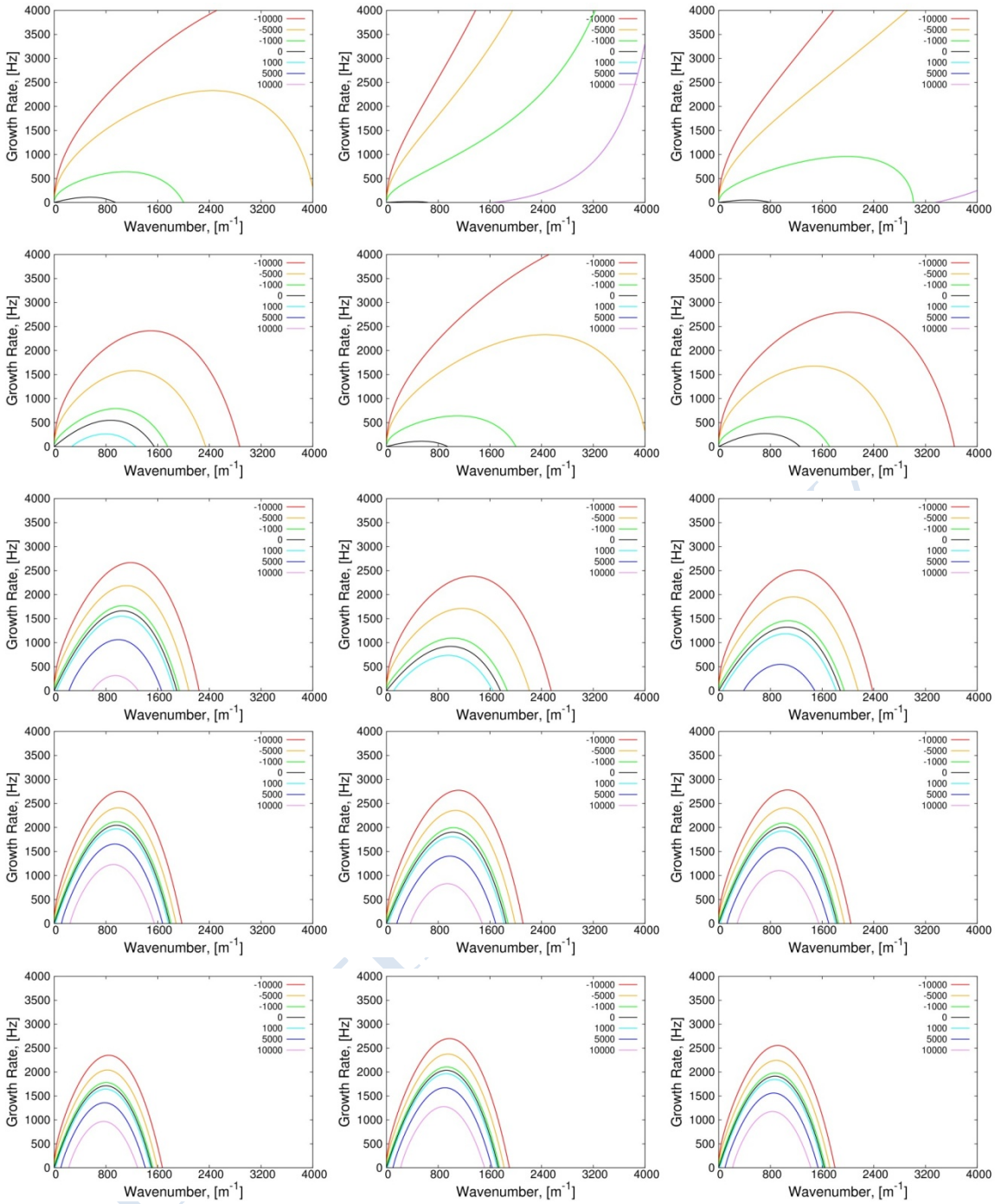

Figure 4.36 Growth rate of the Rayleigh-Taylor instability for H2-air mixtures with different fuel concentrations, From left to right; a) 10., 12.5; b)15., 17.5, 20.; c) 22.5, 25., 27.5; d) 30., 32.5, 35.; e) 37.5, 40., 42.5 H2 %(vol.), Gravity acceleration indicated in the legend.

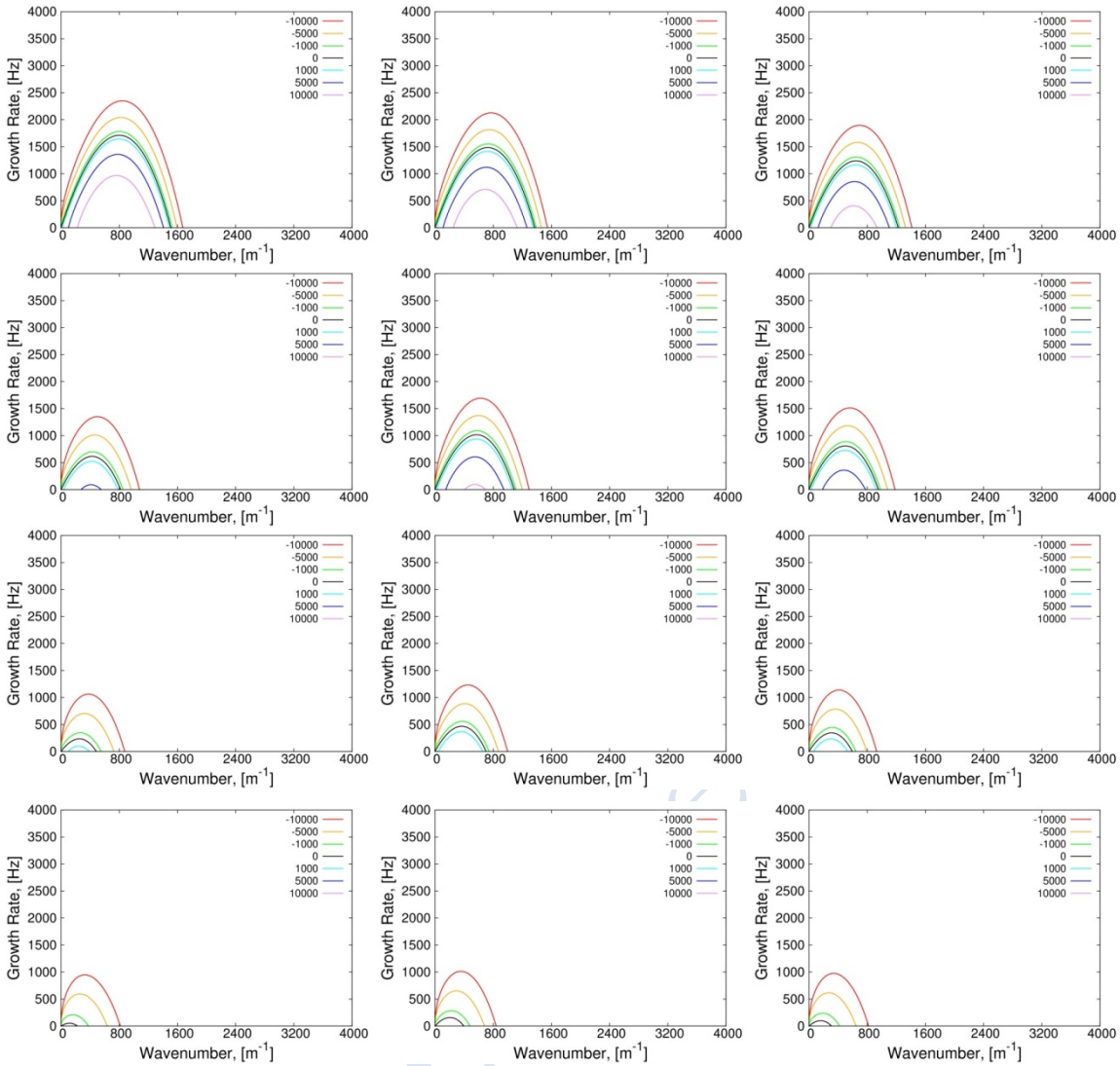

Figure 4.37 Growth rate of the Rayleigh-Taylor instability for H2-air mixtures with different fuel concentrations, From left to right; a) 42.5, 45., 47.5; b) 50., 52.5, 55.; c) 57.5, 60., 62.5; d) 65., 67.5, 70. H2 % (vol.), Gravity acceleration indicated in the legend.

4.2.4.11 Analysis of the RT influence on the maximum overpressures achieved

With knowledge of the growth rate (see previous discussion) it is possible to close the model and obtain the required solution of the equation:

$$\frac{d\Xi}{dt} = 2\sigma\,\kappa\,S_L\,(\Xi - 1) - 4\sqrt{2}\frac{\kappa}{\pi}\,S_L\,(\Xi - 1)^{\frac{3}{2}}$$ Equation 4.136

To make this model coherent, the growth rate and the wavenumbers are point and time dependent, and can be simply obtained on each calculation volume by the code. It is necessary also to remark that the acceleration and the gaseous concentrations are also point and time dependent. The only remaining open point is the selection of the initial values for Ξ. Evidently, the modelled equation is dependent on the initial value selected.

This dependency can be studied using Figure 4.38:

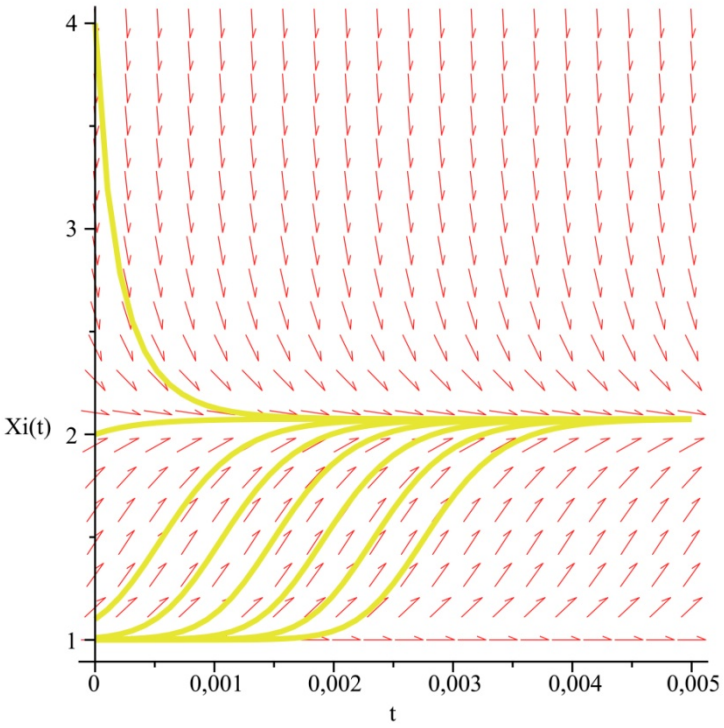

Figure 4.38 Field diagram of a stoichiometric hydrogen air mixture, acceleration = 10000 m/s2 Integral lines obtained for initial values of Ξ0 = 1.000001, 1.00001, 1.0001, 1.001, 1.01, 1.1, 2, 4.

The results depicted show a clear attractor at $\Xi = 2.1$. For this representation the more violent case has been presented, thus timing for the growth rate for less violent accelerations is going to be slower.

For the cases with a very strong deceleration, 10000 m/s^2 taking into account again stoichiometric mixtures, Figure 4.39 is produced, with an analogous attractor at $\Xi = 1.2$.

The results contained in Figure 4.38 and Figure 4.39 show one of the greatest limitations of the model. Taking into account the results obtained for $\Xi = 1.000001, 1.00001, 1.0001, 1.001$, it is clear that the model does not converge to a solution in which grid invariance can be obtained. Even more, the values $\Xi_0 = 1.000001, 1.00001, 1.0001, 1.001$ represent the same physical reality, actually, a planar flame with a negligible perturbation applied. The difference obtained in the figures between the corresponding integral curves, which for transients are significant, show the limited accuracy of the model and its limitative range of utilization.

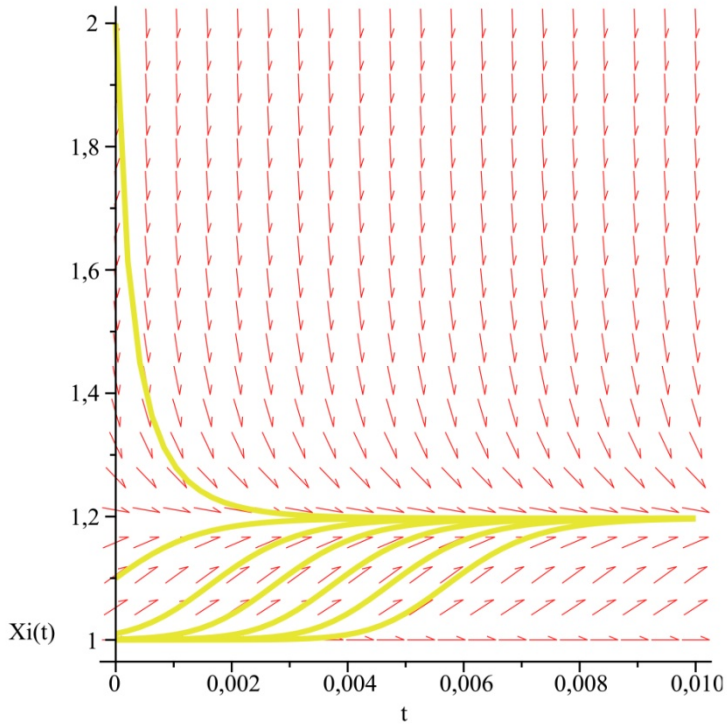

Figure 4.39 Field diagram of a stoichiometric hydrogen air mixture, deceleration = 10000 m/s2 Integral lines obtained for values of Ξ0 = 1.000001, 1.00001, 1.0001, 1.001, 1.01, 1.1, 2.

4.2.5 Modelling and numerical simulation of explosions in stratified mixtures (UU)

The development of predictive methods for explosions in stratified mixtures has so far received limited attention (Marra et al., 2002). Some simplified lumped-parameters models were developed to describe the combustion in stratified layers. Feng et al. (Feng et al., 1975) formulated two analytical models to explain the behaviour for a single roof-layered uniform fuel-air mixture within a gallery of finite and infinite length. The flow was treated as steady, two-dimensional, incompressible and inviscid. For a gallery of infinite height, the ratio of the propagation velocity to the burning velocity is equal to the square root of the ratio of the unburned to burned gas density. For galleries of finite length with open ends, the interesting result is that for all but a gallery of infinite height the flame propagation velocity is unsteady and accelerating. Kaptein and Hermance (Kaptein and Hermance, 1976) developed further the model by Feng et al. (Feng et al., 1975) for a gallery of infinite length. These step-wise premixed layer models were focused on explaining the flame propagation velocities and cannot be applied directly to predict pressure dynamics in unvented/vented enclosures.

Dold (Dold, 1989) performed a theoretical investigation and concluded that the propagation velocity of the triple flame strongly depends upon the transverse mixture fraction gradient. He determined that the flame propagation velocity increases as the mixture fraction gradient decreases, and it is bounded by the maximum adiabatic laminar flame propagation velocity of the system.

The novel aspect of the recent lumped parameter model developed by Tamanini (Tamanini, 2000) is that it includes a dual-mode treatment of the combustion process that affects explosion pressure dynamics. In this model, a premixed flame sweeps horizontally through the corresponding layer at a constant propagation velocity. In the wake of this premixed

flame, the fuel in the rich layer reacts in a convection flame. The second burning mode starts after a delay, which is calculated based on the time required for the buoyant turnover of the combustion products. One of the disadvantages of this model is that the flame propagation velocity is a parameter that needs to be supplied to the model. The burning in the convection flame is essentially treated as a pool fire with a constant burning rate. The most important limitation of the model (Tamanini, 2000) is that it cannot be applied to model explosion dynamics when the flame propagates in the direction of the concentration gradient in an environment similar to Whitehouse et al. (Whitehouse et al., 1996).

Preliminary work on the CFD simulation of stratified fuel-air explosions was performed by (Marra et al., 2002). No significant differences were observed with respect to the flame propagation between the simulation assuming laminar combustion and the simulation using the classical k-ε model. The simulation of the experiment by Tamanini (Tamanini, 2000) has shown that the volume of hot combustion products started to rise due to buoyancy. It has been concluded that calculated flame speeds are in agreement with the experiments and the calculated flow and flame structure are also well reproduced, at least qualitatively. Results in terms of pressure prediction with respect to time were obtained without a turbulence model. In the stratified mixture explosion the pressure rise drops at about 1 s after ignition but is followed by an increase of pressure due to the diffusion/convection flame fed by the rich layer.

4.3 References

Andrews, G.E., Bradley, D., 1972. Determination of burning velocities, a critical review. Combustion and Flame 18, 133–153.

Anthony, E.J., 1978. The use of venting formulae in the design and protection of building and industrial plant from damage by gas or vapor explosions. Journal of Hazardous Materials 2, 23 – 49.

Ardey, N., Mayinger, F., 1996. Highly turbulent hydrogen flames / explosions in partially obstructed confinements, in: Proc. of the 1st. Trabzon Int. Energy and Environment Symp. Karadeniz Techn. Univ., Trabzon, Turkey, July 29th - 31st, pp. 679–692.

Aung, K.T., Hassan, M.I., Faeth, G.M., 1997. Flame stretch interactions of laminar premixed hydrogen/air flames at normal temperature and pressure. Combustion and Flame 109, 1–24. doi:10.1016/S0010-2180(96)00151-4

Babkin, V.S., 2003. Private communication. Institute of Chemical Kinetics and Combustion. Siberian Branch, Russian Academy of Science, Novosibirsk, Russia.

Badr, O., Karim, G., 1984. Flame propagation in stratified methane-air mixtures. Journal of Fire Sciences 2, 415–426.

Baev, V.K., Tretyakov, P.K., 1969. Calculation of flames location in turbulent flow. //Izv. Sib. Otd. Akad. Nauk SSSR, Ser. Tekhn. Nauk (in Russian) 1.

Bailly, P., Garreton, D., Simonin, O., Bruel, P., Champion, M., Deshaies, B., Duplantier, S., Sanquer, S., 1996. Experimental and numerical study of a premixed flame stabilized by a rectangular section cylinder, in: Proceedings of the 1996 26th International Symposium on Combustion. Part 2 (of 2), July 28, 1996 - August 2, 1996, Symposium (International) on Combustion. Combustion Inst, pp. 923–929.

Baker, Q.A., Tang, M.J., Scheier, E.A., Silva, G.J., 1996. Vapor cloud explosion analysis. Process Safety Progress 15, 106–109.

Bakke, J.R., Hjertager, B.H., 1986. Quasi - laminar/turbulent combustion modeling, real cloud generation & boundary conditions in the FLACS - ICE code (No. Report CMI 865402 - 2). Christian Michelsen Institute.

Baraldi, D., Kotchourko, A., Lelyakin, A., Yanez, J., Gavrikov, A., Efimenko, A., Verbecke, F., Makarov, D., Molkov, V., Teodorczyk, A., 2010. An inter-comparison exercise on CFD model capabilities to simulate hydrogen deflagrations with pressure relief vents. International Journal of Hydrogen Energy 35, 12381–12390. doi:10.1016/j.ijhydene.2010.08.106

Baraldi, D., Kotchourko, A., Lelyakin, A., Yanez, J., Middha, P., Hansen, O.R., Gavrikov, A., Efimenko, A., Verbecke, F., Makarov, D., Molkov, V.V., 2009. An inter-comparison exercise on CFD model

capabilities to simulate hydrogen deflagrations in a tunnel. International Journal of Hydrogen Energy 34, 7862–7872.

Bauwens, C.R., Chaffee, J., Dorofeev, S., 2008a. Experimental and Numerical Study of Methane-Air Deflagrations in a Vented Enclosure. Presented at the Sixth International Symposium on Fire Safety Science, Sixth International Symposium on Fire Safety Science, Germany.

Bauwens, C.R., Chaffee, J., Dorofeev, S., 2008b. Experimental and numerical study on hydrogen-air deflagrations in a vented enclosure, in: 7th International Symposium on Hazards, Prevention, and Mitigation of Industrial Explosions. pp. 245–254.

Bauwens, C.R., Chaffee, J., Dorofeev, S.B., 2011. Vented explosion overpressures from combustion of hydrogen and hydrocarbon mixtures. International Journal of Hydrogen Energy 36, 2329–2336. doi:doi: DOI: 10.1016/j.ijhydene.2010.04.005

Bauwens, C.R., Chao, J., Dorofeev, S.B., 2012. Effect of hydrogen concentration on vented explosion overpressures from lean hydrogen-air deflagrations. International Journal of Hydrogen Energy 37, 17599–17605. doi:10.1016/j.ijhydene.2012.04.053

Bauwens, C.R., Dorofeev, S.B., 2014. Effect of initial turbulence on vented explosion overpressures from lean hydrogen-air deflagrations. International Journal of Hydrogen Energy, Int. J. Hydrog. Energy (Netherlands) 39, 20509–15. doi:10.1016/j.ijhydene.2014.04.118

Bazhenova, T.V., Soloukhin, R.I., 1958. Gas ignition behind the shock wave, in: 7th Symposium (International) on Combustion, August 28, 1958 - September 3, 1958, Symposium (International) on Combustion. Combustion Institute, pp. 866–875. doi:10.1016/S0082-0784(58)80130-7

Bechtold, J.K., Matalon, M., 1987. Hydrodynamic and diffusion effects on the stability of spherically expanding flames. Combustion and Flame 67, 77–90.

Benim, A.C., Syed, K.J., 1998. Laminar flamelet modelling of turbulent premixed combustion. Applied Mathematical Modelling 22, 113–136. doi:10.1016/S0307-904X(98)00012-2

Betev, A.S., Karpov, V.P., Lipatnikov, A.N., Yardosanidze, Z.P., 1995. Hydrogen combustion in engines and preferential diffusion effects in laminar and turbulent flames. Archivum Combustionis (The Journal of the Thermodynamics and Combustion Committee of the Polish Academy of Sciences 15, 187–216.

Birkby, P., Cant, R.S., Savill, A.M., 2000. The application of a laminar flamelet model to confined explosion hazards. Flow, Turbulence and Combustion, Flow, Turbul. Combust. (Netherlands) 63, 361–77. doi:10.1023/A:1009932203310

Borghi, R., 1985. On the structure and morphology of turbulent premixed flames. Plenum Press, New York, NY, pp. 117–138.

Bradley, D., 1999. Instabilities and flame speeds in large-scale premixed gaseous explosions. Philosophical Transactions of the Royal Society of London, Series A 357, 3567–3581.

Bradley, D., 1998. Evolution of Flame Propagation in Large Diameter Explosions, in: Proc of the 2nd Int. Seminar on Fire & Explosition Hazard of Substances and Venting of Deflagrations. Presented at the All-Russian Res. Inst. for Fire Protection, pp. 51–59.

Bradley, D., Cresswell, T.M., Puttock, J.S., 2001. Flame acceleration due to flame-induced instabilities in large-scale explosions. Combustion and Flame 124, 9.

Bradley, D., Mitcheson, A., 1978. Venting of gaseous explosions in spherical vessels - 1 Theory. Combustion and Flame 32, 221–236. doi:10.1016/0010-2180(78)90098-6

Bray, K.N.C., 1996. Challenge of turbulent combustion, in: Proceedings of the 1996 26th International Symposium on Combustion. Part 2 (of 2), July 28, 1996 - August 2, 1996, Symposium (International) on Combustion. Combustion Inst, pp. 1–26.

Bray, K.N.C., 1990. Studies of the Turbulent Burning Velocity. Proceedings of the Royal Society of London. Series A: Mathematical and Physical Sciences 431, 315 –335. doi:10.1098/rspa.1990.0133

Brennan, S., Bengaouer, A., Carcassi, M., Cerchiara, G., Evans, G., Friedrich, A., Gentilhomme, O., Houf, W., Kotchourko, A., Kotchourko, N., Kudriakov, S., Makarov, D., Molkov, V., Papanikolaou, E., Pitre, C., Royle, M., Schefer, R., Stern, G., Venetsanos, A.G., Veser, A., Willoughby, D., Yanez, J., 2011. Hydrogen and fuel cell stationary applications: Key findings of modelling and experimental work in the HYPER project. International Journal of Hydrogen Energy, Int. J. Hydrog. Energy (UK) 36, 2711–20. doi:10.1016/j.ijhydene.2010.04.127

British Gas, 1990. Review of the applicability of predictive methods to gas explosions in offshore modules (No. OTH 89 312), Offshore Technology Report. British Gas, Department of Energy, London.

Brizuela, E.A., Bilger, R.W., 1996. On the Eddy Break-Up coefficient. Combustion and Flame 104, 208–212. doi:10.1016/0010-2180(95)00205-7

Burgoyne, J.H., Wilson, M.J.G., 1960. The relief of pentane vapour–air explosion in vessels. The First Symposium on Chemical Process Hazards, I. Chem. E. 25 – 29.

Butlin, R.N., 1975. A review of information on experiments concerning the venting of gas explosions in buildings. Fire Research Note No. 1026, 19 p.

Bychkov, V.V., Liberman, M.A., 2000. Dynamics and stability of premixed fames. Physics Reports 325, 115–237.

Byggstoyl, S., Magnussen, B.F., 1985. Model for flame extinction in turbulent flow, in: Turbulent Shear Flows 4, Selected Papers from the Fourth International Symposium. Springer-Verlag, pp. 381–395.

Cambray, P., Deshaies, B., Clavin, P., 1979. Solution des équations d'Euler associée à l'explosion d'une sphère à vitesse constante. , 40:11. (in French). Journal de Physique Colloq, C8 40, 19–24.

Candel, S., Thevenin, D., Darabiha, N., Veynante, D., 1999. Progress in numerical combustion. Combustion science and technology 149, 297–337.

Cheikhravat, H., Yahyaoui, M., Djebaili-Chaumeix, N., Paillard, C.-E., 2007. Influence of Hydrogen distribution on flame propagation. Presented at the 21st ICDERS, Poitiers, France, July 23rd - 27th.

Chitty, R., 1996. Management summary of `A survey of backdraught'. Fire Engineers Journal 56, 12–12.

Ciccarelli, G., Dorofeev, S., 2008. Flame acceleration and transition to detonation in ducts. Progress in Energy and Combustion Science 34, 499–550.

Ciccarelli, G., Ginsberg, T., Boccio, J., Economos, C., Sato, K., Kinoshita, M., 1994. Detonation cell size measurements and predictions in hydrogen-air-steam mixtures at elevated temperatures. Combustion and Flame 99, 212–220. doi:10.1016/0010-2180(94)90124-4

Clarke, J.F., Kassoy, D.R., Riley, N., 1984. Shocks generated in a confined gas due to rapid heat addition at the boundary. I. Weak shock waves. Proceedings of The Royal Society of London, Series A: Mathematical and Physical Sciences 393, 309–329.

Clavin, P., 1985. Dynamic behavior of premixed flame fronts in laminar and turbulent flows. Progress in Energy and Combustion Science 11, 1–59. doi:10.1016/0360-1285(85)90012-7

Clavin, P., Joulin, G., 1983. Premixed flames in large scale and high intensity turbulent flow. Journal de Physique Lettres, J. Phys. Lett. (France) 44, 1–12. doi:10.1051/jphyslet:019830044010100

Cooper, M.G., Fairweather, M., Tite, J.P., 1986. ON THE MECHANISMS OF PRESSURE GENERATION IN VENTED EXPLOSIONS. Combustion and Flame 65, 1–14.

Cubbage, P.A., Marshall, M.R., 1973. Pressures generated by explosions of gas-air mixtures in vented enclosures (No. 926), Institute of Gas Engineers Communication.

Cubbage, P.A., Simmonds, W.A., 1955. An investigation of explosion reliefs for industrial drying ovens (No. GC23), Gas Council: Research Communication. London: Gas Council.

Dahoe, A.E., 2005. Laminar burning velocities of hydrogen-air mixtures from closed vessel gas explosions. Journal of Loss Prevention in the Process Industries 18, 152–166.

Darrieus, G., 1946. Propagation d''un front de flamme. Essais de théories anormales de déflagration par développement spontané de la turbulence. Presented at the 6th International Congress of applied mechanics, Paris, France (in french).

Darrieus, G., n.d. unpublished work. Presented at the La Technique Moderne, and at Le Congres de Mecanique Appliquee (1945) and (1938).

Daubech, J., Proust, C., Jamois, D., Leprette, E., 2011. Dynamics of vented hydrogen-air deflagrations, in: Proc. of the 4th International Conference on Hydrogen Safety, 12th - 14th Sept. San Francisco, USA.

Deshaies, B., Leyer, J.C., 1981. Flow field induced by unconfined spherical accelerating flames. Combustion and Flame 40, 141–153. doi:10.1016/0010-2180(81)90119-X

Dobashi, R., 1997a. Experimental study on gas explosion behavior in enclosure. Journal of Loss Prevention in the Process Industries 10, 83–89. doi:10.1016/S0950-4230(96)00050-2

Dobashi, R., 1997b. Generating mechanisms of flame front turbulence during gas explosions., in: Proc. of the Second Intl. Seminar on Fire-and-Explosion Hazard of Substances and Venting of Deflagrations, 10th – 15th August. Moscow, pp. 102 – 112.

Dobashi, R., Hirano, T., Tsuruda, T., 1994. Flame front disturbance induced by a weak pressure wave, in: Proceedings of the 25th Symposium (International) on Combustion, Jul 31 - Aug 5 1994, Symposium (International) on Combustion. Combustion Inst, pp. 1415–1415.

Dold, J.W., 2007. Premixed flames modelled with thermally sensitive intermediate branching kinetics. Combustion, Theory and Modelling, Combust. Theory Model. (UK) 11, 909–48. doi:10.1080/13647830701294599

Dold, J.W., 1989. Flame propagation in a nonuniform mixture: Analysis of a slowly varying triple flame. Combustion and Flame 76, 71–88. doi:10.1016/0010-2180(89)90079-5

Domingo, P., Vervisch, L., Bray, K., 2002. Partially premixed flamelets in LES of nonpremixed turbulent combustion. Combustion, Theory and Modelling, Combust. Theory Model. (UK) 6, 529–51. doi:10.1088/1364-7830/6/4/301

Dorofeev, S.B., 2008. Flame acceleration and transition to detonation: a framework for estimating potential explosion hazards in hydrogen mixtures. Presented at the 3rd European Summer School on Hydrogen Safety, Belfast, UK.

Dorofeev, S.B., Kuznetsov, M.S., Alekseev, V.I., Efimenko, A.A., Breitung, W., 2001. Evaluation of limits for effective flame accelaration in hydrogen mixtures. Journal of Loss Prevention in the Process Industries 14, 583–589. doi:10.1016/S0950-4230(01)00050-X

Dorofeev, S.B., Sidorov, V.P., Kuznetsov, M.S., Matsukov, I.D., Alekseev, V.I., 2000. Effect of scale on the onset of detonations. Shock Waves 10, 137–149.

Dragosavic, M., 1973. Structural measures against natural-gas explosions in high-rise blocks of flats. Heron 19, 1–51.

Durst, B., Ardey, N., Mayinger, F., 1996. Interaction of turbulent deflagrations with representative flow obstacles. Presented at the OECD/NEA/CSNI Workshop on the Implementation of Hydrogen Mitigation Techniques, Winnipeg, Manitoba, May 13th - 15th, pp. 433 – 447.

Dyner, H., 1966. Density variation due to reflected shock-boundary- layer interaction. Phys Fluids 6, 879 – 892.

Dzieminska, E., Hayashi, A.K., 2013. Auto-ignition and DDT driven by shock wave-Boundary layer interaction in oxyhydrogen mixture. International Journal of Hydrogen Energy 38, 4185–4193. doi:10.1016/j.ijhydene.2013.01.111

Egerton, A.C., Saunders, O.A., Lefebvre, A.H., Moore, N.P.W., 1953. Some observations by Schlieren technique of the propagation of flame in a closed vessel. 4th Symp. (Int) Comb. 4, 396 – 402.

Ellis, O.C., Wheeler, R.V., 1927. XXVI.-The movement of flame in closed vessels: correlation with development of pressure. J. Chem. Soc. 153–158. doi:10.1039/JR9270000153

Ertesvag, I.S., Magnussen, B.F., 2000. The Eddy dissipation turbulence energy cascade model. Combustion Science and Technology 159, 213–235.

Feng, C.C., Lam, S.H., Glassman, I., 1975. Flame propagation through layered fuel-air mixtures. Combustion Science and Technology 10, 59–71.

Friedrich, A., Grune, J., Jordan, T., Kotchourko, A., Kotchourko, N., Kuznetsov, M., Sempert, K., Stern, G., 2007. Experimental Study of Hydrogen-Air Deflagrations in Flat Layer (Paper 1.3.106), in: Proc. 2nd ICHS International Conference on Hydrogen Safety, September 11th - 13th. San Sebastian – Spain, pp. 1 – 12.

Fureby, C., 2004. A fractal flame-wrinkling large eddy simulation model for premixed turbulent combustion. Proceedings of the Combustion Institute, Proc. Combus. Inst. (USA) 30, 593–601.

Fureby, C., Lofstrom, C., 1994. Large-eddy simulations of bluff body stabilized flames, in: . Proc. of 25th Symp. (Int.) on Comb. pp. 1257 – 1264.

Gaathaug, A.V., Vaagsaether, K., Bjerketvedt, D., 2012. Experimental and numerical investigation of DDT in hydrogen-Air behind a single obstacle. International Journal of Hydrogen Energy 37, 17606–17615. doi:10.1016/j.ijhydene.2012.03.168

Gamezo, V.N., Ogawa, T., Oran, E.S., 2007. Numerical simulations of flame propagation and DDT in obstructed channels filled with hydrogen–air mixture. Proceedings of the Combustion Institute 31, 2463–2471.

Garcia, J., Baraldi, D., Gallego, E., Beccantini, A., Crespo, A., Hansen, O.R., Hoiset, S., Kotchourko, A., Makarov, D., Migoya, E., Molkov, V., Voort, M.M., Yanez, J., 2010. An intercomparison exercise on the capabilities of CFD models to reproduce a large-scale hydrogen deflagration in open atmosphere. International Journal of Hydrogen Energy 35, 4435–4444. doi:10.1016/j.ijhydene.2010.02.011

Girard, P., Huneau, M., Rabasse, C., Leyer, J.C., 1979. Flame propagation through unconfined and confined hemispherical stratified gaseous mixtures. Symposium (International) on Combustion 1247–1255.

Gostintsev, Y.A., Istratov, A.G., Shulenin, Y.V., 1988. Self-similar propagation of a free turbulent flame in mixed gas mixtures. Combustion, Explosion and Shock Waves 24, 563–569.

Gouldin, F.C., 1987. An application of fractals to modeling premixed turbulent flames. Combustion and Flame, Combust. Flame (USA) 68, 249–66. doi:10.1016/0010-2180(87)90003-4

Gouldin, F.C., Hilton, S.M., Lamb, T., 1989. Experimental evaluation of the fractal geometry of flamelets. Symposium (International) on Combustion 22, 541–550. doi:10.1016/S0082-0784(89)80061-X

Grune, J., Sempert, K., Haberstroh, H., Kuznetsov, M., Jordan, T., 2013a. Experimental investigation of hydrogen-air deflagrations and detonations in semi-confined flat layers. Journal of Loss Prevention in the Process Industries 26, 317–323. doi:10.1016/j.jlp.2011.09.008

Grune, J., Sempert, K., Kuznetsov, M., Jordan, T., 2013b. Experimental investigation of fast flame propagation in stratified hydrogen-air mixtures in semi-confined flat layers. Journal of Loss Prevention in the Process Industries, J. Loss Prev. Process Ind. (Netherlands) 26, 1442–51. doi:10.1016/j.jlp.2013.09.008

Guilbert-Duplantier, C., 1993. Etude des effets mécaniques des explosions de gaz sur des structures de forme simple (Thèse de Doctorat de l'Université de Poitiers, no 659 (in French)).

Gulder, O.L., 1991. Turbulent premixed combustion modelling using fractal geometry. Symposium (International) on Combustion 23, 835–842. doi:doi: DOI: 10.1016/S0082-0784(06)80337-1

Gülder, Ö.L., 1991. Turbulent premixed flame propagation models for different combustion regimes. Symposium (International) on Combustion 23, 743–750. doi:10.1016/S0082-0784(06)80325-5

Harmanny, A., 1993. Effect of inertia on effectiveness of explosion venting, Europex Newslett, April.
Harrison, A.J., Eyre, J.A., 1987. "External Explosions" as a Result of Explosion Venting. Combustion Science and Technology 52, 91 – 106.
Heidari, A., Wen, J.X., 2014. Flame acceleration and transition from deflagration to detonation in hydrogen explosions. International Journal of Hydrogen Energy, Int. J. Hydrog. Energy (Netherlands) 39, 6184–200. doi:10.1016/j.ijhydene.2014.01.168
Helie, J., Trouve, A., 1998. Turbulent flame propagation in partially premixed combustion. Symposium (International) on Combustion 1, 891–898.
Hertzberg, A., Bruckner, A.P., Bogdanoff, D.W., 1988. Ram accelerator: a new method for accelerating projectiles to ultrahigh velocities. AIAA journal 26, 195–203.
Hirano, T., Suzuki, T., Mashiko, I., Iwai, K., 1976. Flame propagation through mixtures with concentration gradient. Symp (Int) on Combust, 16th, MIT, August 15, 1976 - August 20, 1976 1307–1315.
Hjertager, B.H., 1993a. Simulation of gas explosions. Modeling, Identification and Control 10, 227–247.
Hjertager, B.H., 1993b. Computer modelling of turbulent gas explosions in complex 2D and 3D geometries. Journal of Hazardous Materials 34, 173–197. doi:10.1016/0304-3894(93)85004-X
Hjertager, B.H., 1982. Numerical simulation of turbulent flame and pressure development in gas explosions, in: Fuel-Air Explosions, Proceedings of the International Conference on Fuel-Air Explosions., Studies Series - University of Waterloo, Solid Mechanics Division, SM Study. Univ of Waterloo, Solid Mechanics Div, pp. 407–426.
Hjertager, B.H., Solberg, T., 1999. A Review of Computional Fluid Dynamics (CFD) Modeling of Gas Explosions, in: Zarko, V.E., Weiser, V., Eisenreich, N., Vasil'ev, A.A. (Eds.), Prevention of Hazardous Fires and Explosions, NATO Science Series. Springer Netherlands, pp. 77–91.
Howard, W.B., 1972. Interpretation of a building explosion accident. Loss Prevention 6, 68 – 73.
Howard, W.B., Karabinis, A.H., 1980. Tests of explosion venting of buildings, in: 3rd International Symposium on Loss Prevention and Safety Promotion in the Process Industries. Swiss Soc of Chem Ind, pp. 13/979–13/1039.
HYPER, 2008. FP6 STREP project "Installation Permitting Guidance for Hydrogen and Fuel Cells Stationary Applications"., Deliverable 4.3 Releases, Fires and Explosions, WP4 Final Report, http://www.hyperproject.eu/.
Ishikawa, N., 1983. Flame propagation in time-dependent concentration gradient fields. Combustion science and technology 35, 207–213.
Kagan, L., Sivashinsky, G., 2003. The transition from deflagration to detonation in thin channels. Combustion and Flame 134, 389–397. doi:10.1016/S0010-2180(03)00138-X
Kaptein, M., Hermance, C.E., 1976. Horizontal propagation of laminar flames through vertically diffusing mixtures above a ground plane. Symp (Int) on Combust, 16th, MIT, August 15, 1976 - August 20, 1976 1295–1306.
Karim, G.A., Lam, H.T., 1986. Ignition and flame propagation within stratified methane-air formed by convective diffusion, in: Proc. 21st Symp. on Combustion. Combustion Institute. pp. 1909 – 1915.
Karim, G.A., Panlilio, V.P., 1993. Flame propagation and extinction within mixtures involving hydrogen and diluent inert gases in air. International Journal of Hydrogen Energy 18, 157–161. doi:10.1016/0360-3199(93)90202-L
Karlovitz, B., Denniston, D.W., Wells, F.E., 1951. Investigation of Turbulent Flames. The Journal of Chemical Physics 19, 541 – 547.
Karpov, V.P., Lipatnikov, A.N. (Eds.), 1995. An Effect of Molecular Thermal Conductivity and Diffusion on Premixed Combustion. Doklady Physical Chemistry 341, 83–85.
Karpov, V.P., Lipatnikov, A.N., Zimont, V.L., 1997. Flame curvature as a determinant of preferential diffusion effects in premixed turbulent combustion. Progress in Astronautics and Aeronautics 173, 235.
Karpov, V.P., Lipatnikov, A.N., Zimont, V.L., 1996. Influence of molecular heat and mass transfer processes on premixed turbulent combustion, Transport Phenomena in Combustion, ed. C.H. Chan. ed. New York: Taylor & Francis.
Karpov, V.P., Severin, E.S., 1980. Effects of molecular-transport coefficients on the rate of turbulent combustion. Combustion, Explosion and Shock Waves 16, 41–46.
Karpov, V.P., Severin, E.S., 1978. Turbulent burn-up rates of propane-air flames determined in a bomb with agitators. Combustion, Explosion and Shock Waves 14, 158–163.
Keenan, J.J., Makarov, D.V., Molkov, V.V., 2014. Rayleigh–Taylor instability: Modelling and effect on coherent deflagrations. International Journal of Hydrogen Energy 39, 20467–20473. doi:10.1016/j.ijhydene.2014.03.230
Kerstein, A.R., 1988. Fractal Dimension of Turbulent Premixed Flames. Combustion Science and Technology 60, 441–445. doi:10.1080/00102208808923997

Kinsella, K.G., 1993. A rapid assessment methodology for the prediction of vapour cloud explosion overpressure, in: Proceedings of the International Conference and Exhibition on Safety, Health and Loss Prevention in the Oil, Chemical and Process Industries. 15th - 19th February. Singapore, pp. 200 – 211.

Koch, C., Drenckhahn, W., 1984. Transition from slow deflagration to detonation, in: Seminar on the Results of the Indirect Action Research Programme, Safety of Thermal Water Reactors (1979-1983), 1-3 Oct. 1984, Seminar on the Results of the Indirect Action Research Programme, Safety of Thermal Water Reactors (1979-1983) (papers in Summary Form Only Received). Comm. Eur. Communities, pp. 31–2.

Kommitten for Explosions Forsok, 1957. Report of Committee for Explosion Testing, Stockholm, 1957, Kommitten for Explosions Forsok, Bromma 1957. Slutrapport, Stockholm, April 1958.

Korotkikh, N.I., 1980. Study on explosion loads on construction during internal local gaseous deflagrations (Ph.D. thesis (in Russian)). Moscow State University of Civil Engineering, Moscow, Russia.

Korotkikh, N.I., Baratov, A.N., 1978. Vent area calculation for enclosures in case of internal gaseous deflagration. Flammability of Substances and Chemical Fire Extinguishing Agents, Transactions of VNIIPO, (in Russian) 3 – 15.

Kuhl, A.L. (Ed.), c1993. Dynamics of heterogeneous combustion and reacting systems /. American Institute of Aeronautics and Astronautics, Inc., American Institute of Aeronautics and Astronautics, Inc.,Washington, DC, 152, 3-24.

Kumar, R.K., 2009. Vented turbulent combustion of hydrogen-air mixtures in a large rectangular volume, in: 47th AIAA Aerospace Sciences Meeting Including the New Horizons Forum and Aerospace Exposition, January 5, 2009 - January 8, 2009, 47th AIAA Aerospace Sciences Meeting Including the New Horizons Forum and Aerospace Exposition. American Institute of Aeronautics and Astronautics Inc.

Kumar, R.K., 2006. Vented combustion of hydrogen-air mixtures in a large rectangular volume, in: 44th AIAA Aerospace Sciences Meeting 2006, January 9, 2006 - January 12, 2006, Collection of Technical Papers - 44th AIAA Aerospace Sciences Meeting. American Institute of Aeronautics and Astronautics Inc., pp. 4398–4406.

Kuznetsov, M., Alekseev, V., Matsukov, I., Dorofeev, S., 2005. DDT in a smooth tube filled with a hydrogen-oxygen mixture. Shock Waves 14, 205–215.

Kuznetsov, M., Grune, J., Friedrich, A., Sempert, K., Breitung, W., Jordan, T., 2011. Hydrogen-Air Deflagrations and Detonations in a Semi-Confined Flat Layer. Presented at the Fire and Explosion Hazards, Proceedings of the Sixth International Seminar (Edited by Bradley, D., Makhviladze, G., and Molkov, V.), pp. 125 – 136.

Kuznetsov, M., Grune, J., Friedrich, A., Sempert, K., Jordan, T., 2010a. Flame acceleration and detonation transition in a semi-confined flat layer of uniform hydrogen-air mixtures (Paper W5P119), in: Proc. of the Thirty-Third Intl. Symp. on Comb., 1st – 6th August. Tsinghua University, Beijing, China.

Kuznetsov, M., Liberman, M., Matsukov, I., 2010b. Experimental study of the preheat zone formation and deflagration to detonation transition. Combustion Science and Technology 182, 1628–1644. doi:10.1080/00102202.2010.497327

Kuznetsov, V.R., Sabel'nikov, V.A., 1990. Turbulence and Combustion, 1st Edition. Hemisphere Publishing Corporation, Moscow, Russia.

Kwon, O.C., Tseng, L.-K., Faeth, G.M., 1992. Laminar burning velocities and transition to unstable flames in H2/O2/N2 and C3H8/O2/N2 mixtures. Combustion and Flame 90, 230–246.

Lahjaily, H., Champion, M., Karmed, D., Bruel, P., 1998. Introduction of dilution in the BML model: Application to a stagnating turbulent flame. Combustion science and technology 135, 153–173.

Lamoureux, N., Djebaili-Chaumeix, N., Paillard, C.-E., 2003. Laminar flame velocity determination for H2-air-He-CO2 mixtures using the spherical bomb method. Experimental Thermal and Fluid Science 27, 385–393.

Lamoureux, N., Djebaili-Chaumeix, N., Paillard, C.E., 2002. Laminar flame velocity determination for H2-air-steam mixtures using the spherical bomb method, in: Proceedings of the Fourth International Symposium on Hazards, Prevention and Mitigation of Industrial Explosions (IV ISHPMIE), October 21, 2002 - October 25, 2002, Journal De Physique. IV : JP. EDP Sciences, Bourges, France, pp. Pr7/445–Pr7/452.

Landau, L., 1944. On the theory of slow combustion, Acta Physicochimica, 19, 77-85.

Lannoy, A., 1984. Analyse des explosions air-hydrocarbure en milieu libre, A (4). Extr. de "Electricité de France. Bulletin de la Direction des études et recherches," Paris.

Law, C.K., 2006. Combustion Physics: Chapter 10 - Aerodynamics of laminar flames, Section 10.9 - Flamefront instabilities, Sub-section 10.9.1 - Mechanisms of Cellular instabilities, 1st ed. Cambridge University Press, pp. 459-460, 504.

Lee, J.H.S., 1988. Cours de 3ème cycle à l'attention des doctorants. Université d'Orléans.
Lee, J.H.S., Knystautas, R., Chan, C.K., 1985. Turbulent Flame Propagation in Obstacle-Filled Tubes. Presented at the . 20th Symp. (Intl.) on Comb., The Combustion Institute, pp. 1663–1672.
Lewis, B., Von Elbe, G., 1987. Combustion, Flames and Explosions of Gases., 3rd Edition. ed. New York: Academic Press.
Leyer, J.C., 1983. Caractéristiques du champ de pression engendré par une flamme accélérée en espace libre (No. EUR 8010 Fr), Commission des Communautes Europeennes (CCE) (in French).
Leyer, J.C., 1982. Explosion Effects of Hydrocarbon/Air Mixtures. Revue generale de thermique 21, 193–208.
Leyer, J.C., Desbordes, D., Saint-Cloud, J.P., Lannoy, A., 1993. Unconfined deflagrative explosion without turbulence: experiments and model. Journal of Hazardous Materials 34, 123–150.
Lipatnikov, A., Chomiak, J., 1998. Lewis Number Effects in Premixed Turbulent Combustion and Highly Perturbed Laminar Flames. Combustion Science and Technology 137, 277–298. doi:10.1080/00102209808952054
Lipatnikov, A.N., 2007. Turbulent combustion of hydrogen-air mixtures, in: Lecture Presented at the 2nd European Summer School on Hydrogen Safety, 30th July - 8th August. Belfast, UK.
Lipatnikov, A.N., Chomiak, J., 2005. Molecular transport effects on turbulent flame propagation and structure. Progress in Energy and Combustion Science 31, 1–73. doi:10.1016/j.pecs.2004.07.001
Lord Rayleigh, 1883.
Magnussen, B.F., 1981. On the structure of turbulence and a generalized eddy dissipation concept for chemical reactions in turbulent flow. Presented at the 19th AIAA Aerospace Sciences Meeting, 12th - 15th January, St. Louis, Missouri, USA.
Magnussen, B.F., Hjertager, B.H., 1976. On mathematical modeling of turbulent combustion with special emphasis on soot formation and combustion. Symp (Int) on Combust, 16th, MIT, August 15, 1976 - August 20, 1976 719–729.
Makarov, D., Molkov, V., 2004. Large Eddy Simulation of Gaseous Explosion Dynamics in an Unvented Vessel. Combustion, Explosion and Shock Waves 40, 136–144.
Makarov, D., Verbecke, F., Molkov, V., Kotchourko, A., Lelyakin, A., Yanez, J., Baraldi, D., Heitsch, M., Efimenko, A., Gavrikov, A., 2010a. An intercomparison of CFD models to predict lean and non-uniform hydrogen mixture explosions. International Journal of Hydrogen Energy 35, 5754–5762. doi:10.1016/j.ijhydene.2010.02.105
Makarov, D., Verbecke, F., Molkov, V., Roe, O., Skotenne, M., Kotchourko, A., Lelyakin, A., Yanez, J., Hansen, O., Middha, P., Ledin, S., Baraldi, D., Heitsch, M., Efimenko, A., Gavrikov, A., 2009. An inter-comparison exercise on CFD model capabilities to predict a hydrogen explosion in a simulated vehicle refuelling environment. International Journal of Hydrogen Energy 34, 2800–2814. doi:10.1016/j.ijhydene.2008.12.067
Makarov, D., Verbecke, F., Molkov, V.V., Keenan, J., 2010b. On Unresolved Mechanisms of Large Scale Deflagrations in Complex Geometries. Presented at the 6th International Seminar on Fire and Explosion Hazards, University of Leeds, UK.
Mandelbrot, B.B., 1982. The Fractal Geometry of Nature. W.H. Freeman & Co Ltd.
Mark, H., 1956. The interaction of a reflected shock wave with the boundary layer in a shock tube. J. Aero. Sci. 24, 304 – 306.
Markstein, G.H., Guenoche, H., Putnam, A.A., 1964. Nonsteady flame propagation. AGARDograph 75 328.
Marra, F.S., Russo, G., Salzano, E., Tamanini, F., 2002. CFD Simulation of Stratified Fuel-Air Explosions. Presented at the 2nd Mediterranean Combustion Symposium, Egypt, pp. 310 – 319.
Marshall, M.R., 1980. Gaseous and dust explosion venting: Determination of explosion relief requirements, in: 3rd International Symposium on Loss Prevention and Safety Promotion in the Process Industries. Swiss Soc of Chem Ind, pp. 16/1210–16/1229.
Matalon, M., 2007. Intrinsic flame instabilities in premixed and nonpremixed combustion. Annual Review of Fluid Mechanics 39, 163–191. doi:10.1146/annurev.fluid.38.050304.092153
Melton, T.A., Marx, J.D., 2009. Estimating flame speeds for use with the BST blast curves. Proc. Safety Prog. 28, 5–10. doi:10.1002/prs.10281
Meneveau, C., Poinsot, T., 1991. Stretching and quenching of flamelets in premixed turbulent combustion. Combustion and Flame, Combust. Flame (USA) 86, 311–32. doi:10.1016/0010-2180(91)90126-V
Moen, I.O., Saber, A.J., 1986. Investigation of the Explosion Hazards of Hydrogen Sulphide: Phase II. Atomic Energy Control Board, Defence Research Establishment Suffield, RN 578, Canada.
Molkov, V., Bragin, M., 2015. Hydrogen-air deflagrations: vent sizing correlation for low-strength equipment and buildings. International Journal of Hydrogen Energy, Int. J. Hydrog. Energy (Netherlands) 40, 1256–66. doi:10.1016/j.ijhydene.2014.11.067
Molkov, V., Dobashi, R., Suzuki, M., Hirano, T., 1999. Modeling of vented hydrogen-air deflagrations and correlations for vent sizing. Journal of Loss Prevention in the Process Industries 12, 147–156.

Molkov, V.V., 2012. Fundamentals of Hydrogen Safety Engineering, parts I & II. bookboon.com, ISBN: 978-87-403-0279-0.
Molkov, V.V., 2010. A Multiphenomena turbulent burning velocity model for large eddy simulation of premixed combustion. Nonequilibrium phenomena, surface physics and chemistry, HySAFER centre, Ulster University 442–450.
Molkov, V.V., 2001. Turbulence generated during vented gaseous deflagrations and scaling issue in explosion protection, in: Proceedings of the Symposium Hazards XVI, I Chem E Symp Series No. 148. pp. 279 – 292.
Molkov, V.V., 1999a. Explosions in buildings: modeling and interpretation of real accidents. Fire Safety Journal 33, 45–56. doi:10.1016/S0379-7112(99)00003-X
Molkov, V.V., 1999b. Explosion safety engineering: NFPA 68 and improved vent sizing technology, in: Proceedings of the 8th International Conference INTERFLAM'99 Fire Science and Engineering, 29th June – 1st July. Edinburgh, pp. 1129 –1134.
Molkov, V.V., 1996. Venting of gaseous deflagrations (D.Sc. Thesis). All-Russian Research Institute for Fire Protection, Moscow.
Molkov, V.V., 1995. Theoretical generalization of international experimental data on vented explosion dynamics, in: Proceedings of the First International Seminar on Fire-and-Explosion Hazards, 17th – 21st July. Moscow, pp. 166 –181.
Molkov, V.V., Baratov, A.N., Korolchenko, A.Y., 1991. Dynamics of gas explosions in vented vessels: A critical review and progress. Progress in Astronautics and Aeronautics 154, 117–131.
Molkov, V.V., Dobashi, R., Suzuki, M., Hirano, T., 2000. Venting of deflagrations: hydrocarbon-air and hydrogen-air systems. Journal of Loss Prevention in the Process Industries 13, 397–409.
Molkov, V., Verbecke, F., Makarov, D., 2008. LES of hydrogen-air deflagrations in a 78.5 m tunnel. Combustion Science and Technology 180, 796–808.
Molkov, V.V., Grigorash, A.V., Eber, R.M., Tamanini, F., Dobashi, R., 2004. Vented gaseous deflagrations with inertial vent covers: State-of-the-art and progress. Process Safety Progress 23, 29–36. doi:10.1002/prs.10002
Molkov, V.V., Makarov, D., 2006. Rethinking the physics of a large-scale vented explosion and its mitigation. Process Safety and Environmental Protection vol. 84, 33 – 39.
Molkov, V.V., Makarov, D.V., 2003. LES of explosion flame wrinkling, in: Proceedings of 4th International Seminar on Fire and Explosion Hazards. Derry, U.K, 8th - 12th September, p. 643.
Molkov, V.V., Makarov, D.V., Schneider, H., 2007. Hydrogen-air deflagrations in open atmosphere: Large eddy simulation analysis of experimental data. International Journal of Hydrogen Energy 32, 2198–2205.
Molkov, V.V., Makarov, D.V., Schneider, H., 2006. LES modelling of an unconfined large-scale hydrogen-air deflagration. Journal of Physics D: Applied Physics 39, 4366–4376.
Molkov, V.V., Nekrasov, V.P., 1981. Dynamics of gaseous combustion in a vented constant volume vessel. Combustion, Explosion and Shock Waves 17, 363–370.
Molkov, V.V., Nekrasov, V.P., Baratov, A.N., Lesnyak, S.A., 1984. Turbulent gas combustion in an unseled vessel. Combustion, Explosion and Shock Waves 20, 149–153. doi:10.1007/BF00751581
Murayama, M., Takeno, T., 1989. Fractal-like character of flamelets in turbulent premixed combustion. Symposium (International) on Combustion 22, 551–559.
NFPA 68, 2007. Standard on Explosion Protection by Deflagration Venting. National Fire Protection Association.
NFPA 68, 2002. Guide for Venting of Deflagrations, 2002 Edition, National Fire Protection Association. USA.
North, G.L., Santivicca, D.A., 1990. The Fractal Nature of Premixed Turbulent Flames. Combustion Science and Technology 72, 215–232. doi:10.1080/00102209008951648
Oppenheim, A.K., 1952. A contribution to the theory of the development and stability of detonation in gases. J. Appl. Mech 9, 63–71.
Oppenheim, A.K., Manson, N., Wagner, H.G., 1963. Recent progress in detonation research. AIAA Journal 1, 2243–2252.
Oppenheim, A.K., Stern, R.A., 1958. On the development of gaseous detonation - Analysis of wave phenomena, in: 7th Symposium (International) on Combustion, August 28, 1958 - September 3, 1958, Symposium (International) on Combustion. Combustion Institute, pp. 837–850. doi:10.1016/S0082-0784(58)80127-7
Oran, E.S., Young, T.R., Boris, J.P., Picone, J.M., Edwars, D.H., 1982. A study of detonation structure: the formation of unreacted gas pockets. Proc Combust Inst 19, 573 – 582.
Pasman, H.J., Groothuisen, T.M., Gooijer, P.H., 1974. Design of Pressure Relief Vents, in: Loss Prevention and Safety Promotion in the Process Industries. Ed. Buschman C.H., Elsevier, New York, pp. 185 – 189.

Pelce, P., Clavin, P., 1982. Influence of hydrodynamics and diffusion upon the stability limits of laminar premixed flames. Journal of Fluid Mechanics, J. Fluid Mech. (UK) 124, 219–37. doi:10.1017/S002211208200247X

Peters, N., 1988. Laminar flamelet concepts in turbulent combustion. Symposium (International) on Combustion 21, 1231–1250. doi:10.1016/S0082-0784(88)80355-2

Philips, H., 1965. Flame in buoyant methane layer. Presented at the Tenth Symposium (Intl) on Combustion, pp. 1277 – 1283.

Pilugin, L.P., 1983. Explosion loadings from internal deflagrations in industrial buildings. Explosion safety in building industry, Transactions of Moscow University of Civil Engineering (in Russian) 77 – 87.

Poinsot, T., Veynante, D., 2012. Theoretical and Numerical Combustion, Third Edition (Editors Poinsot and Veynante). ed. Aquaprint, Bordeaux, France.

Pope, S.B., 2004. Ten questions concerning the large-eddy simulation of turbulent flows. New Journal of Physics 6, 1–24.

Popov, V.A., 1958. On the pre-detonation period of flame propagation, in: 7th Symposium (International) on Combustion, August 28, 1958 - September 3, 1958, Symposium (International) on Combustion. Combustion Institute, pp. 799–806. doi:10.1016/S0082-0784(58)80123-X

Proust, C., 2004. Habilitation à diriger des recherches : mémoires de travaux; Formation-Inflammation-Combustion des atmosphères explosives (ATEX) and effets associés (Authorization to supervise research: dissertation of works; Formation-Ignition-Combustion of explosive atmospheres and their associated effects). Institut National Polytechnique de Lorraine (in French).

Prudnikov, A., 1967. Combustion of homogeneous fuel-air mixtures in turbulent flows., Physical Principles of the Working Process in Combustion Chambers of Jet Engines, pp. 244-336. ed. CFSTI.

Rasbash, D.J., Drysdale, D.D., Kemp, N., 1976. Design of an explosion relief system for a building handling liquefied fuel gases. I Chem E Symp 47, 145 – 156.

Ross, M.C., 1997. Lean combustion characteristics of hydrogen-nitrous oxide-ammonia mixtures in air. California Institute of Technology, Mechanical Engineering, Pasadena, California, USA.

Royle, M., Willoughby, D.B., 2009. Consequences of catastrophic releases of ignited and unignited hydrogen jet releases, in: Proceedings of the Third International Conference on Hydrogen Safety, 16th - 18th September. Ajaccio, France.

Ruetsch, G.R., Vervisch, L., Linan, A., 1995. Effects of heat release on triple flames. Physics of Fluids, Phys. Fluids (USA) 7, 1447–54. doi:10.1063/1.868531

Rust, E.A., 1979. Explosion venting for low-pressure equipment. Chemical Engineering (New York) 86, 102–110.

Said, R., Borghi, R., 1988. A simulation with a cellular automation for turbulent combustion modeling, in: Proceedings of the Combustion Institute. pp. 569 – 577.

Salamandra, G.D., Bazhenova, T.V., Naboko, I.M., 1958. Formation of detonation wave during combustion of gas in combustion tube, in: 7th Symposium (International) on Combustion, August 28, 1958 - September 3, 1958, Symposium (International) on Combustion. Combustion Institute, pp. 851–855. doi:10.1016/S0082-0784(58)80128-9

Sato, K., Mizuno, T., Kokabu, E., 1994. Explosion Caused by Spilt Ethanol in a Vessel. Nensho-no Kagaku to Gijutsu (Combustion Science and Technology, Japanese edition) 2, 201 – 209.

Searby, G.C., 1986. Weakly turbulent, wrinkled flames in pre-mixed gases. Comb. Sci. and Tech 46, 167 – 193.

Searby, G., Rochwerger, D., 1991. A parametric acoustic instability in premixed flames. Journal of Fluid Mechanics, J. Fluid Mech. (UK) 231, 529–43. doi:10.1017/S002211209100349X

Shchelkin, K.I., 1940. Effect of Tube Surface Roughness on Origin and Propagation of Detonation in Gas. J. of Exp. and Th. Phys. (USSR) 10, 823 – 827.

Shepherd, J.E., Lee, J.H.S., 1992. On the Transition from Deflagration to Detonation, in: Major Research Topics in Combustion, Edited by M. Y. Hussaini, A. Kumar, and R. G. Voigt. Springer-Verlag Publishers, pp. 439–487.

Shirvill, L.C., Royle, M., Roberts, T.A., 2007. Hydrogen releases ignited in a simulated vehicle refuelling environment. Presented at the Proceedings of the 2nd International Conference for Hydrogen Safety, Proceedings of the 2nd International Conference for Hydrogen Safety, San Sebastian, Spain.

Sivashinsky, G.I., 1979. On self-turbulization of a laminar flame. Acta Astronautica 6, 569–591. doi:10.1016/0094-5765(79)90019-5

Sochet, I., Guelon, F., Gillard, P., 2002. Deflagrations of non-uniform mixtures: A first experimental approach, in: Proceedings of the Fourth International Symposium on Hazards, Prevention and Mitigation of Industrial Explosions (IV ISHPMIE), October 21, 2002 - October 25, 2002, Journal De Physique. IV : JP. EDP Sciences, pp. Pr7/273–Pr7/279.

Solberg, D.M., 1982. Gas explosion research related to safety of ships and offshore platforms, in: Fuel-Air Explosions, Proceedings of the International Conference on Fuel-Air Explosions., Studies Series -

University of Waterloo, Solid Mechanics Division, SM Study. Univ of Waterloo, Solid Mechanics Div, pp. 787–819.

Solberg, D.M., Pappas, J.A., Skramstad, E., 1981. Observations of flame instabilities in large scale vent gas explosions. Symposium (International) on Combustion 1607–1614.

Solberg, D.M., Pappas, J.A., Skramstad, E., 1980. Experimental investigations on flame acceleration and pressure rise phenomena in large scale vented gas explosions, in: 3rd International Symposium on Loss Prevention and Safety Promotion in the Process Industries. Swiss Soc of Chem Ind, Basle, Switz, pp. 16/1295–16/1303.

Spalding, D.B., 1976. Development of the Eddy Break-Up model of turbulent combustion. Symp (Int) on Combust, 16th, MIT, August 15, 1976 - August 20, 1976 1657–1663.

Spalding, D.B., 1971. Mixing and chemical reaction in steady confined turbulent flames. Proceedings of the Combustion Institute 13, 649 – 657.

Sustek, J., Janovsky, B., 2012. Comparison of empirical and semi-empirical equations for vented gas explosion with experimental data. Presented at the IXth ISHPMIE – International Symposium on Hazard, Prevention and Mitigation of Industrial Explosions, 22nd - 27th July, Krakow, Poland.

Swift, I., Epstein, M., 1987. Performance of low pressure explosion vents. Plant/operations progress 6, 98–105. doi:10.1002/prsb.720060211

Takeno, K., Okabayashi, K., Kouchi, A., Nonaka, T., Hashiguchi, K., Chitose, K., 2007. Dispersion and explosion field tests for 40 MPa pressurized hydrogen. International Journal of Hydrogen Energy 32, 2144–2153.

Takeno, T., Baba, N., Kushida, G., Murayama, M., 1989. Dynamics of Turbulent Premixed Flame Surface. Presented at the Joint Meeting of the Australia/New Zealand and Japanese Sections of The Combustion Institute, pp. 145–147.

Taki, S., Fujiwara, T., 1978. Numerical analysis of two-dimensional nonsteady detonations. AIAA Journal 16, 73–77.

Talantov, A.V., Gorenie, V., 1978. Combustion in flows. Moscow: Mashinostroenie.

Tamanini, F., 2000. Partial-Volume Deflagrations – Characteristics of Explosions in Layered Fuel/Air Mixtures. Presented at the 3rd International Seminar on Fire and Explosion Hazards, Lake Windermere, England, pp. 103 – 117.

Tamanini, F., 1996. Modeling of panel inertia effects in vented dust explosions. Process Safety Progress 15, 247–257.

Tanaka, T., Azuma, T., Evans, J.A., Cronin, P.M., Johnson, D.M., Cleaver, R.P., 2007. Experimental study on hydrogen explosions in a full-scale hydrogen filling station model. International Journal of Hydrogen Energy 32, 2162–2170.

Teodorczyk, A., 1995. Fast Deflagrations and Detonations in Obstacle-Filled Channels. Biuletyn Instytutu Techniki Cieplnej Politechniki Warszawskiej 79, 145 – 178.

Teodorczyk, A., Lee, J.H.S., Knystautas, R., 1988. Propagation Mechanism of Quasi-Detonations. Presented at the Twenty-Second Symposium (Int.) on Combustion, The Combustion Institute, pp. 1723 – 1731.

Thomas, G.O., Sands, C.J., Brambrey, R.J., Jones, S.A., 1997. Experimental Observations of the Onset of Turbulent Combustion Following Shock-Flame Interaction, in: Proceedings of the 16th International Colloquium on the Dynamics of Explosions and Reactive Systems. Cracow, Poland, 3rd - 8th August, pp. 2–5.

Troshin, Y.K., 1958. The generalized hugoniot adiabatic curve, in: 7th Symposium (International) on Combustion, August 28, 1958 - September 3, 1958, Symposium (International) on Combustion. Combustion Institute, pp. 789–798. doi:10.1016/S0082-0784(58)80122-8

Trouve, A., Poinsot, T., 1994. Evolution equation for the flame surface density in turbulent premixed combustion. Journal of Fluid Mechanics 278, 1–31.

Tsuruda, T., Hirano, T., 1987. Growth of Flame Front Turbulence During Flame Propagation Across an Obstacle. Combustion Science and Technology 51, 323–328. doi:10.1080/00102208708960328

Urtiew, P.A., Oppenheim, A.K., 1966. Experimental observations of transition to detonation in explosive gas. Proceedings of the Royal Society of London, Series A: Mathematical and Physical Sciences 295, 13–38.

Van Den Berg, A.C., 1985. The multi-energy method. A framework for vapour cloud explosion blast prediction. Journal of Hazardous Materials 12, 1–10. doi:10.1016/0304-3894(85)80022-4

Van den Berg, A.C., 1980. A 1-D variable flame speed blast simulation code using a Flux Corrected Transport Algorithm (No. Report TNO-PML 1980-162).

Van Den Berg, A.C., Wingerden, C.J., Van, M., Zeeuwen, J.P., Pasman, H.J., 1991. Current research at TNO on vapour cloud explosion modelling. Presented at the International Conference and Workshop on Modeling and Mitigation of the Consequences of Accidental Releases of Hazardous Materials, 20th - 24th May, New Orleans, Louisiana, USA.

Van Wingerden, C.J.M., 1984. Investigation into blast produced by non-steady flames (No. TNO-PML 1984-C-66).
Van Wingerden, C.J.M., Zeeuwen, J.P., 1983. On the role of acoustically driven flame instabilities in vented gas explosions and their elimination. Combustion and Flame, Combust. Flame (USA) 51, 109–11.
Verbecke, F., 2009. Formation and combustion of non-uniform hydrogen-air mixtures (Ph.D.). Ulster University, Jordanstown, N. Ireland, UK.
Verbecke, F., Makarov, D., Molkov, V., 2009. VLES of Lean Hydrogen-Air Deflagrations in a Closed Vessel 5.7m High. Presented at the 6th Mediterranean Combustion Symposium, Ajaccio, France, 7th - 11th June.
Vervisch, L., Veynante, D., 2000. Interlinks between approaches for modeling turbulent flames. Proceedings of the Combustion Institute 28, 175–182.
Whitehouse, D.R., Greig, D.R., Koroll, G.W., 1996. Combustion of stratified hydrogen-air mixtures in the 10.7m3 Combustion Test Facility cylinder. Nuclear Engineering and Design 166 (1996), 453 – 462.
Wilson, M.S.G., 1954. Relief of explosions in closed vessels (Ph.D Thesis). London University, London, UK.
Xiao, H., Makarov, D., Sun, J., Molkov, V., 2012. Experimental and numerical investigation of premixed flame propagation with distorted tulip shape in a closed duct. Combustion and Flame 159 (4), 1523–1538. doi:10.1016/j.combustflame.2011.12.003
Yakhot, V., 1988. Propagation velocity of premixed turbulent flames. Combustion Science and Technology 60, 191–214.
Yakhot, V., Orszag, S.A., 1986. Renormalization group analysis of turbulence. I. Basic theory. Journal of Scientific Computing, J. Sci. Comput. (USA) 1, 3–51.
Yamashita, H., Shimada, M., Takeno, T., 1996. Numerical study on flame stability at the transition point of jet diffusion flames, in: Proceedings of the 1996 26th International Symposium on Combustion. Part 2 (of 2), July 28, 1996 - August 2, 1996, Symposium (International) on Combustion. Combustion Inst, pp. 27–34.
Yanez, J., Kotchourko, A., Kuznetsov, M., Lelyakin, A., Jordan, T., 2011. Modeling of the flame acceleration in flat layer for hydrogen-air mixtures. Presented at the 4th International Conference on Hydrogen Safety, ICHS, 12th - 14th Sept, San Francisco, U.S.A.
Yao, C., 1982. Venting, in: Fuel-Air Explosions, Proceedings of the International Conference on Fuel-Air Explosions., Studies Series - University of Waterloo, Solid Mechanics Division, SM Study. Univ of Waterloo, Solid Mechanics Div, pp. 987–989.
Yao, C., 1974. Explosion venting of low-strength equipment and structures. Loss Prevention: A CEP Technical Manual 8, 1–9.
Yungster, S., 1992. Numerical study of shock-wave/boundary-layer interactions in premixed combustible gases. AIAA journal 30, 2379–2387.
Zalosh, R., 1979. Gas Explosion Tests in Room-Size Vented Enclosures, in: AIChE 13th Loss Prevention Symposium. Presented at the AIChE, Houston.
Zeldovich, Y.B., Barenblatt, G.I., Librovich, V.B., Makhviladze, G.M., 1985. The Mathematical Theory of Combustion and Explosions. Consultants Bur, New York, NY, USA.
Zel'dovich, Y.B., Frank-Kamenetskii, D.A., 1947. Turbulent and Heterogeneous Combustion. MMI (in Russian), Moscow.
Zel'dovich, Y.B., Istratov, A.G., Kidin, N.I., Librovich, V.B., 1980. Flame propagation in tubes: hydrodynamics and stability. Combustion science and technology 24, 1–13.
Zimont, V.L., Lipatnikov, A.N., 1995. A numerical model of premixed turbulent combustion of gases. Chemical Physics Reports 14, 993.

5. Physical and mathematical models of detonations (KIT)

5.1 Hydrogen safety engineering relevant problems and phenomena (KIT)

5.1.1 Detonation propagation (KIT)

5.1.1.1 Structure of the detonation

Detonations have an intrinsic non-stationary and multi-dimensional nature affect the maximum local pressures during detonation process.

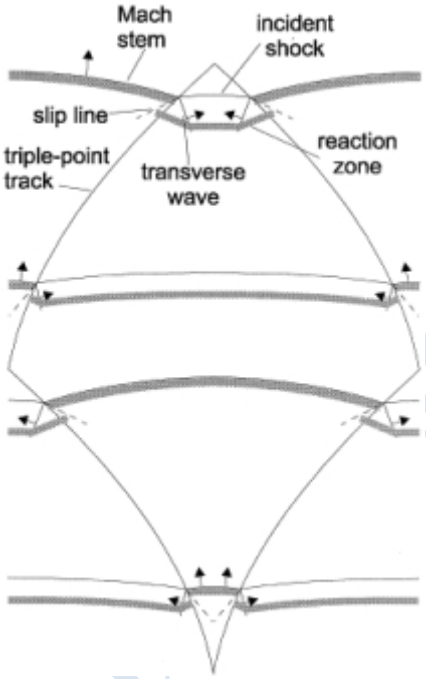

Figure 5.1 Schematic presentation of multi-dimensional detonation front structure (Kuo, 2005).

Detonation waves in the mixtures have internal multi-dimensional structures. Already classical works on the structure of detonation waves, e.g. (Voitsekhovskii et al., 1966, Strehlow 1970, Strehlow 1969b, Strehlow 1969c), have led to the discovery of different type of detonation waves:

1. Front structures, which have highly constant values of main characteristics averaged in time and have a regularly repeated structure;
2. Front structures, which have constant averaged characteristics but no regular structure;
3. Front structures, which exhibit wholely non-stationary behaviour.

In the case of lean or rich mixtures, which are close to the detonation limits for hydrogen, detonations occur usually exhibiting characteristics of the second or third types. Unfortunately, most of the experimental work has only been performed for mixtures far from the detonation limits. Full volume detonations happening for concentrations close to the detonation limits have not been studied so far. Note that the role of front structure, as a rule, appears to be more significant in cases considering lean mixture detonations, which are typical for industrial accidents.

The multi-dimensional structure of the detonation front includes the leading shock wave and a number of transverse waves, which propagate perpendicular to the leading shock, reflecting from each other and from bounding walls. The surface of the leading shock consists of a sequence of convex parts, which instigate the chemical reaction, and concave parts which are fast decaying waves. Additional reaction zones are located behind the transverse waves where the reaction completes.

5.1.1.2Rankine-Hugoniot jump conditions

For the steady, one-dimensional flow of a combustible gas that burns to completion, equations relating initial and final conditions are called the Rankine-Hugoniot relations and they provide jump conditions across the front, from upstream (subscript 0) to downstream (subscript ∞).

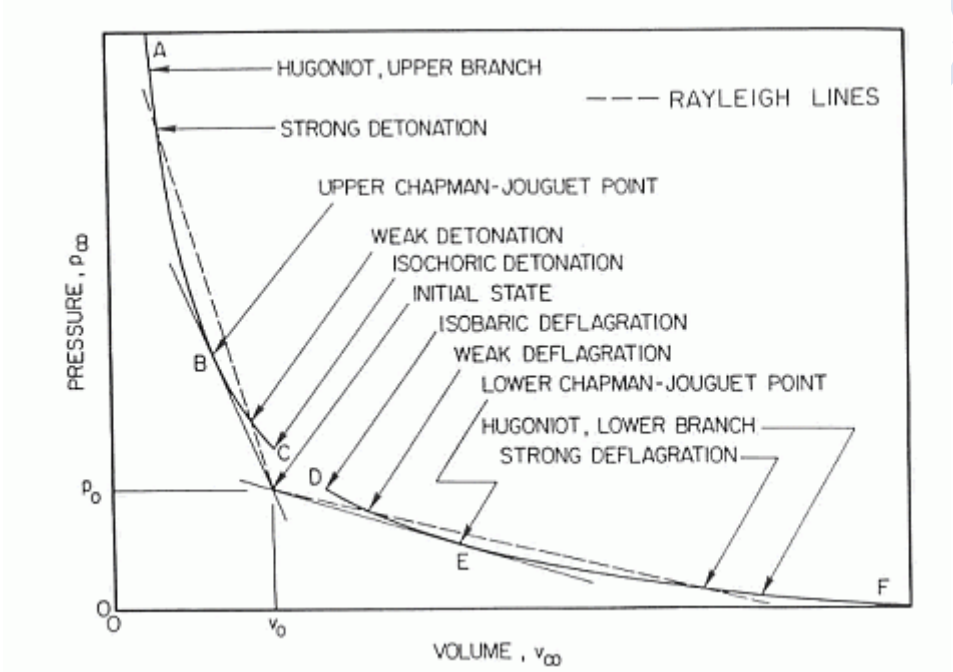

Figure 5.2 Schematic locus of burnt-gas states for combustion waves (Linan and Williams, 1993).

The equations which describe the Rankine-Hugoniot jump conditions can be written as follows:

$$m_0 = \rho_0 u_0 = \rho_\infty u_\infty , \tag{5.1}$$

$$P_0 \equiv \rho_0 u_0^2 + p_0 = \rho_\infty u_\infty^2 + p_\infty . \tag{5.2}$$

The sequence of final states obeying:

$$p_\infty + \frac{m_0^2}{\rho_\infty} = P_0 \equiv p_0 + m_0^2 / \rho_0 . \tag{5.3}$$

Obtained by substituting the first two equations, is the Rayleigh line, which is a straight line in the plane of final pressure, p_∞, and specific volume, $1/\rho_\infty$, as shown in Figure 5.2.

Using the energy conservation equation together with the second jump condition provides a relationship between the thermodynamic properties and the Hugoniot curve, which can be written as:

$$\frac{\gamma}{\gamma-1}\left(\frac{p_\infty}{\rho_\infty} - \frac{P_0}{\rho_0}\right) - \frac{1}{2}\left(\frac{1}{\rho_\infty} + \frac{1}{\rho_0}\right)(p_\infty - p_0) = h_0 , \tag{5.4}$$

where h_0 is the total amount of chemical heat released per unit mass of the mixture. The Hugoniot curve is shown schematically in Figure 5.2 for a representative combustion system. The final state is determined by the intersection of the Rayleigh line with the Hugoniot curve.

As shown in Figure 5.2 the Hugoniot curve has two branches, an upper branch of large p_∞ and ρ_∞, called the detonation branch, and a lower branch of small p_∞ and ρ_∞, called the deflagration branch. There is a minimum propagation velocity for detonations, corresponding to tangency at the upper Chapman-Jouget (CJ) point. The Rankine-Hugoniot equations can be solved using one of the available, and widely utilized, solvers.

Under certain circumstances, it is possible for the detonation wave to move faster than the unique steady-state velocity given by CJ theory. This usually occurs because another event causes the detonation products to move faster than the velocity they would have in a CJ wave. As a result, the pressure associated with such an 'overdriven' detonation front can be significantly higher.

5.1.1.3CJ detonation

One-dimensional detonation theory was developed independently by Chapman (Chapman, 1899) and Jouguet (Jouguet, 1906) and was based on the preceding shock theory, with the inclusion of an addition energy term corresponding to the energy released by the chemical reaction. In this theory, the C-J theory, the chemical reaction is assumed to occur infinitely fast. Further manipulation of equations leads to the following expression:

$$q_{CJ} = \frac{((M_{CJ}^2 - 1)^2 a_1^2)}{2(\gamma_b - 1)M_{CJ}^2(\gamma_b + 1)}, \quad (5.5)$$

which relates the resulting wave Mach number M_{CJ}, the corresponding energy release q_{CJ}, the sound speed in the initial reactants a_1 and the ratio of specific heats of the product gases b. In a CJ detonation, the reactants at an initial pressure, temperature and density are transformed instantaneously to products at a final pressure, temperature and density. The CJ theory gives a remarkably accurate prediction of detonation velocities based only on the knowledge of the initial conditions, despite the actual complexity of a real detonation.

5.1.1.4 Detonations limits

Experiments show that there are definite limits beyond which a detonation cannot exist. These depend on the composition, temperature and pressure of the mixture, and also on the geometry and roughness of the vessel (see Table 5.1 for standard conditions). Approaching the detonation limits the detonation wave first begins to pulsate, then becomes "multi-head" and then changes its character completely: the detonation front starts to move along a helical path – this mode is called spinning detonation.

Table 5.1 Detonation limits for H_2-air and H_2-O_2

Mixture	Lower detonation limit, H_2 %	Upper detonation limit, H_2 %	Referencee
H_2 – air	18.3	59	Kuo, 2005
H_2 – air	12.5		Dorofeev, 2000
H_2 – O_2	15	90	Kuo, 2005
H_2 – O_2	15	63.5	Kogarko 1948

$H_2 – O_2$	13.6	70	Tieszen, 1986

Over the range of detonable concentrations of a given fuel-oxidizer mixture, the wave structure is referred to as a multi-head wave front. This wave is characterized by relatively weak transverse waves in comparison to the axial component, which allows it to be considered roughly one-dimensional as in the Zeldovich (Zeldovich, 1940), Neumann (Neumann, 1942), Doring (Doring, 1943) (ZND) model. It has been observed that, in a given smooth circular tube, as the mixture composition becomes leaner or richer (i.e. closer to the detonation limits), the multi-head, self-sustained detonation becomes a single-head spinning detonation propagating at about the CJ velocity. The critical tube diameter d_c for detonation propagation in an un-confined space outside the tube was discovered to be related to the characteristic transverse wave spacing (detonation cell size) λ, for a circular tube the critical diameter was found to be 13λ and for a planar tube d_c was found to be 10λ.

A schematic illustration of wave motion in a detonation cell is shown in Figure 5.1 (in Section 5.1.1.1 “Detonation front structure”). In Figure 5.3 tube diameter is plotted against fuel concentration around the lean limit. In the region above the curve, known as the self-sustained detonation region, multi-head detonations propagate.

Kogarko (Kogarko and Zeldovich, 1948) proposed that, at the onset of single-head spin in a smooth circular tube, the detonation cell width must be equal to the tube circumference. This limiting tube diameter is designated as d*. Later this criterion was confirmed by Lee (Lee, 1985) and Dupre (Dupre, 1986). Figure 5.4 presents critical tube diameters for hydrogen and some hydrocarbon fuels and Figure 5.5 shows limiting tube diameters for the same fuels (including hydrogen).

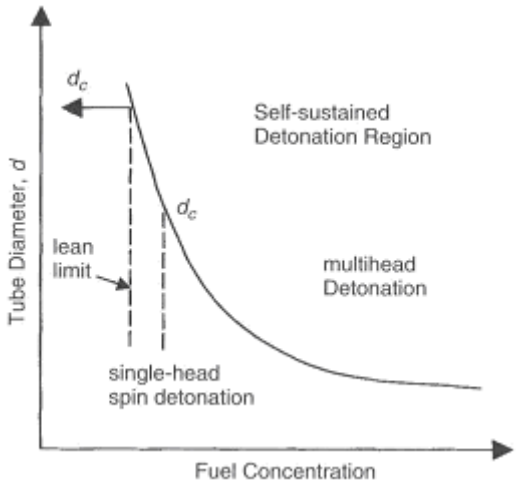

Figure 5.3 Effects of fuel concentration and tube diameter on the onset of single-head spin detonation (Kuo, 2005).

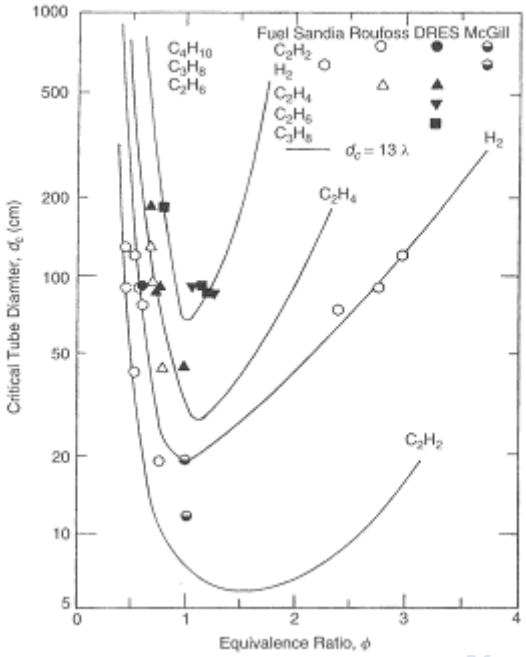

Figure 5.4 Correlation of critical tube diameter with the empirical law d_c=13 λ (Kuo, 2005).

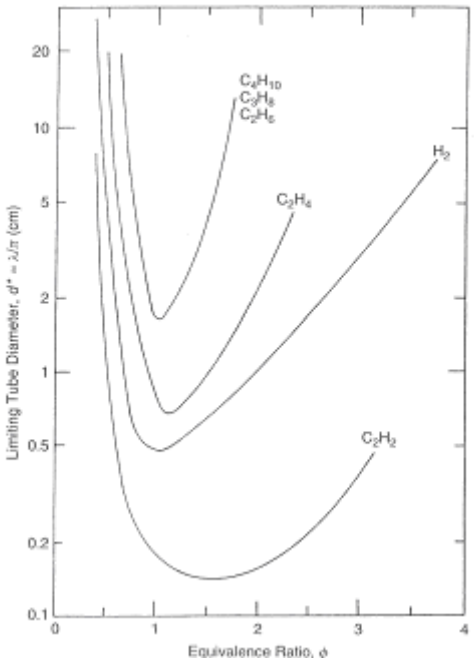

Figure 5.5 Variation of the minimum limiting tube diameter d = λ/π for the stable propagation of detonation in tube (Kuo, 2005).

5.1.1.5 Detonation cell size

As shown in Figure 5.6 the diamond-shaped form of the detonation front structure demonstrates a typical track of triple points from intersecting shock waves. Such a track structure is called a detonation cell and can be easily obtained experimentally on sooted surfaces located in detonating gases. These cells form a cellular structure observed experimentally, and are characterized by their two lengths: longitudinal size, L and transverse

size, S. These two lengths vary depending on the type of burnable gases and on initial conditions, however the relation S ≈ 0.6L normally remains constant.

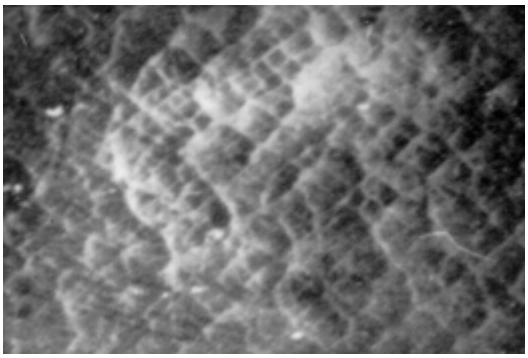

Figure 5.6 Detonation cells in tests(Kuznetsov, 2002).

In Figure 5.6 an example of detonation cells in a stoichiometric hydrogen-air mixture is shown. In the figure a soot track of irregular detonation cellular structures can be observed (Kuznetsov, 2000), (Kuznetsov, 2002). The average transverse cell size, S, obtained from the test shown in the figure was approximately equal to 1 cm. The detonation cell size remained largely constant for the given components for the same initial conditions and can be found to depend only on the mixture composition. Therefore cell size is often used as a measure of mixture reactivity.

Detonation cell size reaches its minimum at the stoichiometry composition and grows for leaner and richer mixtures. In Figure 5.7 a dependence of the detonation cell size for different H_2-air mixtures on initial H_2 concentration and mixture temperature is shown (Ciccarelli, 1994).

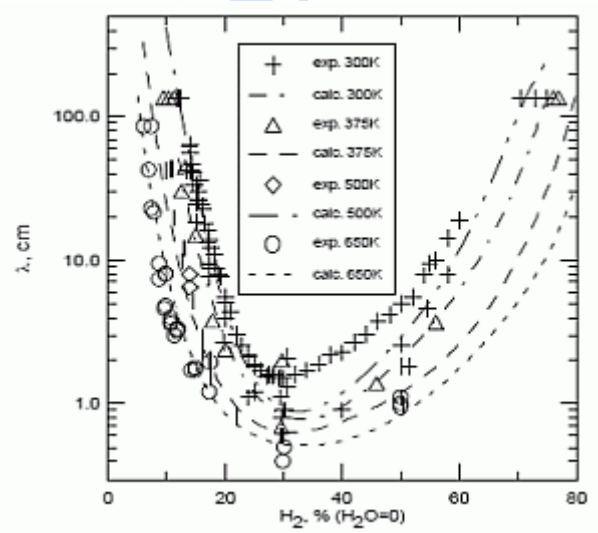

Figure 5.7 Detonations cell sizes (Ciccarelli, 1994).

5.1.2 Reflection (KIT)

Reflections of shock waves lead to an increase in pressure and temperature. Thus they are important both from the point of view of pressure loads on structures and from the point of view of flame acceleration and DDT.

It should be emphasised that behind the detonation wave there is no fuel. Therefore after the reflection of the detonation wave there is only a shock wave without detonation.

The simplest case of shock wave reflection is one-dimensional (1D) reflection, i.e. the reflection of a flat shock wave falling normal to a flat wall. This case is important as it can be completely analysed analytically. It should be noted that the amplitude of any oblique reflection is not greater than the amplitude of a normal reflection.

As an example case let us consider an undisturbed gas with pressure P_0 and specific volume V_0. A shock wave with some velocity D_1 moves towards a wall. Behind this shock wave there is a gas with pressure P_1. The gas behind the shock wave has a velocity U (which is less than D_1). Rankine-Hugoniot conditions provide a relationship between these parameters. In this case one parameter, namely pressure P_1, can be used to determine all the required properties of the shock wave and the gas behind it.

After reflection there will be gas with pressure P_1 moving towards the wall with velocity U (these are the conditions as stated in the paragraph above behind the original shock wave). There will also be a reflected shock wave moving away from the wall with a given velocity, D_2. Between that shockwave and the wall there will be gas with elevated pressure, P_2 with velocity V_2. A sketch of this reflection process is shown in Figure Figure 5.8.

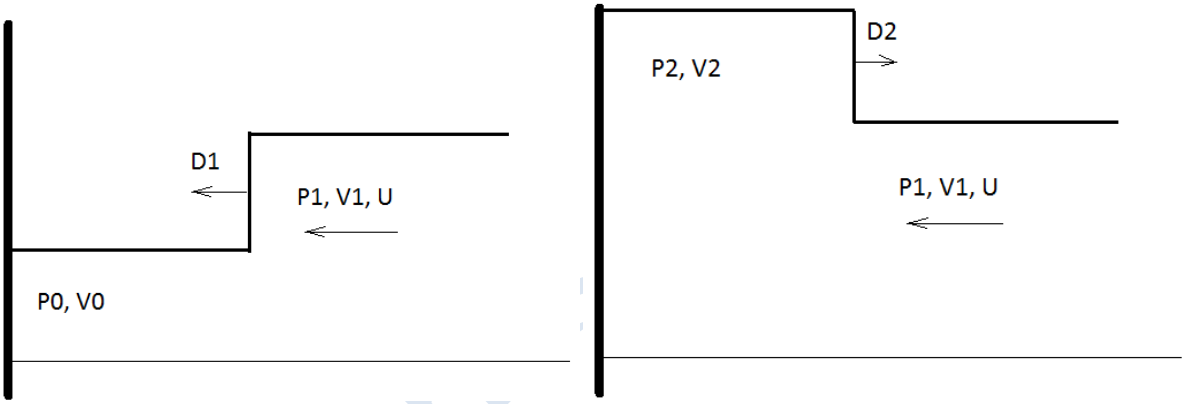

Figure 5.8 Sketch of shock wave reflection: velocities and gas properties before reflection (left) and after reflection (right).

In the case of an ideal gas with constant heat capacity, Rankine-Hugoniot conditions can be reduced to the following relations:

$$\frac{V_1}{V_0} = \frac{(\gamma+1)P_0+(\gamma-1)P_1}{(\gamma+1)P_1+(\gamma-1)P_0}, \tag{5.6}$$

$$U^2 = (P_1 + P_0)(V_1 - V_0). \tag{5.7}$$

The same relations also hold for the reflected shock wave:

$$\frac{V_2}{V_1} = \frac{(\gamma+1)P_1+(\gamma-1)P_2}{(\gamma+1)P_2+(\gamma-1)P_1}, \tag{5.8}$$

$$U^2 = (P_1 + P_2)(V_2 - V_1). \tag{5.9}$$

To solve the problem we need to calculate V_1, and then U. After that we will have a system of two equations to solve for P_2 and V_2. This system can be reduced to a quadratic equation. One solution corresponds to the incident shockwave and the other to the reflected wave.

If we denote relative overpressure in the incident wave as $\alpha = (P_1 - P_0)/P_0$, than we can express relative overpressure in the reflected wave in a completely dimensionless form, i.e.:

$$\beta = \frac{P_2 - P_1}{P_0} = \frac{\alpha^2(\gamma+1)}{2(2\gamma+\alpha(\gamma-1))}\left(1+\sqrt{1+\frac{8\gamma(\alpha+1)(2\gamma+\alpha(\gamma-1))}{(\gamma+1)^2\alpha^2}}\right). \quad (5.10)$$

Figure 5.9 Relative overpressure in reflected wave versus relative overpressure in incident wave for ideal 2-atomic gas.

An example of dependency for a typical 2-atomic gas is presented on Figure 5.9.

As highlighted through the presented formula and as displayed on Figure 5.9 for such weak waves, the reflected wave has almost the same amplitude as the original. However this reflected wave travels in gas that has been compressed by the original wave. Therefore the total overpressure in the weak reflected wave is twice that of the original wave.

For strong waves the reflected wave is significantly stronger than the original wave. The limiting ratio of overpressure between the reflected and original wave can be written as:

$$\lim_{\alpha\to\infty}\frac{\beta}{\alpha} = \frac{\gamma+1}{2(\gamma-1)}\left(1+\sqrt{1+\frac{8\gamma(\gamma-1)}{(\gamma+1)^2}}\right), \quad (5.11)$$

For typical 2-atomic gases with $\gamma = 1.4$ this value is equal to 7. However in reality when considering such strong waves, heat capacity cannot be considered as a constant and therefore the real values will be lower.

5.1.3 Detonation curvature (KIT)

5.1.3.1 General

During the last decades numerous modeling studies e.g. Lee 2008, Sheperd 2009, Oran et al. 1992 and Williams et al. 1999 showed that the detonation process in combustible gaseous mixtures can be successfully reproduced if the internal structure of the detonation wave is resolved. Good practice implies resolving the 3D structure of detonation cells, but not necessary the fine details of the internal structure of the shock or of the chemistry (Oran et al., 1992, Williams et al., 1999).

The thickness of detonations is typically small compared to the characteristic scales of the fluid flow. Thus, a simplified and widely accepted model for detonations can be built by

supposing that the fuel consumption zone shrinks to an infinitely thin surface of discontinuity separating the cold mixture from the hot products.

For deflagrations, e.g. laminar premixed combustion, models considering flames as a gas-dynamic discontinuity have existed since the pioneering works of Darrieus and Landau who derived the jump conditions across the flame.

More recently, Matalon and Matkowsky (Matalon and Matowsky, 1982) considered arbitrary flame shapes for nearly equi-diffusional flames with thermal expansion in general flow fields. In their formulation, they also supposed high activation energy asymptotics and concluded that the leading terms of the jump conditions were exactly those of the Darrieus-Landau model and that a perturbative correction was required in the next order of approximation to take into account the deviation from the Darrieus-Landau conditions.

In a further step, Klimenko and Class (Klimenko and Class, 2000) employed tensor calculus and orthonormal coordinates to simplify the derivation of the flame speed relation of Matalon and Matkowsky (Matalon and Matowsky, 1982). Their approach explicitly exploits the distinctiveness of length scales rather than high activation energy, i.e. large Peclet numbers, *Pe* (defined as the ratio of flow length scale to flame thickness). In a subsequent series of papers, their methodology was applied to multi-step chemistry (Klimenko and Class, 2002) and wider reaction zones (Klimenko and Class, 2002b). Finally, Class et al. (Class et al., 2003) reconsidered the Rankine-Hugoniot jump conditions for the flow field and showed that the perturbative correction of the jump conditions depends on the perturbative correction of the location where these jump conditions are evaluated. Moreover, it was shown that there exists a unique location within the flame structure, where no extra inertia terms arise due to the continuity surface. This corresponds to a vanishing perturbative correction of surface mass.

In a similar manner, Stewart and his co-workers utilized the limit of weak curvature and quasi-steadiness to derive asymptotically their *Detonation Shock Dynamics Theory (DSD)* (see the topical review Stewart, 1998) in order to analyze the initiation, propagation and failure of the detonation. Stewart and Bdzil in their early papers (Stewart and Bdzil, 1988 and Bdzil and Stewart, 1989) studied the influence of curvature on the detonation and obtained a relationship between the normal propagation shock speed and the average curvature. Following the identification of this relationship, a correction to the planar propagation speed was implemented as a function of the curvature.

These fundamental, but initial results, were augmented to also consider the Arrhenius chemical kinetics in a more detailed manner (Klein and Stewart, 1993), thereby extending the formulation to the classical limit of high activation energy. Using this new approach, the reaction zone can be divided into two layers. The shock of the detonation is followed by the *main reaction layer* where most of the material is burnt. After that, the flow passes through a critial sonic state in an adjacent transonic layer. The results obtained in each area can then be finally matched in order to obtain the desired intrinsic relation in the whole reactive domain.

Yao and Stewart further expanded this theory. In their paper (Yao and Stewart, 1995) they utilized the limit of high activation energy to determine the shape of the velocity-curvature relation. They discovered that the relation was multi-valued and also that the turning point of this relation, what the authors termed the *critical curvature*, represents a limit after which extinction of the detonation may occur.

In the next step in the formulation of this developing theory, the formulations which were obtained by considering quasi-steadiness were revised (Yao and D. Stewart, 1996) to account for unsteady corrections. This revision considered the first and second time derivatives of the

normal shock velocity, and the first time derivative of the curvature, in the relationship between the normal propagation shock speed and the average curvature.

Within this context of the constant improvement in the accuracy and generality of results, the DSD theory received a very significant advance following the next development. It should be noted, that the DSD formulations already mentioned have yielded two basic relationships. The first of these was the equation that couples the normal propagation shock speed and the average curvature. The second is the so called *master equation* that couples the velocity of the particle and the conditions of the sonic and thermal locus. This *master equation*, as emphasised by its name, shows the enormous importance that the treatment of the sonic point has received from the DSD authors. A noteworthy point is that early DSD formulations required the superposition of the sonic and thermal locus. This was due to some regularity arguments inside the *master equation*. This condition imposed implicitly some limitations on the generality of the theory and its validity when is applied to unsteady detonations. Therefore it was consequently improved by Kasimov and Stewart in their two exceptionally interesting publications by Kasimov and Stewart (Kasimov and Stewart, 2005 and Stewart and Kasimov, 2005).

Firstly, the generalization of the sonic conditions for a detonation wave was undertaken utilizing the characteristic compatibility conditions of an exceptional surface (Stewart and Kasimov, 2005), see also von Mises (von Mises, 2004, Chapter 9). The results obtained (that have great generality), were applied for the case of a weakly curved, slowly varying, detonation (Kasimov and Stewart, 2005). An improved and generalised curvature to normal detonation shock speed equation was obtained as a result. Additionally, an enhanced understanding of the problematic nature of the failure of detonation was reached as an outcome of this investigation.

5.1.3.2Analysis

5.1.3.2.1 Governing equations

We start our analysis considering the reactive Euler equations:

$$\partial_t \tilde{\phi} + \nabla \cdot J(\tilde{\phi}) = \tilde{Q}(\tilde{\phi}), \tag{5.12}$$

where for continuity; momentum, energy and species are given by:

$$\tilde{\phi} = \begin{pmatrix} \tilde{\rho} \\ \tilde{\rho}\tilde{v} \\ \tilde{\rho}\tilde{e} \\ \tilde{\rho}\tilde{Y} \end{pmatrix}, \; J\begin{pmatrix} \tilde{\rho} \\ \tilde{\rho}\tilde{v} \\ \tilde{\rho}\tilde{e} \\ \tilde{\rho}\tilde{Y} \end{pmatrix} = \begin{pmatrix} \tilde{\rho}\tilde{v} \\ \tilde{\rho}\tilde{v} \otimes \tilde{v} + \tilde{p}\overline{\overline{E}} \\ \tilde{\rho}\tilde{e}\tilde{v} + \tilde{p}\overline{\overline{E}} \cdot \tilde{v} \\ \tilde{\rho}\tilde{Y}\tilde{v} \end{pmatrix}, \; Q\begin{pmatrix} \tilde{\rho} \\ \tilde{\rho}\tilde{v} \\ \tilde{\rho}\tilde{e} \\ \tilde{\rho}\tilde{Y} \end{pmatrix} = \begin{pmatrix} 0 \\ 0 \\ 0 \\ \tilde{\rho}\tilde{W} \end{pmatrix}. \tag{5.13}$$

The system can be made dimensionless with the use of the reference variables $\tilde{\rho}_s, \tilde{c}_s, \tilde{l}_f$ where the sub index s represents the conditions at the Von Neumann peak and $\tilde{l}_f$ is the characteristic scale of the flow motion. The dependent variables can be written as:

$\tilde{\rho} = \rho\tilde{\rho}_s$, $\tilde{v} = v\tilde{c}_s$, $\tilde{p} = p \cdot \tilde{\rho}_s\tilde{c}_s^2/\gamma$, $\tilde{e} = e\tilde{c}_s^2$ and $\tilde{Y} = \lambda\tilde{Y}_s$

while the independent variables become $\tilde{t} = t \cdot \tilde{l}_f/\tilde{c}_s$, and $\tilde{x} = x\tilde{l}_f$.

The Arrhenius chemical consumption rate can be written using the variables $\theta_a = \tilde{E}_a/(\tilde{R}_g\tilde{T}_s)$, and $k = (\tilde{k}\tilde{l}_c)/\tilde{c}_s)$ as:

$$W = k(1-Y)\exp\left(-\frac{\theta_a \rho}{p}\right). \quad (5.14)$$

We assume a large ratio Z of the hydrodynamic typical length to the half detonation thickness $Z = \tilde{l}_f/\tilde{l}_c$. A thin detonation structure corresponds to an intense source term Q which is re-scaled accordingly to $Q = Z/Z \cdot Q = ZQ'$ yielding:

$$\partial_t \phi + \nabla \cdot J(\phi) = ZQ'(\phi). \quad (5.15)$$

It is convenient to transform the equations into a moving generalized curvilinear coordinate system. The coordinate system is attached to the discontinuity surface with its normal direction pointing towards the products. Its tangential direction moves with the local tangential flow. In this system, the flame is at rest with exactly no flow along the flame surface. The tensor calculus utilized in our analysis is described in detail in Aris (Aris, 1989). The coordinates are orthonormal with x^1 direction perpendicular to the surface of the flame, so that x^1 coordinate lines are normal to the surfaces, $x^1 = const$. The contra-variant metric tensor is given by g^{ij}, due to orthogonality $g^{1\alpha} = 0$, and due to normalization $g^{11} = 1$.

In the curvilinear coordinates, the system of differential equations can be written as:

$$\partial_t\left(\sqrt{g}\phi\right) + \partial_{x^j}\left(\sqrt{g}J^j(\phi)\right) = \sqrt{g}ZQ'(\phi), \quad (5.16)$$

with the flux vectors provided as $J^j(\phi) = (v^j - u^j)\phi$ with u^j representing the speed of the moving coordinates relative to fixed Eulerian coordinates.

The fluxes can be expressed according to Class (Class et al. 2003) as:

$$J^j\begin{pmatrix}\rho\\ \rho v^i l_i\\ \rho e\\ \rho\lambda\end{pmatrix} = \begin{pmatrix}m^j\\ \left(m^j v^i + p/\gamma \cdot g^{ij}\right)l_i\\ m^j e + p/\gamma \cdot g^{ij}\cdot m^i/\rho\\ m^j\lambda\end{pmatrix}, \quad (5.17)$$

with mass flux $m^j = (v^j - u^j)\rho$. Decomposing eq.(5.1.3.5) in the normal and tangential directions and introducing the stretched normal spatial variable $X = Zx^1$, Equation 5.1.3.5 yields:

$$Z^{-1}\left[\partial_t\left(\sqrt{g}\phi\right) + \partial_{x^\alpha}\left(\sqrt{g}J^\alpha(\phi)\right)\right] + \partial_X\left(\sqrt{g}J^1(\phi)\right) = \sqrt{g}Q'(\phi)., \quad (5.18)$$

5.1.3.2.2 Asymptotic derivation of the fluid equations and jump conditions

Since Z, i.e. the ratio between the length of the fluid flow and the consumption zone thickness, is assumed to be asymptotically large, the variables are expressed in terms of an asymptotic series expansion in powers of $1/Z$, i.e.:

$$\phi \approx \sum_{n=0} Z^{-n}\phi_{(n)} \approx \phi_{(0)} + Z^{-1}\phi_{(1)} + O(Z^{-1}).$$

The volume element is Taylor expanded around the discontinuity

$$\sqrt{g} = \sqrt{g}_{(0)} + \sqrt{g}_{(1)}Z^{-1}X + o(X^2).$$

Additionally, we make use of the equalities

$$\sqrt{g}_{(1)} = -2H \text{ and } \chi = \partial_t(\sqrt{g}_{(0)})/\sqrt{g}_{(0)}$$

with mean curvature H and stretch χ.

Significantly, the expansion in terms of Z, produces H as one of its terms, therefore (5.1.3.7) becomes:

$$Z^{-1}\left[(\partial_t+\chi)(\phi_{(0)}+Z^{-1}\phi_{(1)})+(g_{(0)})^{-1/2}\,\partial_{x^\alpha}\left(\sqrt{g}_{(0)}(J^\alpha_{(0)}(\phi)+\right.\right.$$
$$\left.\left.Z^{-1}J^\alpha_{(1)})\right)\right]+\partial_X\left[(1-Z^{-1}2HX)(J^1_{(0)}(\phi)+Z^{-1}J^1_{(1)})\right]= \tag{5.19}$$
$$(1-Z^{-1}2HX)(Q'_{(0)}(\phi)+Z^{-1}Q'_{(1)}).$$

Collecting coefficients of like powers in Z^{-n}, the zeroth, Z^0, and first order Z^{-1} terms:

$$\partial_X\left(J^1_{(0)}(\phi)\right)=Q'_{(0)}(\phi)\text{,,} \tag{5.20}$$

$$(\partial_t+\chi)\phi_{(0)}+(g_{(0)})^{-\frac{1}{2}}\partial_{x^\alpha}\left(\sqrt{g}_{(0)}J^\alpha_{(0)}(\phi)\right)+ \tag{5.21}$$
$$+\partial_X\left(J^1_{(1)}-2HXJ^1_{(0)}(\phi)\right)=Q'_{(1)}(\phi)-2HXQ'_{(0)}(\phi).$$

The leading order normal fluxes are:

$$J^1_{(0)}\begin{pmatrix}\rho\\ \rho v^i l_i\\ \rho e\\ \rho\lambda\end{pmatrix}=\begin{pmatrix}m^1_{(0)}\\ m^1_{(0)}\left(v^1_{(0)}l_{1_{(0)}}+v^\alpha_{(0)}l_{\alpha_{(0)}}\right)+p_{(0)}/\gamma\cdot l_{1_{(0)}}\\ m^1_{(0)}e_{(0)}+p_{(0)}/\gamma\cdot g^{i1}_{(0)}\cdot m^i_{(0)}/\rho_{(0)}\\ m^1_{(0)}\lambda_{(0)}\end{pmatrix}\text{,,} \tag{5.22}$$

The fluxes in the momentum equation can be decomposed into the terms emanating from the tangential and normal components. Using a parallel vector field l_i normal to the flame at the point of consideration:

$$J^1_{(0)}(\rho v^i l_\alpha)=m^1_{(0)}v^\alpha_{(0)}l_{\alpha_{(0)}}, \tag{5.23}$$

$$J^1_{(0)}(\rho v^i l_1)=m^1_{(0)}v^1_{(0)}l_{1_{(0)}}+p_{(0)}/\gamma\cdot l_{1_{(0)}}. \tag{5.24}$$

Following this step the perturbative correction (first order) terms require some manipulation.

The first order normal momentum flux is:

$$J^1_{(1)}(\rho v^i l_i)=\left(m^1_{(0)}v^i_{(1)}+m^1_{(1)}v^i_{(0)}+p_{(1)}/\gamma\cdot g^{i1}_{(0)}+p_{(0)}/\gamma\cdot g^{i1}_{(1)}\right)l_{i_{(0)}}+$$
$$+\left(m^1_{(0)}v^i_{(0)}+p_{(0)}/\gamma\cdot g^{i1}_{(0)}\right)l_{i_{(1)}}, \tag{5.25}$$

with $g^{11}=1,\quad g^{11}_{(0)}=1,\quad \Rightarrow g^{11}_{(i)}=0\quad \forall i\neq 0$ and $\left(m^1_{(0)}v^i_{(0)}+p_{(0)}g^{i1}_{(0)}\right)=0$ yielding:

$$J^1_{(1)}(\rho v^i l_i)=\left(m^1_{(0)}v^i_{(1)}+m^1_{(1)}v^i_{(0)}+p_{(1)}/\gamma\cdot g^{i1}_{(0)}\right)l_{i_{(0)}}. \tag{5.26}$$

$J^1_{(1)}(\rho e)$ simplifies substantially due to $g^{i1}=0,\ \forall\ i\neq 1.$

Subsequently, the first order fluxes can be written as:

$$J^1_{(1)}\begin{pmatrix}\rho\\ \rho v^i l_i\\ \rho e\\ \rho\lambda\end{pmatrix}= \tag{5.27}$$

$$\begin{pmatrix} m^1_{(1)} \\ \left(m^1_{(0)} v^i_{(1)} + m^1_{(1)} v^i_{(0)} + p_{(1)}/\gamma \cdot g^{i1}_{(0)}\right) l_{i_{(0)}} \\ m^1_{(1)} e_{(0)} + m^1_{(0)} e_{(1)} + p_{(1)}/\gamma \cdot (m^i_{(0)}/\rho_{(0)}) + p_{(0)}/\gamma \cdot \left(m^i/\rho\right)_{(1)} \\ m^1_{(1)} \lambda_{(0)} + m^1_{(0)} \lambda_{(1)} \end{pmatrix},$$

The asymptotic expansion should also be performed for the source term $Q \approx Q_{(0)} + Q_{(1)} Z^{-1}$. This calculation involves the asymptotic expansion of the variables inside and outside the exponential function plus a Taylor expansion of the latter.

Finally, the first and second order terms can be written as:

$$Q_{(0)} = \rho_{(0)} k (1 - \lambda_{(0)}) e^{\left(-\theta_a/(p_{(0)} \Upsilon_{(0)})\right)}, \tag{5.28}$$

$$Q_{(1)} = \left(\rho_{(1)} k (1 - \lambda_{(0)}) - \rho_{(0)} k \lambda_{(1)}\right) e^{\left(-\theta_a/(p_{(0)} \Upsilon_{(0)})\right)} + \left[\rho_{(0)} k (1 - \lambda_{(0)}) \left(\Upsilon_{(1)}/\Upsilon_{(0)} + p_{(1)}/p_{(0)}\right) \theta_a / \left(p_{(0)} \Upsilon_{(0)}\right)\right] e^{\left(-\theta_a/(p_{(0)} \Upsilon_{(0)})\right)}. \tag{5.29}$$

5.1.3.2.3 Planar detonation

Equation (5.20) combined with Equation (5.22) constitutes an equation system for *planar* detonations. This system is equal to the known equations utilized to derive the classical results of the ZND theory of detonation see publications from Fickett (Fickett, 1989), Lee (Lee, 2008) and Lee and Stewart (Lee and Stewart, 1990). The ZND theory provides an analytic expression for the pressure, velocity and specific volume profiles (Lee and Stewart, 1990) as a function of the reaction progress variable λ:

$$p = a + (1 - a)(1 - b\beta\lambda)^{\frac{1}{2}}, \; v = (1 - p)(\gamma M_S)^{-1} + M_s, \; \Upsilon = v/M_s. \tag{5.30}$$

The auxiliary variables appearing in Equation 5.1.3.19 are, $M_s = \frac{(\gamma-1)D^2+2}{2\gamma D^2-(\gamma-1)}$, where $D = \frac{\tilde{D}}{\tilde{c}_s}$ and $\beta = \tilde{Q}\gamma/\tilde{c}_s^2$.

Additionally:

$$a = \frac{\gamma D^2+1}{2\gamma D^2-(\gamma-1)}, \; b = \frac{M_S^2 2\gamma(\gamma-1)}{(1-a^2)(\gamma+1)}. \tag{5.31}$$

Equations (5.30) allow the half reaction zone length to be expressed as:

$$\tilde{l}_c = \tilde{c}_s k^{-1} \int_0^{\frac{1}{2}} v(\lambda)(1 - \lambda)^{-1} e^{\theta_a/(p(\lambda)\Upsilon(\lambda))} d\lambda. \tag{5.32}$$

Finally, it is interesting to note that the whole system can be converted to the spatial formulation using the following change of variables:

$$X/Z = x = \int_0^{\lambda} v(\zeta)/W(\zeta) d\zeta, \tag{5.33}$$

$$dx/d\lambda = v(\lambda)/W(\chi). \tag{5.34}$$

5.1.3.2.4 Modelling

As previously mentioned a detonation can be considered as a small-thickness layer separating the fresh mixtures of the burned products. To model this phenomenon the following three

dimensional *hydrodynamic* model can be proposed. Within this model the internal structure of the detonation, as well as the chemical reaction, is substituted by modified jump conditions. Conceptually, this construction asymptotically extends the *simplest* planar stationary theory to a three-dimensional non-stationary flow. The derivation of this model can be summarised as follows:

In this derivation we consider two models for detonation simultaneously, the *hydrodynamic* and the *reactive* model. Away from the consumption area, these models are identical. The jump conditions of the *hydrodynamic* model, particularly the position and the amplitude of the discontinuity, are going to be determined from the internal structure of the detonation (*reactive* model).

Therefore, two sets of equations must be considered, each corresponding to one of the models. Capital letters are used to designate the *reactive* model while lower-case letters are used for the *hydrodynamic* model.

The system of Equations (5.27) and Equation (5.28) may be the re-written as:

$$\partial_X \left(J^1_{(0)} \begin{pmatrix} \phi \\ \Phi \end{pmatrix} \right) = \begin{pmatrix} 0 \\ Q'_{(0)}(\Phi) \end{pmatrix}, \tag{5.35}$$

$$\partial_X \left(J^1_{(1)} \begin{pmatrix} \phi \\ \Phi \end{pmatrix} \right) = \begin{pmatrix} 0 \\ Q'_{(1)}(\Phi) - 2HXQ'_{(0)}(\Phi) \end{pmatrix} + 2HJ^1_{(0)} \begin{pmatrix} \phi \\ \Phi \end{pmatrix} - (\partial_t + \chi) \begin{pmatrix} \phi_{(0)} \\ \Phi_{(0)} \end{pmatrix} - (g_0)^{-1/2} \partial_{x^\alpha} \left(\sqrt{g}_{(0)} J^\alpha_{(0)} \begin{pmatrix} \phi_{(0)} \\ \Phi_{(0)} \end{pmatrix} \right). \tag{5.36}$$

In the detonation profile, as provided in Figure 5.10, both models coincide in the initial, rarefaction and final states. The models exclusively differ in a thin zone surrounding the shock, i.e. between the *hydrodynamic* discontinuity and the Chapman-Jouguet point, as shown in Figure 5.11. In the area of appreciable chemical reaction the *hydrodynamic* model is an extrapolation of the rarefaction wave. For simplicity, we set the origin of coordinates in the discontinuity of the *hydrodynamic* model. Therefore Equation 5.1.3.24 and Equation 5.1.3.25 differ with respect to jump position, jump conditions and reaction source term.

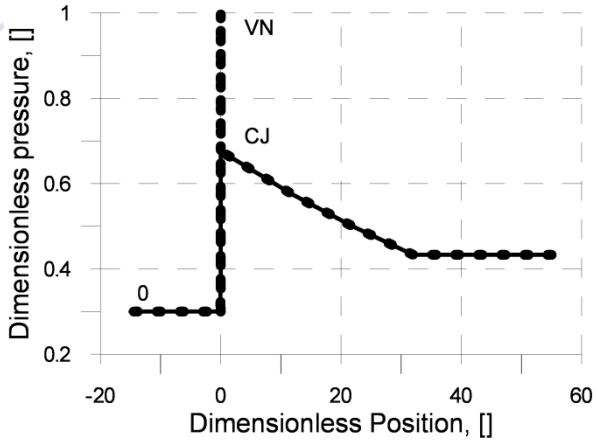

Figure 5.10 Profiles of *hydrodynamic* (solid) and *reactive* (dashed) detonation models: global view. Profile obtained with ZND theory coupled with rarefaction wave, for a gas of

characteristics $p_0 = 100\ kPa, \rho_0 = 1\frac{kg}{m^3}$, $Q = 0.1\ MJ$, $\gamma = 1.4$, $k = 1\ 10^5 s^{-1}$ and $E/R_g = 10000\ K$. *0* = normal status, *VN* = von Neumann peak, *CJ* = Chapman-Jouget point.

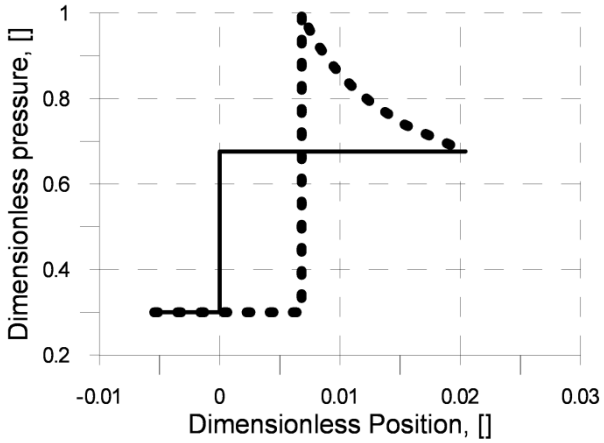

Figure 5.11 Profiles of *hydrodynamic* (solid) and *reactive* (dashed) detonation models: detailed area. Profiles obtained with the same conditions as in Figure 5.10.

Subtracting Equation (5.35) from Equation (5.36) and rearranging leads to:

$$\partial_X\left(J^1_{(0)}(\Phi) - J^1_{(0)}(\phi)\right) = Q'_{(0)}, \tag{5.37}$$

$$\partial_X\left(J^1_{(1)}(\Phi) - J^1_{(1)}(\phi)\right) = Q'_{(1)} - 2HXQ'_{(0)}(\phi) + \partial_X\Big(2HX\big(J^1_{(0)}(\Phi) - J^1_{(0)}(\phi)\big)\Big) - (\partial_t + \chi)(\Phi_{(0)} - \phi_{(0)}) - (g_0)^{-1/2}\,\partial_{x^\alpha}\Big(\sqrt{g}_{(0)}\big(J^\alpha_{(0)}(\Phi) - J^\alpha_{(0)}(\phi)\big)\Big). \tag{5.38}$$

Equation (5.37) and Equation (5.38) can be piecewise integrated from $-\infty$ to ∞.

Taking into account the discontinuities and applying the *Fundamental Calculus Theorem*:

$$\left[J^1_{(0)}(\Phi)\right]_{VN} + \left[J^1_{(0)}(\phi)\right]_{CJ} = \int_{-\infty}^{-\infty} Q_{(0)}(\Phi), \tag{5.39}$$

$$\left[J^1_{(1)}(\Phi)\right]_{VN} + \left[J^1_{(1)}(\phi)\right]_{CJ} = \int_{-\infty}^{-\infty}\left(Q_{(1)}(\Phi) - 2HXQ_{(0)}(\Phi)\right)dX + \\ + \partial_X\Big(\int_{-\infty}^{-\infty} 2HX\big(J^1_{(0)}(\Phi) - J^1_{(0)}(\phi)\big)dX\Big) - (\partial_t + \chi)\int_{-\infty}^{-\infty}(\Phi_{(0)} - \\ \phi_{(0)})dX - -\int_{-\infty}^{-\infty}(g_0)^{-1/2}\,\partial_{x^\alpha}\Big(\sqrt{g}_{(0)}\big(J^\alpha_{(0)}(\Phi) - J^\alpha_{(0)}(\phi)\big)\Big)dX. \tag{5.40}$$

We have designated with the index VN the *reactive* discontinuity and with the index CJ the *hydrodynamic* discontinuity, by analogy of its conditions with the CJ point. The discontinuity in the *reactive* model is a shock. Therefore, it is infinitely thin and the conditions applied for the shock discontinuity (see Landau and Lifshitz, 1987) should also govern the curved case. Furthermore, the composition does not change across the discontinuity since the reaction starts at the high pressure side of the shock.

Therefore:

$$\left\{[J^1(\Phi)]_{VN} = 0,\ \left[J^1_{(0)}(\Phi)\right]_{VN} = 0\right\} \Rightarrow \left[J^1_{(1)}(\Phi)\right]_{VN} = 0. \tag{5.41}$$

Substituting the condition $J^1_{(0)}(\Phi) = J^1_{(0)}(\phi)$ for $X \to -\infty$ into Equation (5.39) we obtain for the vector $\theta = (\rho, \rho v^i l_i, \rho e)$, leading to:

$$\left[J^1_{(0)}(\theta)\right]_{CJ} = 0, \quad J^1_{(0)}(\Theta) = J^1_{(0)}(\theta). \tag{5.42}$$

This has several implications. The mass flux satisfies $M^j_{(0)} - m^j_{(0)} = 0$.

In the moving curvilinear coordinates $M^\alpha_{(0)} = m^\alpha_{(0)} = 0$.

Furthermore, the tangential component of momentum is continuous across the shock. Therefore: $J^\alpha_{(0)}(RV^i l_i) = P_{(0)}/\gamma \cdot g^{i\alpha}_{(0)} l_{i_{(0)}}$ and thus, defining $\Pi = (P_{(0)} - p_{(0)})/\gamma$ we obtain: $J^\alpha_{(0)}(RV^i l_i) - J^\alpha_{(0)}(\rho v^i l_i) = \Pi g^{i\alpha}_{(0)} l_{i_{(0)}}$.

Finally, the normal component of the momentum flux, $J^1_{(0)}\left(RV^i l_i\right) l^1$, is identical in both the *reactive* and CJ *hydrodynamic* models.

Therefore: $\Pi = M^1_{(0)} V^1_{(0)} - m^1_{(0)} v^1_{(0)}$.

Equation (5.40) can be simplified applying the previous considerations.

For continuity of momentum and energy the first two terms in the RHS of Equation (5.40) vanish. Moreover, the last term of the RHS cancels for continuity due to vanishing transverse momentum. Therefore for the continuity Equation (5.40) reduces to:

$$\left[m^1_{(1)}\right]_{CJ} = -(\partial_t + \chi) \int_{-\infty}^{\infty} (R^1_{(0)} - \rho^1_{(0)}) dX. \tag{5.43}$$

The simplifications in the momentum equation are as follows:

$$\begin{aligned} &\left[\left(m^1_{(0)} v^i_{(1)} + m^1_{(1)} v^i_{(0)} + g^{i1}_{(0)} p_{(1)} \gamma^{-1}\right) l_{i_{(0)}}\right]_{CJ} = \\ &- \int_{-\infty}^{\infty} g_0^{-\frac{1}{2}} \partial_{x^\alpha} (g^{\frac{1}{2}}_{(0)} \Pi g^{i\alpha}_{(0)} l_{i_{(0)}}) dX - \int_{-\infty}^{\infty} (\partial_t + \chi)(R_{(0)} V^i_{(0)} - \\ &\rho_{(0)} v^i_{(0)}) l_{i_{(0)}} dX, \end{aligned} \tag{5.44}$$

Referring to the energy equation the simplifications are:

$$\begin{aligned} &\left[m^1_{(1)} e_{(0)} + m^1_{(0)} e_{(1)} + p_{(1)}/\gamma \cdot g^{i1}_{(0)} \cdot m^i_{(0)}/\rho_{(0)} + p_{(0)}/\gamma \cdot g^{i1}_{(0)} (m^i/\right. \\ &\left.\rho)_{(1)}\right]_{CJ} = - \int_{-\infty}^{\infty} (\partial_t + \chi)\left(R_{(0)} E_{(0)} - \rho_{(0)} e_{(0)}\right) dX. \end{aligned} \tag{5.45}$$

Finally for the species equation similar simplifications yield:

$$\begin{aligned} &\left[m^1_{(1)} \lambda_{(0)} + m^1_{(0)} \lambda_{(1)}\right]_{CJ} = \int_{-\infty}^{+\infty} \left(Q_{(1)}(RL) - 2HXQ_{(0)}(RL)\right) dX - \\ &\int_{-\infty}^{+\infty} (\partial_t + \chi)\left(R_{(0)} L_{(0)} - \rho_{(0)} \lambda_{(0)}\right) dX. \end{aligned} \tag{5.46}$$

We may define $I_R = \int_{-\infty}^{\infty} \left(R_{(0)} - \rho_{(0)}\right) dX$, $I_\sigma = \int_{-\infty}^{\infty} \Pi dX$ and $I_\Sigma = \int_{-\infty}^{\infty} (R_{(0)} E_{(0)} - \rho_{(0)} e_{(0)}) dX$. Also using the following equations: $R_{(0)} V^i_{(0)} - \rho_{(0)} v^i_{(0)} = u^i_{(0)} (R_{(0)} - \rho_{(0)})$ and $(g_0)^{-1/2} \cdot \partial_{x^\alpha} (\sqrt{g}_{(0)} g^{i\alpha}_{(0)} l_{i_{(0)}}) = -2H l_1 + (g_0)^{-1/2} \partial_{x^\alpha} (\sqrt{g}_{(0)} g^{\beta\alpha}_{(0)} l_{\beta_{(0)}})$, we can manipulate Equations (5.43), Equation (5.44) and Equation (5.45) to obtain:

$$\left[m^1_{(1)}\right]_{CJ} = -(\partial_t + \chi) I_R, \tag{5.47}$$

$$\left[\left(m^1_{(0)}v^i_{(1)} + m^1_{(1)}v^i_{(0)} + p_{(1)}/\gamma \cdot g^{i1}_{(0)}\right)l_{i_{(0)}}\right]_{CJ} = -(\partial_t + \chi)u^i_{(0)}l_{i(0)}I_R - \left(2Hl_1 + g^{\alpha\beta}l_\beta\,\partial_{x^\alpha}\right)I_\sigma, \tag{5.48}$$

$$\left[m^1_{(1)}e_{(0)} + m^1_{(0)}e_{(1)} + p_{(1)}/\gamma \cdot g^{i1}_{(0)} \cdot m^i_{(0)}/\rho_{(0)} + p_{(0)}/\gamma \cdot g^{i1}_{(0)}\left(m^i/\rho\right)_{(1)}\right]_{CJ} = -(\partial_t + \chi)I_\Sigma. \tag{5.49}$$

The subsequent result can then be obtained following the combination of the leading order jump conditions with the perturbative corrections, and also decomposing the jump condition for the momentum in the normal and tangential components:

$$\begin{bmatrix} m^1 \\ m^1v^1 + p/\gamma \\ m^1v^\beta \\ m^1e + m^1p/\rho\gamma \end{bmatrix}_{CJ} = -\left((\partial_t + \chi)\begin{pmatrix} I_R \\ u^1_{(0)}I_R \\ u^\beta_{(0)}I_R \\ I_\Sigma \end{pmatrix} + \begin{pmatrix} 0 \\ 2HI_\sigma \\ g^{\alpha\beta}\,\partial_{x^\alpha}I_\sigma \\ 0 \end{pmatrix}\right) Z^{-1} + o(Z^{-1}). \tag{5.50}$$

The first row of the Equation (5.50) shows that the normal mass flux m^1 experiences $O(Z^{-1})$ variations in the detonation structure. This represents the excess of mass in the *hydrodynamic* model compared to the *reactive* model. Following the methodology described by Class et al., (Class et al., 2003) we can define, without loss of generality, the position of the artificial discontinuity in the *hydrodynamic* model, requiring identical normal mass flux in the fresh and burned mixtures. A continuous mass flux across the discontinuity surface can be obtained.

The condition $[m^1]_{CJ} = 0$ requires $I_R = 0$ where:

$$I_R = \int_{-\infty}^{0}(R_{(0)} - \rho_{(0)})dX + \int_0^{x_{VN}}(R_{(0)} - \rho_{(0)})dX + \int_{x_{VN}}^{x_{CJ}}(R_{(0)} - \rho_{(0)})dX + \int_{x_{CJ}}^{\infty}(R_{(0)} - \rho_{(0)})dX. \tag{5.51}$$

The areas under the curves in Figure 5.10 and Figure 5.11 delimited by the *hydrodynamic* discontinuity and the Chapman-Jouguet point cancel. Therefore, the first and last term of the RHS of Eq. (5.51) cancel. The difference of slopes, see Figure 5.11, between rarefaction and consumption curves is asymptotically large. In stretched coordinates, the slope of the hydrodynamic model is zero at leading approximation order and does not affect the integral I_R in the consumption area.

After some manipulation we obtain:

$$I_R \approx \int_{x_{VN}}^{x_{CJ}}(R_{(0)} - \rho_{CJ})dX - (\rho_{CJ} - \rho_0)X_{VN}, \tag{5.52}$$

as can be graphically confirmed in Figure 5.10 and Figure 5.11.

The position of the detonation shock relative to the artificial discontinuity is provided by:

$$X_{VN} \approx \left(\rho_{CJ} - \rho_0\right)^{-1}\int_{X_{VN}}^{X_{CJ}}\left(R_{(0)} - \rho_{CJ}\right)dX. \tag{5.53}$$

By similar considerations we find:

$$I_\sigma = \gamma^{-1}\int_{X_{VN}}^{X_{CJ}}\left(P_{(0)} - p_{(0)}\right)dX \approx \gamma^{-1}\left(I_1 - \left(p_{CJ} - p_0\right)X_{VN}\right), \tag{5.54}$$

where $I_1 = \int_{X_{VN}}^{X_{CJ}} \left(P_{(0)} - p_{CJ}\right) dX$.

The terms inside the integral I_1 may be reformulated by changing the leading to the recovery of the more convenient formulation,

$$I_1 = Z \int_0^1 \left(P(\lambda) - p_{CJ}\right) u(\lambda) \cdot (r(\lambda))^{-1} d\lambda = Z I_1{}'.$$

Similarly Equation 5.1.3.42 can also be re-expressed yielding:

$$x_{VN} \approx \frac{\int_0^1 (R^1_{(0)}(\lambda) - \rho_{CJ}) u(\lambda) (r(\lambda))^{-1} d\lambda}{\rho_{CJ} - \rho_0} = \frac{I_\rho}{\rho_{CJ} - \rho_0}. \tag{5.55}$$

Finally, I_σ can be reformulated as:

$$I_\sigma = \gamma^{-1} (I_1{}' - (p_{CJ} - p_0)(\rho_{CJ} - \rho_0)^{-1} I_\rho) Z, \tag{5.56}$$

and I_Σ can be rescaled $I_\Sigma = I'_\Sigma Z$.

Equation (5.50) can thereby be rewritten as:

$$\begin{bmatrix} m^1 \\ m^1 v^1 + p/\gamma \\ m^1 v^\beta \\ m^1 e + m^1 p/\rho\gamma \end{bmatrix}_{CJ} = -(\partial_t + \chi) \begin{pmatrix} 0 \\ 0 \\ 0 \\ I'_\Sigma \end{pmatrix} - \begin{pmatrix} 0 \\ 2H\gamma^{-1} \\ g^{\alpha\beta}\gamma^{-1}\,\partial_{x^\alpha} \\ 0 \end{pmatrix} \left(I_1{}' - \frac{p_{CJ} - p_0}{\rho_{CJ} - \rho_0} I_\rho \right) + \tag{5.57}$$

$$+ o(Z^{-1}).$$

The integrals I_1 and I_ρ can easily be understood using Figure 5.11. Both integrals represent areas contained between the detonation curve and the horizontal CJ conditions. As I_1 and I_ρ depend on the chemistry model, this approach allows for the numerical evaluation of even complex chemistry. In the present work described here, the explicit expressions (referring to Equations (5.40) were selected in the analysis. Obviously, chemical conversion will not fully complete in a layer of finite thickness. This does not however contradict our assumption of a consumption layer of small finite thickness, since the chemical conversion becomes exponentially small for $\lambda \to 1$. Accordingly the integrals I_1 and I_ρ converge for $\lambda \to 1$.

Note that, analogous to the work undertaken by Class (i.e. references Class et al., 2003 and Class, 2003) the stretch χ can be calculated as

$$\chi = |\nabla\rho|^{-1} \nabla \cdot \left(|\nabla\rho| \vec{u}_{(0)} \right)\Big|_{X=0^+}. \tag{5.58}$$

Here the stretch experiences a jump at the *hydrodynamic* discontinuity surface. Thus, the evaluation is taken on the high pressure side of the interface, a fact that is emphasized by the + symbol in Equation (5.58).

5.1.3.2.5 Final jump conditions

A clearer understanding of the jump conditions may be obtained by re-writing Equation 5.1.3.46 in dimensional form. To achieve this I'_1 and I_ρ were transformed, including the reference values $\tilde{l}_f$, $\tilde{p}_s = \tilde{\rho}_s \tilde{c}_s^2/\gamma$ and $\tilde{\rho}_s$ in the kernel and the dummy variable of the integrals. Eq. (5.1.3.39) reads in dimensional notation

$$\begin{bmatrix} \widetilde{m}^1 \\ \widetilde{m}^1\tilde{v}^1 + \tilde{p} \\ \widetilde{m}^1\tilde{v}^\beta \\ \widetilde{m}^1\tilde{e} + \tilde{v}^1\tilde{p} \end{bmatrix}_{CJ} \approx -(\partial_{\tilde{t}} + \tilde{\chi}) \begin{pmatrix} 0 \\ 0 \\ 0 \\ \tilde{I}'_\Sigma \end{pmatrix} - \begin{pmatrix} 0 \\ 2\widetilde{H} \\ g^{\alpha\beta}\,\partial_{\tilde{x}^\alpha} \\ 0 \end{pmatrix} \left(\tilde{I}_1{}' - \frac{\tilde{p}_{CJ} - \tilde{p}_0}{\tilde{\rho}_{CJ} - \tilde{\rho}_0} \tilde{I}_\rho \right). \quad (5.59)$$

It is interesting to note, that the system of equations representing the *planar* detonation (i.e. Equations (5.40)) is, for a gas of known composition, a mono-parametric system dependent on D. The system represented by Equation (5.59) depends not only on D, but also on curvature $\widetilde{H}$ and on stretch $\tilde{\chi}$.

5.1.3.2.6 Virtual surface tension

The normal momentum, as defined in Equation 5.1.3.46, is discontinuous across the jump with linear proportionality on curvature. Following the arguments made by Class (Class et al., 2003), an analogy can be established with an interface separating two immiscible fluids (Landau and E. Lifshitz, 1987) in order to calculate the virtual surface tension of the detonation.

At the interface:

$$[\tilde{p} - \sigma_{nn}] = 2\widetilde{H}\alpha, \quad (5.60)$$

where α represents the surface tension.

Our initial scale considerations suggest that the tangential stress is negligible. Allowing for mass transfer across the surface (e.g. due to evaporation) this equation must be suitably modified:

$$[\widetilde{m}^1\tilde{v}^1 + \tilde{p}] = 2\widetilde{H}\alpha. \quad (5.61)$$

We may, identify terms with eq. (5.59) to obtain

$$\alpha = -\left(\tilde{I}_1{}' - \frac{\tilde{p}_{CJ} - \tilde{p}_0}{\tilde{\rho}_{CJ} - \tilde{\rho}_0} \tilde{I}_\rho \right) = -\tilde{l}_f \left(I'_1 \frac{\rho_s c_s^2}{\gamma} - \frac{\tilde{p}_{CJ} - \tilde{p}_0}{\tilde{\rho}_{CJ} - \tilde{\rho}_0} \rho_s I_\rho \right) = \tilde{l}_f \alpha_0., \quad (5.62)$$

The coefficient of surface tension in an infinitely thin gas-dynamic discontinuity equivalent to a detonation is equal to the difference between the integral of the pressure between the CJ and the VN points minus the integral of the density between the same integration limits normalized by a factor.

The evaluation of α_0 and the partial factors $\alpha_{01} = -I'_1\rho_s c_s^2/\gamma$ and $\alpha_{02} = (\tilde{p}_{CJ} - \tilde{p}_0)(\tilde{\rho}_{CJ} - \tilde{\rho}_0)^{-1}\tilde{n}_s I_\rho$ is included in Figure 5.12 for a gas of the indicated characteristics and different initial pressures p_0. The surface tension exhibits an inverse proportionality to the initial pressure. The existence of a minimum is due to the sum of the α_{01} and α_{02} factors (dashed lines), that combined, creates the final dependency.

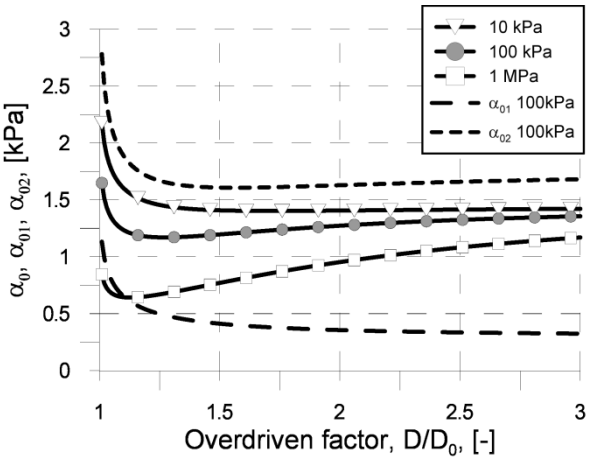

Figure 5.12 Dependence of α_0 factor to the degree of over-driven detonation for a gas with characteristics: $\rho_0 = 1\frac{kg}{m^3}$, $Q = 0.1\ MJ$, $\gamma = 1.4$, $k = 1\ 10^5 s^{-1}$, $E/R_g = 10000\ K$ obtained for different pressures.

Figure 5.13 shows the dependence of the surface stress on the fuel concentration. An increase on the fuel concentration strongly increases the surface tension of the equivalent jump.

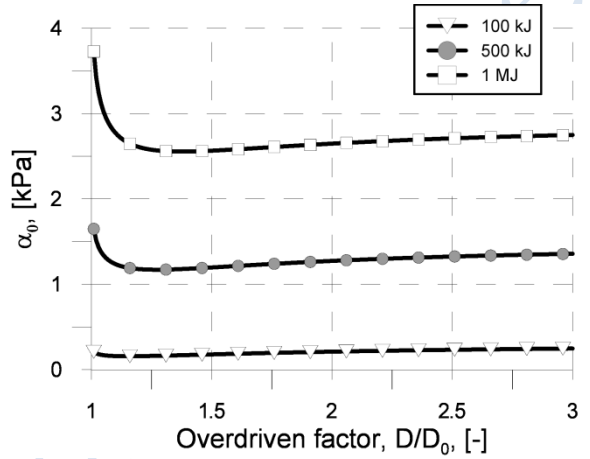

Figure 5.13 Dependence of α_0 factor to the degree of over-driven detonation for a gas with characteristics: $p_0 = 100\ kPa,\ \rho_0 = 1\frac{kg}{m^3}, \gamma = 1.4,\ k = 1\ 10^5 s^{-1}, E/R_g = 10000\ K$ obtained for different enthalpies of formation.

The virtual surface tension has strong connections with the stability of the detonation. In this sense, Equation (5.59) shows that the tangential momentum must not be continuous across the interface.

In this sense, a derivative of the surface tension in the RHS of Equation (5.59) has an analogous meaning to the Marangoni forces. The terms containing I_R in Equation (5.50), which were cancelled in Equation (5.59) contain the dependence of the virtual surface on the inertia that was suppressed thanks to the singular selection for the position of the virtual surface.

5.1.3.2.7 Change of the average curvature in the transverse direction.

The formulation presented allows the variation of the average curvature in the transverse direction to be expressed, i.e. Equation set 5.1.3.48 can be expressed in terms of the surface tension and then derived in the transverse direction.

The second equation in Equation set (5.59) can get transformed into:

$$\partial_{\tilde{x}^\beta}[\tilde{m}^1\tilde{v}^1 + \tilde{p}]_{CJ} = -2\alpha\,\partial_{\tilde{x}^\beta}\tilde{H} - 2\tilde{H}\,\partial_{\tilde{x}^\beta}\alpha. \tag{5.63}$$

This is a very significant form that expresses the change of the average curvature as a function of the jump of pressure and momentum and the equivalent Marangoni forces.

Transforming the third equation of Equation set (5.59) yields:

$$2\tilde{H}[\tilde{m}^1\tilde{v}^\gamma]_{CJ} = -2\tilde{H}g^{\beta\gamma}\,\partial_{\tilde{x}^\beta}\alpha. \tag{5.64}$$

Multiplying by $g^{\beta\gamma}$ and operating:

$$2\alpha g^{\beta\gamma}\,\partial_{\tilde{x}^\beta}\tilde{H} = 2\tilde{H}[\tilde{m}^1\tilde{v}^\gamma]_{CJ} - g^{\beta\gamma}\,\partial_{\tilde{x}^\beta}[\tilde{m}^1\tilde{v}^1 + \tilde{p}]_{CJ}. \tag{5.65}$$

Eliminating α:

$$2g^{\beta\gamma}\,\partial_{\tilde{x}^\beta}\tilde{H} = \left(\tilde{H}g^{\beta\gamma}\,\partial_{\tilde{x}^\beta}[\tilde{m}^1\tilde{v}^1 + \tilde{p}]_{CJ} - 2\tilde{H}^2[\tilde{m}^1\tilde{v}^\gamma]_{CJ}\right)/[\tilde{m}^1\tilde{v}^1 + \tilde{p}]_{CJ}. \tag{5.66}$$

Equation (5.66) expresses the change of the average curvature in the transverse direction as a function of the relative importance of the pressure and normal momentum jump, compared with the transverse one.

Also, Equation (5.63) allows for an increased understanding of the intrinsic mechanism associated with the instability of detonations. A detonation may propagate isotropically in a medium of constant composition without forming cellular structures. The RHS of the tangential impulse in Equation (5.59) would cancel in this case. Still any perturbation in any of the variables would immediately change α, p or v thereby changing the curvature.

5.1.4 Differences between 1D and 3D detonation propagation utilicing detonation curvature modeling (KIT)

We may recall the expression for 1D detonation following the ZND theory. The analytic expression for the pressure, velocity and specific volume profiles (Lee and Stewart, 1990) are provided as a function of the reaction progress variable λ:

These equations have been provided in Section 5.1.3.2.3 and are reproduced here for convenience:

$$p = a + (1-a)(1-b\beta\lambda)^{\frac{1}{2}},\ v = (1-p)(\gamma M_S)^{-1} + M_s,\ \Upsilon = v/M_s. \tag{5.67}$$

The auxiliary variables appearing in Equation (5.67) are, $M_s = \frac{(\gamma-1)D^2+2}{2\gamma D^2-(\gamma-1)}$, where $D = \frac{\tilde{D}}{\tilde{c}_s}$ and $\beta = \tilde{Q}\gamma/\tilde{c}_s^2$.

Additionally:

$$a = \frac{\gamma D^2+1}{2\gamma D^2-(\gamma-1)},\ b = \frac{M_s^2 2\gamma(\gamma-1)}{(1-a^2)(\gamma+1)}. \tag{5.68}$$

The half reaction zone length can be expressed as:

$$\tilde{l}_c = \tilde{c}_s k^{-1}\int_0^{\frac{1}{2}} v(\lambda)(1-\lambda)^{-1}e^{\theta_a/(p(\lambda)\Upsilon(\lambda))}d\lambda, \tag{5.69}$$

$$\begin{bmatrix} \widetilde{m}^1 \\ \widetilde{m}^1\tilde{v}^1 + \tilde{p} \\ \widetilde{m}^1\tilde{v}^\beta \\ \widetilde{m}^1\tilde{e} + \tilde{v}^1\tilde{p} \end{bmatrix}_{CJ} \approx -(\partial_{\tilde{t}} + \tilde{\chi}) \begin{pmatrix} 0 \\ 0 \\ 0 \\ \tilde{I}'_\Sigma \end{pmatrix} - \begin{pmatrix} 0 \\ 2\widetilde{H} \\ g^{\alpha\beta}\,\partial_{\tilde{x}^\alpha} \\ 0 \end{pmatrix} \left(\tilde{I}_1{}' - \frac{\tilde{p}_{CJ} - \tilde{p}_0}{\tilde{\rho}_{CJ} - \tilde{\rho}_0} \tilde{I}_\rho \right). \quad (5.70)$$

It is interesting to note, that the system of equations representing the *planar* detonation (i.e. Equations (5.67)) is, for a gas of known composition, a mono-parametric system dependent on D. The system represented by Equation set (5.59) depends not only on D, but also on curvature $\widetilde{H}$ and on stretch $\tilde{\chi}$.

5.2 Models (KIT)

There are multiple approaches whcich allows to reproduce the detonation process numerically. The most popular of them will be considered in the following sections.

5.2.1 Arrhenius reaction rate (KIT)

The chemistry that describes the detonation processes involved with mixtures of H_2 and Air involves the solution of numerous reactions (Li et al., 2004, Ó'Conaire et al., 2004, Maas et al., 1988 and Marinov, 1995).

The utilization of such schemes would involve resolution requirements in the region of 10^{-7} m. Such highly resolved resolutions are clearly not achievable for practical calculations where the domains of interest can be of the order of cubic hectometres. An evident solution would involve the utilization of a reduced kinetic mechanism (Peters, 1993), considering that fast reactions remain in a stationary state. Still such an approximation would not be sufficient, due to resolution requirements, for engineering calculations. Such calculations would require the utilization of one *brutto* reaction or at most two reactions if the reproduction of the induction time will be required.

These simplifications, that at first glance look to be extremely crude, are in fact much less severe that in equivalent combustion calculations and in most of cases very adequate for obtaining engineering approximations. This is easy to understand if we take into account the ZND theory (Fikett, 1979). Here we see that under this widely accepted theory the propagation velocity of the detonation is independent on the chemistry, it depends only on the polytrophic coefficient and on the enthalpy of formation of the gas. This allows for modelling that considers the chemistry as a simple one step reaction, i.e.:

$$w_y = \mathrm{K}\, \mathrm{y}_{H_2} \exp\left\{\frac{E_a}{RT}\right\}. \quad (5.71)$$

This reaction will have an activation energy obtained from literature sources such as Sun et al. (Sun et al., 1999), from shock tubes experiments, or from calculations performed with Cantera (Goodwin, 2001). The pre-exponential factor will then be determined as an adjusted value that allows the detonation cell size to be mimicked (using information available from experiments). When such a model is utilized, the performance will depend on the resolution utilized in the calculation.

The first case is that in which the resolution is much coarser than the half detonation thickness but much finer than the detonation cell size. In this case, the detonation cell size pattern will

be reproduced. Good practice involves that the resolution is smaller than 1/50 of the detonation cell size.

The second case appears when the cell size is bigger than the last limit. In those cases in which the cell size is bigger than 1/50 of the detonation cell size (for example is of the same order of magnitude), the cellular pattern is not going to be reproduced. The detonation still propagates with an overall adequate velocity (averaged velocity of the cellular detonation).

The third possibility appears when the resolution is even coarser than in the previous case. The model then runs into problems of numerical nature and generates a numerically overdriven detonation. Such difficulties can be overcome with the use of models specially designed for very coarse calculations in which the maximum reaction rate will be limited. Such limitation allows that the propagation remains similar to the one predicted by ZND theory. The Heaviside function, is generally defined as

$$\theta : \Re \to \Re$$

$$\theta(x) = \begin{cases} 0 & x < x_0 \\ 1 & x > x_0 \end{cases}, \tag{5.72}$$

is a good candidate for such limitation. This function allows defining the consumption of fuel as

$$w_y = C_f y_{H_2} \cdot R_r . \tag{5.73}$$

This consumption formula has no real physical interpretation, it is just a mechanism to provide enough variation of the species and heat release to generate and maintain the detonation. C_f is the constant of the model. The model shows almost no influence of the C_f constant as the R_r factor works as a shocking capturing algorithm. The “Heaviside” like factor R_r can be defined with the formula

$$R_r = \begin{cases} 0 & T < T_0 \\ \dfrac{T - T_1}{T_1 - T_0} & T_0 < T < T_1 \\ 1 & T > T_1 \end{cases}, \tag{5.74}$$

where the values of the temperatures, for this model, are T_0=800 and T_1=1700 for an stoichiometric hydrogen air mixture. T_1 can be close to the temperature of the burned gases. T_0 is the real limiter of the reaction and is supposed to simulate the auto-ignition temperature. Therefore, it can be set to a constant value, almost independent for all concentrations, (NASA 1997, IEC, 2000 and Zabetakis 1965). Data for the lower flammability limit (LFL), upper flammability limit (UFL) and self ignition limit are shown in the Figure 5.14.

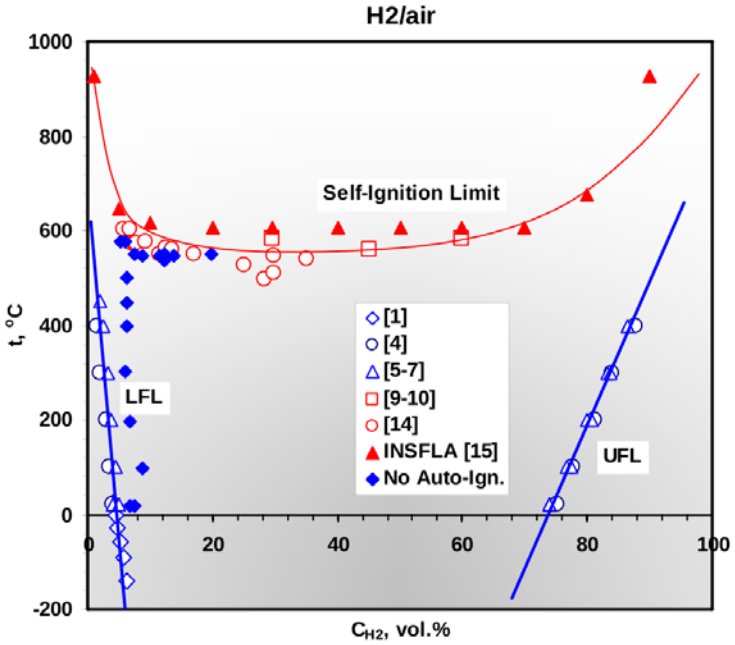

Figure 5.14 Low and upper flammability limits and auto-ignitions temperatures.

5.2.2 Gradient method (UU)

The gradient method, which is used for modelling the specific reaction rate and applied to deflagration modelling, was described previously in Section 4.2.2 of this document. However it may also be applied for the simulation of detonations.

The mathematical model of detonation then includes the governing equations for 3-D filtered mass, momentum and energy equations for a compressible Newtonian fluid. The progress variable equation describes the reaction front propagation and is the same as for the deflagration model accept for the source term:

$$\frac{\partial}{\partial t}\left(\bar{\rho}\,\tilde{c}\right)+\frac{\partial}{\partial x_j}\left(\bar{\rho}\,\tilde{u}_j\tilde{c}\right)=\frac{\partial}{\partial x_j}\left(\frac{\mu_{eff}}{Sc_{eff}}\frac{\partial\,\tilde{c}}{\partial x_j}\right)+\bar{S}_c\,, \tag{5.75}$$

where c = 0 stands for unburned mixture and c = 1 stands for combustion products.

The gradient method (Prudnikov, 1967 and Laskey et al., 1988) is used for the closure of the source term in the progress variable equation $S_c=\rho_u\cdot D\cdot\left|\nabla\tilde{c}\right|$, where ρ_u is density of unburned mixture in front of a shock, D is the detonation wave velocity, and ∇c is a gradient of the progress variable. The difference between deflagration and detonation mathematical models is the substitution in the source term of the turbulent burning velocity S_t by the detonation velocity D. The unique feature of the gradient method is the reproduction of correct mass burning rate per unit area of resolved reaction front, which in case of detonation is $\rho_u\cdot D$. This is achieved due to the fact that the integral of the progress variable gradient in the direction normal to the reaction front is always equal to unity regardless of the number and size of cells throughout the numerical flame front thickness (Molkov, 2012):

$$\int_V \overline{S}_c dV = \int_V \rho_u D\left|\nabla \tilde{c}\right| dV = \int_A \rho_u D dA \int_{c=0}^{c=1} \frac{\partial c}{\partial x} dx = \int_A \rho_u D dA \int_{c=0}^{c=1} dc = \int_A \rho_u D dA = \rho_u D A. \quad (5.76)$$

In work by Zbikowski et al. (Zbikowski et al., 2008, Zbikowski et al., 2009 and Zbikowski et al., 2010) the detonation velocity for a particular hydrogen-air composition was pre-calculated with Shock & Detonation (SD) Toolbox (CANTERRA Toolbox) which uses CANTERA software (Goodwin, 2005). The source term in the energy equation was connected with the source term in the progress variable equation $S_e = \Delta H_c \cdot S_c$, where ΔH_c is the standard heat of combustion which is calculated by CANTERA (Goodwin, 2005). Specific heats of unburned and burnt mixtures were approximated as piecewise-polynomial functions of temperature with polynomial coefficients calculated according to mass-weighted mixing law of composing species.

The gradient method by definition does not track the exact location of the reaction front but represents the change of the progress variable through control volumes (CVs) (Oran and Boris, 2001) and there is a numerical requirement for the flame front to occupy 4-5 CVs (Hawkes and Cant, 2001). This requirement is valid for the shock front as well. When such a treatment is used for the simulation of the reaction in the detonation wave, one should bear in mind that since the reaction zone thickness in a detonation wave is typically of the order of a few millimetres, it is clear that the real detonation wave thickness cannot be resolved when large control volumes are used to tackle industrial scale problems (Zbikowski et al., 2010).

To make the heat release in the numerical reaction zone able to feed the leading shock one should keep the simulated reaction (heat release) zone behind the peak of the leading shock without their numerical "non-physical" overlapping that "kills" the von Neumann spike in numerical simulations when this physics is ignored. Failure to address it results in under-prediction of maximum pressure in the von Neumann spike and hence propagation velocity. To achieve this in simulations the source term for the progress variable is kept equal to zero when the pressure derivative with time in the considered CV is positive (before the pressure peak), and is "switched on" only when the pressure derivative with time becomes negative (after the pressure peak).

This method had been implemented within LES detonation model developed by Ulster University (Zbikowski et al., 2008, 2009, 2010) which had been successfully validated against ZND (Zeldovich 1940, Neumann 1942, Doring 1943) theory. It was shown to be practically grid independent for planar detonation simulations in the range of cell sizes 0.1–1.0 m, not requiring any "calibration" of the heat of combustion and the ratio of specific heats (no Arrhenius chemistry parameters dependence either due to use of pre-calculated detonation velocity), which are often applied in other models to better reproduce experimental data. It was subsequently used in a number of simulations, e.g., simulation of large scale experiment in the RUT facility (Efimenko and Gavrikov, 2007) performed in Russia by Kurchatov Institute as a part of an international collaborative project (Zbikowski et al., 2009), (Zbikowski et al., 2010).

5.3 References

Aris, R. (1989) Tensor vectors and the basic equations of fluid dynamics. Dover.

Bdzil, J. and Stewart, D. (1989) Modelling tow dimensional detonations with detonation shock dynamics. Physics of fluids A. 1:1261–1267.

CANTERA Toolbox
http://www.galcit.caltech.edu/EDL/public/cantera/html/SD_Toolbox/index.html.

Chapman, D.L (1899) On the Rate of Explosion in Gases. Physics of Fluids. 47:90–104.
Doring, W. (1943) On detonation processes in gases. Ann Phys. 43:421–436.
Ciccarelli G., Ginsberg T., Boccio J., Economos C., Sato K. and Kinoshita M.. (1994)Detonation cell size measurements and predictions in hydrogen-air-steam mixtures at elevated temperatures. Comb. and Flame, 99:212–220.
Class, A.G., Matowsky, B., and Klimenko, A. (2003) A unified model of flames as gasdynamics discontinuities. J. Fluid Mech. 491:11–49.
Dorofeev, S.B., Sidorov, V.P., Kuznetsov M.S., Matsukov I.D. and Alekseev V.I. (2000) Effect of scale on the onset of detonations. Shock Waves. 10:137–149.
Dupre G, Knystautas R, Lee JH (1986) Near limit propagation of detonations in tubes. Prog. Aero. Astro. (AIAA, New York) 106:244–252
Efimenko, A. and Gavrikov, A. (2007) Large Scale Hydrogen-Air Detonation Experiments. The Effect of Ignition Location and Hydrogen Concentration on Loads. Description of HySafe SBEP V13.
Fickett, W. and Davis, W.C. (1979) Detonation. University of California press.
Goodwin, D.G. (2001) Cantera User's Guide. California Institute of Technology, Pasadena, CA, November, 2001.
Goodwin, D. (2005) CANTERA – Object-oriented software for reacting flows. Technical report, California Institute of Technology.
Hawkes. E.R. and Cant. R.S. (2001) Implication of a flame surface density approach to large eddy simulation of premixed turbulent combustion. Comb and Flame. 126:1617–1629.
International Electrotechnical Commission (2000) Electrical apparatus for explosive gas atmospheres - Part 20: Data for flammable gases and vapours, relating to the use of electrical apparatus. Standard IEC 60079-20:2000.
Jouguet. E. (1906) On the propagation of chemical reactions in gases, J. de Mathematiques Pures et Appliquees, 1:347–425.
Kasimov. A. and Stewart D. (2005) Asymptotic theory of evolution and failure of self sustained detonations, Journal of Fluids mechanics, 525:161–192.
Klein, R.and Stewart, D. (1993) The relation between curvature, rate state-dependence and detonation velocity. SIAM J. of Applied Mathematics. 53:1401–1435.
Klimenko A. and Class A. (2000) On premixed flames as gasdynamics discontinuities: A simple approach to derive their propagation speed. Comb. Sci. and Tech., 160:23–33.
Klimenko, A. and Class, A. (2002) Propagation of nonstationary curved and stretched premixed flames with multi-step mechanism. Comb. Sci. and Tech. 174:1–43.
Klimenko, A. Class, and S. O'Gorman (2002) Near-equidiffusion disturbed pre-mixed flames with wither reaction zones. Flow Turb. and Comb. 69: 95–122.
Kogarko, S.M. and Zeldovich, Ya.B. (1948) Detonation of gaseous mixture. Academiia Nauk, SSSR Doklady. 63:553–556.
Kuo, K.K. (2005) Principles of combustion. Wiley and Sons.
Kuznetsov, M.S., Alekseev, V.I. and Dorofeev, S.B. (2000) Comparison of critical conditions for {DDT} in regular and irregular cellular detonation systems. Shock Waves. 10:217-224.
Kuznetsov, M., Cicarelli, G., Dorofeev, S., Alekseev, V., Yankin, Yu. and Kim, T.H. (2002) DDT in methane-air mixtures. Shock Waves. 12:215-220.
Landau, L.D. and Lifshitz, E.M. (1987) Fluid Mechanics, v. 6 of Course of Theoretical Physcis. 2nd Ed. New York: Pergamon Press.
Laskey, K.J., Oran, E.S. and Boris J.P. (1988) The gradient method for interface tracking. Naval Research Laboratory report.
Lee, J.H.S. (1985) On the Transition from deflagration to Detonation. Prog. in Astronautics and Aeronautics. 106:3–18.
Lee, J. (2008) The Detonation Phenomenon. Cambridge University Press.
Li, J, Zhao, Z., Kazakov, A. and Dryer F. (2004) An updated comprehensive kinetic model of hydrogen combustio. Intl. J. Chem Kinet. 36:566–75.
Linan, A. and Williams, F.A. (1993) Fundamental Aspects of Combustion. Oxford University Press.
Maas, U. and Warnatz, J. (1988) Ignition processes in hydrogen-oxygen mixtures, Comb. and Flame. 74:53–69.
Marinov, N.M., Westbrook, C.K. and Pitz, W.J. (1995) Detailed and Global Chemical Kinetics Model for Hydrogen. Eighth (International) Symposium on Transport Processes. 1:118–129.
Matalon, M. and Matowsky, B. (1982) Flame as gasdynamics discontinuities. J. Fluid Mech. 124:239–259.
Molkov, V.V. (2012) Fundamentals of hydrogen safety engineering, www.bookboon.com.
National Aeronautics and Space Administration Report (1997) Safety Standard for Hydrogen and Hydrogen Systems. Report NSS 1740.16, 1997, p. A-16.

Ó Conaire, M, Curran, H.J., Simmie, J.M., Pitz, W.J. and Westbrook, C.K. (2004) A comprehensive modelling study of hydrogen oxidation, Intl. J. Chem Kinet, 36:603–622.

Oran, E.S. and Boris, J.P. (2001) Numerical Simulation of Reactive Flow. 2nd Ed. Cambridge: University Press.

Oran, E., Jones, D., and Sichel, M. (1992) Numerical simulations of detonation transmission. Proc. Roy. Soc.A. 436(1): 267–297.

Peters N. (1993) Reduced Kinetic Mechanisms for Applications in Combustion Systems. Springer.

Prudnikov, A.G.(1967) Combustion of homogeneous fuel-air mixtures in turbulent flows. In: B.V. Raushenbakh, editor, Physical Principles of the Working Process in Combustion Chambers of Jet Engines, Chapter 5, pp. 244-336. Clearing House for Federal Scientific & Technical Information, Springfield, 1967.

Shepherd, J. (2009) Detonation in gases, in Proc. of the Comb. Inst. 32(1):83-98.

Stewart, D. (1998) The shock dynamics of multi dymensional condensed and gas-phase detonations, Proc. of the Comb. Inst., 27:2189–2205.

Stewart, D. and Bdzil, J. (1988) The shock dynamics of stable multidimensional detonation, Combustion and flame, 72: 311–323.

Stewart, D. and A. Kasimov (2005) SIAM J. of Applied Math. 66:384–407.

Strehlow, R.A. (1969) Spacings in the hydrogen-oxygen system. AIAA J. 7:323–328.

Strehlow, R.A. (1970) Multi-dimensional wave structure. Prog. in Aeronautics and Astronautics. 15:345–357.

Strehlow, R.A., Maurer, R.E. and Rajan, S. (1969) Transverse waves in detonations: I.,Transverse waves in detonations: II. Structure and spacing in H2-O2, C2H2-O2, C2H4-O2 and CH4-O2 systems. AIAA J. 7:492–496.

Sun, C.J.,. Sung, C.J, He, L. and Law, C.W. (1999). Comb. and flame. 118:108.

Tieszen S.R., Sherman M.P., Benedick W.B., Shepherd J.E., Knystautas R. and Lee J.H.S. (1986) Detonation cell size measurements in hydrogen-air-steam mixtures. Progress in Astronautics Aeronautics. 106:205–219.

Voitsekhovskii B.V., Mitrofanov V.V. and Topchian M.E. (1966) The structure of a detonation front in gases. Technical report FTD-MT-64-527 (AD 633821) Wright-Patterson Air Force Base.

von Mises, R. (2004) Mathematical theory of compressible fluid flow. Dover.

von Neumann, J. (1942) Theory of detonation waves. In: Taub A.J., (ed), John von Neumann, collected works, vol. 6. New York: Macmillan.

Zabetakis, M.G. (1965) Flammability characteristics of combustible gases and vapors, BuMines Bulletin. 627:121.

Williams, D., Bauwens, L. and Oran, E. (1996) Detailed structure and propagation of three-dimensional detonations. Symposium (International) on Combustion. 26(2): 2991–2998.

Yao, J. and Stewart, D. (1995) On the normal detonation shock velocity-curvature relationship for materials with large activation energy. Comb. and flame. 100:519–528.

Yao, J. and Stewart, D. (1996) On the dynamics of multi-dimensional detonation, J. of Fluids dynmaics. 309:225–275

Zbikowski, M., Makarov, D. and Molkov, V. (2008) LES Model of Large Scale Hydrogen-Air Planar Detonations: Verification by the ZND Theory. Intl. J. of Hydrogen Energy. 33:4884–4892.

Zbikowski, M., Makarov, D.V., Molkov and V.V. (2009) LES of a large-Scale detonation experiment in the RUT facility. Presented at 22nd ICDERS. July 27-31, 2009, Minsk, Belorussia.

Zbikowski, M., Makarov, D.V. and Molkov, V.V. (2010) Numerical simulations of large-scale detonation tests in the RUT facility by the LES model. J. of Hazard. Materials, 181:949–956.

Zeldovich, Y.B. (1940). Zh Eksp Teor Fiz. 10: 542–568.